



UNIVERSIDAD NACIONAL AUTÓNOMA DE MÉXICO
POSGRADO EN CIENCIAS DE LA TIERRA
CENTRO DE GEOCIENCIAS

**EL COMPLEJO SIERRA DE JUÁREZ EN EL SUR DE MÉXICO: SU ORIGEN,
EVOLUCIÓN E IMPLICACIONES TECTÓNICAS**

THE SIERRA DE JUÁREZ COMPLEX IN SOUTHERN MEXICO: ITS ORIGIN, EVOLUTION AND TECTONIC
IMPLICATIONS

T E S I S

Que para optar por el grado de
Doctor en Ciencias de la Tierra

PRESENTA:

Guillermo Espejo Bautista

Director de Tesis

Dr. Luigi Solari, Centro de Geociencias, UNAM

Comité tutor

Dra. María Teresa Orozco Esquivel, Centro de Geociencias, UNAM

Dr. Fernando Ortega Gutiérrez, Instituto de Geología, UNAM

Juriquilla, Querétaro.

Mayo 2023



Universidad Nacional
Autónoma de México

Dirección General de Bibliotecas de la UNAM

Biblioteca Central



UNAM – Dirección General de Bibliotecas
Tesis Digitales
Restricciones de uso

DERECHOS RESERVADOS ©
PROHIBIDA SU REPRODUCCIÓN TOTAL O PARCIAL

Todo el material contenido en esta tesis esta protegido por la Ley Federal del Derecho de Autor (LFDA) de los Estados Unidos Mexicanos (México).

El uso de imágenes, fragmentos de videos, y demás material que sea objeto de protección de los derechos de autor, será exclusivamente para fines educativos e informativos y deberá citar la fuente donde la obtuvo mencionando el autor o autores. Cualquier uso distinto como el lucro, reproducción, edición o modificación, será perseguido y sancionado por el respectivo titular de los Derechos de Autor.

COMITÉ DE EXAMEN PREDOCTORAL

Dra. María Teresa Orozco Esquivel
Centro de Geociencias, UNAM

Dr. Mariano Elías Herrera
Instituto de Geología, UNAM

Dr. Juan Alonso Ramírez Fernández
Facultad de Ciencias de la Tierra, UANL

Dr. Ricardo Vega Granillo
Depto. de Geología, Universidad de Sonora

Dr. Ángel Francisco Nieto Samaniego
Centro de Geociencias, UNAM



COMITÉ DE EXAMEN DE GRADO

Dr. Luigi Solari (tutor)
Centro de Geociencias, UNAM

Dra. Susana Alaniz Álvarez
Centro de Geociencias, UNAM

Dr. Michelangelo Martini
Instituto de Geología, UNAM

Dr. Uwe Martens
Centro de Geociencias, UNAM

Dr. Peter Schaaf
Instituto de Geofísica, UNAM

2023 Guillermo Espejo-Bautista
Centro de Geociencias
Universidad Nacional Autónoma de México, Campus Juriquilla
Blvd. Juriquilla 3001, Juriquilla, Querétaro, C.P. 76230, México
gespejo@geociencias.unam.mx / guillermoespejo@hotmail.com

DECLARATORIA DE ÉTICA

DECLARO CONOCER EL CÓDIGO DE ÉTICA DE LA UNIVERSIDAD NACIONAL AUTÓNOMA DE MÉXICO, PLASMADO EN LA LEGISLACIÓN UNIVERSITARIA. CON BASE EN LAS DEFINICIONES DE INTEGRIDAD Y HONESTIDAD AHÍ ESPECIFICADAS, ASEGURO MEDIANTE MI FIRMA AL CALCE QUE EL PRESENTE TRABAJO ES ORIGINAL Y ENTERAMENTE DE MI AUTORÍA.

TODAS LAS CITAS DE, O REFERENCIAS A LA OBRA DE OTROS AUTORES APARECEN DEBIDA Y ADECUADAMENTE SEÑALADAS, ASÍ COMO ACREDITADAS MEDIANTE LOS RECURSOS EDITORIALES CONVENCIONALES.



GUILLERMO ESPEJO BAUTISTA

AGRADECIMIENTOS

Este trabajo fue posible gracias al financiamiento de los proyectos CONACYT Ciencia de Frontera 7351 y PAPIIT, UNAM, IN101520. Agradezco la beca de doctorado otorgada por el CONACYT.

Agradezco al Dr. Luigi Solari por guiarme durante mi desarrollo a lo largo de estos cuatro años de doctorado, por su confianza y la libertad que me garantizó durante la elaboración de este proyecto. Agradezco también la participación de la Dra. Teresa Orozco y al Dr. Fernando Ortega por su participación en mi comité tutor.

Un agradecimiento especial para el Dr. Carlos Ortega por su amplia disposición y amabilidad al trabajar en el área analítica de geocronología y por brindarme conocimientos específicos de manejo de software. Agradezco también a Ofelia Pérez y Rufino Lozano por su apoyo durante la adquisición de datos geoquímicos. A Teodoro Hernández Treviño, Jazmín López Díaz, Juan Tomás Vázquez Ramírez y Manuel Albarrán Murillo por su apoyo en el área técnica.

Agradezco a Roberto Maldonado por su compañía y consejos durante el trabajo de campo de este proyecto. Asimismo, agradezco a Mónica Ramírez Calderón por su apoyo en campo y consejos durante la producción del cuerpo de la tesis.

Agradezco mucho a Melissa Torres Peralta por su paciencia y comprensión durante estos cuatro años de trabajo.

Finalmente, a mi familia por su apoyo incondicional y aliento que me fortalecen cada día.

RESUMEN

El Complejo Sierra de Juárez (CSJ) en el sur de México, consiste en un fragmento de basamento cristalino polimetamórfico que contiene un amplio registro geológico desde el Mesoproterozoico tardío hasta el Cretácico Inferior. Su desarrollo ha estado ligado al origen, evolución y rompimiento de los supercontinentes Rodinia, Gondwana y Pangea; así como a la evolución del sur de México después del rompimiento de Pangea. Con base en trabajo de campo, petrografía, análisis de U-Pb en zircón por LA-ICPMS y geoquímica de roca total de elementos mayores y traza, su compleja geología se clasifica en tres grandes ciclos geotectónicos ocurridos durante el Mesoproterozoico tardío-Neoproterozoico temprano, Paleozoico y Mesozoico. (1) Durante el primer ciclo, el CSJ se originó como un sector peri-Amazónico en un ambiente de magmatismo de arco poco antes del ensamble de Rodinia entre ~1080-1050 Ma. Posteriormente, registró un evento metamórfico de bajo a alto grado, incluyendo anatexis en algunas localidades entre ~950-930 Ma. Este evento termotectónico, sumado a la falta de evidencias relacionadas con la Orogenia Zapoteca (facies de granulita hace ~990 Ma), permiten inferir una evolución tectónica del CSJ diferente con relación al microcontinente Oaxaquia, particularmente al Complejo Oaxaqueño, que representa la porción geográficamente más cercana. (2) Durante el segundo ciclo, entre los periodos Ordovícico y Devónico, el CSJ evolucionó como un terreno peri-Gondwánico, registrando sedimentación y magmatismo (~440 Ma) consistentes con un ambiente de transtensión asociado a la formación del Océano Rheico. Durante el Pérmico inferior se registró actividad magmática y sedimentaria dentro de un ambiente convergente asociado a la formación de Pangea. Al finalizar este ciclo durante la recta final del periodo Pérmico, el CSJ registró un evento metamórfico de grado medio relacionado con un ambiente convergente en la margen occidental del Océano Panthalassa (paleo-Pacífico). (3) El último ciclo se considera a partir de la etapa de ruptura de Pangea y la formación del Golfo de México, durante la cual se registró en el CSJ evidencias de anatexis, magmatismo y deformación milonítica entre ~190-175 Ma. Posteriormente y dentro de un contexto de México peninsular, ocurrió una segunda etapa anatética, magmática y milonítica en el Cretácico Inferior entre ~145-125 Ma, producto de un intrincado grupo de eventos relacionados con la evolución de la cuenca de Arperos. El CSJ es, por lo tanto, un fragmento cortical crucial en el entendimiento de la evolución geológica de México y de alto valor correlativo con los terrenos tipo Rodinia y peri-Gondwánicos del sur de México, Centroamérica y del NW de Sudamérica.

ABSTRACT

The Sierra de Juárez Complex (SJC) in southern Mexico is a polymetamorphic crystalline basement block with a broad geological record from the late Mesoproterozoic to the Early Cretaceous. Its development has been linked to the origin, evolution, and breakup of Rodinia, Gondwana, and Pangea supercontinents and the evolution of southern Mexico after the Pangea breakup. Based on fieldwork, LA-ICPMS zircon U-Pb geochronology, and whole-rock geochemistry, its complex geology is classified into three major geotectonic cycles that occurred during the late Mesoproterozoic-early Neoproterozoic, Paleozoic, and Mesozoic. (1) During the first cycle, the SJC originated as a peri-Amazonian sector within an arc-magmatism environment prior to the Rodinia assembly between ca. 1080-1050 Ma. Subsequently, it recorded a low-to-medium-grade metamorphic event and anatexis between ca. 950-930 Ma. This thermotectonic event and the lack of evidence related to the Zapotecan Orogeny (granulite facies at ca. 990 Ma) indicate a tectonic evolution unrelated to the Oaxaquia microcontinent. (2) During the second cycle, between the Ordovician and Devonian periods, the SJC evolved as a peri-Gondwanan terrane, recording sedimentation and magmatism at ca. 440 Ma, consistent with a transtensional tectonic environment associated with the opening of the Rheic Ocean. During the early Permian, the SJC recorded magmatic and sedimentary activity within a convergent environment associated with the formation of Pangea. At the end of this cycle, the SJC experienced a medium-grade metamorphic event related to a convergent environment on the western margin of the Panthalassa Ocean (paleo-Pacific) during the middle-late Permian. (3) The last cycle starts with the rupture of Pangea and the formation of the Gulf of Mexico, during which the SJC recorded evidence of anatexis, magmatism, and mylonitic deformation between ca. 190-175 Ma. Subsequently, and within the context of peninsular Mexico, a second anatectic, magmatic, and mylonitic stage occurred in the Lower Cretaceous between ca. 145-125 Ma, characterizing an intricate set of events related to the evolution of the Arperos Basin. The SJC is, therefore, a crucial crustal fragment in understanding Mexico's geological evolution, and it's a valuable correlative block with respect to the Rodinia and peri-Gondwanan terranes of southern Mexico, Central America, and NW South America.

ÍNDICE

1.	INTRODUCCIÓN	7
1.1.	Definición del Complejo Sierra de Juárez	7
1.2.	Antecedentes y problemática	7
1.3.	Objetivos	10
1.3.1.	Objetivos particulares del periodo precámbrico	10
1.3.2.	Objetivos particulares del periodo paleozoico	10
1.3.3.	Objetivos particulares del periodo mesozoico	10
1.4.	Metodología analítica	11
1.4.1.	Geocronología	11
1.4.2.	Geoquímica de roca total	12
1.5.	Estructura de la tesis	13
1.6.	Referencias	14
2.	EL COMPLEJO SIERRA DE JUÁREZ: UN NUEVO TERRENO METAMÓRFICO GONDWÁNICO DEL NEOPROTEROZOICO AL PALEOZOICO TEMPRANO EN EL SUR DE MÉXICO	17
3.	EVOLUCIÓN GEOLÓGICA DEL SILÚRICO AL CRETÁCICO DEL SUR DE MÉXICO Y SU CONEXIÓN CON EL ENSAMBLE Y RUPTURA DE LA PANGEA ECUATORIAL OCCIDENTAL: ENFOQUE GEOCRONOLÓGICO EN EL NORTE DEL COMPLEJO SIERRA DE JUÁREZ.	41
4.	MAGMATISMO DE ARCO ESTÉNICO Y METAMORFISMO DE MEDIO A ALTO GRADO TÓNICO A LO LARGO DEL BORDE NORTE DE AMAZONIA DURANTE EL ENSAMBLE DE RODINIA: LA SUITE POCHOTEPEC EN EL SUR DE MÉXICO.	70
5.	DISCUSIÓN Y CONCLUSIONES	87
5.1.	Periodo precámbrico	87
5.1.1.	Magmatismo del Esténico tardío y la suite Pochotepec	87
5.1.2.	Metamorfismo y anatexis del Tónico inferior entre ~950-930 Ma	88
5.2.	Periodo paleozoico	89
5.2.1.	Magmatismo y sedimentación del Ordovícico al Silúrico	89
5.2.2.	Magmatismo y sedimentación del Pérmico temprano	90
5.2.3.	Metamorfismo del Pérmico tardío-Triásico Inferior	90
5.3.	Periodo mesozoico	92
5.3.1.	Milonitización, anatexis y magmatismo del Jurásico Inferior	92
5.3.2.	Migmatización y magmatismo del Cretácico Temprano	92
5.4.	Referencias	95
6.	Anexos	97

1.1. Definición del Complejo Sierra de Juárez

El Complejo Sierra de Juárez (CSJ), antes Complejo Milonítico Sierra de Juárez (Alaniz-Álvarez et al., 1996), es un cinturón metamórfico Precámbrico-Mesozoico orientado ~NNW-SSE (Fig. 1) que forma parte del mosaico de bloques de basamento del sur de México. La extensión del CSJ alcanza aproximadamente 125 km de longitud, abarcando desde el norte de la Ciudad de Oaxaca (San Felipe del Agua) hasta el norte de la ciudad de Teotitlán de Flores Magón, y 15 km de anchura en algunos sectores. Geográficamente, el sector sur del CSJ incluye a la Sierra de Juárez, mientras que el sector norte está constituido por una parte de la Sierra Mazateca (ambas constituyentes de la Sierra Madre del Sur en el estado de Oaxaca). En este trabajo se considera al CSJ como el sector de basamento occidental del Terreno Cuicateco (según la definición de Sedlock et al., 1993), diferenciándose del sector de basamento oriental conocido como el Complejo Mazateco (Fig. 1). Dentro del CSJ se incluyen las unidades estratigráficas del sector norte como la Suite Migmatita Teotitlán, el Esquisto La Nopalera y el Grupo Pochotepec, todas ellas descritas por Ángeles-Moreno et al. (2012). La morfología elongada que caracteriza al CSJ es el resultado de múltiples eventos tectono-estructurales sobreimpuestos. Estadísticamente, el CSJ está dominado por planos de foliación esquistosos, gnéisicos y miloníticos orientados ~NNW-SSE y ~N-S, originados y reactivados en diversas etapas de su evolución geológica, definiendo una orientación estructural general. Adicionalmente, el CSJ estuvo sujeto a un evento de acortamiento ~E-W durante el Cretácico Superior-Eoceno (Graham et al., 2021), originando estructuras de cabalgamiento orientadas ~N-S de las que se destaca la Falla Siempre Viva, que constituye su límite oriental en contacto con unidades del Cretácico Inferior del Terreno Cuicateco. Finalmente, eventos de extensión ~E-W post-eocénicos causaron la reactivación de planos y la formación de la Falla Oaxaca (Fig. 1), orientada ~N-S, de naturaleza normal con una pendiente hacia el oeste, la cual define el límite oriental del CSJ y el límite de los terrenos Cuicateco y Zapoteco (Centeno-García, 1988; Sedlock et al., 1993; Alaniz-Álvarez et al., 1994; Nieto-Samaniego et al., 1995; Campos-Enríquez et al., 2010).

1.2. Antecedentes y problemática

Uno de los objetivos fundamentales de la geología es el reconocimiento y clasificación de los elementos litológicos de un área determinada y su disposición estructural. Definir su naturaleza, origen, evolución e implicaciones tectónicas es crítico en las reconstrucciones paleogeográficas y en el entendimiento de la evolución tectónica de la Tierra, pero también es fundamental en la exploración de recursos naturales. Las primeras descripciones formales del CSJ están contenidas en los trabajos pioneros de los terrenos tectonoestratigráficos de México y sus límites tectónicos (Campa y Coney, 1983; Ortega-Gutiérrez et al., 1990; Sedlock et al., 1993), donde se le consideró como una amplia zona limítrofe entre dos terrenos (Zapoteco y Cuicateco, según la nomenclatura de Sedlock et al., 1993) y en manuscritos que documentan la presencia de cuerpos ultramáficos de importancia económica (p. ej., Delgado-Argote et al., 1992, y referencias contenidas). El CSJ posee

dos atributos que le confieren una distinción especial. (1) Más del ~80 % de su contenido litológico lo integran rocas metamórficas de bajo a medio grado de composición intermedia-básica-ultrabásica; mientras que el 20 % restante está integrado por esquistos pelíticos, mármoles, granitoides, meta-granitoides y anortositas; y (2) las numerosas estructuras miloníticas y cataclásticas que corren ~N-S a lo largo del CSJ. Estas estructuras posiblemente se originaron progresivamente como consecuencia de diferentes eventos tectónicos de carácter compresivo, transformante y extensional posiblemente durante el pre-Mesozoico, Mesozoico y Cenozoico, respectivamente (Centeno-García, 1988; Alaniz-Álvarez et al., 1994; 1996). De estos eventos, el más relevante se produjo durante el periodo jurásico, posiblemente como consecuencia de desplazamientos tectónicos provocados por el rompimiento de Pangea y la apertura del Golfo de México (Alaniz-Álvarez et al., 1996). Este atributo estructural le confirió el término de *Complejo Milonítico Sierra de Juárez* y fue considerado como un laboratorio natural atractivo para el análisis de procesos de reactivación de planos de falla (Nieto-Samaniego et al., 1995). Ambos atributos (petrológico y estructural) permiten considerar al CSJ como un cinturón esencialmente máfico y multi-deformado, con eventos miloníticos ocurridos en diversos niveles corticales, representando un laboratorio natural para el análisis de la deformación de rocas y minerales máficos bajo diferentes condiciones termodinámicas.

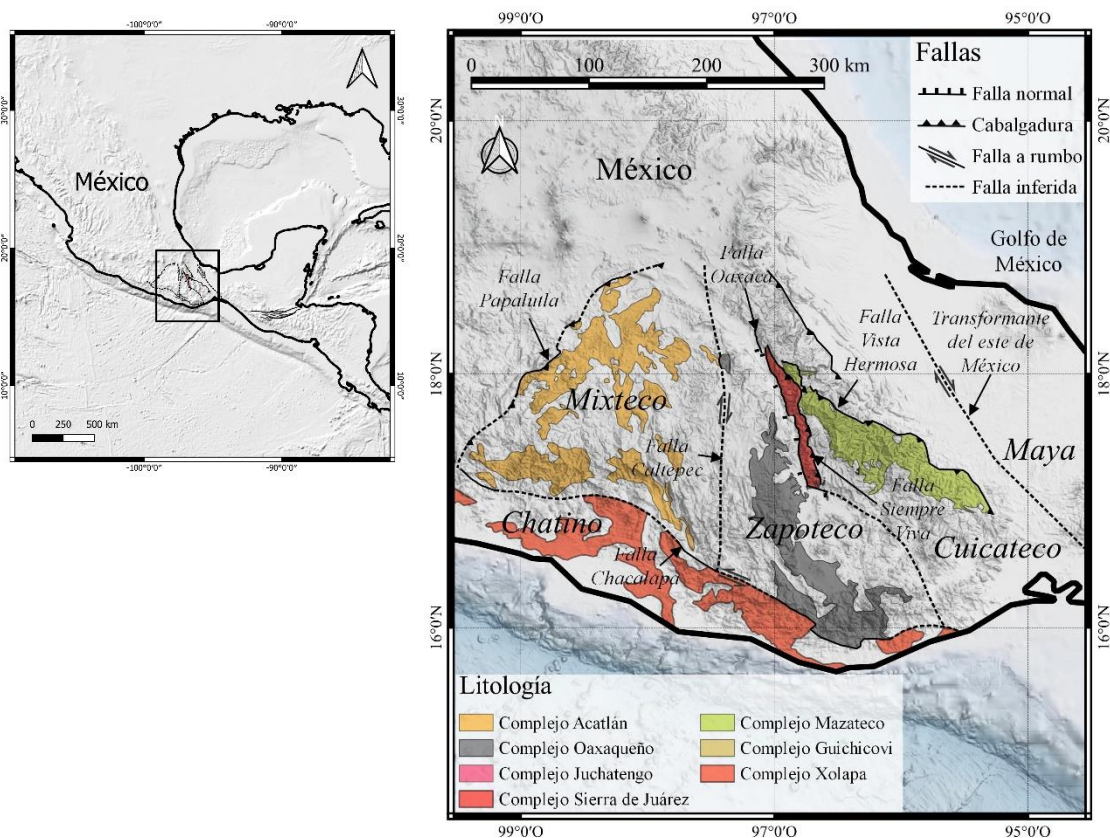


Fig. 1. Mapa geológico del sur de México que muestra los bloques de basamento cristalino, incluyendo al Complejo Sierra de Juárez y las estructuras principales de contacto entre los terrenos tectonoestratigráficos. La nomenclatura de terrenos sigue a Sedlock et al. (1993).

El CSJ ha demostrado poseer múltiples edades de protolitos pre-miloníticos que requieren un análisis muy extenso y cuidadoso, pero que también pueden derivar implicaciones tectónicas significativamente valiosas en términos regionales. Con base en observaciones litológicas y relaciones espaciales regionales (p. ej., [Alaniz-Álvarez et al., 1994](#)), parte de los protolitos pre-miloníticos del CSJ fueron considerados como provenientes del Complejo Oaxaqueño (basamento tipo Grenville), y por lo tanto asumidos de edad meso y neoproterozoica. Esta edad fue confirmada posteriormente mediante edades U-Pb en zircón en un granitoide, anortositas y esquistos de grado bajo a medio en el CSJ ([Coombs, 2016](#); [Espejo-Bautista, 2018](#); [Pindell et al., 2021](#)). Sin embargo, no hay evidencias petrológicas de que estas rocas hayan alcanzado un grado metamórfico alto en facies de granulita, característico del Complejo Oaxaqueño y otros bloques de basamento tipo Grenville, por lo que surge la pregunta: ¿realmente se observa un basamento Precámbrico tipo Grenville en el CSJ? Por otra parte, se han documentado rocas metamórficas con edades máximas de depósito y de protolito magmático que oscilan entre 578-247 Ma en diversos sectores del CSJ, indicando un posible origen en diversas etapas del Paleozoico ([Coombs, 2016](#); [Espejo-Bautista, 2018](#); [Pindell et al., 2021](#)). Las rocas paleozoicas metamórficas en el CSJ relacionadas espacialmente a un basamento precámbrico se distinguen notablemente de las secuencias que sobreyacen discordantemente al el Complejo Oaxaqueño, considerando que éstas últimas aún conservan su naturaleza sedimentaria (formaciones Tiñú, Santiago, Ixtaltepec, etc.; p. ej., [Landing et al., 2007](#)). Esto denota una considerable diferencia entre la evolución tectónica pre-mesozoica del CSJ y el Complejo Oaxaqueño. Además, ¿cuál es el alcance, origen tectónico y correlación de las secuencias Paleozoicas del CSJ? ¿Cuál es la edad y el significado tectónico de su metamorfismo? Por último, en el sector norte del CSJ se documentaron edades $^{40}\text{Ar}/^{39}\text{Ar}$ en hornblenda de ~130 Ma asociadas a cuerpos ultramáficos ([Delgado-Argote et al., 1992](#)) y edades de U-Pb en zircón de ~141 Ma obtenidas en bandas de rocas ígneas de composición intermedias-ácidas, interpretadas como neosomas de un paquete de migmatitas denominado Complejo Migmatítico Teotitlán (CMT, [Ángeles-Moreno, 2006](#); [Ángeles-Moreno et al., 2012](#)). [Ángeles-Moreno \(2006\)](#) también identificó la presencia de esquistos de granate con edades $^{40}\text{Ar}/^{39}\text{Ar}$ en moscovita de ~132 Ma, interpretada como una edad de enfriamiento del evento migmatítico, y anfibolitas que forman parte de los paleosomas del CMT. Estos hallazgos fueron confirmados por trabajos posteriores ([Coombs, 2006](#); [Pindell et al., 2021](#)). Sin embargo, el origen y la naturaleza del paleosoma del CMT permanecen desconocidos, así como los eventos metamórficos pre-migmatíticos que evidencian sus características litológicas.

El CSJ parece tener un registro geológico extenso e intrigante, con múltiples etapas sedimentarias, ígneas, metamórficas y anatéticas que aún permanecen desordenadas e inéditas ([Ortega-Gutiérrez et al., 2018](#)). Descifrar el origen y evolución del CSJ puede conducir a importantes implicaciones sobre el desarrollo geodinámico relacionado con los supercontinentes Rodinia, Gondwana y Pangea. A pesar de ello, la mayor atención sobre el CSJ se ha centrado hasta ahora principalmente en su carácter milonítico y el rol que ha tenido en la tectónica de México peninsular a partir de la Era Mesozoica (p. ej., [Villagómez et al., 2014](#); [Graham et al., 2021](#)).

1.3. Objetivos

En este proyecto de tesis se plantea resolver la problemática abordada anteriormente mediante un enfoque multidisciplinario apoyado en trabajo de campo, geocronología de U-Pb en zircón y geoquímica de roca total de elementos mayores y traza. De manera general se busca revelar el origen y la evolución tectónica pre-milonítica del CSJ desde el Precámbrico hasta el Mesozoico y el ordenamiento cronológico de los eventos geológicos y unidades litológicas que lo constituyen.

De acuerdo con los antecedentes y la problemática planteada anteriormente, se pueden identificar tres periodos geológicos extensos que se abordan de manera específica: (1) Periodo Precámbrico, (2) Periodo Paleozoico y (3) Periodo Mesozoico.

1.3.1. Objetivos particulares del periodo precámbrico

- 1.- Determinar rigurosamente la edad de las unidades precámbricas que constituyen al CSJ y estimar su alcance de exposición en el campo.
- 2.- Identificar la naturaleza litológica de las unidades precámbricas y su origen tectónico mediante observaciones petrográficas y análisis de geoquímica de roca total.
- 3.- Establecer la relación de las unidades precámbricas del CSJ con el Complejo Oaxaqueño y otros bloques de basamento Precámbrico de México, Centroamérica y el NW de Sudamérica.
- 4.- Indagar sobre el origen metamórfico de bajo a medio grado observado en las unidades precámbricas del CSJ.

1.3.2. Objetivos particulares del periodo paleozoico

- 1.- Determinar la naturaleza y alcance de las unidades paleozoicas expuestas en el CSJ.
- 2.- Determinar mediante geocronología de U-Pb en zircón las edades máximas de depósito y grupos de procedencia en rocas paleozoicas meta-sedimentarias del CSJ.
- 3.- Proponer un posible ambiente tectónico de origen para las rocas metasedimentarias y analizar su correlación con otras unidades paleozoicas del sur y sureste de México, Centroamérica y el NW de Sudamérica.
- 4.- Indagar sobre la naturaleza, edad y origen tectónico del metamorfismo observado en la secuencia de rocas paleozoicas del CSJ.

1.3.3. Objetivos particulares del periodo mesozoico

- 1.- Analizar mediante petrografía y geocronología de U-Pb en zircón la naturaleza y edad de los paleosomas que constituyen el Complejo Migmatítico Teotitlán en el norte del CSJ.
- 2.- Determinar la relación de los paleosomas de la Migmatita Teotitlán con otras unidades expuestas en el CSJ.

1.4. Metodología analítica

1.4.1. Geocronología

La separación de zircones se llevó a cabo principalmente en el Centro de Geociencias, UNAM campus Juriquilla, aunque algunas muestras se separaron también en los institutos de Geofísica y Geología de la UNAM (Ciudad Universitaria). De las muestras de composición básica empleadas en este estudio se trituraron aproximadamente entre 5 y 15 kg de roca utilizando una prensa hidráulica de 5 toneladas. En el caso de muestras de composición ácida y rocas de origen sedimentario se utilizaron menos de 5 kg de roca. El material obtenido fue cribado por una malla de 500 μm y posteriormente decantado. El material resultante se filtró mediante métodos húmedos [método de bateo según [Hernández-Treviño y López-Portillo \(2015\)](#)] y separación magnética para obtener concentrados de minerales pesados. Los zircones se reconocieron y separaron mediante técnicas manuales con ayuda de un microscopio binocular. Los granos de zircón fueron posteriormente montados en resina epóxica (Struers Epofix) y desbastados utilizando papel lija (# 800, 1500 y 3000) con el fin de exponer la parte ecuatorial del zircón. Las imágenes de catodoluminiscencia se obtuvieron principalmente por medio de un luminoscopio ELM-3R en el Centro de Geociencias, mientras que algunas otras se obtuvieron a través de un microscopio electrónico de barrido Jeol IT300 acoplado a un sistema de catodoluminiscencia Gatan Chroma CL2 en el Laboratorio de Microscopía Electrónica de la Universidad de Taxco (Guerrero, México).

Todos los análisis de U-Pb fueron realizados en el Laboratorio de Estudios Isotópicos (LEI) del Centro de Geociencias, UNAM, mediante el método de ablación láser (LA-ICPMS). El LEI cuenta con un sistema de ablación láser modelo Resolution M50 de la marca “Resonetics” compuesto por un láser Compex Pro tipo excímero de 193 nm de longitud de onda, que utiliza una mezcla de fluoruro de argón (ArF) para generar la pulsación. Este se encuentra acoplado a un espectrómetro de masas (ICP-MS) cuadrupolo “Thermo ICap Qc”. La metodología empleada para los análisis isotópicos U(Th)-Pb en zircones ([Solarí et al., 2010; 2015; 2018](#)) comienza con la limpieza de la probeta con zircones montados con HNO₃ IM con la finalidad de eliminar o minimizar cualquier posible contaminación por la presencia de Pb común en la superficie de los granos. Los cristales de zircón se ablacionan dentro de una celda en una atmósfera de He. El haz del láser incide sobre la superficie del cristal en el punto previamente seleccionado, con una densidad de energía de $\sim 6 \text{ J/cm}^2$ y a una tasa de repetición de 5 Hz creando un cráter provocado por la volatilización de un área del zircón (spot o punto de análisis) de 23 μm de diámetro y de $\sim 8 \mu\text{m}$ de profundidad para obtener un total de $\sim 30\text{-}35 \text{ ng}$ de masa ablacionada durante cada análisis. La ablación se lleva a cabo por 30 segundos con el fin de minimizar la profundidad del hoyo de ablación y, de la misma manera, el fraccionamiento elemental. Posteriormente, el material ablacionado (vaporizado) es evacuado de la celda de ablación y transportado al espectrómetro de masas en un flujo de He (350 ml/min) que se mezcla con N (ca. 3 ml/min) y con Ar (ca. 0.9 l/min) para después ser analizado. En las secuencias analíticas se intercalan dos análisis de un estándar de vidrio (NIST 610), cinco análisis de un estándar natural de zircón primario (91500, [Wiedenbeck et al., 1995](#)), tres de uno secundario (Plešovice, [Sláma et al., 2008](#)) que sirve como control de calidad y finalmente diez zircones de edad desconocida. Posteriormente, se hace una medición doble de todos los estándares cada diez mediciones en zircones desconocidos. El experimento finaliza con dos zircones estándar y un vidrio NIST. Los análisis del vidrio NIST son utilizados para calcular las concentraciones correctas de U y Th, además

de las otras concentraciones de elementos traza y tierras raras medidas durante cada análisis, mientras que los análisis del estándar de zircón 91500 son usados para recalculas las relaciones isotópicas. La calibración de los datos y correcciones por deriva instrumental (“drift”) se basan en los estándares de zircón 91500 que tiene una edad conocida de 1063 ± 0.5 Ma ([Wiedenbeck et al., 1995](#)).

Los datos isotópicos se adquieren utilizando el software analítico Thermo QTegra con resolución temporal, permitiendo que las relaciones isotópicas sean calculadas de los datos adquiridos en un intervalo de tiempo específico.

Durante el análisis de cada zircón los isótopos de interés principal para el fechamiento U-Pb como ^{206}Pb , ^{207}Pb , ^{208}Pb , ^{232}Th y ^{238}U se determinan, además de otros isótopos importantes como ^{29}Si , ^{31}P , ^{49}Ti , ^{89}Y , ^{96}Zr , REE's y ^{179}Hf . Por ejemplo, el silicio y el zirconio son usados como elementos estándar internos para la cuantificación del contenido de elementos traza, considerando su concentración estequiométrica en el zircón, mientras que elementos como el P, Ti e Y, además de las tierras raras, son monitoreados como indicadores de la presencia de inclusiones dentro de los zircones (p.ej., monacita, apatito o titanita), las cuales podrían modificar las relaciones U(Th)-Pb del zircón y proporcionar edades equívocas y mediciones erróneas como en el caso de la presencia de Pb común. Los mismos elementos se pueden utilizar para obtener indicaciones petrogenéticas sobre las condiciones de cristalización del zircón.

Para llevar a cabo la reducción de datos, el cálculo de edades y concentraciones elementales de los zircones analizados, se utilizó el software Lolite, v. 4.0, cuya licencia me fue otorgada amablemente por los desarrolladores por un periodo de prueba de un año, gracias a un programa de apoyo a estudiantes. La reducción de datos consistente en una serie de instrucciones que incluyen el cálculo de edades y error, así como su propagación ([Patón et al., 2010; 2011](#); [Petrus and Kamber, 2012](#)). En el caso de que una corrección de Pb sea requerida, y dada la precisión limitada de la medición del ^{204}Pb por medio de un cuadrupolo, aunada a la interferencia con ^{204}Hg , para zircones cuya edad es < 250 Ma se puede emplear la macro algebraica de [Andersen \(2002\)](#), así como implementada por [Petrus y Kamber \(2012\)](#).

Los archivos exportados de Lolite se procesan en una macro de Excel desarrollada en el LEI, la cual permite al operador ordenar automáticamente los datos y generar una tabla de datos lista para publicarse con las relaciones isotópicas y edades; la concentración de elementos traza y mayores medidas en los zircones analizados también se despliegan, para desde estos poder producir un diagrama de REE normalizado a condrita con los datos obtenidos. Los diagramas de concordia y las medias ponderadas se grafican usando el programa computacional IsoplotR ([Vermeesch, 2018](#)).

1.4.2. Geoquímica de roca total

Para este trabajo se seleccionaron 11 muestras de distinta composición química con el fin de obtener su contenido de elementos mayores y traza. Las muestras se trituraron mediante una prensa hidráulica de 5 toneladas y posteriormente se pulverizaron empleando un molino oscilatorio en el Centro de Geociencias y en el Instituto de Geofísica, UNAM. Para obtener la concentración de elementos mayores, las muestras fueron analizadas mediante Fluorescencia de rayos X. Las muestras fundidas se analizaron utilizando un espectrómetro secuencial Rigaku ZSX Primus II en el Laboratorio de Fluorescencia de Rayos X del Laboratorio Nacional de Geoquímica y Mineralogía del Instituto de Geología, UNAM. Los errores estimados en las determinaciones de este laboratorio

son menores al 1 % en elementos mayores. Los valores del estándar utilizado para la verificación correcta del equipo (IGLA-1), la metodología y procedimientos de calidad se pueden consultar en [Lozano-Santa Cruz y Bernal \(2005\)](#). La obtención de elementos traza fue realizada en el Laboratorio Ultralimpio e ICP-MS del Laboratorio de Estudios Isotópicos (LEI) del Centro de Geociencias, UNAM. La reproducibilidad de los elementos traza obtenidos en este laboratorio se basa en la medición de los estándares del Servicio Geológico de Estado Unidos (AGV-2, BCR-2 y BHVO-2) y del Servicio Geológico de Japón (JB-2, JR-1). La metodología y procedimientos empleados en este laboratorio pueden consultarse en [Mori et al. \(2009\)](#).

1.5. Estructura de la tesis

El cuerpo principal de esta tesis está constituido por tres artículos publicados en revistas arbitradas. Cada artículo representa un capítulo que resuelve parte de los objetivos y problemática planteados anteriormente.

Capítulo 2. En este capítulo se establece por primera vez la redefinición del Complejo Sierra de Juárez, eliminando el adjetivo “milonítico” con el objetivo de ampliar el significado tectónico del CSJ. Con base en trabajo de campo, petrografía, geocronología U-Pb en zircón y geoquímica de roca total se documenta por primera vez la estratigrafía completa del sector sur del CSJ. Se confirman y reinterpretan las edades de anortositas del CSJ y se investiga una nueva unidad metasedimentaria y metaígneas del Paleozoico inferior denominada Unidad Etlá y se discuten sus implicaciones tectónicas. Finalmente, se describen las características estructurales de meta-granitoides aparentemente sintectónicos con el evento milonítico dominante en el área de estudio y se obtuvo su edad.

Capítulo 3. En esta sección se documenta la estratigrafía de eventos tectónicos y unidades litológicas en el sector norte del CSJ por medio de trabajo de campo, petrografía y geocronología U-Pb en zircón. Los resultados permiten determinar la extensión de la Unidad Etlá a lo largo del CSJ, se reconocieron otros eventos magmáticos, sedimentarios y metamórficos del Paleozoico tardío inéditos en el CSJ y se investigó la procedencia y naturaleza de los paleosomas de la Suite Migmatita Teotitlán. Finalmente, se corroboró la presencia del evento milonítico del Jurásico inferior y se reconocieron nuevos cuerpos intrusivos del Cretácico Inferior y un evento milonítico dúctil adicional. Se estableció una correlación detallada con otros eventos tectónicos en el sur de México, Centroamérica y el NW de Sudamérica y se discuten todos los nuevos hallazgos en función de la evolución geológica del sur de México.

Capítulo 4. En este capítulo se redefine al grupo Pochotepec como suite Pochotepec y se investiga su edad, naturaleza y extensión dentro del CSJ con base en trabajo de campo, petrografía, geocronología y geoquímica de roca total. La importancia de esta unidad es que permite proponer un nuevo tipo de basamento precámbrico “no granulítico”, que difiere principalmente en su evolución tectónica con respecto al Complejo Oaxaqueño y otros bloques asociados al microcontinente Oaxaquia y al Orógeno Putumayo en el sur y este de México y el NW de Sudamérica, respectivamente.

1.6. Referencias

- Alaniz-Álvarez, S.A., Nieto-Samaniego, A.F., Ortega-Gutiérrez, F., 1994. Structural evolution of the Sierra Juárez Mylonitic Complex, state of Oaxaca, Mexico. *Revista Mexicana de Ciencias geológicas*, 11(2), 147–156.
- Alaniz-Álvarez, S.A., van der Heyden, P., Nieto-Samaniego, A.F., Ortega-Gutiérrez, F., 1996. Radiometric and kinematic evidence for Middle Jurassic strike-slip faulting in Southern Mexico related to the opening of the Gulf of Mexico. *Geology* 24(5), 443–446, [https://doi.org/10.1130/0091-7613\(1996\)024<0443:RAKEFM>2.3.CO;2](https://doi.org/10.1130/0091-7613(1996)024<0443:RAKEFM>2.3.CO;2).
- Andersen, T., 2002. Correction of common lead in U–Pb analyses that do not report ²⁰⁴Pb. *Chemical Geology*, 192, p. 59–79, [https://doi.org/10.1016/S0009-2541\(02\)00195-X](https://doi.org/10.1016/S0009-2541(02)00195-X).
- Ángeles-Moreno, E., 2006. Petrografía, geología estructural y geocronología del borde noroccidental del Terreno Cuicateco, Sierra Mazateca, Estado de Oaxaca, México. Universidad Nacional Autónoma de México, tesis de maestría.
- Ángeles-Moreno, E., Elías-Herrera, M., Macías-Romo, C., Sánchez-Zavala, J.L., Ortega-Gutiérrez, F., 2012. Geological Map of the Western Border of the Cuicateco Terrane, Southern Mexico. Geological Society of America, Map and Chart series MCH102, doi: 10.1130/2012.MCH102.
- Campa, M.F. y Coney, P.J., 1983. Tectono-stratigraphic terranes and mineral resource distributions in Mexico. *Can. J. Earth Sci.* 20, 1040-1051, doi: 10.1139/e83-094.
- Campos-Enríquez, J.O., Belmonte-Jiménez, S.I., Keppie, J.D., Ortega-Gutiérrez, F., Arzate, J.A., Martínez-Silva, J., Martínez-Serrano, R.G., 2010. Gravity and magnetic survey of the Oaxaca city region: Cenozoic horst-and-graben structure superimposed on the Oaxaca–Juarez terrane boundary, southern Mexico. *Journal of South American Earth Sciences*, 29, 572-585, doi: 10.1016/j.jsames.2009.11.002.
- Centeno-García, E., 1988. Evolución estructural de la Falla de Oaxaca durante el Cenozoico. Universidad Nacional Autónoma de México, tesis de maestría.
- Coombs, H. 2016. Geochemical and geochronological constraints on terrane definition in Mexico. Cardiff University, tesis de doctorado.
- Delgado-Argote, L.A., López-Martínez, M., York, D., Hall, C.M., 1992. Geologic framework and geochronology of ultramafic complexes of southern Mexico. *Canadian Journal of Earth Sciences*, 29, 1590-1604, doi: 10.1139/e92-125.
- Espejo-Bautista, G., 2018. Caracterización estructural, petrológica y tectónica del Complejo Milonítico Sierra de Juárez. Universidad Nacional Autónoma de México. Tesis de maestría.
- Graham, R., Pindell, J., Villagómez, D., Molina-Garza, R., Granath, J. and Sierra-Rojas, M. 2021. Integrated Cretaceous–Cenozoic plate tectonics and structural Geology in southern Mexico. Geological Society, London, Special Publications, 504, 285–314, doi: 10.1144/SP504-2020-70.
- Hernández-Treviño, J.T., y López-Portillo, P.M., 2015. Método rápido de separación de minerales pesados, para obtener edades de rocas por el método U-Pb. Reunión anual de la Unión Geofísica Mexicana, libro de resúmenes, 35(1), 93.
- Landing, E., Westrop S.R., Keppie, J.D., 2007. Terminal Cambrian and lowest Ordovician succession of Mexican west Gondwana: biotas and sequence stratigraphy of the Tiñú Formation. *Geological Magazine*, 144(6), 909–936, doi: 10.1017/S0016756807003585.

- Lozano-Santa Cruz, R., & Bernal, J.P., 2005. Characterization of a new set of eight geochemical reference materials for XRF major and trace element analysis. *Revista Mexicana de Ciencias Geológicas*, 22, 329–344.
- Mori, L., Gómez-Tuena, A., Cai, Y., Goldstein, S.L., 2007. Effects of prolonged flat subduction on the Miocene magmatic record of the central trans-Mexican volcanic belt. *Chemical Geology*, 244, 452–473, <https://doi.org/10.1016/j.chemgeo.2007.07.002>.
- Nieto-Samaniego, A.F., Alaniz-Álvarez, S.A., Ortega-Gutiérrez, F., 1995. Estructura interna de la Falla de Oaxaca (México) e influencia de las anisotropías litológicas durante su actividad cenozoica. *Revista Mexicana de Ciencias Geológicas*, 12(1), 1–8.
- Ortega-Gutiérrez F., Mitre-Salazar, L.M., Roldán-Quintana, J., Sánchez-Rubio, G., de la Fuente, M., 1990. North American Continent-Ocean transect program, transect H-3–Acapulco trench to the Gulf of Mexico across Southern Mexico. Geological Society of America, Decade of North American Geology Program, scale 1:500,000, <https://doi.org/10.1130/DNAG-COT-H-3>.
- Ortega-Gutiérrez, F., Elías-Herrera, M., Morán-Zenteno, D.J., Solari, L., Weber, B. and Luna-González, L. 2018. The pre-Mesozoic metamorphic basement of Mexico, 1.5 billion years of crustal evolution. *Earth-Science Reviews*, 183, 2–37, doi: 10.1016/j.earscirev.2018.03.006
- Paton, C., Hellstrom, J., Paul, B., Woodhead, J., Hergt, J., 2011. Lolite: Freeware for the visualization and processing of mass spectrometric data. *Journal of Analytical Atomic Spectrometry*, 26, 2508, doi: 10.1039/c1ja10172b.
- Paton, C., Woodhead, J.D., Hellstrom, J.C., Hergt, J.M., Greig, A., Maas, R., 2010. Improved laser ablation U-Pb zircon geochronology through robust downhole fractionation correction. *Geochemistry Geophysics Geosystems*, 11, Q0AA06, doi: 10.1029/2009GC002618.
- Petrus, J.A., and Kamber, B.S., 2012. VizualAge: A Novel Approach to Laser Ablation ICP-MS U-Pb Geochronology Data Reduction. *Geostandards and Geoanalytical Research*, 36, 247–270, doi: 10.1111/j.1751-908X.2012.00158.x.
- Pindell, P., Villagómez, D., Molina-Garza, R., Graham, R. and Weber, B. 2021. A revised synthesis of the rift and drift history of the Gulf of Mexico and surrounding regions in the light of improved age dating of the Middle Jurassic salt. Geological Society, London, Special Publications, 504, 29–76, doi: 10.1144/SP504-2020-43.
- Sedlock, R.L., Ortega-Gutiérrez, F., Speed, R.C., 1993. Tectonostratigraphic terranes and tectonic evolution of Mexico. Geological Society of America, Special Paper, 278, 153, doi: 10.1130/SPE278.
- Sláma, J., Kosler, J., Condon, D., Crowley, J., Gerdes, A., Hanchar, J., Horstwood, M., Morris, G., Nasdala, L., Norberg, N., Schaltegger, U., Schoene, B., Tubrett, M., Whitehouse, M.J., 2008. Plešovice zircon — A new natural reference material for U–Pb and Hf isotopic microanalysis: *Chemical Geology*, 249, 1–35, doi: 10.1016/j.chemgeo.2007.11.005.
- Solari, L. A., González-León, C. M., Ortega-Obregón, C., Valencia-Moreno, M., Rascón-Heimpel, M. A., 2018. The Proterozoic of NW Mexico revisited: U–Pb geochronology and Hf isotopes of Sonoran rocks and their tectonic implications. *International Journal of Earth Sciences*, 107, 845–861, <https://doi.org/10.1007/s00531-017-1517-2>.
- Solari, L. A., Ortega-Obregón, C., Bernal, J. P., 2015. U–Pb zircon geochronology by LAICPMS combined with thermal annealing: Achievements in precision and accuracy on dating standard and unknown samples. *Chemical Geology*, 414, 109–123, <https://doi.org/10.1016/j.chemgeo.2015.09.008>.

- Solari, L., Gómez-Tuena, A., Bernal, J., Pérez-Arvizu, O., Tanner, M., 2010. U-Pb Zircon Geochronology with an Integrated LA-ICP-MS Microanalytical Workstation: Achievements in Precision and Accuracy. *Geostandards and Geoanalytical Research*, 34, 5–18, <https://doi.org/10.1111/j.1751-908X.2009.00027.x>.
- Vermeesch, P., 2018. IsoplotR: a free and open toolbox for geochronology. *Geoscience Frontiers*, 9(5), 1479-1493, doi:10.1016/j.gsf.2018.04.001.
- Villagómez, D. 2014. The Northern Cuicateco Terrane from a Thermochronological Perspective and its Implications on the Pre-, Syn- and Post-Laramide Deformation. Cordillera Program Phase I Technical Report. Tectonic Analysis Ltd, Worthing, West Sussex, UK, doi: 10.13140/RG.2.2.22814.43840.
- Wiedenbeck, M., Allé, P., Corfu, F., Griffin, W., Meier, M., Oberli, F., Quadt, von, A., Roddick, J., Spiegel, W., 1995. Three natural zircon standards for U-Th-Pb, Lu-Hf, Trace element and REE Analyses. *Geostandard Newsletter*, 19, 1–23, <https://doi.org/10.1111/j.1751-908X.1995.tb00147.x>.



2. *EL COMPLEJO SIERRA DE JUÁREZ: UN NUEVO TERRENO METAMÓRFICO GONDWÁNICO DEL NEOPROTEROZOICO AL PALEOZOICO TEMPRANO EN EL SUR DE MÉXICO.*

Guillermo Espejo-Bautista, Fernando Ortega-Gutiérrez, Luigi A. Solari, Roberto Maldonado & Yuly T. Valencia-Morales (2022) The Sierra de Juárez Complex: a new Gondwanan Neoproterozoic-early Palaeozoic metamorphic terrane in southern Mexico, *International Geology Review*, 64:5, 631-653, <https://doi.org/10.1080/00206814.2020.1870172>.

CONTRIBUCIÓN DE AUTORES

Guillermo Espejo-Bautista: Conceptualización, organización e integración de datos, análisis formal, investigación (trabajo de campo), metodología (procesamiento de muestras, separación de zircones, obtención de datos analíticos), propuesta de modelo tectónico, visualización, escritura original del manuscrito, revisión y edición.

Fernando Ortega-Gutiérrez: Adquisición de fondos, supervisión, escritura y revisión del manuscrito.

Luigi A. Solari: Organización e integración de datos, análisis formal, adquisición de fondos, recursos, metodología, supervisión, escritura y revisión del manuscrito.





Roberto Maldonado: Análisis formal, investigación (trabajo de campo), escritura y revisión del manuscrito.

Yuly T. Valencia-Morales: Análisis formal, investigación (trabajo de campo), escritura y revisión del manuscrito.

ARTICLE



The Sierra de Juárez Complex: a new Gondwanan Neoproterozoic-early Palaeozoic metamorphic terrane in southern Mexico

Guillermo Espejo-Bautista ^a, Fernando Ortega-Gutiérrez ^b, Luigi A. Solari ^d, Roberto Maldonado ^d and Yuly T. Valencia-Morales^c

^aPosgrado en Ciencias de la Tierra, Centro De Geociencias, Universidad Nacional Autónoma De México, Campus Juriquilla, Santiago de Querétaro, Querétaro, México; ^bInstituto De Geología, Universidad Nacional Autónoma De México, Ciudad Universitaria, Ciudad De México, México; ^cDivisión De Ciencias De La Tierra, Centro De Investigación Científica Y De Educación Superior De Ensenada (CICESE), Ensenada, Baja California, México; ^dCentro de Geociencias, Universidad Autónoma Nacional de México, Campus Juriquilla, Santiago de Querétaro, Querétaro, México

ABSTRACT

Proterozoic to lower Palaeozoic metamorphic sequences are exposed in southern Mexico providing an important geological record for Rodinia and northwestern Gondwana reconstructions. The Sierra de Juárez Complex (SJC) is an enigmatic basement block in southern Mexico that recorded Jurassic dextral strike-slip mylonitic deformation, likely instigated by Pangea break-up and opening of the Gulf of Mexico. However, the origin and pre-Mesozoic evolution of this block are poorly constrained. In this paper, we present the result of fieldwork, LA-ICP-MS U-Pb zircon geochronology, and major and trace element geochemical analyses that allow us to define the following lithological units in the SJC: (1) an anorthositic-gabbroic metamorphic unit (Viguera Suite) with protolith ages of 979–976 Ma and a thermal disturbance event at ca. 920–880 Ma; (2) a MORB-like metagabbroic unit (San Agustín Orthogneiss) with a protolith age of 441.9 ± 3.6 Ma; (3) a metamorphic supracrustal sequence (Etna Unit) that includes amphibolites and pelitic schists with maximum depositional ages of 422–414 Ma and a detrital provenance sourced in Gondwanan-type terranes; and (4) metagranitic intrusions with a protolith age of 191.9 ± 1 Ma, suspected to be syntectonic with respect to the Jurassic mylonitic event. The Silurian-Devonian San Agustín Orthogneiss and Etna Unit constitute the roots of a formerly undocumented lower Palaeozoic terrane that, together with the Viguera Suite, underwent high-pressure amphibolite facies metamorphism between 398–391 Ma, likely related to contractional tectonics. Based on these data, the SJC is proposed as a Mesoproterozoic to middle Palaeozoic crustal block with a geologic evolution coupled to NW Gondwana and a potential correlation with the Grenville-aged and peri-Gondwanan-type terranes like those currently located in southeastern Mexico, Central America, and northwestern South America.

ARTICLE HISTORY

Received 15 July 2020
Accepted 26 December 2020

KEYWORDS

NW Gondwana connections; cuicateco terrane; southern Mexico; Sierra de Juárez Complex; Neoproterozoic; palaeozoic; metamorphic basement

1. Introduction


The reconstruction and geological evolution of northwestern Gondwana have been a matter of revision during the last decade as new evidence of its geological record has emerged from several pre-Mesozoic basement units in southern Mexico, Central America, and northwestern South America (e.g., Solari *et al.* 2011; Estrada-Carmona *et al.* 2012; Ortega-Obregón *et al.* 2008, 2014; Martens *et al.* 2014; Van der Lelij *et al.* 2016; González-Guzmán *et al.* 2016; Keppie *et al.* 2018; Tazzo-Rangel *et al.* 2018; Maldonado *et al.* 2018; Vega-Granillo *et al.* 2020; Weber *et al.* 2018, 2020. Figure 1A). It is widely accepted that the Palaeozoic basement units of southern Mexico and Central America originated and evolved as peripheral NW-Gondwana blocks, constituting the counterpart of the

Andean basements of Venezuela, Colombia, and Ecuador (Ruiz *et al.* 1999; Dickinson and Lawton 2001; Cardona *et al.* 2006; Ortega-Gutiérrez *et al.* 2007; Weber *et al.* 2010; Martens *et al.* 2014). However, this geological continuity was disrupted and detached after the break-up of Pangea (e.g., Spikings *et al.* 2015, 2016), blurring the original palaeogeographic connections. The geological record of these dismembered pre-Mesozoic blocks is thus critical for deciphering the still-missing links in northwestern Gondwana reconstructions, and more detailed geological and geochronological data are required for suitable correlations.

The peri-Gondwanan blocks that currently constitute the pre-Mesozoic basement of Mexico (Acatlán Complex, Oaxaquia, Maya, etc.) recorded post-Palaeozoic relative tectonic displacements along regional-scale fault zones,

CONTACT Guillermo Espejo-Bautista  gespejo@geociencias.unam.mx; guillermoespejo@hotmail.com  UNAM, Campus Juriquilla, Boulevard Juriquilla 3001, Querétaro 76230, México

This article has been republished with minor changes. These changes do not impact the academic content of the article.

 Supplemental data for this article can be accessed [here](#).

© 2021 Informa UK Limited, trading as Taylor & Francis Group

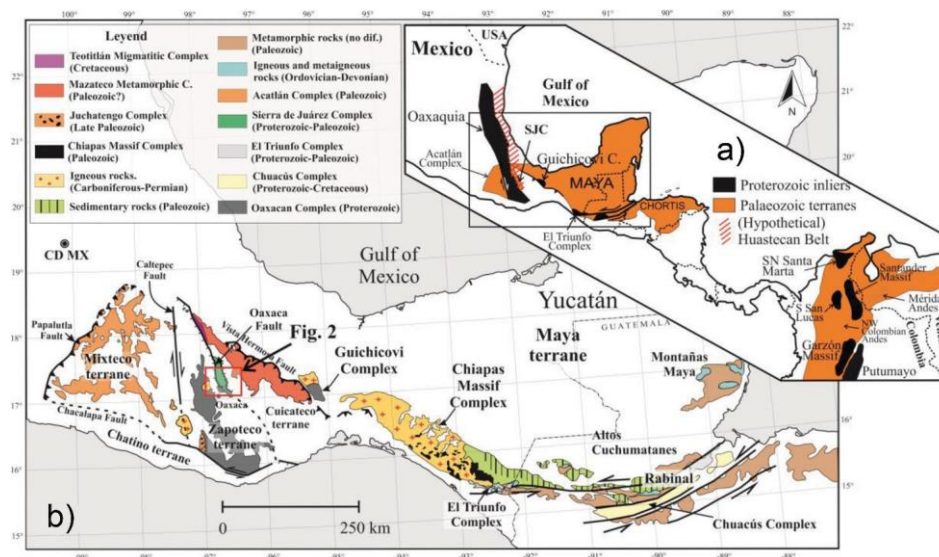


Figure 1. A) Schematic map showing Proterozoic (black) and Palaeozoic (orange) peri-Gondwanan regions exposed in Mexico, Central America, and NW South America. B) Geologic map showing pre-Mesozoic basement rocks of southeastern Mexico and Central America (Modified from Ortega-Gutiérrez *et al.* 2018; Weber *et al.* 2018).

changing their original distribution and structure (e.g., Dickinson and Lawton 2001). The Sierra de Juárez Complex (SJC, Figure 1B; also known as the Sierra de Juárez Mylonitic Complex) is located between the southern Oaxaquia (Precambrian) and the Cuicateco (late Palaeozoic-Mesozoic) terranes in southern Mexico. It is a ~ 15 km wide and more than 60 km long metamorphic belt that recorded an extensive -N-trending strike-slip shear zone, likely related to the opening of the Gulf of Mexico during the Middle Jurassic (Alaniz-Álvarez *et al.* 1994, 1996). The Jurassic mylonitization overprints a set of metamorphic lithologies and structures that resulted from a pre-Mesozoic geologic history with a potential correlation to the NW Gondwana evolution. However, this pre-Mesozoic history of the SJC remains uncertain given the lack of geological and geochronological data.

To gain insight into the pre-Mesozoic evolution of the SJC we use geological mapping and structural-petrological analysis assisted by U-Pb geochronology and major and trace elements geochemistry. We provide first-time evidence for a Neoproterozoic to Lower-Middle Palaeozoic basement unit with sedimentary and igneous protoliths that allows for the re-definition of this metamorphic-mylonitic belt. Finally, the regional tectonic implications of these new findings are discussed, and the central issue of the palaeogeographic connection between the SJC and other Gondwanan-type terranes in southern Mexico, Central America, and NW South America is evaluated.

Regional geologic setting

The SJC is composed of gneissic, intensely mylonitized rocks that show a multi-stage metamorphic and

deformational history (Sedlock *et al.* 1993; Alaniz-Álvarez *et al.* 1994, 1996; Figure 1B). The complex is bordered along its western and eastern sides by reactivated Cenozoic -N-S gently dipping low-angle normal faults, known as the Oaxaca and Siempre Viva faults, respectively, which define the SJC as an elongated horst (González-Ramos *et al.* 2000; Figure 2). The southern border of the complex is truncated by an E-W normal fault, known as the Donají fault, north of Oaxaca City (Centeno-García 1988; Alaniz-Álvarez *et al.* 1994, 1996; Campos-Enríquez *et al.* 2010; Figure 2). The Palaeozoic (?) Mazateco Metamorphic Complex (MMC) and the Cretaceous Teotitlán Migmatitic Complex (TMC) crop out north and east of the SJC, respectively (Ángeles-Moreno 2006; Figure 1B). However, the correlation and the nature of the contact between the SJC and the MMC-TMC block are unknown.

The SJC records two stages of deep brittle-ductile deformation (Sedlock *et al.* 1993; Alaniz-Álvarez *et al.* 1994, 1996). The first one is associated with late Palaeozoic eastward contraction during or after equatorial western-Pangea amalgamation. The SJC likely acted as a thrust belt that emplaced the Zapoteco terrane basement (Oaxacan Complex) over the Cuicateco terrane basement, resulting in a mylonitic belt with foliation planes dipping to the west. The second one took place in Middle Jurassic when the SJC was reactivated during the Pangea break-up by -N-S dextral strike-slip displacement and mylonitization likely due to the opening of the Gulf of Mexico (Alaniz-Álvarez *et al.* 1996).

At its western edge, the SJC is in tectonic contact with the Oaxacan Complex (OC) and its Cambrian-Cenozoic

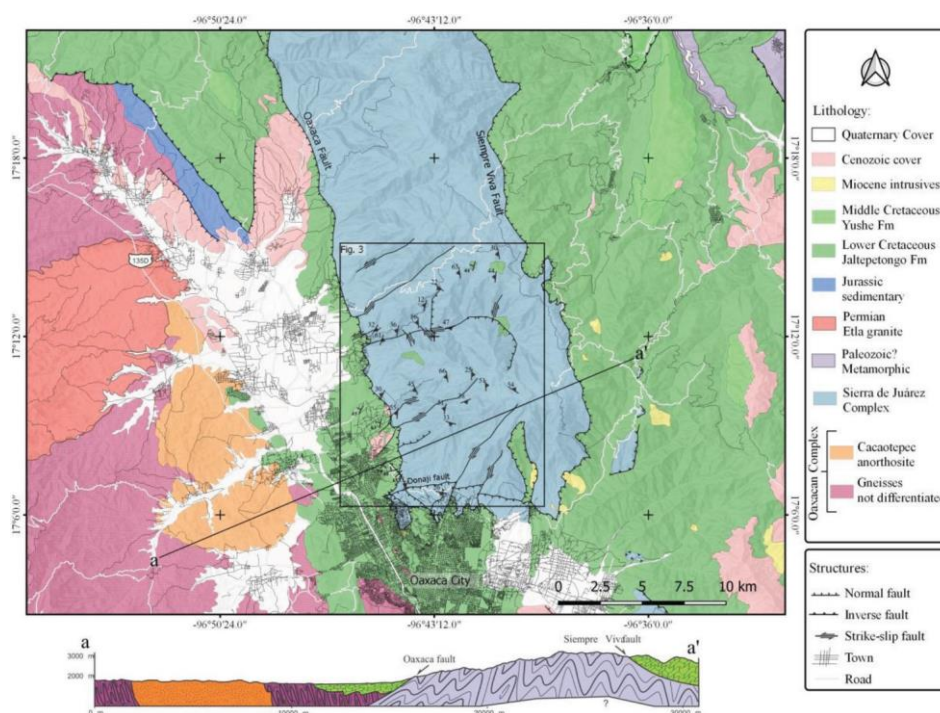


Figure 2. Geologic map of the meridional sector of the SJC compiled from 1:50,000 charts E14-D47 (Oaxaca de Juárez), E14-D48 (Tlaxiact de Cabrera), E14-D38 (Santa Catarina Ixtepeji) and E14-D37 (San Francisco Telixtlahuaca) of the Servicio Geológico Mexicano complemented with the geologic map of the Cacaotepec Anorthosite of Valencia-Morales (2017) and geologic observations in the SJC during this study.

stratigraphic cover (Zapoteco terrane) along the normal Oaxaca fault (Figure 1B, 2, and 3). The OC is conformed by a set of granulitic rocks with magmatic and sedimentary protoliths that span the interval ca. 1.4-0.95 Ga (Keppie *et al.* 2003; Solari *et al.* 2003, 2014; Cameron *et al.* 2004; Keppie and Ortega-Gutiérrez 2010; Weber *et al.* 2010; Weber and Schulze 2014; Ortega-Gutiérrez *et al.* 2018). Associated massif-type anorthosites, interpreted as a part of a ca. 1010 Ma AMCG suite (Anorthosite-Mangerite-Charnockite-Granite) (Solari *et al.* 2003; Keppie *et al.* 2003; Cameron *et al.* 2004; Keppie and Ortega-Gutiérrez 2010) crop out towards the structural base of the complex where they intrude an older unit of polydeformed migmatites. All pre-Neoproterozoic lithologies of the OC underwent granulite-facies metamorphism during the Grenville-aged Zapotecan Orogeny at ca. 1000-980 Ma (Lawlor *et al.* 1999; Weber and Köhler 1999; Solari *et al.* 2003, 2004; Keppie *et al.* 2003; Cameron *et al.* 2004; Weber *et al.* 2010; Keppie and Ortega-Gutiérrez 2010).

The OC is the largest Grenvillian exposure in Mexico that, together with similar outcrops, such as the Huiznopala and Novillo gneisses in northern and central-eastern Mexico (Lawlor *et al.* 1999; Cameron *et al.* 2004), the Guichicovi Complex in southeastern Mexico (Weber and Köhler 1999; Weber and Hecht; Weber and Hecht

2003) and the El Triunfo Complex in southeastern Mexico (Weber *et al.* 2018, 2020), make up the Grenville-aged block known as Oaxaquia (Ortega-Gutiérrez *et al.* 1995), which constitutes the Precambrian backbone of eastern and southern Mexico (Figure 1A). The most recent reconstructions of the supercontinent Rodinia place Oaxaquia in the collisional suture between the Amazonia and Baltica cratons (Li *et al.* 2008; Ortega-Gutiérrez *et al.* 2018; Weber *et al.* 2020). During the Palaeozoic, Oaxaquia was likely located at the northwestern corner of Gondwana, witnessing the opening of the Iapetus and Rheic oceans (Ortega-Gutiérrez *et al.* 2018; Weber *et al.* 2018; Keppie *et al.* 2018).

The Cuicateco terrane (Delgado-Argote 1989; Sedlock *et al.* 1993, Figures 2 and 3), on the other hand, is the least studied geological block of southern Mexico. It essentially consists of a Jurassic-Cretaceous oceanic and volcano-sedimentary basin and a suite of gabbroic and ultramafic rocks interpreted as fragments of an ophiolitic complex that represent the basement (Carfentan 1983; Delgado-Argote 1989; Sedlock *et al.* 1993; Pérez-Gutiérrez *et al.* 2009). Most geologic models for the origin of this terrane place its development within a pull-apart system as a consequence of a transtensional tectonic environment (Sedlock *et al.* 1993; Dickinson and Lawton 2001; Pindell and Kennan

2009), undergoing crustal thinning and anatexis (Ángeles-Moreno 2006) as well as alkaline magmatism during Late Jurassic-Early Cretaceous times (Mendoza-Rosales *et al.* 2010). The extensional setting of the Cuicateco terrane was probably related to either the southeastward displacement of South America relative to North America during or after the final stages of the opening of the Gulf of Mexico (Ángeles-Moreno 2006) or to back-arc extension related to the subduction of the Arperos plate in western Mexico (Coombs 2016). In addition, an inversion stage is recorded in the Cuicateco terrane, probably because of the Late-Cretaceous-Palaeogene Mexican Orogeny (Fitz-Díaz *et al.* 2018) or some other undetermined post-Early Cretaceous tectonic event, that caused incipient metamorphism and different degrees of deformation and shortening (Sedlock *et al.* 1993; Pérez-Gutiérrez *et al.* 2009).

Low- to medium-grade metasedimentary and metaigneous rocks, of possible Palaeozoic age, crop out within the Cuicateco terrane as remnants of a crystalline complex that predates its origin. These metamorphic exposures are known as the Mazateco Metamorphic Complex (MMC; Ángeles-Moreno 2006; Ortega-Gutiérrez *et al.* 2018; Figure 1A). The origin of the MMC has been related to the hypothetical Huastecan orogenic belt, a poorly understood late Palaeozoic suture that may have separated the Mesoproterozoic Oaxaquia block and the Gondwanan-affinity terranes in northwestern South America (Ortega-Gutiérrez *et al.* 2018).

2. Analytical techniques

Sample preparation was performed at the mineral separation labs of the Instituto de Geofísica and the Centro de Geociencias, UNAM. Samples were pulverized utilizing a hydraulic press. For zircon grain separation we used batting, Frantz magnetic separator, and handpicking techniques. Zircon grains were handpicked under a stereoscopic microscope, mounted in epoxy resin, and finally polished for subsequent analysis.

Cathodoluminescence images of zircon grains from anorthositic samples JG50, JG42, and JG24 were taken at the Laboratorio de Microscopía Electrónica de Barrido y Microanálisis at Taxco University, Guerrero state, Mexico, with an SEM Jeol IT300, coupled to Gatan Chroma CL2 cathodoluminescence equipment. Samples JG18, JG46, and JG55 from the Etna Unit and San Agustín Orthogneiss, were imaged at the Centro de Geociencias (CGEO), UNAM, with an SEM Hitachi S-3100 H.

U-Pb zircon geochronology was performed by LA-ICP-MS (laser ablation inductively-coupled plasma mass spectrometry) at the Laboratorio de Estudios Isotópicos

(LEI), CGEO, UNAM. A Thermo iCap Qc ICP-MS coupled to a Resonetics, resolution M050 excimer laser workstation was employed, according to the methodology described in Solari *et al.* (2018). An analytical spot diameter of 23 μm was used, employing an energy density of 6 Jcm^{-2} measured at target. The reference zircon employed during this study was 91,500 (1062 Ma, Wiedenbeck *et al.* 1995), and the secondary (control) reference standard was Plešovice zircon (337 ± 1 Ma, Sláma *et al.* 2008), both run each 10 analyses. The mean $^{206}\text{Pb}/^{238}\text{U}$ age obtained on Plešovice was 339.3 ± 4 Ma ($n = 32$, MSWD = 2.3) in agreement with previously published data. Lolite software (Paton *et al.* 2010, 2011) was employed to reduce raw data, calculate U and Th concentrations and propagate 2σ uncertainties. $^{207}\text{Pb}/^{206}\text{Pb}$ ratios, ages, and errors are calculated according to Petrus and Kamber (2012). Common Pb is not corrected, since the signal of ^{204}Pb is swamped by the isobar ^{204}Hg contained in carrier gasses, and thus all the analyses would become overcorrected, as well as the errors overestimated. Zircon REE data were obtained during the same ablation as the U-Pb analyses employing NIST 610 as the reference standard and normalized with the CI Chondrite values of McDonough and Sun (1995). The cut-off of U-Pb data for metasedimentary rocks was considered at 800 Ma (e.g., Gehrels *et al.* 2008), and the minimum discordant values for age calculus are considered as less than 30%.

Major elements were obtained using a Rigaku Primus II X-ray sequential spectrometer at the X-Ray Fluorescence Lab of the Laboratorio Nacional de Geoquímica at the Instituto de Geología, UNAM. For procedures and standards refer to Lozano-Santa Cruz and Bernal (2005). Trace elements were measured at LEI, CGEO, UNAM, using a Thermo iCap Qc ICP-MS according to the methodology of Mori *et al.* (2007). For the information on the quality of geochemical data and measured standards during trace element acquisition, we referred to Supplementary data 2.

3. Lithology and petrography

The SJC is essentially composed of three main lithologic units: (1) a mafic and anorthositic orthogneiss suite, here referred to as the Viguera Suite; (2) a metagabbroic body, named the San Agustín Orthogneiss; and (3) a metamorphic supracrustal sequence denominated Etna Unit (Figure 3). Most of the SJC is structurally controlled by Jurassic -N-S mylonitic domains (hereafter referred to as $M_2 + D_2$), with sub-vertical foliation planes, a sub-horizontal stretching mineral-lineation, and retrograde greenschist facies mineralogy with chlorite, titanite, and epidote. However, mylonitization occurs in

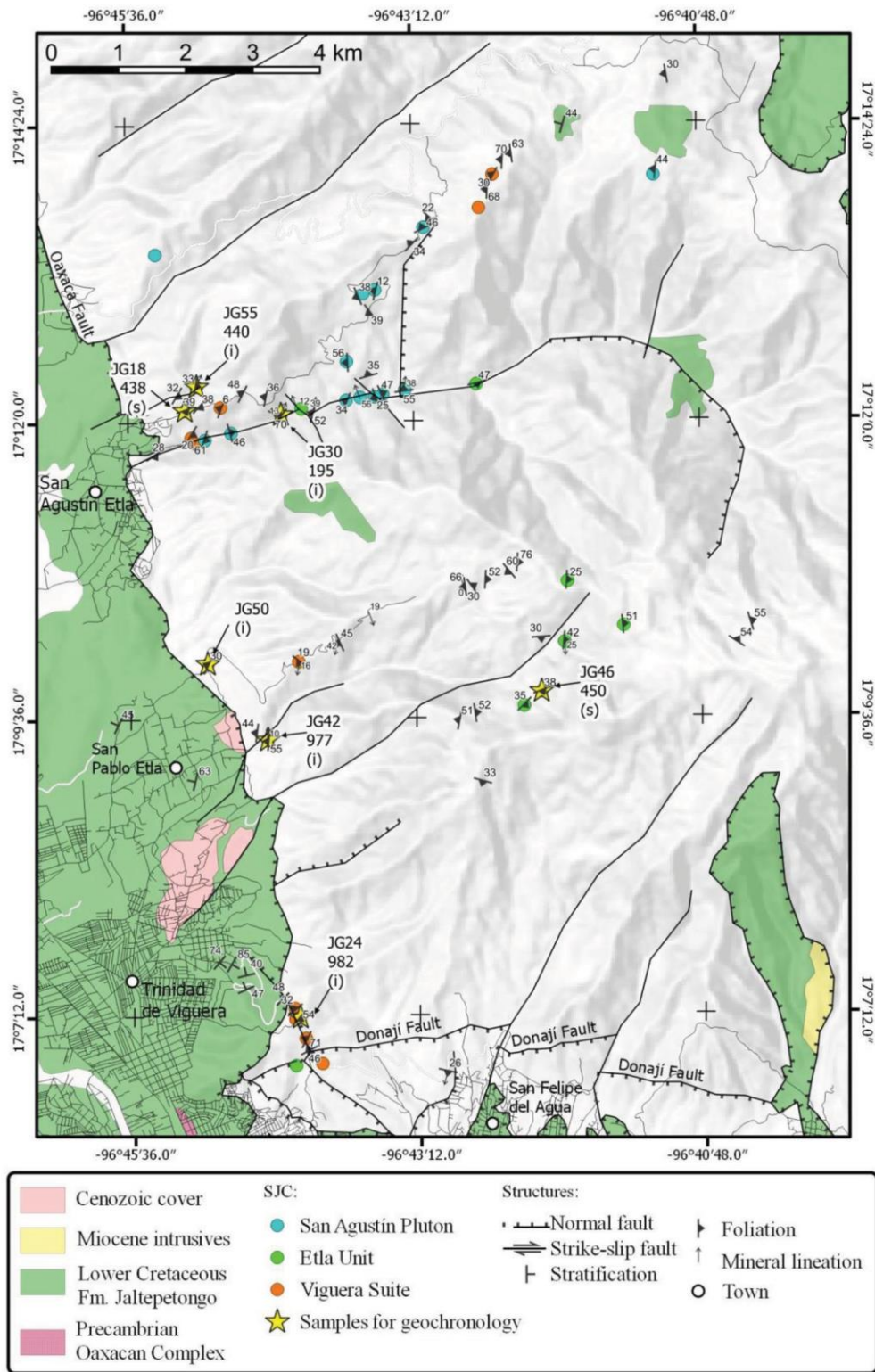


Figure 3. Geologic map of the study area with sample collection sites for petrographic classification and geochronologic analysis. Ages expressed in Ma.

a regionally anastomosing pattern, allowing the preservation of low-strain regions. These relict regions exhibit petrologic and structural features related to a previous tectonic event under higher-grade metamorphic

conditions (hereafter referred to as $M_1 + D_1$) defined by gneissic and schistose foliations, usually affected by asymmetric tight to isoclinal folding with axial surfaces mainly dipping to the NW.

3.1. Viguera Suite

The Viguera Suite is best exposed between San Felipe del Agua and Trinidad de Viguera (Figure 3). It is intercalated on a metre scale by the metanorthositic and mafic components (Figure 4A), although the anorthosite member is also observed as a massive body (Figure 4B). Some exposures show the mafic component as the host rock of anorthosite intrusives (Figure 4A). It is also possible a comagmatic origin for both lithologies, but the field observations are insufficient to establish a reliable correlation.

The mafic gneissic component shows gradual deformation and grain-size reduction, becoming mylonitic and ultramylonitic at the metre scale (Figure 4C-F). The samples analysed are mainly composed of anastomosed patterns of stretched chlorite that surround plagioclase porphyroclasts (Figure 4C-F). Some samples preserve fine-grained amphibole with progressive alteration to chlorite (Figure 4G), which suggests that the chlorite content in this lithotype arises from precursor amphiboles. Variable amounts of calcite are usually present as a secondary phase, probably indicating fluid percolation during mylonitization. Rutile, ilmenite, and apatite are

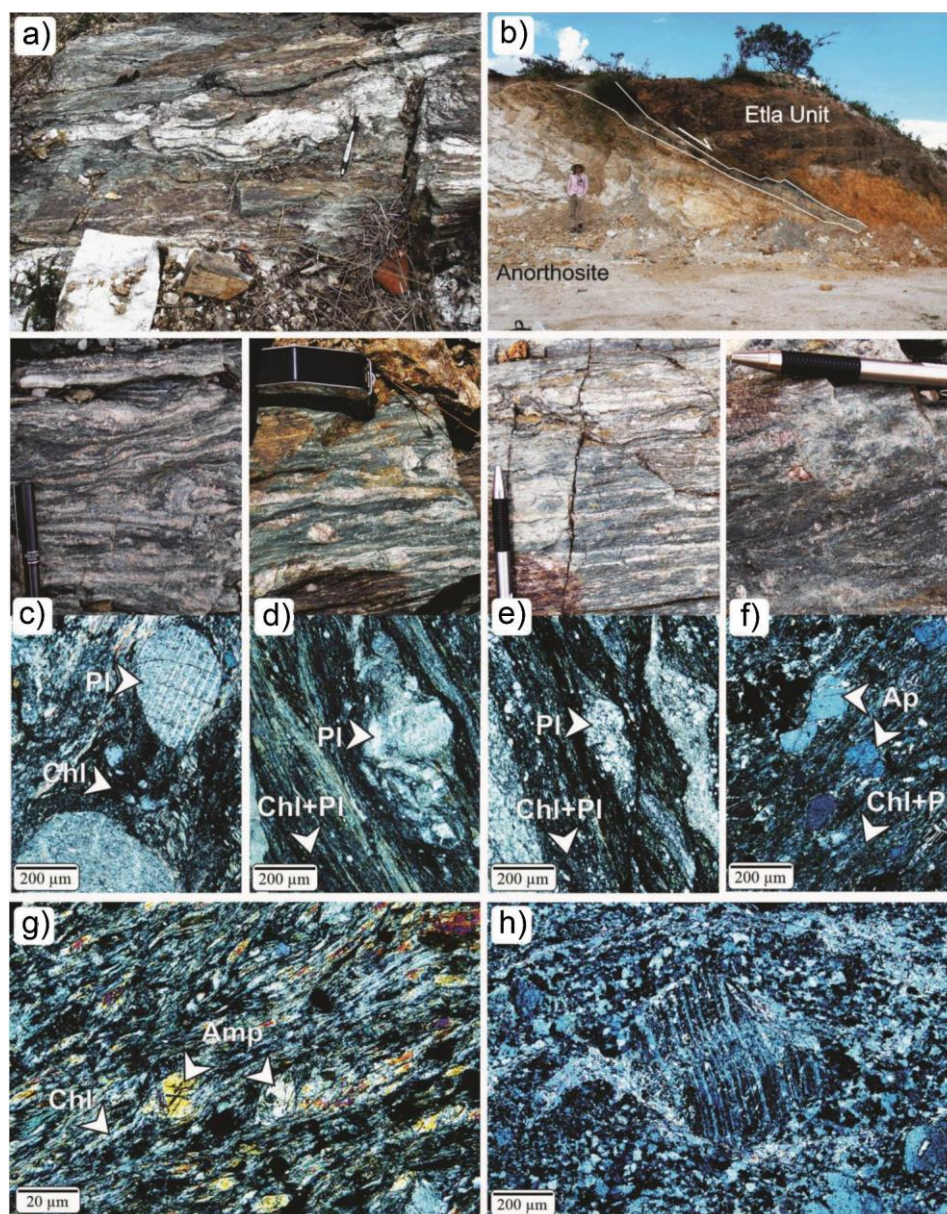


Figure 4. Photographs and photomicrographs of the Viguera Suite. A-B) Field relationships between the anorthositic and mafic members of the suite, as well as with the Esla Unit. C-F) Photographs and photomicrographs showing a progressive transition from gneissic to ultramylonitic textures in the mafic component of the Viguera Suite. E) Photomicrograph showing a mafic sample of the Viguera Suite, with amphiboles been altered to chlorite. F) Typical mylonitic texture of anorthosite in the Viguera Suite.

also found in some highly deformed samples as rigid porphyroclasts associations, suggesting the presence of nelsonite bodies.

The anorthositic component (> 90% Pl; samples JG24, JG42, and JG50) of the suite also shows mylonitic to ultramylonitic textures. Twinned plagioclase porphyroclasts (> 150 μm) exhibits ductile deformation and a strong alteration to sericite and recrystallization to white mica along crystal borders (Figure 4H). The matrix mineralogy is mainly made up of very fine-grained plagioclase (< 30 μm), minor amphibole and apatite, and < 80 μm euhedral rutile grains spatially related to ilmenite. Apatite appear as rigid porphyroclasts (Figure 4F).

3.2. San Agustín orthogneiss

The Viguera Suite is inferred to be intruded by the protolith of the San Agustín Orthogneiss, which is well exposed to the east of the San Agustín ETLA town (Figure 3) and is widely distributed within the SJC. This lithotype is a coarse-grained rutile-bearing mafic orthogneiss composed of planar or anastomosed domains of amphibole and plagioclase (Figure 5A-B). The orthogneiss (samples JG55 and JG09) is equitably composed of > 90% hornblende and low-Ca plagioclase (andesine to albite) (Figure 5C). The remaining 10% is mainly made up of ilmenite, rutile, titanite, epidote-clinozoisite, and chlorite + epidote + plagioclase pseudomorphs likely after garnet. Most samples display a mylonitic fabric (S_2) with anastomosed foliation and amphibole porphyroclasts with asymmetric tails. The mylonitic foliation appears to have reoriented a previous gneissic fabric into its present configuration, inducing recrystallization towards mineral edges, such as chlorite after amphibole and albite after oligoclase and developing greenschist-facies mineralogy in the matrix. These textures and mineralogy suggest a retrograde metamorphic path. Relict cores are related to the pre-mylonitic event ($M_1 + D_1$) and edges or recrystallized areas are linked to the superimposed mylonitization. Rutile, 50-100 μm in size, appears as isolated grains in the matrix and as needle-shaped polygonal aggregates more than 1 cm long (Figure 5C), in both cases commonly rimmed by titanite. According to the textural relations and mineralogy, the $M_1 + D_1$ mineral assembly for this lithotype is thought to be hornblende + plagioclase \pm rutile \pm garnet. The occurrence of rutile in middle-T metabasic rocks suggests pressure conditions of at least ca. 11 kbar (Zack and Kooijman 2017).

3.3. ETLA unit

The ETLA Unit is a supracrustal sequence mainly composed of folded mafic paragneisses with or without garnet (Figure

5D-E), and white-mica pelitic schists (Figure 5F-H). The ETLA Unit is in contact with the Viguera Suite through a normal fault in the San Felipe del Agua-Trinidad de Viguera transect (Figure 4B). This fault is spatially related to the Cenozoic Donají fault (Centeno-García 1988; Alaniz-Álvarez *et al.* 1994, 1996; Campos-Enríquez *et al.* 2010; Figure 3), hence, it was probably active or reactivated during the Cenozoic. The ETLA Unit is usually retrograded and structurally modified by the Jurassic N-S mylonitic event ($M_2 + D_2$) and intruded by thin protomylonitic granitic layers concordant with the mylonitic foliation planes of the country rock, thus suspected to be syntectonic with respect to $M_2 + D_2$ (Figure 5D; sample JG30).

Sample JG18 is a highly altered pelitic schist with anastomosed lepidoblastic foliation (Figure 5G-H). It is composed of > 50% white mica. Rutile appears as > 100 μm subhedral to euhedral elongated grains, with cores and rims composed of ilmenite, oriented parallel to the micaceous planar fabric (Figure 5G-H). Quartz microlithons constitute the lepidoblastic fabric, which also contains pseudomorphs of chlorite and opaques likely after garnet (Figure 5G). Tabular, 1 or 2 cm long and bluish in hand sample sericite + quartz pseudomorphs are also common (Figure 5F and 5H). Since no relict precursors have been observed, we interpret these as likely pseudomorphs after kyanite/sillimanite or staurolite. Mineralogy (including pseudomorphs) and textural observations in this lithotype indicate a $M_1 + D_1$ paragenesis of white mica + quartz + garnet + rutile + pseudomorphs (kyanite/sillimanite/staurolite).

Sample JG49 is a garnet-amphibolite (Figure 5E), mainly composed of hornblende (45%), plagioclase (25%), quartz (25%), garnet (3%), and less than 2% biotite, chlorite, apatite, and epidote-allanite. The sample contains a matrix-mineralogy of 50-300 μm size and ca. 400 μm long sigmoidal apatite and amphibole porphyroclasts. Amphibole is often mantled by biotite and/or chlorite, as recrystallized rims possibly related to the $M_2 + D_2$ phase. Considering the mineral modes and textural relationships, the pre-mylonitic $M_1 + D_1$ mineral assembly is interpreted to have been amphibole + plagioclase + quartz + garnet.

4. Geochronology

The age and provenance of the Viguera Suite and the San Agustín Orthogneiss in the SJC have never been constrained using isotopic methods. Furthermore, the presence of a newly-recognized metasedimentary unit (ETLA Unit) has potentially important implications regarding the correlation of the SJC with other regions of southern Mexico, Central, and northern South America. With this in mind, we analysed zircon

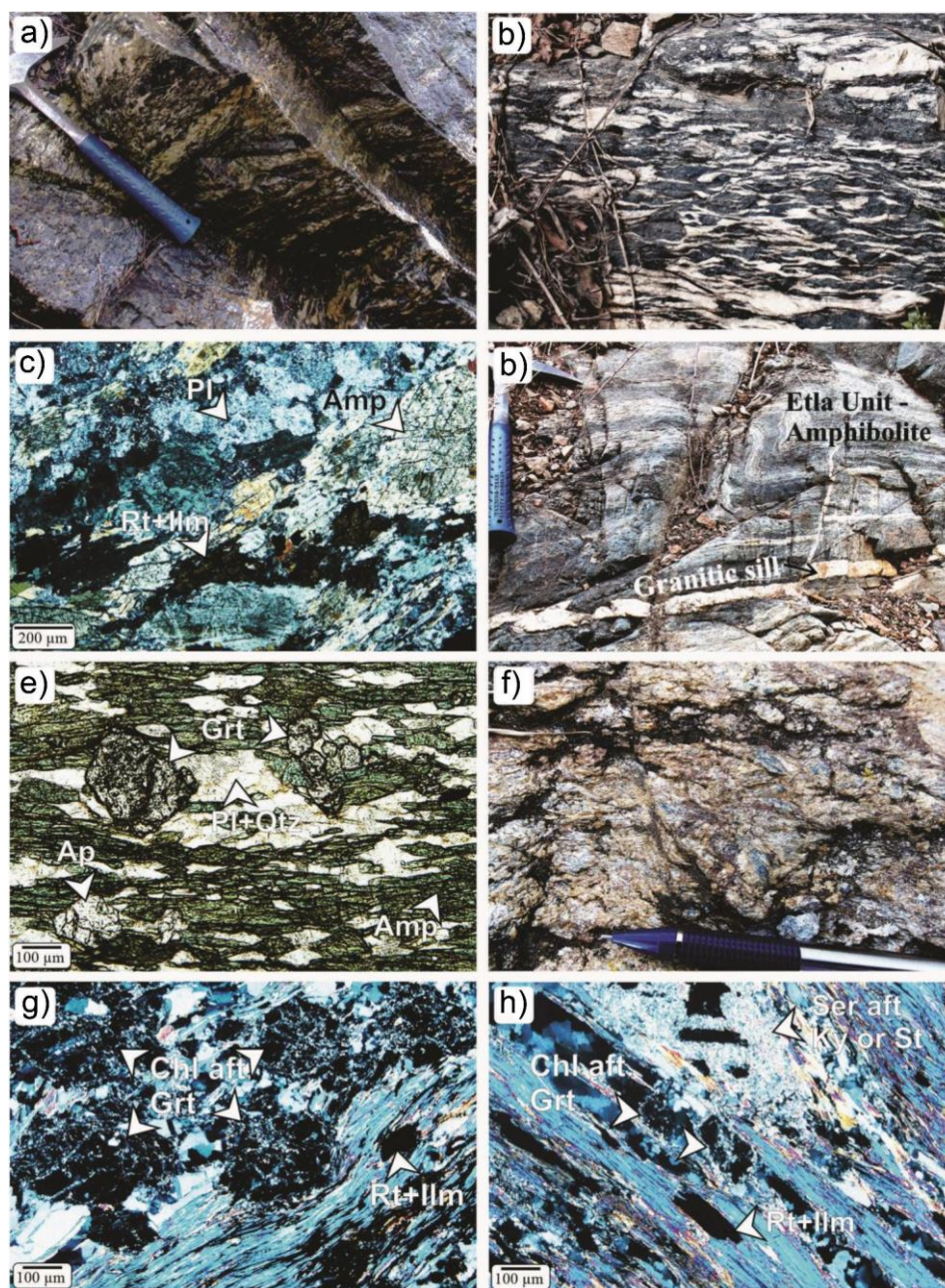


Figure 5. Photographs and photomicrographs of the San Agustín Orthogneiss and Etna Unit. A-B) Typical gneissic and mylonitic textures of the San Agustín Orthogneiss. C) Photomicrograph showing San Agustín Orthogneiss mineralogy and texture. D) Amphibolite from the Etna Unit intruded by a Jurassic granitic layer. Both rocks share similar mylonitic fabrics. E) Photomicrograph of garnet-bearing amphibolite from the Etna Unit. F) White mica pelitic schist from the Etna Unit with blue pseudomorphs of sericite + quartz after kyanite/sillimanite or staurolite. G) Pelitic schist of the Etna Unit with garnet pseudomorphs, rutile/ilmenite and white mica (sample JG18). H) Etna Unit schist showing rutile/ilmenite, chlorite pseudomorphs likely after garnet, and sericite pseudomorphs likely after kyanite/sillimanite or staurolite. No precursor minerals are preserved.

grains from three anorthositic samples of the Viguera Suite; one sample of the San Agustín Orthogneiss; one pelitic schist and one amphibolite from the Etna Unit; and one protomylonitic metagranite to determine the age of the mylonitic event, which represents the youngest event recognized in the SJC. The age and geographic location of the dated samples

are listed in Table 1 and show in Figure 3, whereas the geochronological data is available in Supplementary Data 1.

4.1. Viguera Suite

Anorthositic samples JG24, JG42, and JG50 were collected at the SW corner of the SJC, (sample location

in Figure 3). Zircon grains in all samples range in size from ca. 30 to less than 200 μm , varying in shape from round to slightly elongated, with some fragments of larger crystals. CL images show diffuse luminescent areas and some rim-core structures with low CL contrast (Figure 6A-C).

The anorthosite sample JG24 yielded twenty-two zircon grains. Overall, they show a range of $^{206}\text{Pb}/^{238}\text{U}$ ages (all less than 8.2% discordant) from 993 to 898 Ma, with Th/U ratios > 0.2, low U concentrations (< 201 ppm), and typical igneous REE patterns with a progressive increment from LREE to HREE (Figure 7A; e.g., Hinton and Upton 1991). A weak negative Eu anomaly is present, suggesting coeval crystallization of zircon and plagioclase (e.g., Kaczmarek *et al.* 2008; Grimes *et al.* 2009). The $^{206}\text{Pb}/^{238}\text{U}$ weighted mean age of 979.7 ± 3.7 Ma (MSWD = 2.07, $n = 20$, Figure 7A) is interpreted as the more reliable age for the magmatic protolith crystallization. Two zircon spots show $^{206}\text{Pb}/^{238}\text{U}$ ages between ~919 and 898 Ma possibly due to the effect of a younger tectonothermal event that produced new square-shaped zircon crystallization (Figures 6A and 7A). The REE patterns from these two younger spots exhibit slight LREE depletion, especially in Pr (red REE patterns in Figure 7A), which may indicate a crystallization in the presence of other metamorphic minerals such as monazite or allanite (Rubatto *et al.* 2009; Rubatto 2017).

From sample JG42, 13 zircon grains were analysed. These have low U content in the range ca. 153-27 ppm, Th/U ratios between 0.65 and 0.17, and are less than 13.1% discordant. The chondrite normalized rare-earth elements (Figure 7B) display igneous patterns with an increase of HREE over LREE, a positive anomaly in Ce, and a negative Eu anomaly. Two analyses show a positive Eu anomaly, possibly associated with plagioclase micro-inclusions. One zircon yields a $^{206}\text{Pb}/^{238}\text{U}$ age of 1047 ± 33 Ma (2σ), which could be inherited. All other zircon grains (12 analyses) straddle the concordia curve from ca. 997 to ca. 959 Ma, yielding a mean $^{206}\text{Pb}/^{238}\text{U}$ age of 976.2 ± 5.1 Ma (MSWD = 2.17), interpreted as the best approximation of the anorthosite crystallization age.

Sample JG50 was analysed with 17 zircon grains with Th/U ratios up to 0.46, a discordance of less than 24.5%, and

very low U concentrations ranging between ca. 38 and 13 ppm (only one inherited core show 127 ppm). Two zircon grains with $^{206}\text{Pb}/^{238}\text{U}$ ages of 1076 ± 35 and 1076 ± 15 Ma are probably inherited (Figure 7C). The remaining analyses spread along the concordia curve from ca. 981 to 837 Ma. The REE patterns and the ages show that the younger the zircon, the greater the depletion in its Gd-Lu series (Dy/Gd ratio). Hence, we can infer that this progressively develops flat HREE patterns (shown in reddish in Figure 7C). The flat HREE patterns and the spread of ages are suggestive of recrystallization and Pb loss, probably as a consequence of a superimposed thermal event. However, Pb loss was a variable and partial process, and the ages are not entirely reset. There is also no clear discordant line, and therefore, it is not possible to estimate a reliable igneous or metamorphic age for this sample.

4.2. San Agustín Orthogneiss

From sample JG55 twenty-nine zircon grains less than 60 μm long were analysed. Cathodoluminescence images reveal poorly developed internal structures (Figure 6F). All grains show rounded or slightly elongated anhedral shapes and homogeneous or low-contrasting luminescent domains. The two oldest zircon grains show discordant behaviour, with $^{206}\text{Pb}/^{238}\text{U}$ ages of 869 ± 14 and 731 ± 23 Ma which are interpreted as inherited (Figure 7D). Most of the zircon ages are concordant to nearly concordant, ranging from 460 to 347 Ma, with Th/U ratios of 0.12 to 1.4 and variable U concentrations in the range ca. 56-734 ppm (only one zircon shows 2457 ppm of U). The REE patterns coupled with the weighted mean ages show increasing Dy/Gd ratios as the zircon age decreases, which is probably due to a depletion in LREE rather than an enrichment in HREE (Figure 7D). LREE depletion has been observed in zircons that grow during amphibolite-facies metamorphic conditions in the presence of allanite, titanite, or monazite (Rubatto *et al.* 2009; Rubatto 2017). Thus, a metamorphic overprinting causing partial recrystallization or radiogenic Pb-loss is a likely explanation for the spread of decreasing ages. However, all the ages apparently derive from a single population, so it is permissible to exclude the youngest slightly spreading ages (dashed-line ellipses in

Table 1. Classification and location of the samples collected for U-Pb geochronology.

Sample	Lithology	Unit	Latitude N	Longitude W	U-Pb age (Ma)
JG24	Meta-anorthosite	Viguera Suite	17° 7 11.3 "	96° 44 12.4 "	979.7 ± 3.7
JG42	Meta-anorthosite	Viguera Suite	17° 9 29.9 "	96° 44 33.1 "	976.2 ± 5.1
JG50	Meta-anorthosite	Viguera Suite	17° 10 2.9 "	96° 44 57.1 "	-
JG18	Pelitic Schist	Etla Unit	17° 12 5.7 "	96° 45 7.3 "	ca.422*
JG46	Garnet-bearing para-amphibolite	Etla Unit	17° 9 48.3 "	96° 42 9.0 "	ca. 414*
JG55	Rutile-bearing gabbroic orthogneiss	San Agustín Orthogneiss	17° 12 17.3 "	96° 45 1.3 "	441.9 ± 3.6
JG30	Mylonitic granitic layer		17° 12 3.5 "	96° 44 18.9 "	191 ± 1

*Maximum depositional ages

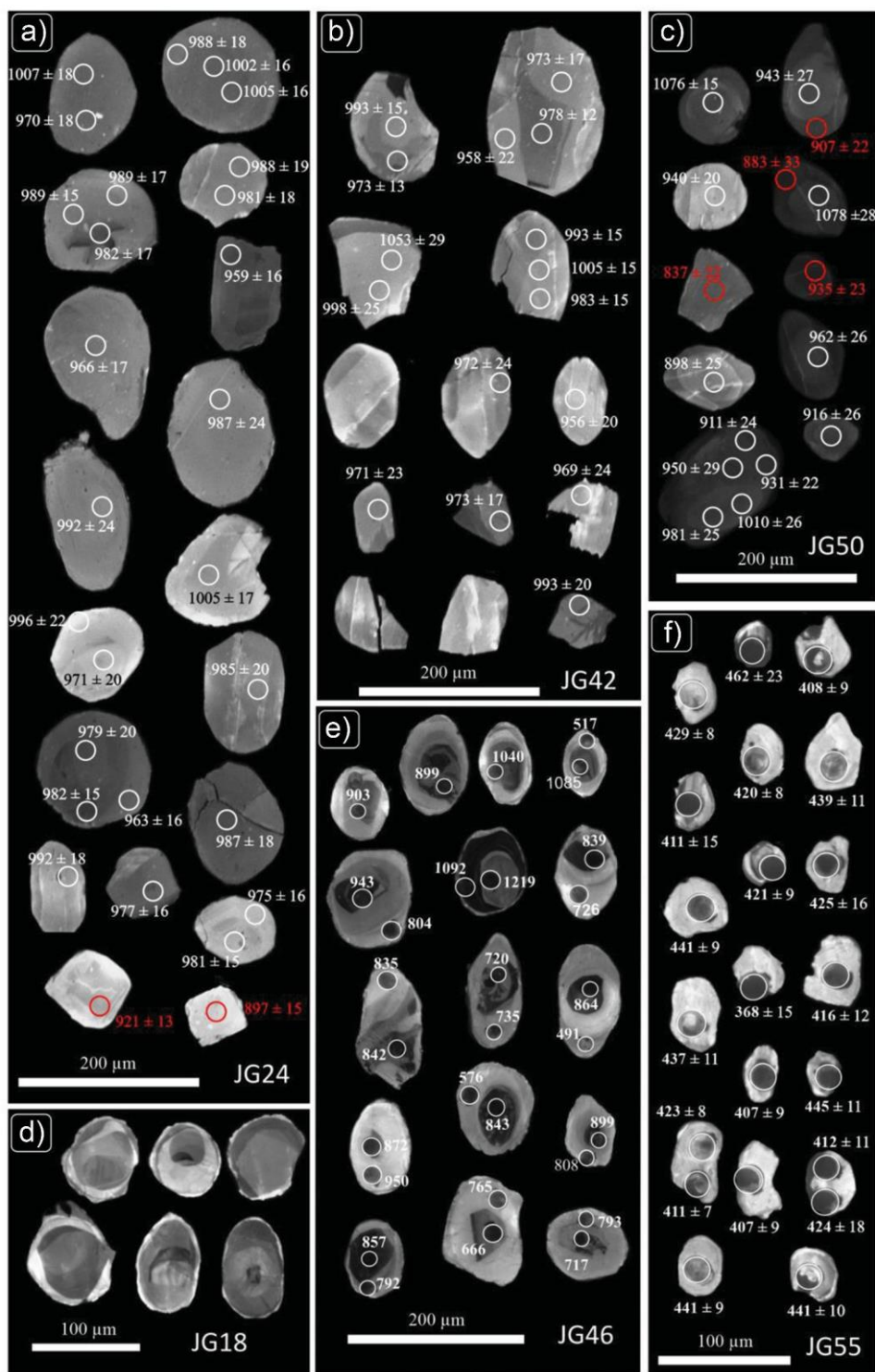


Figure 6. Cathodoluminescence images of zircon grains. Circles represent 23 μm -diameter laser spots. White circles represent ages with igneous REE patterns, whereas red circles represent ages with metamorphic REE patterns. A), B) and C) Meta-anorthositic samples JG24, JG42, and JG50 of the Viguera Suite. D) Pelitic Schist JG18 from the Etna Unit. E) Amphibolite JG46 from the Etna Unit. F) Zircon grains from the San Agustín Orthogneiss (sample JG55).

the concordia diagram of Figure 7D) from the weighted mean as suggested by Taylor *et al.* (2016). The 11 oldest concordant zircon analyses constitute a subset of data that displays a coherent scatter within their analytical errors and

magmatic-related chemistry. These zircons yield a mean age of 441.9 ± 3.6 Ma (MSWD = 0.31, $n = 8/25$) (Lower Silurian) that is interpreted as the crystallization age of the San Agustín Orthogneiss protolith. The LREE-depleted

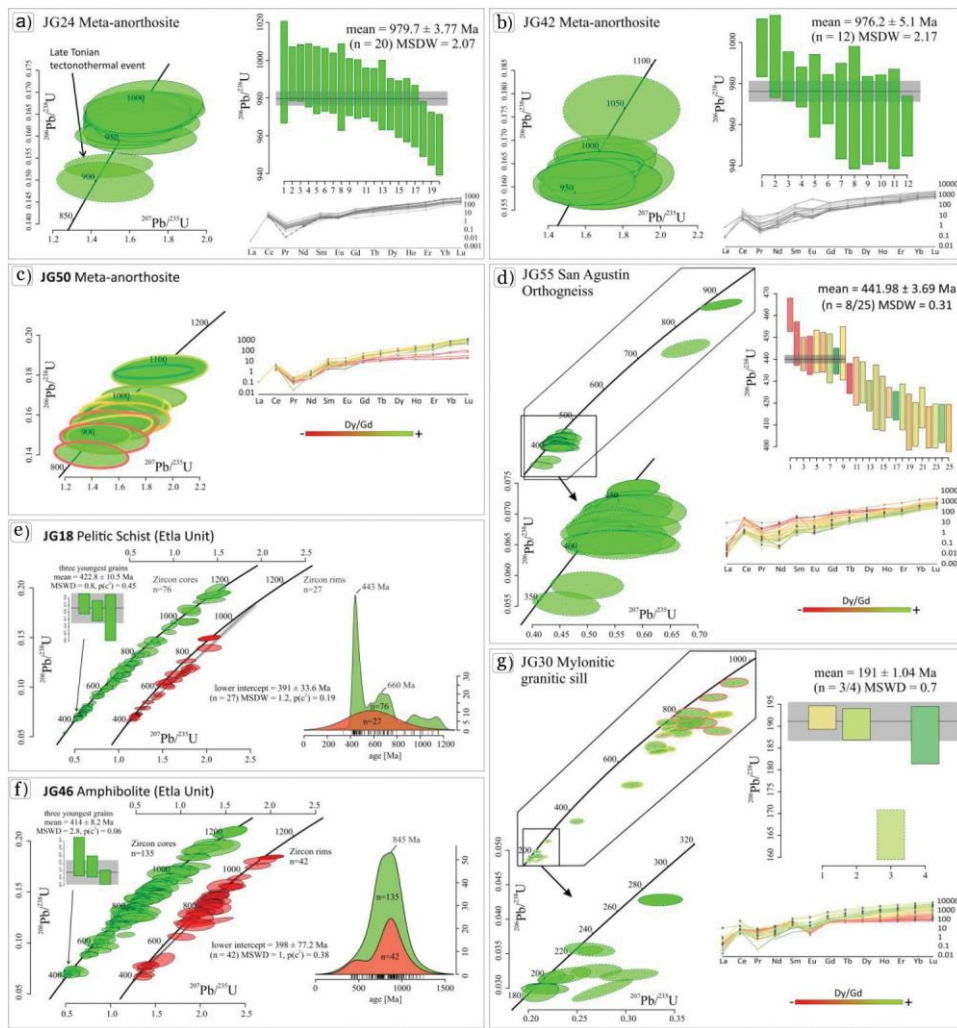


Figure 7. Geochronologic results data for concordia, weighted mean and KDE diagrams from *Isoplot R* programme of Vermeesch (2018). Data-point error ellipses are 2σ . A-C) U-Pb geochronology and zircon trace-element data for meta-anorthosites from the Viguera Suite. D) San Agustin Orthogneiss U-Pb geochronology. Igneous age estimated from analyses with more enriched LREE patterns (reddish patterns). Dashed lines are not considered in mean age calculations. E-F) U-Pb geochronology and zircon trace-element data for pelitic schist JG18 and garnet-bearing amphibolite JG46 of the Etna Unit. Green ellipses represent core analyses whereas red ellipses represent rim analyses. G) U-Pb geochronology for granitic layer intruding amphibolites of the Etna Unit. Crystallization age obtained from the youngest concordant analyses (ellipses with continuous line).

younger zircon group shows a meaningless step pattern in the weighted mean ages; hence they are not discussed further.

4.3. Etna unit

Sample JG18 is a rutile-bearing pelitic schist, from which 103 analyses from detrital zircon grains were made. Cathodoluminescence images (Figure 6D) show rim-core structures in zircon grains. Assuming that most of the rims could represent the effect of the post-depositional metamorphism and cores represent the detrital provenance, they were interpreted separately. Core-ages (using best-age with cut-off at 800 Ma) range between 1156 to

338 Ma (green ellipses in Figure 7E). The oldest scattered group of 7 Mesoproterozoic ages ranges between 1156 and 1021 Ma, followed by a small group of 8 zircon grains that range in age from 997 to 798 Ma. A more abundant but still scattered group of 27 ages range between 766 and 554 Ma, with a major concentration at 660 Ma. The maximum age distribution defines a Palaeozoic population of 34 zircon grains with ages that range between 521 and 338 Ma with a prominent probability peak at ca. 443 Ma. The maximum depositional age was calculated using the three youngest overlapping concordant analyses (e.g., Dickinson and Gehrels 2009), which yielded a mean of 422 ± 10.5 Ma (MSWD = 0.8). The youngest zircon grain of 338 ± 4.3 (2σ) does not constitute part of a group (e.g., Dickinson and

Gehrels 2009) and hence is not discussed further. Zircon rims (red ellipses in Figure 7E) are more discordant than cores and constitute a continuous distribution that forms a discordia line. The lower intercept of 391 ± 33 Ma ($n = 27$, MSWD = 1.2) possibly indicates the age of metamorphism in this rock. However, since it is not clear if all analyses belong to a unique source, this age must be carefully taken.

Sample JG46 is a garnet-bearing amphibolite from which 177 detrital zircon spots (cores and rims) were analysed (Figures 6E, 7F and 9B). The core ages (considering the cut-off at 800 Ma) span continuously from 1206 to 421 Ma, defining a peak population of 845 Ma (green ellipses in Figure 7F). The three youngest overlapping analyses yield an age of 414 ± 8.2 Ma (MSWD = 2.8) which is interpreted as the maximum depositional age for this sample. The zircon rim analyses ($n = 42$) constitute a discordia line whose lower intercept defines an age of 398 ± 77 Ma (MSWD = 1), which is considered to represent the best approximation to the age of metamorphism recorded in this rock. However, the same cautious interpretation on the age of metamorphism expressed for the sample JG18 applies here too.

4.4. Mylonitized granitic intrusion JG30

Sample JG30 is from an 8 to 10 cm-thick granitic layer emplaced parallel to the mylonitic foliation of an amphibolite of the Etna Unit (Figure 5D). The granitic sill shows a protomylonitic fabric and the same kinematic sense of deformation as the host rock, suggesting their intrusion and deformation were syntectonic with respect to the M_2 - D_2 event.

From this sample 31 zircon grains were analysed, all with a Th/U ratio > 0.12 . Most of the analysed grains are discordant, including a poorly defined group that exhibits flat HREE patterns (red colours in the concordia and REE diagrams of Figure 7G), interpreted as inherited metamorphic grains that crystallized in the presence of a garnet-rich paragenesis. A younger zircon group with typical igneous REE patterns contains high concentrations of U (from 440 to 2900 ppm), Th/U ratios ranging between 0.1 and 0.6 and shows less discordance as the age decreases (yellow-green patterns in Figure 7G). A weighted mean calculated from the three most concordant analyses yields an age of 191 ± 1.04 Ma (MSWD = 0.7;), which is considered to be the best approximation of the crystallization age of the granitic intrusion.

5. Geochemistry of the San Agustín Orthogneiss

Due to the regional relevance of the early Silurian (441.9 ± 3.6 Ma) San Agustín Orthogneiss, major and trace-

element analyses of samples JG09 and JG55 were additionally undertaken. For comparative purposes, samples of similar age and composition from the Acatlán Complex of southern Mexico (Ortega-Obregón *et al.* 2010) and the Chiapas Massif Complex of southeastern Mexico (Estrada-Carmona *et al.* 2012) are also presented. The geochemical data from the orthogneisses are tabulated in Supplementary Data 2.

Analysed samples JG09 and JG55 are subalkaline basalts in composition, calc-alkaline to tholeiitic with Mg# of 61.9 and 53.3, respectively (Figure 8A-B). Their poorly evolved compositions are similar to the most primitive within plate/MORB samples of the Acatlán Complex (Ortega-Obregón *et al.* 2010; Figure 8B). REE profiles show MORB-like patterns with a slight depletion in HREE (Figure 8D). Trace elements patterns (Figure 8C) show positive anomalies in the most mobile elements (such as Rb, Ba, K, and Sr), whereas some HSE's, such as Zr (and P in sample JG55), display negative anomalies. The apparently intact Nb indicates no crustal assimilation (Rollison 1993), suggesting that the mobile elements enrichment is related to secondary alteration (fluid percolation, weathering, etc). The negative anomalies in Zr and P, as well as the slightly positive and negative anomalies in Ti, are probably a reflection of zircon, apatite, and Ti-bearing phases crystal fractionation during protolith crystallization.

6. Discussion

The petrological descriptions of samples from the SJC, coupled with the U-Pb geochronology and geochemical data provided by this study point to the following sequence of events: 1) anorthositic-gabbroic magmatism at ca. 979-976 Ma (Viguera Suite) followed by a poorly constrained thermal event at ca. 920-880 Ma; 2) MORB-like magmatism at ca. 441 Ma (San Agustín Orthogneiss); 3) deposition of supracrustal rocks (Etna Unit) with maximum depositional ages of 422 and 414 Ma; 4) a poorly constrained middle to late Palaeozoic high-pressure amphibolite-facies metamorphic event around 391-398 Ma; and 5) the intrusion of granitic layers at ca. 191 Ma.

6.1. Origin and regional correlation of the Viguera Suite

The Viguera Suite crops out mainly along the western edge of the SJC (Figure 3). Apparently, its location, lithologies, and distribution suggest a link to the AMCG suite of the Oaxacan Complex (Oaxaquia), located 7 km west of the SJC (Figure 2; Cacaotepec anorthosite; Valencia-Morales 2017). However, LA-ICP-MS zircon analyses of anorthosite samples

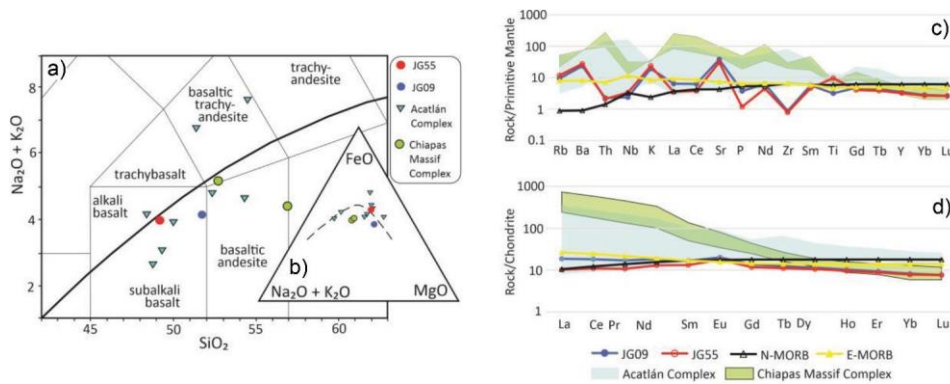


Figure 8. Geochemical data for the San Agustín Orthogneiss (samples JG55 and JG09). The data is plotted together with that from samples of similar composition and age from the Acatlán Complex of Southern Mexico (Ortega-Obregón *et al.* 2010, samples OL-336, OL-332, OL-217, OL-215, OL-221, OL-79, OL-78, and OL-42) and the Chiapas Massif Complex (Estrada-Carmona *et al.* 2012, samples CJ-66B and CJ-48). A) TAS grid for compositional classification. B) AFM (Alkalis- Σ FeO-MgO) plot showing poorly evolved tholeiitic-alkaline chemistry of the San Agustín Orthogneiss. C) Trace element diagram (spidergram). Values normalized to the primitive mantle of McDonough and Sun (1995). D) REE diagram showing MORB-like profiles for the San Agustín Orthogneiss protolith. Values normalized to the chondrite of McDonough and Sun (1995).

JG24 and JG42 yield concordant $^{206}\text{Pb}/^{238}\text{U}$ ages of ca. 979–976 Ma. This time range is considerably younger than the magmatic age of the AMCG suite documented in Oaxaquia, which is constrained between 1035 and 1010 Ma (Solari *et al.* 2003; Keppie *et al.* 2003; Cameron *et al.* 2004). Furthermore, it overlaps the Zapotecan (Grenville) granulite-facies metamorphic event in Oaxaquia at -1000–980 Ma (Lawlor *et al.* 1999; Weber and Köhler 1999; Solari *et al.* 2003, 2004; Keppie *et al.* 2003; Cameron *et al.* 2004; Weber *et al.* 2010).

Although the age of the Viguera Suite could be interpreted as indicative of the Zapotecan event in the Oaxacan Complex granulites rather than its protolith magmatic age, several lines of evidence, such as the zircon morphology, their low uranium contents which are not unique of metamorphic zircons but may also characterize zircons crystallized in basic (anorthositic) magmas (e.g., Rubatto and Gebauer 2000; Kaczmarek *et al.* 2008; Zeh *et al.* 2010), the > 0.1 Th/U ratios and REE patterns with a positive anomaly in Ce, a weak but present negative anomaly in Eu, and a gradual increase from LREE to HREE, are all indicative of a magmatic origin (Figure 7A–B; e.g., Hinton and Upton 1991). The magmatic chemistry of the zircons, on the other hand, might be expected to be present after metamorphic recrystallization, given that phases capable of partitioning elements such as Th and HREE are not really available in the mineralogically monotonous anorthositic rocks. However, this was not the case, since some zircon analyses from the Viguera Suite (samples JG50 and JG24) show altered metamorphic-related REE patterns with late-Tonian ages, suggesting that partitioning mineral phases were sufficiently available to change the typical-magmatic REE patterns in these zircons. The high degree of mylonitic

deformation that affects these anorthositic rocks has altered the original metamorphic or igneous textures, removing also any clue that could give insight into the origin of their zircons, for example, exsolution reactions from Fe-Ti oxides to produce zircon (e.g., Cisneros de León *et al.* 2017; Weber *et al.* 2020). The igneous origin is thus favoured, also in agreement with the apparent lack of relict granulite facies-mineralogy in the entire Viguera Suite. The only high-grade mineral observed was rutile, but this could be related to later metamorphic events (as in the San Agustín Orthogneiss, see below) or could be magmatic in origin. On a regional scale, the magmatic stage of the Viguera Suite could correlate with a 991 ± 4 Ma charnockite reported in the Guichicovi Complex (Weber and Köhler 1999), and/or with 988 ± 3 Ma pegmatites that crosscut the gneissic foliation in the Huiznopala Gneiss (Lawlor *et al.* 1999), as well as post-Zapotecan (ca. 981–963 Ma) pegmatitic dikes that intrude the Oaxacan Complex (Shchepetilnikova *et al.* 2015). The most feasible tectonic interpretation of this post-tectonic magmatism would be the relaxation phase or gravitational collapse of the Grenville-age Orogen. The presence of anorthosites in the Viguera Suite is in agreement with post-contractual models for the origin of massif anorthosites (e.g., McLelland *et al.* 2010).

Analysed zircon crystals belonging to anorthosite samples JG24 and JG50 of the Viguera Suite likely experienced Pb loss and/or zircon regrowth between ca. 920 and 880 Ma (Figure 6A, 6C, 7A, and 7C). Their REE patterns indicate that overgrowth and crystallization likely occurred in the presence of garnet, suggesting a deep metamorphic environment. This is not an isolated case, Weber *et al.* (2018, 2020) reported similar (ca. 920 Ma)

Table 2. Summary of possible correlative early Palaeozoic igneous and metamorphic units in Mexico, Central America, and the Andean regions of Colombia and Venezuela.

Basement unit	Dated rock/event	Rock/event age (Ma)	Interpreted tectonic setting	Main reference
San Agustín Orthogneiss, Sierra de Juárez Complex	Metagabbro	441.9 ± 3.6	MORB-like profile in Middle ocean spreading centre or a back-arc basin	This work
Etlá Unit, Sierra de Juárez Complex	Pelitic metasediments and metavolcanics Medium-grade metamorphism	ca. 422-414 (maximum depositional age) ca. 398-391	Back-arc basin formed between Oaxaquia rifted off the Colombian Grenvillian massifs, or basins followed the opening of the Rheic Ocean	This work
Acatlán Complex, southern Mexico	Bimodal magmatism and coeval sedimentation	470-440	Rifting in western Oaxaquia boundary followed by subduction-collisional events	Ortega-Gutiérrez <i>et al.</i> 2018 and references therein
Chiapas Massif, SE Mexico	Motozintla Suite	ca. 452-446	Rift environment of the nascent Rheic Ocean followed or arc magmatism	Estrada-Carmona <i>et al.</i> 2012; Weber <i>et al.</i> 2020
Altos Cuchumatanes and Chuacús Complex, Guatemala	Igneous intrusions	466-427	Rift magmatism and/or convergence tectonics	Ortega-Obregón <i>et al.</i> 2008; Solari <i>et al.</i> 2010, 2011, 2013; Juárez-Zúñiga <i>et al.</i> 2019
Mérida Andes, Venezuela	Igneous intrusions Sedimentation Magmatism, sedimentation, and metamorphism	500-465 472-452 452-415	Arc magmatism and orogenesis Extensional back-arc basin Contractional orogeny and basin inversion	Van der Lelij <i>et al.</i> 2016; Tazzo-Rangel <i>et al.</i> 2018
NW Colombian Andes	Granitoid orthogneisses and HP metamorphism	479-440	Ordovician magmatic arc	Martens <i>et al.</i> 2014
Santander Massif, Colombia	Igneous intrusions	456-413	Ordovician magmatic arc	Ordóñez-Carmona <i>et al.</i> 2006

metamorphic ages in zircon grains extracted from Grenville-age orthogneisses in the El Triunfo Complex (southern Chiapas), possibly related to post-Grenville major tectonic boundaries activity (Weber *et al.* 2020). However, such ages have not been reported in the Novillo, Huiznopala, and the Oaxacan Complex, suggesting it may be confined to the Grenville-age blocks east of the Oaxaca fault. This would imply a different post-Grenvillian tectonic evolution for a hypothetical eastern Oaxaquia, currently separated from western Oaxaquia by the mylonitic domain of the SJC.

6.2. Origin and regional correlation of the San Agustín Orthogneiss

The San Agustín Orthogneiss is probably the most abundant mafic rock exposed in the SJC. The age of 441.9 ± 3.6 Ma obtained for the crystallization of its protolith documents a lower Silurian magmatic episode. The MORB-like profiles shown by their REE patterns suggest an origin at a mid-ocean or back-arc basin spreading ridge.

Based on its age, many potential correlatives for the orthogneiss exist in southern Mexico, Central America, and northern South America (see Table 2 for a summary).

For example, in the Acatlán Complex (southern Mexico), lower Palaeozoic magmatism is represented by variable deformed granitic and mafic rocks dated between 470 and 440 Ma (Ortega-Gutiérrez *et al.* 1999; Sánchez-Zavala *et al.* 2004). These have been interpreted as a bimodal rift-related suite (Malone *et al.* 2002; Miller *et al.* 2007; Keppie *et al.* 2004, 2006, 2008, 2010; Morales-Gómez *et al.* 2008; Ortega-Obregón *et al.* 2009, 2010), although there is also evidence for a subduction-related origin (Talavera-Mendoza *et al.* 2005; Vega-Granillo *et al.* 2009; Juárez-Zúñiga *et al.* 2019).

The El Triunfo Complex (Chiapas, SE Mexico), is intruded by the Motozintla magmatic suite between 452 and 446 Ma (Estrada-Carmona *et al.* 2012; González-Guzmán *et al.* 2016; Weber *et al.* 2018, 2020). In Guatemala, the Rabinal Suite, Altos Cuchumatanes and Chuacús Complex contain magmatic rocks with ages in the range 466 to 427 Ma (Ortega-Obregón *et al.* 2008; Ratschbacher *et al.* 2009; Solari *et al.* 2010, 2011, 2013; Juárez-Zúñiga *et al.* 2019). The Chiapas-Guatemala magmatic segment has been interpreted as the product of crustal melting in a rifting environment (Ortega-Obregón *et al.* 2008; Solari *et al.* 2010; Estrada-Carmona *et al.* 2012). However, as in the Acatlán Complex, there is also geologic, geochemical and isotopic evidence for

a subduction setting (Estrada-Carmona *et al.* 2012; Weber *et al.* 2018, 2020; Juárez-Zúñiga *et al.* 2019). Bimodal magmatism in both the Acatlán Complex and the Chiapas-Guatemala block is linked to the separation of the Avalonian terranes from northwestern Gondwana during the opening of the Rheic Ocean (e.g., Keppie and Ramos 1999; Murphy *et al.* 2006; Ortega-Obregón *et al.* 2008, 2009, 2010; Solari *et al.* 2010; Keppie *et al.* 2004, 2006, 2008, 2010; Nance *et al.* 2012), whereas arc magmatism would be coeval with the Famatinian Arc in Colombia and Venezuela (Weber *et al.* 2018).

Exposures of Ordovician-Silurian magmatism can also be traced to northwestern South America. Van der Lelij *et al.* (2016) and Tazzo-Rangel *et al.* (2018) report arc magmatism and orogenic stages between 500 and 465 Ma in the Mérida Andes (Venezuela), followed by extensional back-arc sedimentation between 472 and 452 Ma. The last stage recorded is a contractional tectonic phase, during which metamorphism and magmatism occurred between 452 and 415 Ma. The La Miel Unit in the Anaconda terrane of the Colombian Andes, on the other hand, includes granitoid orthogneisses with ages in the 479-440 Ma range (Villagómez *et al.* 2011; Martens *et al.* 2014), as well as high-pressure amphibolite-facies garnet, kyanite, and staurolite-bearing schists (Bustamante and Juliani 2011). Similarly, Ordóñez-Carmona *et al.* (2006) documented intrusion ages ranging between 456 and 413 Ma in the Santander Plutonic Group (Santander Massif).

If the San Agustín Orthogneiss is considered autochthonous with respect to Oaxaquia in palaeogeographic reconstructions for western Gondwana and Pangea (e.g., Elías-Herrera and Ortega-Gutiérrez 2002; Pindell and Kennan 2009; Spikings *et al.* 2016; Weber *et al.* 2018), the SJC would be located between Oaxaquia and the northern South American Gondwanan-type terranes (Figure 10A-B, location 1). In such a position, correlation with the Acatlán Complex would not be feasible since the two terranes would lie on opposite sides of Oaxaquia. The northern Gondwana paleo-position of the Chiapas-Guatemala segment on the Rheic Ocean margin would also be disconnected from the SJC. Geochemical data available for the San Agustín Orthogneiss together with the considered autochthonous position (with respect to Oaxaquia) and the presence of related supracrustal rocks (Etna Unit) suggest an origin in a back-arc setting located between Oaxaquia and the South American terranes. This interpretation would allow a southwestward prolongation of the back-arc magmatic setting of the Venezuelan Mérida Andes through the SJC or a connection between the SJC and the South American terranes in the Tahamí/Anaconda terranes or the Santander Massif. On the other hand, an allochthonous origin for the San Agustín Orthogneiss would point to the

Chiapas-Guatemala block as the best candidate for correlation, in agreement with Jurassic southward translation of the SJC and Yucatan block to their current positions (Figure 10, location 2).

6.3. Origin and regional correlation of the Etna unit

The protoliths of the Etna Unit encompass pelitic, as well as mafic clastic and/or volcano-sedimentary lithologies. The scarcity of outcrops, and the overprinting of the primary stratigraphic relationships by the Jurassic mylonitization, hinder the interpretation of a reliable tectonosedimentary setting for this unit. However, the apparent presence of volcano-sedimentary protoliths suggests an arc-related (arc or backarc) tectonosedimentary setting. Detrital core-zircon populations in samples JG18 (pelitic schist) and JG46 (amphibolite) suggest maximum depositional ages of 422 Ma and 414 Ma respectively. Although the younger analysed zircon rims (assuming most of them represent the effect of overprinted metamorphism) are overlapping the younger core analyses in both samples, it is not assumed that the zircon cores were reset with metamorphism. Thus, the zircon cores are interpreted to represent a reliable detrital source and, consequently, the deposition of the Etna Unit is considered to have occurred after the late Silurian-Lower Devonian. If so, a relatively short interval separates the maximum depositional ages of the Etna Unit and the protolith crystallization age of the San Agustín Orthogneiss (ca. 441 Ma), indicating a nearly coeval origin for the two lithological units. On the other hand, the lower intercept of zircon-rim analyses indicates a poorly constrained metamorphic age of 391-398 Ma. If this is true, it also defines the minimum age for the Etna Unit deposition. This implies a fast process of deposition and inhumation of the basin. More data are required to establish a more reliable age of the pre-mylonitic metamorphism present in the SJC.

A distinctive feature of the zircon-cores from samples of the Etna Unit is the abundance of detrital sources in the ca. 1000-400 Ma age range and the scarcity of Mesoproterozoic ones (> 1 Ga). Both samples share provenance groups that can be found in Gondwanan-type terranes (Figure 7E-F and 9A-B). Mesoproterozoic to early Neoproterozoic (1.4 to 0.9 Ga) ages are typical of Grenvillian peri-Gondwanan terranes, such as Oaxaquia in Mexico (e.g., Solari *et al.* 2014), or the Santander Massif and the Sierra Nevada de Santa Marta in South America (e.g., Restrepo-Pace *et al.* 1997; Restrepo-Pace and Cediél 2010). Possible sources for the ca. 900 to 500 Ma detrital provenance groups exist in the Goiás Magmatic Arc (e.g., Matteini *et al.* 2010) and the Panafrikan/Brazilian terranes (e.g., Rino *et al.* 2008). The youngest detrital group in both samples

with ages between ca. 500 and 412 Ma could represent detritus derived from eroded Famatinian arc-related provinces in W and NW Gondwana and/or the bimodal suites in southern Mexican terranes. In contrast with the amphibolite JG46, this population is the most abundant one in the schist JG18. The scarcity of Mesoproterozoic (or older), and the abundance of Neoproterozoic-Devonian (1000-400 Ma) detritus in the Etna Unit, differs somewhat from other nearby metasedimentary units that usually display strong Mesoproterozoic signatures and weak Neoproterozoic and early-middle Palaeozoic populations (Figure 9). Examples of these can be found in the Jocote and Custepec units of the Chiapas Massif Complex (southeastern Mexico; Figure 1B; Weber *et al.* 2007, Weber *et al.* 2008; González-Guzmán *et al.* 2016), and from the Baldy unit in the Maya Mountains of Belize (Martens *et al.* 2010). Similar inheritance patterns to those of the Etna Unit can be found in the Cosoltepec Formation of the Acatlán Complex (e.g., Talavera-Mendoza *et al.* 2005; Figure 1B) but differ by the presence of Meso and Paleoproterozoic ages and older (Figure 9H). To date, the metasedimentary units that best match with the Etna Unit with respect to their detrital zircon populations are found in the Chuacús Complex in Guatemala (Solari *et al.* 2011; Maldonado 2018b; Figure 9E-F), likely suggesting a close paleo-position for both lithotectonic units in northwestern Gondwana (Figure 10).

Assuming an autochthonous position for the Etna Unit relative to Oaxaquia, two implications are noted: (1) the previous exhumation of the Viguera Suite and the San Agustín Orthogneiss protolith upon which the Etna unit was deposited; and (2) the development of a basin between Oaxaquia and the South American Grenvillian terranes (Santa Marta, Santander Massif, etc.; Figure 10A, location 1). These implications suggest a back-arc basin tectonic off-setting for the Etna Unit, consistent with the presence of the lower Silurian MORB-like San Agustín Orthogneiss.

Assuming an allochthonous model for the Etna Unit (SJC, Figure 10, location 2), on the other hand, permits correlation with the Chiapas Massif Complex and a forearc tectonosedimentary setting following initial rifting of the Rheic Ocean.

6.4. Role of the Pre-Mesozoic metamorphism $M_1 + D_1$

The entire sequence of rocks exposed in the SJC records a metamorphic event estimated to have occurred in the high-pressure amphibolite facies. This interpretation is based on the presence of rutile (without pyroxene or its relicts) in the metagabbroic San Agustín Orthogneiss, the Grt-Hbl-Pl-Qtz paragenesis in amphibolites of the Etna Unit, and the presence of the Grt-Ky/St-Rt association in the pelitic schist of

the Etna Unit. The proposed metamorphic conditions probably occurred in a contractional (accretional or subduction) tectonic setting, consistent with the structural characteristics observed in the SJC.

Depending on whether an autochthonous or allochthonous palaeogeographic position is assumed, there are two likely positions and geodynamic scenarios for the SJC within the NW Gondwana realm. In the first case, Oaxaquia would have moved away from the NW corner of Gondwana during the Late Ordovician-early Silurian, producing magmatism and sedimentation in an extensional back-arc setting. It would then have moved back, resulting in metamorphism and deformation in a compressive setting. The most likely correlative metamorphic events, assuming the lower intercept age of the zircon rims analysed in the Etna Unit in this work (391-398 Ma), would be those described in northern South America: (1) the contractional phase that resulted in metamorphism in the Venezuelan Mérida Andes between 452 and 415 Ma (Van der Lelij *et al.* 2015; Tazzo-Rangel *et al.* 2016); and (2) the metamorphic phase of the La Miel orthogneisses in Colombia's Central Cordillera, which constitutes a potential correlative based on similar mineral metasedimentary associations (Bustamante and Juliani 2011; Martens *et al.* 2014) and its poorly constrained age between 390 and 255 Ma (Martens *et al.* 2014 and references therein). In the second one (allochthonous case), the tectonic setting suggested for the SJC lithologies is a forearc of the Rheic Ocean bordering NW Gondwana. In such a setting, the metamorphic episode could be related to that described in El Triunfo Complex, southeastern Mexico (Chiapas), which is thought to have developed in a subduction complex in northeastern Gondwana at ca. 438 Ma (González-Guzmán *et al.* 2016).

7. Conclusions

The SJC is composed of three lithological units. The oldest is a gabbroic-anorthositic suite (Viguera Suite) dated between 979-976 Ma. It lacks granulitic metamorphic relicts and was probably intruded into the Oaxaquia-type crust during a syntectonic or posttectonic phase of the Grenville orogeny. It also contains evidence for an uncertain ca. 920-880 Ma thermal perturbation.

From the lower Silurian to Lower Devonian, the SJC recorded MORB-like magmatism and sedimentation (San Agustín Orthogneiss and Etna Unit). This event could be linked either to a back-arc setting between Oaxaquia (Mexico) and Grenville-age peri-Gondwanan blocks (today exposed in northern South America) (Figure 10A, location 1) or to a continental margin environment along northern Gondwana during the opening of the Rheic Ocean, thus

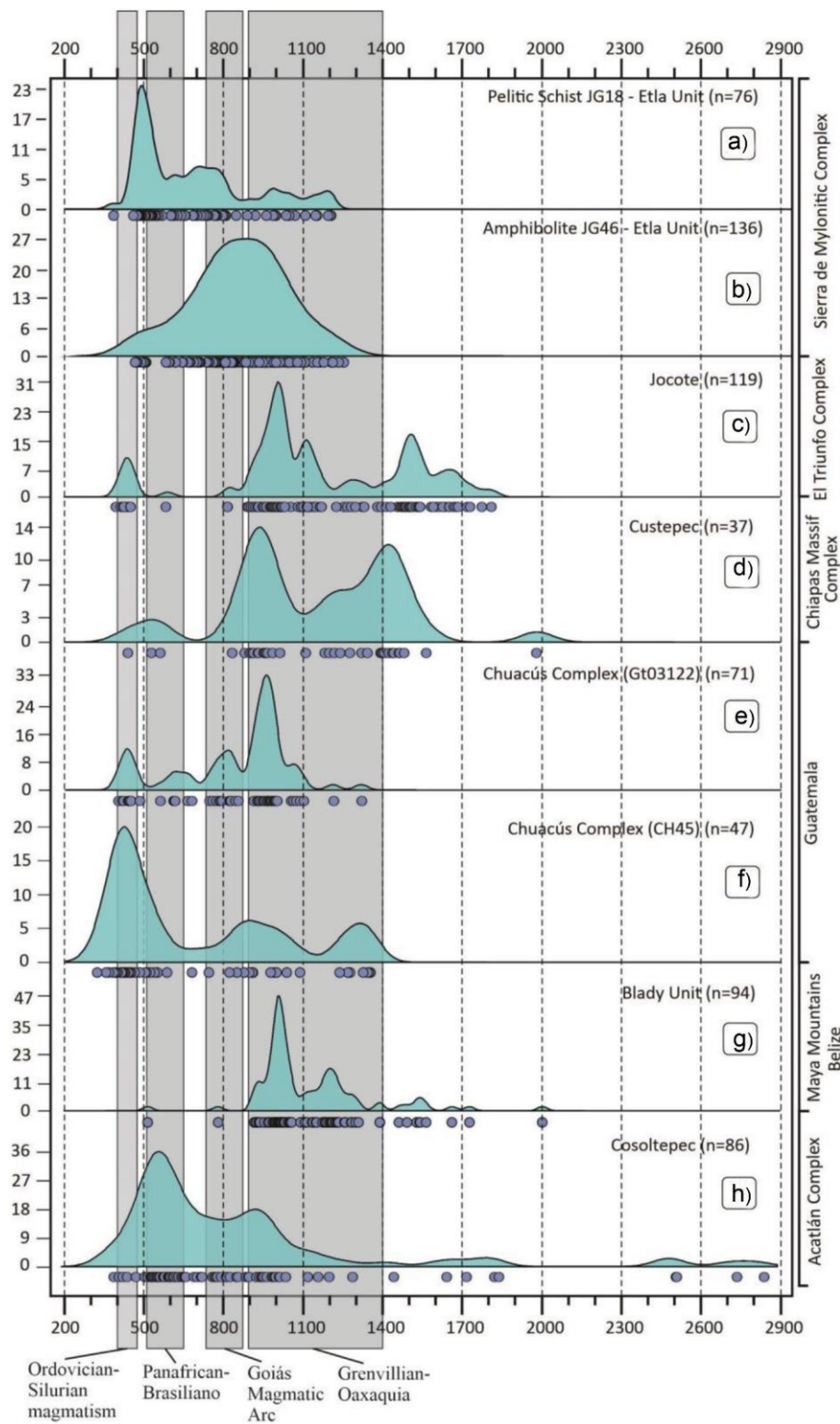


Figure 9. Kernel density estimator diagrams for comparing the detritus provenance of metasedimentary units in southern Mexico and Central America. A) Pelitic schist JG18 from the Etna Unit (this work). B) Amphibolite JG46 from the Etna Unit (this work). C) Jocote Unit, samples CB64, SR05 (Weber *et al.* 2008) and R0907 (González-Guzmán *et al.* 2016). D) Custepec Unit, samples CB45 and CB47 (Weber *et al.* 2007, 2008). E) Chuacús Complex (sample Gt03122, Solari *et al.* 2009). F) Chuacús Complex (sample CH45, Maldonado 2018b). G) Baldy unit (sample BZ03, Martens *et al.* 2010). H) Cosoltepec Fm. (sample ACA-51, Talavera-Mendoza *et al.* 2005).

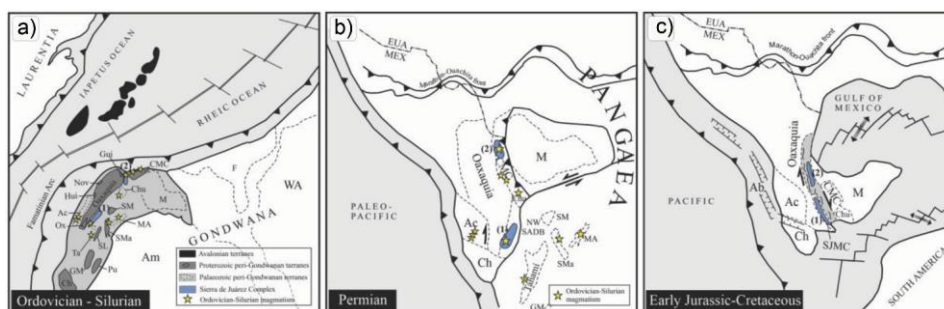


Figure 10. Palaeogeographic model showing the two suggested locations of the SJC in: A) the NW peri-Gondwanan corner during the early Palaeozoic, B) in the Pangea supercontinent during the late Palaeozoic, and C), during the rift-drift stage of Pangea in Jurassic-Cretaceous times. Abbreviations: Ac, Acatlán Complex; Ox, Oaxacan Complex; Hui, Huiznopala Gneiss; Gui, Guichicovi Complex; CMC, Chiapas Massif Complex; M, Maya Block; Chu, Chuacús Complex; SM, Santa Marta; Sma, Santander Massif; SL, Serranía de San Lucas; Pu, Putumayo; GM, Garzón Massif; Ch, Chortis Block. Model-based on Elías-Herrera and Ortega-Gutiérrez *et al.* (2002); Weber *et al.* (2007), Weber *et al.* (2018)); Spikings *et al.* (2015), Spikings *et al.* (2016)); Van der Lelij *et al.* (2016); Tazzo-Rangel *et al.* (2018); Maldonado *et al.* (2018) .

being potentially correlative with the Chiapas Massif Complex and the El Triunfo Complex (Figure 10A, location 2). Detrital zircon provenance patterns in pelitic schist of the Etna Unit suggest a closer source in the Chuacús Complex of Guatemala at the NW corner of Gondwana.

The lithological units of the SJC were subject to a metamorphic event with a poorly constrained age between 398–391 Ma. Petrological characteristics indicate high-pressure amphibolite-facies conditions. This event probably occurred in a contractional setting in which Oaxaquia was emplaced over the back-arc early-Palaeozoic units (SJC) and against the South American Grenville-age blocks. Alternatively, it could be related to the late Palaeozoic Maya block and Oaxaquia amalgamation during the final stages of the assembly of westernmost Pangea.

The final crustal event recorded in the SJC is a dextral mylonitic deformation that occurred between the age of the granitic sill dated in this study (191 ± 1.04 Ma) and the ages obtained by Alaniz-Álvarez *et al.* (1996) (ca. 165 Ma). Development of this major shear zone was probably related to the opening of the Gulf of Mexico after the onset of the Pangea break-up (e.g., Pindell and Kennan 2009) and it is responsible for the present arrangement of Proterozoic and Palaeozoic blocks in Mexico (Figure 10C).

The data presented here allow us to interpret the SJC as a Tonian-early Palaeozoic terrane with a mid-Jurassic mylonitization overprint. For this reason, we propose that the name Sierra de Juárez Mylonitic Complex (Sedlock *et al.* 1993; Alaniz-Álvarez *et al.* 1996) be replaced by the ‘Sierra de Juárez Complex’ to encompass the entire stratigraphic, structural, and lithological features present in this lithotectonic block.

Acknowledgments

The first author acknowledges the Consejo Nacional de Ciencia y Tecnología (CONACyT) for granting him Masters and PhD scholarships. This contribution was financed by the following projects: CONACyT 164454 “Sistemas Tectónicos de México, Origen y Evolución” and PAPIIME, UNAM, PE101615 “Leyendo la Historia de la Tierra: el Poder de la Observación en el Estudio de las Rocas a Macro y Microescala”, both granted to Fernando Ortega Gutiérrez; PAPIIT-DGAPA, UNAM, IN101520, granted to Luigi A. Solari; and a DGAPA-UNAM Postdoc scholarship granted to Roberto Maldonado. We also thank J. Tomás Vázquez Ramírez for thin section preparation; Consuelo Macías Romo, Manuel Albarrán Murillo and Teodoro Hernández Treviño for helping with mineral separation; Carlos Ortega Obregón for acquisition of geochronologic data; Jazmín A. López Díaz and Ma. Concepción Arredondo de la Rosa for help in zircon CL photomicrography; Patricia Girón and Rufino Lozano for major element determinations, and Ofelia Pérez Arvizu for trace element determinations. The first author also thanks Mónica G. Ramírez Calderón and Sandra Guerrero Moreno for early comments that helped to improve this work, and to Daniel Villanueva Lascurain for language revision. The Editorial handling of Dr. R. Stern, as well as the careful journal reviews of Dr. B. Weber as well as two anonymous reviewers are also acknowledged, because they improved the clarity of the concepts described in this manuscript.

Disclosure statement

The first author and co-authors declare that they have no financial interests or personal relationships that could have influenced the work reported in this paper.

Funding

This work was supported by the Consejo Nacional de Ciencia y Tecnología [164454]; PAPIIT-DGAPA, UNAM [IN101520]; PAPIIME, UNAM [PE101615].

ORCID

Guillermo Espejo-Bautista  <http://orcid.org/0000-0001-9206-5108>

Fernando Ortega-Gutiérrez  <http://orcid.org/0000-0002-7475-1216>

Luigi A. Solari  <http://orcid.org/0000-0002-9769-6846>

Roberto Maldonado  <http://orcid.org/0000-0001-5086-6740>

References

- Alaniz-Álvarez, S.A., Nieto-Samaniego, A.F., and Ortega-Gutiérrez, F., 1994, Structural evolution of the Sierra Juárez Mylonitic Complex: State of Oaxaca, Mexico: *Revista Mexicana De Ciencias Geológicas*, v. 11, p. 147-156.
- Alaniz-Álvarez, S.A., van der Heyden, P., Nieto-Samaniego, A.F., and Ortega-Gutiérrez, F., 1996, Radiometric and kinematic evidence for middle jurassic strike-slip faulting in Southern Mexico related to the opening of the gulf of Mexico: *Geology*, v. 24, p.443-446. no. 5 [10.1130/0091-7613\(1996\)024<0443:RAKEFM>2.3.CO;2](https://doi.org/10.1130/0091-7613(1996)024<0443:RAKEFM>2.3.CO;2)
- Ángeles-Moreno, E., 2006, Petrografía, geología estructural y geocronología del borde noroccidental del Terreno Cuicateco, Sierra Mazateca, Estado de Oaxaca, México [M. Sc. thesis], México, Universidad Nacional Autónoma de México, p. 208.
- Bustamante, A., and Juliani, C., 2011, Unravelling an antique subduction process from metamorphic basement around Medellín city: Central Cordillera of Colombian Andes: *Journal of South American Earth Sciences*, v. 32, p. 210-221.
- Cameron, K.L., Lopez, R., Ortega-Gutiérrez, F., Solari, L.A., Keppie, J.D., and Schulze, C., 2004, U-Pb geochronology and Pb isotopic compositions of leached feldspars: Constraints on the origin and evolution of grenville rocks from eastern and southern Mexico: *Geological Society of America Memoir*, v. 197, p. 755-769.
- Campos-Enríquez, J.O., Belmonte-Jiménez, S.I., Keppie, J.D., Ortega-Gutiérrez, F., Arzate, J.A., Martínez-Silva, J., and Martínez-Serrano, R.G., 2010, Gravity and magnetic survey of the Oaxaca city region: cenozoic horst-and-graben structure superimposed on the Oaxaca-Juarez terrane boundary, southern Mexico: *Journal of South American Earth Sciences*, v. 29, p. 572-585. no. 3 [10.1016/j.jsames.2009.11.002](https://doi.org/10.1016/j.jsames.2009.11.002)
- Cardona, M.A., Cordani, U.G., and MacDonald, W.D., 2006, Tectonic correlation of pre-Mesozoic crust from the northern termination of the Colombian Andes, Caribbean region: *Journal of South American Earth Sciences*, v. 21, p. 337-354. no. 4 [10.1016/j.jsames.2006.07.009](https://doi.org/10.1016/j.jsames.2006.07.009)
- Carfantan, J.C., 1983, Les ensembles géologiques du mexique meridional. Evolution géodynamique durante et le Cénozoïque: *Geofísica Internacional*, v. 22, p. 9-37.
- Centeno-García, E., 1988, Evolución estructural de la falla de Oaxaca durante el Cenozoico [M.Sc. thesis], México, Universidad Nacional Autónoma de México, p. 156 p.
- Cisneros de León, A., Weber, B., Ortega-Gutiérrez, F., González-Guzmán, R., Maldonado, R., Solari, L., Schaaf, P., and Manjarrez-Juárez, R., 2017, Grenvillian massif-type anorthosite suite in Chiapas, Mexico: Magmatic to polymetamorphic evolution of anorthosites and their Ti-Fe ores: *Precambrian Research*. v. 195, p. 203-226. [10.1016/j.precamres.2017.04.028](https://doi.org/10.1016/j.precamres.2017.04.028)
- Coombs, H.E., 2016, Geochemical and geochronological constraints on terrane definition in Mexico [Ph.D. thesis], UK, Cardiff University, p. 349 p.
- Delgado-Argote, L.A., 1989, Regional implications of the jurassic-cretaceous volcanosedimentary cuicateco terrane, Oaxaca, Mexico: *Geofísica Internacional*, v. 28-5, p. 939-973.
- Dickinson, W.R., and Lawton, T.F., 2001, Carboniferous to Cretaceous assembly and fragmentation of Mexico: *Geological Society of America Bulletin*, v. 113, 1142-1160. [10.1130/0016-7606\(2001\)113<1142:CTCAAF>2.0.CO;2](https://doi.org/10.1130/0016-7606(2001)113<1142:CTCAAF>2.0.CO;2)
- Eliás-Herrera, M., and Ortega-Gutiérrez, F., 2002, Caltepec fault zone: an early permian dextral transpressional boundary between the proterozoic oaxacan and paleozoic Acatlán complexes, southern Mexico, and regional tectonic implications: *Tectonics*, v. 21, p. 14-18. [10.1029/2000TC001278](https://doi.org/10.1029/2000TC001278)
- Estrada-Carmona, J., Weber, B., Martens, U., and López-Martínez, M., 2012, Petrogenesis of ordovician magmatic rocks in the southern chiapas massif complex: Relations with the early Paleozoic magmatic belts of northwestern Gondwana: *International Geology Review*, v. 54, p. 1918-1943. [10.1080/00206814.2012.685553](https://doi.org/10.1080/00206814.2012.685553)
- Fitz-Díaz, E., Lawton, T.F., Juárez-Arriaga, E., and Chávez-Cabello, G., 2018, The cretaceous-paleogene Mexican orogen: structure, basin development, magmatism and tectonics: *Earth-Science Reviews*, v. 183, 56-84. [10.1016/j.earscirev.2017.03.002](https://doi.org/10.1016/j.earscirev.2017.03.002)
- Gehrels, G.E., Valencia, V.A., and Ruiz, J., 2008, Enhanced precision, accuracy, efficiency, and spatial resolution of U-Pb ages by laser ablation-multicollector-inductively coupled plasma-mass spectrometry: *Geochemistry Geophysics Geosystems*, v. 9, 1-13. [10.1029/2007GC001805](https://doi.org/10.1029/2007GC001805)
- González-Guzmán, R., Weber, B., Manjarrez-Juárez, R., Cisneros de León, A., Hecht, L., and Herguera-García, J.C., 2016, Provenance, age constraints and metamorphism of Ediacaran metasedimentary rocks from the El Triunfo Complex (SE Chiapas, México): Evidence for Rodinia breakup and Iapetus active margin: *International Geology Review*, v. 58, 2065-2091. no. 16 [10.1080/00206814.2016.1207208](https://doi.org/10.1080/00206814.2016.1207208)
- González-Ramos, A., Sánchez-Rojas, L.E., Mota-Mota, S., Arceo Y Cabrilla, F.A., Onofre-Espinosa, L., Zárate-López, J., and Soto-Araiza, R., 2000, Carta Geológico-Minera Oaxaca E14-9, scale 1:250,000: Secretaría de Economía, Servicio Geológico Mexicano, Pachuca, Hidalgo, Mexico, first ed, 1 sheet.
- Grimes, C.B., John, B.E., Cheadle, M.J., Mazdab, F.K., Wooden, J. L., Swapp, S., and Schwartz, J.J., 2009, On the occurrence, trace element geochemistry, and crystallization history of zircon from in situ ocean lithosphere: *Contribution to Mineralogy and Petrology*, v. 158, 757-783. [10.1007/s00410-009-0409-2](https://doi.org/10.1007/s00410-009-0409-2)
- Hinton, R.W., and Upton, B.G.J., 1991, The chemistry of zircon: Variations within and between large crystals from syenite and alkali basalt xenoliths: *Geochimica et Cosmochimica Acta*, v. 55, p, 3287-3302. [10.1016/0016-7037\(91\)90489-R](https://doi.org/10.1016/0016-7037(91)90489-R)
- Juárez-Zúñiga, S., Solari, L., and Ortega-Obregón, C., 2019, Ordovician to Silurian igneous rocks in southern Mexico and Central America: Geochronologic and isotopic constraints on paleogeographic models: *Journal of South American Earth Sciences*, v. 93, no. p, 462-479. [10.1016/j.jsames.2019.04.023](https://doi.org/10.1016/j.jsames.2019.04.023)
- Kaczmarek, M.A., Müntener, O., and Rubatto, D., 2008, Trace element chemistry and U-Pb dating of zircons from oceanic

- gabbros and their relationship with whole rock composition (Lanzo, Italian Alps): Contributions to Mineralogy and Petrology, v.155, 295-312. no. 3 [10.1007/s00410-007-0243-3](https://doi.org/10.1007/s00410-007-0243-3)
- Keppie, J.D., Dostal, J., Cameron, K.L., Solari, L., Ortega-Gutiérrez, F., and Lopez, R., 2003, Geochronology and geochemistry of Grenvillian igneous suites in the northern Oaxacan Complex, Southern Mexico: Tectonic Implications: Precambrian Research, v. 120, 365-389.
- Keppie, J.D., Dostal, J., and Li, J., 2018, Nd isotopic data indicating oaxacan source of ordoevician granitoids in the Acatlán Complex: Southern Mexico: Paleogeographic Implications: Tectonophysics, v. 740-741, p. 1-9.
- Keppie, J.D., Dostal, J., Murphy, J.B., and Nance, D., 2008, Synthesis and tectonic interpretation of the westernmost paleozoic variscan orogen in southern Mexico: from rifted rheic margin to active pacific margin: Tectonophysics, v.461, p. 277-290. [10.1016/j.tecto.2008.01.012](https://doi.org/10.1016/j.tecto.2008.01.012) 1-4
- Keppie, J.D., Dostal, J., Nance, D., Miller, B.V., Ortega-Rivera, A., and Lee, J.K.W., 2006, Circa 546 Ma plume-related dykes in the ~1 Ga Novillo Gneiss (east-central Mexico): Evidence for the initial separation of Avalonia: Precambrian Research, v. 147, p. 342-353. 3-4 [10.1016/j.precamres.2006.01.020](https://doi.org/10.1016/j.precamres.2006.01.020)
- Keppie, J.D., Nance, R.D., Ramos-Arias, M.A., Lee, J.K.W., Dostal, J., Ortega-Rivera, A., and Murphy, J.B., 2010, Late Paleozoic subduction and exhumation of Cambro-Ordovician passive margin and arc rocks in the northern Acatlán Complex, southern Mexico: Geochronological Constraints: Tectonophysics, v. 495, p. 213-229.
- Keppie, J.D., and Ortega-Gutiérrez, F., 2010, 1.3 Ga Oaxaquia (Mexico): Remnant of an arc/backarc on the northern margin of amazonia: Journal of South American Earth Sciences, v. 29, p. 21-27. no. 1 [10.1016/j.jsames.2009.07.001](https://doi.org/10.1016/j.jsames.2009.07.001)
- Keppie, J.D., and Ramos, V., 1999, Odyssey of terranes in the iapetus and rheic oceans during the Paleozoic: Geological Society of America Special Paper, v.336, p. 267-276.
- Keppie, J.D., Solari, L., Ortega-Gutiérrez, F., Ortega-Rivera, A., Lee, J.K.W., Lopez, R., and Hames, W.E., 2004, U-Pb and 40Ar/39Ar constraints on the cooling history of the northern oaxacan complex, southern Mexico: Tectonic implications: Geological Society of America Memoir, v. 197, p. 771-781.
- Lawlor, P.J., Ortega-Gutiérrez, F., Cameron, K.L., Ochoa-Camarillo, H., Lopez, R., and Sampson, D.E., 1999, U-Pb Geochronology, geochemistry, and provenance of the Grenvillian Huiznopala Gneiss of eastern Mexico: Precambrian Research, v. 94, p. 73-99. no. 1-2 [10.1016/S0301-9268\(98\)00108-9](https://doi.org/10.1016/S0301-9268(98)00108-9)
- Li, Z.X., Bogdanova, S.V., Collins, A.S., Davidson, A., De Waele, B., Ernst, R.E., Fitzsimons, I.C.W., Fuck, R.A., Gladkochub, D.P., Jacobs, J., Karlstrom, K.E., Lu, S., Natapov, L.M., Pease, V., Pisarevsky, S.A., Thrane, K., and Vernikovsky, V., 2008, Assembly, configuration, and break-up history of Rodinia: A synthesis: Precambrian Research, v.160, p. 179-210. no. 1-2 [10.1016/j.precamres.2007.04.021](https://doi.org/10.1016/j.precamres.2007.04.021)
- Lozano-Santa Cruz, R., and Bernal, J.P., 2005, Characterization of a new set of eight geochemical reference materials for XRF major and trace element analysis: Revista Mexicana De Ciencias Geológicas, v. 22, p. 329-344.
- Maldonado, R., 2018b, Origen y evolución del basamento metamórfico de la sierra de chuacús, guatemala y sus implicaciones tectónicas [Ph.D. thesis], México, Universidad Nacional Autónoma de México, p. 149.
- Maldonado, R., Ortega-Gutiérrez, F., and Ortiz-Joya, G.A., 2018, Subduction of Proterozoic to Late Triassic continental basement in the Guatemala suture zone: A petrological and geochronological study of high-pressure metagranitoids from the Chuacús complex: Lithos, v. 308-309, p. 83-108. [10.1016/j.lithos.2018.02.030](https://doi.org/10.1016/j.lithos.2018.02.030)
- Malone, J.R., Nance, R.D., Keppie, J.D., and Dostal, J., 2002, Deformational history of part of the acatlán complex: late ordovician-early silurian and early permian orogenesis in southern Mexico: Journal of South American Earth Sciences, v. 15, p. 511-524. no. 5 [10.1016/S0895-9811\(02\)00080-9](https://doi.org/10.1016/S0895-9811(02)00080-9)
- Martens, U., Weber, B., and Valencia, V.A., 2010, U/Pb geochronology of devonian and older paleozoic beds in the south-eastern maya block, Central America: its affinity with peri-gondwanan terranes: Geological Society of America Bulletin, v. 122, p. 815-829. no. 5-6 [10.1130/B26405.1](https://doi.org/10.1130/B26405.1)
- McDonough, W., and Sun, S., 1995, Composition of the Earth: Chemical Geology, v. 120, p. 223-253. no. 3-4 [10.1016/0009-2541\(94\)00140-4](https://doi.org/10.1016/0009-2541(94)00140-4)
- McLelland, J.M., Selleck, B.W., Hamilton, M.A., and Bickford, M. E., 2010, Late- to post-tectonic setting of some major Proterozoic anorthosite-mangerite-charnockite-granite (AMCG) suites: The Canadian Mineralogist, v. 48, p. 1025-1046. 4 [10.3749/canmin.48.4.729](https://doi.org/10.3749/canmin.48.4.729)
- Mendoza-Rosales, C.C., Centeno-García, E., Silva-Romo, G., Campos-Madrigal, E., and Bernal, J.P., 2010, Barremian rift-related turbidites and alkaline volcanism in southern Mexico and their role in the opening of the gulf of Mexico: Earth and Planetary Science Letters, v. 295, p. 419-434. no. 3-4 [10.1016/j.epsl.2010.04.020](https://doi.org/10.1016/j.epsl.2010.04.020)
- Miller, B.V., Dostal, J., Keppie, J.D., Nance, R.D., Ortega-Rivera, A., and Lee, J.K.W., 2007, Ordovician calc-alkaline granitoids in the Acatlán Complex, southern México: Geochemical and geochronologic data and implications for the tectonics of the Gondwanan margin of the Rheic Ocean: Geological Society of America Special Paper, v. 423, p. 465-475.
- Morales-Gómez, M., Keppie, J.D., Lee, J.K.W., and Ortega-Rivera, A., 2008, Paleozoic structures in the xayacatlán area, acatlán complex, southern Mexico: Transtensional rift- and subduction-related deformation along the margin of Oaxaquia: International Geology Review, v. 51, p. 279-303. no. 4 [10.1080/00206810802688659](https://doi.org/10.1080/00206810802688659)
- Mori, L., Gómez-Tuena, A., Cai, Y., and Goldstein, S.L., 2007, Effects of prolonged flat subduction on the Miocene magmatic record of the Central Trans-Mexican Volcanic Belt: Chemical Geology, v. 244, p. 452-473. no. 3-4 [10.1016/j.chemgeo.2007.07.002](https://doi.org/10.1016/j.chemgeo.2007.07.002)
- Murphy, J.B., Gutiérrez-Alonso, G., Nance, R.D., Fernandez-Suarez, J., Keppie, J.D., Quesada, C., Strachan, R.A., and Dostal, J., 2006, Origin of the Rheic Ocean: Rifting along a Neoproterozoic suture?: Geology, v. 34, p. 325-328. no. 5 [10.1130/G22068.1](https://doi.org/10.1130/G22068.1)
- Nance, R.D., Gutiérrez-Alonso, G., Keppie, J.D., Linnemann, U., Murphy, J.B., Quesada, C., Strachan, R.A., and Woodcock, N. H., 2012, A brief history of the Rheic Ocean: Geoscience Frontiers, v. 3, p. p. 125-135. no. 2 [10.1016/j.gsf.2011.11.008](https://doi.org/10.1016/j.gsf.2011.11.008)
- Ordóñez-Carmona, O., Restrepo, Á.J.J., and Martins, P.M., 2006, Geochronological and isotopic review of the pre-Devonian crustal basement of the Colombian Andes: Journal of South American Earth Sciences, v. 21, p. 372-382. no. 4 [10.1016/j.jsames.2006.07.005](https://doi.org/10.1016/j.jsames.2006.07.005)

- Ortega-Gutiérrez, F., Elías-Herrera, M., Morán-Zenteno, D.J., Solari, L., Weber, B., and Luna-González, L., 2018, The pre-Mesozoic metamorphic basement of Mexico, 1.5 billion years of crustal evolution: *Earth-Science Reviews*, v.183, p. 2-37. [10.1016/j.earscirev.2018.03.006](https://doi.org/10.1016/j.earscirev.2018.03.006)
- Ortega-Gutiérrez, F., Elías-Herrera, M., Reyes-Salas, M., Macías-Romo, C., and López, R., 1999, Late Ordovician-Early Silurian continental collisional orogeny in southern Mexico and its bearing on Gondwana-Laurentia connections: *Geology*, v. 27, p. 719-722. no. 8 [10.1130/0091-7613\(1999\)027<0719:LOESSC>2.3.CO;2](https://doi.org/10.1130/0091-7613(1999)027<0719:LOESSC>2.3.CO;2)
- Ortega-Gutiérrez, F., Ruiz, J., and Centeno-García, E., 1995, Oaxaquia, a Proterozoic microcontinent accreted to North America during the late Paleozoic: *Geology*, v. 23, p. 1127-1130. no. 12 [10.1130/0091-7613\(1995\)023<1127:OAPMAT>2.3.CO;2](https://doi.org/10.1130/0091-7613(1995)023<1127:OAPMAT>2.3.CO;2)
- Ortega-Gutiérrez, F., Solari, L.A., Ortega-Obregón, C., Elías-Herrera, M., Martens, U., Morán-Icál, S., Chiquin, M., Keppie, J.D., de León, T., and Schaaf, R., 2007, The Maya-Chortis Boundary: A tectonostratigraphic Approach: *International Geology Review*, v. 49, p. 996-1024. no. 11 [10.2747/0020-6814.49.11.996](https://doi.org/10.2747/0020-6814.49.11.996)
- Ortega-Obregón, C., Keppie, J.D., Murphy, J.B., Lee, J.K.W., and Ortega-Rivera, A., 2009, Geology and Geochronology of Paleozoic rocks in western Acatlán Complex, southern Mexico: Evidence for contiguity across an extruded high-pressure belt and constraints on Paleozoic reconstructions: *Geological Society of America Bulletin*, v. 121, p. 1678-1694. no. 11-12doi:[10.1130/B26597.1](https://doi.org/10.1130/B26597.1)
- Ortega-Obregón, C., Murphy, J.B., and Keppie, J.D., 2010, Geochemistry and Sm-Nd isotopic systematics of Ediacaran, sedimentary and bimodal igneous rocks in the western Acatlán Complex, southern Mexico: Evidence for rifting on the southern margin of the Rheic Ocean: *Lithos*, v. 114, p. 155-167. no. 1-2 [10.1016/j.lithos.2009.08.005](https://doi.org/10.1016/j.lithos.2009.08.005)
- Ortega-Obregón, C., Solari, L., Gómez-Tuena, A., Elías-Herrera, M., Ortega-Gutiérrez, F., and Macías-Romo, C., 2014, Permian-Carboniferous arc magmatism in southern Mexico: U-Pb dating, trace element and Hf isotopic evidence on zircons of earliest subduction beneath the western margin of Gondwana: *International Journal of Earth Sciences*, v. 103, p. 1287-1300. no. 5 [10.1007/s00531-013-0933-1](https://doi.org/10.1007/s00531-013-0933-1)
- Ortega-Obregón, C., Solari, L., Keppie, J.D., Ortega-Gutiérrez, F., Solé, J., and Morán-Icál, S., 2008, Middle-Late Ordovician magmatism and Late Cretaceous collision in the southern Maya block, Rabinal-Salamá area, central Guatemala: Implications for North America-Caribbean plate tectonics: *Geological Society of America Bulletin*, v. 120, p. 556-570. no. 5-6 [10.1130/B26238.1](https://doi.org/10.1130/B26238.1)
- Paton, C., Hellstrom, J., Paul, B., Woodhead, J., and Hergt, J., 2011, Iolite: Freeware for the visualisation and processing of mass spectrometric data: *J. Anal. At. Spectrom.*, v. 26, p. 2508-2518. no. 12 [10.1039/c1ja10172b](https://doi.org/10.1039/c1ja10172b)
- Paton, C., Woodhead, J.D., Hellstrom, J.C., Hergt, J.M., Greig, A., and Maas, R., 2010, Improved laser ablation U-Pb zircon geochronology through robust downhole fractionation correction: *Geochemistry, Geophysics, Geosystems*, v. 11, p. 1-36. [10.1029/2009GC002618](https://doi.org/10.1029/2009GC002618)
- Pérez-Gutiérrez, R., Solari, L.A., Gómez-Tuena, A., and Valencia, V. A., 2009, El terreno Cuicateco: ¿cuenca oceánica con influencia de subducción del Cretácico Superior en el sur de México? Nuevos datos estructurales, geoquímicos y geocronológicos: *Revista Mexicana De Ciencias Geológicas*, v. 26, p. 222-242.
- Petrus, J.A., and Kamber, B.S., 2012, VizualAge: A novel approach to laser ablation ICP-MS U-Pb geochronology data reduction: *Geostandards and Geoanalytical Research*, v. 36 no. 3, p. p. 247-270. [10.1111/j.1751-908X.2012.00158.x](https://doi.org/10.1111/j.1751-908X.2012.00158.x)
- Pindell, J.L., and Kennan, L., 2009, Tectonic evolution of the Gulf of Mexico, Caribbean and northern South America in the mantle reference frame: An update: *Geological Society, London, Special Publications*, v. 328, p. 1-55.
- Ratschbacher, L., Franz, L., Min, M., Bachmann, R., Martens, U., Stanek, K., Stübner, K., Nelson, B.K., Herrmann, U., Weber, B., López-Martínez, M., Jonckheere, R., Sperner, B., Tichomirowa, M., McWilliams, M.O., Gordon, M., Meschede, M., and Bock, P., 2009, The North American-Caribbean plate boundary in Mexico-Guatemala-Honduras: *Geological Society, London, Special Publications*, v. 328, p. 219-293.
- Restrepo-Pace, P.A., and Cediél, F., 2010, Northern South America basement tectonics and implications for paleocontinental reconstructions of the Americas: *Journal of South American Earth Sciences*, v. 29, p. 764-771. no. 4 [10.1016/j.jsames.2010.06.002](https://doi.org/10.1016/j.jsames.2010.06.002)
- Restrepo-Pace, P.A., Ruiz, J., Gehrels, G., and Cosca, M., 1997, Geochronology and Nd isotopic data of Grenville-age rocks in the Colombian Andes: New constraints for Late Proterozoic-Early Paleozoic paleocontinental reconstructions of the Americas: *Earth and Planetary Science Letters*, v. 150, p. 427-441. no. 3-4 [10.1016/S0012-821X\(97\)00091-5](https://doi.org/10.1016/S0012-821X(97)00091-5)
- Rino, S., Kon, Y., Sato, W., Maruyama, S., Santosh, M., and Zhao, D., 2008, The Grenvillian and Pan-African orogens: World's largest orogenies through geologic time, and their implications on the origin of superplume: *Gondwana Research*, v. 14, p. 51-72. no. 1-2 [10.1016/j.gr.2008.01.001](https://doi.org/10.1016/j.gr.2008.01.001)
- Rollison, H., 1993, Using geochemical data: Evaluation, presentation, interpretation, Kingdom, Longman Group UK Limited, p. 352.
- Rubatto, D., 2017, Zircon: The metamorphic mineral: *Reviews in Mineralogy and Geochemistry*, v. 83, p. 261-295. no. 1 [10.2138/rmg.2017.83.9](https://doi.org/10.2138/rmg.2017.83.9)
- Rubatto, D., and Gebauer, D., 2000, Use of cathodoluminescence for U-Pb zircon dating by ion microprobe: Some examples from the western Alps, ed., *Cathodoluminescence in Geosciences*, Springer, Berlin, 372-400.
- Rubatto, D., Hermann, J., Berger, A., and Engi, M., 2009, Protracted fluid-induced melting during Barrovian metamorphism in the Central Alps: Contributions to Mineralogy and Petrology, v. 158, p. 703-722. no. 6 [10.1007/s00410-009-0406-5](https://doi.org/10.1007/s00410-009-0406-5)
- Ruiz, J., Tosdal, R.M., Restrepo, P.A., and Murillo-Muñetón, G., 1999, Pb isotope evidence for Colombia-southern Mexico connections in the Proterozoic: *Geological Society of America Special Paper*, v. 336, p. 183-197.
- Sánchez-Zavala, J.L., Ortega-Gutiérrez, F., Keppie, J.D., Jenner, G.A., Belousova, E., and Macías-Romo, C., 2004, Ordovician and Mesoproterozoic zircons from the Tecomate Formation and Esperanza Granitoids, Acatlán Complex, southern Mexico: Local provenance in the Acatlán and Oaxacan complexes: *International Geology Review*, v. 46, p. 1005-1021. no. 11 [10.2747/0020-6814.46.11.1005](https://doi.org/10.2747/0020-6814.46.11.1005)

- Sedlock, R.L., Ortega-Gutiérrez, F., and Speed, R.C., 1993, Tectonostratigraphic terranes and tectonic evolution of Mexico: Geological Society of America Special Paper, v. 278, p. 153 p.
- Shchepetilnikova, V., Solé, J., Solari, L., and Abdullin, F., 2015, A geochronological and chemical zircon study of some pegmatite dikes and lenses from the central part (Ayoquezco-Ejutla) of the Oaxacan Complex, southern Mexico: *Revista Mexicana De Ciencias Geológicas*, v. 32, p. 123-143.
- Sláma, J., Košler, J., Condon, D.J., Crowley, J.M., Gerdes, A., Hanchar, J.M., Horstwood, S.A., Morris, G.A., Nasdala, L., Norberg, N., Schaltegger, U., Schoene, B., Tubrett, M.N., and Whitehouse, M.J., 2008, Plešovice zircon - A new natural reference material for U-Pb and Hf isotopic microanalysis: *Chemical Geology*, v. 249, p. 1-35. no. 1-2 [10.1016/j.chemgeo.2007.11.005](https://doi.org/10.1016/j.chemgeo.2007.11.005)
- Solari, L.A., García-Casco, A., Martens, U., Lee, J.K.W., and Ortega-Rivera, A., 2013, Late Cretaceous subduction of the continental basement of the Maya block (Rabinal Granite, central Guatemala): Tectonic implications for the geodynamic evolution of Central America: *Geological Society of America Bulletin*, v. 125, p. 625-639. no. 3-4 [10.1130/B30743.1](https://doi.org/10.1130/B30743.1)
- Solari, L.A., Gómez-Tuena, A., Ortega-Gutiérrez, F., and Ortega-Obregón, C., 2011, The Chuacús Metamorphic Complex, central Guatemala: Geochronological and geochemical constraints on its Paleozoic-Mesozoic evolution: *Geologica Acta*, v. 9, p. 329-350.
- Solari, L.A., González-León, C.M., Ortega-Obregón, C., Valencia-Moreno, M., and Rascón-Heimpel, M.A., 2018, The Proterozoic of NW Mexico revisited: U-Pb Geochronology and Hf isotopes of Sonoran rocks and their tectonic implications: *International Journal of Earth Sciences*, v. 107, p. 845-861. no. 3 [10.1007/s00531-017-1517-2](https://doi.org/10.1007/s00531-017-1517-2)
- Solari, L.A., Keppie, J.D., Ortega-Gutiérrez, F., Cameron, K.L., and Lopez, R., 2004, ~990 Ma peak granulitic metamorphism and amalgamation of Oaxaquia, Mexico: U-Pb zircon geochronological and common Pb isotopic data: *Revista Mexicana De Ciencias Geológicas*, v. 21, p. 212-225.
- Solari, L.A., Keppie, J.D., Ortega-Gutiérrez, F., Cameron, K.L., Lopez, R., and Hames, W.E., 2003, 990 and 1100 Ma Grenvillian tectonothermal events in the northern Oaxacan Complex, southern Mexico: Roots of an orogen: *Tectonophysics*, v. 365, p. 257-282. no. 1-4 [10.1016/S0040-1951\(03\)00025-8](https://doi.org/10.1016/S0040-1951(03)00025-8)
- Solari, L.A., Ortega-Gutiérrez, F., Elías-Herrera, M., Gómez-Tuena, A., and Schaaf, P., 2010, Refining the age of magmatism in the Altos Cuchumatanes, western Guatemala, by LA-ICPMS, and tectonic implications: *International Geology Review*, v. 52, p. 977-998. [10.1080/00206810903216962](https://doi.org/10.1080/00206810903216962)
- Solari, L.A., Ortega-Gutiérrez, F., Elías-Herrera, M., Ortega-Obregón, C., and Macías-Romo, C., 2014, Detrital provenance of the Grenvillian Oaxacan Complex, southern Mexico: A zircon perspective: *International Journal of Earth Sciences*, v. 103 no. 5, p. 1301-1315. [10.1007/s00531-013-0938-9](https://doi.org/10.1007/s00531-013-0938-9)
- Solari, L.A., Ortega-Gutiérrez, F., Elías-Herrera, M., Schaaf, P., Norman, M., Torres de León, R., Ortega-Obregón, C., Chiquín, M., and Ical, S.M., 2009, U-Pb zircon Geochronology of Paleozoic units in Western and Central Guatemala: Insights into the tectonic evolution of Middle America, James, K.H., Lorente, M.A., and Pindell, J.L., eds., *The origin and evolution of the Caribbean Plate*: Geological Society, London, Special Publications, v. 328, p. 295-313.
- Spikings, R., Cochrane, R., Villagomez, D., Van der Lelij, R., Vallejo, C., Winkler, W., and Beate, B., 2015, The geological history of northwestern South America: From Pangaea to the early collision of the Caribbean Large Igneous Province (290-75 Ma): *Gondwana Research*, v. 27, p. 95-139. no. 1 [10.1016/j.gr.2014.06.004](https://doi.org/10.1016/j.gr.2014.06.004)
- Spikings, R., Reitsma, M.J., Boekhout, F., Mišković, A., Ulianov, A., Chiaradia, M., Gerdes, A., and Schaltegger, U., 2016, Characterization of Triassic rifting in Peru and implications for the early disassembly of western Pangaea: *Gondwana Research*, v. 35, p. 124-143.
- Talavera-Mendoza, O., Ruiz, J., Gehrels, G.E., Meza-Figueroa, D. M., Vega-Granillo, R., and Campa-Uranga, M.F., 2005, U-Pb Geochronology on the Acatlán Complex and implications for the Paleozoic paleogeography and tectonic evolution of southern Mexico: *Earth and Planetary Science Letters*, v. 235, p. 682-699. no. 3-4 [10.1016/j.epsl.2005.04.013](https://doi.org/10.1016/j.epsl.2005.04.013)
- Taylor, R.J.M., Kirkland, C.L., and Clark, C., 2016, Accessories after the facts: Constraining the timing, duration and conditions of high-temperature metamorphic processes: *Lithos*, v. 264, p. 239-257. [10.1016/j.lithos.2016.09.004](https://doi.org/10.1016/j.lithos.2016.09.004)
- Tazzo-Rangel, M.D., Weber, B., González-Guzmán, R., Valencia, V.A., Frei, D., Schaaf, P., and Solari, L.A., 2018, Multiple metamorphic events in the Paleozoic Mérida Andes basement, Venezuela: Insights from U-Pb geochronology and Hf-Nd isotope systematics: *International Geology Review*, v. 61, p. 1557-1593. no. 13 [10.1080/00206814.2018.1522520](https://doi.org/10.1080/00206814.2018.1522520)
- Valencia-Morales, Y.T., 2017, *Geología y petrología de la Anortosita Cacaotepec, Complejo Oaxaqueño, sur de México* [M.Sc. thesis]: México, Universidad Nacional Autónoma de México, p. 139.
- Van der Lelij, R., Spikings, R., Ulianov, A., Chiaradia, M., and Mora, A., 2016, Paleozoic to Early Jurassic history of the northwestern corner of Gondwana, and implications for the evolution of the Iapetus, Rheic and Pacific Oceans: *Gondwana Research*, v. 31, p. 271-294. [10.1016/j.gr.2015.01.011](https://doi.org/10.1016/j.gr.2015.01.011)
- Vega-Granillo, R., Calmus, T., Meza-Figueroa, D., Ruiz, J., Talavera-Mendoza, O., and López-Martínez, M., 2009, Structural and tectonic evolution of the Acatlán Complex, southern Mexico: Its role in the collisional history of Laurentia and Gondwana: *Tectonics*, v. 28, p. 1-25. no. 4 [10.1029/2007TC002159](https://doi.org/10.1029/2007TC002159)
- Vega-Granillo, R., Sarmiento-Villagrana, A., Vidal-Solano, J.R., Araux-Sánchez, E., and Bourjac-de-Anda, A., 2020, Northern limit of Gondwana in northwestern Mexico from detrital zircon data: *Gondwana Research*, v. 83, p. 232-247.
- Vermeesch, P., 2018, Isoplot R: A free and open toolbox for geochronology: *Geoscience Frontiers*, v. 9, p. 1479-1493. no. 5 [10.1016/j.gsf.2018.04.001](https://doi.org/10.1016/j.gsf.2018.04.001)
- Villagómez, D., Spikings, R., Magna, T., Kammer, A., Winkler, W., and Beltrán, A., 2011, Geochronology, geochemistry and tectonic evolution of the Western and Central cordilleras of Colombia: *Lithos*, v. 125, p. 875-896. no. 3-4 [10.1016/j.lithos.2011.05.003](https://doi.org/10.1016/j.lithos.2011.05.003)
- Weber, B., González-Guzmán, R., Manjarrez-Juárez, R., de León, C., Martens, A., Solari, U., Hecht, L., and Valencia, L., 2018, Late Mesoproterozoic to Early Paleozoic history of metamorphic basement from the southeastern Chiapas

- Massif Complex, Mexico, and implications for the evolution of NW Gondwana: *Lithos*, v. 300-301, p. 177-199. [10.1016/j.lithos.2017.12.009](https://doi.org/10.1016/j.lithos.2017.12.009)
- Weber, B., and Hecht, L., 2003, Petrology and geochemistry of metagneous rocks from a Grenvillian basement fragment in the Maya block: the Guichicovi complex, Oaxaca, southern Mexico: *Precambrian Research*, v. 124, p. 41-67.
- Weber, B., Iriondo, A., Premo, W.R., Hecht, L., and Schaaf, P., 2007, New insights into the history and origin of the southern Maya block, SE México: U-Pb-SHRIMP zircon geochronology from metamorphic rocks of the Chiapas massif: *International Journal of Earth Sciences*, v. 96, p. 253-269. no. 2 [10.1007/s00531-006-0093-7](https://doi.org/10.1007/s00531-006-0093-7)
- Weber, B., and Köhler, H., 1999, Sm-Nd, Rb-Sr and U-Pb geochronology of a Grenville Terrane in southern Mexico: Origin and geologic history of the Guichicovi Complex: *Precambrian Research*, v. 96, p. 245-262.
- Weber, B., Scherer, E.E., Schulze, C., Valencia, V.A., Montecinos, P., Mezger, K., and Ruiz, J., 2010, U-Pb and Lu-Hf isotope systematics of lower crust from central-southern Mexico - Geodynamic significance of Oaxaquia in a Rodinia Realm: *Precambrian Research*, v. 182, p. 149-162.
- Weber, B., Schmitt, A.K., Cisneros de León, A., González-Guzmán, R., and Gerdes, A., 2020, Neoproterozoic extension and the Central Iapetus Magmatic Province in southern Mexico - New U-Pb ages, Hf-O isotopes and trace element data of zircon from the Chiapas Massif Complex: *Gondwana Research*, v. 88
- Weber, B., and Schulze, C.H., 2014, Early Mesoproterozoic (>1.4 Ga) ages from granulite basement inliers of SE Mexico and their implications on the Oaxaquia concept - Evidence from U-Pb and Lu-Hf isotopes on zircon: *Revista Mexicana De Ciencias Geológicas*, v. 31, p. 377-394.
- Weber, B., Valencia, V.A., Schaaf, P., Pompa-Mera, V., and Ruiz, J., 2008, Significance of provenance ages from the Chiapas Massif Complex (Southeastern Mexico): Redefining the Paleozoic basement of the Maya Block and its evolution in a Peri-Gondwanan realm: *Journal of Geology*, v. 116, p. 619-639. no. 6 [10.1086/591994](https://doi.org/10.1086/591994)
- Wiedenbeck, M., Allé, P., Corfu, F., Griffin, W.L., Meier, M., Oberli, F., Von Quadt, A., Roddick, J.C., and Spiegel, W., 1995, Three natural zircon standards for U-Th-Pb, Lu-Hf, trace element and REE analyses: *Geostandards Newsletter*, v. 19, p. 1-23.
- Zack, T., and Kooijman, E., 2017, Petrology and geochronology of rutile: *Reviews in Mineralogy and Geochemistry*, v. 83, p. 443-467. 1 [10.2138/rmg.2017.83.14](https://doi.org/10.2138/rmg.2017.83.14)

Highlights

- The Sierra de Juárez Mylonitic Complex (SJMC) in southern Mexico contains Neoproterozoic - lower Palaeozoic magmatic and sedimentary sequences.
- The Viguera Suite displays protolith ages ranging between 979-975 Ma.
- The Etna Unit is sourced in Neoproterozoic, Cambrian and Ordovician peri-Gondwanan and Rodinian-type terranes.
- The San Agustín Orthogneiss displays a lower Silurian magmatic age with a MORB-like signature
- lithological similarities are found in northwestern peri-Amazonian terranes, the Chiapas Massif Complex and El Triunfo Complex as well as in Guatemala Units.



The
Geological
Society

3. *EVOLUCIÓN GEOLÓGICA DEL SILÚRICO AL CRETÁCICO DEL SUR DE MÉXICO Y SU CONEXIÓN CON EL ENSAMBLE Y RUPTURA DE LA PANGEA ECUATORIAL OCCIDENTAL: ENFOQUE GEOCRONOLÓGICO EN EL NORTE DEL COMPLEJO SIERRA DE JUÁREZ.*

Guillermo Espejo-Bautista, Luigi Solari, Roberto Maldonado & Mónica Ramírez-Calderón (2022) Silurian to Cretaceous geologic evolution of southern Mexico and its connection to the assembly and breakup of western equatorial Pangea: geochronological constraints from the northern Sierra de Juárez Complex. In: Hynes, A.J., and Murphy, J.B., (eds), *The Consummate Geoscientist: A Celebration of the Career of Marteen de Wit*. Geological Society, London, Special Publications, 531, <https://doi.org/10.1144/SP531-2022-2>.

CONTRIBUCIÓN DE AUTORES

Guillermo Espejo-Bautista: Conceptualización, organización e integración de datos, análisis formal, investigación (trabajo de campo), metodología (procesamiento de muestras, separación de zircones, obtención de datos analíticos), propuesta de modelo tectónico, visualización, escritura original del manuscrito, revisión y edición.

Luigi A. Solari: Organización e integración de datos, análisis formal, adquisición de fondos, recursos, metodología, supervisión, escritura y revisión del manuscrito.

Roberto Maldonado: Análisis formal, investigación (trabajo de campo), escritura y revisión del manuscrito.

Mónica Ramírez-Calderón: Análisis formal, investigación (trabajo de campo), escritura y revisión del manuscrito.

Silurian to Cretaceous geological evolution of southern Mexico and its connection to the assembly and break-up of Western Equatorial Pangaea: geochronological constraints from the northern Sierra de Juárez Complex



Guillermo Espejo-Bautista^{1*}, Luigi Solarì¹, Roberto Maldonado² and Mónica Ramírez-Calderón¹

¹Centro de Geociencias, Universidad Nacional Autónoma de México, Campus Juriquilla, Santiago de Querétaro, Querétaro, México

²Instituto de Geología, Universidad Nacional Autónoma de México, Ciudad Universitaria, Ciudad de México, México

GE-B, 0000-0001-9206-5108

*Correspondence: gespejo@geociencias.unam.mx; guillermoespejo@hotmail.com

Abstract: The Sierra de Juárez Complex (SJC) of southern Mexico contains an extensive geological record from Precambrian to Cenozoic, involving Rodinia, NW Gondwana, western equatorial Pangaea, and eastern peninsular Mexico. It is thus critical for palinspastic reconstructions and lithotectonic correlations, mainly between the Mexican and NW South America terranes. In this contribution, we investigate the tectonic evolution of the northern SJC from Silurian to the Lower Cretaceous on the basis of fieldwork, petrography, and zircon U–Pb geochronology by laser ablation–inductively coupled plasma mass spectrometry. Our results allow us to constrain five main geological events: (1) Middle Paleozoic sedimentation along NW Gondwana during transtensional tectonics; (2) volcanosedimentary activity between 292 and 281 Ma in NW Gondwana during Rheic Ocean closure; (3) early–middle Permian metamorphism related to flat-slab subduction postdating Pangaea assembly; (4) Lower–Middle Jurassic anatexis and magmatism coeval with regional shearing at c. 175 Ma influenced by transtensional tectonics along eastern peninsular Mexico during Pangaea tenure; and (5) intermediate to acid magmatism between c. 136 and 129 Ma, correlated with the Zongolica continental arc in southern Mexico, followed by deep-crustal shearing related to either the formation of the extensional Chivillas basin or the Upper Cretaceous–Cenozoic contractional episode documented in the Cuicateco Terrane.

Supplementary material: Zircon U–Pb and trace-element data are available at <https://doi.org/10.6084/m9.figshare.c.6282721>

Unravelling long-lived multitectonic metamorphic complexes is a challenging target that provides fundamental knowledge on the geodynamic evolution of the Earth. Zircon U–Pb geochronology coupled with high spatial resolution techniques such as laser ablation–inductively coupled plasma mass spectrometry (LA–ICP–MS; e.g. [Schaltegger *et al.* 2015](#); [Kylander-Clark 2017](#)) provides a powerful petrochronological tool to elucidate multiple overprinted geotectonic cycles. As zircon incorporates trace elements such as rare earth elements (REE) with the capacity of diffusive re-equilibration sensitive to specific petrogenetic environments (e.g. [Hinton and Upton 1991](#)), zircon REE chemistry along with textural and morphological observations (e.g. [Corfu *et al.* 2003](#); [Olierook *et al.* 2021](#)) allows distinction between magmatic and metamorphic occurrences (e.g. [Rubatto 2017](#)) and discrimination among tectono-magmatic settings (e.g. [Grimes *et al.* 2015](#)) and even among metamorphic facies

(e.g. [Hoskin and Black 2000](#); [Hoskin and Schaltegger 2003](#); [Rubatto and Hermann 2007](#); [Ren-Xu *et al.* 2010](#); [Fornelli *et al.* 2014](#); [2017](#); [Rubatto 2017](#)). Furthermore, the strong resistance of zircon to abrasion and weathering makes it highly useful for evaluating detrital provenance and maximum depositional ages for sedimentary rocks (e.g. [Dickinson and Gehrels 2009](#); [Gehrels 2011](#)), providing essential information on the evolution of tectonic systems. By integrating these aspects of zircon geochronology and including detailed fieldwork and petrographic analysis, it is possible to gain insight into multiple magmatic, metamorphic and sedimentary processes that constitute complex tectonostratigraphic provinces.

The Sierra de Juárez Complex (SJC) is one of the crustal fragments comprising the geological mosaic of southern Mexico. Despite undergoing intense Mesozoic re-working related to the breaking up of Pangaea (e.g. [Alaniz-Álvarez *et al.* 1996](#); [Martini](#)

and Ortega-Gutiérrez 2016; Pindell *et al.* 2021), the SJC has been proved to encompass an intricate multitectonothermal record developed over more than 1100 Ma from the Stenian Period (Espejo-Bautista *et al.* 2023) to the Cenozoic (e.g. Graham *et al.* 2021). As with other crustal blocks in southern Mexico (e.g. Oaxacan Complex, Chiapas Massif Complex), the origin of the SJC is linked to a marginal Amazonian sector involved in the protracted Rodinia suturing process, which concludes its first geodynamic cycle. Geochronological data in the SJC further indicate significant tectonic activity during the Paleozoic and Mesozoic eras (Delgado-Argote *et al.* 1992; Ángeles-Moreno *et al.* 2012; Coombs 2016; Espejo-Bautista *et al.* 2021; Pindell *et al.* 2021). However, the lack of detailed systematic analytical data for the SJC obscures the knowledge about its tectonic evolution. In this paper, geological fieldwork, petrography and LA-ICP-MS-based zircon U-Pb analyses were conducted to synthesize a chronological scheme of geological events recorded in the northern SJC. The results indicate that, after the Precambrian cycle, this metamorphic belt underwent two major geodynamic cycles differentiated by the assembly and disruption of Pangaea. Each cycle encompasses active and passive margin activity, orogenesis, and divergent/transform tectonics related to a complex evolutionary geodynamic system starting in NW Gondwana and ending in peninsular Mexico.

Geological background

Oaxaquia

The Oaxaquia microcontinent (Ortega-Gutiérrez *et al.* 1995; Keppie and Ortega-Gutiérrez 2010) has been interpreted as a crustal fragment accreted to and evolved along the northern margin of Amazonia during the Mesoproterozoic. It records a granulitic metamorphic phase known as the Zapoteca Orogeny (Solari *et al.* 2003), interpreted as occurring during the assembly of the supercontinent Rodinia at *c.* 990 Ma (e.g. Li *et al.* 2008; Weber *et al.* 2010). Currently, crustal vestiges of this Precambrian block can be found in eastern and southern Mexico in the Novillo Gneiss (Cameron *et al.* 2004; Keppie *et al.* 2006; Alemán-Gallardo *et al.* 2019b), the Huiz-nopala Gneiss (Lawlor *et al.* 1999), the Guichicovi Complex (Weber and Köhler 1999; Weber and Hecht 2003) and the Oaxacan Complex (Ortega-Gutiérrez 1981, 1984; Keppie *et al.* 2001, 2003; Solari *et al.* 2003, 2020; Keppie and Dostal 2007; Keppie and Ortega-Gutiérrez 2010; Weber *et al.* 2010; Weber and Schulze 2014; Ortega-Gutiérrez *et al.* 2018). The Oaxacan Complex is the most extensive exposure of Oaxaquia and constitutes the crystalline basement of the Zapoteco Terrane in southern Mexico (Sedlock *et al.* 1993), which is

juxtaposed to the east to the SJC (Cuicateco Terrane) along the Oaxaca Fault (Figs 1 & 2).

The Mazateco Complex

The Mazateco Complex (MC) is a NW–SE-trending belt that constitutes the Paleozoic basement of the eastern Cuicateco Terrane (Sedlock *et al.* 1993). It is obliquely juxtaposed to the SJC at the northwestern corner of the Cuicateco Terrane (Fig. 1). Along its eastern boundary, the MC is thrust eastwards over Jurassic rocks of the Maya Terrane (Todos Santos Formation) along the Paleogene Vista Hermosa Fault (e.g. Ortega-Gutiérrez *et al.* 1991; 2018; Pérez-Gutiérrez *et al.* 2009; Mendoza-Rosales *et al.* 2010; Graham *et al.* 2021). On the opposite side, the SJC is thrust over the MC along the Siempre Viva Fault. In general, the MC consists of a vast low-grade east-verging meta-volcanosedimentary succession. In its northwestern sector (Mazatlán de las Flores Unit), crenulated phyllites, chlorite-white mica schists and intermediate to acid metavolcanic rocks crop out (Ángeles-Moreno *et al.* 2012; this work). The age of the MC has been approximated mainly by K–Ar geochronology. Carfantan (1986) reported a whole-rock K–Ar age of *c.* 233 Ma from a sericitic phyllite. Unpublished reports summarized in Ángeles-Moreno (2006) indicate the presence of scarce Devonian–Carboniferous and Late Permian–Middle Triassic ages (K–Ar in muscovite and whole rock). The vast majority of whole-rock or mineral K–Ar ages reported from the MC are Mesozoic and Cenozoic (Ángeles-Moreno 2006); however, they probably reflect younger tectonic reheating events recorded in the Cuicateco Terrane.

The Sierra de Juárez Complex

The SJC is a NNW-oriented metamorphic belt ~120 km long and *c.* 15 km wide that constitutes the basement of the western Cuicateco Terrane (Sedlock *et al.* 1993). It is bounded to the west by the Cenozoic normal-type Oaxaca Fault that cuts a former thrust contact with the Oaxacan Complex (Alaniz-Álvarez *et al.* 1996; Ortega-Gutiérrez *et al.* 2018; Graham *et al.* 2021). During the Upper Cretaceous–Eocene, the SJC was thrust eastwards over Lower Cretaceous successions (Chivillas and Jaltepetongo formations) along the Siempre Viva Fault, which forms its eastern border (Figs 1 & 2; Ángeles-Moreno *et al.* 2012; Graham *et al.* 2021). The SJC records a highly complex tectonic history and comprises a large variety of metamorphic lithotypes with protolith ages ranging from late Mesoproterozoic to Cretaceous (e.g. Ángeles-Moreno 2006; Espejo-Bautista *et al.* 2021). In this paper, we subdivide the lithology of the SJC into three main metamorphic suites.

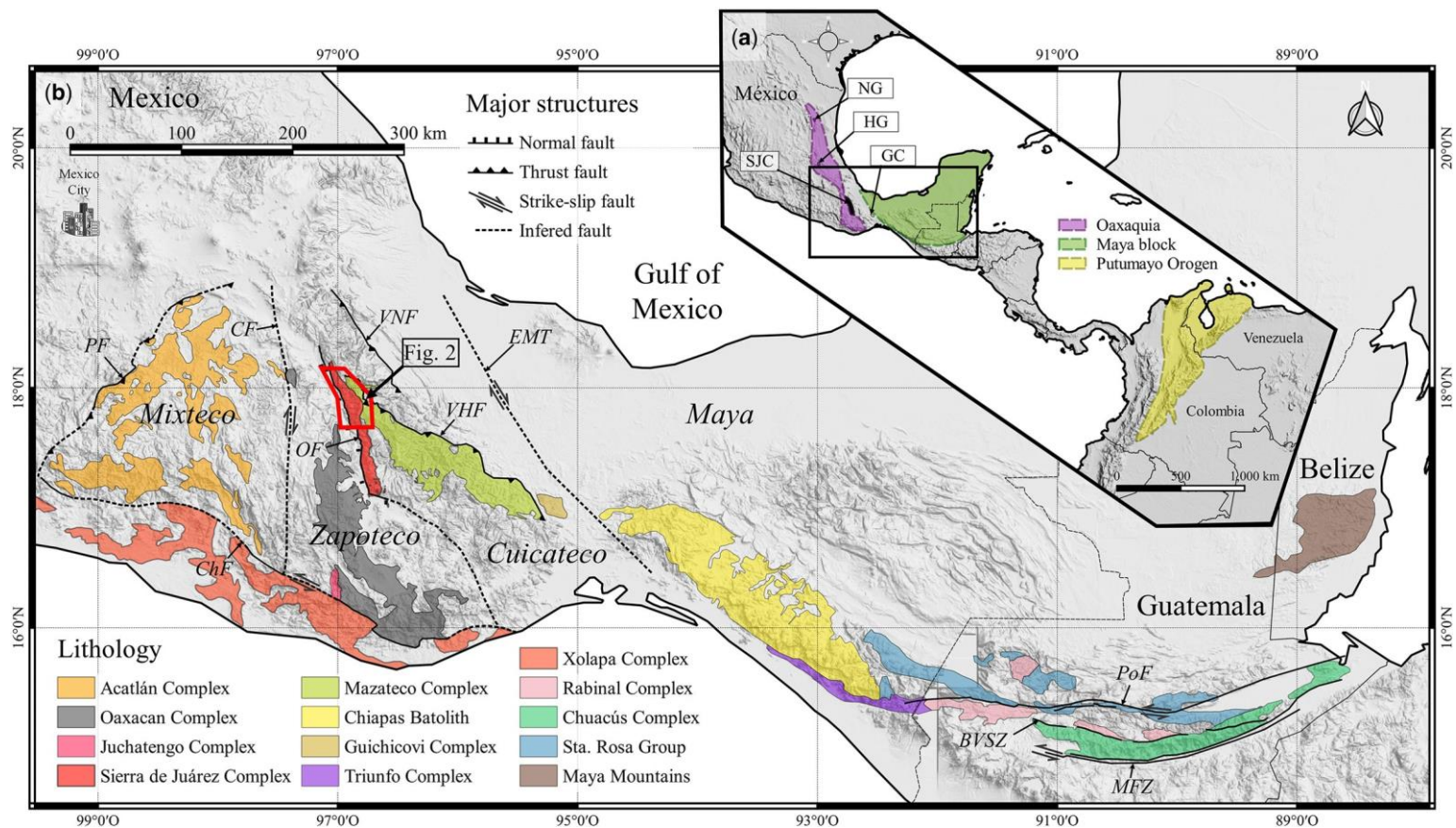


Fig. 1. (a) Simplified map showing the main terranes of NW Gondwana currently exposed in Mexico and northwestern South America. Abbreviations: NG, Novillo Gneiss; HG, Huiznopala Gneiss; GC, Guichicovi Complex; and SJC, Sierra de Juárez Complex. (b) Geological map showing Pre-Mesozoic basement blocks and major structural lineaments in southern Mexico, Belize and Guatemala. Tectonostratigraphic nomenclature in southern Mexico is based on Sedlock *et al.* (1993). Abbreviations: PF, Papalutla Fault; CF, Caltepec Fault; ChF, Chacalapa Fault; OF, Oaxaca Fault; VNF, Valle Nacional Fault; VHF, Vista Hermosa Fault; EMT, Eastern Mexico Transform; PoF, Polochic Fault; BVSZ, Baja Verapaz shear zone; MFZ, Motagua fault zone. Source: (a) modified from Ibanez-Mejia *et al.* (2011), Ortega-Gutiérrez *et al.* (2018) and Weber *et al.* (2018); (b) modified from Ortega-Gutiérrez *et al.* (2018), Maldonado *et al.* (2018, 2020), Weber *et al.* (2018) and Graham *et al.* (2021).

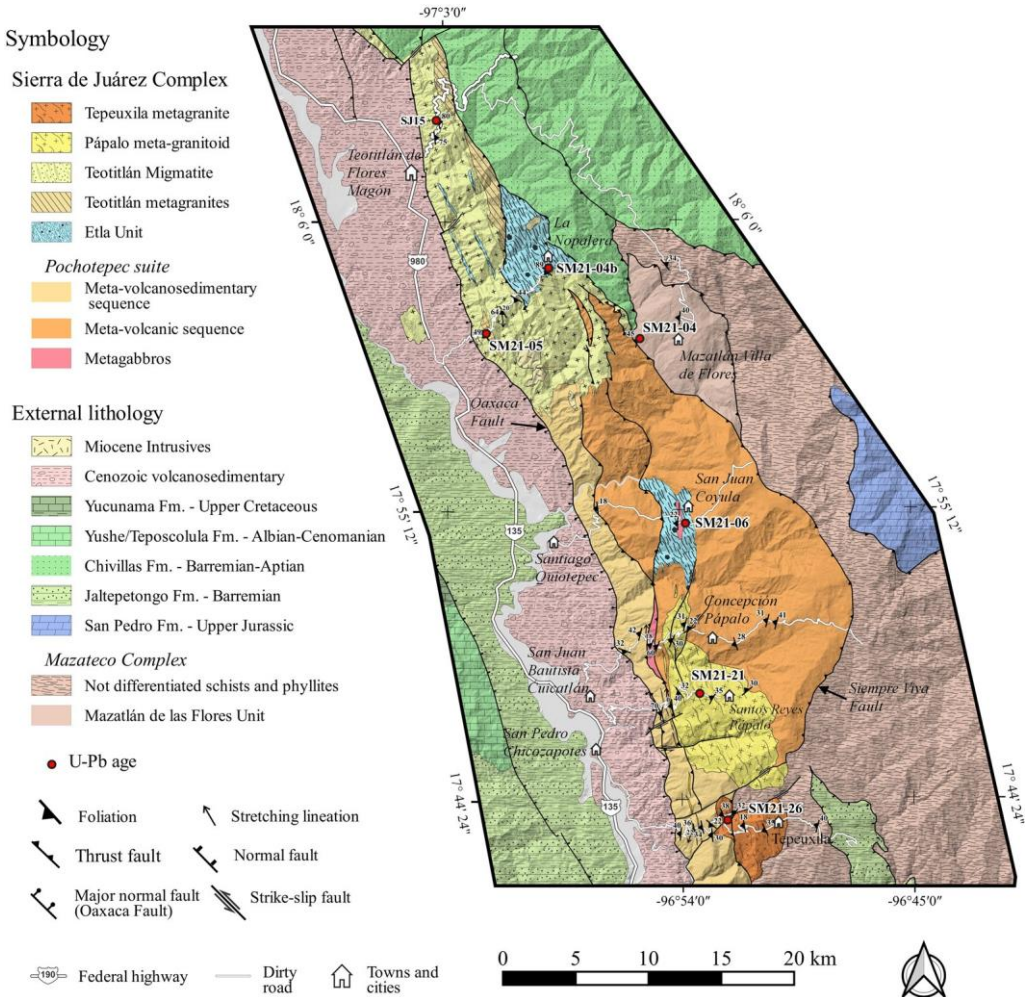


Fig. 2. Geological map of the northern Sierra de Juárez Complex. Source: lithology and structures are based on our field observations and modifications from [Ángeles-Moreno *et al.* \(2012\)](#).

The Pochotepec suite. The Pochotepec suite (PS; [Espejo-Bautista *et al.* 2023](#)) is a medium- to high-grade late Stenian–early Tonian metamorphic sequence that constitutes the most extensive member of the SJC (Fig. 2). It encompasses a meta-volcanosedimentary succession and a package of mafic gneisses and migmatites. The protoliths of these rocks are interpreted as originating in a continental arc along the northern edge of Amazonia prior to the formation of Rodinia between *c.* 1077 and 1044 Ma. The meta-volcanosedimentary succession was intruded by anorthositic bodies at *c.* 979–976 Ma in the southern sector of the SJC ([Espejo-Bautista *et al.* 2021](#)). Given the current proximity between the PS and the Oaxacan Complex (Oaxaquia), some correlation between them might be

expected. However, the PS underwent amphibolite facies metamorphism and anatexis between 953 and 934 Ma, postdating the Oaxacan Complex gran-ulitic phase at *c.* 990 Ma (e.g. [Solarí *et al.* 2003](#); [Weber *et al.* 2010](#)). Hence, a different palaeoposition and tectonic evolution are envisaged for the PS relative to the Oaxacan Complex, at least during the Stenian and Tonian periods ([Espejo-Bautista *et al.* 2023](#)).

The Etla suite. The Etla suite is a medium-grade metamorphic sequence with igneous and sedimentary protoliths originating between the Silurian and Lower Devonian within a back-arc system at the northwestern corner of Gondwana in an extensional tectonic setting related to the opening of

Geological evolution of the Sierra de Juárez Complex

the Rheic Ocean (Espejo-Bautista *et al.* 2021). It is mainly exposed in the southern sector of the SJC and comprises a mid-ocean ridge basalt-like rutile-bearing metagabbro with a protolith age of *c.* 442 Ma, referred to as the San Agustín Orthogneiss, and a succession of garnet-bearing para-amphibolites and pelitic schists named the Etna Unit (hereafter considered as constituent of the Etna suite), with maximum depositional ages ranging between *c.* 422 and 414 Ma. Multiple tectonic overprints have obscured the primary relationship between the Etna suite and the Pochotepec suite in the SJC. However, the supracrustal lithodemic succession (Etna suite) is interpreted to have been unconformably deposited over the extensional basement crust (Pochotepec suite), whereas the San Agustín Orthogneiss may represent oceanic crust originated during back-arc seafloor spreading. Subsequent contractional metamorphism recorded in the Etna suite has been attributed to tectonic switching (Collins 2002) between *c.* 398 and 391 Ma (Espejo-Bautista *et al.* 2021). However, this age is not supported by convincing zircon chemistry or textural evidence; thus, an actual metamorphic age as young as late Paleozoic or Mesozoic and a different tectonic scenario are likely.

The Teotitlán Migmatite. The Teotitlán Migmatite (TM) was recognized by Ángeles-Moreno (2006) and Ángeles-Moreno *et al.* (2012) in the northern sector of the SJC. The TM is in tectonic contact with the Lower Cretaceous Chivillas Formation and the Pochotepec suite along eastward thrusting Upper Cretaceous–Eocene faults, although transitional contacts with the Pochotepec suite are also reported (Ángeles-Moreno 2006; Ángeles-Moreno *et al.* 2012). The TM encompasses neosomes of dioritic/tonalitic to granitic composition and rare palaeosome domains preserved as lenticular-shaped amphibolites. The palaeosome domains show pre-migmatitic folding of banded gneisses (Ángeles-Moreno 2006), suggesting previous deep metamorphic episodes. Coombs (2016) interpreted the TM as an amphibolite-facies metamorphic sequence with volcanosedimentary precursors, followed by granitoid intrusions that triggered partial melting. A wide variety of migmatite structures constitute the TM, from dilatant patch or nebulitic and vein-structured granitic intrusives to stromatic or schlieren, suggesting that more than one anatectic episode took place under different stress systems (this work).

An amphibolite and a Grt-bearing paragneiss interpreted as palaeosomes yielded a protolith magmatic age of *c.* 247 Ma and an apparent maximum depositional age of 354 Ma, respectively (Coombs 2016). The anatectic event was dated by U–Pb in zircon from arc-related granitic and tonalitic intrusives,

which yielded ages between *c.* 141 and 133 Ma (Ángeles-Moreno 2006; Ángeles-Moreno *et al.* 2012; Coombs 2016). Moreover, two Ar/Ar muscovite plateau ages from these intrusive granites yielded *c.* 132 and 133 Ma (Ángeles-Moreno 2006; Ángeles-Moreno *et al.* 2012).

Post-anatectic/magmatic deformation is also observed, implying the occurrence of thermotectonic events after the Berriasian–Valanginian. Different tectonic settings have been suggested for the magmatic–anatectic activity in the TM: (1) extensional tectonics linked to drifting between South America and North America (Ángeles-Moreno 2006) or the development of the extensional Arperos basin in western Mexico (e.g. Graham *et al.* 2021; Pindell *et al.* 2021); (2) crustal thinning and extension related to the opening of the Gulf of Mexico (Mendoza-Rosales *et al.* 2010); and (3) a convergent continental arc produced by the eastward subduction of the Arperos oceanic crust (Coombs 2016). In any of these events, the magmatic–anatectic episode in the TM was followed by, or was nearly coeval with the development of the extensional Berriasian–Barremian Chivillas Formation basin in the Cuicateco Terrane (e.g. Mendoza-Rosales *et al.* 2010; Coombs 2016; Sierra-Rojas *et al.* 2022).

The mylonitic fabric of the Sierra de Juárez Complex. The most noteworthy structural feature of the SJC is a pervasively overprinted mylonitic fabric. The mylonitic foliation dips uniformly westward, and the stretching lineation typically has a subhorizontal *c.* north–south trend, suggesting a strike-slip system. Ductile deformation in the amphibolites suggests that mylonitization occurred at deep-crustal levels; thus, they may represent the root of a crustal discontinuity central to the tectonic evolution of southern Mexico. Different tectonic interpretations have been provided for the mylonitic event. Alaniz-Álvarez *et al.* (1996) suggested that it reflects the development of a right-lateral *c.* north–south transform system along eastern peninsular Mexico in response to the opening of the Gulf of Mexico during the Middle Jurassic. Alternatively, Pindell *et al.* (2021) suggested that it records a west-dipping sinistral shear zone related to the southeastward translation of the ‘Oaxaca Block’ during the Middle–Upper Jurassic.

U–Pb geochronology analytical procedures

About 1 kg of each of the samples selected for U–Pb geochronology was crushed, ground, and the heavy minerals were concentrated using standard techniques (e.g. Solari *et al.* 2007). Between 50 and 100 zircon crystals from each sample were selected and mounted in epoxy resin, polished to expose

their internal structure and targeted for U–Pb *in situ* analyses. In addition, cathodoluminescence imaging was performed before and after ablation in order to observe internal structures such as zoning, choose the analytical target and interpret the U–Pb results (Fig. 4).

Isotope measurements were performed by LA-ICP-MS at the Laboratorio de Estudios Isotópicos, Centro de Geociencias, Universidad Nacional Autónoma de México, using a Thermo ICap Qc quadrupole coupled to a Resolution M050, 193 nm excimer laser ablation workstation. A 23 µm spot was employed, with a repetition rate of 5 Hz and 6 J cm⁻² of fluence, following the analytical procedures described in Solari *et al.* (2018). The standard zircon 91500 (1065.4 ± 0.6 Ma, thermal ionization mass spectrometry age, Wiedenbeck *et al.* 1995) was employed as the primary standard, whereas Plešovice standard zircon (337.13 ± 0.37 Ma, thermal ionization mass spectrometry age, Sláma *et al.* 2008) was employed as a control standard. During the analytical session, the control standard yielded a concordant age of 338.3 ± 0.81 Ma (mean square weighted deviation, MSWD = 0.8, *n* = 111), in agreement with its accepted age. The NIST 610 glass was used as an external standard for recalculating trace and REE element concentrations, employing ²⁹Si as an internal standard, assuming a stoichiometric value of 15.323 mol. Data processing was performed offline using Iolite software v. 4.5 (Paton *et al.* 2010) and the VizualAge data reduction scheme of Petrus and Kamber (2012). No common Pb correction was applied since the isobar ²⁰⁴Hg swamps the ²⁰⁴Pb signal (non-radiogenic Pb). Data were exported from Iolite, and the concordia diagrams and mean ages were plotted and calculated using IsoplotR (Vermeesch 2018). The calculated age uncertainties are reported at the 2σ level.

Field relationships and samples description

We discriminate four main metamorphic Paleozoic–Mesozoic lithological domains based on field observations: (1) pelitic schists with or without garnet; (2) the Teotitlán Migmatite; (3) widespread ultramylonitized intrusives with tonalitic–granitic composition; and (4) the MC.

Pelitic schists

The pelitic schists include the La Nopalera Schist, formerly included in the MC (Ángeles-Moreno 2006; Ángeles-Moreno *et al.* 2012). Metapelite SM21-04b is a highly altered rock cropping out around the village of La Nopalera. Its close

proximity to, and diffuse contacts with, the Teotitlán Migmatite allow us to infer that it was partially affected by anatectic processes. The sample contains white mica, quartz, chlorite and centimetre-sized garnet (Fig. 3a). The accessory phases include tourmaline, epidote, apatite and zircon. Near the village of San Juan Coyula, highly mylonitized wedges of low-grade pelitic schists (sample SM21-06) are tectonically intercalated with the Pochotepec suite (Fig. 2). These rocks are made up of white mica distributed along sheared bands with abundant quartz, minor amounts of epidote and chlorite and accessory phases such as apatite and zircon.

Teotitlán Migmatite

Along the road from Teotitlán de Flores Magón to Mazatlán de las Flores, intricate metamorphic, migmatitic and magmatic structures occur. On the basis of cross-cutting relationships, we categorize them into four groups:

- (1) The oldest rocks comprise subvertical east-dipping, layered and mylonitic schlieren-type migmatites. They formed within a *c.* north-south strike-slip system with dextral kinematics at the outcrop scale (Fig. 3c). Some gneisses with igneous and sedimentary protoliths (Fig. 3b, c) are hosted by the migmatites and constitute the palaeosome. One palaeosome sample from this group was analysed and classified as a mylonitic Grt–Bt paragneiss (SJ15 sample; Fig. 3d, e). Under the microscope, two generations of metamorphic biotite are observed (Fig. 3d): the first one was preserved as idiomorphic inclusions in garnet, probably representing primary minerals growing in a low-strain metamorphic environment. The second generation is stretched and oriented along the foliation planes, together with quartz and garnet, indicating that the mylonitic foliation overprinted the primary metamorphic texture. Inequigranular neosome patches of two-mica granitic composition are widespread (Fig. 3d, e). They are oriented roughly parallel to the foliation, suggesting that the mylonitic and anatectic events were coeval.
- (2) The second group includes granoblastic to slightly foliated amphibolites and scarce ultramafic rocks. The amphibolites exhibit migmatization under low-directed stress, forming metatexites with dilatant patches and nebular structures (Fig. 3f, right side). Groups 1 and 2 are in tectonic contact (Fig. 3f), probably owing to later compressional events (e.g. Grahame *et al.* 2021).
- (3) Granitic to granodioritic dykes with variable post-magmatic deformation intruding parallel

Geological evolution of the Sierra de Juárez Complex

or obliquely to the foliation of the banded migmatites of group 1 and cross-cutting the granoblastic amphibolites of group 2. These dykes were dated by [Ángeles-Moreno \(2006\)](#) and [Coombs \(2016\)](#) as Valanginian (141–133 Ma).

Exposures of massive amphibolite and associated ultramafic rocks (group 2) are dominant along the road to La Nopalera village ([Fig. 2](#)). Along this transect, a different lithotype composed of dioritic gneisses crops out. Because of their foliation, they are inferred to be older than the rocks from group 2; however, the contact between both lithotypes was not observed. The dioritic gneisses are intruded by non-foliated 3–4 m-thick granitic dykes ([Fig. 3g](#)), triggering local partial melting. A sample collected from the dioritic gneisses (SM21-05) is mainly composed of plagioclase, K-feldspar and hornblende with a minor amount of interstitial quartz. Accessory phases include chlorite, titanite, apatite, opaques, epidote, zircon and biotite.

Ultramytonitic intrusives

Highly mylonitized meta-volcanosedimentary sequences composed of pelitic schists, meta-arkoses, meta-andesites and marble belonging to the Precambrian Pochotepec suite crop out along the southwestern margin of the SJC ([Fig. 2](#)). These sequences contain planar ultramytonitic domains (resembling pelitic schists) parallel to the foliation, composed of white mica, quartz and epidote/amphibole, that increase their presence to the east until they become the dominant lithology. Near the town of Santos Reyes Pápalo, a low-strain zone reveals that the protolith of these ultramytonites is an extensive dioritic/tonalitic intrusive (SM21-21 – hereafter referred to as Pápalo meta-granitoid; [Fig. 2](#)). Petrographically, this rock shows coarse-grained hornblende, epidote, K-feldspar, plagioclase, white mica and highly deformed quartz with bulging recrystallization. Quartz subgrains and the white mica, resulting from the alteration of feldspar, form the matrix. Allanite and zircon are abundant accessory phases. As mylonitic strain increases, the quartz white mica matrix extends, epidote crystals are reduced in size and amphibole grains develop stretched sigmoidal textures ([Fig. 3j](#)).

Near Tepeuxila village, an ultramytonitic granite crops out (SM21-26 – hereafter referred to as Tepeuxila meta-granite; [Fig. 2](#)). This rock is in tectonic contact with anastomosed black phyllites interpreted as part of the MC. Petrographically, a low-strain meta-granitic sample shows sigmoidal K-feldspar porphyroclasts and plagioclase surrounded by asymmetric pressure shadows of quartz, altogether embedded in a matrix composed of quartz and muscovite ([Fig. 3k](#)).

Mazateco Complex

Around the village of Mazatlán Villa de Flores, anastomosed phyllites and low-grade metavolcanic successions composed of meta-andesites, meta-rhyolites and chlorite schists belonging to the MC crop out. This lithological package was named by [Ángeles-Moreno et al. \(2012\)](#) as the Mazatlán de las Flores Schist. From the metavolcanic succession, a meta-rhyolite was collected (SM21-04). It is made up of quartz, plagioclase and K-feldspar equally distributed along a spaced (disjunctive) foliation defined by cleavage domains of micaceous fine-grained material ([Fig. 3l](#)).

U–Pb zircon geochronology

To reconstruct the tectonic history of the northern SJC and evaluate its regional implications, we focus on protolith and metamorphic ages of the different recognized lithologic units. Sample locations and a summary of ages are shown in [Table 1](#). The U–Pb geochronological data are available in the [Supplementary material](#).

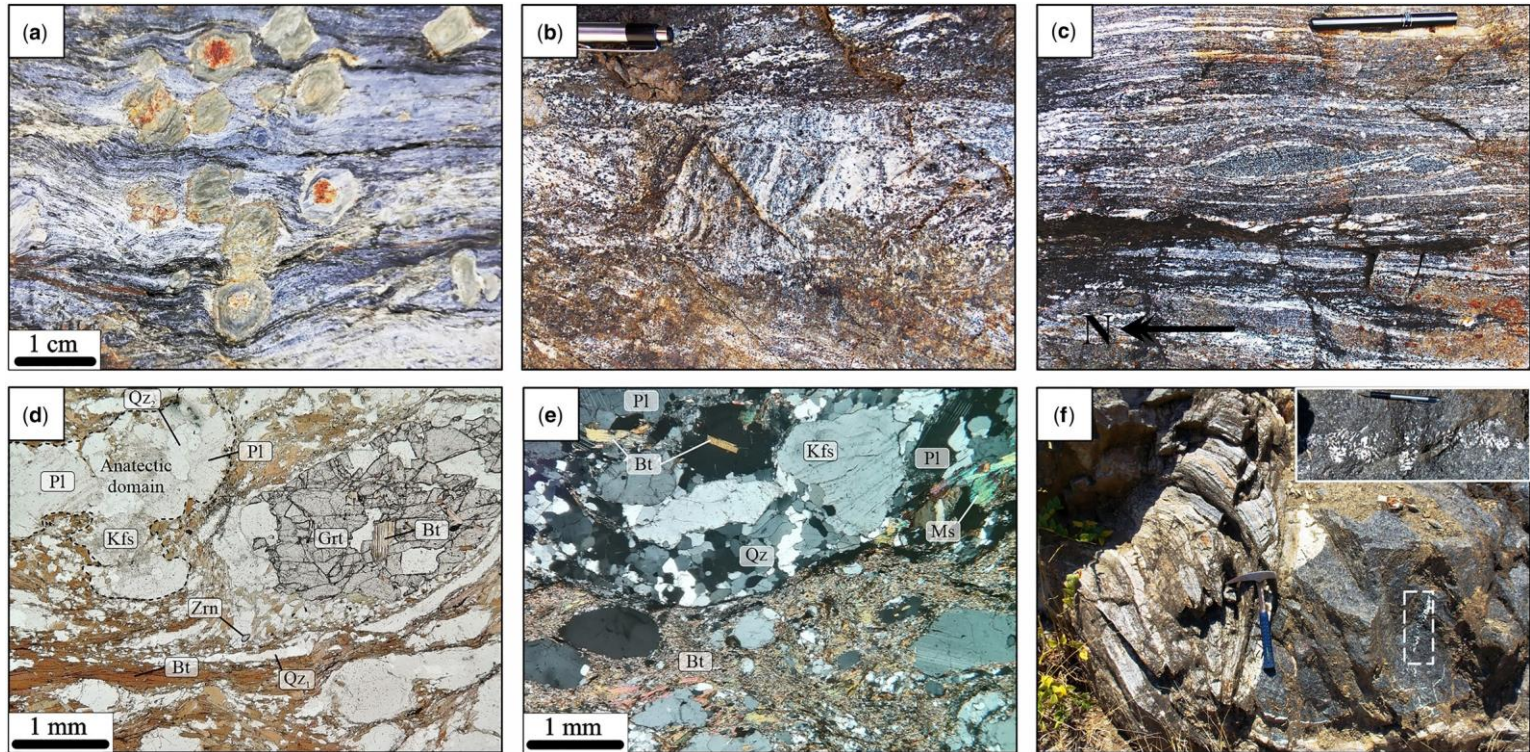
Grt-bearing pelitic schist (SM21-04b)

From this sample, 93 detrital zircon cores and rims were analysed. Zircon grains show a diverse morphology from stubby to elongated prismatic crystals. Cathodoluminescence images ([Fig. 4a](#)) reveal inner zircon textures such as zoned cores with overgrowth rims and core–rim structures with homogeneous contrasting luminescent zones.

The analyses exhibit a small Mesoproterozoic provenance age population of 1300–990 Ma ($n = 14$), peaking at 1154 Ma, and a late Proterozoic population with ages ranging from 651 to 542 Ma ($n = 5$) ([Fig. 5a](#)). Three isolated ages of 1515 ± 50 and 1486 ± 48 Ma (both $^{207}\text{Pb}/^{206}\text{Pb}$ ages) and 778 ± 23 Ma do not represent statistically meaningful detrital sources. The most populated group contains Paleozoic ages ranging from 493 to 404 Ma, with a density peak at 456 Ma ([Fig. 5a](#)). The youngest age population between 393 and 377 Ma yields a concordia age of 392 ± 4 Ma (MSWD 1.2, $n = 8$), which is considered the maximum depositional age of the sample ([Fig. 5b](#)). Finally, zircon rim analyses yield highly discordant ages that range from 292 to 250 Ma ($n = 6$). They exhibit an increase in light REE (LREE) and a decrease in their Th/U ratios relative to the detrital cores ([Fig. 5a, b](#)). These ages probably represent a thermal overprint related to the metamorphism recorded in this sample.

Garnet-free pelitic schist (SM21-06)

This sample yielded 67 detrital zircon analyses. The oldest grain yielded a $^{207}\text{Pb}/^{206}\text{Pb}$ age of



G. Espejo-Bautista *et al.*

Fig. 3. (a) Hand sample of metapelite SM21-04b showing altered garnet crystals. (b, c) Banded structures in the Teotitlán Migmatite containing asymmetric palaeosome lenses that indicate shear sense and pre-anatectic gneissic fabrics. (d) Photomicrograph of paragneiss SJ15 (Teotitlán Migmatite palaeosome). The metamorphic assemblage includes biotite, garnet (with biotite inclusions), elongated quartz (Qz1), muscovite and secondary phases such as apatite, zircon and opaques. Granitic blebs cutting the foliated texture constitute evidence for post-metamorphic anatexis. View in plain polarized light (PPL). (e) Photomicrograph of paragneiss SJ15 showing a granitic anatectic domain oriented according to the mylonitic foliation. View with crossed nicols. (f) Outcrop exhibiting banded migmatites in tectonic contact with granoblastic amphibolites containing nebulitic anatectic structures.

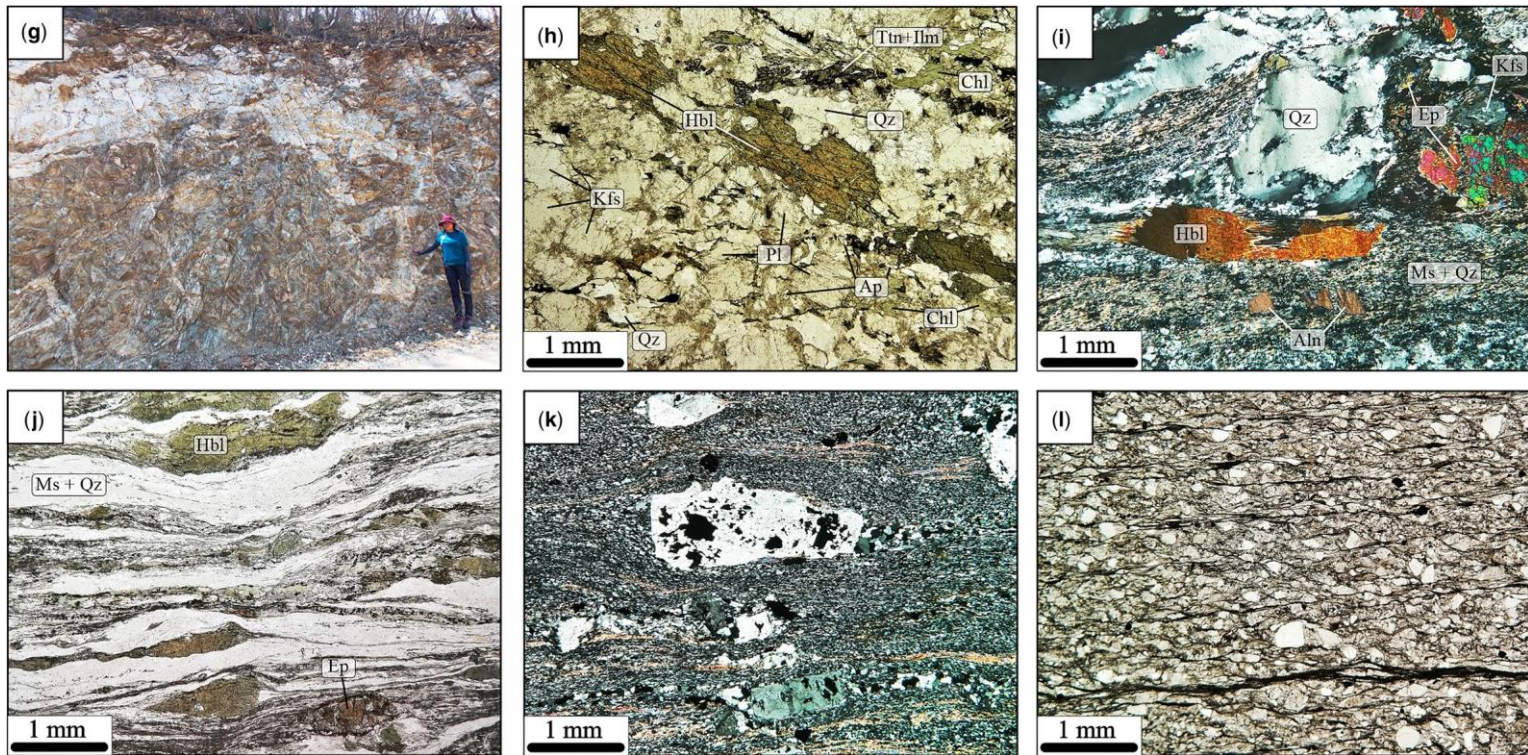


Fig. 3. *Continued.* (g) Outcrop showing granitic layers intruding dioritic gneisses and causing partial melting. (h) Photomicrograph of sample SM21-05, composed of quartz, plagioclase, K feldspar and hornblende. Accessory phases such as titanite, chlorite, ilmenite, apatite and epidote are also present. Amphibole crystals are crudely oriented, defining a weak foliation. View in PPL. (i, j) Meta-granitoid SM21-21 containing quartz, muscovite, plagioclase, hornblende, epidote, allanite, apatite and opaques. Ductile behaviour in this rock is indicated by subgrain rotation recrystallization (SGR) in quartz and undulose extinction in hornblende. (k) Meta-granite SM21-26 showing mylonitic deformation with semi-ductile behaviour based on the brittle response of feldspar crystals. (l) Meta-rhyolite SM21-04 composed of quartz, K-feldspar and plagioclase grains. Pressure solution and solution transfer are the active deformation mechanisms in this rock. The dissolved and transferred material of mineral grains forms dark horizontal seams that constitute a spaced foliation.

Table 1. Summary of ages and sample locations from the northern Sierra de Juárez Complex

Sample	Rock type	x-Coordinate	y-Coordinate	Interpretation	Igneous protolith (IP) or maximum depositional age (MDE) (Ma)	Metamorphic age (Ma)
SM21-04b	Grt-bearing metapelite	-96° 58' 58.44"	18° 04' 15.25"	Pelitic schist related to the Etla Unit	392 ± 4 (MDE)	292-250
SM21-06	Grt-free metapelite	-96° 53' 45.50"	17° 54' 41.90"	Pelitic schist related to the Etla Unit	468 ± 7 (MDE)	246 ± 1.9
SJ15	Grt-bearing paragneiss	-97° 03' 17.20"	18° 09' 47.5"	Palaeosome from the Teotitlán Migmatite	281 ± 5 (MDE)	176 ± 1
SM21-04	Low-grade meta-rhyolite	-96° 55' 26.90"	18° 01' 35.10"	Meta-volcanic rock from the Mazateco Complex	292 ± 1.8 (IP)	
SM21-05	Amphibolite	-97° 01' 25.60"	18° 01' 50.00"	Palaeosome from the Teotitlán Migmatite	175 ± 1 (IP)	
SM21-21	Meta-diorite/tonalite	-96° 53' 16.30"	17° 48' 20.90"	Lower Cretaceous magmatism	136 ± 0.7 (IP)	
SM21-26	Meta-granite	-96° 52' 14.62"	17° 43' 37.21"	Lower Cretaceous magmatism	129 ± 0.8 (IP)	

2752 ± 43 Ma. Eight zircon grains constitute a scattered provenance population with ages of 1983–1491 Ma, followed by a more conspicuous population of 22 ages ranging between 1237 and 924 Ma peaking at 1026 Ma. The largest detrital population ranges in age from 856 to 453 Ma, with a probability peak at 552 Ma (Fig. 5c). The three youngest concordant and overlapping ages, selected to estimate the most reliable maximum depositional age, give a concordia age of 468 ± 7 Ma (Fig. 5c). Three younger analyses of c. 325, 252 and 247 Ma with discordance values between 5.6 and 8.5% do not constitute a reliable provenance group (e.g. Dickinson and Gehrels 2009) and probably reflect Pb lost.

Garnet–Bt paragneiss SJ15 (Teotitlán Migmatite palaeosome)

From this sample, we report 79 core and rim zircon analyses. Cathodoluminescence images (Fig. 4b) show moderately rounded, yellowish zircon crystals with convoluted metamorphic rims surrounding dark or zoned cores considered detrital in origin. Cores yielded ages that span from c. 1551 to 259 Ma ($n = 47$), with igneous-like features such as Th/U values ≈ 0.1 and steeply increasing patterns from LREE to heavy REE (HREE) with positive Ce and negative Eu anomalies (e.g. Rubatto and Gebauer 2000; Belousova *et al.* 2002; Hoskin and Schaltegger 2003; Fig. 6c). Three provenance groups are defined by these ages, peaking at 1075, 742 and 486 Ma (Fig. 6a). To constrain the maximum depositional age, the youngest overlapping concordant ($\approx 5\%$ disc.) igneous-like core analyses were chosen, which yielded a concordia age of 281 ± 5 Ma ($n = 3$). On the other hand, the rims with diffuse textures, which represent recrystallized or reprecipitated domains, exhibit two different concordant clusters of ages that probably reflect two metamorphic imprints. The first cluster contains concordant ages chemically characterized by ≈ 0.1 Th/U values, chaotic LREE contents, positive steep medium REE (MREE)–HREE patterns, and an abrupt increase in Yb and Lu (Fig. 6b, c). This cluster yielded a early Middle Triassic concordia age of 246 ± 1.9 Ma (MSWD = 0.9; $n = 14$), which is probably related to the pre-anatectic/mylonitic (Grt–Bt) metamorphic episode of this sample. The second cluster contains ages with Th/U values grouped around 0.01, a positive Pr anomaly, negative Nd and Eu anomalies, and concave-down positive steep MREE–HREE patterns (Fig. 6c). This cluster yielded a Lower Jurassic (Toarcian) concordia age of 176 ± 1 Ma (MSWD = 0.41; $n = 8$) which is considered to date the anatectic/mylonitic overprint in this sample.

Geological evolution of the Sierra de Juárez Complex

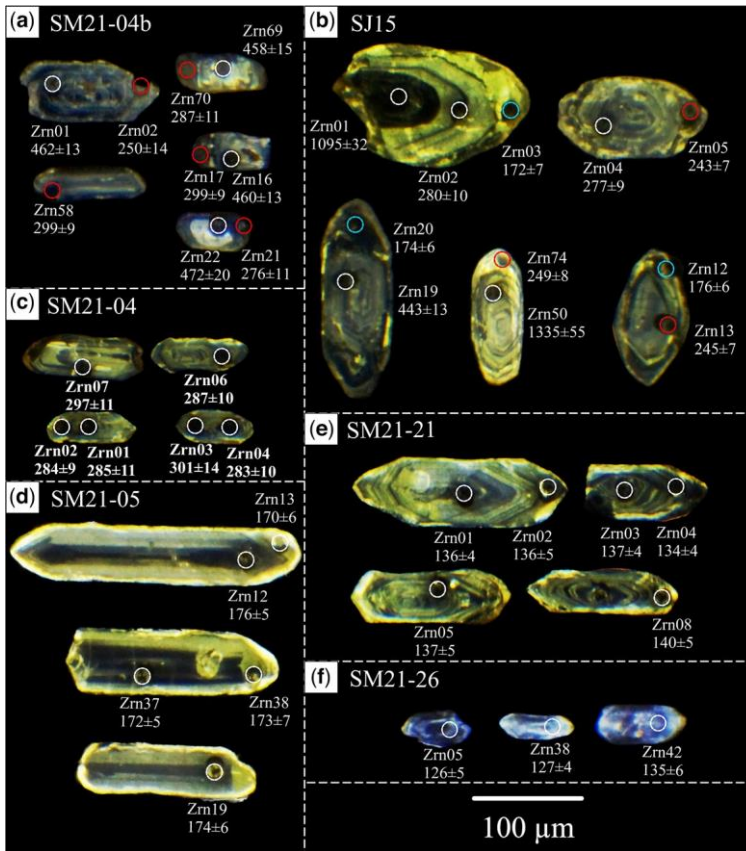


Fig. 4. After-ablation cathodoluminescence images of representative zircon grains showing inherited/igneous analyses (white ellipses), Permian–Triassic metamorphic rims (red ellipses) and Jurassic metamorphic rims (blue ellipses).

Meta-rhyolite SM21-04 (Mazateco Complex)

From this sample, 38 analyses were obtained from euhedral bipyramidal zircon grains with oscillatory zoning (Fig. 4c). The results include four zircon grains with Paleozoic and Precambrian ages assumed to be inherited. The magmatic oscillatory zircon defines a concordant cluster with Th/U values ~ 0.1 and igneous-like REE patterns (Fig. 7a), providing a concordia age of 292 ± 1.8 Ma (MSWD = 1.4; $n = 29$).

Dioritic gneiss SM21-05 (Teotitlán Migmatite palaeosome)

From this sample, 38 zircon U–Pb analyses were carried out. Zircon grains are prismatic and display planar zoning, typical of intermediate magmas (Corfu *et al.* 2003). The crystals often contain small disrupting bright patches, probably produced by late-magmatic resorption (Fig. 4d). Zircon

compositions show Th/U values ~ 0.1 , and REE distributions with typical igneous-like trends (e.g. Belousova *et al.* 2002; Hoskin and Schaltegger 2003) that group into two differentiated groups of trace-element patterns (Fig. 7b). This could be due to magmatic resorption and reprecipitation of new zircon by injection of a more evolved magma depleted in MREE and HREE (e.g. Zhong *et al.* 2021). Regardless of their chemical features, the ages constitute a concordant cluster that yields a Toarcian concordia age of 175 ± 1 Ma (MSWD = 0.67; $n = 35$), interpreted to be the protolith magmatic age of this sample.

Pápalo meta-granitoid SM21-21

Forty-five zircon U–Pb analyses were performed on this sample. Cathodoluminescence images (Fig. 4e) show euhedral zircon with oscillatory zoning. Their normalized REE distribution exhibits typical igneous patterns with positive slopes from LREE to

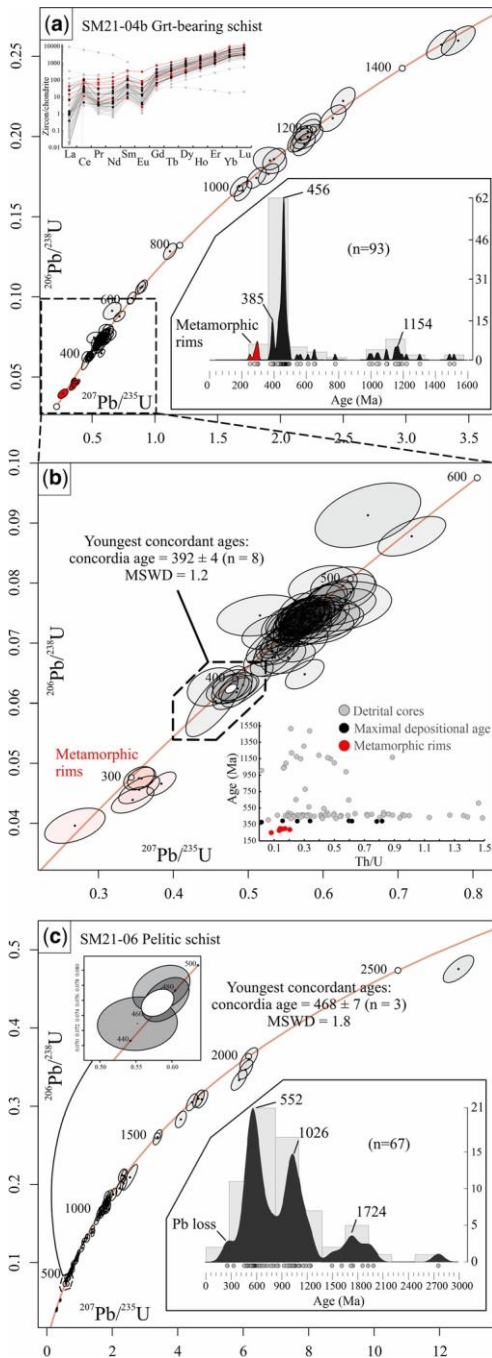


Fig. 5. U-Pb concordia diagrams and kernel density estimation (KDE) plots with histogram for metapelites SM21-04b and SM21-06.

HREE, positive Ce anomalies and negative Eu anomalies (Fig. 7c). These analyses represent the magmatic protolith age and yield a Lower

Cretaceous (Valanginian) concordia age of 136 ± 0.7 Ma (MSWD = 1.2; $n = 43$).

Tepeuxila meta-granite SM21-26

Thirty-eight ~ 100 μm long bipyramidal zircon crystals with diffuse oscillatory zoning were analysed from this sample (Fig. 4f). The chemical and geochronological analyses of these zircons are characterized by steeply increasing patterns from LREE to HREE with positive Ce and negative Eu anomalies, ~ 0.1 Th/U ratios, and concordant to nearly concordant ages (Fig. 7d). A concordia age of 129 ± 0.8 Ma (MSWD = 1.8; $n = 35$) on this sample is indicative of the age of the magmatic protolith.

Discussion

The early-middle Paleozoic meta-sedimentary belt (Eita suite)

Time of deposition. Differences in provenance sources and maximum depositional ages between metapelites SM21-04b and SM21-06 (Fig. 8) suggest two different sedimentation stages. Based on this interpretation, the maximum depositional age of sample SM21-04b represents the minimum depositional age for sample SM21-06. Furthermore, the zircon metamorphic-rim ages between 299 and 250 Ma of metapelite SM21-04b constitute the minimum age for the deposition of its sedimentary protolith. In summary, metapelite SM21-06 is considered to represent sedimentation between Upper Ordovician–Middle Devonian, whereas metapelite SM21-04b is indicative of Middle Devonian–Upper Pennsylvanian sedimentation.

Detrital provenance. Both metapelite samples display a relatively scarce contribution from Proterozoic sources (in the range $c. 1300$ – 900 Ma). The largest provenance group in sample SM21-06, ranging in age between 600 and 500 Ma, was probably sourced from the orogenic provinces related to the assembly of Gondwana (Pan-African–Brasiliano; e.g. Meert and Lieberman 2008). The Pan-African–Brasiliano signal is not strongly present in sample SM21-04b, which instead has a dominant Upper Ordovician–Devonian detrital content ($c. 493$ – 377 Ma; $n = 67$)—with barely to slightly rounded zircon grains with ~ 0.1 Th/U values, probably derived from a proximal magmatic source. Ordovician–Devonian magmatism is widely recognized in southern Mexico, Central America and NW South America (see Table 2 for references). These rocks belong to an extensive magmatic belt along the NW boundary of Gondwana, coeval with the Famatinian arc in western South America (e.g. Otamendi *et al.*

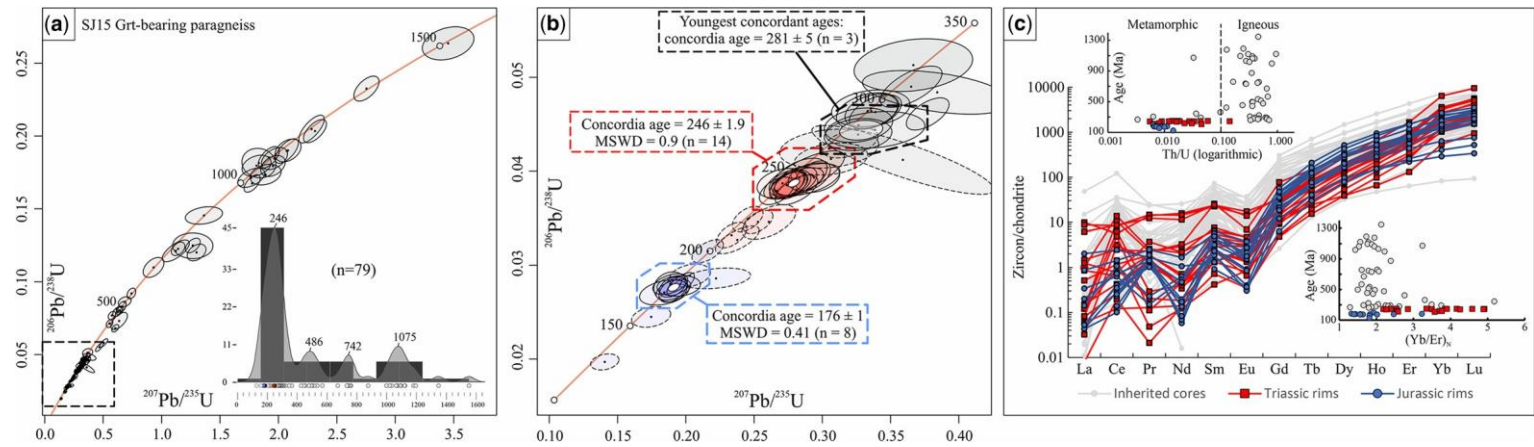


Fig. 6. (a) U–Pb concordia diagram and KDE plot with histogram for paragneiss SJ15. (b) Detail of (a) showing the youngest detrital ages and the two clusters of metamorphic zircon rims. (c) Zircon rare earth elements (REE), age v. Th/U and Yb/Er v. age diagrams.

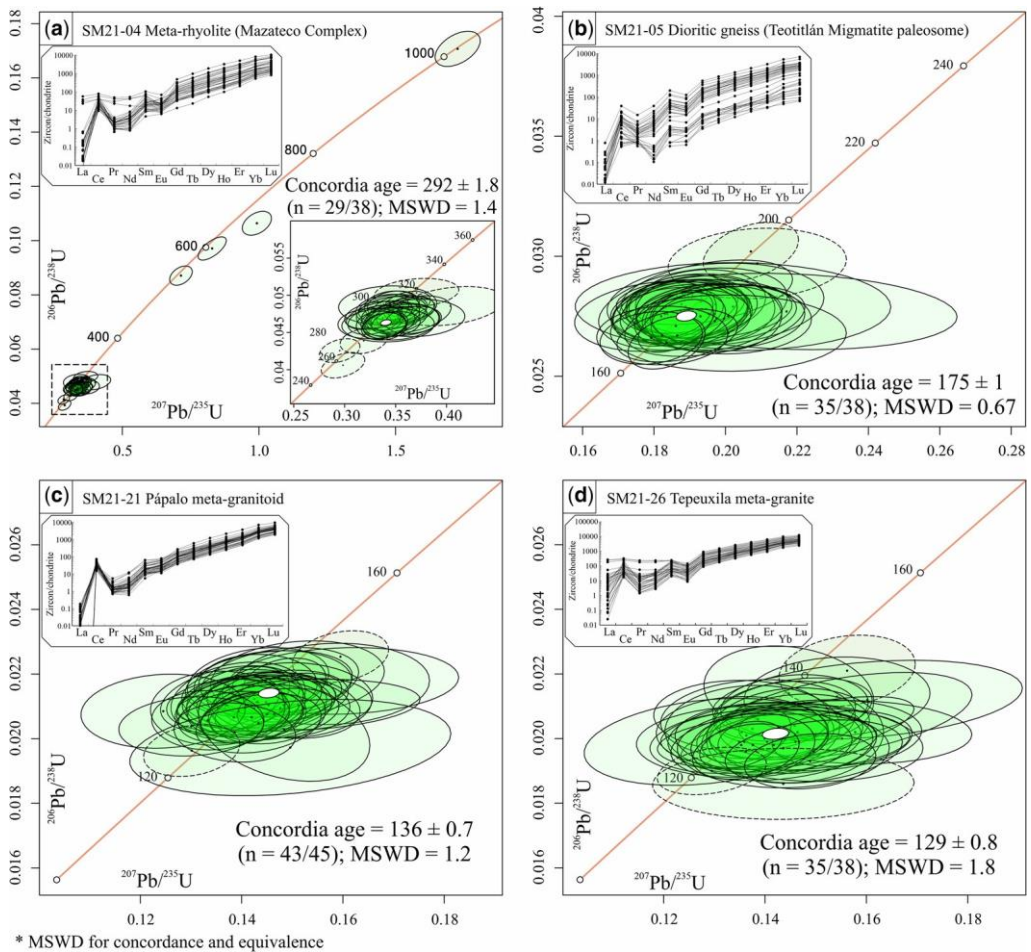


Fig. 7. U–Pb concordia diagrams and REE diagrams for different igneous samples of the SJC.

2020). Different tectonic scenarios have been proposed to explain the magmatism in NW Gondwana, ranging from extensional tectonics (e.g. Keppie *et al.* 2008; Ortega-Obregón *et al.* 2010; Ramos-Arias and Keppie 2011; Estrada-Carmona *et al.* 2012) to convergent arc-related scenarios (e.g. Weber *et al.* 2012; 2018; Juárez-Zúñiga *et al.* 2019). It is plausible that both tectonic schemes took place in a complex and evolutionary subduction model involving tectonic switching (Collins 2002) as the Venezuelan Mérida Andes basement (e.g. Tazzo-Rangel *et al.* 2018).

Correlation and extension. The dominance of Ordovician–Devonian over Precambrian detritus and the maximum depositional age of metapelite SM21-04b (c. 392 Ma) are features correlative with the Etlá suite of the southern SJC (Espejo-Bautista *et al.* 2021; Fig. 8). This correlation suggests the

existence of different sedimentary basins within the SJC, spanning from the Devonian to the Carboniferous periods. The Ordovician–Devonian signal seems to be a ubiquitous and diagnostic detrital source in these metasedimentary rocks, except for sample SM21-06, which represents pre-late Silurian sedimentation. This sedimentary system also could include areas currently exposed within the MC, as indicated by the presence of Devonian–Carboniferous ages (K–Ar in muscovite and whole rock; reported in Angeles-Moreno 2006); however, the validity of these ages is unclear, and this correlation remains uncertain. Detrital patterns similar to the Etlá suite (excepting sample SM21-06) occur in the Acatlán Complex in southwestern Mexico (e.g. the high-grade Xayacatlán Formation; Talavera-Mendoza *et al.* 2005), the Granjeno Schist in NE Mexico (Barboza-Gudiño *et al.* 2011), the Chuacús Complex in Guatemala (e.g. Solari *et al.* 2009;

Geological evolution of the Sierra de Juárez Complex

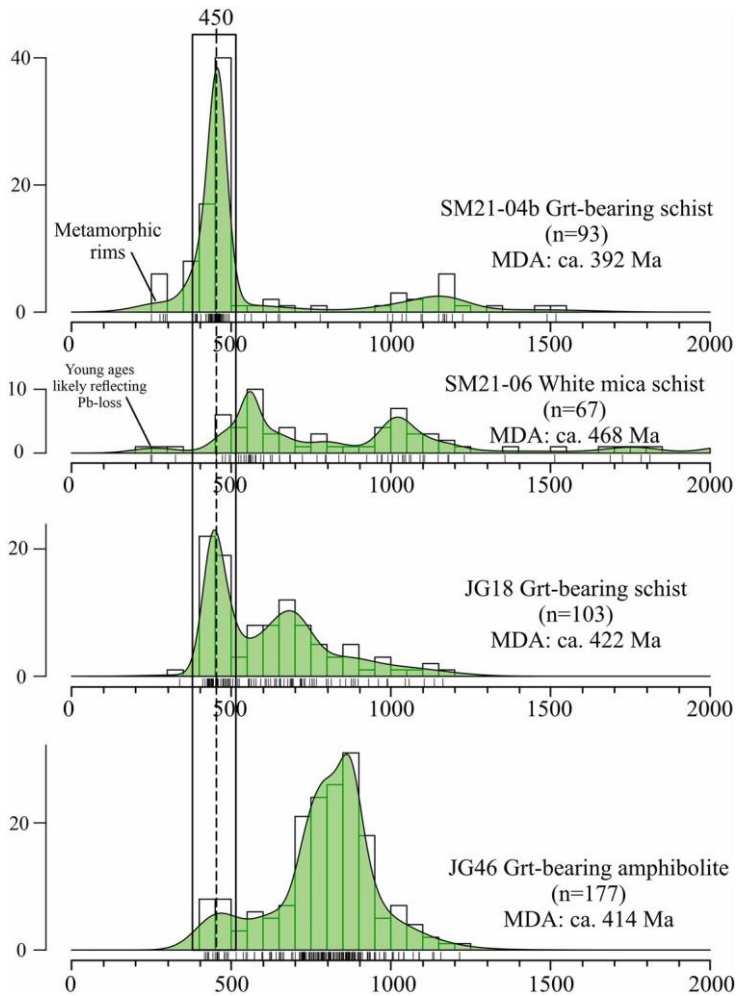


Fig. 8. KDE with histogram plots of samples representative of the SJC. SM21-04b and SM21-06 from this work, and JG18 and JG46 from the southern SJC (Espejo-Bautista *et al.* 2021).

Maldonado *et al.* 2018), the Macal Formation of the Maya Mountains in Belize (Martens *et al.* 2010), and even along the eastern cordillera of Perú (e.g. Reimann *et al.* 2010). These similarities suggest the existence of a wide Upper Ordovician–Devonian or later interconnected sedimentary basin system proximal to the Ordovician–Silurian–Devonian magmatic belt in NW Gondwana (Fig. 9a).

Tectonic interpretation. The period of deposition of the protolith of metapelites SM21-06 and SM21-04b between *c.* 468 and 300 Ma is coeval with the long-lived Ordovician–Devonian magmatic belt of NW Gondwana, and various sedimentary settings are consequently possible. However, the nearby occurrence of mid-ocean ridge basalt-like igneous rocks

of *c.* 441 Ma in the southern SJC (San Agustín Orthogneiss; Espejo-Bautista *et al.* 2021) suggests the presence of within-plate magmatism in the SJC during the early Silurian. Based on this consideration, transtensional basins related to the opening of the Rheic Ocean (e.g. Murphy *et al.* 2006; Nance *et al.* 2012) are consistent with the Silurian magmatic–sedimentary features observed in the SJC.

The opening of the Rheic Ocean is characterized by the separation of the Avalonian terranes from the northern margin of Gondwana, which followed a sinistral displacement until their accretion to North America. This tectonic scenario produced sinistral transtensional troughs along the northern and northwestern Gondwana margin (Solari *et al.* 2010; Weber *et al.* 2012), probably resulting in oceanic

Table 2. Summary of Ordovician–Devonian magmatic ages recognized in Mexico and Central–South America

Name/location	Lithology	Magmatic (protolith) age (Zircon U–Pb; Ma)	References
<i>Mexico</i>			
Esperanza Granitoids (Acatlán Complex)	Megacrystic granitoids	440 + 14 471 + 13 478 – 471 461 – 440 461 – 467	Ortega-Gutiérrez <i>et al.</i> (1999) Sánchez-Zavala <i>et al.</i> (2004) Talavera-Mendoza <i>et al.</i> (2005)
Xayacatlán Gabbro (Acatlán Complex)	Gabbroic dyke	440 + 15 442 + 1	Miller <i>et al.</i> (2007) Vega-Granillo <i>et al.</i> (2007) Keppie <i>et al.</i> (2008)
Sn M. Las Minas Granite (Acatlán Complex)	Megacrystic granite	473 + 32/–24	Keppie <i>et al.</i> (2010)
Amate Unit (Acatlán Complex)	Granitic dykes	452 – 447	Morales-Gámez <i>et al.</i> (2008)
Western Acatlán Complex	Granitic intrusives	462 – 472	Ortega-Obregón <i>et al.</i> (2009)
Chiapas Massif Complex	Felsic to mafic intrusives	448 – 470	Estrada-Carmona <i>et al.</i> (2012)
Motozintla (Chiapas Massif Complex)	Granite	482 + 5	Weber <i>et al.</i> (2008)
Candelaria Unit (Chiapas Massif Complex)	Deformed amphibolites	457 – 444	Weber <i>et al.</i> (2018)
Palo Liso Granite (Acatlán Complex)	Granite	470 + 1	Juárez-Zúñiga <i>et al.</i> (2019)
Peregrina Tonalite (Novillo Gneiss/Granjeno Schist)	Tonalite	449 + 2	Alemán-Gallardo <i>et al.</i> (2019a)
San Agustín Orthogneiss (Sierra de Juárez Complex)	Gabbroic gneiss	442 + 3	Espejo-Bautista <i>et al.</i> (2021)
<i>Central America (Guatemala and Belize)</i>			
Maya Mountains (Belize)	Granite – granodiorite	410 – 420	Steiner and Walker (1996)
Rabinal Suite (Guatemala)	Granitic intrusives	496 – 417	Ortega-Obregón <i>et al.</i> (2008)
Rabinal suite (Guatemala)	K-Feldspar porphyroblastic orthogneiss	485 – 410	Ratschbacher <i>et al.</i> (2009)
Maya Mountains (Belize)	Rhyolite	406 + 7/–6	Martens <i>et al.</i> (2010)
Altos Cuchumatanes (Guatemala)	Granite	461 + 6/–3	Solari <i>et al.</i> (2010)
Chuacús Complex	Granitic orthogneiss Granitic dyke Migmatitic gneiss	449 + 1/–3 466 + 27 450 + 2/–4	Solari <i>et al.</i> (2011)
Rabinal granite	Granite	471 + 3/–5	Solari <i>et al.</i> (2013)
Maya Mountains (Belize)	Granitoids	414 – 400	Weber <i>et al.</i> (2012)
Altos Cuchumatanes (Guatemala)	Granodiorite	457 + 1	Juárez-Zúñiga <i>et al.</i> (2019)
Sierra de las Minas Gneiss (Chuacús Complex)	Migmatitic gneiss	444 + 1.2	
Rabinal Suite (Guatemala)	Granite	456 – 427	
<i>NW South America</i>			
Tahami Terrane (La Miel Orthogneiss; Colombia)	Gneiss	470 – 440	Villagómez <i>et al.</i> (2011)
Anacona Terrane (Colombia)	Orthogneisses	479 – 443	Martens <i>et al.</i> (2014)
Mérida Andes (Venezuela)	Volcanosedimentary rocks and continental arc-magmatism	453 – 415	Van der Lelij <i>et al.</i> (2016)
Mérida Andes (Venezuela)	Complex protracted magmatism	487 – 420	Tazzo-Rangel <i>et al.</i> (2018)
Rio Piedras Gneiss-Sierra Nevada de Santa Marta (Colombia)	Quartzfeldspathic gneiss	449 + 3/–1	Piraquive <i>et al.</i> (2021)

Geological evolution of the Sierra de Juárez Complex

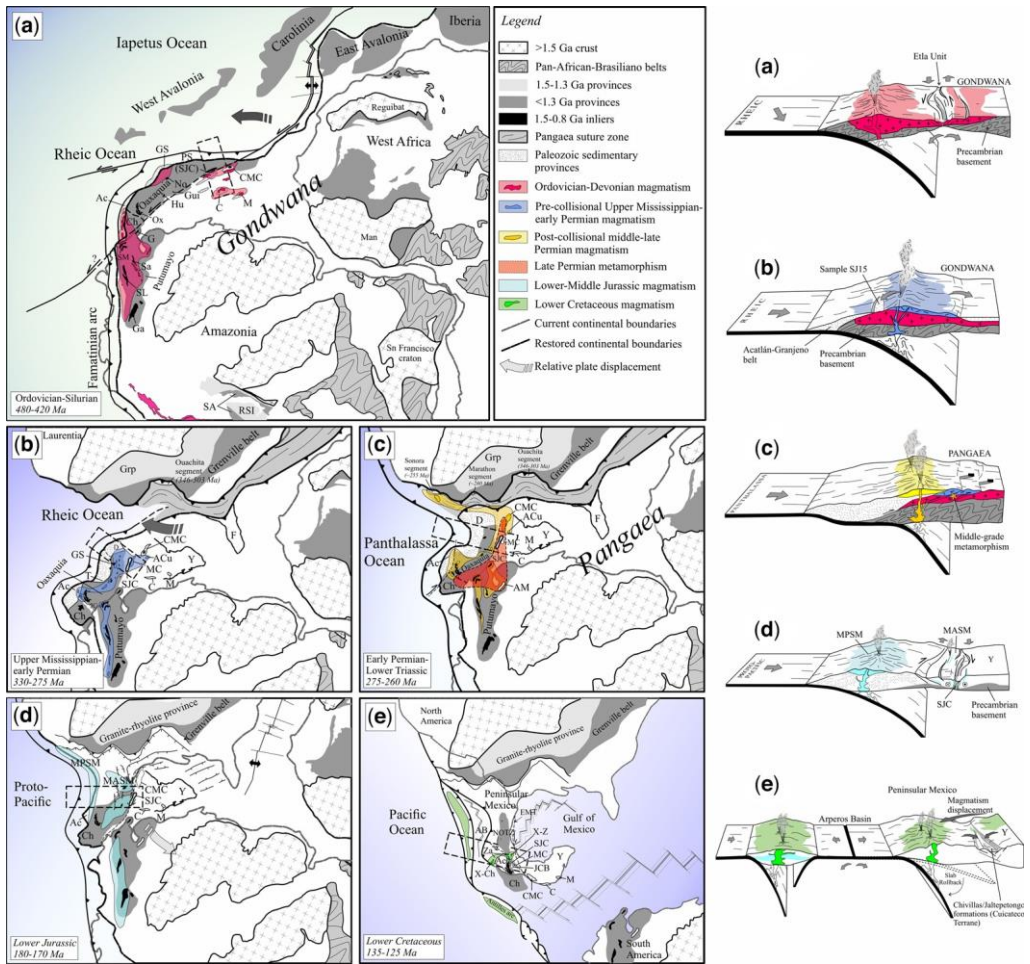


Fig. 9. Evolutionary palaeogeographic model from Middle Ordovician to Lower Cretaceous illustrating each geological stage recorded in the SJC. Abbreviations: AB, Arperos Basin; Ac, Acatlán Complex; ACu, Altos Cuchumatanes; AM, Andes Mérida; C, Chuacús Complex; Ch, Chortís Block; CMC, Chiapas Massif Complex; D, Delicias Fm.; EMT, East Mexico Transform; F, Florida; G, Guajira; Ga, Garzón Massif; Grp, Granite-rhyolite province; GS, Granjeno Schist; Gui, Guichicovi Complex; Hu, Huiznopala Gneiss; JC, Juchatengo Complex; JCB, Jaltepetongo-Chivillas Basin; M, Montañas Maya; MC, Mazateco Complex; MASM, Mesozoic Atlantic System of Mexico; MPSM, Mesozoic Pacific System of Mexico; No, Novillo Gneiss; Ox, Oaxacan Complex; PS, Pochotepec suite; RSI, Rondonian-San Ignacio; SJC, Sierra de Juárez Complex; SM, Sierra Nevada de Santa Marta; Sa, Santander; SL, Serranía de San Lucas; SA, Sunsás-Aguapei; T, Tuzancoa Formation; X-Ch, Xolapa-Chapolapa; X-Z, Xonomanca-Zongolica; Y, Yucatan (Maya Block); Za, Zongolica arc. Source: the geology of Amazonia is based on Ibanez-Mejía (2020), Ramos (2018) and Rodríguez-García *et al.* (2019); the geology of Western Africa is based on Youbi *et al.* (2013), and the geology of Laurentia is based on Johansson (2009). The model of Gondwana and Avalonian terranes was modified from Nance *et al.* (2012). The ages and architecture of the Ouachita-Marathon-Sonora belt are based on Poole *et al.* (2005). The Jurassic-Cretaceous tectonic evolution follows Martini and Ortega-Gutiérrez (2016), Maldonado *et al.* (2017) and Pindell *et al.* (2021). The western equatorial Pangaea model was modified from Elías-Herrera and Ortega-Gutiérrez (2002) and Weber *et al.* (2007, 2012).

lithosphere formation in some cases such as the SJC (Fig. 9a). The transtensional/convergent stage lasted until the end of the Lower Devonian (Martens *et al.* 2010; Weber *et al.* 2012), and was followed by the

development of a passive margin, interpreted on the basis of the absence of magmatism, until the Upper Mississippian-Middle Pennsylvanian when a new magmatic stage started (e.g. Kirsch *et al.* 2012).

Early Permian volcanosedimentary event

Two analysed samples are representative of this event: the Grt-Bt paragneiss SJ15 (palaeosome of the Mesozoic Teotitlán Migmatite – SJC) and the meta-rhyolite SM21-04 (Mazatlán de las Flores unit – MC). The former encompasses detrital zircon provenance groups with probability peaks at *c.* 1075, 742 and 486, probably sourced from nearby Precambrian exposures such as the Oaxacan Complex (e.g. [Solari *et al.* 2014](#)), from Gondwanan Pan-African-Brasiliano orogens (e.g. [Meert and Lieberman 2008](#)), and from the Ordovician–Devonian magmatic belt in NW Gondwana (e.g. [Juárez-Zúñiga *et al.* 2019](#), and references therein), respectively. The youngest concordant igneous-like xenocrysts constituting the maximum depositional age at *c.* 281 Ma point to a nearby igneous source. The metamorphic age of *c.* 246 Ma for this rock (discussed below) also represents a minimum depositional age, constraining the time of deposition to the Permian.

The second sample yielded an igneous protolith age of *c.* 292 Ma, recording volcanic activity in the northern MC, which could have been the source of early Permian detrital zircon in paragneiss SJ15. Based on these findings, it is feasible that both samples were roughly coeval and constituted an early–middle Permian volcanosedimentary succession. If so, it is plausible that part of the protoliths of the Teotitlán Migmatite derive from the NW MC. Therefore, the MC and the SJC share, at least in part, a common pre-Mesozoic geological evolution.

Several correlative Upper Mississippian–Middle Triassic granitoids and volcanosedimentary successions constitute a protracted magmatic belt that cut across Mexico, Central America and NW South America ([Table 3](#)). This belt was active during the closure of the Rheic Ocean (e.g. [Hatcher 2010](#); [Nance *et al.* 2010](#)) and continued after the assembly of Pangaea ([Coombs *et al.* 2020](#)).

The pre-orogenic magmatic stage of this belt (*c.* 330–286 Ma) is attributed to convergence between the North America and Gondwana continents ([Coombs *et al.* 2020](#)) that was coeval with convergent tectonics documented along the Ouachita–Marathon–Sonora orogenic belt during the final stages of western equatorial Pangaea assembly ([Poole *et al.* 2005](#)). In contrast, the post-orogenic stage (*c.* 274–243 Ma) is related to either eastward subduction of the Panthalassa Ocean crust beneath the western margin of the recently assembled Pangaea (e.g. [Ortega-Gutiérrez *et al.* 2014](#); [Spikings and Paul 2019](#)) or to post-collisional crustal relaxation ([Coombs *et al.* 2020](#); further discussed below). The age of the meta-rhyolite SM21-04 (*c.* 292 Ma) implies that the magmatic episode recorded in the northern MC–SJC belongs to the former magmatic phase ([Fig. 9b](#)).

Late Permian–Middle Triassic metamorphism

Field, petrographical and geochronological data suggest that paragneiss SJ15 (palaeosome of the Teotitlán Migmatite) underwent two post-sedimentary thermotectonic events. The first event produced middle-grade metamorphism developing gneissic fabrics and Grt-Bt assemblages, whereas the second induced partial melting and shearing (discussed in ‘Early Jurassic anatectic/magmatic and mylonitic episode’ section). In this section, we focus on the former. *In situ* zircon U–Pb analyses reveal the presence of two generations of metamorphic rims that probably typify each of the aforementioned thermotectonic episodes. Based on this evidence, the concordia age obtained from the first generation of zircon rims (246 ± 1.9 Ma; [Fig. 6b](#)) is taken to represent the time of Grt-Bt metamorphism. However, these analyses exhibit positive steep MREE–HREE patterns ([Fig. 6c](#)), suggesting that the zircon domains did not form coevally with garnet (e.g. [Rubatto 2017](#)); hence, they may not be precisely representative of the metamorphic peak. Given the increase in Yb and Lu relative to the other HREE observed in their REE patterns, it is probable that these zircon domains precipitated during a post-metamorphic peak with garnet breaking down and releasing HREE – perhaps a retrograde path during exhumation. Therefore, the result obtained from these analyses (246 ± 1.9 Ma) is considered to be a minimum metamorphic age.

Late Permian–Middle Triassic metamorphism constitutes a rare thermotectonic imprint post-dating the assembly of Pangaea and the post-collisional mid-late Permian magmatism in NW Gondwana. Compressive deformation, medium- to high-grade metamorphism and anatexis occurred in the Chiapas Massif Complex (the Maya Block in southeastern Mexico) between *c.* 255 and 245 Ma ([Weber *et al.* 2007](#); [Valencia-Morales *et al.* 2022](#)). This event may be attributed to either eastwards accretion of the Mexican Precambrian terranes (Oaxaquia, Chortís and Acatlán) against the Maya Block, or eastward flat-slab subduction of Panthalassa oceanic lithosphere beneath western Pangaea, triggering crustal thickening ([Weber *et al.* 2007](#); [Spikings and Paul 2019](#)). Similarly, orthogneisses with a protolith age of *c.* 273 Ma from the Las Ovejas Complex (Chortís Block) underwent high-*T* metamorphism, interpreted as the result of Middle Triassic eastward flat-subduction at *c.* 245 Ma ([Ratschbacher *et al.* 2009](#)). Likewise, a late Permian–Lower Triassic thermal disturbance in rocks from the Sierra Nevada de Santa Marta (NW Colombia) is ascribed to terrane accretion or plate coupling ([Cardona *et al.* 2010](#)). Finally, recent findings by [Tazzo-Rangel *et al.* \(2021\)](#) in the crystalline basement of the Mérida Andes (western Venezuela) indicate the presence

Geological evolution of the Sierra de Juárez Complex

Table 3. Summary of Mississippian–Permian magmatic ages recognized in Mexico and Central–South America

Name/location	Lithology	Magmatic (protolith) age (Zircon U–Pb; Ma)	References
<i>Mexico</i>			
Aserradero Rhyolite (Novillo Gneiss)	Rhyolite	334 + 39	Stewart <i>et al.</i> (1999)
La Pezuña Rhyolite	Rhyolite	331 + 4	Lopez <i>et al.</i> (1996)
Maxala Granite	Cataclastic granite	330 – 327	Martínez-Sánchez <i>et al.</i> (2016)
Juchatengo Complex	Plagiogranites–tonalites	313 – 260	Grajales-Nishimura <i>et al.</i> (2018)
Cuanana intrusive	Quartzdiorite–diorite–tonalite	310.8 + 18	Ortega-Obregón <i>et al.</i> (2014)
Totoltepec Pluton (Acatlán Complex)	Gabbro–trondhjemitic–diorite–tonalite	306 – 283	Kirsch <i>et al.</i> (2012)
Western Gulf of Mexico	Buried granitoids	294 – 243	Coombs <i>et al.</i> (2020)
Honduras Batholith	Tonalite–quartzdiorite	290.4 + 2	Ortega-Obregón <i>et al.</i> (2014)
Tuzancoa Formation	Volcanosedimentary rocks	290–260	Rosales-Lagarde <i>et al.</i> (2005)
Zaniza Batholith	Granite–tonalite	287.7 + 1	Ortega-Obregón <i>et al.</i> (2014)
Matzitzi Formation (boulders)	Felsic to intermediate volcanic clasts	285 – 269	Juárez-Zúñiga <i>et al.</i> (2021)
Caborca	Granitoids	280 – 270	Arvizu <i>et al.</i> (2009)
Cozahuico Granite (Acatlán Complex)	Granite	275 – 270	Elías-Herrera <i>et al.</i> (2007)
La Carbonera Stock (Oaxacan Complex)	Quartzdiorite–granodiorite	275 – 272	Ortega-Obregón <i>et al.</i> (2014)
Xolapa Complex	Tonalitic gneiss	272 + 10	Ducea <i>et al.</i> (2004)
Chiapas Batholith	Gabbro–granite	271.9 + 2	Weber <i>et al.</i> (2007)
Sosola Rhyolite	Rhyolite	270.5 + 2	Ortega-Obregón <i>et al.</i> (2014)
Sierra Pinta	Granites–Granodiorites	258 – 266	Arvizu <i>et al.</i> (2009)
Etla Granite (Oaxacan Complex)	Granodiorite–granite	255.2 + 1	Ortega-Obregón <i>et al.</i> (2014)
La Mixtequita Batholith (Guichicovi Complex)	Monzonite	254 + 7	Weber and Köhler (1999)
<i>Central America (Guatemala)</i>			
Altos Cuchumatanes (Maya Block)	Granites–granodiorites	312 – 318	Solari <i>et al.</i> (2010)
Las Ovejas Complex (Chortis)	Gneisses	273 + 2	Ratschbacher <i>et al.</i> (2009)
<i>NW South America</i>			
Sierra Nevada de Santa Marta (Colombia)	Granitic orthogneisses	288 – 264	Cardona <i>et al.</i> (2010)
Andes of Colombia	S-type metagranites	275 – 240	Cochrane <i>et al.</i> (2014)
Tahamí Terrane (Colombia)	Granite	271	Villagómez <i>et al.</i> (2011)
Paraguán Peninsula (Venezuela)	Diorite	272	Van der Lelij <i>et al.</i> (2016)
Guajira Arch (Colombia)	Mafic gneiss	272	Piraquive <i>et al.</i> (2021)
Colombian Andes	Granitoids and gneisses	294 – 260	Rodríguez-García <i>et al.</i> (2019)

of amphibolite-facies rocks with peak metamorphic ages between *c.* 251 and 249 Ma that were interpreted as resulting from crustal collapse after Pangaea assembly.

The late Permian–Lower Triassic metamorphism in western equatorial Pangaea constitutes a crucial correlative element for palinspastic reconstructions. However, its geodynamic nature is unclear as it may represent either contractional or extensional tectonics. The interpretation of the post-orogenic crustal relaxation based on negative $\epsilon_{\text{Hf}(t)}$ values (Coombs

et al. 2020) implies a dominantly extensional setting between *c.* 274 and 243 Ma. Likewise, Martini *et al.* (2021) described evidence from the Matzitzi Formation in southern Mexico suggesting initial fragmentation of Pangaea at *c.* 260 Ma. However, assuming that the sedimentary protolith of paragneiss SJ15 (this study) was deposited after 281 Ma (see Section ‘Early Permian volcanosedimentary event’) and its minimal metamorphic age was estimated in 246 + 1.9 Ma, it is essential to consider contractional tectonic burial during this

interval that resulted in middle-grade metamorphism. Furthermore, the increasing input of continental crustal material into the magma that occurs in the subduction front of a progressive slab flattening (Manea *et al.* 2017) would explain the negative $\epsilon_{\text{Hf}(t)}$ values in granites from eastern Mexico. Thus, we suggest flat-slab subduction and crustal thickening as the cause for Grt Bt metamorphism in sample SJ15 during the middle-late Permian (c. 275–260 Ma), followed by extensional tectonics during the late Permian–Middle Triassic that would evolve into the break-up of Pangaea (Fig. 9c).

Early Jurassic anatectic/magmatic and mylonitic episode

Partial melting occurring within a simple-shear strain system in the Teotitlán Migmatite of the northern SJC produced magmas that either cross-cut or rearranged the gneissic fabric of metamorphic rocks. The timing of anatexis is recorded by a second generation of metamorphic zircon rims in sample SJ15, which yielded a concordia age of 176 ± 1 Ma (Fig. 6b). This thermal disturbance is consistent with intermediate magmatism recorded by metadiorite SM21-05, dated at 175 ± 1 Ma. These findings document an anatectic/magmatic episode prior to the Valanginian anatectic/magmatic event (Ángeles-Moreno 2006; Coombs 2016). The presence of two Mesozoic anatectic episodes in the Teotitlán Migmatite is consistent with field relationships showing partial melting occurring during lateral shearing (schlieren migmatites), followed by extension-related anatectic structures (nebulitic migmatites and granitic dykes; Fig. 3b–g).

Similar Lower to Middle Jurassic magmatic ages from meta-granites are recognized within the SJC. In the northern sector, Pindell *et al.* (2021) report an age of 178 ± 3 Ma from a meta-quartzdiorite, whereas, in the southern SJC, Alaniz-Álvarez *et al.* (1996) and Espejo-Bautista *et al.* (2021) obtained ages from meta-granites suspected to be syntectonic with lateral mylonitic deformation at c. 165 and c. 191 Ma, respectively. Alaniz-Álvarez *et al.* (1996) attributed the Lower–Middle Jurassic mylonitic deformation and syntectonic magmatism to an extensive right-lateral transform system related to the opening of the Gulf of Mexico during the break-up of western Pangaea. This divergent event transferred the Maya Block (Yucatan peninsula) southwards into its current position, giving rise to right transtensional displacements along the eastern margin of Mexico.

Contemporary eastward supra-subduction of the Pacific plate beneath the North American plate led to the development of a complex magmatic arc subdivided by Martini and Ortega-Gutiérrez (2016) into

two systems: (1) the Mesozoic Pacific System of Mexico (MPSM) along the western margin of Mexico, composed of calc-alkaline granitoids with ages ranging between 190 and 164 Ma; and (2) the eastern Mesozoic Atlantic System of Mexico (MASM) which, being influenced by transtensional tectonics related to rifting Gulf of Mexico, was characterized by crustal thinning and the development of extensional sedimentary basins along with arc-related magmatism between 193 and 168 Ma (Fig. 9d). The end of the MASM during the Bajocian is coeval with the onset of salt deposition in the Gulf of Mexico, which is indicative of rifting transitioning into a drifting phase and the beginning of seafloor spreading during the southward transfer of the Yucatan peninsula (Pindell *et al.* 2021).

To avoid the overlapping problem of the Colombian and Mexican terranes in palinspastic reconstructions of Pangaea (e.g. Bullard *et al.* 1965), Pindell *et al.* (2021) proposed a pre-Jurassic palaeoposition for the MC–SJC together with the Oaxacan Complex (Oaxaca Block) in western peninsular Mexico, which would probably imply correlation of the Lower Jurassic anatectic/magmatic episode of the northern SJC (samples SJ15 and SM21-05) with the MPSM. According to this model, the Oaxaca Block would have been sinistrally transferred to its current position along the so-called ‘North Oaxaca Transfer Zone’ during the Upper Jurassic, similar to the model suggested by Le Pichon and Fox (1971). However, Lower Jurassic anatexis, magmatism and syntectonic dextral c. north–south strike-slip deformation in the northern SJC (this work) correlate more closely with the MASM than the MPSM, favouring the hypothesis proposed by Alaniz-Álvarez *et al.* (1996). This hypothesis is further supported by the presence of pre-Jurassic lithotectonic elements in the MC–SJC correlative with eastern Mexico and NW South America, such as the late Permian–Lower Triassic metamorphism, the early–middle Permian volcanosedimentary sequences and the Tonian (Neoproterozoic) metamorphism of the Pochotepec suite, which correlates with the Catarina Unit of the El Triunfo Complex in the Maya Block (Valencia-Morales *et al.* 2022; Espejo-Bautista *et al.* 2023). Therefore, we consider the SJC and the MC to have been located in an eastern Mexico pre-Jurassic palaeoposition and not part of the Oaxaca Block.

Lower Cretaceous magmatism and the last mylonitic episode

The Pápalo meta-diorite/tonalite and the Tepeuxila meta-granite represent intermediate to granitic Lower Cretaceous magmatism in the northern SJC.

Geological evolution of the Sierra de Juárez Complex

Their protolith magmatic ages (136 ± 0.7 and 129 ± 0.8 Ma, respectively) are broadly similar and thus considered representative of the same event.

The Pápalo and Tepeuxila intrusives correlate with a wide spectrum of igneous exposures and volcanosedimentary successions spanning the Berriasian to Barremian in southern Mexico, for instance, the Xonamanca Formation (Zongolica basin) in the eastern Cuicateco Terrane, which consists of a volcanosedimentary sequence dating to *c.* 140–137 Ma (Coombs 2016; Sierra-Rojas *et al.* 2022), and granitic-intermediate dykes and probably nebulitic migmatites of the Teotitlán Migmatite (northern SJC), dated at *c.* 141–133 Ma (Ángeles-Moreno 2006; Coombs 2016). Coombs (2016) referred to this Lower Cretaceous magmatic belt as the Zongolica arc, which probably also encompasses several intrusives and volcanosedimentary rocks within the Xolapa Complex of southern Mexico between *c.* 139 and 119 Ma (e.g. Solari *et al.* 2007; Pérez-Gutiérrez *et al.* 2009; Maldonado *et al.* 2020), as well as the *c.* 133 and 126 Ma volcanosedimentary Chapolapa Formation (Campa-Uranga and Iriando 2004; Hernández-Treviño *et al.* 2004), among others (Sierra-Rojas *et al.* 2022 and references therein).

The Zongolica arc was produced by eastward oceanic-crust subduction of either the Farallon or the Arperos plate beneath eastern Mexico between 140 and 119 Ma (Coombs 2016; Sierra-Rojas *et al.* 2022). The Arperos basin opened in response to extensional tectonics related to the subduction system along the eastern Pacific flank between 150 and 143 Ma. During this interval, seafloor spreading and passive margins characterized the Arperos basin (Martini and Ortega-Gutiérrez 2016), whereas the extension in the Gulf of Mexico slowed down until it reached its maximum size at *c.* 139 Ma (Pindell *et al.* 2021). The final stage of opening in the Gulf of Mexico is coeval with the onset of the eastward subduction of the Farallon or Arperos oceanic lithosphere triggered by tectonic switching, thereby giving rise to the development of the Zongolica arc. Extensional deep-marine sedimentation (the Jaltepetongo and Chivillas formations) occurred in the Cuicateco Terrane during the Hauterivian and Barremian (e.g. Mendoza-Rosales *et al.* 2010; Sierra-Rojas *et al.* 2022), coeval with the late stage of the Zongolica arc, indicating overlapping extensional and convergent tectonics between *c.* 133 and 120 Ma. To explain the divergence, Sierra-Rojas *et al.* (2022) suggested a slab rollback mechanism in the Farallon or Arperos plate that transferred the Zongolica arc westward from the Xonamanca-Zongolica region to the Xolapa-Chapolapa region. This led to extensional back-arc tectonics in the Cuicateco Terrane, followed by the separation of the Sierra de Juárez and Mazateco complexes by oblique sinistral transtensional displacement (Graham *et al.* 2021)

and the deposition of the Jaltepetongo–Chivillas formations in deep tectonic basins located between both lithotectonic belts. Alternatively, a faster subduction rate relative to the ridge spreading rate could have led the Arperos oceanic ridge to be subducted eastward beneath the North America plate, leading to back-arc extensional tectonics and the Jaltepetongo–Chivillas basin opening between *c.* 123 and 120 Ma (Coombs 2016; Fig. 9e).

Finally, it is clear from the age and structural fabric of the Pápalo and Tepeuxila intrusives that a syn- or post-Lower Cretaceous deep mylonitic event occurred in the northern SJC. Syn-magmatic shearing could have occurred in response to transtensional back-arc tectonics related to the opening of the Jaltepetongo/Chivillas basin in the Cuicateco Terrane (e.g. Graham *et al.* 2021; Pindell *et al.* 2021; Sierra-Rojas *et al.* 2022). Alternatively, post-magmatic mylonitic deformation could have occurred as a result of Late Cretaceous–Eocene eastward contractional tectonics in the Cuicateco Terrane (Graham *et al.* 2021).

Conclusions

Zircon U–Pb geochronological data presented in this study document the geological record of the northern Sierra de Juárez Complex in southern Mexico from the early Paleozoic to the late Mesozoic. The results demonstrate the existence of five main geological events implying a protracted geodynamic evolution of NW Gondwana, western equatorial Pangaea, and peninsular Mexico.

- (1) Meta-sedimentary rocks with Ordovician–Devonian minimum depositional ages and provenance of detritus from Gondwanan sources constitute a significant lithological component throughout the SJC. Their deposition is related to a transtensional tectonic regime along the NW margin of Gondwana during the separation of the Avalonian terranes and opening of the Rheic Ocean.
- (2) Meta-sedimentary palaeosomes from the Teotitlán Migmatite and meta-volcanic successions in the Mazateco Complex indicate volcanosedimentary activity between 292 and 281 Ma before the final amalgamation of western equatorial Pangaea.
- (3) After the amalgamation of Pangaea, the 292–281 Ma volcanosedimentary successions were tectonically buried and metamorphosed during the middle Permian. Convergent tectonics and metamorphism resulted from flat-slab subduction of the Panthalassa oceanic crust beneath the western Pangaea margin and the consequent crust thickening. The metamorphic peak was followed by crustal decompression and

the onset of the break-up of Pangaea after 260 Ma.

- (4) The northern SJC recorded two anatectic/magmatic and mylonitic stages. The first one comprises schlieren-type migmatites produced at *c.* 175 Ma in a dextral strike-slip regime and is related to the onset of rifting in the Gulf of Mexico along the eastern margin of peninsular Mexico during the break-up of Pangaea.
- (5) The second anatectic/magmatic and mylonitic episode corresponds to a 136–129 Ma magmatism represented by massive intrusives. This magmatism is attributed to the eastward subduction of the Arperos basin oceanic crust beneath the North American plate. This episode is taken as part of the Zongolica arc and correlated with the Xolapa Complex and the Chapolapa Formation in southern Mexico. The Cretaceous intrusives exhibit a strong mylonitic deformation, which is pervasive throughout the SJC. Its origin remains enigmatic and is tentatively attributed either to the opening of the Cretaceous Chivillas–Jaltepetongo basin or the Upper Cretaceous–Cenozoic Mexican Orogeny.

Acknowledgements The first author acknowledges the Consejo Nacional de Ciencia y Tecnología (CONACyT) for granting him a PhD scholarship. We thank Juan Tomás Vázquez Ramírez for thin section preparation, Manuel Albarrán Murillo for helping with the separation of zircon grains and Carlos Ortega Obregón for the acquisition of geochronological data (all from Centro de Geociencias, UNAM). We are grateful to Jarda Dostal, an anonymous reviewer and the editor Brendan Murphy for their constructive reviews that improved the manuscript's clarity.

Competing interests The authors declare that they have no known competing financial interests or personal relationships that could have appeared to influence the work reported in this paper.

Author contributions GE-B: conceptualization (lead), data curation (lead), formal analysis (lead), investigation (lead), methodology (lead), project administration (lead), visualization (lead), writing – original draft (lead); LS: data curation (equal), funding acquisition (lead), resources (lead), supervision (lead), writing – review & editing (supporting); RM: formal analysis (equal), investigation (equal), writing – original draft (supporting), writing – review & editing (supporting); MR-C: formal analysis (supporting), investigation (equal), writing – original draft (supporting), writing – review & editing (supporting).

Funding This paper was financed by CONACyT Ciencia de Frontera 7351 and PAPIIT-DGAPA, UNAM, IN101520, both granted to Luigi A. Solari, and by a PhD

scholarship from Consejo Nacional de Ciencia y Tecnología (CONACyT) to Guillermo Espejo-Bautista.

Data availability All data generated or analysed during this study are included in this published article as 'Supplementary data'.

References

- Alaniz-Álvarez, S.A., van der Heyden, P., Nieto-Samaniego, A.F. and Ortega-Gutiérrez, F. 1996. Radiometric and kinematic evidence for Middle Jurassic strike-slip faulting in southern Mexico related to the opening of the Gulf of Mexico. *Geology*, 24, 443–446, [https://doi.org/10.1130/0091-7613\(1996\)024<0443:RAKEFM>2.3.CO;2](https://doi.org/10.1130/0091-7613(1996)024<0443:RAKEFM>2.3.CO;2)
- Alemán-Gallardo, E.A., Ramírez-Fernández, J.A. *et al.* 2019a. Evidence for an Ordovician continental arc in the pre-Mesozoic basement of the Huizachal–Peregrina Anticlinorium, Sierra Madre Oriental, Mexico: Peregrina Tonalite. *Mineralogy and Petrology*, 113, 505–525, <https://doi.org/10.1007/s00710-019-00660-4>
- Alemán-Gallardo, E.A., Ramírez-Fernández, J.A., Weber, B., Velasco-Tapia, F. and Casas-Peña, J.M. 2019b. Novillo Metamorphic Complex, Huizachal–Peregrina Anticlinorium, Tamaulipas, Mexico: characterization and development based on whole-rock geochemistry and Nd-isotopic ratios. *Journal of South American Earth Sciences*, 96, 102382, <https://doi.org/10.1016/j.jsames.2019.102382>
- Ángeles-Moreno, E. 2006. *Petrografía, Geología estructural y geocronología del borde noroccidental del terreno Cuicateco, sierra Mazateca, estado de Oaxaca, México*. Msc thesis, Universidad Nacional Autónoma de México.
- Ángeles-Moreno, E., Elías-Herrera, M., Macías-Romo, C., Sánchez-Zavala, J.L. and Ortega-Gutiérrez, F. 2012. Geological map of the western border of the Cuicateco terrane, southern Mexico. *Geological Society of America, Map & Chart Series*, MCH102.
- Arvizu, H.E., Iriando, A. *et al.* 2009. Rocas graníticas pérmicas en la Sierra Pinta, NW de Sonora, México: Magmatismo de subducción asociado al inicio del margen continental activo del SW de Norteamérica. *Revista Mexicana de Ciencias Geológicas*, 26, 709–728, https://www.scielo.org.mx/scielo.php?pid=S1026-87742009000300013&script=sci_arttext
- Barboza-Gudiño, J.R., Ramírez-Fernández, J.A., Torres-Sánchez, S.A. and Valencia, V. 2011. Geocronología de circones detríticos de diferentes localidades del Esquisto Granjeno en el noreste de México. *Revista Mexicana de Ciencias Geológicas*, 63, 201–216, <https://doi.org/10.18268/BSGM2011v63n2a5>
- Belousova, E.A., Griffin, W.L., Suzanne, Y. and Fisher, N.I. 2002. Igneous zircon: trace element composition as an indicator of source rock type. *Contributions to Mineralogy and Petrology*, 143, 602–622, <https://doi.org/10.1007/s00410-002-0364-7>
- Bullard, E., Everett, J.E. and Smith, G. 1965. The fit of the continents around the Atlantic. *Philosophical Transactions of the Royal Society of London, Series A, Mathematical and Physical Sciences*, 528, 41–51, <https://doi.org/10.1098/rsta.1965.0020>

Geological evolution of the Sierra de Juárez Complex

- Cameron, K.L., Lopez, R., Ortega-Gutiérrez, F., Solari, L.A., Keppie, J.D. and Schulze, C. 2004. U–Pb geochronology and Pb isotopic compositions of leached feldspars: Constraints on the origin and evolution of Grenville rocks from eastern and southern Mexico. *Geological Society of America*, 197, 755–769, <https://doi.org/10.1130/0-8137-1197-5.755>
- Campa-Uranga, M.F. and Iriondo, A. 2004. Significado de dataciones cretácicas de los arcos volcánicos de Taxco, Taxco el Viejo y Chapolapa, en la evolución de la Plataforma Guerrero Morelos. Paper presented at IV Reunión Nacional de Ciencias de la Tierra, Sociedad Geológica Mexicana, 76, Juriquilla, Querétaro.
- Cardona, A., Valencia, V., Garzón, A., Montes, C., Ojeda, G., Ruiz, J. and Weber, M. 2010. Permian to Triassic I to S-type magmatic switch in the northeast Sierra Nevada de Santa Marta and adjacent regions, Colombian Caribbean: Tectonic setting and implications within Pangea paleogeography. *Journal of South American Earth Sciences*, 29, 772–783, <https://doi.org/10.1016/j.jsames.2009.12.005>
- Carfantan, J.C. 1986. *Du système Cordillerain nord-américain au domaine Caraïbe: étude Géologique du Mexique méridional*. PhD thesis, Université de Savoie, Chambéry, France.
- Cochrane, R., Spikings, R. et al. 2014. Permo-Triassic anatectis, continental rifting and the disassembly of western Pangaea. *Lithos*, 190–191, 383–402, <https://doi.org/10.1016/j.lithos.2013.12.020>
- Collins, W.J. 2002. Hot orogens, tectonic switching, and creation of continental crust. *Geology*, 30, 535–538, [https://doi.org/10.1130/0091-7613\(2002\)030<0535:HOTSAC>2.0.CO;2](https://doi.org/10.1130/0091-7613(2002)030<0535:HOTSAC>2.0.CO;2)
- Coombs, H. 2016. *Geochemical and geochronological constraints on terrane definition in Mexico*. PhD thesis, Cardiff University.
- Coombs, H., Kerr, A.C., Pindell, J., Buchs, D., Weber, B. and Solari, L. 2020. Petrogenesis of the crystalline basement along the western Gulf of Mexico: postcollisional magmatism during the formation of Pangea. *Geological Society of America, Special Paper*, 546, [https://doi.org/10.1130/2020.2546\(02\)](https://doi.org/10.1130/2020.2546(02))
- Corfu, F., Hanchar, J.M., Hoskin, P.W.O. and Kinny, P. 2003. Atlas of zircon textures. *Reviews in Mineral Geochemistry*, 53, 469–500, <https://doi.org/10.2113/0530469>
- Delgado-Argote, L.A., López-Martínez, M., York, and Hall, C.M. 1992. Geologic framework and geochronology of ultramafic complexes of southern Mexico. *Canadian Journal of Earth Sciences*, 29, 1590–1604, <https://doi.org/10.1139/e92-125>
- Dickinson, W.R. and Gehrels, G.E. 2009. Use of U–Pb ages of detrital zircons to infer maximum depositional ages of strata: a test against a Colorado Plateau Mesozoic database. *Earth and Planetary Science Letters*, 288, 115–125, <https://doi.org/10.1016/j.epsl.2009.09.013>
- Ducea, M.N., Gehrels, G.E., Shoemaker, S., Ruiz, J. and Valencia, V.A. 2004. Geologic evolution of the Xolapa Complex, southern Mexico: evidence from U–Pb zircon geochronology. *Geological Society of America Bulletin*, 116, 1016–1025, <https://doi.org/10.1130/B25467.1>
- Elías-Herrera, M. and Ortega-Gutiérrez, F. 2002. Caltepec fault zone: an Early Permian dextral transpressional boundary between the Proterozoic Oaxacan and Paleozoic Acatlán complexes, southern Mexico, and regional tectonic implications. *Tectonics*, 21, 4-1–4-18, <https://doi.org/10.1029/2000TC001278>
- Elías-Herrera, M., Ortega-Gutiérrez, F., Sánchez-Zavala, J.L., Macías-Romo, C., Ortega-Rivera, A. and Iriondo, A. 2007. The Caltepec fault zone: exposed roots of a long-lived tectonic boundary between two continental terranes of southern México. *Geological Society of America, Special Papers*, 422, 317–342, [https://doi.org/10.1130/2007.2422\(11\)](https://doi.org/10.1130/2007.2422(11))
- Espejo-Bautista, G., Ortega-Gutiérrez, F., Solari, L.A., Maldonado, R. and Valencia-Morales, Y.T. 2021. The Sierra de Juárez Complex: a new Gondwanan Neoproterozoic–early Palaeozoic metamorphic terrane in southern Mexico. *International Geology Review*, 64, 631–653, <https://doi.org/10.1080/00206814.2020.1870172>
- Espejo-Bautista, G., Solari, L.A., Maldonado, R. and Ramírez-Calderón, M. 2023. Stenian arc-magmatism and early Tonian metamorphism along the northern border of Amazonia during the Rodinia assembly: the Pochotepec suite in southern Mexico. *Journal of South American Earth Sciences*, 124, 104248, <https://doi.org/10.2139/ssm.4297747>
- Estrada-Carmona, J., Weber, B., Martens, U. and López-Martínez, M. 2012. Petrogenesis of Ordovician magmatic rocks in the southern Chiapas Massif Complex: relations with the early Paleozoic magmatic belts of northwestern Gondwana. *International Geology Review*, 54, 1918–1943, <https://doi.org/10.1080/00206814.2012.685553>
- Fornelli, A., Langone, A., Micheletti, F., Pascazio, A. and Piccarreta, G. 2014. The role of trace element partitioning between garnet, zircon and orthopyroxene on the interpretation of zircon U–Pb ages: an example from high-grade basement in Calabria. *International Journal of Earth Sciences*, 103, 487–507, <https://doi.org/10.1007/s00531-013-0971-8>
- Fornelli, A., Langone, A., Micheletti, F. and Piccarreta, G. 2017. REE partition among zircon, orthopyroxene, amphibole and garnet in a high-grade metabasic system. *Geological Magazine*, 155, 1705–1726, <https://doi.org/10.1017/S001675681700067X>
- Gehrels, G. 2011. Detrital zircon U–Pb geochronology: current methods and new opportunities. In: Cathy, B. and Azor, A. (eds) *Tectonics of Sedimentary Basins: Recent Advances*. Blackwell, 47–62.
- Graham, R., Pindell, J., Villagómez, D., Molina-Garza, R., Granath, J. and Sierra-Rojas, M. 2021. Integrated Cretaceous–Cenozoic plate tectonics and structural geology in southern Mexico. *Geological Society, London, Special Publications*, 504, 285–314, <https://doi.org/10.1144/SP504-2020-70>
- Grajales-Nishimura, J.M., Ramos-Arias, M.A., Solari, L., Murillo-Muñetón, G., Centeno-García, E., Schaaf, P. and Torres-Vargas, R. 2018. The Juchatengo complex: an upper-level ophiolite assemblage of late Paleozoic age in Oaxaca, southern Mexico. *International Journal of Earth Sciences*, 107, 1005–1031, <https://doi.org/10.1007/s00531-017-1580-8>
- Grimes, C.B., Wooden, J.L., Cheadle, M.J. and John, B.E. 2015. ‘Fingerprinting’ tectono-magmatic provenance

- using trace elements in igneous zircon. *Contributions to Mineralogy and Petrology*, 170, <https://doi.org/10.1007/s00410-015-1199-3>
- Hatcher, R.D., Jr 2010. The Appalachian orogen: A brief summary. *Geological Society of America, Memoirs*, 206, 1–19, [https://doi.org/10.1130/2010.1206\(01\)](https://doi.org/10.1130/2010.1206(01))
- Hernández-Treviño, T., Torres de León, R., Solís-Pichardo, G., Schaaf, P., Hernández-Bernal, M.S. and Morales-Contreras, J.J. 2004. Edad de la Formación Chapolapa en la localidad del Río Cochoapa al este del Ocotito, estado de Guerrero. Paper presented at the IV Reunión Mexicana de Ciencias de la Tierra, Juriquilla, Querétaro, 338.
- Hinton, R.W. and Upton, B.G.J. 1991. The chemistry of zircon: variations within and between large crystals from syenite and alkali basalt xenoliths. *Geochimica et Cosmochimica Acta*, 55, 3287–3302, [https://doi.org/10.1016/0016-7037\(91\)90489-R](https://doi.org/10.1016/0016-7037(91)90489-R)
- Hoskin, P.W.O. and Black, L.P. 2000. Metamorphic zircon formation by solid-state recrystallization of protolith igneous zircon. *Journal of Metamorphic Geology*, 18, 423–439, <https://doi.org/10.1046/j.1525-1314.2000.00266.x>
- Hoskin, P.W.O. and Schaltegger, U. 2003. The composition of zircon and igneous and metamorphic petrogenesis. *Reviews in Mineralogy and Geochemistry*, 53, 27–62, <https://doi.org/10.2113/0530027>
- Ibanez-Mejia, M. 2020. The Putumayo Orogen of Amazonia: a synthesis. In: Gómez, J. and Mateus-Zabala, D. (eds) *The Geology of Colombia, Volume 1 Proterozoic – Paleozoic. Servicio Geológico Colombiano, Publicaciones Geológicas Especiales*, 35, 101–131,
- Ibanez-Mejia, M., Ruiz, J., Valencia, V.A., Cardona, A., Gehrels, G.E. and Mora, A.R. 2011. The Putumayo Orogen of Amazonia and its implications for Rodinia reconstructions: new U–Pb geochronological insights into the Proterozoic tectonic evolution of northwestern South America. *Precambrian Research*, 191, 58–77, <https://doi.org/10.1016/j.precamres.2011.09.005>
- Johansson, Å. 2009. Baltica, Amazonia and the SAMBA connection – 1000 million years of neighbourhood during the Proterozoic? *Precambrian Research*, 175, 221–234, <https://doi.org/10.1016/j.precamres.2009.09.011>
- Juárez-Zúñiga, S., Solari, L. and Ortega-Obregón, C. 2019. Ordovician to Silurian igneous rocks in southern Mexico and Central America: geochronologic and isotopic constraints on paleogeographic models. *Journal of South American Earth Sciences*, 93, 462–479, <https://doi.org/10.1016/j.jsames.2019.04.023>
- Juárez-Zúñiga, S., Solari, L. and Ortega-Obregón, C. 2021. Permian igneous clasts from the Matzitz Formation, southern Mexico: isotopic constraints on the final amalgamation of Pangea. *Geological Society, London, Special Publications*, 503, 481–496, <https://doi.org/10.1144/SP503-2019-238>
- Keppie, J.D. and Dostal, J. 2007. Rift-related basalts in the 1.2–1.3 Ga granulites of the northern Oaxacan Complex, southern Mexico: evidence for a rifted arc on the northwestern margin of Amazonia. *Proceedings of the Geologists' Association*, 118, 63–74, [https://doi.org/10.1016/S0016-7878\(07\)80048-4](https://doi.org/10.1016/S0016-7878(07)80048-4)
- Keppie, J.D. and Ortega-Gutiérrez, F. 2010. 1.3 Ga Oaxaquia (Mexico): remnant of an arc/backarc on the northern margin of Amazonia. *Journal of South American Earth Sciences*, 29, 21–27, <https://doi.org/10.1016/j.jsames.2009.07.001>
- Keppie, J.D., Dostal, J., Ortega-Gutiérrez, F. and Lopez, R. 2001. A Grenvillian arc on the margin of Amazonia: evidence from the southern Oaxacan Complex, southern Mexico. *Precambrian Research*, 112, 165–181, [https://doi.org/10.1016/S0301-9268\(00\)00150-9](https://doi.org/10.1016/S0301-9268(00)00150-9)
- Keppie, J.D., Dostal, J., Cameron, K.L., Solari, L., Ortega-Gutiérrez, F. and Lopez, R. 2003. Geochronology and geochemistry of Grenvillian igneous suites in the northern Oaxacan Complex, southern Mexico: tectonic implications. *Precambrian Research*, 120, 365–389, [https://doi.org/10.1016/S0301-9268\(02\)00166-3](https://doi.org/10.1016/S0301-9268(02)00166-3)
- Keppie, J.D., Dostal, J., Nance, D., Miller, B.V., Ortega-Rivera, A. and Lee, J.K.W. 2006. Circa 546 Ma plume-related dykes in the c. 1 Ga Novillo Gneiss (east-central Mexico): evidence for the initial separation of Avalonia. *Precambrian Research*, 147, 342–353, <https://doi.org/10.1016/j.precamres.2006.01.020>
- Keppie, J.D., Dostal, J. *et al.* 2008. Ordovician–earliest Silurian rift tholeiites in the Acatlán Complex, southern Mexico: evidence of rifting on the southern margin of the Rheic Ocean. *Tectonophysics*, 461, 130–156, <https://doi.org/10.1016/j.tecto.2008.01.010>
- Keppie, J.D., Nance, R.D., Ramos-Arias, M.A., Lee, J.K.W., Dostal, J., Ortega-Rivera, A. and Murphy, J.B. 2010. Late Paleozoic subduction and exhumation of Cambro-Ordovician passive margin and arc rocks in the northern Acatlán Complex, southern Mexico: geochronological constraints. *Tectonophysics*, 495, 213–229, <https://doi.org/10.1016/j.tecto.2010.09.019>
- Kirsch, M., Keppie, J.D., Murphy, J.B. and Solari, L.A. 2012. Permian–Carboniferous arc magmatism and basin evolution along the western margin of Pangea: geochemical and geochronological evidence from the eastern Acatlán Complex, southern Mexico. *Geological Society of America Bulletin*, 124, 1607–1628, <https://doi.org/10.1130/B30649.1>
- Kylander-Clark, A.R.C. 2017. Petrochronology by laser-ablation inductively coupled plasma mass spectrometry. *Reviews in Mineralogy and Geochemistry*, 83, 183–198, <https://doi.org/10.2138/rmg.2017.83.6>
- Lawlor, P.J., Ortega-Gutiérrez, F., Cameron, K.L., Ochoa-Camarillo, H., Lopez, R. and Sampson, D.E. 1999. U–Pb Geochronology, geochemistry, and provenance of the Grenvillian Huiznopala Gneiss of eastern Mexico. *Precambrian Research*, 94, 73–99, [https://doi.org/10.1016/S0301-9268\(98\)00108-9](https://doi.org/10.1016/S0301-9268(98)00108-9)
- Le Pichon, X. and Fox, P.J. 1971. Marginal offsets, fracture zones, and the early opening of the North Atlantic. *Journal of Geophysical Research*, 76, 6294–6308, <https://doi.org/10.1029/JB076i026p06294>
- Li, Z.X., Bogdanova, S.V. *et al.* 2008. Assembly, configuration, and break-up history of Rodinia: a synthesis. *Precambrian Research*, 160, 179–210, <https://doi.org/10.1016/j.precamres.2007.04.021>
- Lopez, R., Jones, N.W. and Cameron, K.L. 1996. The pre-Jurassic evolution of the Coahuila terrane, Mexico: no evidence of a major change in magmatic source during the course of the Ouachita orogeny. *Eos (Transactions, American Geophysical Union)*, 77, F759.

Geological evolution of the Sierra de Juárez Complex

- Maldonado, R., Weber, W., Ortega-Gutiérrez, F. and Solari, L. 2017. High-pressure metamorphic evolution of eclogite and associated metapelite from the Chuacús complex (Guatemala Suture Zone): Constraints from phase equilibria modelling coupled with Lu–Hf and U–Pb geochronology. *Journal of Metamorphic Geology*, 36, 1–30, <https://doi.org/10.1111/jmg.12285>
- Maldonado, R., Ortega-Gutiérrez, F. and Ortíz-Joya, G.A. 2018. Subduction of Proterozoic to Late Triassic continental basement in the Guatemala suture zone: a petrological and geochronological study of high-pressure metagranitoids from the Chuacús complex. *Lithos*, 308–309, 83–108, <https://doi.org/10.1016/j.lithos.2018.02.030>
- Maldonado, R., Corona-Chávez, P., Solari, L., Ortega-Obregón, C. and Poli, S. 2020. Petrology and U–Pb geochronology of high-grade metavolcano-sedimentary rocks from central Xolapa Complex, southern Mexico. *Lithos*, 378, 105802, <https://doi.org/10.1016/j.lithos.2020.105802>
- Manea, V.C., Manea, M., Ferrari, L., Orozco-Esquivel, T., Valenzuela, R.W., Husker, A. and Kostoglodov, V. 2017. A review of the geodynamic evolution of flat slab subduction in Mexico, Peru, and Chile. *Tectonophysics*, 695, 27–52, <https://doi.org/10.1016/j.tecto.2016.11.037>
- Martens, U., Weber, B. and Valencia, V.A. 2010. U/Pb geochronology of Devonian and older Paleozoic beds in the southeastern Maya block, Central America: its affinity with peri-Gondwanan terranes. *Geological Society of America Bulletin*, 122, 815–829, <https://doi.org/10.1130/B26405.1>
- Martens, U., Restrepo, J.J., Ordóñez-Carmona, O. and Correa-Martínez, A.M. 2014. The Tahamí and Anaconda terranes of the Colombian Andes: missing links between the South American and Mexican Gondwana Margins. *The Journal of Geology*, 122, 507–530, <https://doi.org/10.1086/677177>
- Martínez-Sánchez, E., Hernández-Treviño, T., Villanueva-Lascaraín, D., Espejo-Bautista, G., López-Díaz, F., Solari, L. and Solís-Pichardo, G. 2016. Magmatism in the Sierra Madre Oriental: geology, geochemistry and geochronology from Maxala Granitoid, Hidalgo and Veracruz, Mexico. Paper presented at the 10th South American Symposium on Isotope Geology, Puerto Vallarta, Mexico.
- Martini, M. and Ortega-Gutiérrez, F. 2016. Tectono-stratigraphic evolution of eastern Mexico during the break-up of Pangea: a review. *Earth-Science Reviews*, 183, 38–55, <https://doi.org/10.1016/j.earscirev.2016.06.013>
- Martini, M., Anaya-Guarneros, J.A., Solari, L., Bedoya, A., Martínez-Zepeda, M. and Villanueva-Amadoz, U. 2021. The Matzitzi Formation in southern Mexico: a record of Pangea final assembly or breakup initiation along inherited suture belts? *Basin Research*, 34, 1–21, <https://doi.org/10.1111/bre.12638>
- Meert, J.G. and Lieberman, B.S. 2008. The Neoproterozoic assembly of Gondwana and its relationship to the Ediacaran–Cambrian radiation. *Gondwana Research*, 14, 5–21, <https://doi.org/10.1016/j.gr.2007.06.007>
- Mendoza-Rosales, C.C., Centeno-García, E., Silva-Romo, G., Campos-Madrugal, E. and Bernal, J.P. 2010. Barremian rift-related turbidites and alkaline volcanism in southern Mexico and their role in the opening of the Gulf of Mexico. *Earth and Planetary Science Letters*, 295, 419–434, <https://doi.org/10.1016/j.epsl.2010.04.020>
- Miller, B.V., Dostal, J., Keppie, J.D., Nance, R.D., Ortega-Rivera, A. and Lee, J.K.W. 2007. Ordovician calc-alkaline granitoids in the Acatlán Complex, southern Mexico: geochemical and geochronologic data and implications for the tectonics of the Gondwanan margin of the Rheic Ocean. *Geological Society of America, Special Paper*, 423, 465–475, [https://doi.org/10.1130/2007.2423\(23\)](https://doi.org/10.1130/2007.2423(23))
- Morales-Gámez, M., Keppie, J.D., Lee, J.K.W. and Ortega-Rivera, A. 2008. Paleozoic structures in the Xayacatlán area, Acatlán Complex, southern Mexico: transtensional rift- and subduction-related deformation along the margin of Oaxaquia. *International Geology Review*, 51, 279–303, <https://doi.org/10.1080/00206810802688659>
- Murphy, J.B., Gutiérrez-Alonso, G. et al. 2006. Origin of the Rheic Ocean: rifting along a Neoproterozoic suture? *Geology*, 34, 325–328, <https://doi.org/10.1130/G22068.1>
- Nance, R.D., Gutiérrez-Alonso, G. et al. 2010. Evolution of the Rheic Ocean. *Gondwana Research*, 17, 194–222, <https://doi.org/10.1016/j.gr.2009.08.001>
- Nance, R.D., Gutiérrez-Alonso, G. et al. 2012. A brief history of the Rheic Ocean. *Geoscience Frontiers*, 3, 125–135, <https://doi.org/10.1016/j.gsf.2011.11.008>
- Olierook, H.K.H., Kirkland, C.L., Barham, M., Daggitt, M.L., Hollis, J. and Hartnady, M. 2021. Extracting meaningful U–Pb ages from core–rim mixtures. *Gondwana Research*, 92, 102–112, <https://doi.org/10.1016/j.gr.2020.12.021>
- Ortega-Gutiérrez, F. 1981. Metamorphic belts of southern Mexico and their tectonic significance. *Geofísica Internacional*, 20, 177–202, <https://doi.org/10.22201/igeof.00167169p.1981.20.3.1085>
- Ortega-Gutiérrez, F. 1984. Evidence of Precambrian evaporites in the Oaxacan granulite complex of southern Mexico. *Precambrian Research*, 23, 377–393, [https://doi.org/10.1016/0301-9268\(84\)90051-2](https://doi.org/10.1016/0301-9268(84)90051-2)
- Ortega-Gutiérrez, F., Mitre-Salazar, L.M., Rodán-Quintana, J., Sánchez-Rubio, G. and de la Fuente, M. 1991. North American Continent Ocean Transects Program, Transect H-3, Acapulco Trench to the Gulf of Mexico Across Southern Mexico. *Geological Society of America, Boulder, CO*, Decade of North American Geology Program, 9.
- Ortega-Gutiérrez, F., Ruiz, J. and Centeno-García, E. 1995. Oaxaquia, a Proterozoic microcontinent accreted to North America during the late Paleozoic. *Geology*, 23, 1127–1130, [https://doi.org/10.1130/0091-7613\(1995\)023<1127:OAPMAT>2.3.CO;2](https://doi.org/10.1130/0091-7613(1995)023<1127:OAPMAT>2.3.CO;2)
- Ortega-Gutiérrez, F., Elías-Herrera, M., Reyes-Salas, M., Macías-Romo, C. and López, R. 1999. Late Ordovician–Early Silurian continental collisional orogeny in southern Mexico and its bearing on Gondwana–Laurentia connections. *Geology*, 27, 719–722, [https://doi.org/10.1130/0091-7613\(1999\)027<0719:LOESCC>2.3.CO;2](https://doi.org/10.1130/0091-7613(1999)027<0719:LOESCC>2.3.CO;2)
- Ortega-Gutiérrez, F., Elías-Herrera, M., Morán-Zenteno, D.J., Solari, L., Luna-González, L. and Schaaf, P. 2014. A review of batholiths and other plutonic

- intrusions of Mexico. *Gondwana Research*, 26, 834–868, <https://doi.org/10.1016/j.gr.2014.05.002>
- Ortega-Gutiérrez, F., Elías-Herrera, M., Morán-Zenteno, D.J., Solari, L., Weber, B. and Luna-González, L. 2018. The pre-Mesozoic metamorphic basement of Mexico, 1.5 billion years of crustal evolution. *Earth- Science Reviews*, 183, 2–37, <https://doi.org/10.1016/j.earscirev.2018.03.006>
- Ortega-Obregón, C., Solari, L., Ortega-Gutiérrez, F., Solé, J. and Morán-Ical, S. 2008. Middle–Late Ordovician magmatism and Late Cretaceous collision in the southern Maya block, Rabinal–Salamá area, central Guatemala: implications for North America–Caribbean plate tectonics. *Geological Society of America Bulletin*, 120, 556–570, <https://doi.org/10.1130/B26238.1>
- Ortega-Obregón, C., Keppie, J.D., Murphy, J.B., Lee, J.K.W. and Ortega-Rivera, A. 2009. Geology and geochronology of Paleozoic rocks in western Acatlán Complex, southern Mexico: evidence for contiguity across an extruded high-pressure belt and constraints on Paleozoic reconstructions. *Geological Society of America Bulletin*, 121, 1678–1694, <https://doi.org/10.1130/B26597.1>
- Ortega-Obregón, C., Murphy, J.B. and Keppie, J.D. 2010. Geochemistry and Sm–Nd isotopic systematics of Ediacaran, sedimentary and bimodal igneous rocks in the western Acatlán Complex, southern Mexico: evidence for rifting on the southern margin of the Rheic Ocean. *Lithos*, 114, 155–167, <https://doi.org/10.1016/j.lithos.2009.08.005>
- Ortega-Obregón, C., Solari, L., Gómez-Tuena, A., Elías-Herrera, M., Ortega-Gutiérrez, F. and Macías-Romo, C. 2014. Permian–Carboniferous arc magmatism in southern Mexico: U–Pb dating, trace element and Hf isotopic evidence on zircons of earliest subduction beneath the western margin of Gondwana. *International Journal of Earth Sciences*, 103, 1287–1300, <https://doi.org/10.1007/s00531-013-0933-1>
- Otamendi, J.E., Cristofolini, E.A., Morosini, A., Armas, P., Tibaldi, A.M. and Camilietti, G.C. 2020. The geodynamic history of the Famatinian arc, Argentina: a record of exposed geology over the type section (latitudes 27°–33° south). *Journal of South American Earth Sciences*, 100, 102558, <https://doi.org/10.1016/j.jsames.2020.102558>
- Paton, C., Woodhead, J.D., Hellstrom, J.C., Hergt, J.M., Greig, A. and Maas, R. 2010. Improved laser ablation U–Pb zircon geochronology through robust downhole fractionation correction. *Geochemistry, Geophysics, Geosystems*, 11, 1–36, <https://doi.org/10.1029/2009GC002618>
- Pérez-Gutiérrez, R., Solari, L.A., Gómez-Tuena, A. and Valencia, V.A. 2009. El terreno Cuicateco: ¿cuencia oceánica con influencia de subducción del Cretácico Superior en el sur de México? Nuevos datos estructurales, geoquímicos y geocronológicos. *Revista Mexicana de Ciencias Geológicas*, 26, 222–242.
- Petrus, J.A. and Kamber, B.S. 2012. VizualAge: a novel approach to laser ablation ICP–MS U–Pb geochronology data reduction. *Geostandards and Geoanalytical Research*, 36, 247–270, <https://doi.org/10.1111/j.1751-908X.2012.00158.x>
- Pindell, P., Villagómez, D., Molina-Garza, R., Graham, R. and Weber, B. 2021. A revised synthesis of the rift and drift history of the Gulf of Mexico and surrounding regions in the light of improved age dating of the Middle Jurassic salt. *Geological Society, London, Special Publications*, 504, 29–76, <https://doi.org/10.1144/SP504-2020-43>
- Piraquive, A., Kammer, A., Bernet, M., Cramer, T., von Quadt, A. and Gómez, C. 2021. Neoproterozoic to Jurassic tectono-metamorphic events in the Sierra Nevada de Santa Marta Massif, Colombia: insights from zircon U–Pb geochronology and trace element geochemistry. *International Geology Review*, 64, 1933–1965, <https://doi.org/10.1080/00206814.2021.1961317>
- Poole, F.G., Perry, W.J., Madrid, R.J. and Amaya-Martínez, R. 2005. Tectonic synthesis of the Ouachita–Marathon–Sonora orogenic margin of southern Laurentia. *Geological Society of America, Special Papers*, 393, <https://doi.org/10.1130/0-8137-2393-0.543>
- Ramos, V.A. 2018. Tectonic evolution of the central Andes: from terrane accretion to crustal delamination. *AAPG Memoirs*, 117, 1–34, <https://doi.org/10.1306/13622115M1172855>
- Ramos-Arias, M.A. and Keppie, J.D. 2011. U–Pb Neoproterozoic–Ordovician protolith age constraints for high- to medium-pressure rocks thrust over low-grade metamorphic rocks in the Ixcamilpa area, Acatlán Complex, southern Mexico. *Canadian Journal of Earth Sciences*, 48, 45–61, <https://doi.org/10.1139/E10-082>
- Ratschbacher, L., Franz, L. *et al.* 2009. The North American–Caribbean plate boundary in Mexico–Guatemala–Honduras. *Geological Society, London, Special Publications*, 328, 219–293, <https://doi.org/10.1144/SP328.11>
- Reimann, C.R., Bahlburg, H., Kooijman, E., Berndt, J., Gerdes, A., Carlotto, V. and López, S. 2010. Geodynamic evolution of the early Paleozoic Western Gondwana margin 14°–17°S reflected by the detritus of the Devonian and Ordovician basins of southern Peru and northern Bolivia. *Gondwana Research*, 18, 370–384, <https://doi.org/10.1016/j.gr.2010.02.002>
- Ren-Xu, C., Yong-Fei, Z. and Xie, L. 2010. Metamorphic growth and recrystallization of zircon: Distinction by simultaneous in-situ analyses of trace-elements, U–Th–Pb and Lu–Hf isotopes in zircons from eclogite-facies rocks in the Sulu orogen. *Lithos*, 114, 132–154, <https://doi.org/10.1016/j.lithos.2009.08.006>
- Rodríguez-García, G., Correa-Martínez, A.M., Zapata-Villada, J.P. and Obando-Erazo, G. 2019. Fragments of a Permian Arc on the western margin of the Neoproterozoic Basement of Colombia. In: Gómez, J. and Mateus-Zabala, D. (eds) *The Geology of Colombia, v. 1 Proterozoic–Paleozoic*. Servicio Geológico Colombiano, Publicaciones Geológicas Especiales, 35, 205–239, <https://doi.org/10.32685/pub.esp.35.2019.10>
- Rosales-Lagarde, L., Centeno-García, E., Dostal, J., Sour-Tovar, F., Ochoa-Camarillo, H. and Quiroz-Barroso, S. 2005. The Tuzancoa Formation: evidence of an Early Permian submarine continental arc in east-central Mexico. *International Geology Review*, 47, 901–919, <https://doi.org/10.2747/0020-6814.47.9.901>

Geological evolution of the Sierra de Juárez Complex

- Rubatto, D. 2017. Zircon: The metamorphic mineral. *Reviews in Mineralogy and Geochemistry*, 83, 261–295, <https://doi.org/10.2138/rmg.2017.83.9>
- Rubatto, D. and Gebauer, D. 2000. Use of cathodoluminescence for U–Pb zircon dating by ion microprobe: some examples from the western Alps. In: Pagel, M., Barbin, V., Blanc, P. and Ohnenstetter, D. (eds) *Cathodoluminescence in Geosciences*. Springer, Berlin, 373–400, https://doi.org/10.1007/978-3-662-04086-7_15
- Rubatto, D. and Hermann, J. 2007. Experimental zircon/melt and zircon/garnet trace element partitioning and implications for the geochronology of crustal rocks. *Chemical Geology*, 241, 38–61, <https://doi.org/10.1016/j.chemgeo.2007.01.027>
- Sánchez-Zavala, J.L., Ortega-Gutiérrez, F., Keppie, J.D., Jenner, G.A., Belousova, E. and Macías-Romo, C. 2004. Ordovician and Mesoproterozoic zircons from the Tecamate Formation and Esperanza Granitoids, Acatlán Complex, southern Mexico: local provenance in the Acatlán and Oaxacan complexes. *International Geology Review*, 46, 1005–1021, <https://doi.org/10.2747/0020-6814.46.11.1005>
- Schaltegger, U., Schmitt, A.K. and Horstwood, M.S.A. 2015. U–Th–Pb zircon geochronology by ID-TIMS, SIMS, and laser ablation ICP-MS: recipes, interpretations, and opportunities. *Chemical Geology*, 402, 89–110, <https://doi.org/10.1016/j.chemgeo.2015.02.028>
- Sedlock, R.L., Ortega-Gutiérrez, F. and Speed, R.C. 1993. Tectonostratigraphic terranes and tectonic evolution of Mexico. *Geological Society of America, Special Papers*, 278, <https://doi.org/10.1130/SPE278-p1>
- Sierra-Rojas, M.L., Molina-Garza, R.S., Pindell, J., Rodríguez-Rodríguez, R.A. and Serrano-García, D. 2022. Paleomagnetism, magnetostratigraphy, provenance, and tectonic setting of the Lower Cretaceous of nuclear southern Mexico. *Journal of South American Earth Sciences*, 115, 103719, <https://doi.org/10.1016/j.jsames.2022.103719>
- Sláma, J., Košler, J. et al. 2008. Plešovice zircon – a new natural reference material for U–Pb and Hf isotopic microanalysis. *Chemical Geology*, 249, 1–35, <https://doi.org/10.1016/j.chemgeo.2007.11.005>
- Solari, L.A., Keppie, J.D., Ortega-Gutiérrez, F., Cameron, K.L., Lopez, R. and Hames, W.E. 2003. 990 and 1100 Ma Grenvillian tectonothermal events in the northern Oaxacan Complex, southern Mexico: roots of an orogen. *Tectonophysics*, 365, 257–282, [https://doi.org/10.1016/S0040-1951\(03\)00025-8](https://doi.org/10.1016/S0040-1951(03)00025-8)
- Solari, L.A., Torres de León, R., Hernández-Pineda, G., Solé, J., Solís-Pichardo, G. and Hernández-Treviño, T. 2007. Tectonic significance of Cretaceous–Tertiary magmatic and structural evolution of the northern margin of the Xolapa Complex, Tierra Colorada area, southern Mexico. *Geological Society of America Bulletin*, 119, 1265–1279, <https://doi.org/10.1130/B26023.1>
- Solari, L.A., Ortega-Gutiérrez, F. et al. 2009. U–Pb zircon geochronology of Palaeozoic units in Western and Central Guatemala: Insights into the tectonic evolution of Middle America. *Geological Society, London, Special Publications*, 328, 298–313, <https://doi.org/10.1144/SP328.12>
- Solari, L.A., Ortega-Gutiérrez, F., Elías-Herrera, M., Gómez-Tuena, A. and Schaaf, P. 2010. Refining the age of magmatism in the Altos Cuchumatanes, western Guatemala, by LA-ICP-MS, and tectonic implications. *International Geology Review*, 52, 977–998, <https://doi.org/10.1080/00206810903216962>
- Solari, L.A., Gómez-Tuena, A., Ortega-Gutiérrez, F. and Ortega-Obregón, C. 2011. The Chuacús Metamorphic Complex, central Guatemala: geochronological and geochemical constraints on its Paleozoic–Mesozoic evolution. *Geologica Acta*, 9, 329–350, <https://doi.org/10.1344/105.000001695>
- Solari, L.A., García-Casco, A., Martens, U., Lee, J.K.W. and Ortega-Rivera, A. 2013. Late Cretaceous subduction of the continental basement of the Maya block (Rabinal Granite, central Guatemala): tectonic implications for the geodynamic evolution of Central America. *Geological Society of America Bulletin*, 125, 625–639, <https://doi.org/10.1130/B30743.1>
- Solari, L.A., Ortega-Gutiérrez, F., Elías-Herrera, M., Ortega-Obregón, C. and Macías-Romo, C. 2014. Detrital provenance of the Grenvillian Oaxacan Complex, southern Mexico: a zircon perspective. *International Journal of Earth Sciences*, 103, 1301–1315, <https://doi.org/10.1007/s00531-013-0938-9>
- Solari, L.A., González-León, C.M., Ortega-Obregón, C., Valencia-Moreno, M. and Rascón-Heimpel, M.A. 2018. The Proterozoic of NW Mexico revisited: U–Pb Geochronology and Hf isotopes of Sonoran rocks and their tectonic implications. *International Journal of Earth Sciences*, 107, 845–861, <https://doi.org/10.1007/s00531-017-1517-2>
- Solari, L.A., Ortega-Obregón, C., Ortega-Gutiérrez, F. and Elías-Herrera, M. 2020. Origin and evolution of the Grenvillian Oaxacan Complex, southern Mexico: Hf isotopic and U–Pb geochronologic constraints. *Geological Society of America, Special Papers*, 546, [https://doi.org/10.1130/2020.2546\(03\)](https://doi.org/10.1130/2020.2546(03))
- Spikings, R. and Paul, A. 2019. The Permian–Triassic history of magmatic rocks of the northern Andes (Colombia and Ecuador): supercontinent assembly and disassembly. In: Gómez, J. and Pinilla-Pachon, A.O. (eds) *The Geology of Colombia, Volume 2, Mesozoic*. Servicio Geológico Colombiano, Publicaciones Geológicas Especiales, 36, 1–43, <https://doi.org/10.32685/pub.esp.36.2019.01>
- Steiner, M.B. and Walker, J.D. 1996. Late Silurian plutons in Yucatan. *Journal of Geophysical Research*, 101, 17727–17735, <https://doi.org/10.1029/96JB00174>
- Stewart, J.H., Blodgett, R.B., Boucot, A.J., Carter, J.L. and López, R. 1999. Exotic Paleozoic strata of Gondwana provenance near Ciudad Victoria, Tamaulipas, México. *Geological Society of America, Special Papers*, 336, 227–252, <https://doi.org/10.1130/0-8137-2336-1.227>
- Talavera-Mendoza, O., Ruiz, J., Gehrels, G.E., Meza-Figueroa, D.M., Vega-Granillo, R. and Campa-Uranga, M.F. 2005. U–Pb geochronology on the Acatlán Complex and implications for the Paleozoic paleogeography and tectonic evolution of southern Mexico. *Earth and Planetary Science Letters*, 235, 682–699, <https://doi.org/10.1016/j.epsl.2005.04.013>
- Tazzo-Rangel, M.D., Weber, B., González-Guzmán, R., Valencia, V.A., Frei, D., Schaaf, P. and Solari, L.A. 2018. Multiple metamorphic events in the Paleozoic Mérida Andes basement, Venezuela: insights from U–

- Pb geochronology and Hf-Nd isotope systematics. *International Geology Review*, 61, 1557–1593, <https://doi.org/10.1080/00206814.2018.1522520>
- Tazzo-Rangel, D., Weber, B., Schmitt, A.K., González-Guzmán, R., Cisneros de Leon, A. and Hecht, L. 2021. Permo-Triassic metamorphism in the Mérida Andes, Venezuela: new insights from geochronology, O-isotopes, and geothermobarometry. *International Journal of Earth Sciences*, 110, 2465–2493, <https://doi.org/10.1007/s00531-020-01926-5>
- Valencia-Morales, Y.T., Weber, B., Tazzo-Rangel, M.D., González-Guzmán, R., Frei, D., Quintana-Delgado, J.A. and Rivera-Moreno, E.N. 2022. Early Mesoproterozoic inliers in the Chiapas Massif Complex of southern Mexico: Implications on Oaxaquia–Amazonia–Baltica configuration. *Precambrian Research*, 373, 106611, <https://doi.org/10.1016/j.precamres.2022.106611>
- Van der Lelij, R., Spikings, R., Ulianov, A., Chiaradia, M. and Mora, A. 2016. Paleozoic to Early Jurassic history of the northwestern corner of Gondwana, and implications for the evolution of the Iapetus, Rheic and Pacific Oceans. *Gondwana Research*, 31, 271–294, <https://doi.org/10.1016/j.gr.2015.01.011>
- Vega-Granillo, R., Talavera-Mendoza, O., Meza-Figueroa, D., Ruiz, J., Gehrels, G.E., López-Martínez, M. and de la Cruz-Vargas, J.C. 2007. Pressure-temperature-time evolution of Paleozoic high-pressure rocks of the Acatlán Complex (southern Mexico): implications for the evolution of the Iapetus and Rheic Oceans. *GSA Bulletin*, 119, 1249–1264, <https://doi.org/10.1130/B226031.1>
- Vermeesch, P. 2018. Isoplot R: a free and open toolbox for geochronology. *Geoscience Frontiers*, 9, 1479–1493, <https://doi.org/10.1016/j.gsf.2018.04.001>
- Villagómez, D., Spikings, R., Magna, T., Kammer, A., Winkler, W. and Beltrán, A. 2011. Geochronology, geochemistry and tectonic evolution of the Western and Central cordilleras of Colombia. *Lithos*, 125, 875–896, <https://doi.org/10.1016/j.lithos.2011.05.003>
- Weber, B. and Hecht, L. 2003. Petrology and geochemistry of metaigneous rocks from a Grenvillian basement fragment in the Maya block: the Guichicovi complex, Oaxaca, southern Mexico. *Precambrian Research*, 124, 41–67, [https://doi.org/10.1016/S0301-9268\(03\)00078-0](https://doi.org/10.1016/S0301-9268(03)00078-0)
- Weber, B. and Köhler, H. 1999. Sm–Nd, Rb–Sr and U–Pb geochronology of a Grenville Terrane in southern Mexico: origin and geologic history of the Guichicovi Complex. *Precambrian Research*, 96, 245–262, [https://doi.org/10.1016/S0301-9268\(99\)00012-1](https://doi.org/10.1016/S0301-9268(99)00012-1)
- Weber, B. and Schulze, C.H. 2014. Early Mesoproterozoic (~1.4 Ga) ages from granulite basement inliers of SE Mexico and their implications on the Oaxaquia concept – evidence from U–Pb and Lu–Hf isotopes on zircon. *Revista Mexicana de Ciencias Geológicas*, 31, 377–394.
- Weber, B., Iriando, A., Premo, W.R., Hecht, L. and Schaaf, P. 2007. New insights into the history and origin of the southern Maya block, SE México: U–Pb–SHRIMP zircon geochronology from metamorphic rocks of the Chiapas massif. *International Journal of Earth Sciences*, 96, 253–269, <https://doi.org/10.1007/s00531-006-0093-7>
- Weber, B., Valencia, V.A., Schaaf, P., Pompa-Mera, V. and Ruiz, J. 2008. Significance of provenance ages from the Chiapas Massif Complex (Southeastern Mexico): redefining the Paleozoic basement of the Maya Block and its evolution in a Peri-Gondwanan realm. *The Journal of Geology*, 116, 619–639, <https://doi.org/10.1086/591994>
- Weber, B., Scherer, E.E., Schulze, C., Valencia, V.A., Montecinos, P., Mezger, K. and Ruiz, J. 2010. U–Pb and Lu–Hf isotope systematics of lower crust from central-southern Mexico – geodynamic significance of Oaxaquia in a Rodinia Realm. *Precambrian Research*, 182, 149–162, <https://doi.org/10.1016/j.precamres.2010.07.007>
- Weber, B., Scherer, E.E., Martens, U.K. and Mezger, K. 2012. Where did the lower Paleozoic rocks of Yucatan come from? A U–Pb, Lu–Hf, and Sm–Nd isotope study. *Chemical Geology*, 312–313, 1–17, <https://doi.org/10.1016/j.chemgeo.2012.04.010>
- Weber, B., González-Guzmán, R. *et al.* 2018. Late Mesoproterozoic to Early Paleozoic history of metamorphic basement from the southeastern Chiapas Massif Complex, Mexico, and implications for the evolution of NW Gondwana. *Lithos*, 300–301, 177–199, <https://doi.org/10.1016/j.lithos.2017.12.009>
- Wiedenbeck, M., Allé, P. *et al.* 1995. Three natural zircon standards for U–Th–Pb, Lu–Hf, trace element and REE analyses. *Geostandards Newsletter*, 19, 1–23, <https://doi.org/10.1111/j.1751-908X.1995.tb00147.x>
- Youbi, N., Kouyaté, D. *et al.* 2013. The 1750 Ma magmatic event of the West African Craton (Anti-Atlas, Morocco). *Precambrian Research*, 236, 106–123, <https://doi.org/10.1016/j.precamres.2013.07.003>
- Zhong, S., Li, S., Seltmann, R., Lai, Z. and Zhou, J. 2021. The influence of fractionation of REE-enriched minerals on the zircon partition coefficients. *Geoscience Frontiers*, 12, 101094, <https://doi.org/10.1016/j.gsf.2020.10.002>



4. *MAGMATISMO DE ARCO ESTÉNICO Y METAMORFISMO DE MEDIO A ALTO GRADO TÓNICO A LO LARGO DEL BORDE NORTE DE AMAZONIA DURANTE EL ENSAMBLE DE RODINIA: LA SUITE POCHOTEPEC EN EL SUR DE MÉXICO.*

Guillermo Espejo-Bautista, Luigi Solari, Roberto Maldonado & Mónica Ramírez-Calderón (2023) Stenian arc-magmatism and early Tonian metamorphism and anatexis along the northern border of Amazonia during the Rodinia assembly: The Pochotepec suite in southern Mexico, *Journal of South American Earth Sciences*, 124, 104248, <https://doi.org/10.1016/j.jsames.2023.104248>.

CONTRIBUCIÓN DE AUTORES

Guillermo Espejo-Bautista: Conceptualización, organización e integración de datos, análisis formal, investigación (trabajo de campo), metodología (procesamiento de muestras, separación de zircones, obtención de datos analíticos), propuesta de modelo tectónico, visualización, escritura original del manuscrito, revisión y edición.

Luigi A. Solari: Organización e integración de datos, análisis formal, adquisición de fondos, recursos, metodología, supervisión, escritura y revisión del manuscrito.

Roberto Maldonado: Análisis formal, investigación (trabajo de campo), escritura y revisión del manuscrito.

Mónica Ramírez-Calderón: Análisis formal, investigación (trabajo de campo), escritura y revisión del manuscrito.



ELSEVIER

Contents lists available at [ScienceDirect](https://www.sciencedirect.com)

Journal of South American Earth Sciences

journal homepage: www.elsevier.com/locate/james

Stenian arc-magmatism and early Tonian metamorphism and anatexis along the northern border of Amazonia during the Rodinia assembly: The Pochotepec suite in southern Mexico

Guillermo Espejo-Bautista ^{a,*}, Luigi Solari ^a, Roberto Maldonado ^b, Mónica Ramírez-Calderón ^a

^a Centro de Geociencias, Universidad Nacional Autónoma de México, Campus Juriquilla, Santiago de Querétaro, Querétaro, México

^b Instituto de Geología, Universidad Nacional Autónoma de México, Ciudad Universitaria, Ciudad de México, México

ARTICLE INFO

Keywords:

Rodinia
U–Pb LA-ICPMS Geochronology
Anatexis
Pochotepec suite
Proterozoic
Amazonia

ABSTRACT

The eastern and southern Precambrian basement of Mexico is composed of crustal blocks linked to northern Amazonia before and during the assembly of the Rodinia supercontinent. In this paper, we examine an extensive basement block known as the Sierra de Juárez Complex (SJC) in southern Mexico by integrating fieldwork, in-situ zircon U–Pb geochronology by LA-ICPMS and whole-rock geochemistry by X-ray fluorescence. The results provide evidence for a continuous low- to high-grade metamorphic succession here re-defined as the Pochotepec suite (PS), which comprises an upper lithodeme with volcanosedimentary precursors and a lower lithodeme that includes mafic to intermediate orthogneisses and migmatites. The analytical results suggest that the PS protoliths originated in a continental-arc tectonic setting ca. 1080–1050 Ma along the northern edge of Amazonia before the consolidation of Rodinia. In addition, xenocrystic zircon U–Pb analyses indicate the presence of a recycled older crust of ca. 1200–1300 Ma. Finally, U–Pb data of recrystallized zircon rims and younger metamorphic zircon grains recorded the timing of metamorphism and anatexis of the PS during the early Tonian (954–933 Ma). The crystallization ages of two trondhjemitic leucosomes of 954 and 933 Ma strongly support the migmatization age. The Tonian metamorphic/anatectic episode of the PS differs in grade and age from the typical metamorphism related to the amalgamation of Rodinia reported in Mexico and Colombia (granulite-facies at ca. 990 Ma). Therefore, we interpret this event as produced by either post-orogenic crustal collapse or contractive tectonics.

1. Introduction

The recognition of new geological provinces and the sophistication of different analytical techniques since the advent of plate tectonics allowed us to reconstruct paleogeographic models and understand the geodynamic evolution throughout the Earth's history. However, because of the continuous generation and recycling of the continental crust, the further we look into the past, the more challenging the paleotectonic task becomes and the more variable and controversial the paleogeographic models will result. In this context, although it is a consensus that a triple junction among Amazonia, Laurentia, and Baltica assembled the core of the Proterozoic Rodinia supercontinent (e.g., Li et al., 2008; Merdith et al., 2017), the pre-collisional configuration is envisaged through two different main models. The first model (SAMBA) suggests that Amazonia and Baltica formed a continuous lineal arrangement and followed a clockwise rotation until colliding with

Laurentia (Johansson, 2009). The second model (e.g., Elmg et al., 2009; Cawood and Pisarevsky, 2017) predicts a displacement of Amazonia from a distant location, ending with a lateral collision and sinistral shearing between Amazonia and Laurentia (e.g., Tohver et al., 2006; D'Agrella-Filho et al., 2008) and a frontal collision between northern Amazonia (leading edge) and Baltica. These models chiefly differ in Amazonia's paleoposition and translation, but most notably in its tectonic interaction with Baltica during the Stenian period; hence, determinant evidence could be held along the northern border (leading edge) of Amazonia.

Following the formation and breakup of Rodinia, multiple Phanerozoic tectonic events related to the formation, evolution, and breakup of Gondwana and Pangea pervasively affected the Precambrian architecture of northern Amazonia (e.g., Van der Lelij et al., 2016; Espejo-Bautista et al., 2022). As a result, the northern peri-Amazonian edge was modified and disrupted into multiple Mesoproterozoic to early

* Corresponding author.

E-mail addresses: gespejo@geociencias.unam.mx, guillermoespejo@hotmail.com (G. Espejo-Bautista).

<https://doi.org/10.1016/j.james.2023.104248>

Received 5 December 2022; Received in revised form 2 February 2023; Accepted 4 February 2023

Available online 17 February 2023

0895-9811/© 2023 Elsevier Ltd. All rights reserved.

Neoproterozoic metamorphic crustal fragments encompassing crucial geological records related to the formation of Rodinia. These fragments were subsequently spread throughout current Mexico (e.g., Keppie and Ortega-Gutiérrez, 2010; Weber et al., 2018; Alemán-Gallardo et al., 2019; Valencia-Morales et al., 2022), Central America (e.g., Maldonado et al., 2018), and northern South America (e.g., Ibañez-Mejía et al., 2011; Ibañez-Mejía, 2020). Therefore, with the aim of a better understanding of the formation of Rodinia, it is critical to identify and characterize these Amazonian inliers and rebuild the Precambrian geological puzzle.

The Precambrian basement of Mexico contains inliers encompassing a complex record of pre-, syn-, and post-Rodinian tectonism. From them, the Sierra de Juárez Complex (SJC; Espejo-Bautista et al., 2021) has remained relatively enigmatic so far. Since it underwent Phanerozoic orogenesis and lacks modern geochronological analyses, the reconstruction of its Precambrian history is hampered. The present study attempts to unravel the history of an extensive Proterozoic lower-to-high-grade metamorphic area of the SJC, redefined here as the Pochotepec suite (PS). In order to constrain the magmatic timing and petrogenesis of their protoliths and the age of metamorphism, we performed in-situ zircon U–Pb analyses by LA-ICPMS supported by whole-rock geochemistry by X-ray fluorescence. The results lead us to propose that the PS constitutes a late Stenian continental arc emplaced into a Mesoproterozoic crust belonging to the northern edge of Amazonia. Moreover, the PS underwent considerably younger Tonian metamorphism and anatexis than the typical metamorphism related to the assembly of Rodinia (the Zapotecan Orogeny: granulite facies at ca. 990 Ma in Oaxaquia, e.g., Weber and Köhler, 1999; Solari et al., 2003, 2004), implying a different tectonic evolution than other Precambrian blocks in Mexico.

2. Geological setting

2.1. Oaxaquia

Oaxaquia has been interpreted as a microcontinent of Grenvillian age (a concept proposed by Ortega-Gutiérrez et al., 1995) that incorporates similar dispersed Precambrian granulitic blocks cropping out in eastern and southern Mexico into a single terrane, including the Novillo Complex (Cameron et al., 2004; Keppie et al., 2006; Alemán-Gallardo et al., 2019), the Huiznopala Gneiss (Lawlor et al., 1999), the Guichicovi Complex (Weber and Köhler, 1999; Weber and Hecht, 2003), and the Oaxacan Complex (Ortega-Gutiérrez, 1981, 1984; Ortega-Gutiérrez et al., 2018; Keppie et al., 2001, 2003; Solari et al., 2003, 2020; Keppie and Dostal, 2007; Weber et al., 2010; Keppie and Ortega-Gutiérrez, 2010; Weber and Schulze, 2014). Oaxaquia originated as a peripheral island-arc terrane accreted along the northern boundary of Amazonia during the late Mesoproterozoic. It is widely documented that it was part of an extensive suture zone related to the assembly of Rodinia, undergoing granulite facies-metamorphism at ca. 990 Ma (e.g., Solari et al., 2003; Weber et al., 2010). The Oaxacan Complex is the most extensive exposure of Oaxaquia and constitutes the crystalline basement of the Zapotecan Terrane, which is in tectonic contact with the Sierra de Juárez Complex.

2.2. The Sierra de Juárez Complex

The Sierra de Juárez Complex (SJC) is a ca. 120 km long, NNW-SSE trending composite metamorphic belt delimited by Cenozoic faults (Oaxaca and Siempre Viva faults) between the Zapoteco and Cuicateco terranes in southern Mexico (Figs. 1 and 2). The lithologies and structure of the SJC were pervasively modified by extensive Middle Jurassic and Lower Cretaceous strike-slip shearing events, likely related to the opening of the Gulf of Mexico and the evolution of Mexico peninsular

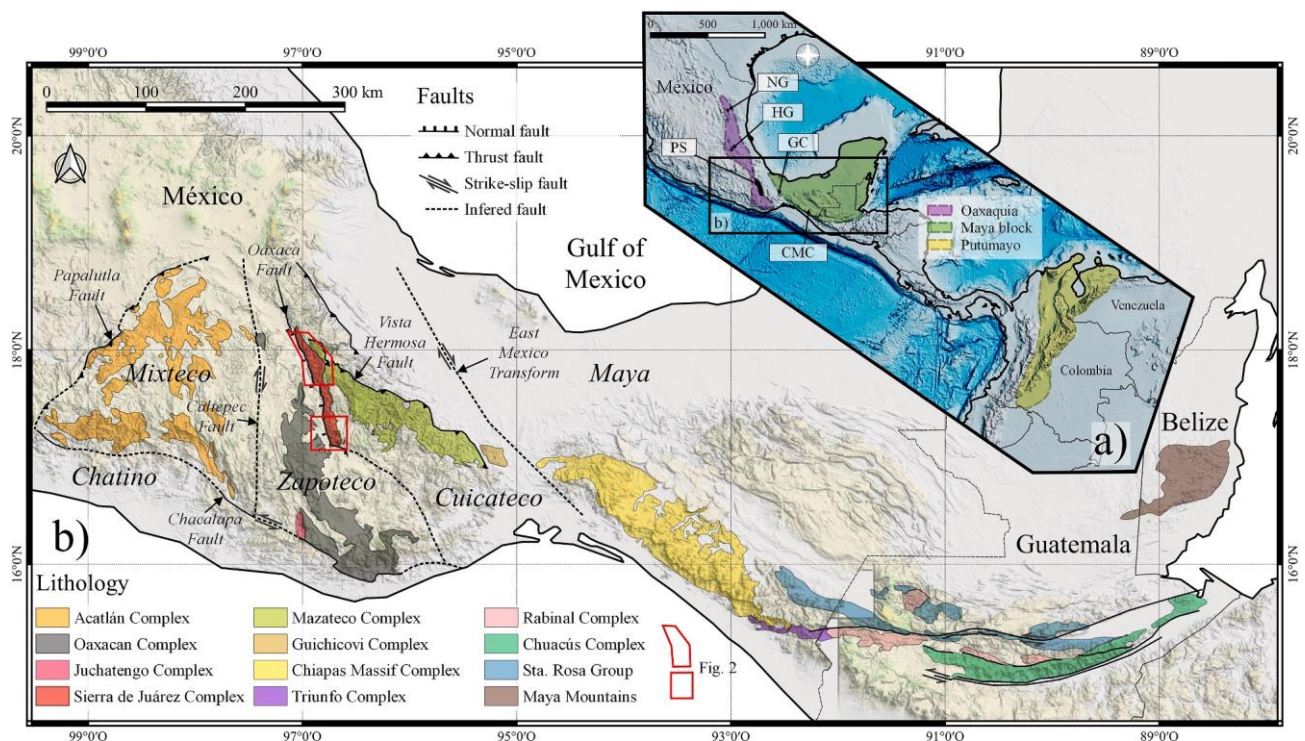


Fig. 1. a) Simplified geological map showing the main Rodinian blocks of Mexico and northwestern South America, modified from Ibañez-Mejía (2020); Ortega-Gutiérrez et al. (2018); Weber et al. (2018). Abbreviations: NG, Novillo Complex; HG, Huiznopala Gneiss; GC, Guichicovi Complex; PU, Pochotepec Suite; CMC, Chiapas Massif Complex. b) Pre-Mesozoic basement blocks in southern Mexico, Belize, and Guatemala; modified from Ratschbacher et al. (2009); Ortega-Gutiérrez et al. (2018); Maldonado et al. (2018); Weber et al. (2018); Valencia-Morales et al. (2022); tectonostratigraphic nomenclature in southern Mexico is based on Sedlock et al. (1993).

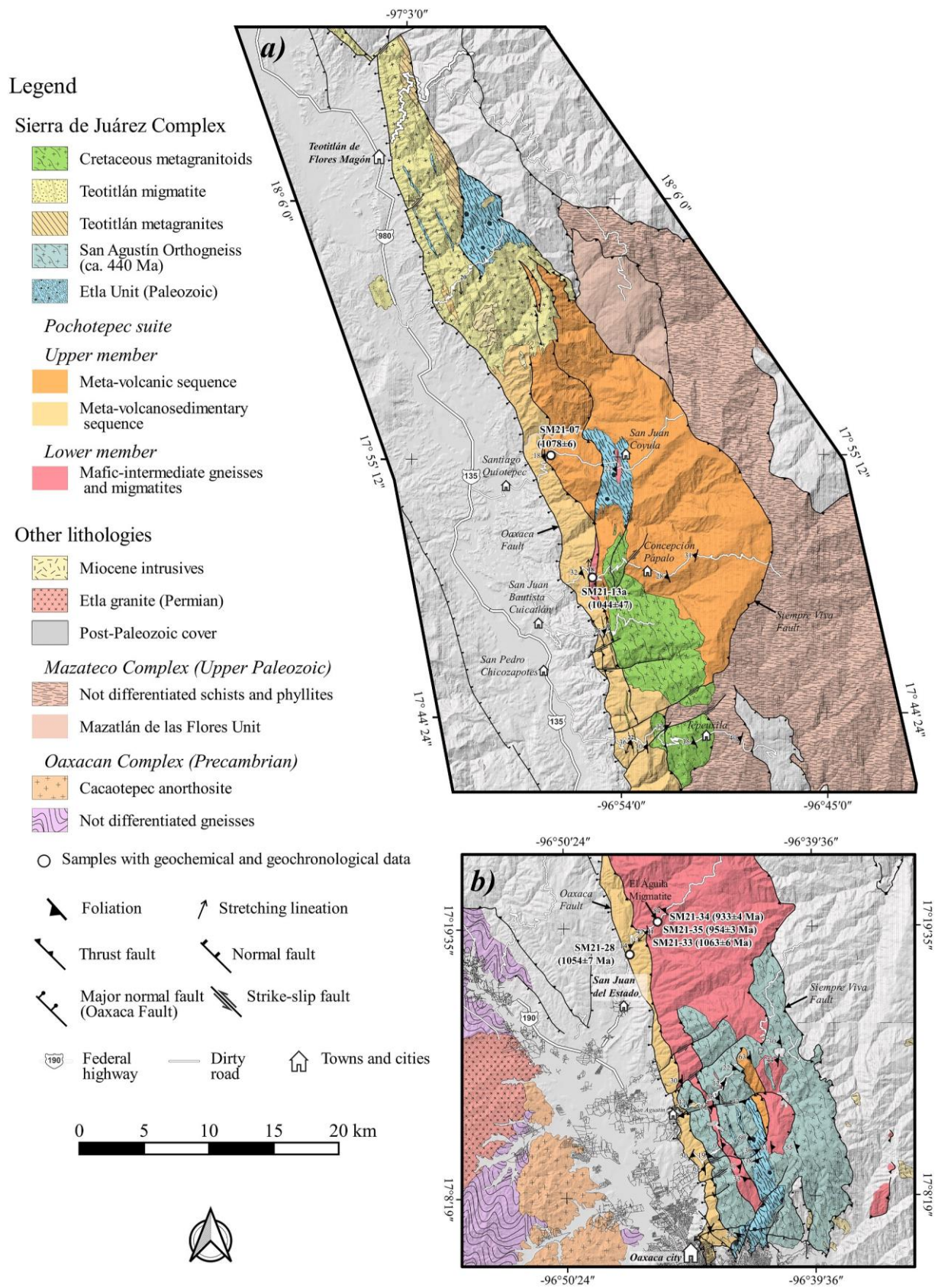


Fig. 2. Geological map of the (a) northern and (b) southern sectors of the Sierra de Juárez Complex and external pre-Mesozoic lithologies. The mapped areas are indicated in Fig. 1. Lithology and structures of the SJC are based on our field observations and modifications from Ángeles-Moreno et al. (2012) and Espejo-Bautista et al. (2022).

(Alaniz-Álvarez et al., 1996; Martini and Ortega-Gutiérrez, 2016; Pindell et al., 2021; Espejo-Bautista et al., 2022). Mylonitic foliation dips 50–30° to the west, and the stretching lineation usually exhibits a sub-horizontal ~ N–S orientation. Ductile deformation was accommodated by 10-m scale anastomosed shearing bands wrapping regional low-strain sectors. The relict non-mylonitic zones preserve gneisses and schists with prograde amphibolite-facies assemblages and variable degrees of folding, reflecting pre-mylonitic deep-crustal tectonic events (Sedlock et al., 1993; Alaniz-Álvarez et al., 1996; Espejo-Bautista et al., 2021). The overprinting Mesozoic mylonitization has two critical tectonic implications: (1) the SJC represents an extinct transform along the current eastern border of the Oaxacan Complex, and (2) the SJC is allochthonous relative to the Oaxacan Complex.

Three main lithostratigraphic elements constitute the SJC, formed during successive geodynamic cycles.

2.2.1. The Etna suite

The Etna suite comprises medium-grade metapelites, amphibolites, and rutile-bearing MORB-type mafic orthogneisses. Their protolith's origin is related to transtensional tectonic activity in NW-Gondwana from Silurian to Devonian (Espejo-Bautista et al., 2021, 2022). Due to similar petrologic characteristics, the La Nopalera Schist, recognized by Ángeles-Moreno et al. (2012), is included in this suite. These rocks crop out dispersed along the northern and southern sectors of the SJC (Fig. 2).

2.2.2. The Teotitlán migmatite

The northern sector of the SJC encompasses a Jurassic-Cretaceous package of migmatites known as the Teotitlán migmatitic complex (Ángeles-Moreno et al., 2012; Espejo-Bautista et al., 2022). It comprises dioritic/tonalitic to granitic neosome domains and rare paleosome lenses constituted by para- and ortho-amphibolites. Related ultramafic rocks are also present (Delgado-Argote et al., 1992). It is characterized by intricate anatectic structures, including schlieren to nebulitic migmatites. The origin of anatexis has been attributed to the tectonic evolution of the Caribbean (Ángeles-Moreno, 2006), eastward subduction in southern peninsular Mexico (Coombs, 2016), and crustal strike-slip crustal displacements related to the opening of the Gulf of Mexico (Espejo-Bautista et al., 2022).

2.2.3. The Pochotepec suite

The Pochotepec suite (PS) is the major constituent of the SJC and extends for 110 km long, with ca. 700 km² of exposure. The PS (Fig. 2) was described in the northern sector of the SJC by Carfantán (1983) and Delgado-Argote et al. (1992) as a sequence of metatuffs and andesitic meta-lavas related to the Cretaceous Chivillas Formation. It was subsequently named Pochotepec Group by Ángeles-Moreno et al. (2012). They interpreted it as an independent low-grade Upper Jurassic-Lower Cretaceous sequence composed of marbles, meta-pyroclastic rocks, meta-rhyolites, greenschists, pelitic schists, meta-basalts, meta-gabbros, and serpentinites. Given its metamorphic nature, we consider the term “suite” the correct form to refer to this succession.

3. Field relationships and sample descriptions

The PS encompasses (1) an upper supracrustal lithodeme made up of meta-volcanosedimentary successions cropping out mainly in the northern section and small areas along the western border of the SJC; and (2) a lower lithodeme consisting of mafic gneisses and migmatites mainly exposed in the southern sector of the PS (Fig. 2).

3.1. Upper lithodeme

This lithodeme is subdivided into two members with transitional contacts. The first member comprises a meta-volcanosedimentary sequence of mafic to intermediate meta-volcanic rocks intercalated

with low-grade pelitic and calc-silicate schists made up of variable amounts of calcite, white mica, quartz, biotite, and chlorite; and marbles composed of calcite (>90 vol %) and some quartz and white mica. The second member contains a monotonous succession of mafic to intermediate meta-volcanic rocks (Fig. 3a) composed of coarse green amphibole, probably of igneous origin, wrapped in a fine-grained foliated matrix containing plagioclase + epidote + chlorite + quartz (Fig. 3c), indicating low-grade metamorphism. Highly deformed to undeformed granitoid layers intruded parallel to the foliation planes are commonly present (Fig. 3a). Their origin is unknown, although they could have arisen from deeper anatectic levels. The sequence also hosts tabular anorthositic intrusives with variable degrees of deformation (Fig. 3b) near San Juan del Estado and Etna towns at the southwestern border of the SJC (Fig. 2). These intrusives were dated by Espejo-Bautista et al. (2021) at 979–976 Ma and named Viguera Suite, which we include into the Pochotepec suite in the present work.

3.2. Lower lithodeme

The lower lithodeme encompasses mafic to intermediate amphibolites and migmatites. In the northern sector of the SJC, coarse-grained gabbroic orthogneisses crop out (Fig. 3d), forming tectonic lenses among meta-volcanic rocks from the upper lithodeme (Fig. 2). These orthogneisses exhibit a paragenesis of hornblende + oligoclase ± titanite and accessory phases such as apatite and Ti–Fe oxides, indicating typical amphibolite facies metamorphism. The primary metamorphic fabric is overprinted by metasomatism and mylonitic deformation within a ductile-fragile regime, producing retrograde mineral reactions such as chlorite after amphibole and saussuritization. The most extensive exposure of the lower lithodeme crops out along the road from San Juan del Estado to San Miguel Aloapam (Oaxaca state). Along this transect, the contact between the lower and upper lithodemes is inferred to be tectonic. The amphibolite from the lower lithodeme are coarse-grained banded orthogneisses with gneissic and mylonitic fabrics (Fig. 3e). They are usually intruded by granitoid layers of unknown age, concordant with the foliation (Fig. 3e). In this area, the paleo-geothermal gradient increases eastward, as can be noted by the appearance of conspicuous diatexite migmatites, here referred to as El Águila Migmatite (Figs. 2 and 3f–i). The melanosome domain in this migmatite is made up of >90 vol % amphibole (hand-specimen observations), whereas the leucosome consists of plagioclase (<30_{Ab}) + quartz, and <2 vol% of Fe–Ti oxides, epidote, and chlorite (Fig. 3g, i, and 3k). Rare paleosome pods are present among the neosome domains. These are coarse-grained amphibolite with anastomosed texture and millimetric to centimetric quartz + feldspar anatectic pods, suggestive of incipient partial melting (Fig. 3j).

4. Analytical procedures

4.1. Major and trace elements geochemistry

Whole-rock major elements were obtained by X-ray fluorescence at the Laboratorio Nacional de Geoquímica y Mineralogía of the Instituto de Geología, Universidad Nacional Autónoma de México (UNAM) using a Rigaku Primus II X-Ray sequential spectrometer and according to the methodology and internal quality controls (IGLa1) reported by Lozano-Santa Cruz and Bernal (2005). Trace-element analyses were performed at the Laboratorio de Estudios Isotópicos (LEI) of Centro de Geociencias, UNAM, by inductively-coupled plasma mass spectrometry (ICP-MS), employing a Thermo ICap Qc ICP-MS. The analytical procedures follow the methodology reported by Mori et al. (2007), and the instrument calibration employs the standards AGV-2, BCR-2, BHVO-2, JB-2, JR-1, and ZZ.

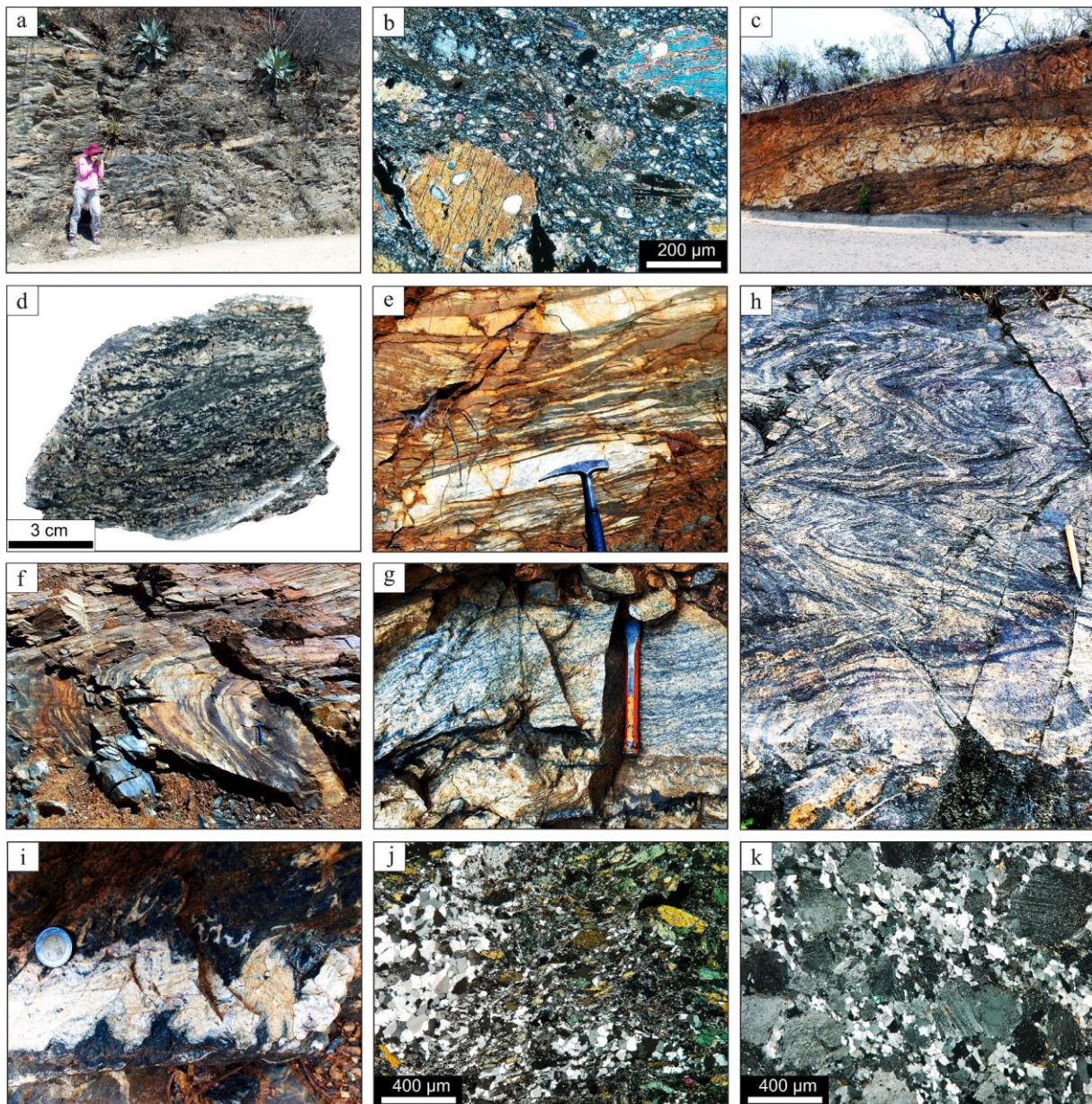


Fig. 3. a) View of meta-basalts at outcrop scale from the upper lithodeme of the PS. b) Photomicrograph of meta-basalt SM21-07 showing amphibole crystals surrounded by a matrix composed of Pl + Chl + Ep + Qtz. View with crossed nicols. c) Upper supracrustal lithodeme of the PS intruded by anorthositic dikes. d) Hand sample of an amphibolite (SM21-13a) representative of the lower lithodeme of the PS. e) View of amphibolites from the lower lithodeme of the PS with mylonitic foliation and intrusive granitoid layers. f) Symmetric open fold of interlayered leuco and melanosome domains. g) Trondhjemitic leucosome SM21-35 at outcrop scale. h) Representative view of El Águila Migmatite with close-to-tight folds. i) Ptygmatic folding observed in the trondhjemitic leucosome SM21-34. j) Photomicrograph of mafic paleosome SM21-33 showing quartz-felspathic anatectic zones and melanocratic domains composed of amphibole. View with crossed nicols. k) Photomicrograph of a trondhjemitic leucosome (sample SM21-35). View with crossed nicols.

4.2. Zircon U–Pb geochronology

Samples were processed at Centro de Geociencias, UNAM. From 5 to 15 kg of rock were crushed by using a hydraulic press. We used panning, magnetic separator, and handpicking techniques for zircon separation under a binocular microscope. Zircons were cast in different mounts according to their size, glued with epoxy resin, and carefully polished to reveal their equatorial sections. Cathodoluminescence imaging was carried out before and after ablation for more detailed textural observations.

U–Pb zircon geochronology and REE data were obtained by LA-ICP-MS at the Laboratorio de Estudios Isotópicos (LEI), Centro de Geociencias, UNAM. The samples were studied using a Resonetics resolution

M050 excimer laser-ablation workstation coupled to a Thermo iCap Qc ICP-MS, following the methodology of [Solari et al. \(2010\)](#). Isotopic content and zircon chemistry (REE) were measured simultaneously employing the quadrupole ICP-MS. The reference standard NIST 610 was used for REE, and the elements were normalized to CI Chondrite values after [McDonough and Sun \(1995\)](#). Zircon grains were ablated with a laser spot diameter of 23 μm using an energy density of 6 Jcm^{-2} at the target. The reference 91,500 zircon (1062 Ma, [Wiedenbeck et al., 1995](#)) was employed as the primary standard, whereas Plešovice zircon (337 ± 1 Ma, [Slařma et al., 2008](#)) as the control standard. Both standards were run every ten unknown analyses. The Plešovice reference zircon yielded a mean age of 338.2 ± 1.4 Ma, in agreement with previously published data. The raw data reduction, the estimation of U and Th

concentration, and the propagation of 2σ uncertainties were performed using Iolite software version 4.5.1 (Paton et al., 2011). $^{207}\text{Pb}/^{206}\text{Pb}$ ratios, ages, and errors are calculated according to Petrus and Kamber (2012). The Online IsoplotR program (Vermeesch, 2018) was employed for concordia plotting, mean diagrams, and age calculation. The cutoff between $^{206}\text{Pb}/^{238}\text{U}$ and $^{207}\text{Pb}/^{206}\text{Pb}$ ages is established at 1500 Ma (which means we consider the $^{206}\text{Pb}/^{238}\text{U}$ ages below that cutoff), as suggested by Spencer et al. (2016), and a discordance filter of $\pm 10\%$

was considered for meaningful ages. Descriptions of zircon textures are based on Corfu et al. (2003) and Rubatto and Gebauer (2000).

5. Results

Two mafic-intermediate meta-volcanic samples (upper lithodeme; SM21-07 and SM21-28), three amphibolites (lower lithodeme; SM21-33–paleosome, SM21-13a, and SM21-13 b), and two leucosomes from El

Table 1
Whole-rock geochemistry.

	Meta-basalt	Meta-andesite	Amphibolites		Amphibolite (paleosome)	Leucosomes		Standards	
	SM21-07	SM21-28	SM21-13 A	SM21-13 B	SM21-33	SM21-34	SM21-35	IGLa1	IGLa1
Major elements (wt.%)									
SiO ₂	57.11	55.70	48.36	49.48	55.72	79.71	77.39	60.74	60.76
TiO ₂	0.82	1.05	1.32	0.98	1.30	0.07	0.27	1.08	1.08
Al ₂ O ₃	15.26	14.41	16.46	17.10	15.71	12.16	12.04	17.36	17.34
Fe ₂ O ₃ t	7.36	7.38	11.74	10.13	11.04	0.61	2.74	6.03	6.02
MnO	0.10	0.08	0.20	0.16	0.22	bdl	0.01	0.1	0.1
MgO	3.58	3.17	5.19	4.28	2.91	0.16	0.22	1.99	1.99
CaO	5.13	5.76	8.90	10.77	5.88	0.84	1.11	5.28	5.27
Na ₂ O	3.39	4.40	3.68	3.98	4.29	5.57	5.06	4.66	4.68
K ₂ O	0.84	0.87	0.94	0.37	0.39	0.26	0.40	2.21	2.21
P ₂ O ₅	0.18	0.33	0.70	0.36	0.50	bdl	0.01	0.38	0.39
LOI	6.20	6.85	2.41	2.28	1.93	0.51	0.65	0.12	0.12
Total	99.96	100.00	99.90	99.90	99.90	99.90	99.90	100	99.99
Trace elements (ppm)									
Li	34.71	25.79	6.54	4.28	6.60	0.73	0.98	10.63	9.28
Be	1.24	1.30	1.26	1.11	1.26	1.00	1.43	2.28	2.49
B	15.93	4.89	3.74	4.61	3.89	3.65	4.33	6.61	5.16
Sc	18.51	16.97	31.74	35.31	28.21	0.47	2.38	14.18	33.48
V	96.62	124.32	218.93	262.21	116.76	7.60	9.71	117.4	415.35
Cr	173.49	78.08	79.34	167.55	21.60	4.89	2.72	16.19	16.61
Co	16.80	19.59	24.56	26.82	19.02	1.80	2.97	15.55	37.29
Ni	15.95	37.45	30.73	51.82	9.25	3.72	8.92	18.45	12.91
Cu	15.15	65.75	54.38	74.76	38.08	7.40	14.00	53.86	30.04
Zn	79.97	74.99	86.64	71.36	117.04	9.34	12.35	84.61	128.73
Ga	18.14	18.03	18.25	19.46	19.59	11.50	18.89	20.7	22.43
Rb	21.21	19.28	11.53	3.03	2.83	1.47	2.40	69.06	48.69
Sr	272.49	409.34	489.11	503.11	396.65	147.29	134.16	657.27	341.68
Y	12.75	28.56	30.76	23.87	34.45	0.89	4.30	20.13	37.53
Zr	90.50	208.36	85.04	58.10	104.36	5.80	301.94	232.71	188.07
Nb	7.40	11.37	6.69	4.00	8.27	0.27	1.04	14.94	13.26
Mo	0.09	0.29	0.08	0.11	0.46	0.02	0.16	1.59	247.98
Sn	0.58	1.27	1.03	0.93	1.20	0.33	0.90	2.01	2.15
Sb	2.10	0.87	0.33	0.41	0.68	0.12	0.16	0.45	0.31
Cs	12.19	1.66	0.19	0.05	0.22	0.05	0.10	1.16	1.14
Ba	256.64	361.49	368.22	215.46	247.72	190.41	201.08	1141.99	674.46
La	17.33	27.82	24.74	16.79	22.02	4.35	13.41	37.88	25.08
Ce	32.12	56.84	55.51	37.85	50.92	6.54	22.23	68.48	52.76
Pr	3.95	7.52	7.74	5.33	7.21	0.66	2.50	8.19	6.89
Nd	15.68	30.33	33.60	23.41	31.63	2.65	9.20	30.23	28.61
Sm	3.13	6.38	7.37	5.32	7.40	0.35	1.27	5.64	6.78
Eu	1.16	1.66	2.06	1.53	2.14	0.67	1.54	1.64	1.94
Tb	0.44	0.88	0.97	0.73	1.03	0.05	0.15	0.69	1.07
Gd	3.06	5.96	6.86	5.04	7.06	0.39	1.17	4.94	6.85
Dy	2.49	5.19	5.57	4.31	6.19	0.20	0.73	3.62	6.68
Ho	0.50	1.02	1.09	0.86	1.23	0.06	0.17	0.69	1.34
Er	1.34	2.86	2.96	2.34	3.42	0.10	0.50	1.88	3.69
Yb	1.21	2.69	2.64	2.14	3.25	0.10	0.62	1.68	3.47
Lu	0.18	0.40	0.39	0.32	0.49	0.02	0.11	0.25	0.51
Hf	2.16	4.85	2.01	1.47	2.58	0.03	7.05	4.98	4.77
Ta	0.30	0.56	0.30	0.21	0.34	0.01	0.04	0.89	0.83
W	0.15	0.46	0.15	0.22	0.31	0.16	0.16	0.4	0.41
Tl	0.18	0.15	0.09	0.02	0.03	0.01	0.02	0.28	0.27
Pb	5.57	3.53	5.58	6.81	5.78	1.95	2.28	13.25	10.49
Th	0.17	1.50	0.48	0.70	0.26	0.15	0.19	6.01	5.84
U	0.06	0.64	0.16	0.26	0.09	bdl	0.18	1.88	1.69
(La/Yb) _N	10	7	7	6	5	29	14		
Sr/Y	21	14	16	21	12	166	31		
Nb/Ta	25	20	22	19	24	27	26		
Mg#	49	46	47	46	34	34	14		

*bdl: below detection limits.

*The certificated values of the IGLa standards for major elements can be consulted in Lozano-Santa Cruz and Bernal (2005). The values of AGV-2 and BCR-2 standards for trace elements can be consulted in the US Geological Survey rock standards.

Águila Migmatite (lower lithodeme; SM21-34 and SM21-35) were selected for geochemical and geochronological analyses. The location of all samples and resulting ages are summarized in Table 2, whereas zircon U–Pb data is available in Supplementary data. The whole-rock geochemical data are summarized in Table 1.

5.1. Zircon U–Pb geochronology and REE geochemistry

5.1.1. Mafic to intermediate meta-volcanic rocks and amphibolites

The four samples selected for geochronological analyses contain abundant zircon with dimensions spanning from 70 to 200 μm (Fig. 4a–d). Zircon grains exhibit a wide range of morphologies with nearly equant stubby to elliptical shapes and textures characterized by broad-banded concentric zoning and unzoned homogeneous or convoluted luminescent fields.

Three zircon-age typologies can be recognized based on the obtained ages, their distribution, and zircon chemistry. The first type encompasses core grains with homogeneous or convoluted luminescent fields with highly concordant (76% are less than 3% discordant) but slightly overlapping ages arranged along the concordia, forming clusters with concordia ages of 1148–1200 Ma (Fig. 5a–d). Additionally, sample SM21-33 exhibits a small group of ages ($n = 3$) around 1300 Ma. All these analyses show (1) an increase from LREE to HREE with a positive steep MREE–HREE pattern, $(\text{Lu}/\text{Gd})_N$ ratios averaging between 22 and 34, and $(\text{Lu})_N$ contents regularly above 1000; (2) positive Ce and negative Eu anomalies; and (3) Th/U values above 0.1 (Fig. 6a–d, gray data). These are typical igneous chemical features (e.g., Hoskin and Schaltegger, 2003; Rubatto and Gebauer, 2000; Belousova et al., 2002).

The ages constituting the second type also belong to zircon cores. Some core textures are similar to type 1, whereas others contain broad-banded concentric zoning (e.g., Fig. 4a, white targets). Their chemical compositions present igneous-like REE patterns, as well as Y and Th/U values similar to type 1. However, unlike type 1, these analyses constitute coherent fractions of highly overlapping ellipses (Fig. 5a–d, black ellipses). They yielded concordia ages of 1078 ± 6 Ma (MSWD = 0.95, $n = 14$), 1054 ± 7 Ma (MSWD = 0.38, $n = 8$), and 1063 ± 6 Ma (MSWD = 1, $n = 15$). Sample SM21-13a yielded an approximate upper intercept (discordant analyses) of 1044 ± 47 Ma (MSWD = 1.1; $n = 6$).

The U–Pb analyses from stubby to elongated unzoned small bright grains and rims surrounding igneous-like zircon cores define the third type of zircon populations (e.g., Fig. 4a, red targets). They are interpreted as newly grown or entirely reprecipitated/recrystallized zircon crystals chemically distinguished by positive low-steep to-flat MREE–HREE slopes with $(\text{Lu}/\text{Gd})_N$ averages of 1–15 and $(\text{Lu})_N$ contents usually below 1000 (except in sample SM21-28, which show a wide range of HREE content) (Fig. 6a–d, red data). In addition, meta-volcanic SM21-07 and amphibolite SM21-33 show less scattered and lower values or decreasing trends in Y and Th/U relative to the 1 and 2 types. The resulting ages of the third type are highly concordant and produce coherent clusters with concordia ages of 934 ± 7 Ma (MSWD = 0.48, $n = 13$), 934 ± 6 Ma (MSWD = 0.68, $n = 12$), 948 ± 6.7 Ma (MSWD = 0.66; $n = 9$), and 952 ± 5 Ma (MSWD = 0.46, $n = 19$).

5.1.2. Leucosomes

Leucosome SM21-34 contains scarce subhedral to rounded $<90 \mu\text{m}$

long zircon grains with dark cores rimmed by barely zoned domains and convoluted or homogeneous luminescent fields (Fig. 4e). In leucosome SM21-35, abundant zircon occurs as elliptical grains with sharp luminescent sectors, core-rim textures, and broad-banded oscillatory zoning (Fig. 4f). The ages distribution in both samples follows two types of arrays (Fig. 5e and f). In the first one, the ages are randomly spread along the concordia from 1344 to 956 Ma with apparent low isotopic disturbance (70% are less than 3% discordant). Analyses from the second type are related to zoned textures and show nearly concordant, overlapping ages that form coherent populations. All data contain similar igneous-like chemical signatures. Therefore, only based on age distribution and zircon texture, the second type is interpreted to have originated during magmatic crystallization, whereas the first type is related to inherited grains or cores. Based on this criterion, the leucosomes crystallization ages were estimated by employing the analyses of the second type, yielding concordia ages of 954 ± 3 Ma (MSWD = 0.62, $n = 35$) and 933 ± 4 Ma (MSWD = 0.4, $n = 19$). Finally, some analyses of zircon rims show younger scattered ages, interpreted as recrystallization or Pb-loss caused by post-magmatic thermal disturbance.

5.2. Whole-rock major and trace element geochemistry

To inquire about the tectonic setting that originated the mafic-intermediate PS igneous protoliths, whole-rock major and trace element analyses (Table 1) were obtained for five meta-volcanics and amphibolites (SM21-07, SM21-28, SM21-13a, SM21-13 b, and SM21-33). Additionally, two leucosomes from El Águila Migmatite (SM21-34 and SM21-35) were analyzed to evaluate their composition and relationship with the suspected paleosomes.

Whole-rock chemical analyses of mafic to intermediate meta-volcanics and amphibolites indicate subalkaline basalt-andesite compositions that follow roughly a calc-alkaline trend as observed in the Zr/Ti vs. Nb/Y and AFM diagrams (Fig. 7a and b). The multi-element diagram reveals roughly similar patterns (Fig. 7e). They display decreasing content from most incompatible to the least incompatible elements (left to right) and negative anomalies in HFSEs such as Nb, Ta, Ti, and Zr relative to LILEs such as K and La, likely indicating fractionation processes and crustal involvement during the magma evolution (Rollison, 1993). Rb, U, and Th also present variable negative anomalies. Chondrite-normalized REEs (Fig. 7f) display moderate negative steep patterns from LREE to HREE and negligible Eu anomalies.

Leucosomes are weakly peraluminous, low K_2O ($<1 \text{ wt } \%$), and high-silica ($>75 \text{ wt } \%$ SiO_2) rocks, classified as low-Al trondhjemites ($<15 \text{ wt } \%$ Al_2O_3) according to the classification of Barker (1979) (Fig. 7d). The multi-element and REE diagrams reveal moderately fractionated patterns ($\text{La}_N/\text{Yb}_N = 29$ and 14) with negative Nb, Ta, P, and Ti anomalies, and a slight increase in HREE (especially in sample SM21-35). Zr and U show negative anomalies in leucosome SM21-34 and positive anomalies in leucosome SM21-35, likely reflecting zircon inheritance or fractionation. Both samples display lower Sr contents ($<300 \text{ ppm}$), though a slight positive anomaly is present in leucosome SM21-34. The REE abundances show plagioclase-like patterns (e.g., Rollison, 1993), with lower REE content than the amphibolite SM21-33 (paleosome) and a strong positive Eu anomaly.

Table 2
Ages and location of samples from the Pochotepec Suite.

	Sample	Rock type	Longitude	Latitude	Protolith/igneous age (Ma)	Metamorphic age (Ma)
Lower lithodeme	SM21-33	Amphibolite (paleosome)	$-96^{\circ}46'19.30''$	$17^{\circ}19'50.59''$	1063 ± 6	952 ± 5
	SM21-35	Leucosome	$-96^{\circ}46'19.30''$	$17^{\circ}19'50.59''$	954 ± 3	
	SM21-34	Leucosome	$-96^{\circ}46'19.30''$	$17^{\circ}19'50.59''$	933 ± 4	
	SM21-13a and b	Amphibolite	$-96^{\circ}55'09.70''$	$17^{\circ}50'10.50''$	1044 ± 47	948 ± 6.7
Upper lithodeme	SM21-07	Meta-basalt	$-96^{\circ}57'4.84''$	$17^{\circ}55'17.77''$	1078 ± 6	934 ± 7
	SM21-28	Meta-andesite	$-96^{\circ}47'32.8''$	$17^{\circ}18'29.2''$	1054 ± 7	934 ± 6

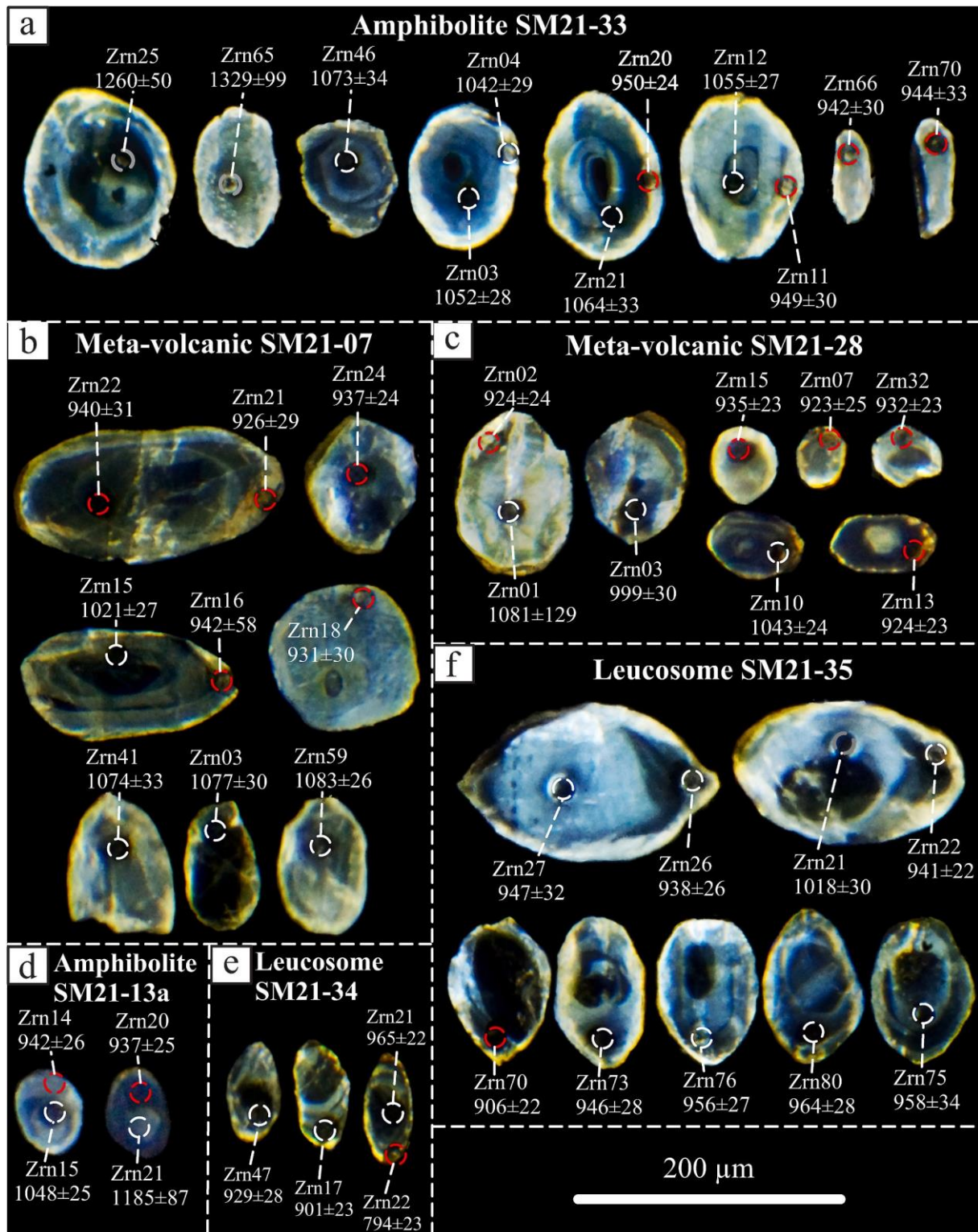


Fig. 4. After-ablation Cl images of representative zircon grains showing inherited (gray targets), igneous (white targets), and metamorphic (red targets) ages. $^{206}\text{Pb}/^{238}\text{U}$ ages are considered below 1200 Ma, and $^{207}\text{Pb}/^{206}\text{Pb}$ ages above that cutoff.

6. Discussion

6.1. Interpretation of the whole-rock geochemistry and zircon U–Pb data

6.1.1. Mafic to intermediate metavolcanics and amphibolites

Based on texture, grain size, and field relationships, we interpret the mafic to intermediate metamorphic rocks from the Pochotepec suite

(PS) as having two types of protolith representing different lithodemes. Fine-grained low-grade mafic to intermediate meta-volcanic rocks (SM21-28 and SM21-07), commonly intercalated with pelitic schists and marbles, are inferred to have formed in a supracrustal volcanosedimentary environment. In contrast, coarse-grained amphibolites (SM21-13a, SM21-13 b, SM21-33), reaching partial melting in some sectors, are thought to derive from gabbroic-dioritic protoliths and represent a lower

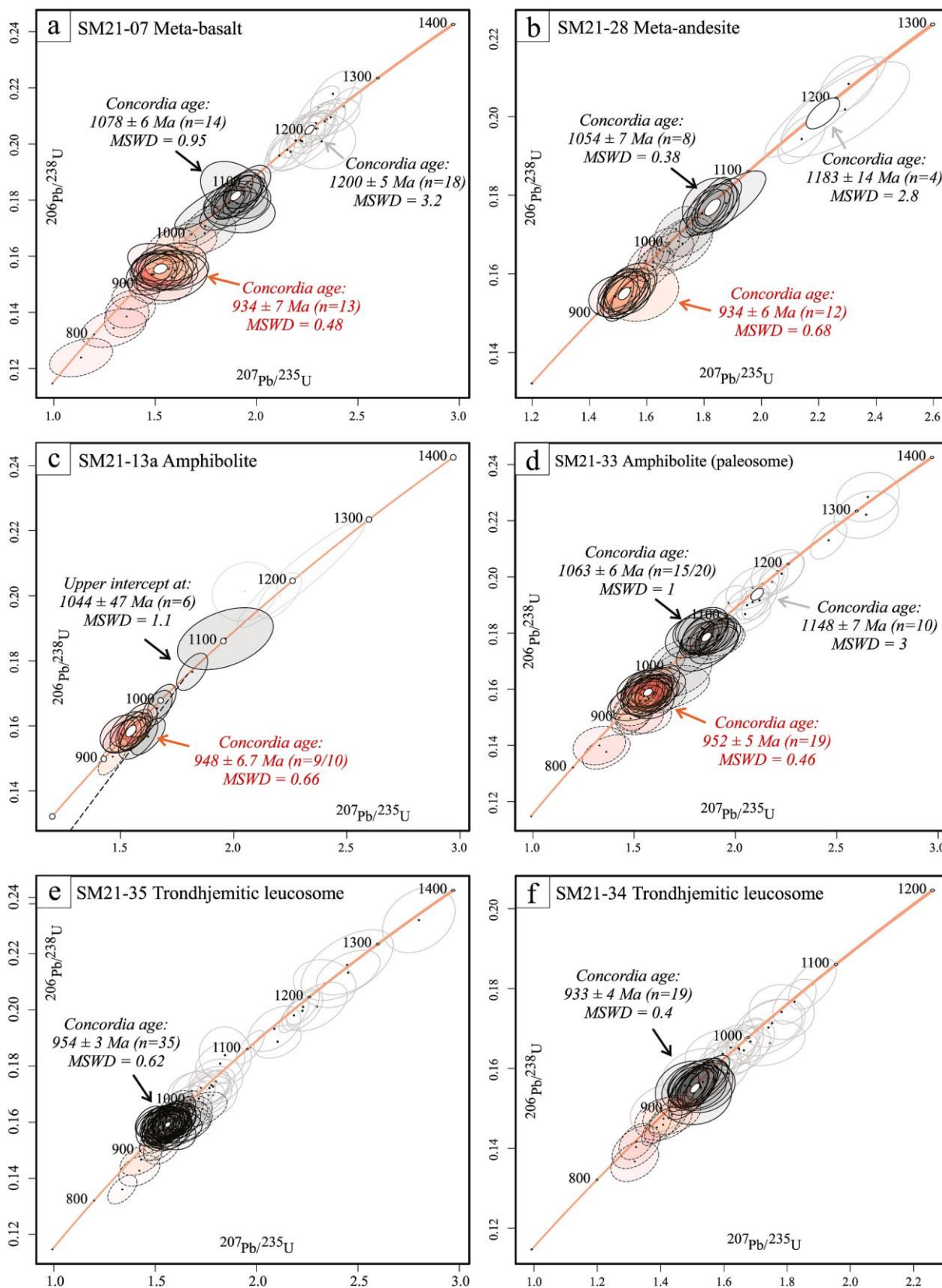


Fig. 5. Concordia diagrams representing the zircon U–Pb analyses. All uncertainties are 2σ . The color of ellipses relates to the age interpretation: gray, inherited; black, igneous; and red, metamorphic/anatectic or Pb loss. Dashed ellipses are not considered in age calculus as they represent Pb loss or mixed ages.

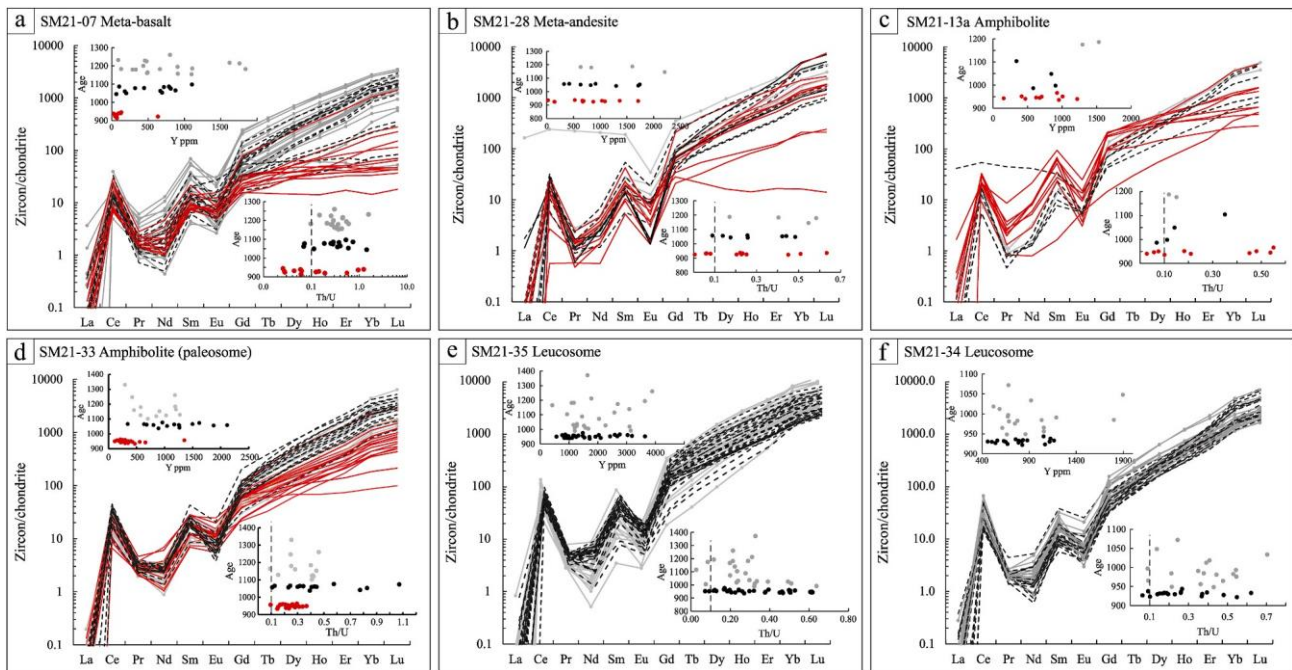


Fig. 6. Chondrite-normalized zircon REE abundances, age vs. Y, and age vs. Th/U diagrams. Normalizing values for REE diagrams are after [McDonough and Sun \(1995\)](#). Gray symbology indicates inherited analyses, black symbology represents igneous-type analyses (including dashed lines), and red symbology represents metamorphic analyses.

crustal level.

Whole-rock geochemistry of all mafic to intermediate samples from the PS suggests arc-related magmas that interacted with a continental crust ([Fig. 7](#)). Although amphibolite SM21-33 is considered a paleosome and contains slight melting reactions, its chemical composition is quite similar to the other mafic to intermediate samples. Therefore, it is considered to maintain intact its protolith chemical composition. The multi-element patterns of all mafic to intermediate meta-volcanics and amphibolites show a depletion in Rb, Th, and U, and perhaps K as well, likely driven by dissolution in anatectic or fluoride-rich fluids ([Dostal and Capedri, 1978](#); [Keppler and Wyllie, 1990](#)). Therefore, Th-free tectonic discrimination diagrams such as Ti–Zr (after [Pearce et al., 1981](#), [Fig. 7g](#)), Nb/8-Y/5- La/10 (after [Cabani and Lecolle, 1989](#), [Fig. 7h](#)), and Nb/La–La/Yb (after [Hollocher et al., 2012](#), [Fig. 7i](#)) are suitable to gain insight into the tectonic environment of the magmatic protoliths. The samples plot in the arc, calc-alkaline, and continental arc fields, respectively. Therefore, we interpret a continental arc as the most plausible tectonic setting where the igneous series of the PS originated.

Even though zircon U–Pb dating is one of the most widely used and sophisticated geochronological techniques, there remain debatable issues or analytical difficulties that require a careful approach. For instance, given the habitual scarceness of zircon as a primary accessory phase in mafic or ultramafic rocks (low-Zr melts), the syn-magmatic nature of zircon, when present, is usually doubtful. This is because the low-Zr contents and high zircon-saturation points in mafic and ultramafic melts restrict the syn-magmatic zircon precipitation (e.g., [Watson and Harrison, 1983](#); [Shao et al., 2019](#)). However, this fact is constantly challenged by natural observations where primary zircon commonly occurs in mafic and ultramafic rocks from different tectonic settings, even in the oceanic crust (e.g., [Grimes et al., 2007](#); [2009](#) and references therein; [Schwartz et al., 2010](#)). Therefore, additional mechanisms could intervene to trigger zircon precipitation during the crystallization of low-Zr melts, such as the formation of local zircon-saturated confined volumes ([Bea et al., 2022](#)). Except for amphibolite SM21-13 b, all the mafic-intermediate samples investigated in the present study contain low to moderate zircon grain amounts that yielded multiple populations and complex distributions of U–Pb analyses. Careful analysis must be

made to infer the nature and age meaning of these types of U–Pb data. The ages distribution shows three main populations (differentiated by color in [Fig. 5](#)). To discuss their geological meaning, we consider the three following attributes: (1) the zircon chemistry, including the behavior of Y, Th/U ratios, and HREE; (2) the zircon textures; and (3) the U–Pb ages distribution. Given some similarities between the two oldest types of U–Pb ages populations, we discuss them together (type 1 from ca. 1150 to 1300 Ma and type 2 from ca. 1050 to 1080 Ma; [Fig. 6a–d](#), gray and black symbology). First, they are chemically similar, exhibiting increasing contents from LREE to HREE and positive steep MREE–HREE patterns, positive Ce and negative Eu anomalies, and scattered Th/U values usually above 0.1; likely suggesting that both types originated in a magmatic environment (e.g., [Rubatto and Gebauer, 2000](#); [Belousova et al., 2002](#); [Hoskin and Schaltegger, 2003](#)). In addition, they show highly scattered Y contents ([Fig. 6](#)). From a textural perspective, both types of U–Pb analyses were acquired from unzoned or convoluted zircon cores; however, the zircon cores of type 2 differ by additionally exhibiting broad-banded concentric zoning ([Fig. 4a–d](#)). Finally, the U–Pb analyses distribution along the concordia of type 1 (except in amphibolite SM21-13a) form clusters with somewhat scattered ages, whereas those of type 2 constitute coherent populations of concordant and overlapped ages ([Fig. 5](#)). Based on the U–Pb ages and their distribution along the concordia and the zircon textural differences of both types, we consider the first one as representing xenocrystic cores extracted from an older igneous-type crust. In contrast, the second type is inferred to reflect the crystallization of the magmatic protoliths. Given that some zircon textures are similar between types 1 and 2, it is plausible that, during the magmatic event, some xenocrysts recrystallized by coupled dissolution-precipitation or diffusion-reaction processes, resetting their U–Pb isotopic system (e.g., [Tomaschek et al., 2003](#); [Geisler et al., 2007](#)). In turn, the broad-banded concentric zoning textures of type 2 are thought to represent syn-magmatic growths.

A significant reworking of an older crust during magmatism is evident from the inherited zircon ages in all the mafic-intermediate samples. Although they show some dispersion along concordia, likely caused by Pb loss, relatively coherent clusters occur at ca. 1200–1150 Ma in all samples and an additional cluster at ca. 1300 Ma in amphibolite

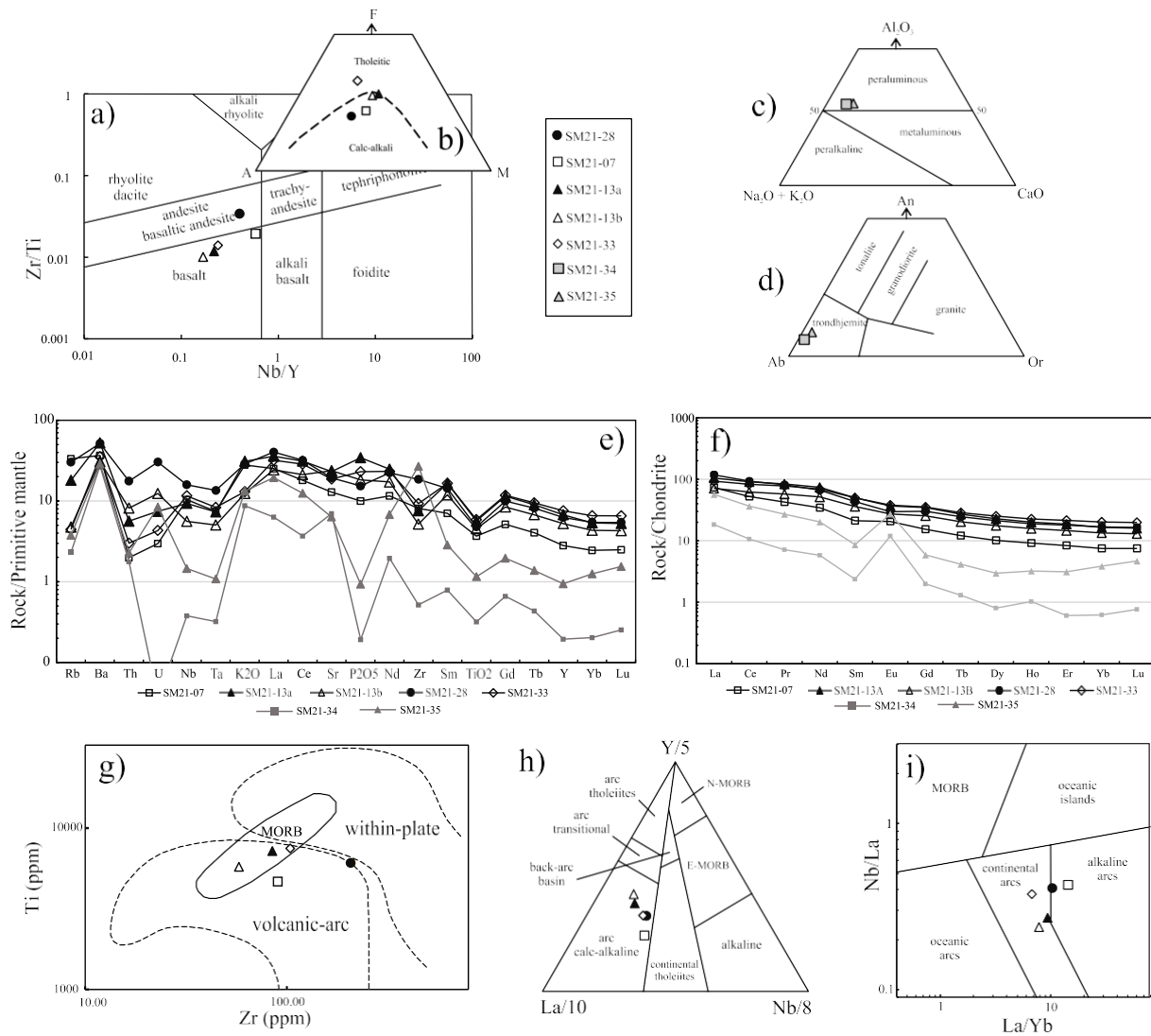


Fig. 7. a) Zr/Ti–Nb/Y classification diagram for altered or metamorphosed volcanic rocks after [Pearce \(1996\)](#). The samples graph into the sub-alkali field. b) AFM ($\text{Na}_2\text{O} + \text{K}_2\text{O}$; ΣFeO ; ΣMgO) ternary diagram with the tholeiitic and calc-alkali sub-division suggested by [Irvine and Baragar \(1971\)](#). c) Ternary plot with the peraluminous, metaluminous, and peralkaline fields. Modified from [Gill \(2010\)](#). Whole rock Al_2O_3 , $\text{Na}_2\text{O} + \text{K}_2\text{O}$, and CaO contents are in molar proportions. d) Normative feldspar diagram for granitoids after [Baker \(1979\)](#). e) Multi-element diagram. Normalizing values are after [Sun and McDonough \(1989\)](#). f) REE abundances normalized to the CI chondrite values after [McDonough and Sun \(1995\)](#). g) Ti vs. Zr tectonic discrimination diagram after [Pearce et al. \(1981\)](#). h) Nb/8–Y/5–La/10 ternary plot for tectonic discrimination after [Cabanis and Lecolle \(1989\)](#). i) Nb/La–La/Yb tectonic discrimination diagram after [Hollocher et al. \(2012\)](#).

SM21-33, yielding insight into the age of the hosting crust. The concordia ages of type 2 reflect a magmatic stage spanning 1078–1054 Ma (late Stenian). Amphibolite SM21-13a contains a few discordant igneous-type ages that yielded an upper intercept of 1044 ± 47 Ma, a crystallization age similar to the other mafic-intermediate samples (meta-volcanics and amphibolites); however, given its significant error and the low number of analyses, it is not considered to define the Stenian interval of magmatism in the PS.

The U–Pb analyses forming the third type of age populations (from ca. 950 to 930 Ma) were measured from rims surrounding the igneous/inherited zircon cores of types 1 and 2 and from stubby to elongated unzoned small bright zircon grains ([Fig. 4](#), red targets). Meta-volcanic SM21-07 and amphibolite SM21-33 show decreasing trends and gathered values of Y and Th/U ratios (some of them lower than 0.1) relative to the igneous-like types 1 and 2 ([Fig. 6a](#) and d). These characteristics are related to metamorphism; as elements Y, Th, and U contain greater ionic radii than Zr, they tend to be expelled from the zircon lattice when pressure increases (e.g., [Wann and Griffin, 2004](#)). However, the zircon chemistry changes also depend on how open or close the system is or the

composition of acting fluids, among other variables (e.g., [Ren-Xu et al., 2010](#)), which could leave unaltered the chemistry of zircon despite undergoing metamorphism, as can be observed in the Y contents of meta-volcanic SM21-28 and amphibolite SM21-13a ([Fig. 6b](#) and c). The third type of U–Pb analyses is also distinguished by lower HREE contents (especially in meta-volcanic SM21-07 and amphibolites SM21-33 and SM21-13a), leading to relatively flat HREE patterns compared with the igneous-like slopes of the zircon populations of types 1 and 2 ([Fig. 6](#)). However, a lack of garnet in the rock precludes the traditional garnet effect as the cause of Gd–Lu depletion (e.g., [Rubatto, 2017](#)), hence calling for a different explanation. We suggest that zircon precipitated in equilibrium with an HREE-depleted anatectic/metamorphic fluid formed in situ by dissolution or incongruent melting (without assimilation or contribution of HREE-rich phases) of a rock whose precursor magma underwent zircon fractionation ([Zhong et al., 2021](#)). In this scenario, as the system evolves, the melt/fluid incorporates more elements buffered by surrounding phases, including inherited/magmatic zircon itself, favoring new zircon rims or crystals to precipitate with higher HREE content, as observed in meta-volcanic SM21-28 ([Fig. 6b](#)).

Therefore, the zircon textural and chemical characteristics of the third type U–Pb analyses are consistent with metamorphic zircon growth or recrystallization (e.g., Ren-Xu et al., 2010; Rubatto, 2017), which mainly occurs as newly grown or entirely reprecipitated/recrystallized grains or rims, resulting in isotopically reset and highly concordant U–Pb ages. The obtained metamorphic zircon ages constrain the metamorphism/anatexis timing in the PS between 952 and 934 Ma.

6.1.2. Leucosomes

Whole rock geochemical data of leucosomes SM21-34 and SM21-35 show typical low-Al TTGs compositions (<15 wt % Al_2O_3 ; tonalite-trondhjemite-granodiorite) in terms of low contents of Y (<5 wt %), Yb (<1 wt %), Nb (≤ 1 wt %), Sr (<300 ppm), Mg, Ni, and Cr, as well as Mg numbers (34 and 14, respectively), among others (e.g., Condie, 2005). TTGs result from the partial melting of rocks with hydrated basaltic compositions in different tectonic settings, including continental orogens (Beard and Lofgren, 1991; Rapp et al., 1991; Nehring et al., 2009; Kendrick and Yakymchuk, 2020). The leucosome samples are spatially related to the amphibolite SM21-33 (paleosome); thereby, the amphibolite SM21-33 is considered part of the mafic source from which anatectic melts derive. Furthermore, the coherent chemical composition of amphibolite SM21-33 and the other mafic-intermediate meta-volcanics and amphibolites allows us to consider the general arc-related signature of the PS protoliths as representing the source composition. However, the content of incompatible elements in the leucosomes is slightly lower than that of the mafic source (Fig. 7e and f), which is noteworthy as higher contents of these elements in anatectic fluids should be expected. The low content in incompatible elements could be attributable to that (1) the leucosomes analyzed rather derive from a different, more depleted source; (2) the leucosomes are late anatectic fluids after high-melting rates; (3) the leucosomes are depleted cumulates left after enriched fluids extraction. The first possibility is less likely considering the close spatial relation between leucosomes and the amphibolite SM21-33. Hypothesis 2 is reasonable, considering that diatexitic structures, as observed in the El Águila Migmatite, are related to high-melting rates (e.g., Sawyer, 2008). Finally, the third option is probable only in leucosome SM21-34 by considering the positive anomaly in Sr, which is likely related to the accumulation of plagioclase (e.g., Condie, 2005).

TTGs are produced during pressure melting conditions of at least 10 kb from the stability field of plagioclase to high-pressure conditions with garnet + rutile in the residue (e.g., Moyen, 2011; Kendrick and Yakymchuk, 2020). High values in Sr/Y and $L_{\text{AN}}/Y_{\text{BN}}$ ratios, as well as depletion in Ta, Nb, and HREE, indicate the presence of residual garnet and rutile and hence, of high-pressure conditions during melting (e.g., Moyen and Martin, 2012). However, other factors, such as the source composition or melt-loss, are also determinants in the trace elements and REE composition of resulting melts (Kendrick and Yakymchuk, 2020). The REE patterns and high positive Eu anomalies in the leucosomes (Fig. 7f) indicate a high input of plagioclase into the melts. However, the generally low Sr values (<300 ppm) suggest that plagioclase was also present in the residue (e.g., Condie, 2005), thus indicating that melting occurred under lower-pressure conditions, which is consistent with the absence overall in the field of high-pressure minerals such as garnet. HREE and Y show no depletion trends in the leucosomes, indicating the absence of residual garnet. Although, inherited zircon could increase the HREE content, especially in sample SM21-35, which also shows positive anomalies in Zr and U. The lack of petrographically observations of the melanosome (residue) from the El Águila Migmatite precludes a conclusive interpretation; however, amphibolite SM21-33 (paleosome) exhibits local partial melting reactions where anatectic pods of plagioclase and quartz are formed, while amphibole is left as a residual phase (Fig. 3j). Given the absence of dehydrating reactions such as growth pyroxene after amphibole, it is suggested that partial melting was enhanced by external fluids rather than hydrous-phases breakdown. In addition, melting under fluid-saturated conditions reduces the

resistance of plagioclase, and it requires lower P–T conditions to produce anatexis relative to those for hydrated phase breakdown reactions (e.g., Beard and Lofgren, 1991). The water-saturated system increases the plagioclase contribution and reduces amphibole involvement in melting reactions; hence, melt compositions of leucosomes from the PS are controlled mainly by the source composition, plagioclase breakdown, and residual amphibole.

The leucosomes contain igneous-like zircon U–Pb analyses forming inherited and magmatic clusters in a similar way as in the mafic-intermediate samples. Therefore, we consider the same criteria for distinguishing inherited from magmatic ages (see section 6.1.1.). Their magmatic-related clusters yielded ages of 954 ± 3 (SM21-35) and 933 ± 4 Ma (SM21-34), supporting the metamorphic/anatectic age of the PS. Interestingly, the amphibolites (SM21-33 and SM21-13a) exhibit older metamorphic ages (952–948 Ma) than those with extrusive protoliths (SM21-07 and SM21-28; ca. 935 Ma). Moreover, each leucosome age perfectly matches these ages (ca. 954 and 933 Ma). This fact likely reflects progressive metamorphism affecting the rocks according to their original crustal position and the existence of two overprinted anatectic pulses in the PS lower lithodeme.

6.2. Tectonic implications

6.2.1. Origin of the Pochotepec suite in a pre-Rodinian scenario

The geochronological data evaluated in this paper document Precambrian ages in the Pochotepec suite for the first time. Furthermore, the recognition of late-Stenian magmatism in Mexican basement inliers has important implications for the pre-Rodinian geodynamic evolution of Amazonia. The interpretation of a continental arc involves an older hosting crust, which is demonstrated by the abundant presence of inherited zircon cores, especially in meta-volcanic SM21-07 and amphibolite SM21-33 (Fig. 5). Although some dispersion is present in the xenocrystic zircon U–Pb ages attributable to variable Pb loss, they indicate igneous-type inherited components of ca. 1300, 1200, and 1150 Ma. Given the multiple igneous pulses between ca. 1230 and 1150 Ma widely recognized throughout the different Oaxaquia-related inliers (e.g., Solari et al., 2020 and references therein), this is the most likely geological province representing the country rock for the PS.

The Oaxaquia microcontinent (Ortega-Gutiérrez et al., 1995) has been widely interpreted as a Mesoproterozoic peri-Amazonian arc-related composite terrane that originated and evolved between ca. 1400–1150 Ma (e.g., Weber et al., 2010; Weber and Schulze, 2014; Solari et al., 2020 and references therein). Numerous lines of evidence strongly suggest that exposed and buried lithologic units in Colombia (Putumayo Orogen) evolved together with Oaxaquia (Ibañez-Mejía et al., 2011; Ibañez-Mejía, 2020) and perhaps with other peri-Amazonian blocks such as Chortís and Maya, constituting a long-lived fringing arc system bordering the Amazon craton (Keppie and Ortega-Gutiérrez, 2010; Solari et al., 2014, 2010). It is interpreted that a >1400 Ma proto-Oaxaquia-Putumayo oceanic arc underwent back-arc spreading tectonics, separating from the Amazon craton, leading it to evolve as a juvenile intra-oceanic arc (“typical-Oaxaquia”; Weber et al., 2010; Ibañez-Mejía, 2020) and producing sedimentation and alkaline magmatism in the back-arc between ca. 1250 and 1160 Ma (e.g., Ibañez-Mejía, 2020). Subsequently, switching tectonics led the Oaxaquia-Putumayo arc to accrete to continental Amazonia between 1050 and 1020 Ma, recording amphibolite-facies metamorphism in some Putumayo Orogen inliers (Ibañez-Mejía, 2020).

The palinspastic evolution from the Columbia supercontinent to Rodinia during the Mesoproterozoic is traditionally approached through two main paleogeographic models (Fig. 8). Both show the Oaxaquia-Putumayo fringing arc as constituting the Amazonian leading margin that underwent continent-continent collision when Rodinia formed at ca. 1000–990 Ma (e.g., Solari et al., 2003; Weber et al., 2010; Ibañez-Mejía, 2020). During the pre-collisional geodynamic framework between ca. 1100–1000 Ma, a subduction system between the

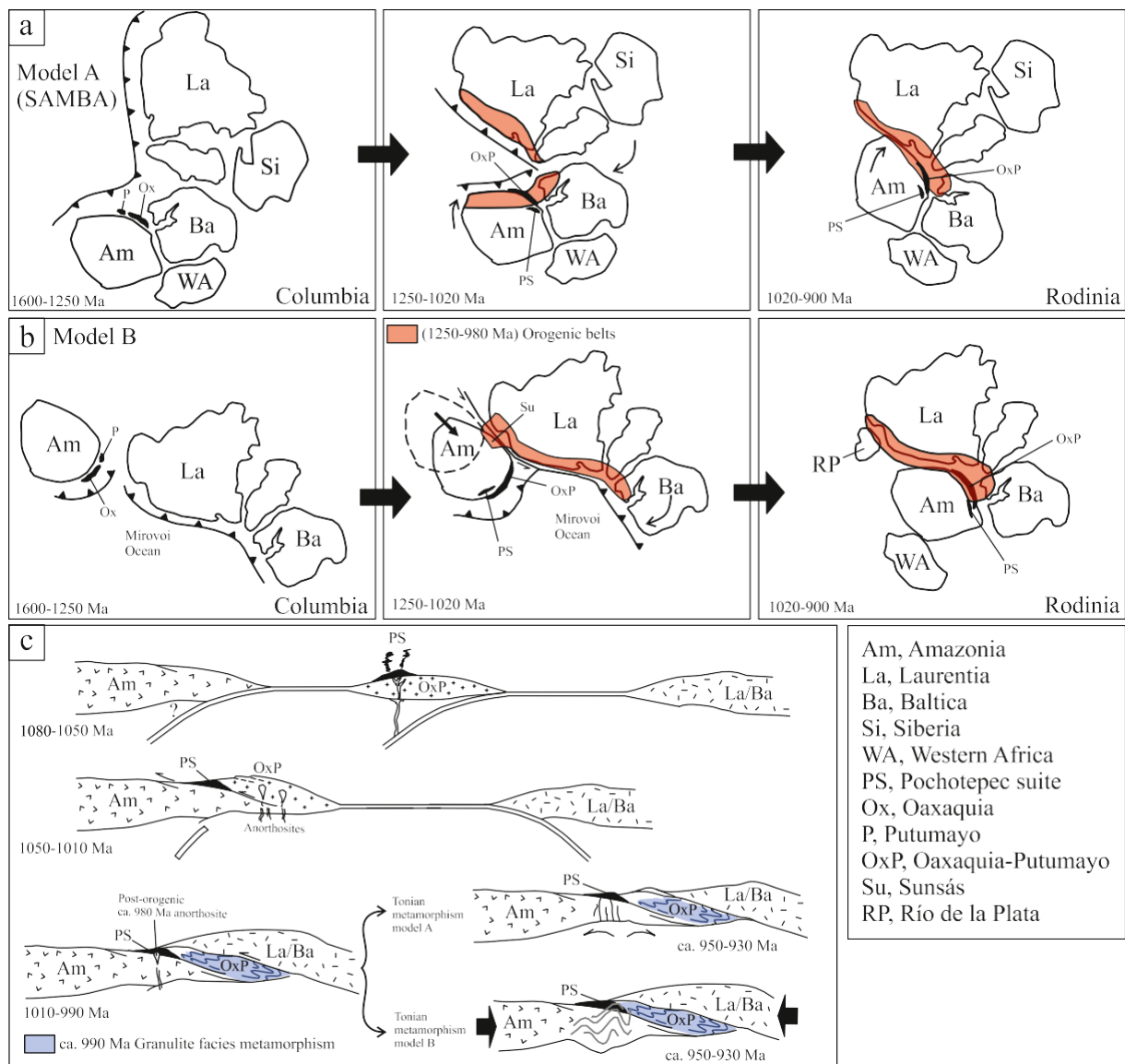


Fig. 8. Proposed tectonic model for the origin and evolution of the Pochotepec suite in a Rodinia-forming context. a) Model A (SAMBA) after Johansson (2009). b) Model B follows Elmg et al. (2009) and Cawood and Pisarevsky (2017). c) Schematic illustration showing the tectonic evolution of the PS and the two possible scenarios considered for the origin of the Tonian metamorphism.

approaching cratons must have been active contemporaneously with the accretion of the Oaxaquia-Putumayo arc onto continental Amazonia. However, a magmatic gap in this time interval has been noted along the Oaxaquia-Putumayo province (Solari et al., 2020; Ibañez-Mejía, 2020). In this context, we propose that the Pochotepec suite mafic-intermediate protoliths, which crystallized at 1078-1054 Ma within a continental arc tectonic setting, represent part of the missing arc-related magmatism along the Oaxaquia-Putumayo arc before the formation of Rodinia.

6.2.2. The formation of Rodinia and the tectonic significance of tonian metamorphism in the Pochotepec suite

The geochronological results in this work are consistent with the cessation of arc-related magmatism in the Pochotepec suite at ca. 1050 Ma, likely instigated by the proximity of continental plates (Amazonia and Oaxaquia-Putumayo) and the eventual break-off of the subducting slab that likely triggered the emplacement of the AMCG suite (anorthosite, mangerite, charnockite, granite) within Oaxaquia (ca. 1020-1000 Ma, e.g., Weber et al., 2010). The AMCG magmatism was followed by a continent-continent collision, leading to the thrusting of Baltica or

Laurentia over the accreted Oaxaquia-Putumayo arc (Amazonia). As a result, the Oaxaquia-Putumayo province reached granulite facies metamorphism peaking at ca. 990 Ma with about 7.5 ± 1 kbar and $730-850$ °C (Solari et al., 2020 and references therein).

The PS underwent burying during the Rodinia assembly, as demonstrated by the presence of anorthosite intrusions dated at 980 Ma, potentially produced by post-orogenic collapse (Espejo-Bautista et al., 2021). However, unlike the Oaxacan Complex, most anorthosites in the PS occur as minor intrusives and dikes into the upper volcanosedimentary lithodeme (Fig. 3c) rather than massif-type plutons in deep crustal levels. More importantly, the metamorphic record in the PS exhibits progressive green-schists to amphibolite-facies metamorphism and partial melting between ca. 952-934 Ma, without any structural, petrological, or geochronological record of ca. 990 Ma granulite-facies, as occurred in the Oaxaquia-Putumayo province. Based on this, the tectonic evolution in the PS did not follow the same tectonometamorphic path as the typical orogenic phase in the Oaxaquia-Putumayo province.

Correlative tectonothermal activity at ca. 950-930 Ma is present in

southeastern Mexico's Chiapas Massif Complex (CMC). [Valencia-Morales et al. \(2022\)](#) document gneisses with Calymmian (>1500 Ma) arc-related protoliths that underwent Tonian amphibolite-facies metamorphism and partial melting between ca. 960–940 Ma (The Catarina Unit). This event correlates with a metamorphic imprint at ca. 920 Ma recorded by gneisses from the Candelaria Unit, also in the CMC ([Cisneros de León et al., 2017](#); [Weber et al., 2018](#)). It is proposed that these units followed a similar trajectory as the composite Oaxaca-Putumayo orogen during the formation of Rodinia. Furthermore, based on low zircon $\delta^{18}\text{O}$ values in the CMC ([Weber et al., 2020](#)), it is likely that these rocks underwent post-orogenic collapse that may have triggered the Tonian anatectic episode ([Valencia-Morales et al., 2022](#)).

Despite the absence of ca. 1080–1050 magmatism in the CMC and of a ca. 1500 Ma crustal component in the PS, the resemblance in metamorphic grade and age between the PS and the Precambrian units of the CMC, their spatial proximity, and similar evolution since the Paleozoic (e.g., [Espejo-Bautista et al., 2022](#)) support a correlation between both provinces. Consequently, extending the CMC Tonian extensional tectonometamorphic interpretation to the PS is suitable. Moreover, the water-saturated melting reactions interpreted for rocks in the PS agree with an early Tonian extensional metamorphic environment ([Fig. 8c](#); metamorphic model A). However, one area for improvement in this model is the complete absence of ca. 990 Ma granulite-facies metamorphism in both provinces. A paleogeographic position for the PS and the CMC far enough from the Rodinian suture zone into the foreland to cause burial into the middle crust but not to reach granulite-facies metamorphism seems plausible. However, highly folding structures observed in the PS also sustain (although not conclusively) the possibility of compressive metamorphism rather than extensional as a result of a late contractional phase near the core of Rodinia ([Fig. 8c](#); metamorphic model B). The lack of thermobarometric evidence for this tectonic event precludes a more definitive interpretation but is a target for future research.

7. Conclusions

1. The Sierra de Juárez Complex in southern Mexico comprises an extensive exposure of mafic to intermediate metamorphic rocks (Pochotepc suite; PS). For the first time, zircon U–Pb geochronological data and whole-rock geochemistry document a Stenian continental arc occurring between 1080 and 1050 Ma as the origin for the PS protoliths.
2. Based on inherited zircon cores dated between 1300 and 1150 Ma, it is likely that the continental arc (PS) occurred along the Oaxaquia-Putumayo block during its docking to continental Amazonia before the final amalgamation of Rodinia.
3. The PS underwent Tonian folding, low-to medium-grade metamorphism, and anatexis between 954 and 933 Ma and lacks structural, petrological, and geochronological evidence for the typical ca. 990 Ma granulite-facies metamorphism recorded in the Oaxaquia-Putumayo province related to the amalgamation of Rodinia.
4. The tectonometamorphic features observed in the PS imply a different evolution and paleo-position than the Oaxaquia-Putumayo one. The “eastern Oaxaquia” term is suggested to refer to this non-granulitic province which may be separated from the “typical Oaxaquia” by the Mesozoic lateral mylonitic structures that run along the Sierra de Juárez Complex.

CRediT authorship contribution statement

Guillermo Espejo-Bautista: Writing – original draft, Visualization, Project administration, Methodology, Investigation, Formal analysis, Data curation, Conceptualization. **Luigi Solari:** Writing – review & editing, Supervision, Resources, Project administration, Funding acquisition, Formal analysis. **Roberto Maldonado:** Writing – review & editing, Validation, Investigation, Formal analysis. **Mónica Ramírez-**

Calderón: Writing – review & editing, Validation, Investigation.

Declaration of competing interest

The authors declare that they have no known competing financial interests or personal relationships that could have appeared to influence the work reported in this paper.

Data availability

Data will be made available on request.

Acknowledgments

The first author acknowledges the Consejo Nacional de Ciencia y Tecnología (CONACyT) for granting him the Ph.D. scholarship. The following projects financed this paper: CONACyT Frontiers of Science 7351, and PAPIIT-DGAPA, UNAM, IN101520, both granted to Luigi A. Solari. We are grateful to Juan Toma's Vázquez Ramírez for thin section preparation; Manuel Albarrán Murillo for helping with mineral separation; Carlos Ortega Obregón for the acquisition of geochronologic data; Ofelia Pérez Arvizu for trace element determinations (all from Centro de Geociencias, UNAM) and with Rufino Lozano (Instituto de Geología, UNAM) for major element determinations. We are also grateful to Juan Alonso Ramírez Fernández for his companionship during fieldwork and for providing some field photographs. We are grateful to Aaron J. Martin, an anonymous reviewer, and the editor Michelangelo Martini for their constructive reviews that improved the manuscript's clarity.

Appendix A. Supplementary data

Supplementary data to this article can be found online at <https://doi.org/10.1016/j.jsames.2023.104248>.

References

- Alaniz-Álvarez, S.A., van der Heyden, P., Nieto-Samaniego, A.F., Ortega-Gutiérrez, F., 1996. Radiometric and kinematic evidence for Middle Jurassic strike-slip faulting in southern Mexico related to the opening of the Gulf of Mexico. *Geology* 24, 443–446. [https://doi.org/10.1130/0091-7613\(1996\)024<0443:RAKEFM>2.3.CO](https://doi.org/10.1130/0091-7613(1996)024<0443:RAKEFM>2.3.CO).
- Alamán-Gallardo, E.A., Ramírez-Fernández, J.A., Weber, B., Velasco-Tapia, F., Casas-Peña, J.M., 2019. Novillo Metamorphic Complex, Huizachal-Peregrina Anticlinorium, Tamaulipas, Mexico: characterization and development based on whole-rock geochemistry and Nd-isotopic ratios. *J. S. Am. Earth Sci.* 96, 102382 <https://doi.org/10.1016/j.jsames.2019.102382>.
- Ángeles-Moreno, 2006. Petrografía, Geología estructural y geocronología del borde noroccidental del terreno Cuicateco, sierra Mazateca, estado de Oaxaca, México. M. Sc. thesis. Universidad Nacional Autónoma de México.
- Ángeles-Moreno, E., Elías-Herrera, M., Macías-Romo, C., Sánchez-Zavala, J.L., Ortega-Gutiérrez, F., 2012. Geological map of the western border of the Cuicateco Terrane, Southern Mexico. *Map Chart Ser. (Geol. Soc. Am.)*. <https://doi.org/10.1130/2012.MCH102>.
- Bea, F., Bortnikov, N., Cambeses, A., Chakraborty, S., Molina, J.F., Montero, P., Morales, I., Solantiev, S., Zinger, T., 2022. Zircon crystallization in low-Zr mafic magmas: possible or impossible? *Chem. Geol.* 602, 120898 <https://doi.org/10.1016/j.chemgeo.2022.120898>.
- Beard, J.S., Lofgren, G.E., 1991. Dehydration melting and water-saturated melting of basaltic and andesitic greenstones and amphibolites at 1, 3, and 6.9 kb. *J. Petrol.* 32, 365–401. <https://doi.org/10.1093/petrology/32.2.365>.
- Belousova, E.A., Griffin, W.L., Suzanne, Y., Fisher, N.I., 2002. Igneous zircon: trace element composition as an indicator of source rock type. *Contrib. Mineral. Petrol.* 143, 602–622. <https://doi.org/10.1007/s00410-002-0364-7>.
- Cabanis, B., Lecolle, M., 1989. Le diagramme La/10-Y/15-Nb/8: un outil pour la discrimination des séries volcaniques et la mise en évidence des processus de mélange et/ou de contamination crustale. *Comptes Rendus de l'Académie des Sciences, Paris, Series 2*, 2023–2029.
- Cameron, K.L., Lopez, R., Ortega-Gutiérrez, F., Solari, L.A., Keppie, J.D., Schulze, C., 2004. U–Pb geochronology and Pb isotopic compositions of leached feldspars: constraints on the origin and evolution of Grenville rocks from Eastern and Southern Mexico. *Geol. Soc. Am. vol. 197*, 755–769. <https://doi.org/10.1130/0-8137-1197-5755>.
- Carfantán, J.C., 1983. Les ensembles géologiques du Mexique méridional. Evolution géodynamique durant le Mésozoïque et le Cénozoïque. *Geofisc. Int.* 22 (1), 9–37.

- Cawood, P.A., Pisarevsky, S.A., 2017. Laurentia-Baltica-Amaozonia relations during Rodinia assembly. *Precambrian Res.* 292, 386–397. <https://doi.org/10.1016/j.precamres.2017.01.031>.
- Cisneros de León, A., Weber, B., Ortega-Gutiérrez, F., González-Guzmán, R., Maldonado, R., Solari, L., Schaaf, P., Manjarrez-Juárez, R., 2017. Grenvillian massif-type anorthosite suite in Chiapas, Mexico: magmatic to polymetamorphic evolution of anorthosites and their Ti-Fe ores. *Precambrian Res.* 195, 203–226. <https://doi.org/10.1016/j.precamres.2017.04.028>.
- Condie, K.C., 2005. TTGs and adakites: are they both slab melts? *Lithos* 80, 33–44. <https://doi.org/10.1016/j.lithos.2003.11.001>.
- Coombs, H., 2016. *Geochemical and Geochronological Constraints on Terrane Definition in Mexico*. Ph.D. Thesis. Cardiff University.
- Corfu, F., Hanchar, J.M., Hoskin, P.W.O., Kinny, P., 2003. Atlas of zircon textures. *Rev. Mineral. Geochem.* 53 (1), 469–500. <https://doi.org/10.2113/0530469>.
- D'Agrella-Filho, M.S., Tohver, E., Santos, J.O.S., Elming, S.Å., Trindade, R.I.F., Pacca, I.I.G., Geraldes, M.C., 2008. Direct dating of paleomagnetic results from Precambrian sediments in the Amazon craton: evidence for Grenvillian emplacement of exotic crust in SE Appalachians of North America. *Earth Planet Sci. Lett.* 267, 188–199. <https://doi.org/10.1016/j.epsl.2007.11.030>.
- Delgado-Argote, L.A., López-Martínez, M., York, D., Hall, C.M., 1992. Geologic framework and geochronology of ultramafic complexes of southern Mexico. *Can. J. Earth Sci.* 29, 1590–1604. <https://doi.org/10.1139/e92-125>.
- Dostal, J., Capedri, S., 1978. Uranium in metamorphic rocks. *Contrib. Mineral. Petrol.* 66, 409–414. <https://doi.org/10.1007/BF00403426>.
- Elmig, S.Å., D'Agrella-Filho, M.S., Page, L.M., Tohver, E., Trindade, R.I.F., Pacca, I.I.G., Geraldes, M.C., Teixeira, W., 2009. A palaeomagnetic and ⁴⁰Ar/³⁹Ar study of late Precambrian sills in the SW part of the Amazonian craton: Amazonia in the Rodinia reconstruction. *Geophys. J. Int.* 178 (1), 106–122. <https://doi.org/10.1111/j.1365-246X.2009.04149.x>.
- Espejo-Bautista, G., Ortega-Gutiérrez, F., Solari, L.A., Maldonado, R., Valencia-Morales, Y.T., 2021. The Sierra de Juárez complex: a new gondwanan neoproterozoic-early palaeozoic metamorphic terrane in southern Mexico. *Int. Geol. Rev.* 64 (5), 631–653. <https://doi.org/10.1080/00206814.2020.1870172>.
- Espejo-Bautista, G., Solari, L., Maldonado, R., Ramírez-Calderón, M., 2022. Silurian to Cretaceous geologic evolution of southern Mexico and its connection to the assembly and breakup of western equatorial Pangea: geochronological constraints from the northern Sierra de Juárez Complex. *Geological Society of London*. <https://doi.org/10.6084/m9.figshare.c.6282721.v1>. Collection.
- Geisler, T., Schaltegger, U., Tomaschek, F., 2007. Re-equilibration of zircon in aqueous fluids and melts. *Elements* 3, 43–50. <https://doi.org/10.2113/gselements.3.1.43>.
- Gill, R., 2010. *Igneous Rocks and Processes a Practical Guide, first ed.* Wiley-Blackwell, UK.
- Grimes, C.B., John, B.E., Kelemen, P.B., Mazdab, F.K., Wooden, J.L., Cheadle, M.J., Høghøj, K., Schwartz, J.J., 2007. Trace element chemistry of zircons from oceanic crust: A method for distinguishing detrital zircon provenance. *Geology* 35 (7), 643–646. <https://doi.org/10.1130/G23603A.1>.
- Grimes, C.B., John, B.E., Cheadle, M.J., Mazdab, F.K., Wooden, J.L., Swapp, S., Schwartz, J.J., 2009. On the occurrence, trace element geochemistry, and crystallization history of zircon from in situ ocean lithosphere. *Contrib. Mineral. Petrol.* 158, 757–783. <https://doi.org/10.1007/s00410-009-0409-2>.
- Hollocher, K., Robinson, P., Walsh, E., Roberts, D., 2012. Geochemistry of amphibolite-facies volcanics and gabbros of the Støren nappe in extensions west and southwest of Trondheim, western gneiss region, Norway: a key to correlations and paleotectonic settings. *Am. J. Sci.* 312, 357–416. <https://doi.org/10.2475/04.2012.01>.
- Hoskin, P.W.O., Schaltegger, U., 2003. The composition of zircon and igneous and metamorphic petrogenesis. *Rev. Mineral. Geochem.* 53 (1), 27–62. <https://doi.org/10.2113/0530027>.
- Ibanéz-Mejía, M., Ruiz, J., Valencia, V.A., Cardona, A., Gehrels, G.E., Mora, A.R., 2011. The Putumayo Orogen of Amazonia and its implications for Rodinia reconstructions: new U-Pb geochronological insights into the Proterozoic tectonic evolution of northwestern South America. *Precambrian Res.* 191, 58–77. <https://doi.org/10.1016/j.precamres.2011.09.005>.
- Ibanéz-Mejía, M., 2020. The Putumayo orogen of Amazonia: a synthesis. In: Gómez, J., Mateus-Zabala, D. (Eds.), *The Geology of Colombia, Volume 1 Proterozoic – Paleozoic*, vol. 35. Servicio Geológico Colombiano, Publicaciones Geológicas Especiales, pp. 101–131. <https://doi.org/10.32685/pub.esp.35.2019.06>.
- Irvine, T.N., Baragar, W.R.A., 1971. A guide to the chemical classification of the common volcanic rocks. *Can. J. Earth Sci.* 8, 523–548. <https://doi.org/10.1139/e71-055>.
- Johansson, Å., 2009. Baltica, Amazonia and the SAMBA connection—1000 million years of neighbourhood during the Proterozoic? *Precambrian Res.* 175, 221–234. <https://doi.org/10.1016/j.precamres.2009.09.011>.
- Kendrick, J., Yakymchuk, C., 2020. Garnet fractionation, progressive melt loss and bulk composition variations in anatectic metabasites: complications for interpreting the geodynamic significance of TTGs. *Geosci. Front.* 11, 745–763. <https://doi.org/10.1016/j.gsf.2019.12.001>.
- Keppie, J.D., Dostal, J., 2007. Rift-related basalts in the 1.2–1.3 Ga granulites of the northern Oaxacan Complex, southern Mexico: evidence for a rifted arc on the northwestern margin of Amazonia. *PGA (Proc. Geol. Assoc.)* 118, 63–74. [https://doi.org/10.1016/S0016-7878\(07\)80048-4](https://doi.org/10.1016/S0016-7878(07)80048-4).
- Keppie, J.D., Ortega-Gutiérrez, F., 2010. 1.3 Ga Oaxaquia (Mexico): remnant of an arc/backarc on the northern margin of Amazonia. *J. S. Am. Earth Sci.* 29, 21–27. <https://doi.org/10.1016/j.jsames.2009.07.001>.
- Keppie, J.D., Dostal, J., Ortega-Gutiérrez, F., López, R., 2001. A Grenvillian arc on the margin of Amazonia: evidence from the southern Oaxacan Complex, southern Mexico. *Precambrian Res.* 112, 165–181. [https://doi.org/10.1016/S0301-9268\(00\)00150-9](https://doi.org/10.1016/S0301-9268(00)00150-9).
- Keppie, J.D., Dostal, J., Cameron, K.L., Solari, L.A., Ortega-Gutiérrez, F., López, R., 2003. Geochronology and geochemistry of Grenvillian igneous suites in the northern Oaxacan Complex, southern Mexico. Tectonic implications. *Precambrian Res.* 120, 365–389. [https://doi.org/10.1016/S0301-9268\(02\)00166-3](https://doi.org/10.1016/S0301-9268(02)00166-3).
- Keppie, J.D., Dostal, J., Nance, D., Miller, B.V., Ortega-Rivera, A., Lee, J.K.W., 2006. Circa 546 Ma plume-related dykes in the ~1 Ga Novillo gneiss (east-central Mexico): evidence for the initial separation of Avalonia. *Precambrian Res.* 147, 342–353. <https://doi.org/10.1016/j.precamres.2006.01.020>.
- Keppeler, H., Wyllie, P.J., 1990. Role of fluids in transport and fractionation of uranium and thorium in magmatic processes. *Nature* 348, 531–533. <https://doi.org/10.1038/348531a0>.
- Lawlor, P.J., Ortega-Gutiérrez, F., Cameron, K.L., Ochoa-Camarillo, H., López, R., Sampson, D.E., 1999. U-Pb geochronology, geochemistry, and provenance of the Grenvillian Huiznopala gneiss of eastern Mexico. *Precambrian Res.* 94, 73–99. [https://doi.org/10.1016/S0301-9268\(98\)00108-9](https://doi.org/10.1016/S0301-9268(98)00108-9).
- Li, Z.X., Bogdanova, S.V., Collins, A.S., Davidson, A., De Waele, B., Ernst, R.E., Fitzsimons, I.C.W., Fuck, R.A., Gladkochub, D.P., Jacobs, J., Karlstrom, K.E., Lu, S., Natapov, L.M., Pease, V., Pisarevsky, S.A., Thrane, K., Vernikovsky, V., 2008. Assembly, configuration, and break-up history of Rodinia: a synthesis. *Precambrian Res.* 160, 179–210. <https://doi.org/10.1016/j.precamres.2007.04.021>.
- Lozano-Santa Cruz, R., Bernal, J.P., 2005. Characterization of a new set of eight geochemical reference materials for XRF major and trace element analysis. *Rev. Mex. Ciencias Geol.* 22, 329–344.
- Maldonado, R., Ortega-Gutiérrez, F., Ortiz-Joya, G.A., 2018. Subduction of Proterozoic to Late Triassic continental basement in the Guatemala suture zone: a petrological and geochronological study of high-pressure metagranitoids from the Chuacús complex. *Lithos* 308, 83–108. <https://doi.org/10.1016/j.lithos.2018.02.030>.
- Martini, M., Ortega-Gutiérrez, F., 2016. Tectono-stratigraphic evolution of eastern Mexico during the break-up of Pangea: a review. *Earth Sci. Rev.* 183, 38–55. <https://doi.org/10.1016/j.earscirev.2016.06.013>.
- McDonough, W., Sun, S., 1995. The composition of the Earth. *Chem. Geol.* 120 (3), 223–253. [https://doi.org/10.1016/0009-2541\(94\)00140-4](https://doi.org/10.1016/0009-2541(94)00140-4).
- Merdith, A.S., Collins, A.S., Williams, S.E., Pisarevsky, S., Foden, J.D., Archibald, D.B., Blades, M.L., Alessio, B.L., Armistead, S., Plavsa, D., 2017. A full-plate global reconstruction of the Neoproterozoic. *Gondwana Res.* 50, 84–134. <https://doi.org/10.1016/j.jgr.2017.04.001>.
- Mori, L., Gómez-Tuena, A., Cai, Y., Goldstein, S.L., 2007. Effects of prolonged flat subduction on the miocene magmatic record of the central trans-Mexican volcanic belt. *Chem. Geol.* 244, 452–473. <https://doi.org/10.1016/j.chemgeo.2007.07.002>.
- Moyen, J.F., 2011. The composite Archaean grey gneisses: petrological significance, and evidence for a non-unique tectonic setting for Archaean crustal growth. *Lithos* 123 (1–4), 21–36. <https://doi.org/10.1016/j.lithos.2010.09.015>.
- Moyen, J.F., Martin, H., 2012. Forty years of TTG research. *Lithos* 148, 312–336. <https://doi.org/10.1016/j.lithos.2012.06.010>.
- Nehring, F., Foley, S.F., Hołtta, P., Van den Kerkhof, A.M., 2009. Internal differentiation of the Archaean continental crust: fluid-controlled partial melting of granulites and TTG-amphibolite associations in central Finland. *J. Petrol.* 50 (1), 3–35. <https://doi.org/10.1093/petrology/egn070>.
- Ortega-Gutiérrez, F., 1981. Metamorphic belts of southern Mexico and their tectonic significance. *Geofisc. Int.* 20 (3), 177–202. <http://www.revistas.unam.mx/index.php/geofisica/article/view/39229>.
- Ortega-Gutiérrez, F., 1984. Evidence of Precambrian evaporites in the Oaxacan granulite complex of southern Mexico. *Precambrian Res.* 23 (3–4), 377–393. [https://doi.org/10.1016/0301-9268\(84\)90051-2](https://doi.org/10.1016/0301-9268(84)90051-2).
- Ortega-Gutiérrez, F., Ruiz, J., Centeno-García, E., 1995. Oaxaquia, a Proterozoic microcontinent accreted to North America during the late Paleozoic. *Geology* 23, 1127–1130. doi: 10.1130/0091-7613(1995)023<1127:OAPMAT>2.3.CO;2.
- Ortega-Gutiérrez, F., Elías-Herrera, M., Morañ-Zenteno, D.J., Solari, L., Weber, B., Luna-González, L., 2018. The pre-Mesozoic metamorphic basement of Mexico, 1.5 billion years of crustal evolution. *Earth Sci. Rev.* 183, 2–37. <https://doi.org/10.1016/j.earscirev.2018.03.006>.
- Paton, C., Hellstrom, J., Paul, B., Woodhead, J., Hergt, J., 2011. Lolite: freeware for the visualisation and processing of mass spectrometric data. *J. Anal. At. Spectrom.* 26, 2508–2518. <https://doi.org/10.1039/C1JA10172B>.
- Pearce, J.A., Alabaster, T., Shelton, A.W., Searle, M.P., 1981. The Oman ophiolite as a Cretaceous arc-basin complex: evidence and implications. *Phil. Trans. Roy. Soc. Lond.* 300 (1454), 1454.
- Pearce, J.A., 1996. A user's guide to basalt discrimination diagrams. In: Wyman, D.A. (Ed.), *Trace Element Geochemistry of Volcanic Rocks: Applications for Massive Sulphide Exploration*, vol. 12. Geological Association of Canada, Short Course Notes, pp. 79–113.
- Petrus, J.A., Kamber, B.S., 2012. VizualAge: a novel approach to laser ablation ICP-MS U-Pb geochronology data reduction. *Geostand. Geoanal. Res.* 36 (3), 247–270. <https://doi.org/10.1111/j.1751-908X.2012.00158.x>.
- Pindell, P., Villagoñe, D., Molina-Garza, R., Graham, R., Weber, B., 2021. A revised synthesis of the rift and drift history of the Gulf of Mexico and surrounding regions in the light of improved age dating of the Middle Jurassic salt. In: Davison, I., Hull, J.N.F., Pindell, J. (Eds.), *The Basins, Orogens and Evolution of the Southern Gulf of Mexico and Northern Caribbean*, vol. 504. Geological Society, London, Special Publications, pp. 29–76. <https://doi.org/10.1144/SP504-2020-43>.
- Rapp, R.P., Watson, E.B., Miller, C.F., 1991. Partial melting of amphibolite/eclogite and the origin of Archaean trondhjemites and tonalites. *Precambrian Res.* 51, 1–25. [https://doi.org/10.1016/0301-9268\(91\)90092-0](https://doi.org/10.1016/0301-9268(91)90092-0).
- Ratschbacher, L., Franz, L., Min, M., Bachmann, R., Martens, U., Stanek, K., Stübner, K., Nelson, B.K., Herrmann, U., Weber, B., López-Martínez, M., Jonckheere, R., Sperner, B., Tichomirowa, M., McWilliams, M.O., Gordon, M., Meschede, M.,

- Bock, P., 2009. The North American-Caribbean plate boundary in Mexico-Guatemala-Honduras. In: James, K.H., Lorente, M.A., Pindel, J.L. (Eds.), *The Origin and Evolution of the Caribbean Plate*, vol. 328. Geological Society, London, Special Publications, pp. 219–293. <https://doi.org/10.1144/SP328.11>.
- Ren-Xu, C., Yong-Fei, Z., Xie, L., 2010. Metamorphic growth and recrystallization of zircon: distinction by simultaneous in-situ analyses of trace-elements, U-Th-Pb and Lu-Hf isotopes in zircons from eclogite-facies rocks in the Sulu orogen. *Lithos* 114, 132–154. <https://doi.org/10.1016/j.lithos.2009.08.006>.
- Rollison, H., 1993. *Using Geochemical Data: Evaluation, Presentation, Interpretation*. Kingdom. Longman Group, UK.
- Rubatto, D., Gebauer, D., 2000. Use of cathodoluminescence for U-Pb zircon dating by ion microprobe: some examples from the western Alps. In: Pagel, M., Barbin, V., Blanc, P., Ohnenstetter, D. (Eds.), *Cathodoluminescence in Geosciences*. Springer, Berlin Heidelberg New York, pp. 373–400. https://doi.org/10.1007/978-3-662-04086-7_15.
- Rubatto, D., 2017. Zircon: the metamorphic mineral. *Rev. Mineral. Geochem.* 83 (1), 261–295. <https://doi.org/10.2138/rmg.2017.83.9>.
- Sawyer, E., 2008. *Atlas of Migmatites*, vol. 9. The Canadian Mineralogist, Special Publication. <https://doi.org/10.1139/9780660197876>.
- Sedlock, R.L., Ortega-Gutiérrez, F., Speed, R.C., 1993. Tectonostratigraphic terranes and tectonic evolution of Mexico. *Geol. Soc. Am. vol. 278*, 155. <https://doi.org/10.1130/SPE278>.
- Shao, T., Xia, Y., Ding, X., Cai, Y., Song, M., 2019. Zircon saturation in terrestrial basaltic melts and its geological implications. *Solid Earth Sci.* 4, 27–42. <https://doi.org/10.1016/j.sesci.2018.08.001>.
- Schwartz, J.J., John, B.E., Cheadle, M.J., Wooden, J.L., Mazdab, F., Swapp, S., Grimes, C. B., 2010. Dissolution-reprecipitation of igneous zircon in mid-ocean ridge gabbro, Atlantis Bank, Southwest Indian Ridge. *Chem. Geol.* 274, 68–81. <https://doi.org/10.1016/j.chemgeo.2010.03.017>.
- Slařma, J., Kořsler, J., Condon, D.J., Crowley, J.M., Gerdes, A., Hanchar, J.M., Horstwood, S.A., Morris, G.A., Nasdala, L., Norberg, N., Schaltegger, U., Schoene, B., Tubrett, M.N., Whitehouse, M.J., 2008. Pleistocene zircon – a new natural reference material for U-Pb and Hf isotopic microanalysis. *Chem. Geol.* 249, 1–35. <https://doi.org/10.1016/j.chemgeo.2007.11.005>.
- Solari, L.A., Ortega-Gutiérrez, F., Elías-Herrera, M., Gómez-Tuena, A., Schaaf, P., 2010. Refining the age of magmatism in the Altos Cuchumatanes, western Guatemala, by LA-ICPMS, and tectonic implications. *Int. Geol. Rev.* 52, 977–998. <https://doi.org/10.1080/00206810903216962>.
- Solari, L.A., Keppie, J.D., Ortega-Gutiérrez, F., Cameron, K.L., Lopez, R., Hames, W.E., 2003. 990 and 1100 Ma Grenvillian tectonothermal events in the northern Oaxacan Complex, southern Mexico: roots of an orogen. *Tectonophysics* 365, 257–282. [https://doi.org/10.1016/S0040-1951\(03\)00025-8](https://doi.org/10.1016/S0040-1951(03)00025-8).
- Solari, L.A., Keppie, J.D., Ortega-Gutiérrez, F., Cameron, K.L., Lopez, R., 2004. ~990 Ma peak granulitic metamorphism and amalgamation of Oaxaquia, Mexico: U-Pb zircon geochronological and common Pb isotopic data. *Rev. Mex. Ciencias Geol.* 21 (2), 212–225.
- Solari, L.A., Ortega-Gutiérrez, F., Elías-Herrera, M., Ortega-Obregón, C., Macías-Romo, C., 2014. Detrital provenance of the Grenvillian Oaxacan Complex, southern Mexico: a zircon perspective. *Int. J. Earth Sci.* 103 (5), 1301–1315. <https://doi.org/10.1007/s00531-013-0938-9>.
- Solari, L.A., Ortega-Obregón, C., Ortega-Gutiérrez, F., Elías-Herrera, M., 2020. Origin and evolution of the Grenvillian Oaxacan Complex, southern Mexico: Hf isotopic and U-Pb geochronologic constraints. In: Martens, U.C., Molina-Garza, M. (Eds.), *Southern and Central Mexico: Basement Framework, Tectonic Evolution, and Provenance of Mesozoic-Cenozoic Basins*, vol. 546. The Geological Society of America. [https://doi.org/10.1130/2020.2546\(03\)](https://doi.org/10.1130/2020.2546(03)).
- Spencer, C.J., Kirkland, C.L., Taylor, R.J.M., 2016. Strategies towards statistically robust interpretations of *in situ* U-Pb zircon geochronology. *Geosci. Front.* 7, 581–589. <https://doi.org/10.1016/j.gsf.2015.11.006>.
- Sun, S.S., McDonough, W.S., 1989. Chemical and isotopic systematics of oceanic basalts: implications for mantle composition and processes. Geological Society, London, Special Publications 42 (1), 313–345. <https://doi.org/10.1144/GSL.SP.1989.042.01.19>.
- Tohver, E., Teixeira, W., van der Pluijm, B., Geraldes, M.C., Beltencourt, J.S., Rizzotto, G., 2006. Restored transect across the exhumed Grenville orogen of Laurentia and Amazonia, with implications for crustal architecture. *Geology* 34 (8), 669–772. <https://doi.org/10.1130/G22534.1>.
- Tomaschek, F., Kennedy, A.K., Villa, I.M., Lagos, M., Ballhaus, C., 2003. Zircons from Syros, Cyclades, Greece. Recrystallization and mobilization of zircon during high-pressure metamorphism. *J. Petrol.* 44 (11), 1977–2002. <https://doi.org/10.1093/ptrology/egg067>.
- Van der Lelij, R., Spikings, R., Ulianov, A., Chiaradia, M., Mora, A., 2016. Palaeozoic to early Jurassic history of the northwestern corner of Gondwana, and implications for the evolution of the Iapetus, Rheic and Pacific oceans. *Gondwana Res.* 31, 271–294. <https://doi.org/10.1016/j.jgr.2015.01.011>.
- Valencia-Morales, Y.T., Weber, B., Tazzo-Rangel, M.D., González-Guzmán, R., Frei, D., Quintana-Delgado, J.A., Rivera-Moreno, E.N., 2022. Early Mesoproterozoic inliers in the Chiapas massif complex of southern Mexico: implications on Oaxaquia-Amazonia-Baltica configuration. *Precambrian Res.* 373, 106611. <https://doi.org/10.1016/j.precamres.2022.106611>.
- Vermeesch, P., 2018. Isoplot R: a free and open toolbox for geochronology. *Geosci. Front.* 9, 1479–1493. <https://doi.org/10.1016/j.gsf.2018.04.001>.
- Wann, X., Griffin, W.L., 2004. Unusual Hf contents in metamorphic zircon from coesite-bearing eclogites of the Dabie Mountains, east-central China: implications for the dating of ultrahigh-pressure metamorphism. *J. Metamorphic Geol.* 22, 629–637. <https://doi.org/10.1111/j.1525-1314.2004.00538.x>.
- Watson, E.B., Harrison, T.M., 1983. Zircon saturation revisited: temperature and composition effects in a variety of crustal magma types. *Earth Planet. Sci. Lett.* 64, 295–304. [https://doi.org/10.1016/0012-821X\(83\)90211-X](https://doi.org/10.1016/0012-821X(83)90211-X).
- Weber, B., Hecht, L., 2003. Petrology and geochemistry of metagneiss rocks from a Grenvillian basement fragment in the Maya block: the Guichicovi complex, Oaxaca, southern Mexico. *Precambrian Res.* 124, 41–67. [https://doi.org/10.1016/S0301-9268\(03\)00078-0](https://doi.org/10.1016/S0301-9268(03)00078-0).
- Weber, B., Köhler, H., 1999. Sm-Nd, Rb-Sr and U-Pb geochronology of a Grenville Terrane in southern Mexico: origin and geologic history of the Guichicovi Complex. *Precambrian Res.* 96, 245–262. [https://doi.org/10.1016/S0301-9268\(99\)00012-1](https://doi.org/10.1016/S0301-9268(99)00012-1).
- Weber, B., Schulze, C.H., 2014. Early Mesoproterozoic (>1.4 Ga) ages from granulite basement inliers of SE Mexico and their implications on the Oaxaquia concept – evidence from U-Pb and Lu-Hf isotopes on zircon. *Rev. Mex. Ciencias Geol.* 31, 377–394.
- Weber, B., Scherer, E.E., Schulze, C., Valencia, V.A., Montecinos, P., Mezger, K., Ruiz, J., 2010. U-Pb and Lu-Hf isotope systematics of lower crust from central-southern Mexico – geodynamic significance of Oaxaquia in a Rodinia Realm. *Precambrian Res.* 182, 149–162. <https://doi.org/10.1016/j.precamres.2010.07.007>.
- Weber, B., González-Guzmán, R., Manjarrez-Juárez, R., Cisneros de León, A., Martens, U., Solari, L., Hecht, L., Valencia, V., 2018. Late Mesoproterozoic to early Paleozoic history of metamorphic basement from the southeastern Chiapas massif complex, Mexico, and implications for the evolution of NW Gondwana. *Lithos* 300–301, 177–199. <https://doi.org/10.1016/j.lithos.2017.12.009>.
- Weber, B., Schmitt, A.K., Cisneros de León, A., González-Guzmán, R., Gerdes, A., 2020. Neoproterozoic extension and the central Iapetus magmatic province in southern Mexico – new U-Pb ages, Hf-O isotopes and trace element data of zircon from the Chiapas massif complex. *Gondwana Res.* 88, 1–20. <https://doi.org/10.1016/j.jgr.2020.06.022>.
- Wiedenbeck, M., Allé, P., Corfu, F., Griffin, W.L., Meier, M., Oberli, F., Von Quadt, A., Roddick, J.C., Spiegel, W., 1995. Three natural zircon standards for U-Th-Pb, Lu-Hf, trace element and REE analyses. *Geostand. Newsl.* 19, 1–23. <https://doi.org/10.1111/j.1751-908X.1995.tb00147.x>.
- Zhong, S., Li, S., Seltmann, R., Lai, Z., Zhou, J., 2021. The influence of fractionation of REE-enriched minerals on the zircon partition coefficients. *Geosci. Front.* 12, 101094. <https://doi.org/10.1016/j.gsf.2020.10.002>.

5. DISCUSIÓN Y CONCLUSIONES

El Complejo Sierra de Juárez (CSJ) en el sur de México, contiene un registro muy extenso de la historia geológica de México desde el Mesoproterozoico tardío hasta el Cenozoico. Las relaciones de campo, así como los datos geocronológicos y geoquímicos obtenidos en este trabajo documentan por primera vez que la estratigrafía del CSJ está construida por múltiples etapas orogénicas y extensionales constituidas por episodios magmáticos, sedimentarios y metamórficos. Con el objetivo de plantear un ordenamiento cronológico de dichos eventos, se clasifican dentro de tres periodos geodinámicos, cada uno de ellos se corresponde al Mesoproterozoico tardío-Neoproterozoico temprano, Paleozoico y Mesozoico. El primer periodo está delimitado aproximadamente entre 1080 y 930 Ma y contiene registros de magmatismo de arco durante el Esténico tardío, antes de la formación final de Rodinia, y metamorfismo y anatexis durante el Tónico temprano, poco después de la formación de Rodinia. El segundo periodo transcurre entre el inicio de la formación del Océano Rheico, en los dominios del NW de Gondwana, y termina con eventos tectónicos ocurridos dentro de un ambiente de formación de Pangea, aproximadamente entre 460 y 240 Ma. El último periodo inicia con la fragmentación de Pangea y se extiende durante la formación y evolución de México peninsular entre 240 y 130 Ma.

5.1. Periodo precámbrico

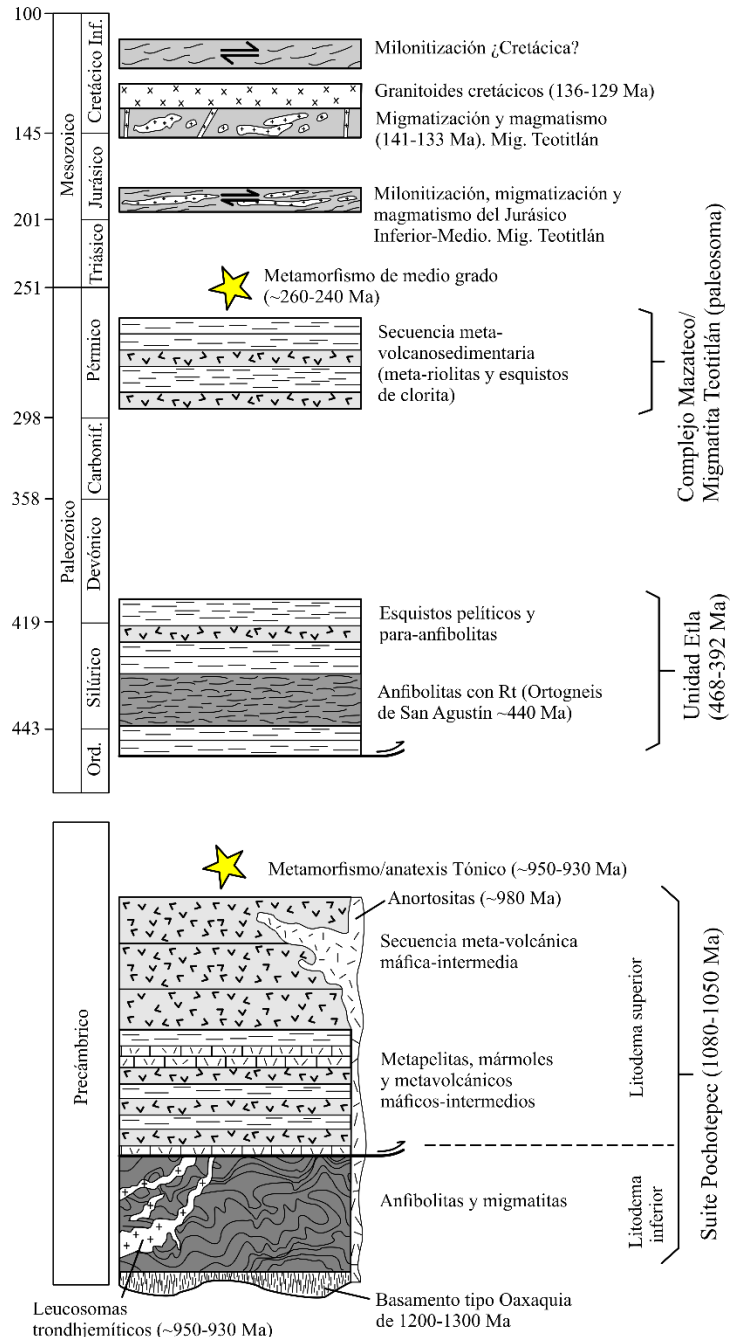
5.1.1. Magmatismo del Esténico tardío y la suite Pochotepec

La unidad más antigua documentada en el CSJ corresponde a la denominada suite Pochotepec (SP; Fig. 2), la cual fue concebida originalmente como Cretácica (Ángeles-Moreno et al., 2012). Esta unidad metamórfica de origen volcanosedimentario consta de un litodema supracortical compuesto por meta-andesitas y meta-basaltos, en algunos casos intercalados con esquistos pelíticos y mármoles y por un litodema metaplutónico intermedio-máfico compuesto por gneises y migmatitas. La SP representa la base estratigráfica del CSJ, y por su edad, es correlacionable con otros bloques de basamento precámbricos en el sur de México como el Complejo Oaxaqueño. La edad magmática de sus protolitos (Esténico tardío, entre 1080-1050 Ma) es crucial en el contexto geológico regional del sur de México y de la evolución geodinámica de Amazonia durante la formación de Rodinia. Las evidencias geoquímicas y geocronológicas documentadas en este trabajo indican que este evento magmático ocurrió en un entorno tectónico de arco continental a lo largo de una corteza tipo Oaxaquia (~1300-1250 Ma), lo cual confirma la presencia de un sistema de subducción en el margen de avance de Amazonia previo a la consolidación de Rodinia. Este es un hecho valioso que contribuye sustancialmente a la reconstrucción paleo-tectónica de la formación de Rodinia durante el Mesoproterozoico tardío.

5.1.2. Metamorfismo y anatexis del Tónico inferior entre ~950-930 Ma

Las observaciones de campo y datos geocronológicos obtenidos en este trabajo documentan la presencia de un evento metamórfico y anatéctico en la suite Pochotepec ocurrido entre ~950-930 Ma. En los últimos años ha incrementado el reconocimiento de este evento termotectónico en provincias precámbricas del sur de México (Complejo Macizo de Chiapas, Cisneros de León et al., 2017; Weber et al., 2018; Valencia-Morales et al., 2022). Debido a su escasa extensión, identificarlo

Fig. 2. Columna estratigráfica que ilustra las unidades litológicas y eventos tectónicos documentados en este trabajo en el Complejo Sierra de Juárez.



es crucial en la reconstrucción paleogeográfica y correlación de estas provincias geológicas dentro de Rodinia. Este evento tectónico parece tener una fuerte presencia en las provincias que se localizan al este de las estructuras miloníticas del CSJ (excluyendo al Complejo Guichicovi); mientras que en dominios precámbricos granulíticos (tipo Grenville) como en el Complejo Guichicovi o el Complejo Novillo se ha identificado escasamente (Keppie et al., 2006; Weber y Köhler, 1999). La presencia de pegmatitas en el Complejo Oaxaqueño con edades entre ~963-981 Ma (p. ej., Shchepetilnikova et al., 2015), producto del colapso orogénico de la Orogenia Zapoteca, no parecen estar relacionados al evento de 950-930 Ma debido a que las edades no se traslapan. Otra distinción notable es que las provincias con fuerte presencia de metamorfismo de ~950-930 Ma carecen a su vez, de evidencias petrológicas o geocronológicas indicativas de haber registrado la Orogenia Zapoteca, relacionada al ensamble de Rodinia, ocurrida en condiciones metamórficas en facies de granulita hace 990 Ma. Algunos autores (e. ej., Weber et al., 2018; Valencia-Morales, 2022) sugieren una fuerte retrogresión metamórfica como causa de la ausencia de dichas condiciones en el Complejo Macizo de Chiapas. Sin embargo, las condiciones metamórficas de grado bajo del litodema superior de la suite Pochotepec permite sugerir fuertemente que el sector precámbrico del CSJ y probablemente también el Macizo de Chiapas, no estuvieron sujetos a la Orogenia Zapoteca durante la formación de Rodinia. Derivado de esto, se propone considerar al sector precámbrico del sur de México localizado al este de las estructuras miloníticas del CSJ (excepto el Complejo Guichicovi) como una provincia precámbrica no granulítica (y por lo tanto, no grenvilliana), posiblemente originado dentro del mismo entorno tectónico del bloque considerado como Oaxaquia, pero con una evolución termotectónica neoproterozoica diferente. Se propone el término “Oaxaquia oriental” para referirse a estas provincias no granulíticas. La posición del Complejo Guichicovi entre el Terreno Cuicateco (y por lo tanto el CSJ) y el terreno Maya (Complejo Macizo de Chiapas) sugiere que sufrió un desplazamiento desde una posición originalmente en el norte (posiblemente cercana al Complejo Novillo) hasta su posición actual, debido a desplazamientos tectónicos laterales complejos, posiblemente jurásicos, y asociados a la apertura del Golfo de México durante la ruptura de Pangea.

5.2. *Periodo paleozoico*

5.2.1. *Magmatismo y sedimentación del Ordovícico al Silúrico*

En este trabajo se ha documentado únicamente en el sur del CSJ la presencia de ortogneises máficos (Ortogneis de San Agustín), cuyo protolito posee una edad de ~440 Ma y una composición tipo MORB, aunque su alcance podría extenderse hacia el norte. Asociado a este magmatismo Ordovícico, se ha identificado una amplia, aunque discontinua, presencia de rocas meta-sedimentarias (esquistos pelíticos y para-anfibolitas) de grado bajo a medio. La relación entre las rocas metasedimentarias con el Ortogneis de San Agustín se sustenta principalmente en relaciones espaciales y en la similitud entre las edades máximas de depósito de los protolitos sedimentarios y la edad del protolito del Ortogneis (468-392 Ma). A esta secuencia coherente de rocas se le denomina en este trabajo como Unidad Etlá. Esta correlación permite asumir un sistema tectónico extensional conformado por una cuenca, o un sistema de cuencas con desarrollo de corteza oceánica. Con base en la presencia de rocas de basamento Precámbrico asociado a una corteza tipo Oaxaquia (suite Pochotepec) y a las edades de proveniencia detrítica (zircón), se infiere que este evento ocurrió en el sector NW de Gondwana. Tanto la paleo-posición, como las características

tectónicas interpretadas para la Unidad Etna son consistentes con un sistema tectónico más amplio asociado al origen del Océano Rheico, del cual se derivan sistemas transtensionales a lo largo del borde NW de Gondwana (p. ej., [Solarí et al., 2010](#)).

5.2.2. *Magmatismo y sedimentación del Pérmico temprano*

La presencia de secuencias meta-volcanosedimentarias (Unidad Mazatlán de las Flores, Complejo Mazateco) con edad de protolito magmático de ~292 Ma (meta-riolita) y el reconocimiento de paragneises de grado medio (paleosoma de la Migmatita Teotitlán) con edad máxima de depósito de ~281 Ma, permiten asumir la existencia de eventos volcano-sedimentarios durante el Pérmico temprano en el CSJ. Aunque la mayor parte de esta secuencia se extiende dentro del Complejo Mazateco, en menor medida también forma parte del sector norte del CSJ, lo que implica que ambos complejos mantienen cierta relación genética. Únicamente basado en la edad magmática de la Unidad Mazatlán de las Flores, este evento se asocia a la etapa de magmatismo de arco que ocurrió durante la conformación de Pangea en su sector occidental y mantiene una amplia correlación con rocas de la misma edad en el este y sur de México, así como en Centroamérica (Figs. 3 y 4).

5.2.3. *Metamorfismo del Pérmico tardío-Triásico Inferior*

El espectro amplio de rocas metamórficas de grado bajo a medio que conforma al CSJ con protolitos post-proterozoicos es indicativo de un evento metamórfico ampliamente extendido que posfecha al metamorfismo tónico de la suite Pochotepec. La litología relacionada a este evento incluye anfibolitas con o sin rutilo, esquistos pelíticos con o sin granate y paragneises de biotita y granate. Este conjunto de litologías están incluidos en la Unidad Etna (Ortogneis de San Agustín e intercalaciones de esquistos pelíticos y para-anfibolitas), el Esquisto de la Nopalera (esquisto pelítico de granate con turmalina), la secuencia meta-volcanosedimentaria de grado bajo del Complejo Mazateco y los paleosomas del Complejo Migmatítico Teotitlán (paragneises y anfibolitas). La edad de este evento ha sido aproximada a partir de sobrecrecimientos metamórficos en granos de zircón de un paragneis de Bt + Gr interpretado como un paleosoma del Complejo Migmatítico Teotitlán. El resultado indica una edad de ~246 Ma. Sin embargo, el alto contenido de HREE en los bordes metamórficos de zircón (principalmente de Yb y Lu) sugieren que no cristalizaron en equilibrio con granate, por lo tanto, esta edad posiblemente posfecha el pico metamórfico y debe ser considerada como una edad mínima. La edad máxima se obtuvo a partir de las edades de zircón detrítico más jóvenes en la misma muestra (~281 Ma), por lo que la edad metamórfica se constriñe entre ~281-246 Ma. El origen tectónico de este evento puede ser debatible, lo que está claro es que ocurrió después del ensamble final de Pangea occidental. Tal como lo proponen algunos autores (p. ej., [Ratschbacher et al., 2009](#); [Cardona et al., 2010](#)), en este trabajo se sugiere que el origen del metamorfismo está relacionado con una dinámica compresiva, resultado de un cambio de ángulo en la placa de subducción, lo que condujo a un aplanamiento de la placa y engrosamiento de la corteza continental (Fig. 2). Este evento no parece haber perturbado las litologías que constituyen a la suite Pochotepec, por lo que se considera que esta última se comportó como un bloque rígido y relativamente alejado del núcleo orogénico permo-triásico. También se debe considerar los desplazamientos horizontales N-S que afectaron al CSJ durante el Jurásico y Cretácico, así como el

acortamiento tectónico E-W ocurrido al final del Periodo Cretácico y principios de la Era Cenozoica (Graham et al., 2021) como agentes estructurales que han puesto en contacto diferentes sectores corticales. Este evento está pobremente documentado en otros bloques de basamento; sin embargo, se aprecia una amplia correlación con el Complejo Macizo de Chiapas (sureste de México), Complejo Chuacús (Guatemala) y diferentes exposiciones de basamento en el NW de Sudamérica (Colombia y Venezuela).

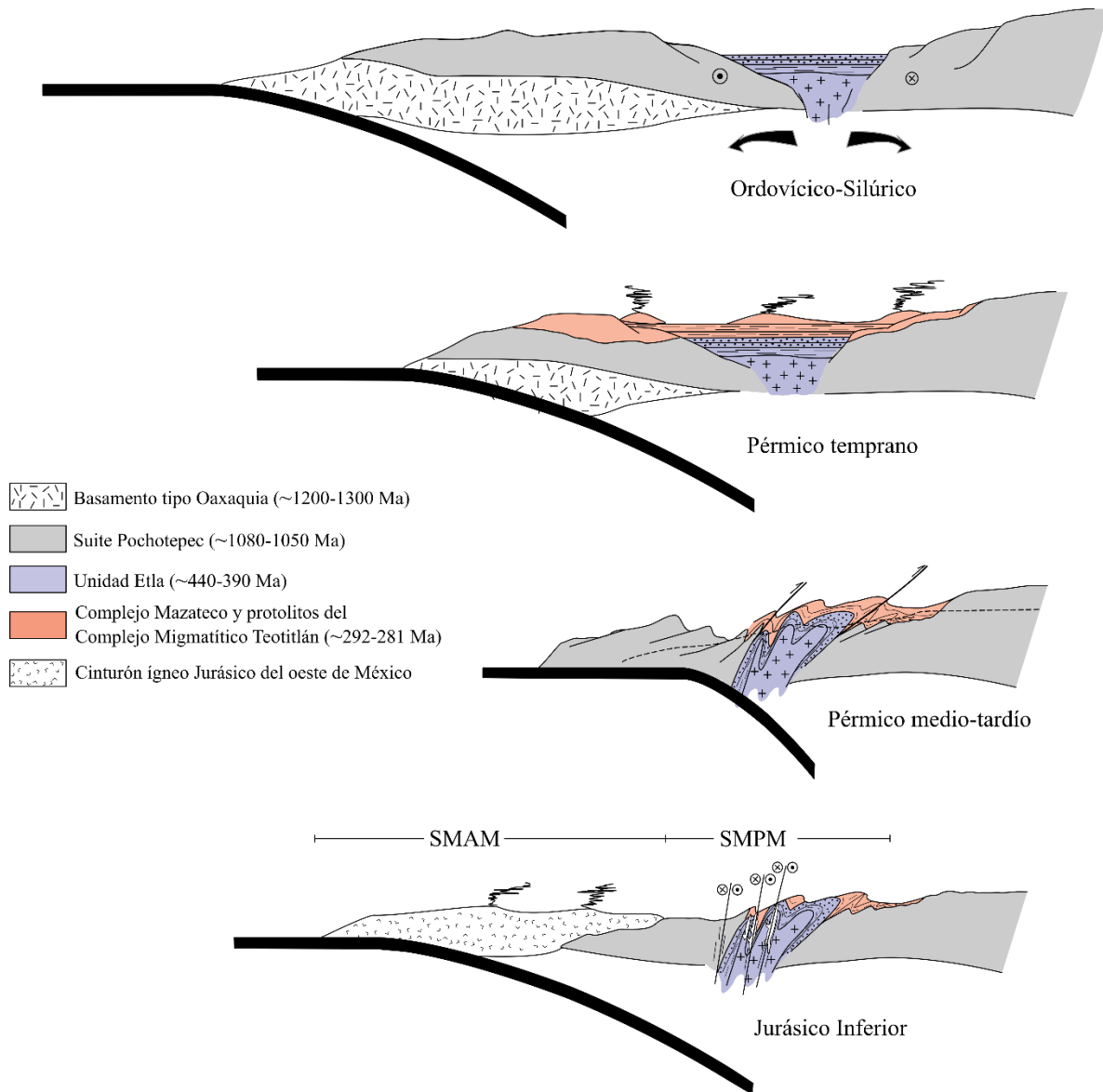


Fig. 3. Secciones esquemáticas que ilustran la evolución tectónica del Complejo Sierra de Juárez desde el Ordovícico al Jurásico inferior. SMAM, Sistema Mesozoico Atlántico de México; SMPM, Sistema Mesozoico del Pacífico de México.

5.3. Periodo mesozoico

5.3.1. Milonitización, anatexis y magmatismo del Jurásico Inferior

Este es un evento en donde participan aspectos estructurales de deformación milonítica, producción de fundidos anatéticos y emplazamiento de magmas de composición intermedia. De acuerdo con observaciones de campo, del Complejo Migmatítico Teotitlán en el norte del CSJ está constituido por lo menos por dos familias de estructuras anatéticas. La primera contiene estructuras tipo Schlieren en donde coexisten armónicamente flujos de fundido anatético y estructuras miloníticas de carácter lateral derecho orientadas ~N-S. La edad de este evento se data en ~176 Ma (Jurásico Inferior) mediante un segundo conjunto de sobrecrecimientos de zircón metamórfico en un paragneis de Grt+Bt considerado como un paleosoma. También se identificó y dató un cuerpo de anfibolita no milonítico embebido dentro del Complejo Migmatítico Teotitlán. La edad de protolito magmático obtenida fue de ~175 Ma, por lo que se asume que, de manera simultánea, tomaron lugar episodios magmáticos, anatéticos y miloníticos en el norte del CSJ. Por otra parte, en el sur del CSJ se documentó la presencia de bandas proto-miloníticas de composición félsica emplazadas dentro de planos miloníticos de carácter lateral derecho, orientados ~N-S, en anfibolitas de la Unidad Etlá. No se descarta que estas bandas leucocráticas se hayan formado por procesos anatéticos *in-situ* derivados de las anfibolitas de la Unidad Etlá. Debido a su disposición estructural, se asumen sintectónicos a la deformación de la roca encajonante. Su edad fue obtenida mediante U-Pb en zircón, arrojando una edad de ~191 Ma (Fig. 3). Las características estructurales de las migmatitas con texturas Schlieren del Complejo Migmatítico Teotitlán en el norte del CSJ y de las anfibolitas miloníticas de la Unidad Etlá en el sur del CSJ son similares, aunque su actividad tectónica parece haber ocurrido con ~15 Ma de diferencia. Con base en las características de deformación y edades, se considera que el CSJ estuvo sujeto a esfuerzos tectónicos en un sistema transformante asociados a la apertura del Golfo de México durante la ruptura de Pangea, como fue sugerido originalmente por [Alaniz-Álvarez et al. \(1994; 1996\)](#). Se especula que este evento haya ocurrido a través de múltiples pulsos y reactivaciones durante el Jurásico Inferior y posiblemente hasta el Jurásico Medio. En el modelo de actividad magmática en México durante el Jurásico, sugerido por [Martini y Ortega-Gutiérrez \(2016\)](#), este evento registrado en el CSJ corresponde al sector magmático oriental o MASM (Mesozoic Atlantic System of Mexico). La segunda familia de estructuras migmatíticas del Complejo Migmatítico Teotitlán posfecha este evento y se aborda en la siguiente sección.

5.3.2. Migmatización y magmatismo del Cretácico Temprano

La última etapa documentada en el CSJ dentro del ciclo Mesozoico incluye la segunda familia de estructuras de fusión parcial observadas en el Complejo Migmatítico Teotitlán, las cuáles se distinguen por carecer de una orientación u ordenamiento restringido por esfuerzos dirigidos. El resultado son estructuras nebulíticas. Estas estructuras están acompañadas por la presencia de diques de composición félsica, los cuáles fueron datados entre ~141-133 Ma ([Ángeles-Moreno et al., 2012](#); [Coombs, 2016](#)). Basado en el tipo de estructuras y edad, se asume que este evento anatético no sólo es posterior al del evento

Jurásico Inferior, sino que posiblemente tiene un origen tectónico distinto. Adicionalmente, se documentó la presencia de cuerpos intrusivos de composición granítica-tonalítica emplazados principalmente en la suite Pochotepec precámbrica y esquistos de grado bajo del Complejo Mazateco. Estos cuerpos poseen evidencias de una deformación milonítica fuerte. La edad obtenida de estas rocas indica una etapa de emplazamiento entre ~136-129 Ma, edad que también indica la edad mínima para este evento milonítico registrado en el CSJ. El origen tectónico del episodio magmático/anatóctico del Cretácico Inferior se asocia a la subducción de la placa oceánica relacionada con la cuenca de Arperos, o en su defecto a la placa del paleo-Pacífico. Un probable cambio de ángulo podría haber originado una migración del magmatismo del Cretácico Inferior desde el oriente hacia el occidente de México y haber ocasionado un sistema extensional en la corteza continental que dio origen a la Formación Chivillas en el Terreno Cuicateco, entre otras (p. ej., [Coombs, 2016](#)).

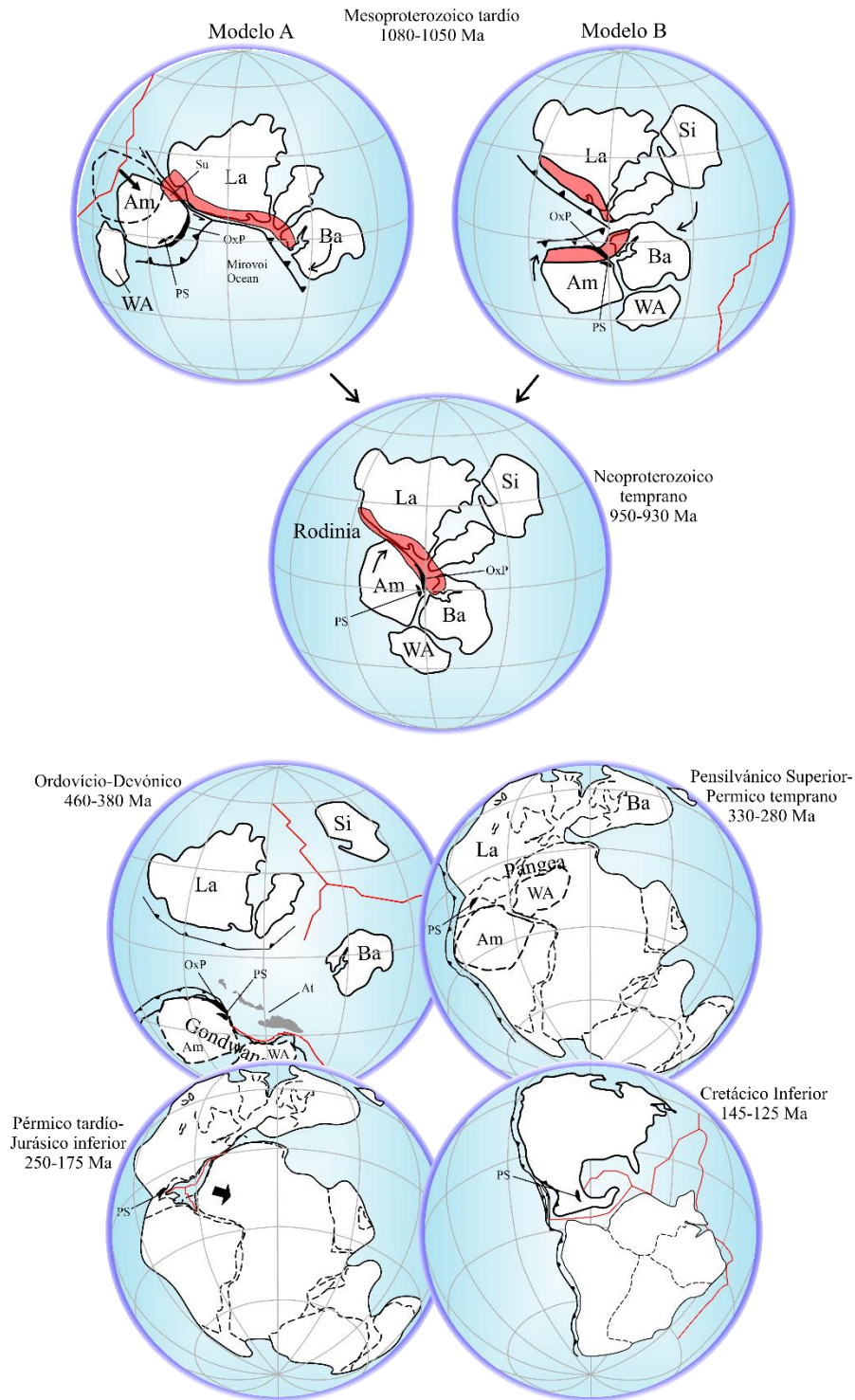


Fig. 4. Reconstrucciones paleogeográficas que ilustran la evolución continental desde el Mesoproterozoico al Cretácico y la posición de la suite Pochotepec (o Complejo Sierra de Juárez). Abreviaturas: La, Laurencia; Ba, Báltica; Am, Amazonia; PS, suite Pochotepec; Wa, África occidental; Si, Siberia; OxP, Oaxaquia-Putumayo; At, terrenos avalonianos. Modelo de Rodinia A después de [Johansson \(2009\)](#); modelo B después de [Cawood y Pisarevsky \(2017\)](#).

5.4. Referencias

- Alaniz-Álvarez, S.A., Nieto-Samaniego, A.F., Ortega-Gutiérrez, F., 1994. Structural evolution of the Sierra Juárez Mylonitic Complex, state of Oaxaca, Mexico. *Revista Mexicana de Ciencias geológicas*, 11(2), 147–156.
- Alaniz-Álvarez, S.A., van der Heyden, P., Nieto-Samaniego, A.F., Ortega-Gutiérrez, F., 1996. Radiometric and kinematic evidence for Middle Jurassic strike-slip faulting in Southern Mexico related to the opening of the Gulf of Mexico. *Geology*, 24(5), 443–446, doi: [10.1130/0091-7613\(1996\)024<0443:RAKEFM>2.3.CO;2](https://doi.org/10.1130/0091-7613(1996)024<0443:RAKEFM>2.3.CO;2).
- Ángeles-Moreno, E., Elías-Herrera, M., Macías-Romo, C., Sánchez-Zavala, J.L., Ortega-Gutiérrez, F., 2012. Geological Map of the Western Border of the Cuicateco Terrane, Southern Mexico, Geological Society of America, Map and Chart series, MCH102.
- Cardona, A., Valencia, V., Garzón, A., Montes, C., Ojeda, G., Ruiz, J. and Weber, M. 2010. Permian to Triassic I to S-type magmatic switch in the northeast Sierra Nevada de Santa Marta and adjacent regions, Colombian Caribbean: Tectonic setting and implications within Pangea paleogeography. *Journal of South American Earth Sciences*, 29, 772–783, doi: [10.1016/j.jsames.2009.12.005](https://doi.org/10.1016/j.jsames.2009.12.005).
- Cawood, P.A., Pisarevsky, S.A., 2017. Laurentia-Baltica-Azononia relations during Rodinia assembly. *Precambrian Research*. 292, 386–397, <https://doi.org/10.1016/j.precamres.2017.01.031>.
- Cisneros de León, A., Weber, B., Ortega-Gutiérrez, F., González-Guzmán, R., Maldonado, R., Solari, L., Schaaf, P., Manjarrez-Juárez, R., 2017. Grenvillian massif- type anorthosite suite in Chiapas, Mexico: magmatic to polymetamorphic evolution of anorthosites and their Ti-Fe ores. *Precambrian Research*, 195, 203–226, doi: [10.1016/j.precamres.2017.04.028](https://doi.org/10.1016/j.precamres.2017.04.028).
- Coombs, H. 2016. Geochemical and geochronological constraints on terrane definition in Mexico. Cardiff University, tesis de doctorado.
- Graham, R., Pindell, J., Villagómez, D., Molina-Garza, R., Granath, J. and Sierra-Rojas, M. 2021. Integrated Cretaceous–Cenozoic plate tectonics and structural Geology in southern Mexico. Geological Society, London, Special Publications, 504, 285–314, doi: [10.1144/SP504-1020-70](https://doi.org/10.1144/SP504-1020-70).
- Johansson, Å., 2009. Baltica, Amazonia and the SAMBA connection– 1000 million years of neighborhood during the Proterozoic? *Precambrian Research*. 175, 221–234. <https://doi.org/10.1016/j.precamres.2009.09.011>.
- Keppie, J.D., Dostal, J., Nance, D., Miller, B.V., Ortega-Rivera, A., Lee, J.K.W., 2006. Circa 546 Ma plume-related dykes in the ~1 Ga Novillo gneiss (east-central Mexico): evidence for the initial separation of Avalonia. *Precambrian Research*, 147, 342–353, doi: [10.1016/j.precamres.2006.01.020](https://doi.org/10.1016/j.precamres.2006.01.020).
- Maldonado, R., Ortega-Gutiérrez, F., Ortíz-Joya, G.A., 2018. Subduction of Proterozoic to Late Triassic continental basement in the Guatemala suture zone: a petrological and geochronological study of high-pressure metagranitoids from the Chuacús complex. *Lithos*, 308, 83–108, doi: [10.1016/j.lithos.2018.02.030](https://doi.org/10.1016/j.lithos.2018.02.030).
- Martini, M. and Ortega-Gutiérrez, F. 2016. Tectonostratigraphic evolution of eastern Mexico during the break-up of Pangea: a review. *Earth-Science Reviews*, 183, 38–55, doi: [10.1016/j.earscirev.2016.06.013](https://doi.org/10.1016/j.earscirev.2016.06.013).

- Ratschbacher, L., Franz, L. et al. 2009. The North American–Caribbean plate boundary in Mexico–Guatemala–Honduras. Geological Society, London, Special Publications, 328, 219–293, doi: [10.1144/SP328.11](https://doi.org/10.1144/SP328.11).
- Shchepetilnikova, V., Solé, J., Solari, L., Abdullin, F., 2015. A chronological and chemical zircon study of some pegmatite dikes and lenses from the central part (Ayoquezco-Ejutla) of the Oaxacan Complex, southern Mexico. *Revista Mexicana de Ciencias Geológicas*, 32(1), 123-143.
- Solari, L.A., Ortega-Gutiérrez, F., Elías-Herrera, M., Gómez-Tuena, A., Schaaf, P., 2010. Refining the age of magmatism in the Altos Cuchumatanes, western Guatemala, by LA-ICPMS, and tectonic implications. *International Geology Review*, 52, 977–998, doi: [10.1080/00206810903216962](https://doi.org/10.1080/00206810903216962).
- Valencia-Morales, Y.T., Weber, B., Tazzo-Rangel, M.D., González-Guzmán, R., Frei, D., Quintana-Delgado, J.A., Rivera-Moreno, E.N., 2022. Early mesoproterozoic inliers in the Chiapas massif complex of southern Mexico: implications on Oaxaquia–Amazonia–Baltica configuration. *Precambrian Research*, 373, 106611, doi: [10.1016/j.precamres.2022.106611](https://doi.org/10.1016/j.precamres.2022.106611).
- Weber, B., González-Guzmán, R., Manjarrez-Juárez, R., Cisneros de León, A., Martens, U., Solari, L., Hecht, L., Valencia, V., 2018. Late mesoproterozoic to early paleozoic history of metamorphic basement from the southeastern Chiapas massif complex, Mexico, and implications for the evolution of NW Gondwana. *Lithos*, 300–301, 177–199, doi: [10.1016/j.lithos.2017.12.009](https://doi.org/10.1016/j.lithos.2017.12.009).
- Weber, B., Köhler, H., 1999. Sm–Nd, Rb–Sr and U–Pb geochronology of a Grenville Terrane in southern Mexico: origin and geologic history of the Guichicovi Complex. *Precambrian Research*, 96, 245–262, doi: [10.1016/S0301-9268\(99\)00012-1](https://doi.org/10.1016/S0301-9268(99)00012-1).

6. Anexos

6.1. Datos isotópicos de U-Pb en zircón

JG24 Meta-anortosita		Espejo-Bautista et al., 2021																
Zircón	U ppm	Th/U	Relaciones isotópicas corregidas							rho	Edades corregidas					Mejor edad		Discordancia %
			$\frac{Pb^{207}}{Pb^{206}}$	$\pm 2\sigma$	$\frac{Pb^{207}}{U^{235}}$	$\pm 2\sigma$	$\frac{Pb^{206}}{U^{238}}$	$\pm 2\sigma$	$\frac{Pb^{206}}{U^{238}}$		$\pm 2\sigma$	$\frac{Pb^{207}}{U^{235}}$	$\pm 2\sigma$	$\frac{Pb^{207}}{Pb^{206}}$	$\pm 2\sigma$	Ma	$\pm 2\sigma$	
Zircon_36	80	0.33	0.0720	0.0033	1.6144	0.2089	0.1630	0.0031	0.11	973.2	17.3	972.1	82.8	958.7	98.2	973.2	17.3	-1.5
Zircon_39	35	0.24	0.0730	0.0046	1.6997	0.2366	0.1663	0.0031	0.12	991.5	17.4	997.7	86.6	990.2	133.7	991.5	17.4	-0.1
Zircon_42	84	0.27	0.0723	0.0032	1.6545	0.2132	0.1665	0.0027	-0.03	992.6	15.0	986.9	82.2	960.9	95.9	992.6	15.0	-3.2
Zircon_43	201	0.21	0.0714	0.0026	1.6161	0.2042	0.1645	0.0026	0.06	981.9	14.8	974.4	78.5	953.3	76.4	981.9	14.8	-2.9
Zircon_44	82	0.30	0.0738	0.0033	1.6697	0.2140	0.1651	0.0029	-0.09	985.2	16.5	993.5	82.4	1004.1	96.4	985.2	16.5	1.8
Zircon_45	69	0.41	0.0726	0.0033	1.6562	0.2167	0.1659	0.0033	0.30	989.5	18.5	992.0	77.2	989.1	90.2	989.5	18.5	0.0
Zircon_46	62	0.51	0.0742	0.0039	1.6793	0.2186	0.1654	0.0032	-0.21	986.8	17.8	995.7	83.2	1000.6	111.9	986.8	17.8	1.3
Zircon_49	42	0.66	0.0734	0.0045	1.7065	0.2344	0.1664	0.0029	-0.12	992.1	16.4	1002.3	85.1	1015.5	131.4	992.1	16.4	2.3
Zircon_51	70	0.41	0.0757	0.0056	1.6612	0.2352	0.1595	0.0030	0.00	954.2	17.2	986.3	88.3	1034.1	152.2	954.2	17.2	7.7
Zircon_54	79	0.51	0.0718	0.0036	1.6138	0.2087	0.1631	0.0030	-0.21	974.2	17.0	972.4	81.6	950.5	107.1	974.2	17.0	-2.4
Zircon_56	57	0.48	0.0719	0.0044	1.6256	0.2157	0.1651	0.0032	-0.26	984.8	18.2	973.4	86.1	987.5	115.2	984.8	18.2	0.2
Zircon_58	75	0.45	0.0728	0.0036	1.6551	0.2143	0.1659	0.0032	-0.07	989.1	18.0	992.4	76.2	989.0	95.3	989.1	18.0	0.0
Zircon_59	75	0.27	0.0716	0.0039	1.6199	0.2128	0.1645	0.0035	-0.02	981.8	19.4	972.4	84.0	928.6	115.9	981.8	19.4	-5.7
Zircon_60	167	0.41	0.0712	0.0025	1.6190	0.2048	0.1647	0.0024	0.18	982.7	13.3	975.0	79.3	946.3	71.7	982.7	13.3	-3.8
Zircon_61	74	0.28	0.0711	0.0040	1.5742	0.2107	0.1603	0.0026	0.03	958.5	14.4	953.4	86.7	966.6	106.1	958.5	14.4	0.8
Zircon_62	105	0.32	0.0726	0.0035	1.6152	0.2106	0.1612	0.0027	0.10	963.7	15.2	971.1	82.1	966.4	101.4	963.7	15.2	0.2
Zircon_65	95	0.27	0.0754	0.0035	1.6960	0.2211	0.1624	0.0030	0.16	970.0	16.7	1003.5	81.5	1056.8	94.7	970.0	16.7	8.2
Zircon_66	97	0.32	0.0733	0.0031	1.6655	0.2143	0.1636	0.0025	0.19	976.7	14.1	992.1	83.4	999.3	90.3	976.7	14.1	2.2
Zircon_68	130	0.24	0.0705	0.0024	1.4921	0.1881	0.1533	0.0022	0.14	919.4	12.6	925.3	75.8	927.7	69.7	919.4	12.6	0.9
Zircon_69	92	0.21	0.0718	0.0056	1.4731	0.2061	0.1495	0.0037	-0.12	898.1	21.2	913.6	85.7	926.3	162.8	898.1	21.2	3.0
Zircon_75	35	0.50	0.0723	0.0048	1.6437	0.2253	0.1652	0.0043	0.08	985.3	23.9	978.2	88.5	975.2	130.6	985.3	23.9	-1.0
Zircon_76	22	0.56	0.0732	0.0063	1.6778	0.2491	0.1666	0.0050	0.18	993.0	27.6	987.6	96.2	1006.3	160.9	993.0	27.6	1.3

JG42 Meta-anortosita		Espejo-Bautista et al., 2021																
Zircón	U ppm	Th/U	Relaciones isotópicas corregidas						rho	Edades corregidas						Mejor edad		Discordancia %
			$\frac{Pb^{207}}{Pb^{206}}$	$\pm 2\sigma$	$\frac{Pb^{207}}{U^{235}}$	$\pm 2\sigma$	$\frac{Pb^{206}}{U^{238}}$	$\pm 2\sigma$		$\frac{Pb^{206}}{U^{238}}$	$\pm 2\sigma$	$\frac{Pb^{207}}{U^{235}}$	$\pm 2\sigma$	$\frac{Pb^{207}}{Pb^{206}}$	$\pm 2\sigma$	Ma	$\pm 2\sigma$	
Zircon_01	153	0.55	0.0707	0.0026	1.5910	0.2019	0.1628	0.0022	0.20	972.4	12.3	964.4	78.4	933.4	73.5	972.4	12.3	-4.1
Zircon_03	48	0.21	0.0768	0.0059	1.7044	0.2430	0.1607	0.0045	0.10	960.8	25.3	1002.6	87.4	1063.7	148.2	960.8	25.3	9.6
Zircon_04	18	0.39	0.0775	0.0086	1.7228	0.2859	0.1618	0.0055	0.17	966.5	30.7	999.3	106.6	1078.5	211.9	966.5	30.7	10.3
Zircon_05	55	0.57	0.0737	0.0038	1.7039	0.2225	0.1663	0.0039	-0.08	991.5	22.0	1005.7	82.4	1020.5	112.9	991.5	22.0	2.8
Zircon_06	68	0.17	0.0726	0.0029	1.6073	0.2093	0.1618	0.0043	0.39	966.6	24.3	975.0	74.2	1000.1	76.3	966.6	24.3	3.3
Zircon_07	152	0.45	0.0725	0.0026	1.6098	0.2047	0.1605	0.0027	0.27	959.3	15.1	971.0	79.2	981.5	74.1	959.3	15.1	2.2
Zircon_08	42	0.37	0.0770	0.0059	1.7089	0.2463	0.1609	0.0039	0.11	961.5	21.6	1003.9	93.6	1107.0	152.6	961.5	21.6	13.1
Zircon_09	98	0.65	0.0742	0.0031	1.7130	0.2204	0.1673	0.0026	0.14	997.2	14.8	1009.9	82.1	1023.9	86.2	997.2	14.8	2.6
Zircon_11	87	0.65	0.0730	0.0029	1.6542	0.2109	0.1648	0.0022	0.10	983.6	12.6	992.9	74.3	991.7	82.3	983.6	12.6	0.8
Zircon_12	51	0.35	0.0733	0.0041	1.6290	0.2156	0.1631	0.0037	0.25	973.9	21.0	984.5	94.1	982.7	120.5	973.9	21.0	0.8
Zircon_13	129	0.62	0.0729	0.0024	1.6460	0.2075	0.1639	0.0018	0.27	978.7	10.0	985.7	80.7	996.9	67.8	978.7	10.0	1.8
Zircon_14	27	0.34	0.0721	0.0053	1.5930	0.2237	0.1609	0.0040	0.06	961.6	22.5	956.1	87.2	946.7	142.5	961.6	22.5	-1.5
Zircon_15	30	0.51	0.0746	0.0060	1.7926	0.2554	0.1765	0.0061	0.02	1047.4	33.4	1043.0	85.9	1050.3	150.0	1047.4	33.4	0.2

JG50 Meta-anortosita		Espejo-Bautista et al., 2021																
Zircón	U ppm	Th/U	Relaciones isotópicas corregidas						rho	Edades corregidas						Mejor edad		Discordancia %
			$\frac{Pb^{207}}{Pb^{206}}$	$\pm 2\sigma$	$\frac{Pb^{207}}{U^{235}}$	$\pm 2\sigma$	$\frac{Pb^{206}}{U^{238}}$	$\pm 2\sigma$		$\frac{Pb^{206}}{U^{238}}$	$\pm 2\sigma$	$\frac{Pb^{207}}{U^{235}}$	$\pm 2\sigma$	$\frac{Pb^{207}}{Pb^{206}}$	$\pm 2\sigma$	Ma	$\pm 2\sigma$	
Zircon_17	28	0.71	0.0711	0.0084	1.5169	0.2721	0.1532	0.0054	0.45	919.0	30.6	920.5	110.3	926.6	238.5	919.0	30.6	0.8
Zircon_18	26	0.66	0.0744	0.0068	1.5997	0.2453	0.1553	0.0046	0.21	930.4	25.8	956.4	102.0	1129.4	157.7	930.4	25.8	17.6
Zircon_19	36	0.92	0.0753	0.0063	1.6725	0.2466	0.1583	0.0064	-0.03	946.9	36.1	987.4	89.7	1039.6	180.3	946.9	36.1	8.9
Zircon_20	23	0.65	0.0772	0.0061	1.7820	0.2561	0.1686	0.0049	0.04	1003.8	27.5	1026.0	94.1	1091.0	159.2	1003.8	27.5	7.9
Zircon_21	25	0.69	0.0757	0.0055	1.6978	0.2308	0.1645	0.0051	-0.15	981.6	28.6	1001.2	88.1	1024.8	151.8	981.6	28.6	4.2
Zircon_22	30	0.64	0.0729	0.0052	1.5576	0.2202	0.1561	0.0046	0.20	934.4	26.0	942.3	86.2	999.1	135.0	934.4	26.0	6.4
Zircon_24	38	0.55	0.0750	0.0053	1.6549	0.2255	0.1636	0.0059	0.22	976.5	33.1	996.5	97.2	1018.6	148.7	976.5	33.1	4.1
Zircon_25	30	0.57	0.0764	0.0066	1.9018	0.2890	0.1819	0.0064	0.28	1076.8	35.3	1067.0	105.0	1088.5	154.2	1076.8	35.3	1.0
Zircon_26	13	0.91	0.0751	0.0110	1.4915	0.2670	0.1482	0.0061	-0.14	890.1	34.1	894.7	117.5	1179.3	237.7	890.1	34.1	24.5
Zircon_28	31	0.59	0.0738	0.0067	1.5841	0.2215	0.1588	0.0061	-0.27	949.6	33.9	956.3	84.8	975.8	169.6	949.6	33.9	2.6
Zircon_29	33	0.54	0.0712	0.0072	1.3961	0.2227	0.1400	0.0054	-0.25	844.2	30.7	875.2	94.0	1057.0	213.3	844.2	30.7	20.1
Zircon_30	37	0.62	0.0689	0.0048	1.4457	0.2071	0.1504	0.0038	0.16	902.8	21.6	895.4	86.3	902.9	148.2	902.8	21.6	0.0
Zircon_31	23	0.86	0.0735	0.0087	1.5497	0.2508	0.1548	0.0059	-0.15	927.6	33.1	937.2	97.6	1012.7	214.8	927.6	33.1	8.3
Zircon_32	26	0.65	0.0728	0.0048	1.5360	0.2105	0.1550	0.0056	0.16	928.3	31.2	937.4	84.5	946.6	139.3	928.3	31.2	1.9
Zircon_33	127	0.46	0.0742	0.0029	1.8570	0.2382	0.1817	0.0027	0.32	1076.5	15.1	1062.7	84.6	1027.8	82.0	1076.5	15.1	-4.7
Zircon_34	35	0.47	0.0715	0.0042	1.4518	0.1917	0.1495	0.0048	0.06	897.6	27.3	905.7	80.9	924.0	121.8	897.6	27.3	2.8
Zircon_48	38	0.53	0.0748	0.0055	1.6113	0.2178	0.1585	0.0043	-0.34	948.5	24.3	969.5	84.9	1043.6	169.5	948.5	24.3	9.1

JG55 Ortogneis de San Agustín		Espejo-Bautista et al., 2021																
Zircón	U ppm	Th/U	Relaciones isotópicas corregidas							rho	Edades corregidas					Mejor edad		Discordancia %
			$\frac{Pb^{207}}{Pb^{206}}$	$\pm 2\sigma$	$\frac{Pb^{207}}{U^{235}}$	$\pm 2\sigma$	$\frac{Pb^{206}}{U^{238}}$	$\pm 2\sigma$	$\frac{Pb^{206}}{U^{238}}$		$\pm 2\sigma$	$\frac{Pb^{207}}{U^{235}}$	$\pm 2\sigma$	$\frac{Pb^{207}}{Pb^{206}}$	$\pm 2\sigma$	Ma	$\pm 2\sigma$	
JG55-03_Zrn-01	116	0.62	0.0616	0.0085	0.5557	0.0844	0.0654	0.0016	0.09	408.7	9.8	441.4	56.9	876.2	198.2	408.7	9.8	7.4
JG55-03_Zrn-02	92	0.57	0.0614	0.0063	0.4614	0.0499	0.0554	0.0016	-0.24	347.8	10.0	381.7	34.7	872.5	172.8	347.8	10.0	8.8
JG55-03_Zrn-05	82	0.57	0.0555	0.0038	0.5292	0.0494	0.0689	0.0016	0.41	429.7	10.0	426.9	32.7	607.8	110.1	429.7	10.0	-0.6
JG55-03_Zrn-06	148	0.60	0.0568	0.0030	0.5390	0.0412	0.0691	0.0012	0.00	431.0	7.6	436.0	27.0	547.1	100.5	431.0	7.6	1.1
JG55-03_Zrn-07	206	0.73	0.0559	0.0026	0.5425	0.0405	0.0705	0.0010	0.21	439.6	6.3	438.5	26.5	503.8	84.3	439.6	6.3	-0.2
JG55-03_Zrn-11	158	0.76	0.0753	0.0039	1.2492	0.1082	0.1201	0.0041	0.61	731.2	23.8	818.9	49.3	1088.8	91.5	731.2	23.8	10.7
JG55-03_Zrn-12	68	0.54	0.0647	0.0076	0.5825	0.0696	0.0658	0.0019	-0.39	411.3	12.0	461.8	43.2	733.4	231.3	411.3	12.0	10.9
JG55-04_Zrn-14	253	0.70	0.0588	0.0043	0.5869	0.0544	0.0717	0.0017	0.17	446.7	10.3	467.8	34.5	537.2	160.3	446.7	10.3	4.5
JG55-04_Zrn-16	143	1.41	0.0599	0.0046	0.5374	0.0515	0.0654	0.0017	0.16	408.7	10.6	433.3	34.7	789.8	102.5	408.7	10.6	5.6
JG55-04_Zrn-17	102	1.08	0.0542	0.0032	0.5137	0.0434	0.0679	0.0012	0.02	423.6	7.8	418.4	28.8	517.6	108.2	423.6	7.8	-1.2
JG55-04_Zrn-18	56	0.56	0.0622	0.0065	0.5970	0.0671	0.0705	0.0022	-0.06	439.1	13.5	470.1	41.8	803.2	182.5	439.1	13.5	6.5
JG55-04_Zrn-19	141	0.48	0.0597	0.0053	0.5801	0.0601	0.0710	0.0017	0.00	442.2	10.5	462.4	38.3	594.5	178.8	442.2	10.5	4.3
JG55-04_Zrn-22	69	0.62	0.0596	0.0055	0.5758	0.0591	0.0708	0.0017	-0.20	441.3	10.2	456.9	37.6	779.1	167.1	441.3	10.2	3.4
JG55-04_Zrn-23	118	0.32	0.0603	0.0048	0.4994	0.0538	0.0584	0.0018	-0.05	366.0	11.4	408.7	36.0	751.4	164.3	366.0	11.4	10.4
JG55-04_Zrn-24	517	0.31	0.0572	0.0035	0.5202	0.0490	0.0661	0.0022	0.58	413.1	13.4	424.5	32.4	488.2	137.7	413.1	13.4	2.6
JG55-04_Zrn-25	2457	0.12	0.0568	0.0020	0.5833	0.0388	0.0740	0.0013	0.26	460.7	7.9	466.4	24.8	481.9	77.3	460.7	7.9	1.2
JG55-04_Zrn-29	81	0.99	0.0597	0.0069	0.5501	0.0704	0.0674	0.0026	0.05	420.6	15.9	441.3	46.2	813.1	151.5	420.6	15.9	4.7
JG55-04_Zrn-30	99	0.79	0.0565	0.0047	0.5256	0.0524	0.0673	0.0012	0.00	419.8	7.4	425.4	35.1	664.9	128.8	419.8	7.4	1.3
JG55-04_Zrn-31	400	0.64	0.0567	0.0029	0.5246	0.0407	0.0671	0.0011	0.19	419.0	7.0	427.1	26.8	488.7	109.7	419.0	7.0	1.8
JG55-04_Zrn-32	271	0.61	0.0572	0.0029	0.5606	0.0446	0.0710	0.0015	0.42	442.4	9.4	450.7	29.1	480.1	113.4	442.4	9.4	1.8
JG55-04_Zrn-34	74	0.82	0.0568	0.0045	0.5363	0.0521	0.0689	0.0019	0.11	429.9	11.7	433.5	34.2	601.8	149.3	429.9	11.7	0.8
JG55-04_Zrn-35	90	0.64	0.0621	0.0073	0.5506	0.0689	0.0650	0.0019	-0.04	406.4	11.9	439.8	44.7	798.3	208.7	406.4	11.9	7.6
JG55-04_Zrn-36	124	0.37	0.0631	0.0050	0.5718	0.0586	0.0660	0.0017	0.38	412.5	10.5	456.9	38.2	756.4	149.7	412.5	10.5	9.7
JG55-04_Zrn-37	67	0.82	0.0583	0.0067	0.5347	0.0683	0.0669	0.0018	0.05	417.5	11.2	427.7	44.9	722.3	186.1	417.5	11.2	2.3
JG55-04_Zrn-38	99	1.38	0.0569	0.0039	0.5548	0.0501	0.0710	0.0013	0.08	442.6	8.2	444.8	32.0	575.9	124.6	442.6	8.2	0.4
JG55-04_Zrn-39	734	0.29	0.0729	0.0019	1.4434	0.0938	0.1443	0.0025	0.67	869.3	14.4	906.5	39.0	1009.1	53.1	869.3	14.4	4.0
JG55-04_Zrn-40	133	0.97	0.0558	0.0032	0.5424	0.0451	0.0707	0.0019	0.33	440.5	11.5	437.4	30.4	600.1	97.5	440.5	11.5	-0.7
JG55-04_Zrn-41	70	0.34	0.0614	0.0080	0.5672	0.0833	0.0673	0.0021	0.24	420.1	13.2	450.2	52.0	787.5	227.1	420.1	13.2	6.6
JG55-04_Zrn-42	141	0.30	0.0619	0.0039	0.5565	0.0466	0.0654	0.0015	0.09	408.6	9.3	447.5	30.5	703.1	120.3	408.6	9.3	8.6

JG18 Esquisto pelítico (U. Etlá)		Espejo-Bautista et al., 2021																
Zircón	U ppm	Th/U	Relaciones isotópicas corregidas							Edades corregidas					Mejor edad		Discordancia %	
			$\frac{Pb^{207}}{Pb^{206}}$	$\pm 2\sigma$	$\frac{Pb^{207}}{U^{235}}$	$\pm 2\sigma$	$\frac{Pb^{206}}{U^{238}}$	$\pm 2\sigma$	rho	$\frac{Pb^{206}}{U^{238}}$	$\pm 2\sigma$	$\frac{Pb^{207}}{U^{235}}$	$\pm 2\sigma$	$\frac{Pb^{207}}{Pb^{206}}$	$\pm 2\sigma$	Ma		$\pm 2\sigma$
JG18-01_Zrn-b-01	63	0.73	0.0650	0.0043	1.0193	0.0956	0.1133	0.0027	0.09	691.9	15.7	708.2	48.6	789.1	132.6	691.9	15.7	10.2
JG18-01_Zrn-b-03	267	0.05	0.0571	0.0027	0.6215	0.0519	0.0788	0.0012	0.14	489.2	7.4	489.2	32.5	506.6	105.0	489.2	7.4	3.4
JG18-01_Zrn-b-05	158	0.12	0.0649	0.0040	0.9071	0.0819	0.1016	0.0021	0.00	624.2	12.3	652.7	43.3	754.0	128.3	624.2	12.3	13.4
JG18-01_Zrn-b-07	123	0.04	0.0617	0.0043	0.8959	0.0906	0.1047	0.0025	0.37	642.3	14.9	644.4	49.3	680.7	129.6	642.3	14.9	5.3
JG18-01_Zrn-b-10	491	0.44	0.0603	0.0024	0.7109	0.0557	0.0849	0.0013	0.03	525.4	7.8	544.5	33.2	616.0	81.8	525.4	7.8	11.6
JG18-01_Zrn-b-12	190	0.18	0.0558	0.0033	0.5312	0.0494	0.0670	0.0012	0.00	418.6	7.5	430.6	32.1	518.1	134.3	418.6	7.5	16.8
JG18-01_Zrn-b-14	155	0.08	0.0726	0.0034	1.4065	0.1160	0.1394	0.0029	0.14	841.5	16.4	889.5	49.5	1009.1	85.2	1009.1	85.2	11.8
JG18-01_Zrn-b-18	249	0.27	0.0639	0.0035	0.9399	0.0891	0.1063	0.0032	0.57	651.5	18.8	670.2	46.5	716.8	122.0	651.5	18.8	6.4
JG18-01_Zrn-b-20	246	0.31	0.0584	0.0030	0.5879	0.0494	0.0730	0.0014	0.00	454.5	8.7	468.3	31.7	569.9	100.9	454.5	8.7	17.8
JG18-01_Zrn-b-21	698	0.11	0.0682	0.0021	1.4072	0.1066	0.1494	0.0024	0.50	897.5	13.4	891.2	45.2	882.5	57.5	882.5	57.5	-0.9
JG18-01_Zrn-b-23	318	0.07	0.0657	0.0025	1.1452	0.0909	0.1263	0.0019	0.38	766.8	11.2	773.3	42.8	782.8	82.8	766.8	11.2	1.2
JG18-01_Zrn-n-02	844	0.58	0.0785	0.0024	2.0793	0.1586	0.1928	0.0036	0.63	1136.6	19.9	1141.1	52.3	1156.7	61.6	1156.7	61.6	1.3
JG18-01_Zrn-n-04	322	0.07	0.0591	0.0028	0.6359	0.0534	0.0780	0.0011	0.22	484.1	6.9	498.6	32.9	548.4	104.1	484.1	6.9	9.0
JG18-01_Zrn-n-06	353	0.06	0.0681	0.0031	1.0007	0.0817	0.1065	0.0014	-0.08	652.4	8.3	702.9	41.5	857.4	98.9	652.4	8.3	18.0
JG18-01_Zrn-n-08	903	0.59	0.0784	0.0022	2.0297	0.1507	0.1869	0.0023	0.57	1104.8	12.8	1124.8	50.5	1154.8	56.5	1154.8	56.5	2.5
JG18-01_Zrn-n-09	292	0.03	0.0576	0.0026	0.6079	0.0494	0.0762	0.0010	0.04	473.5	6.4	480.9	31.5	536.8	84.3	473.5	6.4	10.4
JG18-01_Zrn-n-11	255	0.03	0.0585	0.0034	0.6261	0.0549	0.0777	0.0019	0.10	482.3	11.8	492.3	34.4	561.6	116.2	482.3	11.8	12.3
JG18-01_Zrn-n-13	187	0.07	0.0681	0.0028	1.3478	0.1070	0.1425	0.0024	0.19	859.0	13.6	864.6	45.9	871.0	90.9	871.0	90.9	0.7
JG18-01_Zrn-n-17	474	0.44	0.0763	0.0026	1.7498	0.1315	0.1662	0.0023	0.16	991.1	12.8	1026.5	48.6	1097.7	68.0	1097.7	68.0	6.4
JG18-01_Zrn-n-19	396	0.48	0.0572	0.0023	0.5768	0.0455	0.0728	0.0011	0.10	453.1	6.9	461.6	29.2	507.0	83.3	453.1	6.9	8.9
JG18-01_Zrn-n-22	210	0.14	0.0704	0.0035	1.3091	0.1138	0.1345	0.0037	0.42	813.3	21.3	846.8	51.0	949.5	89.1	949.5	89.1	10.8
JG18-01_Zrn-n-24	355	0.07	0.0653	0.0025	1.1013	0.0865	0.1227	0.0025	0.30	746.4	14.7	752.9	42.1	773.5	84.3	746.4	14.7	2.6
Zircon_01_JGE-18	211	0.06	0.0576	0.0041	0.6477	0.0501	0.0815	0.0016	0.00	505.1	9.5	504.1	31.5	628.9	111.0	505.1	9.5	19.6
Zircon_10_1	270	0.06	0.0559	0.0024	0.5388	0.0286	0.0697	0.0010	0.14	434.6	6.5	436.3	18.8	493.2	84.1	434.6	6.5	11.8
Zircon_100	215	0.02	0.0564	0.0033	0.5524	0.0333	0.0714	0.0014	-0.27	444.5	8.8	444.7	22.0	565.6	98.1	444.5	8.8	21.4
Zircon_103	204	0.02	0.0687	0.0022	1.1742	0.0521	0.1240	0.0023	0.24	753.6	13.6	787.3	24.4	876.4	67.4	753.6	13.6	14.0
Zircon_104	415	0.02	0.0658	0.0032	0.9438	0.0578	0.1037	0.0022	0.31	636.1	13.2	672.9	29.9	779.7	103.7	636.1	13.2	18.4
Zircon_105	139	0.01	0.0614	0.0036	0.7627	0.0482	0.0913	0.0019	0.17	563.6	11.3	577.8	30.2	671.7	113.9	563.6	11.3	16.0
Zircon_106	324	0.02	0.0550	0.0030	0.5290	0.0328	0.0697	0.0013	0.01	434.5	8.2	429.8	22.4	475.9	84.9	434.5	8.2	8.6
Zircon_107	388	0.23	0.0735	0.0040	1.2204	0.0663	0.1202	0.0024	-0.24	731.9	14.3	808.8	30.4	1014.1	106.0	731.9	14.3	27.8
Zircon_108	711	0.02	0.0704	0.0019	1.1474	0.0516	0.1178	0.0020	0.55	717.9	11.5	774.9	24.5	933.5	56.8	717.9	11.5	23.0
Zircon_11_1	195	0.07	0.0676	0.0047	1.1669	0.0865	0.1251	0.0035	0.04	759.9	20.2	783.6	39.9	841.1	150.4	759.9	20.2	9.6
Zircon_110	245	0.06	0.0567	0.0037	0.5344	0.0366	0.0683	0.0013	-0.05	426.4	8.0	437.1	26.9	632.5	121.9	426.4	8.0	32.5
Zircon_12_1	171	0.06	0.0675	0.0040	0.7797	0.0548	0.0835	0.0019	0.36	517.3	11.6	582.7	31.7	858.5	107.6	517.3	11.6	39.7
Zircon_13_1	357	0.08	0.0602	0.0025	0.6339	0.0319	0.0765	0.0009	-0.03	475.1	5.4	497.5	19.6	608.6	81.9	475.1	5.4	21.9
Zircon_14_1	352	0.08	0.0605	0.0041	0.6447	0.0491	0.0771	0.0027	0.29	478.9	16.6	503.9	30.4	597.5	152.3	478.9	16.6	19.8
Zircon_15_1	228	0.14	0.0646	0.0042	0.7406	0.0582	0.0826	0.0018	0.39	512.0	11.2	560.1	34.0	772.3	118.8	512.0	11.2	33.7
Zircon_16_1	73	0.30	0.0574	0.0049	0.6009	0.0528	0.0762	0.0021	0.00	473.7	13.1	472.8	33.4	689.1	140.0	473.7	13.1	31.2
Zircon_17_1	210	0.06	0.0686	0.0040	0.9492	0.0599	0.1003	0.0020	0.01	616.2	11.8	675.2	31.0	857.3	117.7	616.2	11.8	28.1
Zircon_18_1	189	0.07	0.0690	0.0042	1.0197	0.0696	0.1070	0.0020	0.15	655.3	11.9	712.0	34.7	880.4	121.6	655.3	11.9	25.5
Zircon_19_1	225	0.04	0.0564	0.0027	0.5356	0.0325	0.0687	0.0012	0.31	428.4	7.4	434.6	21.3	448.2	106.1	428.4	7.4	4.4
Zircon_2_1	198	0.06	0.0571	0.0037	0.5817	0.0460	0.0736	0.0021	0.40	458.0	12.7	463.3	29.7	581.7	110.7	458.0	12.7	21.2
Zircon_21_1	235	0.06	0.0628	0.0039	0.6586	0.0450	0.0760	0.0017	0.04	472.1	10.4	511.8	27.7	753.3	110.8	472.1	10.4	37.3
Zircon_22_1	179	0.02	0.0605	0.0051	0.5944	0.0519	0.0712	0.0015	0.03	443.3	9.5	469.7	33.0	668.9	147.1	443.3	9.5	33.7
Zircon_23_1	202	0.02	0.0564	0.0043	0.5475	0.0449	0.0703	0.0020	0.10	438.1	12.3	441.5	29.6	604.2	124.0	438.1	12.3	27.4
Zircon_24_1	327	0.03	0.0784	0.0030	1.7949	0.0930	0.1656	0.0029	0.35	988.0	16.5	1041.3	33.2	1145.9	77.1	1145.9	77.1	13.7
Zircon_25_1	501	0.01	0.0635	0.0021	0.8446	0.0383	0.0963	0.0017	0.27	593.0	10.5	621.0	20.8	716.2	68.8	593.0	10.5	17.1
Zircon_26_1	297	0.03	0.0685	0.0027	1.0622	0.0575	0.1121	0.0021	0.41	685.2	12.5	732.9	28.6	867.9	86.9	685.2	12.5	21.0
Zircon_27_1	229	0.06	0.0610	0.0039	0.6005	0.0393	0.0715	0.0015	-0.15	445.1	9.1	475.8	24.8	652.1	123.1	445.1	9.1	31.7

Continúa

Continuación

JG18 Esquisto pelítico (U. Etlá) Espejo-Bautista et al., 2021

Zircón	U ppm	Th/U	Relaciones isotópicas corregidas							Edades corregidas				Mejor edad		Discordancia %		
			$\frac{Pb^{207}}{Pb^{206}}$	$\pm 2\sigma$	$\frac{Pb^{207}}{U^{235}}$	$\pm 2\sigma$	$\frac{Pb^{206}}{U^{238}}$	$\pm 2\sigma$	ρ	$\frac{Pb^{206}}{U^{238}}$	$\pm 2\sigma$	$\frac{Pb^{207}}{U^{235}}$	$\pm 2\sigma$	$\frac{Pb^{207}}{Pb^{206}}$	$\pm 2\sigma$		Ma	$\pm 2\sigma$
Zircon_28_l	338	0.06	0.0707	0.0021	1.4475	0.0606	0.1478	0.0022	0.18	888.5	12.5	907.6	25.1	937.0	60.5	937.0	60.5	5.1
Zircon_29_l	265	0.04	0.0672	0.0027	1.2200	0.0605	0.1318	0.0020	0.20	798.2	11.5	808.3	27.1	830.0	81.3	798.2	11.5	3.8
Zircon_3_l	219	0.07	0.0677	0.0028	1.3721	0.0679	0.1467	0.0032	0.15	882.3	18.4	875.0	29.4	841.2	87.3	841.2	87.3	-4.8
Zircon_30_l	101	0.06	0.0667	0.0060	0.8565	0.0875	0.0927	0.0026	0.35	571.9	15.3	623.5	46.9	824.9	169.2	571.9	15.3	30.6
Zircon_31_l	639	0.12	0.0581	0.0022	0.5943	0.0300	0.0739	0.0011	0.22	460.0	6.9	472.7	18.8	528.1	79.9	460.0	6.9	12.8
Zircon_33_l	228	0.01	0.0653	0.0028	0.6221	0.0323	0.0691	0.0013	-0.02	431.0	8.2	490.1	20.1	758.6	96.3	431.0	8.2	43.1
Zircon_34_l	317	0.06	0.0593	0.0028	0.6578	0.0395	0.0802	0.0014	0.30	497.4	8.4	511.9	24.1	576.7	103.2	497.4	8.4	13.7
Zircon_35_l	242	0.02	0.0555	0.0027	0.5297	0.0291	0.0693	0.0014	0.05	432.2	9.0	430.2	19.6	518.2	84.9	432.2	9.0	16.5
Zircon_36_l	281	0.24	0.0767	0.0023	2.0978	0.0986	0.1977	0.0051	0.57	1162.7	27.8	1146.0	32.9	1104.4	59.6	1104.4	59.6	-5.2
Zircon_37_l	633	0.06	0.0555	0.0016	0.5047	0.0224	0.0658	0.0008	0.47	411.2	5.2	414.3	15.1	461.1	56.6	411.2	5.2	10.8
Zircon_38_l	422	0.04	0.0557	0.0030	0.5350	0.0351	0.0695	0.0013	0.27	433.2	8.0	433.9	23.3	466.7	109.1	433.2	8.0	7.1
Zircon_39_l	591	0.07	0.0687	0.0022	1.1232	0.0511	0.1184	0.0028	0.38	721.2	16.3	763.8	24.7	883.7	69.4	721.2	16.3	18.3
Zircon_4_l	359	0.14	0.0655	0.0034	0.8385	0.0523	0.0927	0.0020	0.24	571.5	11.8	616.8	29.0	771.2	114.4	571.5	11.8	25.8
Zircon_40_l	484	0.04	0.0579	0.0033	0.6342	0.0390	0.0793	0.0018	0.01	492.3	11.2	497.8	24.2	546.0	107.0	492.3	11.2	9.8
Zircon_41	244	0.05	0.0597	0.0034	0.5973	0.0393	0.0725	0.0016	0.20	451.3	9.9	473.9	25.1	610.7	116.9	451.3	9.9	26.0
Zircon_43	291	0.05	0.0578	0.0029	0.5830	0.0325	0.0730	0.0011	-0.17	454.6	6.9	465.2	20.7	572.3	90.0	454.6	6.9	20.5
Zircon_44	221	0.01	0.0569	0.0030	0.5892	0.0339	0.0752	0.0012	-0.21	467.8	7.4	468.4	21.8	568.5	96.5	467.8	7.4	17.7
Zircon_45	303	0.06	0.0682	0.0022	1.1033	0.0569	0.1182	0.0020	-0.09	720.6	11.8	758.8	23.9	864.4	69.1	720.6	11.8	16.6
Zircon_48	351	0.16	0.0565	0.0020	0.6243	0.0313	0.0800	0.0017	0.40	496.5	10.2	491.2	19.4	479.0	70.8	496.5	10.2	-3.6
Zircon_49	151	0.01	0.0637	0.0045	0.9934	0.0753	0.1138	0.0047	0.17	694.5	27.3	696.3	37.7	764.2	118.5	694.5	27.3	9.1
Zircon_5	311	0.11	0.0659	0.0024	0.8094	0.0497	0.0900	0.0025	0.50	555.6	15.2	599.9	28.1	788.7	79.5	555.6	15.2	29.5
Zircon_50	88	0.36	0.0732	0.0039	1.8006	0.1066	0.1783	0.0037	-0.03	1057.6	20.2	1041.5	38.4	988.9	111.2	988.9	111.2	-6.9
Zircon_51	187	0.01	0.0560	0.0031	0.5281	0.0325	0.0684	0.0012	0.00	426.6	7.8	428.5	21.3	518.5	106.4	426.6	7.8	17.7
Zircon_52	517	0.04	0.0709	0.0019	1.1083	0.0491	0.1129	0.0015	0.44	689.5	9.0	756.5	23.8	948.7	59.1	689.5	9.0	27.3
Zircon_53	213	0.06	0.0577	0.0031	0.5842	0.0355	0.0733	0.0014	0.09	456.4	8.5	465.2	22.6	566.0	105.7	456.4	8.5	19.3
Zircon_54	179	0.08	0.0654	0.0045	1.0559	0.0752	0.1175	0.0037	0.08	715.9	21.6	727.3	37.1	769.3	133.1	715.9	21.6	6.9
Zircon_56	336	0.05	0.0656	0.0020	0.9935	0.0465	0.1107	0.0026	0.63	676.9	15.0	699.4	23.7	786.1	66.3	676.9	15.0	13.8
Zircon_58	235	0.05	0.0653	0.0032	0.9861	0.0709	0.1088	0.0023	0.76	666.1	13.8	695.0	35.6	773.5	102.1	666.1	13.8	13.8
Zircon_6	360	0.19	0.0594	0.0036	0.5861	0.0418	0.0713	0.0013	0.24	444.3	8.2	466.9	26.3	554.4	130.2	444.3	8.2	19.8
Zircon_60	586	0.10	0.0522	0.0016	0.3883	0.0171	0.0539	0.0007	0.13	338.4	4.3	332.7	12.5	319.1	60.9	338.4	4.3	-6.0
Zircon_61	230	0.05	0.0728	0.0025	1.4650	0.0711	0.1456	0.0024	0.29	876.3	13.5	914.4	28.8	997.6	71.5	997.6	71.5	12.1
Zircon_62	235	0.07	0.0626	0.0038	0.6842	0.0480	0.0789	0.0016	0.21	489.8	10.0	526.8	28.7	685.1	123.5	489.8	10.0	28.5
Zircon_63	650	0.04	0.0707	0.0028	1.1084	0.0702	0.1133	0.0034	0.68	692.1	20.0	755.6	33.5	938.7	85.2	692.1	20.0	26.2
Zircon_64	369	0.03	0.0617	0.0023	0.7761	0.0416	0.0902	0.0019	0.51	557.0	11.4	582.2	24.0	652.4	83.5	557.0	11.4	14.6
Zircon_65	542	0.23	0.0735	0.0020	1.5752	0.0630	0.1553	0.0018	-0.08	930.7	10.5	959.8	24.8	1021.7	55.7	1021.7	55.7	8.9
Zircon_66	98	0.02	0.0584	0.0069	0.5059	0.0591	0.0629	0.0019	0.02	393.5	11.6	409.6	39.8	849.5	181.1	393.5	11.6	53.6
Zircon_67	122	0.05	0.0598	0.0043	0.7599	0.0560	0.0938	0.0021	0.11	578.2	12.4	577.3	35.3	682.5	138.7	578.2	12.4	15.2
Zircon_68	176	0.05	0.0584	0.0036	0.5744	0.0384	0.0714	0.0017	0.07	445.0	10.7	458.5	25.0	617.7	112.1	445.0	10.7	27.9
Zircon_69	312	0.04	0.0708	0.0019	1.5750	0.0721	0.1608	0.0029	0.55	961.0	16.1	958.6	28.4	943.5	57.7	943.5	57.7	-1.8
Zircon_7	195	0.09	0.0633	0.0043	0.7651	0.0539	0.0877	0.0023	-0.06	542.2	13.8	574.2	31.8	801.5	109.5	542.2	13.8	32.3
Zircon_70	387	0.09	0.0715	0.0034	1.0252	0.0618	0.1041	0.0019	0.64	638.5	11.1	715.0	31.3	998.2	125.4	638.5	11.1	36.0
Zircon_71	642	0.08	0.0608	0.0021	0.7062	0.0325	0.0841	0.0014	0.23	521.0	8.8	542.0	19.4	625.5	74.2	521.0	8.8	16.7
Zircon_72	237	0.01	0.0593	0.0050	0.5636	0.0472	0.0689	0.0019	0.01	429.9	11.6	452.5	31.4	606.0	155.8	429.9	11.6	29.0
Zircon_73	273	0.09	0.0577	0.0031	0.5490	0.0335	0.0689	0.0013	0.09	430.0	7.8	443.1	21.8	525.1	113.2	430.0	7.8	18.1
Zircon_74	117	0.12	0.0626	0.0064	0.6331	0.0597	0.0760	0.0023	0.15	472.3	13.9	505.2	43.8	768.4	173.4	472.3	13.9	38.5
Zircon_75	190	0.02	0.0693	0.0029	1.0762	0.0560	0.1126	0.0024	0.19	688.2	14.2	740.2	27.6	890.7	90.7	688.2	14.2	22.7
Zircon_77	130	0.22	0.0723	0.0045	1.1739	0.0725	0.1182	0.0031	-0.01	720.1	18.2	786.2	33.9	966.1	121.8	720.1	18.2	25.4

Continúa

Continuación

JG18 Esquisto pelítico (U. Etlá) Espejo-Bautista et al., 2021																		
Zircón	U ppm	Th/U	Relaciones isotópicas corregidas							Edades corregidas					Mejor edad		Discordancia %	
			$\frac{Pb^{207}}{Pb^{206}}$	$\pm 2\sigma$	$\frac{Pb^{207}}{U^{235}}$	$\pm 2\sigma$	$\frac{Pb^{206}}{U^{238}}$	$\pm 2\sigma$	rho	$\frac{Pb^{206}}{U^{238}}$	$\pm 2\sigma$	$\frac{Pb^{207}}{U^{235}}$	$\pm 2\sigma$	$\frac{Pb^{207}}{Pb^{206}}$	$\pm 2\sigma$	Ma		$\pm 2\sigma$
Zircon_78	146	0.10	0.0573	0.0043	0.5404	0.0498	0.0681	0.0022	0.43	424.9	13.8	437.5	31.8	484.8	159.4	424.9	13.8	12.3
Zircon_79	845	0.03	0.0635	0.0019	0.7990	0.0350	0.0913	0.0020	0.36	563.2	12.2	595.7	19.7	716.3	66.7	563.2	12.2	21.3
Zircon_8	295	0.06	0.0584	0.0030	0.7274	0.0454	0.0897	0.0016	0.29	554.2	9.5	554.2	27.0	534.5	117.8	554.2	9.5	-3.6
Zircon_80	592	0.03	0.0637	0.0032	0.7029	0.0396	0.0798	0.0020	0.10	495.0	12.1	540.1	23.6	722.9	107.6	495.0	12.1	31.5
Zircon_81	313	0.05	0.0699	0.0026	1.2823	0.0633	0.1327	0.0024	0.27	803.4	13.8	836.5	28.1	913.4	78.7	913.4	78.7	12.0
Zircon_82	592	0.05	0.0573	0.0027	0.5569	0.0311	0.0702	0.0013	0.03	437.7	7.9	448.8	20.0	513.8	96.2	437.7	7.9	14.8
Zircon_83	259	0.05	0.0563	0.0033	0.5368	0.0319	0.0694	0.0014	-0.26	432.9	8.7	434.9	21.3	530.3	105.4	432.9	8.7	18.3
Zircon_84	461	0.13	0.0672	0.0025	1.1099	0.0520	0.1195	0.0022	0.11	728.0	12.9	757.2	24.9	833.7	77.4	728.0	12.9	12.6
Zircon_85	795	0.00	0.0653	0.0018	0.9456	0.0401	0.1046	0.0015	0.21	641.7	9.0	675.4	20.9	779.2	60.8	641.7	9.0	17.6
Zircon_86	135	0.52	0.0569	0.0035	0.5674	0.0406	0.0712	0.0014	0.02	443.6	8.7	453.3	26.7	604.7	98.8	443.6	8.7	26.6
Zircon_87	489	0.17	0.0589	0.0034	0.5913	0.0418	0.0726	0.0019	0.39	452.2	11.5	470.6	26.8	582.2	113.6	452.2	11.5	22.3
Zircon_88	141	0.10	0.0751	0.0033	1.8240	0.0897	0.1761	0.0036	-0.08	1045.9	20.1	1052.5	32.4	1058.7	90.6	1058.7	90.6	1.2
Zircon_9	334	0.06	0.0566	0.0025	0.5506	0.0296	0.0704	0.0008	-0.06	438.6	4.9	444.0	19.1	523.0	84.5	438.6	4.9	16.1
Zircon_90	625	0.68	0.0655	0.0019	0.9664	0.0424	0.1065	0.0018	0.29	652.5	10.8	686.0	22.2	785.2	66.5	652.5	10.8	16.8
Zircon_91	534	0.17	0.0677	0.0023	1.1613	0.0554	0.1241	0.0019	0.34	754.3	11.4	781.0	26.4	847.7	73.5	754.3	11.4	11.0
Zircon_92	377	0.36	0.0549	0.0023	0.5235	0.0276	0.0686	0.0013	0.02	427.7	7.8	426.2	18.4	475.8	74.0	427.7	7.8	10.1
Zircon_94	179	0.02	0.0554	0.0040	0.5362	0.0348	0.0707	0.0026	-0.12	440.7	15.6	434.8	23.2	562.0	125.3	440.7	15.6	21.5
Zircon_95	176	0.01	0.0579	0.0033	0.5660	0.0387	0.0709	0.0019	0.27	441.8	11.6	453.2	24.7	593.3	98.6	441.8	11.6	25.5
Zircon_96	373	0.04	0.0644	0.0042	0.9225	0.0456	0.1038	0.0050	-0.04	636.6	29.4	663.5	24.2	746.7	135.9	636.6	29.4	14.7
Zircon_97	201	0.01	0.0631	0.0031	0.8598	0.0562	0.0986	0.0031	0.46	606.3	18.5	625.9	30.3	719.0	97.1	606.3	18.5	15.6
Zircon_99	300	0.35	0.0637	0.0033	0.8766	0.0537	0.0992	0.0017	0.20	609.6	10.3	636.8	28.1	703.5	103.7	609.6	10.3	13.3

JG46 Anfibolita (U. Etna) Espejo-Bautista et al., 2021

Zircón	U ppm	Th/U	Relaciones isotópicas corregidas							Edades corregidas					Mejor edad		Discordancia %	
			$\frac{Pb^{207}}{Pb^{206}}$	$\pm 2\sigma$	$\frac{Pb^{207}}{U^{235}}$	$\pm 2\sigma$	$\frac{Pb^{206}}{U^{238}}$	$\pm 2\sigma$	rho	$\frac{Pb^{206}}{U^{238}}$	$\pm 2\sigma$	$\frac{Pb^{207}}{U^{235}}$	$\pm 2\sigma$	$\frac{Pb^{207}}{Pb^{206}}$	$\pm 2\sigma$	Ma		$\pm 2\sigma$
JG46-01_Zrn-b-101	882	0.09	0.0696	0.0027	1.3913	0.1070	0.1457	0.0024	-0.21	876.8	13.5	884.8	45.2	911.8	81.4	911.8	81.4	2.9
JG46-01_Zrn-b-103	84	0.17	0.0632	0.0045	1.0457	0.1040	0.1201	0.0022	0.14	731.4	12.8	722.0	52.6	769.9	121.4	731.4	12.8	-1.2
JG46-01_Zrn-b-105	136	0.58	0.0714	0.0031	1.3387	0.1085	0.1360	0.0025	0.15	822.3	14.4	861.3	46.5	957.2	90.1	957.2	90.1	10.0
JG46-01_Zrn-b-107	305	0.25	0.0673	0.0026	1.3370	0.1041	0.1463	0.0027	0.59	880.0	15.4	865.4	51.9	835.6	80.7	835.6	80.7	-3.5
JG46-01_Zrn-b-116	54	0.21	0.0582	0.0064	0.5990	0.0726	0.0769	0.0022	0.03	477.8	13.2	479.0	48.5	647.0	194.4	477.8	13.2	0.2
JG46-01_Zrn-b-132	212	0.29	0.0671	0.0034	1.1978	0.1003	0.1290	0.0022	0.05	782.4	12.7	797.4	46.6	821.0	104.9	782.4	12.7	1.8
JG46-01_Zrn-b-33	44	0.64	0.0756	0.0076	1.2995	0.1530	0.1251	0.0035	0.03	760.1	20.4	835.0	66.1	994.7	196.3	760.1	20.4	8.9
JG46-01_Zrn-b-39	139	1.23	0.0726	0.0031	1.5699	0.1255	0.1558	0.0024	0.01	933.7	13.6	956.0	49.5	984.4	91.8	984.4	91.8	2.8
JG46-01_Zrn-b-41	100	0.13	0.0592	0.0048	0.6451	0.0679	0.0792	0.0021	0.19	491.4	12.5	502.2	42.0	640.0	164.0	491.4	12.5	2.1
JG46-01_Zrn-b-43	244	1.05	0.0756	0.0030	1.8812	0.1502	0.1806	0.0030	0.31	1070.1	16.8	1072.7	53.1	1075.2	82.8	1075.2	82.8	0.2
JG46-01_Zrn-b-51	82	0.45	0.0680	0.0036	1.3772	0.1188	0.1475	0.0027	0.17	887.2	15.4	880.7	47.1	873.7	100.6	873.7	100.6	-0.8
JG46-01_Zrn-b-58	78	0.89	0.0699	0.0077	1.0064	0.1266	0.1062	0.0030	-0.14	650.6	17.8	699.1	64.9	938.3	209.6	650.6	17.8	6.9
JG46-01_Zrn-b-68	205	0.66	0.0648	0.0028	1.1028	0.0914	0.1229	0.0026	0.43	747.4	15.2	752.0	43.7	746.9	93.7	747.4	15.2	0.6
JG46-01_Zrn-b-74	35	0.08	0.0677	0.0052	1.3036	0.1330	0.1393	0.0037	0.17	840.5	21.2	837.3	57.5	815.8	149.7	815.8	149.7	-2.6
JG46-01_Zrn-b-77	133	0.24	0.0692	0.0029	1.3984	0.1142	0.1461	0.0036	0.39	879.0	20.5	885.4	47.9	886.6	89.7	886.6	89.7	0.1
JG46-01_Zrn-b-82	39	0.31	0.0577	0.0112	0.6119	0.1217	0.0776	0.0034	0.16	481.7	20.6	470.6	75.6	885.9	314.7	481.7	20.6	-2.3
JG46-01_Zrn-b-84	24	0.26	0.0721	0.0097	1.1592	0.1755	0.1179	0.0049	0.05	718.4	28.3	759.8	82.3	1086.4	223.0	718.4	28.3	5.4
JG46-01_Zrn-b-88	23	0.23	0.0745	0.0078	1.3577	0.1659	0.1335	0.0051	0.19	807.4	29.5	859.0	71.6	992.6	205.1	992.6	205.1	13.4
JG46-01_Zrn-b-91	27	0.26	0.0648	0.0065	1.1402	0.1424	0.1293	0.0044	0.19	783.9	25.5	759.5	66.4	866.4	166.2	783.9	25.5	-3.2
JG46-01_Zrn-b-95	49	0.30	0.0644	0.0087	0.6021	0.0880	0.0688	0.0020	-0.07	429.1	12.5	468.9	52.8	868.3	226.6	429.1	12.5	8.4
JG46-01_Zrn-n-100	281	0.23	0.0683	0.0025	1.4294	0.1131	0.1506	0.0024	0.43	904.4	13.4	899.2	46.7	864.6	79.5	864.6	79.5	-4.0
JG46-01_Zrn-n-102	228	0.57	0.0683	0.0037	1.2052	0.1020	0.1277	0.0022	-0.09	775.0	12.9	801.0	48.4	856.5	119.4	775.0	12.9	3.2
JG46-01_Zrn-n-104	718	0.77	0.0725	0.0027	1.5944	0.1245	0.1587	0.0022	0.28	949.9	12.5	967.1	49.2	995.2	77.2	995.2	77.2	2.8
JG46-01_Zrn-n-106	7	0.06	0.0654	0.0129	1.2920	0.2401	0.1496	0.0085	-0.03	896.8	47.7	785.0	115.2	1221.7	262.1	1221.7	262.1	35.7
JG46-01_Zrn-n-108	924	0.35	0.0689	0.0027	1.1633	0.0968	0.1229	0.0026	0.65	747.6	15.5	782.6	45.6	892.3	83.8	747.6	15.5	4.4
JG46-01_Zrn-n-110	23	0.35	0.0716	0.0061	1.4981	0.1548	0.1518	0.0041	-0.08	916.2	26.0	918.8	62.6	941.8	159.8	941.8	159.8	2.4
JG46-01_Zrn-n-111	164	0.37	0.0552	0.0028	0.5212	0.0454	0.0683	0.0012	0.30	426.1	7.6	424.2	30.1	497.4	96.4	426.1	7.6	-0.4
JG46-01_Zrn-n-112	43	1.01	0.0684	0.0048	1.2275	0.1229	0.1300	0.0038	0.24	787.5	21.7	806.3	54.4	883.4	130.7	787.5	21.7	2.3
JG46-01_Zrn-n-113	299	0.36	0.0682	0.0023	1.3920	0.1061	0.1478	0.0019	0.00	888.8	10.8	884.4	45.2	864.1	74.9	864.1	74.9	-2.3
JG46-01_Zrn-n-114	549	0.20	0.0641	0.0029	1.0035	0.0834	0.1135	0.0017	0.28	693.5	10.4	704.5	42.3	735.9	98.6	693.5	10.4	1.5
JG46-01_Zrn-n-115	367	0.21	0.0716	0.0049	1.2207	0.1307	0.1226	0.0030	0.72	745.5	17.4	807.7	58.9	962.5	138.5	745.5	17.4	7.6
JG46-01_Zrn-n-117	200	0.71	0.0644	0.0033	1.0731	0.0951	0.1209	0.0025	0.41	735.9	14.9	737.4	46.5	755.8	103.7	735.9	14.9	0.2
JG46-01_Zrn-n-118	225	0.17	0.0610	0.0027	0.8287	0.0679	0.0974	0.0014	-0.05	599.6	8.7	611.1	37.6	646.9	101.9	599.6	8.7	1.8
JG46-01_Zrn-n-119	101	0.24	0.0757	0.0039	2.0069	0.1794	0.1918	0.0040	0.49	1131.0	21.6	1112.0	60.7	1061.4	107.7	1061.4	107.7	-4.7
JG46-01_Zrn-n-120	56	0.77	0.0695	0.0045	1.4305	0.1295	0.1499	0.0032	-0.12	900.4	18.4	895.8	54.7	901.7	126.1	901.7	126.1	0.6
JG46-01_Zrn-n-121	64	0.36	0.0772	0.0037	1.8001	0.1522	0.1693	0.0047	0.34	1007.8	26.3	1041.9	55.9	1105.8	99.6	1105.8	99.6	5.7
JG46-01_Zrn-n-122	108	1.01	0.0704	0.0035	1.5074	0.1278	0.1549	0.0026	0.11	928.7	14.6	929.0	52.1	929.1	115.6	929.1	115.6	0.0
JG46-01_Zrn-n-124	26	0.21	0.0698	0.0081	1.1865	0.1510	0.1258	0.0062	0.00	763.5	35.7	781.0	71.5	1017.1	200.4	763.5	35.7	2.2
JG46-01_Zrn-n-125	115	0.56	0.0671	0.0037	1.2420	0.1070	0.1344	0.0027	-0.01	812.8	15.6	816.7	49.6	858.8	100.2	858.8	100.2	4.9
JG46-01_Zrn-n-126	37	0.35	0.0585	0.0071	0.5697	0.0746	0.0711	0.0021	-0.15	442.7	13.0	448.0	48.7	854.9	185.7	442.7	13.0	1.1
JG46-01_Zrn-n-127	351	0.31	0.0649	0.0022	1.1013	0.0864	0.1228	0.0023	0.57	747.0	13.2	752.5	41.5	760.6	74.3	747.0	13.2	0.7
JG46-01_Zrn-n-129	47	0.17	0.0691	0.0072	0.8801	0.1055	0.0929	0.0022	-0.09	572.7	13.1	632.9	55.6	874.5	189.0	572.7	13.1	9.5
JG46-01_Zrn-n-130	37	0.25	0.0661	0.0068	1.1921	0.1461	0.1313	0.0035	0.01	795.3	19.9	779.6	69.2	980.7	158.0	795.3	19.9	-2.0
JG46-01_Zrn-n-131	224	0.42	0.0726	0.0035	1.5877	0.1338	0.1592	0.0034	0.22	952.3	19.2	964.1	51.9	995.9	98.2	995.9	98.2	3.1
JG46-01_Zrn-n-133	20	0.27	0.0712	0.0070	1.6490	0.1977	0.1686	0.0051	0.14	1003.9	28.5	966.6	76.3	1059.1	174.0	1059.1	174.0	8.7
JG46-01_Zrn-n-31	90	1.16	0.0679	0.0040	1.2468	0.1094	0.1330	0.0026	-0.07	805.1	15.0	818.9	49.3	831.9	125.2	831.9	125.2	1.5
JG46-01_Zrn-n-32	370	0.29	0.0690	0.0028	1.2694	0.0996	0.1332	0.0021	0.00	806.0	12.4	831.1	44.6	888.1	83.9	888.1	83.9	6.4
JG46-01_Zrn-n-34	506	0.14	0.0682	0.0033	1.1717	0.0977	0.1247	0.0018	0.12	757.7	10.6	786.5	46.3	867.4	103.4	757.7	10.6	3.6

Continúa

Continuación

JG46 Anfibolita (U. Etna) Espejo-Bautista et al., 2021

Zircón	U ppm	Th/U	Relaciones isotópicas corregidas						rho	Edades corregidas						Mejor edad		Discordancia %
			$\frac{Pb^{207}}{Pb^{206}}$	$\pm 2\sigma$	$\frac{Pb^{207}}{U^{235}}$	$\pm 2\sigma$	$\frac{Pb^{206}}{U^{238}}$	$\pm 2\sigma$		$\frac{Pb^{206}}{U^{238}}$	$\pm 2\sigma$	$\frac{Pb^{207}}{U^{235}}$	$\pm 2\sigma$	$\frac{Pb^{207}}{Pb^{206}}$	$\pm 2\sigma$	Ma	$\pm 2\sigma$	
JG46-01_Zrn-n-35	55	0.20	0.0681	0.0047	1.1859	0.1184	0.1259	0.0033	0.24	764.4	19.1	787.7	53.9	817.2	148.0	764.4	19.1	2.9
JG46-01_Zrn-n-36	755	0.08	0.0681	0.0030	1.2600	0.1011	0.1343	0.0016	-0.29	812.6	9.1	827.3	45.3	864.5	92.7	864.5	92.7	4.3
JG46-01_Zrn-n-38	224	0.29	0.0625	0.0038	0.9274	0.0966	0.1065	0.0042	0.69	652.3	24.9	662.2	51.5	741.1	91.4	652.3	24.9	1.4
JG46-01_Zrn-n-40	726	0.16	0.0693	0.0023	1.3189	0.1011	0.1380	0.0019	0.28	833.8	10.9	853.2	44.3	901.6	71.6	901.6	71.6	5.3
JG46-01_Zrn-n-42	571	0.07	0.0675	0.0023	1.2386	0.0970	0.1331	0.0020	0.55	806.0	11.7	817.3	43.0	849.5	69.7	849.5	69.7	3.7
JG46-01_Zrn-n-44	6	0.16	0.0820	0.0159	1.5680	0.3056	0.1435	0.0092	0.06	862.4	52.4	900.6	135.3	1490.6	281.3	1490.6	281.3	39.5
JG46-01_Zrn-n-45	58	1.01	0.0734	0.0046	1.6552	0.1529	0.1639	0.0032	0.08	978.6	17.9	983.9	59.3	995.6	126.7	995.6	126.7	1.1
JG46-01_Zrn-n-46	15	0.47	0.0629	0.0094	0.8782	0.1449	0.1021	0.0047	0.20	626.2	27.7	612.0	80.2	1096.6	212.8	626.2	27.7	-2.3
JG46-01_Zrn-n-47	115	0.61	0.0627	0.0051	0.7686	0.0783	0.0892	0.0021	-0.21	550.7	12.4	575.4	44.3	731.5	151.2	550.7	12.4	4.2
JG46-01_Zrn-n-48	38	1.13	0.0740	0.0096	1.3273	0.1882	0.1307	0.0045	0.00	791.7	25.7	847.9	82.1	956.7	267.3	791.7	25.7	6.6
JG46-01_Zrn-n-49	75	0.30	0.0790	0.0049	1.9014	0.1738	0.1753	0.0028	-0.08	1041.4	15.6	1072.9	60.0	1116.3	127.9	1116.3	127.9	3.8
JG46-01_Zrn-n-50	22	0.06	0.0745	0.0068	1.5514	0.1708	0.1545	0.0045	0.00	925.6	25.2	934.6	70.5	1164.9	145.7	1164.9	145.7	19.7
JG46-01_Zrn-n-52	909	0.06	0.0723	0.0022	1.4509	0.1087	0.1458	0.0018	0.39	877.8	10.6	909.7	45.3	1001.2	53.2	1001.2	53.2	9.1
JG46-01_Zrn-n-53	65	0.94	0.0714	0.0078	1.2429	0.1640	0.1273	0.0026	0.29	772.9	14.8	814.7	72.0	925.6	211.2	772.9	14.8	5.1
JG46-01_Zrn-n-55	177	0.32	0.0717	0.0024	1.6223	0.1251	0.1649	0.0025	0.42	983.9	14.2	977.3	48.6	969.5	72.2	969.5	72.2	-0.7
JG46-01_Zrn-n-56	94	0.30	0.0795	0.0042	2.1460	0.1828	0.1965	0.0046	0.10	1156.7	25.0	1160.7	57.9	1166.7	104.4	1166.7	104.4	0.5
JG46-01_Zrn-n-57	593	0.04	0.0734	0.0022	1.7338	0.1311	0.1722	0.0022	0.59	1024.7	12.6	1020.0	48.9	1019.5	63.1	1019.5	63.1	0.0
JG46-01_Zrn-n-59	245	1.06	0.0714	0.0029	1.4794	0.1185	0.1509	0.0024	0.24	906.4	13.9	920.5	47.6	957.7	83.9	957.7	83.9	3.8
JG46-01_Zrn-n-60	168	0.22	0.0703	0.0033	1.3925	0.1179	0.1441	0.0038	0.41	872.5	19.2	882.6	50.0	916.1	99.3	916.1	99.3	3.6
JG46-01_Zrn-n-61	270	0.43	0.0696	0.0027	1.4271	0.1145	0.1509	0.0036	0.21	905.9	20.4	902.0	44.1	917.2	71.0	917.2	71.0	1.6
JG46-01_Zrn-n-62	132	0.46	0.0582	0.0051	0.5897	0.0648	0.0738	0.0016	-0.15	459.3	9.7	473.1	37.7	749.5	129.6	459.3	9.7	2.9
JG46-01_Zrn-n-63	66	0.67	0.0549	0.0048	0.5538	0.0617	0.0734	0.0016	0.12	456.7	10.1	441.4	40.1	690.4	146.0	456.7	10.1	-3.4
JG46-01_Zrn-n-64	39	0.05	0.0671	0.0054	1.3129	0.1326	0.1432	0.0036	-0.14	862.7	20.6	841.2	59.6	917.5	141.5	917.5	141.5	8.3
JG46-01_Zrn-n-66	32	0.44	0.0565	0.0094	0.5398	0.0957	0.0689	0.0025	-0.07	429.8	15.3	439.5	71.9	909.5	197.3	429.8	15.3	2.2
JG46-01_Zrn-n-67	563	0.32	0.0647	0.0029	1.0574	0.0880	0.1184	0.0015	0.39	721.4	9.2	731.8	43.9	756.6	99.7	721.4	9.2	1.4
JG46-01_Zrn-n-69	30	0.62	0.0694	0.0075	1.3660	0.1726	0.1432	0.0045	0.01	862.5	25.7	857.5	76.2	1032.1	188.1	1032.1	188.1	16.9
JG46-01_Zrn-n-70	55	0.73	0.0726	0.0061	0.9668	0.1025	0.0969	0.0026	-0.08	596.1	15.8	681.2	51.3	1003.2	153.1	596.1	15.8	12.4
JG46-01_Zrn-n-71	75	0.86	0.0704	0.0051	1.3762	0.1423	0.1409	0.0033	0.29	849.6	19.1	870.1	59.2	908.5	142.9	908.5	142.9	4.2
JG46-01_Zrn-n-73	890	0.04	0.0760	0.0032	1.9237	0.1542	0.1839	0.0026	0.04	1088.4	14.2	1088.6	54.1	1090.1	88.9	1090.1	88.9	0.1
JG46-01_Zrn-n-75	13	0.50	0.0661	0.0131	0.6193	0.1102	0.0723	0.0043	-0.28	449.8	26.4	481.9	75.8	1297.4	306.4	449.8	26.4	6.6
JG46-01_Zrn-n-76	294	0.10	0.0634	0.0032	0.9044	0.0759	0.1045	0.0022	0.29	641.2	13.0	658.0	46.1	723.1	97.9	641.2	13.0	2.5
JG46-01_Zrn-n-78	66	0.75	0.0737	0.0034	1.7566	0.1467	0.1723	0.0033	0.22	1024.8	18.5	1025.2	54.9	1006.4	104.4	1006.4	104.4	-1.8
JG46-01_Zrn-n-79	48	0.11	0.0611	0.0050	0.7585	0.0840	0.0885	0.0021	0.09	546.7	12.9	565.4	47.2	753.0	158.5	546.7	12.9	3.2
JG46-01_Zrn-n-81	269	0.12	0.0633	0.0029	1.0459	0.0853	0.1197	0.0017	-0.10	728.9	10.0	725.7	42.3	704.9	100.1	728.9	10.0	-0.4
JG46-01_Zrn-n-83	294	0.27	0.0674	0.0031	1.2025	0.0997	0.1291	0.0027	0.28	783.0	15.7	800.4	45.9	840.3	98.9	783.0	15.7	2.1
JG46-01_Zrn-n-86	337	0.25	0.0635	0.0027	0.9455	0.0768	0.1086	0.0022	0.31	664.8	12.9	674.8	39.9	714.2	90.9	664.8	12.9	1.4
JG46-01_Zrn-n-87	36	0.20	0.0652	0.0067	1.1599	0.1342	0.1313	0.0046	-0.09	795.0	26.4	772.7	61.4	828.0	175.1	795.0	26.4	-2.8
JG46-01_Zrn-n-89	72	0.67	0.0727	0.0047	1.4370	0.1328	0.1444	0.0035	0.08	869.3	19.9	899.4	54.1	964.5	130.2	964.5	130.2	6.7
JG46-01_Zrn-n-90	216	0.41	0.0663	0.0030	1.2228	0.1068	0.1339	0.0037	0.63	810.4	21.0	808.7	48.0	803.3	97.9	803.3	97.9	-0.6
JG46-01_Zrn-n-92	24	0.27	0.0805	0.0073	2.1304	0.2564	0.1925	0.0069	0.44	1134.2	37.2	1143.1	85.2	1188.4	166.8	1188.4	166.8	3.8
JG46-01_Zrn-n-93	61	0.89	0.0730	0.0067	1.4677	0.1740	0.1460	0.0044	0.35	878.4	25.2	908.1	69.6	953.9	182.8	953.9	182.8	4.8
JG46-01_Zrn-n-94	97	0.82	0.0655	0.0030	1.1529	0.0969	0.1283	0.0027	0.42	778.0	15.5	775.4	45.3	764.4	97.5	778.0	15.5	-0.3
JG46-01_Zrn-n-96	297	0.32	0.0645	0.0029	1.1480	0.0973	0.1293	0.0042	0.58	784.1	24.0	774.4	46.1	744.9	94.0	784.1	24.0	-1.2
JG46-01_Zrn-n-97	19	0.24	0.0752	0.0096	1.2957	0.1848	0.1266	0.0045	0.05	768.3	26.3	822.3	79.3	1096.5	219.2	768.3	26.3	6.5
JG46-01_Zrn-n-99	124	0.39	0.0709	0.0029	1.4677	0.1186	0.1500	0.0027	0.32	901.3	15.6	915.0	49.0	940.6	88.0	940.6	88.0	2.7
JG46-02_Zrn-b-02	186	0.70	0.0734	0.0025	1.5632	0.1014	0.1550	0.0025	0.00	929.0	14.3	954.7	39.7	1017.2	68.6	1017.2	68.6	6.1
JG46-02_Zrn-b-05	63	0.35	0.0605	0.0072	0.6082	0.0793	0.0731	0.0019	-0.07	455.0	11.5	473.5	49.7	798.7	185.5	455.0	11.5	3.9

Continúa

Continuación

JG46 Anfibolita (U. Etna) Espejo-Bautista et al., 2021

Zircón	Relaciones isotópicas corregidas									Edades corregidas				Mejor edad		Discordancia %		
	U ppm	Th/U	Pb ²⁰⁷ / Pb ²⁰⁶	±2σ	Pb ²⁰⁷ / U ²³⁵	±2σ	Pb ²⁰⁶ / U ²³⁸	±2σ	rho	Pb ²⁰⁶ / U ²³⁸	±2σ	Pb ²⁰⁷ / U ²³⁵	±2σ	Pb ²⁰⁷ / Pb ²⁰⁶	±2σ		Ma	±2σ
JG46-02_Zrn-b-07	26	0.58	0.0683	0.0066	1.4950	0.1687	0.1562	0.0053	0.27	935.4	29.8	913.1	72.6	936.8	161.2	936.8	161.2	2.5
JG46-02_Zrn-b-10	17	0.23	0.0729	0.0080	1.1983	0.1380	0.1245	0.0048	-0.02	755.9	27.9	794.7	69.0	1206.9	158.9	755.9	27.9	4.8
JG46-02_Zrn-b-12	55	0.80	0.0699	0.0040	1.3463	0.1145	0.1392	0.0031	0.40	839.9	17.8	859.5	49.2	881.9	122.4	881.9	122.4	2.5
JG46-02_Zrn-b-13	40	0.68	0.0697	0.0052	1.3136	0.1241	0.1368	0.0032	0.14	826.8	18.5	841.3	54.8	988.8	126.5	988.8	126.5	14.9
JG46-02_Zrn-b-15	35	0.20	0.0732	0.0060	1.3221	0.1260	0.1319	0.0032	-0.17	798.7	18.5	844.7	53.7	986.1	146.9	798.7	18.5	5.4
JG46-02_Zrn-b-18	146	0.47	0.0673	0.0022	1.3384	0.0871	0.1438	0.0018	0.09	866.4	10.5	861.1	38.3	832.4	73.1	832.4	73.1	-3.4
JG46-02_Zrn-b-20	25	0.25	0.0706	0.0072	1.3707	0.1562	0.1414	0.0037	-0.05	852.7	20.9	858.9	66.9	1059.7	166.3	1059.7	166.3	18.9
JG46-02_Zrn-b-22	166	0.51	0.0685	0.0026	1.4238	0.0971	0.1500	0.0021	0.19	900.8	12.0	900.9	37.6	897.9	66.4	897.9	66.4	-0.3
JG46-02_Zrn-b-24	177	0.40	0.0693	0.0036	1.2669	0.0968	0.1304	0.0023	0.09	790.1	13.4	828.2	42.9	881.6	109.2	790.1	13.4	4.6
JG46-02_Zrn-b-25	116	0.22	0.0688	0.0032	1.3229	0.1022	0.1388	0.0033	0.41	838.1	19.0	852.3	44.0	870.6	98.5	870.6	98.5	2.0
JG46-02_Zrn-b-28	2043	0.04	0.0776	0.0016	2.0015	0.1219	0.1840	0.0019	0.49	1089.1	10.6	1115.7	41.6	1135.4	41.8	1135.4	41.8	1.7
JG46-02_Zrn-b-30	59	0.06	0.0671	0.0041	1.3112	0.1152	0.1388	0.0031	0.21	837.8	18.0	842.6	49.5	834.8	127.4	834.8	127.4	-0.9
JG46-02_Zrn-b-32	55	0.97	0.0776	0.0110	1.3055	0.2279	0.1202	0.0041	0.86	731.6	24.0	831.3	93.7	1221.0	316.3	731.6	24.0	11.9
JG46-02_Zrn-b-34	988	0.26	0.0686	0.0016	1.2877	0.0806	0.1356	0.0016	0.45	819.7	9.2	839.8	35.7	883.9	51.5	883.9	51.5	4.9
JG46-02_Zrn-b-36	60	0.21	0.0589	0.0051	0.6352	0.0615	0.0785	0.0021	-0.12	487.2	12.6	493.9	37.9	789.7	148.6	487.2	12.6	1.3
JG46-02_Zrn-b-38	100	1.00	0.0696	0.0034	1.4176	0.1053	0.1469	0.0026	0.05	883.5	14.7	892.1	44.1	881.4	103.1	881.4	103.1	-1.2
JG46-02_Zrn-b-40	23	0.97	0.0639	0.0093	0.5770	0.0830	0.0667	0.0027	-0.05	416.2	16.7	448.9	53.2	1051.3	233.7	416.2	16.7	7.2
JG46-02_Zrn-b-41	441	0.20	0.0725	0.0019	1.6509	0.1060	0.1641	0.0024	0.50	979.6	13.6	988.6	40.3	992.6	54.7	992.6	54.7	0.4
JG46-02_Zrn-b-44	54	0.36	0.0653	0.0046	1.1868	0.1075	0.1297	0.0031	-0.05	786.3	18.0	785.0	51.6	903.3	118.4	786.3	18.0	-0.1
JG46-02_Zrn-b-46	23	0.21	0.0790	0.0107	1.4507	0.2034	0.1339	0.0046	-0.09	809.8	26.1	883.8	91.7	1371.0	191.9	1371.0	191.9	35.5
JG46-02_Zrn-b-48	279	0.55	0.0768	0.0020	1.8589	0.1179	0.1751	0.0025	0.42	1040.3	13.7	1065.6	41.7	1111.6	53.3	1111.6	53.3	4.1
JG46-02_Zrn-b-50	26	0.32	0.0693	0.0082	0.7944	0.1128	0.0833	0.0056	0.44	515.4	33.6	581.0	66.4	959.9	197.9	515.4	33.6	11.2
JG46-02_Zrn-n-01	390	0.59	0.0777	0.0037	1.7567	0.1271	0.1614	0.0029	-0.12	964.5	16.4	1028.5	46.2	1130.6	91.4	1130.6	91.4	9.0
JG46-02_Zrn-n-04	350	0.28	0.0788	0.0026	1.8254	0.1201	0.1688	0.0029	0.29	1005.7	16.4	1053.4	43.2	1159.7	66.2	1159.7	66.2	9.1
JG46-02_Zrn-n-06	33	0.39	0.0603	0.0070	0.6060	0.0722	0.0743	0.0027	-0.09	461.9	16.6	472.8	45.4	855.9	209.3	461.9	16.6	2.3
JG46-02_Zrn-n-08	179	0.36	0.0671	0.0024	1.3351	0.0882	0.1447	0.0022	-0.02	871.1	12.6	859.6	38.3	824.1	77.0	824.1	77.0	-4.3
JG46-02_Zrn-n-09	397	0.09	0.0786	0.0031	1.1679	0.0823	0.1080	0.0020	0.25	661.1	11.7	784.4	38.1	1152.7	81.8	661.1	11.7	15.7
JG46-02_Zrn-n-11	359	0.93	0.0620	0.0037	0.7926	0.0634	0.0930	0.0017	-0.08	573.3	10.3	591.4	35.8	655.1	127.6	573.3	10.3	3.0
JG46-02_Zrn-n-14	280	1.29	0.0701	0.0035	1.3522	0.1009	0.1401	0.0025	-0.03	845.2	14.3	867.2	43.3	921.0	106.4	921.0	106.4	5.8
JG46-02_Zrn-n-16	574	0.18	0.0680	0.0025	1.4925	0.1021	0.1558	0.0039	0.32	933.3	21.7	926.8	41.3	865.5	76.8	865.5	76.8	-7.0
JG46-02_Zrn-n-17	146	0.43	0.0714	0.0033	1.4200	0.1008	0.1445	0.0023	-0.13	870.3	13.1	895.2	41.9	949.6	94.2	949.6	94.2	5.7
JG46-02_Zrn-n-19	368	0.21	0.0709	0.0030	1.5618	0.1082	0.1585	0.0026	-0.09	948.8	14.5	953.8	43.3	943.3	90.8	943.3	90.8	-1.1
JG46-02_Zrn-n-23	1704	0.18	0.0677	0.0018	1.3379	0.0847	0.1427	0.0032	0.59	860.2	18.1	862.0	36.8	856.4	55.5	856.4	55.5	-0.6
JG46-02_Zrn-n-26	490	0.46	0.0690	0.0025	1.3814	0.0932	0.1449	0.0021	0.13	872.8	11.9	880.1	40.2	891.7	78.7	891.7	78.7	1.3
JG46-02_Zrn-n-27	155	0.01	0.0808	0.0025	2.3331	0.1544	0.2086	0.0048	0.51	1221.0	26.0	1220.0	47.2	1206.9	63.1	1206.9	63.1	-1.0
JG46-02_Zrn-n-29	594	0.08	0.0719	0.0024	1.1874	0.0838	0.1192	0.0025	0.62	725.8	14.8	793.5	38.6	976.9	70.6	725.8	14.8	8.5
JG46-02_Zrn-n-31	258	0.63	0.0688	0.0042	1.1235	0.0893	0.1171	0.0033	-0.09	714.1	19.3	763.6	41.8	879.2	127.5	714.1	19.3	6.4
JG46-02_Zrn-n-33	454	1.14	0.0727	0.0026	1.4990	0.1017	0.1490	0.0022	0.27	895.8	12.4	928.8	40.8	997.6	71.5	997.6	71.5	6.8
JG46-02_Zrn-n-35	594	0.36	0.0684	0.0020	1.3587	0.0907	0.1432	0.0028	0.62	863.1	16.1	869.9	38.9	875.4	60.2	875.4	60.2	0.6
JG46-02_Zrn-n-37	168	0.61	0.0675	0.0040	1.2151	0.1033	0.1296	0.0036	0.38	785.8	20.6	805.5	47.8	838.7	126.2	785.8	20.6	2.4
JG46-02_Zrn-n-39	451	0.35	0.0681	0.0033	1.3883	0.1110	0.1459	0.0021	0.61	877.9	11.8	881.6	46.2	857.2	99.2	857.2	99.2	-2.8
JG46-02_Zrn-n-42	37	1.15	0.0733	0.0058	1.4870	0.1450	0.1471	0.0039	0.13	884.5	22.1	916.1	60.9	992.5	163.1	992.5	163.1	7.7
JG46-02_Zrn-n-43	650	0.30	0.0666	0.0023	1.0922	0.0759	0.1173	0.0021	0.47	715.2	12.6	748.5	36.3	818.2	74.6	715.2	12.6	4.4
JG46-02_Zrn-n-45	706	0.22	0.0743	0.0025	1.5550	0.1053	0.1495	0.0023	0.46	898.2	12.9	951.8	42.1	1046.9	68.1	1046.9	68.1	9.0
JG46-02_Zrn-n-47	760	0.16	0.0693	0.0020	1.3907	0.0913	0.1447	0.0020	0.45	871.2	11.6	883.8	38.5	901.0	60.5	901.0	60.5	1.9
JG46-02_Zrn-n-49	238	0.42	0.0759	0.0024	1.9320	0.1296	0.1841	0.0030	0.49	1089.4	16.4	1090.7	44.9	1087.1	64.6	1087.1	64.6	-0.3

Continúa

Continuación

JG46 Anfibolita (U. Etna) Espejo-Bautista et al., 2021

Zircón	U ppm	Th/U	Relaciones isotópicas corregidas							Edades corregidas				Mejor edad		Discordancia %		
			$\frac{Pb^{207}}{Pb^{206}}$	$\pm 2\sigma$	$\frac{Pb^{207}}{U^{235}}$	$\pm 2\sigma$	$\frac{Pb^{206}}{U^{238}}$	$\pm 2\sigma$	rho	$\frac{Pb^{206}}{U^{238}}$	$\pm 2\sigma$	$\frac{Pb^{207}}{U^{235}}$	$\pm 2\sigma$	$\frac{Pb^{207}}{Pb^{206}}$	$\pm 2\sigma$		Ma	$\pm 2\sigma$
Zircon_01	79	0.96	0.0642	0.0028	1.2101	0.0615	0.1367	0.0028	-0.04	826.1	16.1	802.4	28.3	749.3	89.7	749.3	89.7	-10.2
Zircon_02	113	0.51	0.0708	0.0030	1.3460	0.0728	0.1355	0.0018	-0.07	819.2	10.6	862.5	31.1	942.9	98.0	942.9	98.0	13.1
Zircon_03	82	2.56	0.0673	0.0032	1.3238	0.0739	0.1425	0.0027	0.07	858.6	15.6	857.5	30.1	848.5	93.5	848.5	93.5	-1.1
Zircon_04	63	0.70	0.0666	0.0053	1.1149	0.0844	0.1221	0.0034	-0.25	742.8	19.6	755.0	40.8	887.7	151.5	742.8	19.6	1.6
Zircon_05	213	0.77	0.0668	0.0031	0.9876	0.0519	0.1071	0.0023	-0.01	656.1	13.7	696.3	26.1	814.4	96.8	656.1	13.7	5.7
Zircon_06	86	0.49	0.0686	0.0036	1.3309	0.0844	0.1404	0.0035	0.27	846.8	20.2	853.7	36.7	889.6	99.5	889.6	99.5	4.8
Zircon_07	100	0.45	0.0695	0.0043	1.3967	0.0810	0.1458	0.0050	-0.11	877.5	28.1	886.2	34.2	896.9	125.5	896.9	125.5	2.1
Zircon_08	208	0.31	0.0647	0.0036	1.0239	0.0629	0.1148	0.0025	0.01	700.8	14.9	713.5	31.6	761.4	115.0	700.8	14.9	1.7
Zircon_09	502	0.37	0.0629	0.0022	0.8885	0.0399	0.1020	0.0014	-0.14	626.5	8.3	645.2	21.5	700.9	78.0	626.5	8.3	2.9
Zircon_10	1216	0.39	0.0695	0.0016	1.3831	0.0545	0.1437	0.0011	0.16	865.9	6.3	881.1	23.1	909.2	48.2	909.2	48.2	4.7
Zircon_11	216	0.77	0.0642	0.0022	1.0916	0.0545	0.1228	0.0024	0.42	746.9	13.8	746.9	26.5	728.9	75.7	746.9	13.8	0.0
Zircon_13	487	0.49	0.0675	0.0014	1.3174	0.0529	0.1401	0.0013	0.30	845.6	7.7	852.5	22.9	858.3	49.6	858.3	49.6	1.4
Zircon_14	142	0.71	0.0673	0.0030	1.2572	0.0810	0.1343	0.0035	0.66	812.3	20.0	820.9	37.4	817.5	94.6	817.5	94.6	0.6
Zircon_15	98	0.74	0.0671	0.0042	1.1762	0.0811	0.1271	0.0032	0.13	771.3	18.7	785.3	37.2	827.0	123.2	771.3	18.7	1.7
Zircon_16	129	0.82	0.0691	0.0028	1.2816	0.0635	0.1355	0.0023	0.28	819.1	13.5	840.2	31.1	878.5	82.7	878.5	82.7	6.7
Zircon_17	315	1.03	0.0561	0.0028	0.5262	0.0303	0.0675	0.0012	0.07	421.2	7.7	428.1	20.4	516.5	89.3	421.2	7.7	1.6
Zircon_18	41	0.09	0.0694	0.0041	1.4826	0.1140	0.1550	0.0065	0.45	927.6	36.8	912.3	46.1	911.4	118.0	911.4	118.0	-1.7
Zircon_19	1101	0.83	0.0704	0.0012	1.3738	0.0549	0.1410	0.0023	0.74	850.2	13.0	877.0	23.4	936.7	37.9	936.7	37.9	9.2
Zircon_20	551	0.17	0.0704	0.0016	1.4313	0.0594	0.1469	0.0024	0.47	883.5	13.5	901.1	24.7	935.7	50.3	935.7	50.3	5.5
Zircon_21	172	1.14	0.0688	0.0031	1.3563	0.0725	0.1430	0.0036	0.15	861.4	20.5	868.4	30.5	875.5	94.2	875.5	94.2	1.6
Zircon_22	157	0.24	0.0556	0.0037	0.5252	0.0354	0.0688	0.0015	-0.10	429.1	9.3	425.9	23.7	587.3	123.2	429.1	9.3	-0.7
Zircon_23	448	0.16	0.0668	0.0021	1.0428	0.0462	0.1128	0.0016	0.20	689.0	9.7	724.1	22.8	820.4	65.4	689.0	9.7	4.8
Zircon_24	81	0.75	0.0681	0.0046	1.1052	0.0691	0.1187	0.0028	-0.35	723.0	16.2	751.5	33.0	866.9	124.8	723.0	16.2	3.7
Zircon_25	111	0.38	0.0679	0.0029	1.2590	0.0710	0.1333	0.0027	0.40	806.7	15.6	823.4	31.8	837.0	89.5	837.0	89.5	3.6
Zircon_26	795	0.61	0.0656	0.0020	1.0908	0.0456	0.1203	0.0014	-0.22	732.6	8.3	748.4	22.2	786.3	67.0	732.6	8.3	2.1
Zircon_27	194	0.48	0.0657	0.0029	0.9239	0.0504	0.1016	0.0016	0.15	624.1	9.6	662.5	26.8	797.1	87.6	624.1	9.6	5.7
Zircon_28	257	0.30	0.0639	0.0030	0.8555	0.0460	0.0970	0.0019	-0.01	596.7	11.5	626.1	25.0	734.4	94.4	596.7	11.5	4.6
Zircon_29	106	0.52	0.0605	0.0036	0.7258	0.0468	0.0870	0.0021	0.03	537.6	12.7	551.7	27.2	646.5	111.5	537.6	12.7	2.5
Zircon_30	77	0.63	0.0638	0.0035	1.0784	0.0764	0.1200	0.0039	0.30	730.4	22.9	739.4	37.6	773.7	124.3	730.4	22.9	1.2
Zircon_31	80	1.17	0.0656	0.0039	1.0919	0.0760	0.1190	0.0021	-0.01	724.9	12.5	743.1	36.0	837.7	115.2	724.9	12.5	2.4
Zircon_32	584	1.09	0.0721	0.0018	1.5053	0.0597	0.1509	0.0017	0.07	906.2	9.6	931.9	24.3	982.8	52.6	982.8	52.6	7.7
Zircon_33	136	0.43	0.0630	0.0032	0.8765	0.0498	0.1010	0.0019	-0.09	620.1	11.6	636.3	26.7	715.1	102.7	620.1	11.6	2.5
Zircon_34	102	0.81	0.0661	0.0039	1.1460	0.0815	0.1236	0.0039	0.16	751.3	22.8	770.8	38.6	835.6	127.6	751.3	22.8	2.5
Zircon_35	292	0.05	0.0670	0.0033	1.1470	0.0693	0.1238	0.0026	0.30	752.8	15.0	775.1	32.6	830.7	101.2	752.8	15.0	2.8
Zircon_36	44	1.76	0.0712	0.0055	1.2893	0.1048	0.1328	0.0050	-0.07	803.4	28.5	833.0	46.8	952.6	148.8	952.6	148.8	15.6
Zircon_37	74	0.88	0.0705	0.0030	1.4533	0.0750	0.1506	0.0035	0.56	904.5	19.8	908.3	30.9	917.2	92.2	917.2	92.2	1.3
Zircon_38	1574	0.50	0.0690	0.0022	1.1421	0.0508	0.1195	0.0015	0.07	727.7	9.1	772.9	24.1	893.0	68.9	727.7	9.1	5.8
Zircon_39	212	1.69	0.0672	0.0020	1.2945	0.0638	0.1376	0.0023	0.60	831.4	13.1	840.6	28.1	842.9	60.9	842.9	60.9	1.3
Zircon_40	322	1.80	0.0691	0.0020	1.3609	0.0611	0.1423	0.0019	0.37	857.7	11.2	870.4	25.9	890.2	61.5	890.2	61.5	3.6

JG30 Meta-granitoide milonítico		Espejo-Bautista et al., 2021																	
Zircón	U ppm	Th/U	Relaciones isotópicas corregidas							rho	Edades corregidas						Mejor edad		Discordancia %
			$\frac{Pb^{207}}{Pb^{206}}$	$\pm 2\sigma$	$\frac{Pb^{207}}{U^{235}}$	$\pm 2\sigma$	$\frac{Pb^{206}}{U^{238}}$	$\pm 2\sigma$	$\frac{Pb^{206}}{U^{238}}$		$\pm 2\sigma$	$\frac{Pb^{207}}{U^{235}}$	$\pm 2\sigma$	$\frac{Pb^{207}}{Pb^{206}}$	$\pm 2\sigma$	Ma	$\pm 2\sigma$		
Zircon_16_2	252	2.21	0.0744	0.0026	1.5675	0.0746	0.1528	0.0024	0.19	916.8	13.7	955.8	29.6	1040.1	74.8	916.8	13.7	4.0	
Zircon_9_1	344	2.33	0.0726	0.0028	1.4291	0.0732	0.1425	0.0019	0.27	859.0	10.8	899.1	30.5	990.2	79.5	859.0	10.8	4.4	
Zircon_11_2	85	1.16	0.0714	0.0044	1.2908	0.0922	0.1310	0.0033	-0.02	793.5	19.0	835.4	40.2	949.7	119.9	793.5	19.0	5.0	
Zircon_4_2	344	2.32	0.0817	0.0023	1.4729	0.0652	0.1306	0.0017	0.36	791.3	10.1	917.8	26.8	1229.0	58.3	791.3	10.1	13.7	
Zircon_8_1	452	0.51	0.0690	0.0022	1.2175	0.0549	0.1278	0.0016	0.12	775.4	9.4	807.7	25.0	891.9	67.9	775.4	9.4	3.9	
Zircon_31_2	332	1.67	0.0705	0.0022	1.2248	0.0543	0.1255	0.0016	0.19	762.5	9.3	810.5	24.6	929.8	65.6	762.5	9.3	5.9	
Zircon_5_1	526	0.48	0.0650	0.0026	1.1225	0.0552	0.1249	0.0021	0.07	759.1	12.4	763.2	26.5	762.9	86.1	759.1	12.4	0.5	
Zircon_29_2	174	2.76	0.0781	0.0047	1.3417	0.0895	0.1247	0.0028	0.10	757.9	16.1	860.5	39.1	1120.6	124.4	757.9	16.1	11.9	
Zircon_32_2	145	0.27	0.0733	0.0031	1.2790	0.0771	0.1247	0.0034	0.35	757.5	19.8	833.6	34.0	1029.1	99.1	757.5	19.8	9.1	
Zircon_10_2	106	1.36	0.0724	0.0046	1.2047	0.0755	0.1229	0.0029	0.02	747.2	17.0	806.5	38.9	983.7	119.1	747.2	17.0	7.3	
Zircon_12_2	349	1.41	0.0682	0.0022	1.1403	0.0480	0.1208	0.0021	0.08	735.3	12.0	771.6	22.7	859.4	67.7	735.3	12.0	4.7	
Zircon_2_2	239	0.86	0.0880	0.0042	1.4556	0.0754	0.1193	0.0022	-0.06	726.7	12.7	910.2	31.0	1364.9	91.2	726.7	12.7	20.1	
Zircon_14_2	155	1.43	0.0743	0.0038	1.2080	0.0673	0.1182	0.0027	-0.06	720.6	15.8	802.0	30.7	1023.3	106.6	720.6	15.8	10.1	
Zircon_18_2	1128	0.18	0.0686	0.0015	1.0990	0.0439	0.1163	0.0014	0.47	709.5	8.3	752.3	21.2	883.9	46.7	709.5	8.3	5.6	
Zircon_26_2	146	0.51	0.0695	0.0034	1.0484	0.0596	0.1083	0.0033	0.03	662.6	19.5	725.6	29.5	910.2	116.3	662.6	19.5	8.6	
Zircon_20_2	657	0.19	0.0761	0.0020	1.1209	0.0471	0.1066	0.0015	0.17	653.4	9.0	762.9	22.4	1094.5	52.3	653.4	9.0	14.3	
Zircon_28_2	175	2.14	0.0734	0.0028	1.0658	0.0564	0.1051	0.0016	0.42	644.6	9.7	734.9	27.6	1011.1	79.1	644.6	9.7	12.2	
Zircon_35	158	1.82	0.0784	0.0048	0.8912	0.0607	0.0818	0.0021	0.19	507.3	13.0	644.0	32.6	1121.0	123.9	507.3	13.0	21.2	
Zircon_33_2	515	0.57	0.0671	0.0039	0.5252	0.0357	0.0566	0.0013	0.21	355.0	7.9	427.5	23.6	814.0	128.6	355.0	7.9	16.9	
Zircon_6_1	1890	0.31	0.0567	0.0026	0.3354	0.0186	0.0428	0.0007	0.07	270.6	4.5	293.3	14.1	478.4	100.8	270.6	4.5	7.7	
Zircon_23_2	697	0.60	0.0537	0.0044	0.2629	0.0211	0.0356	0.0008	-0.23	225.5	5.1	236.3	16.8	511.9	146.5	225.5	5.1	4.5	
Zircon_19_2	2100	0.24	0.0537	0.0014	0.2633	0.0105	0.0355	0.0005	0.18	225.2	3.4	237.3	8.4	353.0	59.6	225.2	3.4	5.0	
Zircon_3_2	499	0.16	0.0597	0.0040	0.2701	0.0210	0.0325	0.0008	0.19	206.2	5.2	242.1	16.5	596.9	127.4	206.2	5.2	14.8	
Zircon_22_2	1938	0.29	0.0691	0.0043	0.3034	0.0242	0.0319	0.0007	0.38	202.9	4.9	267.8	18.7	892.7	146.6	202.9	4.9	24.2	
Zircon_17_2	440	0.12	0.0538	0.0040	0.2370	0.0223	0.0318	0.0010	0.49	202.2	6.7	215.4	17.9	429.8	159.2	202.2	6.7	6.1	
Zircon_34_2	2022	0.36	0.0512	0.0017	0.2238	0.0113	0.0315	0.0008	0.49	200.1	5.6	204.8	9.3	299.0	59.1	200.1	5.6	2.2	
Zircon_1	2932	0.36	0.0540	0.0015	0.2335	0.0106	0.0313	0.0005	0.50	198.7	3.7	212.9	8.7	363.4	66.4	198.7	3.7	6.6	
Zircon_7_1	817	0.23	0.0517	0.0032	0.2147	0.0139	0.0301	0.0005	-0.27	191.5	3.5	197.3	11.6	406.2	97.1	191.5	3.5	2.9	
Zircon_25_2	1041	0.63	0.0526	0.0045	0.2170	0.0198	0.0299	0.0006	-0.04	190.2	3.8	199.1	16.7	461.7	102.6	190.2	3.8	4.4	
Zircon_30_2	1735	0.47	0.0662	0.0034	0.2757	0.0252	0.0297	0.0013	0.87	188.7	8.3	245.6	20.0	778.6	109.1	188.7	8.3	23.1	
Zircon_27_2	924	0.53	0.0524	0.0036	0.2123	0.0153	0.0294	0.0011	0.30	187.3	7.3	195.1	12.7	375.6	132.6	187.3	7.3	3.9	

SM21-04b Esquisto pelítico con Grt (U. Etna) Espejo-Bautista et al., 2022																		
Zircón	U ppm	Th/U	Relaciones isotópicas corregidas						rho	Edades corregidas						Mejor edad		Discordancia %
			$\frac{Pb^{207}}{Pb^{206}}$	$\pm 2\sigma$	$\frac{Pb^{207}}{U^{235}}$	$\pm 2\sigma$	$\frac{Pb^{206}}{U^{238}}$	$\pm 2\sigma$		$\frac{Pb^{206}}{U^{238}}$	$\pm 2\sigma$	$\frac{Pb^{207}}{U^{235}}$	$\pm 2\sigma$	$\frac{Pb^{207}}{Pb^{206}}$	$\pm 2\sigma$	Ma	$\pm 2\sigma$	
M2_SM21_04b_Zrn01	483	0.29	0.0570	0.0022	0.5817	0.0237	0.0743	0.0022	0.31	462.0	13.3	464.7	15.2	467.6	88.6	462.0	13.3	0.6
M2_SM21_04b_Zrn02	209	0.08	0.0487	0.0053	0.2685	0.0330	0.0396	0.0024	-0.02	250.2	14.6	240.1	25.8	58.9	234.1	250.2	14.6	-4.2
M2_SM21_04b_Zrn03	197	0.40	0.0795	0.0028	2.2186	0.0831	0.2032	0.0061	0.25	1192.4	32.7	1184.5	26.1	1178.3	76.0	1192.4	32.7	-1.2
M2_SM21_04b_Zrn04	551	0.25	0.0611	0.0021	0.9005	0.0326	0.1064	0.0034	0.41	651.9	19.7	651.4	17.4	631.0	72.9	651.9	19.7	-0.1
M2_SM21_04b_Zrn05	171	0.50	0.0768	0.0028	1.9487	0.0742	0.1859	0.0055	0.08	1099.3	29.8	1100.4	27.6	1102.2	71.1	1099.3	29.8	0.3
M3_SM21_04b_Zrn07	290	0.25	0.0561	0.0024	0.5726	0.0234	0.0747	0.0023	0.45	464.5	13.7	461.3	16.4	427.9	95.0	464.5	13.7	-0.7
M3_SM21_04b_Zrn08	659	0.51	0.0598	0.0031	0.5531	0.0297	0.0676	0.0022	0.16	421.4	13.6	446.2	19.3	575.7	109.2	421.4	13.6	5.6
M3_SM21_04b_Zrn09	186	0.37	0.0578	0.0028	0.5758	0.0290	0.0722	0.0023	0.15	449.4	13.7	459.9	18.7	478.7	110.1	449.4	13.7	2.3
M3_SM21_04b_Zrn10	331	0.41	0.0561	0.0026	0.5822	0.0271	0.0749	0.0025	0.09	465.8	15.1	465.1	17.4	432.5	108.1	465.8	15.1	-0.2
M3_SM21_04b_Zrn11	456	0.59	0.0561	0.0022	0.5689	0.0223	0.0740	0.0023	0.39	460.1	14.0	458.9	15.5	431.7	87.3	460.1	14.0	-0.3
M3_SM21_04b_Zrn12	292	0.89	0.0784	0.0025	2.1560	0.0804	0.1986	0.0068	0.32	1167.3	36.8	1165.9	25.9	1151.1	65.2	1167.3	36.8	-1.4
M3_SM21_04b_Zrn14	340	0.46	0.0792	0.0024	2.1633	0.0701	0.1978	0.0059	0.48	1163.6	31.9	1168.2	22.3	1169.2	58.3	1163.6	31.9	0.5
M3_SM21_04b_Zrn15	1077	0.06	0.0646	0.0021	0.5753	0.0211	0.0648	0.0020	0.14	404.7	12.0	461.1	13.5	753.5	67.5	404.7	12.0	12.2
M3_SM21_04b_Zrn16	568	0.50	0.0569	0.0025	0.5773	0.0254	0.0740	0.0023	0.37	460.2	13.6	461.9	16.2	466.3	94.6	460.2	13.6	0.4
M3_SM21_04b_Zrn17	513	0.17	0.0536	0.0025	0.3540	0.0167	0.0475	0.0016	0.36	299.1	9.8	307.0	12.5	318.9	108.7	299.1	9.8	2.6
M3_SM21_04b_Zrn18	437	0.20	0.0585	0.0025	0.6367	0.0279	0.0785	0.0025	0.41	487.2	15.0	499.3	17.2	527.7	93.7	487.2	15.0	2.4
M3_SM21_04b_Zrn19	501	0.29	0.0592	0.0047	0.5873	0.0439	0.0730	0.0026	0.36	453.9	15.4	468.3	27.6	555.1	158.0	453.9	15.4	3.1
M3_SM21_04b_Zrn20	526	0.27	0.0563	0.0019	0.5660	0.0205	0.0729	0.0021	0.20	453.8	12.8	454.9	13.3	473.1	63.4	453.8	12.8	0.2
M3_SM21_04b_Zrn21	560	0.13	0.0564	0.0031	0.3457	0.0232	0.0439	0.0018	-0.01	276.8	11.3	301.2	17.3	457.3	120.0	276.8	11.3	8.1
M3_SM21_04b_Zrn22	101	0.75	0.0602	0.0054	0.6228	0.0560	0.0761	0.0034	0.27	472.5	20.4	488.7	35.0	546.3	208.1	472.5	20.4	3.3
M3_SM21_04b_Zrn23	196	0.32	0.0558	0.0025	0.5702	0.0270	0.0742	0.0024	0.14	461.2	14.2	459.9	16.1	435.1	91.1	461.2	14.2	-0.3
M3_SM21_04b_Zrn24	309	1.46	0.0598	0.0020	0.8143	0.0286	0.0992	0.0031	0.48	609.8	18.4	604.1	15.9	581.1	73.8	609.8	18.4	-0.9
M3_SM21_04b_Zrn25	385	0.80	0.0594	0.0027	0.5726	0.0277	0.0699	0.0025	0.22	435.3	14.8	458.8	17.9	563.0	100.0	435.3	14.8	5.1
M3_SM21_04b_Zrn26	498	0.12	0.0576	0.0020	0.5887	0.0226	0.0743	0.0022	0.07	461.9	13.5	469.3	14.6	498.1	77.8	461.9	13.5	1.6
M3_SM21_04b_Zrn27	364	0.42	0.0564	0.0023	0.5373	0.0223	0.0695	0.0021	0.38	433.2	12.7	435.7	14.8	439.4	94.6	433.2	12.7	0.6
M3_SM21_04b_Zrn28	107	0.33	0.0525	0.0042	0.6597	0.0576	0.0913	0.0044	0.16	563.2	26.0	510.9	34.7	241.5	190.7	563.2	26.0	-10.2
M3_SM21_04b_Zrn29	453	0.32	0.0586	0.0020	0.5975	0.0217	0.0744	0.0022	0.37	462.4	13.2	475.1	13.8	552.9	68.5	462.4	13.2	2.7
M3_SM21_04b_Zrn30	478	0.41	0.0571	0.0019	0.5666	0.0199	0.0728	0.0022	0.32	452.9	13.3	455.4	12.9	493.7	66.6	452.9	13.3	0.6
M3_SM21_04b_Zrn31	295	0.02	0.0726	0.0022	1.6716	0.0582	0.1688	0.0050	0.17	1005.6	27.8	996.8	22.0	996.4	61.7	1005.6	27.8	-0.9
M3_SM21_04b_Zrn32	355	0.43	0.0596	0.0025	0.7182	0.0371	0.0878	0.0027	-0.32	542.6	16.1	548.3	21.8	573.2	88.4	542.6	16.1	1.0
M3_SM21_04b_Zrn33	506	0.34	0.0931	0.0024	3.2816	0.0960	0.2573	0.0074	0.34	1475.8	37.9	1476.2	23.0	1486.7	48.3	1486.7	37.9	0.7
M3_SM21_04b_Zrn34	180	0.29	0.0562	0.0025	0.5715	0.0255	0.0746	0.0024	0.45	464.0	14.2	457.7	16.6	445.3	98.1	464.0	14.2	-1.4
M3_SM21_04b_Zrn35	106	0.83	0.0555	0.0035	0.5996	0.0375	0.0796	0.0027	0.34	493.4	15.9	474.3	23.4	365.9	143.3	493.4	15.9	-4.0
M3_SM21_04b_Zrn36	393	0.60	0.0610	0.0020	0.8861	0.0325	0.1056	0.0033	0.15	647.1	19.2	643.8	17.5	634.4	70.8	647.1	19.2	-0.5
M3_SM21_04b_Zrn37	129	0.18	0.0752	0.0052	1.9165	0.1085	0.1851	0.0067	0.78	1094.7	36.4	1085.5	38.6	1057.9	143.0	1094.7	36.4	-3.5
M3_SM21_04b_Zrn38	89	0.47	0.0789	0.0030	2.2125	0.0897	0.2060	0.0068	0.28	1207.1	36.3	1181.6	28.5	1149.8	74.8	1149.8	36.3	-5.0
M3_SM21_04b_Zrn39	472	0.19	0.0574	0.0025	0.5753	0.0256	0.0738	0.0023	0.31	458.8	13.6	460.7	16.5	488.2	97.5	458.8	13.6	0.4
M4_SM21_04b_Zrn40	2023	0.78	0.0578	0.0019	0.4843	0.0168	0.0618	0.0020	0.50	386.8	11.9	400.9	11.4	517.3	73.9	386.8	11.9	3.5
M4_SM21_04b_Zrn41	525	0.29	0.0559	0.0019	0.5737	0.0222	0.0748	0.0024	-0.03	465.1	14.5	459.5	14.5	440.7	73.8	465.1	14.5	-1.2
M4_SM21_04b_Zrn42	315	0.50	0.0576	0.0024	0.6088	0.0268	0.0775	0.0023	0.25	481.3	13.9	481.8	17.0	508.1	87.7	481.3	13.9	0.1
M4_SM21_04b_Zrn43	492	0.17	0.0544	0.0020	0.5437	0.0214	0.0732	0.0023	0.09	455.2	13.6	440.2	14.0	383.3	87.6	455.2	13.6	-3.4
M4_SM21_04b_Zrn44	258	0.23	0.0561	0.0021	0.5569	0.0221	0.0728	0.0023	0.23	453.2	13.6	448.8	14.4	440.3	81.6	453.2	13.6	-1.0
M4_SM21_04b_Zrn45	709	0.25	0.0552	0.0022	0.4760	0.0204	0.0624	0.0020	0.15	390.1	11.9	394.9	14.0	408.1	88.5	390.1	11.9	1.2
M4_SM21_04b_Zrn46	219	1.00	0.0595	0.0026	0.5985	0.0265	0.0736	0.0023	0.32	457.9	13.9	475.4	17.0	563.0	99.3	457.9	13.9	3.7
M4_SM21_04b_Zrn48	758	1.13	0.0555	0.0019	0.5263	0.0237	0.0696	0.0025	0.03	433.8	15.2	428.3	15.9	418.2	77.2	433.8	15.2	-1.3
M4_SM21_04b_Zrn49	103	0.97	0.0585	0.0049	0.5862	0.0515	0.0737	0.0032	0.05	458.4	18.9	464.8	32.4	514.1	215.5	458.4	18.9	1.4
M4_SM21_04b_Zrn50	670	0.95	0.0547	0.0020	0.5652	0.0209	0.0755	0.0023	0.53	469.2	14.0	454.6	13.6	387.4	83.9	469.2	14.0	-3.2
M4_SM21_04b_Zrn51	275	0.46	0.0562	0.0029	0.5739	0.0303	0.0744	0.0025	0.19	462.7	15.2	458.8	19.7	451.7	98.0	462.7	15.2	-0.8
M4_SM21_04b_Zrn52	267	0.54	0.0569	0.0025	0.5814	0.0244	0.0735	0.0023	0.36	457.0	14.0	464.4	15.6	477.1	91.2	457.0	14.0	1.6
M4_SM21_04b_Zrn53	343	0.30	0.0573	0.0023	0.5911	0.0286	0.0746	0.0023	-0.21	463.5	13.9	469.9	18.2	473.4	91.9	463.5	13.9	1.4

Continúa

Continuación

SM21-04b Esquisto pelítico con Grt (U. Etlá) Espejo-Bautista et al., 2022																		
Zircón	U ppm	Th/U	Relaciones isotópicas corregidas							Edades corregidas						Mejor edad		Discordancia %
			$\frac{Pb^{207}}{Pb^{206}}$	$\pm 2\sigma$	$\frac{Pb^{207}}{U^{235}}$	$\pm 2\sigma$	$\frac{Pb^{206}}{U^{238}}$	$\pm 2\sigma$	rho	$\frac{Pb^{206}}{U^{238}}$	$\pm 2\sigma$	$\frac{Pb^{207}}{U^{235}}$	$\pm 2\sigma$	$\frac{Pb^{207}}{Pb^{206}}$	$\pm 2\sigma$	Ma	$\pm 2\sigma$	
M4_SM21_04b_Zrn54	557	0.44	0.0564	0.0019	0.5811	0.0225	0.0741	0.0022	0.35	460.5	13.3	464.5	14.4	470.1	83.9	460.5	13.3	0.9
M4_SM21_04b_Zrn55	329	0.58	0.0743	0.0021	1.7030	0.0574	0.1660	0.0051	0.15	990.0	28.1	1008.5	21.8	1043.5	57.3	990.0	28.1	5.1
M4_SM21_04b_Zrn56	1317	0.19	0.0564	0.0017	0.5658	0.0188	0.0731	0.0022	0.38	455.0	13.3	455.0	12.2	460.9	67.7	455.0	13.3	0.0
M4_SM21_04b_Zrn57	1253	1.39	0.0558	0.0016	0.5396	0.0180	0.0705	0.0020	0.15	439.3	12.3	437.8	11.9	435.2	63.4	439.3	12.3	-0.3
M4_SM21_04b_Zrn58	1010	0.14	0.0550	0.0024	0.3575	0.0154	0.0475	0.0015	0.50	299.1	9.2	310.2	11.6	398.1	101.8	299.1	9.2	3.6
M4_SM21_04b_Zrn59	591	1.49	0.0568	0.0019	0.5325	0.0208	0.0687	0.0021	0.41	428.3	12.9	432.8	13.9	470.1	75.7	428.3	12.9	1.0
M4_SM21_04b_Zrn60	284	0.72	0.0601	0.0035	0.6233	0.0386	0.0760	0.0025	0.04	472.0	14.8	490.2	24.4	571.4	139.2	472.0	14.8	3.7
M4_SM21_04b_Zrn61	415	0.64	0.0570	0.0020	0.6091	0.0249	0.0775	0.0025	0.21	481.4	14.7	482.0	15.6	483.1	83.8	481.4	14.7	0.1
M4_SM21_04b_Zrn62	431	1.27	0.0552	0.0020	0.5632	0.0222	0.0744	0.0022	0.10	462.7	13.2	452.9	14.4	400.7	81.4	462.7	13.2	-2.2
M4_SM21_04b_Zrn63	762	0.34	0.0550	0.0018	0.5507	0.0209	0.0733	0.0022	-0.11	455.8	13.1	444.9	13.7	399.4	74.5	455.8	13.1	-2.4
M4_SM21_04b_Zrn64	106	0.89	0.0507	0.0045	0.5156	0.0468	0.0746	0.0028	0.11	463.4	17.0	420.6	32.3	80.5	219.2	463.4	17.0	-10.2
M4_SM21_04b_Zrn65	532	0.83	0.0576	0.0033	0.5948	0.0329	0.0751	0.0024	0.41	466.5	14.3	472.6	20.6	480.1	124.1	466.5	14.3	1.3
M4_SM21_04b_Zrn66	806	0.17	0.0782	0.0025	1.9051	0.0666	0.1766	0.0053	0.25	1048.1	29.2	1082.1	23.1	1146.6	61.9	1048.1	29.2	8.6
M4_SM21_04b_Zrn67	248	0.22	0.0812	0.0025	2.4989	0.0782	0.2222	0.0069	0.49	1293.2	36.6	1271.2	22.7	1219.7	62.8	1219.7	62.8	-6.0
M4_SM21_04b_Zrn68	669	0.28	0.0813	0.0025	2.1898	0.0726	0.1953	0.0059	0.44	1149.8	31.7	1177.1	23.2	1223.6	60.8	1149.8	31.7	6.0
M4_SM21_04b_Zrn69	224	1.36	0.0593	0.0044	0.5980	0.0459	0.0738	0.0025	0.05	458.7	15.3	473.1	29.4	517.0	170.6	458.7	15.3	3.0
M4_SM21_04b_Zrn70	1101	0.20	0.0570	0.0028	0.3544	0.0224	0.0456	0.0019	-0.26	287.4	11.4	307.4	16.8	473.5	111.8	287.4	11.4	6.5
M4_SM21_04b_Zrn71	460	0.33	0.0560	0.0018	0.5709	0.0210	0.0741	0.0022	0.14	460.6	13.5	458.0	13.5	448.0	66.3	460.6	13.5	-0.6
M4_SM21_04b_Zrn72	236	0.31	0.0638	0.0022	1.1202	0.0424	0.1284	0.0041	0.33	778.6	23.4	761.8	20.2	721.8	74.7	778.6	23.4	-2.2
M4_SM21_04b_Zrn73	570	0.72	0.0562	0.0020	0.5685	0.0227	0.0733	0.0022	0.12	456.0	13.3	456.2	14.7	441.8	79.6	456.0	13.3	0.1
M4_SM21_04b_Zrn74	134	0.45	0.0579	0.0034	0.6260	0.0350	0.0795	0.0026	0.06	493.3	15.6	491.1	21.9	464.0	127.6	493.3	15.6	-0.5
M4_SM21_04b_Zrn75	217	0.54	0.0567	0.0026	0.5657	0.0262	0.0722	0.0023	0.32	449.6	14.0	453.9	17.0	460.4	97.2	449.6	14.0	0.9
M4_SM21_04b_Zrn76	2826	0.15	0.0601	0.0020	0.3840	0.0159	0.0466	0.0016	-0.09	293.6	10.0	329.7	11.7	600.8	71.9	293.6	10.0	11.0
M4_SM21_04b_Zrn77	172	0.25	0.0800	0.0032	2.2169	0.0996	0.1999	0.0063	-0.09	1174.8	33.9	1183.4	31.6	1183.6	77.4	1174.8	33.9	0.7
M4_SM21_04b_Zrn78	463	0.21	0.0569	0.0022	0.5321	0.0240	0.0675	0.0025	0.12	421.1	15.0	434.9	14.7	482.2	81.5	421.1	15.0	3.2
M4_SM21_04b_Zrn79	758	0.28	0.0550	0.0017	0.5397	0.0200	0.0702	0.0022	-0.05	437.5	13.5	437.8	13.2	402.7	67.6	437.5	13.5	0.1
M4_SM21_04b_Zrn80	775	0.23	0.0561	0.0016	0.5531	0.0187	0.0708	0.0023	0.38	441.0	13.9	446.7	12.2	449.9	64.5	441.0	13.9	1.3
M4_SM21_04b_Zrn81	330	0.21	0.0945	0.0025	3.4161	0.1105	0.2598	0.0075	-0.18	1489.0	38.5	1507.1	25.2	1515.0	50.1	1515.0	50.1	1.7
M4_SM21_04b_Zrn82	336	0.42	0.0564	0.0034	0.5354	0.0339	0.0676	0.0026	0.13	421.6	15.8	434.5	22.5	446.0	134.1	421.6	15.8	3.0
M4_SM21_04b_Zrn83	380	0.21	0.0573	0.0024	0.6016	0.0229	0.0766	0.0025	0.55	475.9	14.8	480.4	16.3	483.0	95.3	475.9	14.8	1.0
M4_SM21_04b_Zrn84	600	0.02	0.0545	0.0028	0.4564	0.0325	0.0603	0.0048	0.61	377.1	29.4	380.7	22.7	417.4	153.2	377.1	29.4	0.9
M4_SM21_04b_Zrn85	99	0.54	0.0534	0.0031	0.5324	0.0333	0.0719	0.0024	0.14	447.6	14.7	430.5	21.8	269.9	143.4	447.6	14.7	-4.0
M4_SM21_04b_Zrn86	488	0.16	0.0559	0.0025	0.4931	0.0329	0.0630	0.0033	-0.14	393.6	19.8	405.4	22.5	428.7	102.9	393.6	19.8	2.9
M4_SM21_04b_Zrn87	526	0.32	0.0574	0.0021	0.5671	0.0204	0.0723	0.0023	0.36	449.9	14.1	458.5	15.3	495.3	81.0	449.9	14.1	1.9
M4_SM21_04b_Zrn88	1156	0.82	0.0569	0.0022	0.4860	0.0209	0.0624	0.0018	-0.07	390.3	11.2	402.0	14.3	481.9	86.6	390.3	11.2	2.9
M4_SM21_04b_Zrn89	414	0.62	0.0564	0.0031	0.4790	0.0287	0.0625	0.0021	0.00	390.9	13.0	396.4	20.0	439.8	132.9	390.9	13.0	1.4
M4_SM21_04b_Zrn90	724	0.16	0.0764	0.0025	1.8088	0.0642	0.1742	0.0053	0.31	1035.1	28.8	1047.7	23.1	1097.9	67.5	1035.1	28.8	5.7
M4_SM21_04b_Zrn91	502	0.34	0.0525	0.0033	0.4524	0.0276	0.0627	0.0026	0.37	392.0	15.8	378.2	19.4	274.3	148.8	392.0	15.8	-3.6
M4_SM21_04b_Zrn92	1013	0.20	0.0565	0.0018	0.5484	0.0196	0.0713	0.0023	0.27	443.9	13.7	445.2	11.9	461.0	70.7	443.9	13.7	0.3
M4_SM21_04b_Zrn93	871	0.30	0.0847	0.0028	2.4167	0.0862	0.2114	0.0068	0.38	1235.8	36.1	1246.5	25.3	1302.1	63.2	1302.1	63.2	5.1
M4_SM21_04b_Zrn94	589	0.86	0.0580	0.0023	0.6016	0.0252	0.0766	0.0027	0.40	476.0	15.9	477.4	16.0	526.6	83.6	476.0	15.9	0.3
M4_SM21_04b_Zrn95	765	0.60	0.0567	0.0027	0.4790	0.0217	0.0630	0.0021	0.36	393.7	12.8	399.9	16.7	452.8	107.6	393.7	12.8	1.6
M4_SM21_04b_Zrn96	1367	0.94	0.0585	0.0022	0.5428	0.0208	0.0690	0.0021	0.40	429.9	12.6	440.0	13.7	538.2	82.0	429.9	12.6	2.3

SM21-06 Esquisto pelítico sin Grt (U. Etna)

Espejo-Bautista et al., 2022

Zircón	U ppm	Th/U	Relaciones isotópicas corregidas						rho	Edades corregidas						Mejor edad		Discordancia %
			$\frac{Pb^{207}}{Pb^{206}}$	$\pm 2\sigma$	$\frac{Pb^{207}}{U^{235}}$	$\pm 2\sigma$	$\frac{Pb^{206}}{U^{238}}$	$\pm 2\sigma$		$\frac{Pb^{206}}{U^{238}}$	$\pm 2\sigma$	$\frac{Pb^{207}}{U^{235}}$	$\pm 2\sigma$	$\frac{Pb^{207}}{Pb^{206}}$	$\pm 2\sigma$	Ma	$\pm 2\sigma$	
M2_SM21_06_Zrn01	141	0.30	0.0575	0.0032	0.6724	0.0366	0.0846	0.0026	0.38	523.6	15.6	519.4	22.2	474.1	119.0	523.6	15.6	-0.8
M2_SM21_06_Zrn02	330	0.13	0.0564	0.0024	0.5911	0.0268	0.0761	0.0024	0.11	473.0	14.6	470.6	17.2	445.2	95.7	473.0	14.6	-0.5
M2_SM21_06_Zrn05	182	0.78	0.1271	0.0035	5.8760	0.1977	0.3333	0.0106	0.21	1853.9	51.3	1956.2	29.3	2054.2	49.1	1853.9	51.3	9.8
M2_SM21_06_Zrn06	257	0.15	0.0677	0.0034	1.2349	0.0620	0.1312	0.0043	0.34	794.5	24.6	815.0	27.6	844.2	100.0	794.5	24.6	2.5
M2_SM21_06_Zrn07	925	0.33	0.0604	0.0019	0.7734	0.0250	0.0934	0.0029	0.64	575.5	16.9	581.4	14.3	612.2	68.5	575.5	16.9	1.0
M2_SM21_06_Zrn08	219	0.45	0.0787	0.0036	1.8309	0.0885	0.1687	0.0051	0.16	1004.6	28.3	1057.5	34.1	1152.0	99.6	1004.6	28.3	12.8
M2_SM21_06_Zrn04	117	0.43	0.1910	0.0047	12.5802	0.3821	0.4755	0.0142	0.27	2507.2	62.0	2647.5	28.0	2752.1	43.9	2752.1	43.9	8.9
M4_SM21_06_Zrn09_1	1209	1.59	0.0552	0.0033	0.3014	0.0243	0.0399	0.0026	0.05	252.3	16.1	267.2	19.0	408.6	132.0	252.3	16.1	5.6
M4_SM21_06_Zrn09_2	487	0.68	0.0549	0.0049	0.5520	0.0454	0.0729	0.0029	0.45	453.9	17.5	445.7	29.4	390.3	197.6	453.9	17.5	-1.8
M4_SM21_06_Zrn10	1318	0.07	0.0655	0.0024	0.9149	0.0359	0.1024	0.0033	0.36	628.7	19.3	659.4	18.7	785.8	76.4	628.7	19.3	4.7
M4_SM21_06_Zrn11	88	0.66	0.0750	0.0033	1.7409	0.0794	0.1687	0.0058	0.25	1004.8	32.0	1019.9	29.9	1042.3	90.9	1004.8	32.0	3.6
M4_SM21_06_Zrn13	488	0.06	0.0598	0.0034	0.7519	0.0443	0.0906	0.0033	0.23	558.9	19.5	568.1	25.6	573.1	130.4	558.9	19.5	1.6
M4_SM21_06_Zrn14	125	0.39	0.0596	0.0038	0.8079	0.0504	0.0979	0.0038	0.33	602.0	22.4	599.5	28.3	559.7	136.6	602.0	22.4	-0.4
M4_SM21_06_Zrn15	189	0.43	0.0943	0.0028	3.3867	0.1104	0.2603	0.0079	0.22	1491.3	40.4	1500.1	25.5	1507.3	56.2	1491.3	40.4	1.1
M4_SM21_06_Zrn16	589	0.26	0.0632	0.0022	0.9677	0.0367	0.1119	0.0033	0.16	683.5	19.4	686.4	19.0	702.4	75.2	683.5	19.4	0.4
M4_SM21_06_Zrn17	727	0.19	0.0569	0.0019	0.6316	0.0232	0.0804	0.0025	0.20	498.6	14.6	496.6	14.6	475.8	75.2	498.6	14.6	-0.4
M4_SM21_06_Zrn18	210	0.83	0.1091	0.0030	4.6371	0.1418	0.3096	0.0092	0.51	1738.7	45.4	1754.9	25.5	1779.7	50.5	1738.7	45.4	2.3
M4_SM21_06_Zrn19	246	0.13	0.0787	0.0032	2.0323	0.0898	0.1872	0.0064	0.24	1106.1	34.6	1124.4	30.2	1151.6	83.5	1106.1	34.6	4.0
M4_SM21_06_Zrn20	319	0.21	0.1235	0.0036	6.1717	0.2237	0.3603	0.0119	0.12	1983.1	56.5	1999.3	32.0	2005.0	51.3	1983.1	56.5	1.1
M4_SM21_06_Zrn21	217	0.29	0.0757	0.0049	1.7459	0.1208	0.1685	0.0059	0.03	1003.9	32.5	1021.5	44.0	1064.2	127.6	1003.9	32.5	5.7
M4_SM21_06_Zrn22	314	0.15	0.0841	0.0028	2.2206	0.0890	0.1950	0.0080	0.10	1147.8	43.0	1185.4	28.4	1285.7	65.5	1147.8	43.0	10.7
M4_SM21_06_Zrn23	55	0.71	0.0619	0.0044	0.7194	0.0500	0.0858	0.0029	0.31	530.4	17.5	544.7	29.8	588.3	159.7	530.4	17.5	2.6
M4_SM21_06_Zrn24	94	0.53	0.0793	0.0029	2.3029	0.0938	0.2117	0.0067	0.13	1237.7	35.8	1209.9	29.2	1163.3	75.8	1237.7	35.8	-6.4
M4_SM21_06_Zrn25	96	0.95	0.0737	0.0031	1.6858	0.0747	0.1662	0.0054	0.28	991.0	30.0	1000.5	28.6	1015.0	87.6	991.0	30.0	2.4
M4_SM21_06_Zrn26	231	0.19	0.0753	0.0026	1.9255	0.0716	0.1863	0.0055	0.33	1101.0	29.8	1088.1	25.0	1063.8	72.1	1101.0	29.8	-3.5
M4_SM21_06_Zrn27	373	0.35	0.0597	0.0019	0.7863	0.0273	0.0963	0.0028	0.27	592.6	16.4	588.4	15.6	579.4	69.7	592.6	16.4	-0.7
M4_SM21_06_Zrn28	406	0.18	0.0586	0.0019	0.7222	0.0271	0.0897	0.0027	0.12	553.8	16.0	551.2	15.9	541.0	71.3	553.8	16.0	-0.5
M4_SM21_06_Zrn29	862	0.09	0.0601	0.0018	0.7521	0.0247	0.0910	0.0026	0.48	561.5	15.5	569.1	14.3	598.4	68.1	561.5	15.5	1.3
M4_SM21_06_Zrn30	479	0.46	0.0713	0.0021	1.5828	0.0520	0.1625	0.0048	0.27	970.8	26.7	962.9	20.4	961.4	60.1	970.8	26.7	-1.0
M4_SM21_06_Zrn31	189	0.47	0.0724	0.0025	1.8327	0.0674	0.1845	0.0056	0.30	1091.4	30.5	1055.3	24.4	983.7	72.4	1091.4	30.5	-11.0
M4_SM21_06_Zrn32	306	0.26	0.0625	0.0020	0.9078	0.0309	0.1063	0.0032	0.45	651.0	18.8	655.3	16.5	680.2	69.3	651.0	18.8	0.7
M4_SM21_06_Zrn33	362	0.53	0.0670	0.0029	1.0807	0.0541	0.1187	0.0042	0.12	723.0	24.4	742.7	26.2	826.6	87.8	723.0	24.4	2.6
M4_SM21_06_Zrn34	181	0.20	0.0601	0.0035	0.7142	0.0403	0.0874	0.0031	0.37	539.9	18.4	545.5	23.7	572.8	125.5	539.9	18.4	1.0
M4_SM21_06_Zrn35	739	0.20	0.0638	0.0019	1.1152	0.0365	0.1267	0.0037	0.26	768.7	21.4	760.2	17.5	728.2	61.4	768.7	21.4	-1.1
M4_SM21_06_Zrn36	495	0.53	0.0613	0.0019	0.8546	0.0286	0.1015	0.0031	0.43	623.3	17.9	626.6	15.7	637.1	69.9	623.3	17.9	0.5
M4_SM21_06_Zrn37	188	0.49	0.0551	0.0030	0.5853	0.0325	0.0776	0.0025	0.27	481.6	15.2	465.4	20.8	377.0	120.2	481.6	15.2	-3.5
M4_SM21_06_Zrn38	162	0.16	0.1057	0.0029	4.4340	0.1381	0.3050	0.0090	0.29	1715.7	44.4	1717.6	25.8	1721.6	51.4	1715.7	44.4	0.3
M4_SM21_06_Zrn39	250	0.79	0.0747	0.0024	1.8470	0.0636	0.1793	0.0055	0.34	1063.0	30.1	1061.3	22.8	1053.0	64.9	1063.0	30.1	-1.0
M4_SM21_06_Zrn40	180	0.69	0.0581	0.0028	0.4129	0.0221	0.0518	0.0017	0.07	325.3	10.6	349.6	15.7	490.0	109.1	325.3	10.6	6.9
M4_SM21_06_Zrn41	243	0.58	0.0736	0.0026	1.7706	0.0640	0.1752	0.0054	0.51	1040.7	29.8	1033.6	23.1	1018.5	71.3	1040.7	29.8	-2.2

Continúa

Continuación																		
SM21-06 Esquisto pelítico sin Grt (U. Etna)			Espejo-Bautista et al., 2022															
Zircón	U ppm	Th/U	Relaciones isotópicas corregidas							Edades corregidas						Mejor edad		Discordancia %
			$\frac{Pb^{207}}{Pb^{206}}$	$\pm 2\sigma$	$\frac{Pb^{207}}{U^{235}}$	$\pm 2\sigma$	$\frac{Pb^{206}}{U^{238}}$	$\pm 2\sigma$	rho	$\frac{Pb^{206}}{U^{238}}$	$\pm 2\sigma$	$\frac{Pb^{207}}{U^{235}}$	$\pm 2\sigma$	$\frac{Pb^{207}}{Pb^{206}}$	$\pm 2\sigma$	Ma	$\pm 2\sigma$	
SM21_06_Zrn42	375	1.24	0.0628	0.0038	0.6328	0.0357	0.0728	0.0025	0.50	453.1	14.9	497.0	22.5	681.4	135.2	453.1	14.9	8.8
SM21_06_Zrn43	562	0.66	0.0696	0.0026	1.3856	0.0577	0.1422	0.0045	0.20	856.9	25.6	882.0	24.4	911.0	77.3	856.9	25.6	2.8
SM21_06_Zrn44	328	0.71	0.0764	0.0025	1.8490	0.0619	0.1762	0.0052	0.24	1046.4	28.6	1062.2	22.0	1096.4	63.2	1046.4	28.6	4.6
SM21_06_Zrn45	591	0.38	0.0722	0.0019	1.6038	0.0475	0.1601	0.0047	0.43	957.5	25.8	971.3	18.5	988.3	53.5	957.5	25.8	3.1
SM21_06_Zrn46	176	0.33	0.0869	0.0035	2.5411	0.1889	0.2090	0.0135	-0.03	1220.3	70.7	1271.6	51.3	1343.6	78.4	1220.3	70.7	9.2
SM21_06_Zrn47	282	0.64	0.0624	0.0027	0.9196	0.0428	0.1063	0.0035	0.58	651.2	20.2	660.9	22.6	673.4	90.2	651.2	20.2	1.5
SM21_06_Zrn48	477	0.31	0.0761	0.0024	1.8784	0.0626	0.1784	0.0054	0.44	1058.0	29.5	1072.9	22.1	1092.9	62.9	1058.0	29.5	3.2
SM21_06_Zrn49	560	0.11	0.0591	0.0025	0.7319	0.0344	0.0902	0.0030	0.03	556.6	17.7	556.9	20.0	561.2	92.0	556.6	17.7	0.1
SM21_06_Zrn50	689	0.47	0.0596	0.0019	0.7605	0.0258	0.0920	0.0027	0.34	567.5	15.8	573.8	14.8	578.8	67.7	567.5	15.8	1.1
SM21_06_Zrn51	114	0.41	0.0738	0.0028	1.6775	0.0788	0.1628	0.0053	0.08	971.9	29.6	997.9	29.4	1044.9	88.2	971.9	29.6	7.0
SM21_06_Zrn52	89	0.99	0.0769	0.0038	1.8378	0.0932	0.1720	0.0055	0.24	1023.0	30.2	1054.9	33.3	1090.7	99.5	1023.0	30.2	6.2
SM21_06_Zrn53	254	0.95	0.1035	0.0034	4.0964	0.1385	0.2832	0.0087	0.52	1607.1	43.9	1652.9	27.1	1684.3	59.1	1607.1	43.9	4.6
SM21_06_Zrn54_1	592	0.32	0.0594	0.0021	0.7559	0.0302	0.0911	0.0028	0.16	562.3	16.5	571.1	17.3	574.5	79.4	562.3	16.5	1.5
SM21_06_Zrn54_2	2628	0.38	0.0573	0.0029	0.3057	0.0116	0.0392	0.0016	0.83	247.8	10.2	270.8	9.0	492.5	111.7	247.8	10.2	8.5
SM21_06_Zrn55	263	0.94	0.1108	0.0031	4.7353	0.1508	0.3089	0.0092	0.29	1735.1	45.3	1772.6	26.8	1808.3	52.1	1735.1	45.3	4.0
SM21_06_Zrn56	505	0.22	0.1263	0.0033	6.0744	0.1798	0.3468	0.0101	0.39	1919.3	48.3	1986.1	25.9	2044.5	46.4	1919.3	48.3	6.1
SM21_06_Zrn57	93	0.93	0.0617	0.0041	0.7803	0.0533	0.0905	0.0031	0.31	558.4	18.3	579.9	29.7	596.5	150.0	558.4	18.3	3.7
SM21_06_Zrn58	241	0.40	0.0814	0.0029	2.3587	0.0844	0.2110	0.0068	0.55	1234.1	36.0	1229.2	25.8	1223.7	71.5	1234.1	36.0	-0.8
SM21_06_Zrn59	839	0.55	0.0741	0.0025	1.4076	0.0466	0.1387	0.0044	0.58	837.3	24.7	891.9	19.7	1038.9	66.0	837.3	24.7	6.1
SM21_06_Zrn60	388	0.20	0.0614	0.0024	0.7887	0.0310	0.0937	0.0028	0.40	577.6	16.6	589.7	17.7	638.2	85.9	577.6	16.6	2.1
SM21_06_Zrn62	136	0.48	0.0605	0.0030	0.7350	0.0359	0.0885	0.0029	0.39	546.3	17.2	557.5	21.0	581.5	110.6	546.3	17.2	2.0
SM21_06_Zrn63	876	0.15	0.0661	0.0018	1.2040	0.0414	0.1317	0.0041	0.01	797.7	23.6	801.8	19.1	813.1	49.9	797.7	23.6	0.5
SM21_06_Zrn64	334	0.26	0.0626	0.0021	0.9654	0.0353	0.1122	0.0034	0.28	685.6	19.7	687.4	17.1	690.2	66.7	685.6	19.7	0.3
SM21_06_Zrn65	160	0.58	0.0596	0.0043	0.6404	0.0454	0.0796	0.0030	0.02	493.3	18.0	504.4	30.2	512.2	151.4	493.3	18.0	2.2
SM21_06_Zrn66	582	0.44	0.0840	0.0029	2.3455	0.0826	0.2012	0.0068	0.50	1181.6	36.4	1225.3	25.1	1285.5	68.0	1181.6	36.4	8.1
SM21_06_Zrn67	463	0.90	0.0728	0.0025	1.5316	0.0592	0.1542	0.0048	0.09	924.4	26.8	947.6	19.5	1001.3	72.2	924.4	26.8	7.7
SM21_06_Zrn68	335	0.50	0.0750	0.0026	1.7889	0.0686	0.1744	0.0052	0.20	1036.1	28.9	1040.1	25.0	1061.2	69.9	1036.1	28.9	2.4

SJ15 Paragneis Grt-Bt (Paleosoma T.)			Espejo-Bautista et al., 2022																
Zircón	Relaciones isotópicas corregidas									Edades corregidas						Mejor edad		Discordancia %	
	U ppm	Th/U	$\frac{Pb^{207}}{Pb^{206}}$	$\pm 2\sigma$	$\frac{Pb^{207}}{U^{235}}$	$\pm 2\sigma$	$\frac{Pb^{206}}{U^{238}}$	$\pm 2\sigma$	rho	$\frac{Pb^{206}}{U^{238}}$	$\pm 2\sigma$	$\frac{Pb^{207}}{U^{235}}$	$\pm 2\sigma$	$\frac{Pb^{207}}{Pb^{206}}$	$\pm 2\sigma$	Ma	$\pm 2\sigma$		
M1_SJ15_Zrn01	492	0.22	0.0745	0.0024	1.9181	0.0735	0.1853	0.0061	0.14	1095.6	32.9	1086.5	25.4	1051.3	64.7	1095.6	32.9	-4.2	
M1_SJ15_Zrn02	122	0.38	0.0550	0.0048	0.3387	0.0298	0.0444	0.0016	0.10	280.2	9.6	294.1	23.1	342.9	223.1	280.2	9.6	4.7	
M1_SJ15_Zrn03	261	0.01	0.0495	0.0038	0.1842	0.0148	0.0271	0.0011	-0.18	172.2	6.9	170.9	12.8	117.9	194.4	172.2	6.9	-0.8	
M2_SJ15_Zrn04	249	0.65	0.0540	0.0035	0.3262	0.0203	0.0439	0.0014	0.39	277.0	8.9	285.3	15.5	292.5	147.5	277.0	8.9	2.9	
M2_SJ15_Zrn05	1290	0.01	0.0515	0.0017	0.2744	0.0107	0.0385	0.0012	0.05	243.7	7.4	245.9	8.5	249.0	79.9	243.7	7.4	0.9	
M2_SJ15_Zrn06	94	0.47	0.0524	0.0051	0.3667	0.0355	0.0513	0.0023	0.24	322.5	14.0	317.3	27.7	153.9	235.3	322.5	14.0	-1.6	
M2_SJ15_Zrn07	1585	0.02	0.0530	0.0017	0.2529	0.0089	0.0346	0.0010	0.33	219.6	6.3	228.8	7.2	314.8	75.9	219.6	6.3	4.0	
M2_SJ15_Zrn08	173	0.61	0.0521	0.0037	0.3355	0.0235	0.0467	0.0016	0.31	294.1	9.9	292.4	17.7	209.8	164.9	294.1	9.9	-0.6	
M2_SJ15_Zrn09	799	0.01	0.0517	0.0018	0.2740	0.0103	0.0385	0.0012	0.25	243.3	7.4	245.7	8.2	270.1	71.9	243.3	7.4	1.0	
M2_SJ15_Zrn10	599	0.36	0.0582	0.0022	0.6438	0.0257	0.0804	0.0024	0.31	498.7	14.2	503.8	15.7	519.2	82.7	498.7	14.2	1.0	
M2_SJ15_Zrn11	223	0.01	0.0513	0.0031	0.2030	0.0123	0.0289	0.0010	0.17	183.9	6.6	187.1	10.4	208.2	156.7	183.9	6.6	1.7	
M2_SJ15_Zrn12	1024	0.01	0.0516	0.0036	0.1948	0.0130	0.0278	0.0009	0.41	176.9	5.9	180.5	11.0	240.8	157.0	176.9	5.9	2.0	
M2_SJ15_Zrn13	422	0.14	0.0520	0.0023	0.2763	0.0125	0.0387	0.0012	0.20	245.0	7.4	247.3	10.0	270.4	94.2	245.0	7.4	0.9	
M2_SJ15_Zrn14	65	0.65	0.0621	0.0044	0.9315	0.0726	0.1099	0.0056	0.27	671.7	32.7	660.5	37.6	619.3	153.6	671.7	32.7	-1.7	
M2_SJ15_Zrn15	362	0.01	0.0492	0.0025	0.1886	0.0105	0.0280	0.0009	-0.04	178.1	5.9	175.0	8.9	98.9	121.6	178.1	5.9	-1.8	
M2_SJ15_Zrn16	353	0.16	0.0964	0.0052	3.4521	0.1803	0.2637	0.0093	0.43	1508.4	47.5	1515.4	41.3	1551.1	101.7	1551.1	101.7	2.8	
M2_SJ15_Zrn17	725	0.01	0.0496	0.0033	0.1889	0.0101	0.0277	0.0013	0.65	176.4	8.4	175.6	8.7	148.7	146.5	176.4	8.4	-0.4	
M2_SJ15_Zrn18	396	0.01	0.0526	0.0035	0.1746	0.0117	0.0245	0.0009	0.23	155.8	5.8	163.0	10.1	292.2	132.4	155.8	5.8	4.4	
M2_SJ15_Zrn19	325	0.36	0.0570	0.0024	0.5553	0.0234	0.0713	0.0022	0.37	443.7	13.4	447.6	15.4	487.4	83.9	443.7	13.4	0.9	
M2_SJ15_Zrn20	884	0.01	0.0504	0.0025	0.1909	0.0104	0.0274	0.0009	-0.02	174.1	5.8	177.1	8.8	184.7	116.9	174.1	5.8	1.7	
M2_SJ15_Zrn22	930	0.01	0.0506	0.0021	0.1901	0.0079	0.0277	0.0009	0.17	175.9	5.5	176.5	6.7	193.8	94.0	175.9	5.5	0.4	
M2_SJ15_Zrn23	59	0.95	0.0803	0.0036	2.0819	0.0914	0.1901	0.0064	0.48	1121.5	34.8	1138.9	30.2	1175.6	92.5	1121.5	34.8	4.6	
M2_SJ15_Zrn24	89	0.00	0.0527	0.0051	0.3050	0.0297	0.0424	0.0017	0.08	267.9	10.2	266.4	23.2	81.6	265.8	267.9	10.2	-0.6	
M2_SJ15_Zrn25	218	0.36	0.0571	0.0028	0.6231	0.0329	0.0795	0.0027	0.03	493.3	16.3	489.7	20.5	458.1	106.8	493.3	16.3	-0.7	
M2_SJ15_Zrn26	228	0.51	0.0585	0.0025	0.6625	0.0287	0.0830	0.0029	0.25	513.7	17.0	514.7	17.8	531.1	101.2	513.7	17.0	0.2	
M2_SJ15_Zrn27	105	0.45	0.0579	0.0037	0.6841	0.0446	0.0863	0.0028	0.26	533.3	16.7	524.8	26.8	426.8	164.9	533.3	16.7	-1.6	
M2_SJ15_Zrn28	25	0.33	0.0708	0.0154	0.3590	0.0545	0.0412	0.0030	-0.15	259.9	18.4	304.1	39.3	376.4	472.1	259.9	18.4	14.5	
M2_SJ15_Zrn29	109	0.36	0.0798	0.0035	1.9530	0.0856	0.1794	0.0059	0.42	1063.3	32.3	1096.2	28.9	1167.8	84.9	1063.3	32.3	8.9	
M2_SJ15_Zrn30	28	0.47	0.0763	0.0096	1.2672	0.1411	0.1248	0.0072	0.52	757.6	41.2	819.3	62.7	957.6	277.6	757.6	41.2	7.5	
M2_SJ15_Zrn31	1473	0.01	0.0512	0.0018	0.2453	0.0092	0.0349	0.0011	0.23	221.2	6.7	222.6	7.5	232.7	83.2	221.2	6.7	0.6	
M3_SJ15_Zrn32	543	0.40	0.0531	0.0025	0.3359	0.0158	0.0464	0.0015	0.38	292.2	9.0	293.5	12.1	323.0	101.9	292.2	9.0	0.4	
M3_SJ15_Zrn33	911	0.03	0.0515	0.0029	0.2708	0.0152	0.0387	0.0013	0.15	244.6	8.3	243.0	12.1	237.5	129.6	244.6	8.3	-0.7	
M3_SJ15_Zrn34	566	0.45	0.0537	0.0025	0.3205	0.0167	0.0430	0.0013	0.28	271.6	8.2	281.6	12.7	343.3	117.3	271.6	8.2	3.5	
M3_SJ15_Zrn35	85	0.32	0.0744	0.0035	1.7672	0.0947	0.1713	0.0054	0.09	1018.8	29.8	1027.4	34.7	1034.3	104.0	1018.8	29.8	1.5	
M3_SJ15_Zrn36	218	0.01	0.0584	0.0081	0.3842	0.0448	0.0484	0.0019	-0.02	304.6	11.8	324.8	25.3	327.6	127.3	304.6	11.8	6.2	
M3_SJ15_Zrn37	1123	0.33	0.0542	0.0021	0.3651	0.0185	0.0490	0.0018	-0.27	308.2	10.8	315.3	13.8	359.8	85.6	308.2	10.8	2.2	
M3_SJ15_Zrn38	97	0.36	0.0778	0.0034	1.9660	0.0913	0.1845	0.0062	0.27	1091.0	33.6	1099.7	31.5	1114.0	91.0	1091.0	33.6	2.1	
M3_SJ15_Zrn39	403	0.25	0.0828	0.0024	2.3128	0.0804	0.2034	0.0065	0.19	1193.3	35.1	1214.6	24.6	1257.6	57.7	1193.3	35.1	5.1	
M3_SJ15_Zrn40	264	0.67	0.0594	0.0025	0.7420	0.0304	0.0920	0.0030	0.30	567.2	17.4	562.4	17.5	555.7	89.0	567.2	17.4	-0.9	
M3_SJ15_Zrn41	2905	0.03	0.0540	0.0024	0.2828	0.0148	0.0389	0.0012	0.57	245.9	7.7	252.7	11.7	362.8	101.3	245.9	7.7	2.7	

Continúa

Continuación

SJ15 Paragneis Grt-Bt (Paleosoma T.)		Espejo-Bautista et al., 2022																
Zircón	U ppm	Th/U	Relaciones isotópicas corregidas						Edades corregidas						Mejor edad		Discordancia %	
			$\frac{Pb^{207}}{Pb^{206}}$	$\pm 2\sigma$	$\frac{Pb^{207}}{U^{235}}$	$\pm 2\sigma$	$\frac{Pb^{206}}{U^{238}}$	$\pm 2\sigma$	rho	$\frac{Pb^{206}}{U^{238}}$	$\pm 2\sigma$	$\frac{Pb^{207}}{U^{235}}$	$\pm 2\sigma$	$\frac{Pb^{207}}{Pb^{206}}$	$\pm 2\sigma$	Ma		$\pm 2\sigma$
M3_SJ15_Zrn42	1857	0.01	0.0529	0.0019	0.2765	0.0101	0.0385	0.0012	0.41	243.8	7.2	247.7	8.0	308.5	77.7	243.8	7.2	1.6
M3_SJ15_Zrn43	2716	0.02	0.0524	0.0019	0.2666	0.0104	0.0379	0.0012	-0.19	239.7	7.6	242.2	10.4	295.4	83.7	239.7	7.6	1.0
M3_SJ15_Zrn44	387	0.56	0.0548	0.0024	0.5752	0.0258	0.0769	0.0023	0.37	477.4	13.9	460.1	16.5	369.0	99.2	477.4	13.9	-3.8
M3_SJ15_Zrn45	613	0.65	0.0529	0.0029	0.3332	0.0187	0.0464	0.0016	0.30	292.1	9.6	291.1	14.1	301.5	113.0	292.1	9.6	-0.4
M3_SJ15_Zrn46	118	0.40	0.0740	0.0041	1.8128	0.1016	0.1796	0.0059	0.30	1064.4	32.5	1045.6	37.0	1039.9	100.5	1064.4	32.5	-2.4
M3_SJ15_Zrn47	533	0.01	0.0521	0.0032	0.1406	0.0085	0.0197	0.0007	0.35	126.0	4.7	133.2	7.6	226.8	144.2	126.0	4.7	5.5
M3_SJ15_Zrn48	397	0.48	0.0532	0.0034	0.3265	0.0205	0.0449	0.0015	0.35	283.1	9.1	285.8	15.7	306.7	135.7	283.1	9.1	0.9
M3_SJ15_Zrn49_1	151	0.03	0.0729	0.0060	1.8328	0.1188	0.1814	0.0083	0.68	1074.3	45.5	1055.9	43.2	995.0	162.4	1074.3	45.5	-8.0
M3_SJ15_Zrn49_3	3256	0.06	0.0533	0.0028	0.2832	0.0166	0.0393	0.0017	0.22	248.5	10.8	253.0	13.3	331.3	123.5	248.5	10.8	1.8
M3_SJ15_Zrn50	381	0.46	0.0866	0.0025	2.7532	0.0881	0.2326	0.0070	0.38	1347.7	36.8	1341.9	23.8	1346.3	55.1	1346.3	55.1	-0.1
M3_SJ15_Zrn51	944	0.01	0.0499	0.0018	0.2160	0.0094	0.0315	0.0010	0.00	200.2	6.3	198.3	7.8	180.7	83.3	200.2	6.3	-0.9
M3_SJ15_Zrn52	892	0.04	0.0545	0.0032	0.2890	0.0196	0.0391	0.0014	0.44	246.9	8.5	257.4	15.4	371.0	135.9	246.9	8.5	4.1
M3_SJ15_Zrn54	710	0.01	0.0538	0.0020	0.2810	0.0128	0.0380	0.0013	-0.03	240.3	8.1	250.9	10.1	339.6	84.3	240.3	8.1	4.3
M3_SJ15_Zrn55	384	0.40	0.0533	0.0022	0.3389	0.0156	0.0463	0.0015	0.16	292.0	9.4	295.8	11.8	337.8	109.4	292.0	9.4	1.3
M3_SJ15_Zrn56	264	0.01	0.0545	0.0030	0.2939	0.0154	0.0393	0.0013	0.45	248.7	8.1	261.0	12.0	344.7	124.6	248.7	8.1	4.7
SJ15_Zrn57	693	0.12	0.0634	0.0024	0.6040	0.0247	0.0681	0.0021	0.17	424.6	12.5	479.2	15.7	706.3	82.7	424.6	12.5	11.4
SJ15_Zrn58_a	244	0.27	0.0654	0.0040	1.1217	0.0948	0.1213	0.0061	-0.24	737.8	35.3	761.3	44.4	773.5	125.3	737.8	35.3	3.1
SJ15_Zrn58_b	1196	0.10	0.0628	0.0022	0.5056	0.0272	0.0580	0.0024	-0.13	363.1	14.9	414.4	17.9	692.0	75.2	363.1	14.9	12.4
SJ15_Zrn59_a	97	0.28	0.0775	0.0045	1.8901	0.1084	0.1735	0.0058	0.32	1031.4	31.7	1074.6	38.7	1112.4	119.5	1031.4	31.7	7.3
SJ15_Zrn60	494	0.04	0.0610	0.0022	0.4673	0.0269	0.0551	0.0025	0.86	345.3	15.2	390.8	19.9	621.7	78.8	345.3	15.2	11.6
SJ15_Zrn61	996	0.01	0.0505	0.0022	0.1906	0.0084	0.0274	0.0011	0.52	174.0	7.1	177.0	7.1	200.1	105.1	174.0	7.1	1.7
SJ15_Zrn62	272	0.13	0.0794	0.0023	2.2835	0.0890	0.2048	0.0078	0.24	1200.7	41.5	1205.4	27.6	1177.9	56.2	1177.9	56.2	-1.9
SJ15_Zrn63	2259	0.01	0.0564	0.0050	0.2221	0.0207	0.0286	0.0009	-0.22	181.7	5.5	203.5	17.0	452.0	179.7	181.7	5.5	10.7
SJ15_Zrn64_a	132	0.35	0.0663	0.0061	1.3626	0.1301	0.1454	0.0049	0.11	874.9	27.8	869.5	55.0	785.8	200.3	874.9	27.8	-11.3
SJ15_Zrn64_b	1338	0.03	0.0547	0.0029	0.2608	0.0161	0.0346	0.0015	0.13	219.0	9.1	235.1	12.9	387.8	120.5	219.0	9.1	6.8
SJ15_Zrn65	114	0.24	0.0622	0.0045	0.6367	0.0578	0.0731	0.0048	0.08	454.1	28.5	494.1	35.0	605.8	152.3	454.1	28.5	8.1
SJ15_Zrn66	1342	0.01	0.0508	0.0018	0.2335	0.0091	0.0332	0.0011	0.13	210.6	6.7	212.9	7.4	217.4	83.0	210.6	6.7	1.1
SJ15_Zrn67	777	0.01	0.0522	0.0030	0.2867	0.0242	0.0396	0.0021	-0.20	250.0	13.1	254.9	18.8	263.6	135.8	250.0	13.1	1.9
SJ15_Zrn68	327	0.30	0.0787	0.0025	2.0712	0.0805	0.1897	0.0069	0.26	1119.5	37.7	1138.1	26.8	1158.1	63.9	1119.5	37.7	3.3
SJ15_Zrn69	209	0.72	0.0534	0.0038	0.3063	0.0220	0.0413	0.0014	0.24	260.7	8.9	269.8	17.2	280.9	167.5	260.7	8.9	3.4
SJ15_Zrn70	2879	0.05	0.0528	0.0021	0.2377	0.0131	0.0327	0.0012	-0.40	207.2	7.7	216.3	10.8	309.9	91.2	207.2	7.7	4.2
SJ15_Zrn72	1009	0.02	0.0517	0.0022	0.2805	0.0127	0.0389	0.0013	0.24	245.9	7.9	250.7	10.0	245.7	101.7	245.9	7.9	1.9
SJ15_Zrn73	212	0.45	0.0668	0.0027	1.1410	0.0475	0.1227	0.0038	0.28	746.0	21.8	771.1	22.5	811.6	83.8	746.0	21.8	3.2
SJ15_Zrn74	912	0.02	0.0530	0.0019	0.2931	0.0105	0.0395	0.0013	0.19	249.8	8.3	261.0	8.2	320.4	80.0	249.8	8.3	4.3
SJ15_Zrn75	1810	0.04	0.0587	0.0017	0.3772	0.0128	0.0461	0.0014	0.01	290.8	8.4	324.7	9.5	546.5	65.4	290.8	8.4	10.5
SJ15_Zrn76	477	0.80	0.0762	0.0021	1.7749	0.0566	0.1674	0.0049	0.22	997.8	27.2	1035.5	20.6	1094.8	56.1	997.8	27.2	8.9
SJ15_Zrn77	1966	0.01	0.0505	0.0016	0.1962	0.0082	0.0280	0.0010	0.01	178.0	6.3	181.7	7.0	205.8	74.7	178.0	6.3	2.0
SJ15_Zrn78	103	0.28	0.0787	0.0040	1.2994	0.0657	0.1202	0.0047	0.35	731.4	27.0	842.9	29.2	1141.7	98.5	731.4	27.0	13.2
SJ15_Zrn79	252	0.16	0.0725	0.0027	1.2673	0.0516	0.1250	0.0041	0.15	759.4	23.8	829.7	23.2	987.5	78.9	759.4	23.8	8.5

SM21-04 Meta-riolita (C. Mazateco)

Espejo-Bautista et al., 2022

Zircón	U ppm	Th/U	Relaciones isotópicas corregidas							Edades corregidas						Mejor edad		Discordancia %
			$\frac{Pb^{207}}{Pb^{206}}$	$\pm 2\sigma$	$\frac{Pb^{207}}{U^{235}}$	$\pm 2\sigma$	$\frac{Pb^{206}}{U^{238}}$	$\pm 2\sigma$	rho	$\frac{Pb^{206}}{U^{238}}$	$\pm 2\sigma$	$\frac{Pb^{207}}{U^{235}}$	$\pm 2\sigma$	$\frac{Pb^{207}}{Pb^{206}}$	$\pm 2\sigma$	Ma	$\pm 2\sigma$	
M3_SM21_04_Zrn01	83	0.68	0.0518	0.0050	0.3193	0.0291	0.0453	0.0018	0.29	285.7	11.1	278.5	21.9	138.9	203.8	285.7	11.1	-2.6
M3_SM21_04_Zrn02	163	1.14	0.0540	0.0032	0.3326	0.0186	0.0450	0.0015	0.47	284.0	9.4	290.4	14.2	298.6	140.2	284.0	9.4	2.2
M3_SM21_04_Zrn03	33	0.42	0.0517	0.0067	0.3358	0.0420	0.0479	0.0023	0.36	301.4	14.4	286.7	32.4	152.4	309.0	301.4	14.4	-5.1
M3_SM21_04_Zrn04	191	0.35	0.0540	0.0040	0.3292	0.0215	0.0450	0.0017	0.60	283.9	10.5	288.2	16.5	306.7	179.4	283.9	10.5	1.5
M3_SM21_04_Zrn05	59	0.92	0.0587	0.0070	0.3656	0.0416	0.0461	0.0022	0.25	290.5	13.4	310.8	30.4	317.0	280.0	290.5	13.4	6.5
M3_SM21_04_Zrn06	117	0.69	0.0552	0.0039	0.3360	0.0231	0.0456	0.0017	0.05	287.5	10.4	295.7	19.1	329.0	167.5	287.5	10.4	2.8
M3_SM21_04_Zrn07	93	0.63	0.0514	0.0043	0.3360	0.0275	0.0473	0.0018	0.32	297.9	11.0	291.2	20.7	162.6	194.8	297.9	11.0	-2.3
M4_SM21_04_Zrn08	111	0.73	0.0548	0.0050	0.3592	0.0351	0.0466	0.0022	0.19	293.4	13.4	308.8	26.1	311.0	244.8	293.4	13.4	5.0
M4_SM21_04_Zrn09	205	0.49	0.0552	0.0068	0.3362	0.0396	0.0451	0.0020	0.31	284.2	12.4	293.0	30.2	341.8	303.6	284.2	12.4	3.0
M4_SM21_04_Zrn10	143	1.28	0.0514	0.0035	0.3220	0.0228	0.0458	0.0017	0.13	288.7	10.2	281.5	17.4	210.3	180.1	288.7	10.2	-2.5
M4_SM21_04_Zrn11	342	0.86	0.0536	0.0029	0.3562	0.0198	0.0481	0.0015	0.18	302.6	9.3	308.7	15.0	318.9	133.1	302.6	9.3	2.0
M4_SM21_04_Zrn12	118	0.49	0.0532	0.0052	0.3659	0.0362	0.0497	0.0017	0.00	312.6	10.6	313.9	26.7	211.8	238.0	312.6	10.6	0.4
M4_SM21_04_Zrn13	152	0.76	0.0546	0.0033	0.3437	0.0211	0.0459	0.0015	0.18	289.1	9.5	298.6	15.9	320.8	144.9	289.1	9.5	3.2
M4_SM21_04_Zrn14	45	0.78	0.0602	0.0066	0.4013	0.0461	0.0478	0.0023	0.31	301.0	14.3	335.6	32.9	352.0	309.3	301.0	14.3	10.3
M4_SM21_04_Zrn15	182	0.69	0.0518	0.0037	0.3397	0.0231	0.0479	0.0017	0.36	301.9	10.2	295.4	17.4	183.7	171.8	301.9	10.2	-2.2
M4_SM21_04_Zrn16	336	0.63	0.0505	0.0037	0.3208	0.0246	0.0465	0.0016	0.11	293.1	10.1	281.3	18.5	154.2	166.8	293.1	10.1	-4.2
M4_SM21_04_Zrn17	141	0.81	0.0508	0.0039	0.3271	0.0283	0.0465	0.0017	-0.26	292.9	10.5	291.5	24.5	190.9	200.4	292.9	10.5	-0.5
M4_SM21_04_Zrn18	286	1.46	0.0499	0.0029	0.2856	0.0173	0.0414	0.0014	0.19	261.5	8.7	254.2	13.7	129.3	146.5	261.5	8.7	-2.9
M4_SM21_04_Zrn19	367	0.57	0.0542	0.0029	0.3466	0.0185	0.0465	0.0015	0.35	293.1	8.9	301.4	14.0	331.8	126.6	293.1	8.9	2.8
M4_SM21_04_Zrn20	149	0.45	0.0537	0.0031	0.3327	0.0197	0.0450	0.0016	0.27	283.6	9.6	290.4	15.0	307.1	153.5	283.6	9.6	2.3
M4_SM21_04_Zrn21	218	0.56	0.0593	0.0027	0.7147	0.0337	0.0871	0.0029	0.31	538.5	16.9	545.9	19.8	549.0	100.0	538.5	16.9	1.4
M4_SM21_04_Zrn22	65	0.86	0.0528	0.0046	0.3397	0.0300	0.0468	0.0020	0.20	294.7	12.3	293.9	22.7	231.9	236.3	294.7	12.3	-0.3
M4_SM21_04_Zrn23	183	0.38	0.0731	0.0027	1.7274	0.0674	0.1707	0.0053	0.29	1016.0	29.4	1016.8	25.2	1001.4	74.4	1016.0	29.4	-1.5
M4_SM21_04_Zrn24	100	0.63	0.0575	0.0039	0.3627	0.0239	0.0458	0.0016	0.36	288.5	10.0	312.1	17.6	435.2	142.4	288.5	10.0	7.6
M4_SM21_04_Zrn25	293	0.92	0.0554	0.0030	0.3612	0.0198	0.0472	0.0015	0.26	297.3	9.4	312.0	14.8	374.2	125.9	297.3	9.4	4.7
M4_SM21_04_Zrn26	197	0.89	0.0550	0.0039	0.3408	0.0237	0.0452	0.0015	0.26	284.7	9.0	296.3	17.7	333.5	166.6	284.7	9.0	3.9
M4_SM21_04_Zrn27	90	0.60	0.0557	0.0052	0.3495	0.0326	0.0455	0.0021	0.27	287.1	13.0	301.6	24.2	303.3	219.3	287.1	13.0	4.8
M4_SM21_04_Zrn28	77	0.77	0.0524	0.0045	0.3412	0.0295	0.0474	0.0017	0.22	298.6	10.5	295.1	22.3	179.1	205.3	298.6	10.5	-1.2
M4_SM21_04_Zrn29	254	0.61	0.0544	0.0032	0.3580	0.0215	0.0474	0.0015	0.09	298.5	9.2	309.6	16.2	366.3	120.3	298.5	9.2	3.6
M4_SM21_04_Zrn30	400	0.02	0.0615	0.0023	0.8289	0.0422	0.0971	0.0035	-0.44	597.3	20.5	610.5	23.1	640.2	78.2	597.3	20.5	2.2
M4_SM21_04_Zrn31	166	0.34	0.0674	0.0029	0.9926	0.0436	0.1064	0.0036	0.31	651.8	20.7	698.7	22.0	831.7	87.8	651.8	20.7	6.7
M4_SM21_04_Zrn32	377	0.30	0.0516	0.0035	0.3418	0.0223	0.0479	0.0017	0.39	301.8	10.7	297.7	16.8	213.9	161.0	301.8	10.7	-1.4
M4_SM21_04_Zrn33	252	0.59	0.0554	0.0034	0.3481	0.0237	0.0458	0.0016	0.09	288.5	9.9	302.0	17.7	369.4	146.3	288.5	9.9	4.5
M4_SM21_04_Zrn34	234	0.96	0.0534	0.0035	0.3107	0.0202	0.0428	0.0015	-0.09	269.9	9.3	273.9	15.8	333.8	187.4	269.9	9.3	1.4
M4_SM21_04_Zrn35	343	0.60	0.0522	0.0025	0.3372	0.0169	0.0471	0.0017	0.12	296.4	10.4	294.3	13.0	276.9	104.4	296.4	10.4	-0.7
M4_SM21_04_Zrn36	460	0.78	0.0533	0.0033	0.3305	0.0181	0.0461	0.0015	0.24	290.2	9.4	292.9	15.9	297.7	137.1	290.2	9.4	0.9
M4_SM21_04_Zrn37	88	1.06	0.0564	0.0054	0.3515	0.0318	0.0459	0.0019	0.30	289.0	11.6	302.4	23.3	338.3	217.9	289.0	11.6	4.4
M4_SM21_04_Zrn38	349	0.92	0.0537	0.0032	0.2890	0.0186	0.0393	0.0015	0.18	248.7	9.6	256.6	14.5	288.8	141.9	248.7	9.6	3.1

SM21-05 Anfibolita (Paleosoma s. Teot.) Espejo-Bautista et al., 2022

Zircón	U ppm	Th/U	Relaciones isotópicas corregidas						rho	Edades corregidas						Mejor edad		Discordancia %
			$\frac{Pb^{207}}{Pb^{206}}$	$\pm 2\sigma$	$\frac{Pb^{207}}{U^{235}}$	$\pm 2\sigma$	$\frac{Pb^{206}}{U^{238}}$	$\pm 2\sigma$		$\frac{Pb^{206}}{U^{238}}$	$\pm 2\sigma$	$\frac{Pb^{207}}{U^{235}}$	$\pm 2\sigma$	$\frac{Pb^{207}}{Pb^{206}}$	$\pm 2\sigma$	Ma	$\pm 2\sigma$	
M2_SM21_05_Zrn01	284	0.38	0.0497	0.0035	0.1888	0.0136	0.0279	0.0009	0.17	177.3	5.8	174.8	11.6	106.1	164.9	177.3	5.8	-1.4
M2_SM21_05_Zrn02	494	0.45	0.0499	0.0034	0.1792	0.0117	0.0266	0.0009	0.39	169.2	5.5	166.9	10.2	91.1	185.3	169.2	5.5	-1.4
M2_SM21_05_Zrn03	392	0.28	0.0497	0.0036	0.1869	0.0134	0.0276	0.0010	0.25	175.2	6.4	173.2	11.5	104.4	166.8	175.2	6.4	-1.2
M2_SM21_05_Zrn04	525	0.49	0.0500	0.0025	0.2071	0.0109	0.0302	0.0010	0.33	192.0	6.1	190.7	9.2	174.3	113.9	192.0	6.1	-0.7
M2_SM21_05_Zrn05	198	0.36	0.0505	0.0055	0.1909	0.0216	0.0278	0.0014	0.06	177.0	8.5	176.4	18.5	71.1	303.9	177.0	8.5	-0.3
M2_SM21_05_Zrn06	127	0.15	0.0513	0.0052	0.2089	0.0204	0.0297	0.0012	0.47	188.9	7.3	191.3	17.1	198.0	226.5	188.9	7.3	1.3
M2_SM21_05_Zrn07	275	0.48	0.0511	0.0031	0.1918	0.0117	0.0276	0.0010	0.31	175.4	6.5	177.6	10.0	201.1	134.2	175.4	6.5	1.2
M2_SM21_05_Zrn08	168	0.27	0.0499	0.0046	0.1948	0.0196	0.0285	0.0011	-0.13	181.0	6.8	179.5	16.6	37.1	243.1	181.0	6.8	-0.9
M2_SM21_05_Zrn09	76	0.20	0.0523	0.0067	0.1972	0.0248	0.0280	0.0014	0.64	178.1	8.9	185.9	23.5	228.1	319.4	178.1	8.9	4.2
M2_SM21_05_Zrn10	288	0.55	0.0516	0.0034	0.1930	0.0115	0.0275	0.0009	0.50	174.9	5.7	178.6	9.8	180.9	152.5	174.9	5.7	2.1
M2_SM21_05_Zrn11	159	0.18	0.0520	0.0050	0.1970	0.0206	0.0273	0.0012	0.11	173.9	7.8	181.9	17.1	213.4	232.6	173.9	7.8	4.4
M2_SM21_05_Zrn12	545	0.47	0.0504	0.0034	0.1908	0.0130	0.0277	0.0009	0.13	176.4	5.8	177.1	11.2	231.9	128.4	176.4	5.8	0.4
M2_SM21_05_Zrn13	126	0.03	0.0498	0.0044	0.1823	0.0150	0.0267	0.0010	0.31	170.0	6.2	169.2	12.8	47.3	201.0	170.0	6.2	-0.5
M2_SM21_05_Zrn14	323	0.37	0.0512	0.0036	0.1865	0.0138	0.0267	0.0009	-0.14	169.6	5.8	173.2	11.9	185.6	186.3	169.6	5.8	2.1
M2_SM21_05_Zrn15	218	0.25	0.0488	0.0034	0.1877	0.0130	0.0280	0.0010	0.19	178.0	6.0	173.9	11.1	54.5	180.5	178.0	6.0	-2.4
M2_SM21_05_Zrn16	153	0.04	0.0495	0.0043	0.1875	0.0161	0.0277	0.0010	0.23	175.9	6.6	173.5	13.7	12.5	230.7	175.9	6.6	-1.4
M2_SM21_05_Zrn17	283	0.25	0.0500	0.0041	0.1930	0.0149	0.0281	0.0011	0.21	178.6	6.6	178.2	12.7	34.5	217.6	178.6	6.6	-0.2
M2_SM21_05_Zrn18	365	0.39	0.0504	0.0043	0.1899	0.0144	0.0278	0.0010	0.23	176.5	6.4	176.0	12.4	112.5	219.7	176.5	6.4	-0.3
M2_SM21_05_Zrn19	483	0.51	0.0524	0.0040	0.1975	0.0150	0.0274	0.0011	0.27	174.3	6.9	182.5	12.7	240.1	178.9	174.3	6.9	4.5
M2_SM21_05_Zrn20	836	0.78	0.0503	0.0024	0.1835	0.0088	0.0264	0.0009	0.16	167.8	5.4	170.9	7.6	172.1	109.6	167.8	5.4	1.8
M2_SM21_05_Zrn21	238	0.01	0.0532	0.0053	0.1953	0.0167	0.0276	0.0013	0.30	175.3	8.1	184.4	16.4	202.7	240.3	175.3	8.1	5.0
M2_SM21_05_Zrn22	263	0.02	0.0519	0.0049	0.1970	0.0187	0.0276	0.0010	0.14	175.5	6.4	181.4	15.9	230.4	201.3	175.5	6.4	3.2
M2_SM21_05_Zrn23	690	0.38	0.0498	0.0028	0.1873	0.0104	0.0274	0.0009	0.39	174.0	5.7	174.0	8.9	134.8	142.4	174.0	5.7	0.0
M2_SM21_05_Zrn24	48	0.03	0.0519	0.0097	0.2021	0.0361	0.0279	0.0015	-0.16	177.1	9.1	179.6	30.7	246.5	323.3	177.1	9.1	1.4
M2_SM21_05_Zrn25	410	0.47	0.0484	0.0053	0.1820	0.0198	0.0275	0.0012	0.26	175.1	7.8	169.4	17.0	65.5	290.8	175.1	7.8	-3.3
M2_SM21_05_Zrn26	123	0.05	0.0493	0.0043	0.1886	0.0166	0.0277	0.0011	0.17	175.9	6.6	174.4	14.1	94.1	218.6	175.9	6.6	-0.9
M2_SM21_05_Zrn27	136	0.01	0.0578	0.0111	0.2171	0.0390	0.0277	0.0013	0.41	175.9	8.0	197.7	32.8	243.4	599.5	175.9	8.0	11.0
M2_SM21_05_Zrn28	709	0.30	0.0490	0.0021	0.1866	0.0081	0.0276	0.0008	0.18	175.3	5.2	173.5	7.0	115.4	104.3	175.3	5.2	-1.0
M2_SM21_05_Zrn29	169	0.01	0.0512	0.0049	0.1934	0.0167	0.0278	0.0012	0.09	176.6	7.5	178.6	14.4	224.5	264.8	176.6	7.5	1.1
M2_SM21_05_Zrn30	582	0.56	0.0515	0.0053	0.1945	0.0197	0.0278	0.0010	0.17	176.5	6.3	180.0	16.8	190.5	252.7	176.5	6.3	2.0
M2_SM21_05_Zrn31	357	0.38	0.0485	0.0033	0.1830	0.0118	0.0276	0.0011	0.42	175.5	6.8	170.3	10.1	106.8	148.0	175.5	6.8	-3.1
M2_SM21_05_Zrn32	155	0.01	0.0496	0.0039	0.1893	0.0140	0.0278	0.0010	0.25	176.9	6.4	175.0	12.1	59.7	243.1	176.9	6.4	-1.0
M2_SM21_05_Zrn34	85	0.16	0.0537	0.0050	0.2008	0.0175	0.0275	0.0011	0.41	175.0	7.1	187.4	16.1	223.8	245.6	175.0	7.1	6.6
M2_SM21_05_Zrn35	70	0.19	0.0552	0.0079	0.2008	0.0270	0.0268	0.0013	0.27	170.6	8.0	183.4	22.4	200.4	300.7	170.6	8.0	7.0
M2_SM21_05_Zrn36	274	0.43	0.0484	0.0033	0.1837	0.0128	0.0276	0.0009	0.15	175.5	5.9	170.6	10.9	55.6	160.4	175.5	5.9	-2.9
M2_SM21_05_Zrn37	1369	0.68	0.0502	0.0021	0.1861	0.0086	0.0271	0.0009	-0.12	172.3	5.3	173.1	7.4	186.1	98.7	172.3	5.3	0.5
M2_SM21_05_Zrn38	185	0.10	0.0537	0.0059	0.1996	0.0200	0.0274	0.0012	0.35	173.9	7.7	183.8	17.0	203.4	279.0	173.9	7.7	5.4

Zircón	U ppm	Th/U	Relaciones isotópicas corregidas						rho	Edades corregidas						Mejor edad		Discordancia %
			$\frac{Pb^{207}}{Pb^{206}}$	$\pm 2\sigma$	$\frac{Pb^{207}}{U^{235}}$	$\pm 2\sigma$	$\frac{Pb^{206}}{U^{238}}$	$\pm 2\sigma$		$\frac{Pb^{206}}{U^{238}}$	$\pm 2\sigma$	$\frac{Pb^{207}}{U^{235}}$	$\pm 2\sigma$	$\frac{Pb^{207}}{Pb^{206}}$	$\pm 2\sigma$	Ma	$\pm 2\sigma$	
M2_SM21_21_Zrn01	403	0.92	0.0505	0.0044	0.1431	0.0107	0.0213	0.0008	0.47	136.1	4.8	138.0	10.9	188.7	175.8	136.1	4.8	1.3
M2_SM21_21_Zrn02	482	0.71	0.0523	0.0045	0.1507	0.0120	0.0213	0.0008	0.41	136.0	5.2	142.1	10.6	212.0	212.0	136.0	5.2	4.3
M2_SM21_21_Zrn03	304	0.91	0.0494	0.0045	0.1457	0.0137	0.0215	0.0007	0.03	137.2	4.7	137.5	12.1	27.3	240.0	137.2	4.7	0.2
M2_SM21_21_Zrn04	499	0.82	0.0504	0.0031	0.1447	0.0089	0.0210	0.0007	0.28	134.3	4.3	136.9	7.9	140.1	148.6	134.3	4.3	1.9
M2_SM21_21_Zrn05	243	0.47	0.0506	0.0042	0.1477	0.0120	0.0215	0.0008	0.27	137.1	5.0	139.3	10.6	156.4	181.1	137.1	5.0	1.6
M2_SM21_21_Zrn06	538	0.65	0.0520	0.0027	0.1634	0.0083	0.0230	0.0007	0.30	146.3	4.6	153.4	7.2	244.3	115.4	146.3	4.6	4.6
M2_SM21_21_Zrn07	158	0.46	0.0541	0.0061	0.1614	0.0170	0.0221	0.0011	0.39	140.7	6.8	150.7	14.8	209.3	258.4	140.7	6.8	6.7
M2_SM21_21_Zrn08	510	0.65	0.0485	0.0038	0.1460	0.0102	0.0221	0.0008	0.52	140.7	5.1	138.1	9.0	38.6	197.2	140.7	5.1	-1.9
M2_SM21_21_Zrn09	311	0.66	0.0507	0.0031	0.1513	0.0101	0.0216	0.0007	0.17	137.7	4.6	142.6	8.9	189.0	158.1	137.7	4.6	3.4
M2_SM21_21_Zrn10	363	0.59	0.0487	0.0041	0.1418	0.0116	0.0216	0.0010	0.53	137.5	6.2	134.4	10.1	110.4	241.9	137.5	6.2	-2.3
M3_SM21_21_Zrn11	342	0.50	0.0477	0.0045	0.1375	0.0116	0.0213	0.0010	0.52	135.7	6.0	130.4	10.4	-58.6	249.5	135.7	6.0	-4.1
M3_SM21_21_Zrn12	231	0.79	0.0498	0.0047	0.1452	0.0125	0.0216	0.0008	0.40	137.7	5.2	137.0	11.0	11.5	219.6	137.7	5.2	-0.5
M3_SM21_21_Zrn13	288	0.64	0.0496	0.0037	0.1434	0.0103	0.0214	0.0008	0.32	136.3	5.0	135.5	9.1	23.7	186.9	136.3	5.0	-0.6
M3_SM21_21_Zrn14	392	0.83	0.0474	0.0036	0.1393	0.0103	0.0214	0.0007	0.27	136.5	4.6	132.1	9.1	52.8	156.6	136.5	4.6	-3.3
M3_SM21_21_Zrn15	271	0.78	0.0481	0.0029	0.1418	0.0089	0.0217	0.0008	0.26	138.2	5.2	134.3	7.9	56.3	139.3	138.2	5.2	-2.9
M3_SM21_21_Zrn16	409	0.46	0.0492	0.0034	0.1409	0.0096	0.0210	0.0007	0.28	134.3	4.4	133.5	8.5	101.7	174.5	134.3	4.4	-0.6
M3_SM21_21_Zrn18	455	0.47	0.0506	0.0030	0.1446	0.0088	0.0210	0.0007	0.21	134.2	4.6	136.9	7.8	173.3	148.1	134.2	4.6	2.0
M3_SM21_21_Zrn19	341	0.61	0.0491	0.0047	0.1483	0.0144	0.0221	0.0009	0.22	140.7	5.5	139.9	12.7	105.7	209.2	140.7	5.5	-0.6
M3_SM21_21_Zrn20	421	0.49	0.0477	0.0040	0.1460	0.0122	0.0222	0.0009	0.40	141.8	5.8	137.9	10.8	133.5	239.0	141.8	5.8	-2.8
M3_SM21_21_Zrn21	283	0.82	0.0441	0.0052	0.1260	0.0142	0.0212	0.0010	0.35	135.5	6.0	120.0	12.7	-298.7	321.3	135.5	6.0	-12.9
M3_SM21_21_Zrn22	455	0.54	0.0476	0.0029	0.1395	0.0090	0.0214	0.0008	0.08	136.7	5.3	132.3	8.0	10.1	153.2	136.7	5.3	-3.3
M3_SM21_21_Zrn23	199	0.54	0.0474	0.0039	0.1401	0.0120	0.0216	0.0009	0.15	137.7	5.9	137.2	13.9	79.0	230.3	137.7	5.9	-0.3
M3_SM21_21_Zrn24	305	0.95	0.0501	0.0037	0.1461	0.0108	0.0208	0.0008	0.41	132.9	4.8	137.9	9.6	166.4	179.9	132.9	4.8	3.6
M3_SM21_21_Zrn25	358	0.69	0.0511	0.0045	0.1411	0.0105	0.0205	0.0008	0.32	131.1	5.0	133.7	9.3	160.6	193.3	131.1	5.0	2.0
M3_SM21_21_Zrn26	246	0.92	0.0540	0.0073	0.1515	0.0148	0.0206	0.0014	0.72	131.6	9.1	143.2	13.0	344.6	293.3	131.6	9.1	8.1
M3_SM21_21_Zrn28	559	0.70	0.0509	0.0039	0.1511	0.0114	0.0217	0.0007	0.21	138.1	4.6	142.5	10.0	156.8	179.8	138.1	4.6	3.1
M3_SM21_21_Zrn30	546	0.82	0.0496	0.0027	0.1482	0.0092	0.0214	0.0008	0.14	136.4	4.7	140.0	8.1	153.4	136.3	136.4	4.7	2.6
M3_SM21_21_Zrn31	206	0.88	0.0519	0.0050	0.1543	0.0130	0.0217	0.0009	0.52	138.4	5.6	145.2	11.5	167.0	230.0	138.4	5.6	4.7
M3_SM21_21_Zrn32	427	0.55	0.0488	0.0032	0.1419	0.0088	0.0212	0.0007	0.40	135.3	4.7	134.5	7.8	60.8	163.7	135.3	4.7	-0.6
M3_SM21_21_Zrn33	651	0.72	0.0467	0.0046	0.1319	0.0125	0.0207	0.0008	0.25	132.3	5.2	125.5	11.2	26.0	192.7	132.3	5.2	-5.4
M3_SM21_21_Zrn34	143	0.49	0.0563	0.0098	0.1528	0.0277	0.0200	0.0013	0.24	127.6	8.0	142.3	23.9	321.6	446.6	127.6	8.0	10.4
M3_SM21_21_Zrn35	467	0.88	0.0528	0.0070	0.1545	0.0210	0.0214	0.0007	-0.16	136.5	4.1	145.5	18.3	262.0	295.1	136.5	4.1	6.2
M3_SM21_21_Zrn36	267	0.63	0.0532	0.0040	0.1558	0.0116	0.0213	0.0008	0.45	135.8	4.8	146.4	10.2	305.6	173.9	135.8	4.8	7.2
M3_SM21_21_Zrn37	614	0.53	0.0521	0.0054	0.1514	0.0132	0.0214	0.0009	0.75	136.6	5.5	142.9	11.7	218.0	250.7	136.6	5.5	4.4
M3_SM21_21_Zrn38	330	0.70	0.0514	0.0037	0.1494	0.0112	0.0211	0.0007	0.13	134.8	4.6	140.8	9.8	215.6	172.8	134.8	4.6	4.3
M3_SM21_21_Zrn39	841	0.64	0.0475	0.0039	0.1354	0.0097	0.0209	0.0008	0.63	133.5	5.0	128.8	8.7	21.8	200.1	133.5	5.0	-3.6
M3_SM21_21_Zrn40	370	0.53	0.0493	0.0028	0.1460	0.0078	0.0215	0.0008	0.11	137.1	4.8	138.1	7.0	135.3	123.5	137.1	4.8	0.7
M3_SM21_21_Zrn41	153	0.86	0.0492	0.0046	0.1452	0.0134	0.0213	0.0009	0.21	135.8	5.4	137.2	12.0	153.0	229.7	135.8	5.4	1.0
M3_SM21_21_Zrn42	180	0.58	0.0496	0.0047	0.1491	0.0136	0.0221	0.0009	0.40	141.1	5.7	140.3	12.0	10.2	269.0	141.1	5.7	-0.5
M3_SM21_21_Zrn43	248	0.70	0.0497	0.0044	0.1506	0.0136	0.0222	0.0009	0.02	141.6	5.7	142.1	12.1	209.1	312.7	141.6	5.7	0.4

Continúa

Continuación

SM21-21 Meta-granitoide Pápalo		Espejo-Bautista et al., 2022																
Zircón	U ppm	Th/U	Relaciones isotópicas corregidas						rho	Edades corregidas						Mejor edad		Discordancia %
			$\frac{Pb^{207}}{Pb^{206}}$	$\pm 2\sigma$	$\frac{Pb^{207}}{U^{235}}$	$\pm 2\sigma$	$\frac{Pb^{206}}{U^{238}}$	$\pm 2\sigma$		$\frac{Pb^{206}}{U^{238}}$	$\pm 2\sigma$	$\frac{Pb^{207}}{U^{235}}$	$\pm 2\sigma$	$\frac{Pb^{207}}{Pb^{206}}$	$\pm 2\sigma$	Ma	$\pm 2\sigma$	
M3_SM21_21_Zrn44	390	0.77	0.0515	0.0038	0.1479	0.0101	0.0211	0.0008	0.53	134.3	4.8	139.8	8.9	175.9	187.5	134.3	4.8	3.9
M3_SM21_21_Zrn45	292	0.79	0.0541	0.0067	0.1640	0.0199	0.0222	0.0009	0.19	141.7	5.4	153.7	17.2	296.8	264.7	141.7	5.4	7.8
M3_SM21_21_Zrn46	362	0.77	0.0482	0.0031	0.1320	0.0083	0.0199	0.0007	0.29	127.3	4.1	125.5	7.5	40.2	153.0	127.3	4.1	-1.4
M3_SM21_21_Zrn47	352	0.48	0.0503	0.0050	0.1543	0.0150	0.0223	0.0010	0.28	142.3	6.0	145.4	13.2	146.2	240.5	142.3	6.0	2.1
M3_SM21_21_Zrn50	1801	0.41	0.0499	0.0025	0.1515	0.0072	0.0221	0.0007	0.43	140.7	4.6	143.1	6.3	147.7	119.2	140.7	4.6	1.6

SM21-26 Meta-granitoide Tepeuxila			Espejo-Bautista et al., 2022							Relaciones isotópicas corregidas						Edades corregidas			Mejor edad		Discordancia %
Zircón	U ppm	Th/U	$\frac{Pb^{207}}{Pb^{206}}$	$\pm 2\sigma$	$\frac{Pb^{207}}{U^{235}}$	$\pm 2\sigma$	$\frac{Pb^{206}}{U^{238}}$	$\pm 2\sigma$	rho	$\frac{Pb^{206}}{U^{238}}$	$\pm 2\sigma$	$\frac{Pb^{207}}{U^{235}}$	$\pm 2\sigma$	$\frac{Pb^{207}}{Pb^{206}}$	$\pm 2\sigma$	Ma	$\pm 2\sigma$				
M4_SM21_26_Zrn01	691	1.64	0.0560	0.0041	0.1489	0.0106	0.0193	0.0007	0.35	123.4	4.4	140.6	9.4	379.4	176.7	123.4	4.4	12.2			
M4_SM21_26_Zrn02	496	0.95	0.0515	0.0054	0.1464	0.0188	0.0202	0.0009	0.03	129.0	5.9	137.6	16.6	208.0	303.5	129.0	5.9	6.3			
M4_SM21_26_Zrn03	728	1.24	0.0505	0.0032	0.1362	0.0086	0.0196	0.0007	0.23	125.4	4.6	129.4	7.8	143.0	167.7	125.4	4.6	3.1			
M4_SM21_26_Zrn04	414	0.87	0.0549	0.0064	0.1500	0.0171	0.0201	0.0009	0.22	128.1	5.6	141.2	14.9	255.3	269.5	128.1	5.6	9.2			
M4_SM21_26_Zrn05	649	1.30	0.0511	0.0040	0.1376	0.0100	0.0198	0.0008	0.27	126.3	5.1	130.5	8.8	155.9	197.2	126.3	5.1	3.2			
M4_SM21_26_Zrn08	293	0.85	0.0522	0.0074	0.1440	0.0201	0.0200	0.0008	0.02	127.7	5.4	135.9	17.8	254.4	268.0	127.7	5.4	6.0			
M4_SM21_26_Zrn09	124	0.86	0.0554	0.0051	0.1496	0.0143	0.0196	0.0008	0.11	125.1	5.2	140.6	12.6	279.8	233.6	125.1	5.2	11.0			
M4_SM21_26_Zrn10	128	0.66	0.0496	0.0059	0.1386	0.0157	0.0206	0.0010	0.23	131.5	6.1	130.6	14.0	48.0	274.9	131.5	6.1	-0.7			
M4_SM21_26_Zrn11	142	1.15	0.0492	0.0054	0.1354	0.0138	0.0202	0.0009	0.53	128.7	5.7	128.3	12.3	64.9	241.2	128.7	5.7	-0.3			
M4_SM21_26_Zrn12	199	1.19	0.0504	0.0043	0.1458	0.0119	0.0210	0.0008	0.20	134.1	5.0	137.7	10.5	151.0	183.1	134.1	5.0	2.6			
M4_SM21_26_Zrn15	590	1.64	0.0481	0.0055	0.1354	0.0142	0.0207	0.0009	0.49	131.9	5.9	128.7	12.8	31.4	318.5	131.9	5.9	-2.5			
M4_SM21_26_Zrn16	712	0.31	0.0509	0.0039	0.1411	0.0102	0.0202	0.0007	0.32	129.2	4.5	133.8	9.0	191.2	165.1	129.2	4.5	3.5			
M4_SM21_26_Zrn17	114	0.58	0.0569	0.0073	0.1578	0.0188	0.0202	0.0008	0.33	129.1	5.1	147.2	16.4	158.4	351.6	129.1	5.1	12.3			
M4_SM21_26_Zrn18	896	1.65	0.0490	0.0032	0.1295	0.0088	0.0190	0.0006	0.22	121.6	4.0	123.5	7.9	166.7	133.2	121.6	4.0	1.5			
M4_SM21_26_Zrn19	296	0.70	0.0516	0.0060	0.1417	0.0166	0.0198	0.0009	0.14	126.5	5.7	133.7	14.9	135.1	295.8	126.5	5.7	5.4			
M4_SM21_26_Zrn20	376	1.02	0.0514	0.0044	0.1458	0.0121	0.0204	0.0008	0.49	130.2	5.3	137.4	10.7	142.0	226.4	130.2	5.3	5.3			
M4_SM21_26_Zrn21	381	0.52	0.0518	0.0061	0.1447	0.0137	0.0214	0.0012	0.21	136.7	7.4	136.9	12.2	158.8	292.4	136.7	7.4	0.1			
M4_SM21_26_Zrn22	757	1.48	0.0511	0.0038	0.1562	0.0110	0.0221	0.0009	0.39	140.8	5.5	147.1	9.7	174.5	189.1	140.8	5.5	4.3			
M4_SM21_26_Zrn23	252	1.03	0.0490	0.0052	0.1349	0.0144	0.0199	0.0008	0.10	127.2	5.3	127.5	12.9	43.9	267.6	127.2	5.3	0.2			
M4_SM21_26_Zrn25	195	1.07	0.0569	0.0087	0.1436	0.0211	0.0186	0.0009	0.27	119.0	5.9	134.7	18.6	167.0	403.6	119.0	5.9	11.6			
M4_SM21_26_Zrn26	728	1.40	0.0494	0.0026	0.1363	0.0072	0.0201	0.0007	0.29	128.2	4.1	129.6	6.4	132.7	122.1	128.2	4.1	1.1			
M4_SM21_26_Zrn27	151	0.91	0.0504	0.0067	0.1359	0.0174	0.0199	0.0009	0.34	126.9	5.9	131.2	17.1	175.3	311.0	126.9	5.9	3.3			
M4_SM21_26_Zrn28	258	1.06	0.0502	0.0057	0.1375	0.0141	0.0203	0.0011	0.35	129.7	7.0	130.3	12.6	146.6	224.6	129.7	7.0	0.5			
M4_SM21_26_Zrn29	637	1.44	0.0493	0.0023	0.1353	0.0067	0.0198	0.0006	0.32	126.6	3.9	128.7	6.0	133.4	120.1	126.6	3.9	1.6			
M4_SM21_26_Zrn30	223	0.94	0.0540	0.0049	0.1460	0.0125	0.0199	0.0008	0.29	127.2	4.8	137.9	11.1	264.7	216.3	127.2	4.8	7.8			
M4_SM21_26_Zrn31	275	0.98	0.0502	0.0042	0.1456	0.0127	0.0209	0.0008	0.30	133.2	4.8	137.3	11.2	138.8	211.5	133.2	4.8	3.0			
M4_SM21_26_Zrn32	64	0.72	0.0477	0.0071	0.1284	0.0197	0.0199	0.0011	0.18	126.8	6.7	120.7	17.4	29.2	331.9	126.8	6.7	-5.1			
M4_SM21_26_Zrn33	625	1.01	0.0495	0.0057	0.1399	0.0156	0.0200	0.0009	0.24	127.5	5.5	132.7	13.8	213.5	396.5	127.5	5.5	3.9			
M4_SM21_26_Zrn34	560	2.65	0.0517	0.0063	0.1404	0.0177	0.0199	0.0007	-0.03	127.1	4.4	133.0	15.8	178.1	307.6	127.1	4.4	4.4			
M4_SM21_26_Zrn35	216	1.05	0.0550	0.0061	0.1459	0.0143	0.0201	0.0012	0.52	128.4	7.8	137.4	12.7	218.0	317.3	128.4	7.8	6.6			
M4_SM21_26_Zrn36	216	0.99	0.0551	0.0084	0.1467	0.0200	0.0199	0.0010	0.40	126.8	6.5	138.2	17.8	234.5	366.7	126.8	6.5	8.3			
M4_SM21_26_Zrn37	94	0.74	0.0550	0.0082	0.1602	0.0250	0.0212	0.0010	-0.03	135.3	6.6	148.3	21.8	163.8	407.5	135.3	6.6	8.8			
M4_SM21_26_Zrn38	709	0.55	0.0563	0.0042	0.1552	0.0113	0.0200	0.0007	0.30	127.4	4.6	146.2	9.9	467.2	136.6	127.4	4.6	12.9			
M4_SM21_26_Zrn39	275	1.16	0.0509	0.0041	0.1438	0.0115	0.0208	0.0008	0.30	132.4	5.1	135.8	10.2	171.6	189.4	132.4	5.1	2.5			
M4_SM21_26_Zrn42	256	0.52	0.0537	0.0056	0.1542	0.0150	0.0213	0.0010	0.39	135.6	6.5	145.1	13.0	250.3	226.4	135.6	6.5	6.6			
M4_SM21_26_Zrn43	227	0.83	0.0524	0.0063	0.1549	0.0212	0.0207	0.0011	0.19	131.8	7.3	145.4	18.6	158.3	322.8	131.8	7.3	9.4			
M4_SM21_26_Zrn44	440	1.16	0.0511	0.0047	0.1429	0.0134	0.0201	0.0008	0.50	128.4	5.1	135.0	11.7	139.5	241.8	128.4	5.1	4.9			
M4_SM21_26_Zrn45	261	1.01	0.0543	0.0070	0.1436	0.0171	0.0197	0.0010	0.42	125.9	6.4	135.4	15.2	152.1	353.8	125.9	6.4	7.0			

SM21-33 Anfibolita (Paleosoma-Pochotepec) Espejo-Bautista et al., 2022																		
Zircón	U ppm	Th/U	Relaciones isotópicas corregidas						rho	Edades corregidas						Mejor edad		Discordancia %
			$\text{Pb}^{207}/\text{Pb}^{206}$	$\pm 2\sigma$	$\text{Pb}^{207}/\text{U}^{235}$	$\pm 2\sigma$	$\text{Pb}^{206}/\text{U}^{238}$	$\pm 2\sigma$		$\text{Pb}^{206}/\text{U}^{238}$	$\pm 2\sigma$	$\text{Pb}^{207}/\text{Pb}^{206}$	$\pm 2\sigma$	$\text{Pb}^{207}/\text{Pb}^{206}$	$\pm 2\sigma$	Ma	$\pm 2\sigma$	
MI_SM21_33_Zrn01	80	0.21	0.0705	0.0041	1.5750	0.1010	0.1602	0.0058	0.36	957.6	32.4	956.4	39.8	916.8	124.7	957.6	32.4	-4.5
MI_SM21_33_Zrn02	46	0.44	0.0756	0.0036	2.0848	0.1070	0.1959	0.0063	0.11	1152.7	33.8	1144.5	32.8	1112.2	87.0	1152.7	33.8	-3.6
MI_SM21_33_Zrn03	142	0.85	0.0736	0.0030	1.8233	0.0798	0.1774	0.0052	0.27	1052.8	28.3	1051.4	29.2	1015.3	84.4	1052.8	28.3	-3.7
MI_SM21_33_Zrn04	104	0.76	0.0772	0.0036	1.8950	0.0990	0.1755	0.0054	0.41	1042.0	29.4	1073.2	36.0	1136.1	80.1	1042.0	29.4	8.3
MI_SM21_33_Zrn05	82	0.24	0.0742	0.0057	1.8594	0.1364	0.1800	0.0062	0.00	1066.7	33.6	1059.9	48.2	999.4	152.4	1066.7	33.6	-6.7
MI_SM21_33_Zrn06	80	0.20	0.0751	0.0052	1.7313	0.1258	0.1657	0.0068	0.23	987.7	37.4	1013.5	48.1	1023.5	160.0	987.7	37.4	3.5
MI_SM21_33_Zrn07	52	0.18	0.0705	0.0059	1.5851	0.1378	0.1606	0.0058	0.24	960.1	32.2	956.6	55.2	886.0	188.3	960.1	32.2	-8.4
MI_SM21_33_Zrn08	75	0.20	0.0723	0.0054	1.5713	0.1041	0.1567	0.0059	0.27	938.4	32.8	955.2	41.5	959.4	148.6	938.4	32.8	2.2
MI_SM21_33_Zrn09	71	0.16	0.0707	0.0044	1.3637	0.0955	0.1375	0.0050	0.43	830.5	28.5	868.3	40.5	913.3	126.5	830.5	28.5	9.1
MI_SM21_33_Zrn10	395	0.10	0.0686	0.0023	1.5488	0.0513	0.1600	0.0042	0.27	956.9	23.6	949.3	20.4	895.0	60.0	956.9	23.6	-6.9
MI_SM21_33_Zrn11	58	0.22	0.0728	0.0045	1.5975	0.1018	0.1588	0.0055	0.25	949.8	30.9	964.7	39.1	974.5	126.6	949.8	30.9	2.5
MI_SM21_33_Zrn12	126	0.48	0.0778	0.0039	1.9315	0.0959	0.1779	0.0049	-0.06	1055.4	27.0	1088.6	33.4	1117.8	101.3	1055.4	27.0	5.6
MI_SM21_33_Zrn13	151	0.41	0.0782	0.0022	2.0860	0.0666	0.1908	0.0051	0.31	1125.4	27.8	1143.0	21.7	1143.8	54.9	1125.4	27.8	1.6
MI_SM21_33_Zrn14	78	0.33	0.0748	0.0039	1.6487	0.0909	0.1572	0.0046	0.23	940.9	25.5	985.3	35.2	1038.6	107.6	940.9	25.5	9.4
MI_SM21_33_Zrn16	54	0.39	0.0763	0.0043	1.8618	0.1241	0.1747	0.0069	0.51	1037.6	37.9	1061.3	43.8	1072.5	113.6	1037.6	37.9	3.3
MI_SM21_33_Zrn18	114	0.21	0.0715	0.0037	1.4979	0.0733	0.1507	0.0046	-0.07	904.5	25.9	925.9	29.9	935.0	106.1	904.5	25.9	3.3
MI_SM21_33_Zrn19	170	0.35	0.0729	0.0030	1.8378	0.0808	0.1798	0.0056	0.27	1065.5	30.5	1057.6	29.1	1001.7	84.9	1065.5	30.5	-6.4
MI_SM21_33_Zrn20	90	0.26	0.0725	0.0030	1.6065	0.0693	0.1588	0.0044	0.06	950.0	24.4	969.3	26.5	972.2	83.5	950.0	24.4	2.3
MI_SM21_33_Zrn21	69	0.32	0.0737	0.0033	1.8475	0.0921	0.1797	0.0061	0.39	1064.8	33.0	1058.6	32.4	1009.7	88.3	1064.8	33.0	-5.5
MI_SM21_33_Zrn22	216	0.40	0.0721	0.0024	1.8119	0.0652	0.1787	0.0054	0.47	1059.4	29.4	1048.1	23.8	991.0	62.0	1059.4	29.4	-6.9
MI_SM21_33_Zrn23	60	0.40	0.0787	0.0038	2.0486	0.1038	0.1865	0.0054	0.20	1102.0	29.4	1125.5	34.1	1128.8	96.2	1102.0	29.4	2.4
MI_SM21_33_Zrn24	88	0.33	0.0723	0.0032	1.5955	0.0747	0.1582	0.0048	0.25	946.3	26.6	964.6	29.5	967.2	91.4	946.3	26.6	2.2
MI_SM21_33_Zrn25	217	0.46	0.0829	0.0022	2.4606	0.0736	0.2128	0.0055	0.21	1243.9	29.2	1259.7	21.5	1260.5	50.6	1243.9	29.2	1.3
MI_SM21_33_Zrn26	80	0.22	0.0712	0.0033	1.5809	0.0760	0.1594	0.0045	0.14	953.5	25.1	959.8	31.0	962.8	87.4	953.5	25.1	1.0
MI_SM21_33_Zrn28	26	0.24	0.0839	0.0044	2.6536	0.1268	0.2282	0.0072	-0.11	1324.5	38.0	1309.2	34.8	1246.5	101.9	1324.5	38.0	-6.3
M2_SM21_33_Zrn29	518	0.21	0.0754	0.0020	1.8778	0.0620	0.1781	0.0051	0.55	1056.3	27.9	1072.4	21.8	1074.6	53.1	1056.3	27.9	1.7
M2_SM21_33_Zrn31	302	0.30	0.0766	0.0022	1.9102	0.0696	0.1787	0.0051	0.63	1059.7	27.7	1085.3	25.2	1100.5	58.0	1059.7	27.7	3.7
M2_SM21_33_Zrn32	172	0.39	0.0775	0.0036	1.9213	0.0971	0.1774	0.0055	0.36	1052.8	29.8	1085.5	34.3	1117.5	92.3	1052.8	29.8	5.8
M2_SM21_33_Zrn33	157	0.32	0.0696	0.0046	1.5357	0.1254	0.1580	0.0057	0.64	945.3	31.7	942.1	48.4	904.6	126.8	945.3	31.7	-4.5
M2_SM21_33_Zrn34	221	0.27	0.0776	0.0026	2.1352	0.0864	0.1972	0.0056	0.49	1160.1	30.1	1157.8	27.4	1126.9	64.7	1160.1	30.1	-2.9
M2_SM21_33_Zrn35	331	0.31	0.0763	0.0026	1.9148	0.0763	0.1793	0.0049	0.50	1063.1	26.6	1084.3	27.0	1091.8	68.4	1063.1	26.6	2.6
M2_SM21_33_Zrn36	188	0.41	0.0758	0.0025	1.8846	0.0664	0.1787	0.0049	0.07	1062.2	24.7	1073.6	23.1	1074.4	66.9	1062.2	24.7	1.1
M2_SM21_33_Zrn37	66	0.15	0.0735	0.0048	1.5275	0.0971	0.1498	0.0050	0.05	899.6	27.9	934.9	38.8	973.6	131.9	899.6	27.9	7.6
M2_SM21_33_Zrn38	176	0.41	0.0787	0.0033	2.0583	0.0887	0.1897	0.0055	0.26	1119.4	29.9	1137.9	31.7	1146.2	80.6	1119.4	29.9	2.3
M2_SM21_33_Zrn39	145	0.75	0.0727	0.0040	1.8340	0.1063	0.1817	0.0053	0.12	1076.4	29.2	1054.5	37.9	983.1	114.6	1076.4	29.2	-9.5
M2_SM21_33_Zrn40	83	0.22	0.0706	0.0045	1.5536	0.0972	0.1589	0.0051	0.02	950.6	28.4	947.7	39.1	908.1	136.3	950.6	28.4	-4.7
M2_SM21_33_Zrn41	106	0.24	0.0709	0.0047	1.5731	0.0962	0.1605	0.0051	-0.21	959.1	28.5	954.4	38.3	902.0	144.2	959.1	28.5	-6.3
M2_SM21_33_Zrn42	588	0.21	0.0715	0.0022	1.6834	0.0604	0.1694	0.0047	0.44	1008.4	25.6	1000.4	23.1	960.3	63.3	1008.4	25.6	-5.0
M2_SM21_33_Zrn43	100	0.16	0.0745	0.0074	1.6560	0.1779	0.1603	0.0067	0.32	958.4	37.3	983.1	68.7	997.4	223.5	958.4	37.3	3.9
M2_SM21_33_Zrn44	190	0.33	0.0718	0.0025	1.5720	0.0572	0.1586	0.0042	0.08	949.0	23.2	960.5	23.9	961.8	72.0	949.0	23.2	1.3
M2_SM21_33_Zrn45	45	0.12	0.0690	0.0057	1.3292	0.1058	0.1398	0.0056	0.12	843.1	31.9	859.9	53.6	878.2	178.4	843.1	31.9	4.0
M2_SM21_33_Zrn46	69	1.02	0.0733	0.0039	1.8427	0.1023	0.1813	0.0063	0.21	1073.8	34.3	1055.2	37.3	983.6	118.0	1073.8	34.3	-9.2
M2_SM21_33_Zrn47	830	0.11	0.0795	0.0020	2.1824	0.0627	0.1980	0.0051	0.19	1164.4	27.2	1175.0	20.0	1180.5	48.9	1164.4	27.2	1.4
M2_SM21_33_Zrn49	85	0.39	0.0764	0.0035	1.8897	0.0913	0.1786	0.0054	0.21	1058.9	29.3	1072.4	32.0	1073.0	95.6	1058.9	29.3	1.3
M2_SM21_33_Zrn51	311	0.17	0.0795	0.0024	2.1197	0.0722	0.1914	0.0056	0.38	1128.8	30.1	1153.9	23.6	1175.2	60.2	1128.8	30.1	4.0
M2_SM21_33_Zrn52	79	0.14	0.0712	0.0054	1.5279	0.1290	0.1558	0.0057	0.59	933.2	32.0	935.9	50.0	984.6	176.0	933.2	32.0	5.2
M2_SM21_33_Zrn53	65	0.17	0.0690	0.0032	1.5385	0.0681	0.1600	0.0050	0.16	956.6	27.8	942.5	27.3	885.8	91.2	956.6	27.8	-8.0

Continúa

Continuación

SM21-33 Anfíbolita (Paleosoma-Pochotepec) Espejo-Bautista et al., 2022

Zircón	U ppm	Th/U	Relaciones isotópicas corregidas							Edades corregidas					Mejor edad		Discordancia %	
			$\frac{Pb^{207}}{Pb^{206}}$	$\pm 2\sigma$	$\frac{Pb^{207}}{U^{235}}$	$\pm 2\sigma$	$\frac{Pb^{206}}{U^{238}}$	$\pm 2\sigma$	ρ	$\frac{Pb^{206}}{U^{238}}$	$\pm 2\sigma$	$\frac{Pb^{207}}{U^{235}}$	$\pm 2\sigma$	$\frac{Pb^{207}}{Pb^{206}}$	$\pm 2\sigma$	Ma		$\pm 2\sigma$
M2_SM21_33_Zrn54	62	0.12	0.0744	0.0064	1.5420	0.1170	0.1514	0.0059	-0.27	908.5	33.2	941.8	46.6	993.1	184.0	908.5	33.2	8.5
M2_SM21_33_Zrn55	67	0.23	0.0712	0.0036	1.4826	0.0771	0.1494	0.0046	-0.05	897.2	25.6	918.7	31.4	941.9	113.5	897.2	25.6	4.7
M2_SM21_33_Zrn56	44	0.39	0.0792	0.0037	2.2077	0.1062	0.2018	0.0063	0.23	1184.2	34.1	1177.8	33.6	1146.4	90.7	1184.2	34.1	-3.3
M2_SM21_33_Zrn57	133	0.40	0.0746	0.0025	1.9664	0.0725	0.1905	0.0050	0.11	1123.9	27.3	1101.5	24.9	1053.8	65.1	1123.9	27.3	-6.6
M2_SM21_33_Zrn58	690	0.13	0.0742	0.0019	1.8281	0.0567	0.1783	0.0047	0.42	1057.7	25.5	1055.0	20.5	1041.7	52.6	1057.7	25.5	-1.5
M2_SM21_33_Zrn61	207	0.31	0.0728	0.0034	1.6148	0.0899	0.1611	0.0062	0.58	962.6	34.1	974.5	35.3	999.5	95.5	962.6	34.1	3.7
M2_SM21_33_Zrn62	71	0.17	0.0729	0.0047	1.7281	0.1220	0.1710	0.0058	0.31	1017.6	31.9	1013.8	44.8	979.4	137.5	1017.6	31.9	-3.9
M2_SM21_33_Zrn64	164	0.25	0.0805	0.0029	2.2289	0.0917	0.2009	0.0061	0.38	1179.8	32.8	1186.6	28.9	1203.4	68.2	1179.8	32.8	2.0
M2_SM21_33_Zrn65	47	0.25	0.0868	0.0045	2.6457	0.1296	0.2219	0.0069	-0.07	1291.5	36.4	1309.2	36.1	1329.9	99.9	1291.5	36.4	2.9
M3_SM21_33_Zrn66	51	0.23	0.0715	0.0037	1.5478	0.0847	0.1575	0.0054	0.29	942.4	30.2	943.2	34.0	950.0	97.1	942.4	30.2	0.8
M3_SM21_33_Zrn67	96	0.23	0.0726	0.0033	1.5571	0.0726	0.1559	0.0046	0.09	936.7	23.8	948.7	28.9	965.5	96.5	936.7	23.8	3.0
M3_SM21_33_Zrn68	77	0.16	0.0718	0.0041	1.5060	0.0851	0.1526	0.0047	-0.04	915.5	26.0	927.5	33.9	934.2	118.7	915.5	26.0	2.0
M3_SM21_33_Zrn69	95	0.22	0.0724	0.0039	1.5654	0.0819	0.1575	0.0050	0.04	942.8	28.0	952.2	32.5	958.9	112.3	942.8	28.0	1.7
M3_SM21_33_Zrn70	34	0.15	0.0716	0.0050	1.5726	0.1152	0.1579	0.0060	0.03	944.3	33.3	955.9	48.2	979.3	150.9	944.3	33.3	3.6

SM21-07 Meta-basalto (s. Pochotepec) Espejo-Bautista et al., 2022

Zircón	U ppm	Th/U	Relaciones isotópicas corregidas						rho	Edades corregidas						Mejor edad		Discordancia %
			$\frac{Pb^{207}}{Pb^{206}}$	$\pm 2\sigma$	$\frac{Pb^{207}}{U^{235}}$	$\pm 2\sigma$	$\frac{Pb^{206}}{U^{238}}$	$\pm 2\sigma$		$\frac{Pb^{206}}{U^{238}}$	$\pm 2\sigma$	$\frac{Pb^{207}}{U^{235}}$	$\pm 2\sigma$	$\frac{Pb^{207}}{Pb^{206}}$	$\pm 2\sigma$	Ma	$\pm 2\sigma$	
M1_SM21_07_Zrn01	75	0.26	0.0708	0.0050	1.4823	0.1029	0.1535	0.0060	0.35	920.2	33.3	917.9	42.9	904.2	154.3	920.2	33.3	-1.8
M1_SM21_07_Zrn02	216	0.42	0.0762	0.0029	1.8813	0.0746	0.1796	0.0051	0.41	1064.6	27.9	1072.7	26.9	1087.1	81.6	1064.6	27.9	2.1
M1_SM21_07_Zrn03	1041	0.11	0.0767	0.0018	1.9084	0.0612	0.1819	0.0056	0.04	1077.0	30.4	1083.1	21.3	1110.8	46.2	1077.0	30.4	3.0
M1_SM21_07_Zrn04	50	0.09	0.0665	0.0070	1.1342	0.1274	0.1239	0.0056	-0.05	752.2	32.4	756.6	61.5	776.9	195.2	752.2	32.4	3.2
M1_SM21_07_Zrn07	66	0.87	0.0759	0.0073	1.8902	0.1360	0.1836	0.0083	0.76	1086.1	45.0	1074.5	46.4	1055.7	183.4	1086.1	45.0	-2.9
M1_SM21_07_Zrn08	621	0.07	0.0759	0.0021	1.8652	0.0645	0.1790	0.0048	0.01	1061.7	26.2	1068.1	22.9	1088.5	56.5	1061.7	26.2	2.5
M1_SM21_07_Zrn09	30	0.16	0.0740	0.0066	1.5963	0.1370	0.1550	0.0058	0.30	928.8	32.6	958.5	53.0	959.2	182.0	928.8	32.6	3.2
M1_SM21_07_Zrn10	535	0.10	0.0802	0.0021	2.2168	0.0678	0.2013	0.0053	0.27	1182.3	28.4	1185.7	21.4	1196.5	50.9	1182.3	28.4	1.2
M1_SM21_07_Zrn11	274	0.26	0.0793	0.0020	2.1930	0.0664	0.2012	0.0050	0.21	1181.8	27.1	1177.7	21.0	1172.9	50.9	1181.8	27.1	-0.8
M1_SM21_07_Zrn12	43	0.71	0.0757	0.0052	1.7442	0.1254	0.1682	0.0060	0.12	1001.7	33.3	1017.5	46.7	1038.2	146.9	1001.7	33.3	3.5
M1_SM21_07_Zrn15	310	0.26	0.0732	0.0024	1.7278	0.0714	0.1717	0.0051	0.02	1021.2	27.9	1017.5	26.3	1011.3	68.2	1021.2	27.9	-1.0
M1_SM21_07_Zrn17	46	0.03	0.0703	0.0044	1.5811	0.1004	0.1634	0.0053	0.09	975.1	29.4	953.4	40.4	893.3	131.1	975.1	29.4	-9.1
M1_SM21_07_Zrn18	47	0.05	0.0733	0.0049	1.5673	0.1125	0.1555	0.0054	0.05	931.4	30.2	948.8	43.5	966.3	134.5	931.4	30.2	3.6
M1_SM21_07_Zrn19	251	0.27	0.0764	0.0029	1.9283	0.0764	0.1835	0.0053	0.34	1085.8	29.0	1088.9	27.2	1091.4	79.2	1085.8	29.0	0.5
M1_SM21_07_Zrn20	40	0.03	0.0722	0.0051	1.3590	0.0899	0.1385	0.0060	0.35	835.3	33.8	862.0	39.0	905.6	140.4	835.3	33.8	7.8
M1_SM21_07_Zrn21	67	0.16	0.0729	0.0067	1.5341	0.1220	0.1546	0.0052	0.67	926.8	29.0	937.5	47.5	942.2	182.3	926.8	29.0	1.6
M1_SM21_07_Zrn22	55	1.05	0.0708	0.0047	1.5226	0.0952	0.1571	0.0057	0.46	940.4	31.6	933.6	39.5	933.3	132.8	940.4	31.6	-0.8
M2_SM21_07_Zrn23	170	0.27	0.0804	0.0024	2.2926	0.0834	0.2074	0.0059	0.19	1215.0	31.8	1208.4	25.7	1199.9	60.7	1215.0	31.8	-1.3
M2_SM21_07_Zrn24	46	0.95	0.0705	0.0038	1.5180	0.0820	0.1565	0.0044	0.32	937.3	24.6	931.4	32.6	891.2	111.1	937.3	24.6	-5.2
M2_SM21_07_Zrn25	294	0.32	0.0781	0.0019	2.1124	0.0621	0.1959	0.0051	0.38	1153.3	27.2	1152.0	20.2	1144.5	49.5	1153.3	27.2	-0.8
M2_SM21_07_Zrn26	113	0.21	0.0761	0.0034	1.9087	0.1076	0.1820	0.0072	0.03	1077.8	39.0	1082.1	38.0	1088.1	93.0	1077.8	39.0	0.9
M2_SM21_07_Zrn27	15	0.06	0.0753	0.0069	1.5824	0.1435	0.1525	0.0068	0.23	913.4	37.7	938.0	59.9	952.8	199.5	913.4	37.7	4.1
M2_SM21_07_Zrn28	32	0.02	0.0742	0.0059	1.5996	0.1232	0.1580	0.0055	0.09	945.1	30.8	957.0	47.6	982.3	173.2	945.1	30.8	3.8
M2_SM21_07_Zrn29	94	0.30	0.0704	0.0048	1.4041	0.0967	0.1466	0.0045	0.28	881.5	25.6	884.8	39.9	890.6	140.0	881.5	25.6	1.0
M2_SM21_07_Zrn30	195	0.51	0.0694	0.0030	1.4922	0.0780	0.1535	0.0047	0.37	920.7	26.4	925.2	31.2	929.9	108.4	920.7	26.4	1.0
M2_SM21_07_Zrn31	102	0.48	0.0731	0.0034	1.7494	0.1252	0.1774	0.0064	0.10	1052.8	35.2	1039.4	33.7	1005.5	95.4	1052.8	35.2	-4.7
M2_SM21_07_Zrn32	177	0.30	0.0791	0.0026	2.1511	0.0761	0.1979	0.0052	0.30	1163.8	28.2	1163.0	24.5	1159.4	63.8	1163.8	28.2	-0.4
M2_SM21_07_Zrn33	403	0.32	0.0828	0.0021	2.4300	0.0715	0.2133	0.0055	0.33	1246.3	29.0	1250.7	21.0	1259.7	48.6	1246.3	29.0	1.1
M2_SM21_07_Zrn34	47	0.28	0.0805	0.0042	2.2249	0.1438	0.2009	0.0083	0.04	1179.0	44.3	1176.8	44.8	1160.9	111.3	1179.0	44.3	-1.6
M2_SM21_07_Zrn35	230	0.64	0.0799	0.0024	2.2543	0.0767	0.2053	0.0054	0.30	1203.4	28.8	1196.2	23.8	1182.0	61.4	1203.4	28.8	-1.8
M2_SM21_07_Zrn36	121	1.86	0.0821	0.0037	2.3660	0.1169	0.2095	0.0054	-0.07	1225.9	28.9	1229.0	35.0	1231.9	87.6	1225.9	28.9	0.5
M2_SM21_07_Zrn37	55	0.06	0.0713	0.0054	1.3786	0.1005	0.1412	0.0055	0.25	851.2	30.8	871.2	42.8	887.6	156.7	851.2	30.8	4.1
M2_SM21_07_Zrn38	179	0.49	0.0772	0.0029	1.9722	0.0801	0.1855	0.0056	0.27	1096.9	30.5	1104.4	27.6	1115.2	74.2	1096.9	30.5	1.6
M2_SM21_07_Zrn39	34	0.03	0.0751	0.0066	1.5282	0.1291	0.1496	0.0054	0.37	898.2	30.5	926.1	51.8	929.5	198.4	898.2	30.5	3.4
M2_SM21_07_Zrn40	53	0.05	0.0716	0.0056	1.5236	0.1152	0.1557	0.0050	0.37	932.3	28.1	928.3	45.8	873.3	169.0	932.3	28.1	-6.7
M2_SM21_07_Zrn41	128	0.37	0.0768	0.0042	1.9128	0.1129	0.1814	0.0062	0.14	1074.5	33.9	1082.3	39.2	1098.3	109.0	1074.5	33.9	2.2
M2_SM21_07_Zrn42	206	0.50	0.0811	0.0022	2.2938	0.0709	0.2055	0.0053	0.28	1204.9	28.2	1209.1	21.8	1216.4	52.7	1204.9	28.2	0.9
M2_SM21_07_Zrn44	225	0.39	0.0787	0.0021	2.3060	0.0829	0.2128	0.0064	0.07	1243.0	33.9	1211.9	25.3	1156.3	53.2	1243.0	33.9	-7.5
M2_SM21_07_Zrn45	91	0.47	0.0808	0.0032	2.2424	0.0787	0.2036	0.0058	0.62	1194.2	30.9	1197.4	27.6	1200.5	79.1	1194.2	30.9	0.5
M2_SM21_07_Zrn46	87	0.13	0.0761	0.0038	1.8609	0.1159	0.1769	0.0063	-0.16	1049.6	34.5	1061.9	41.0	1073.7	101.4	1049.6	34.5	2.2
M2_SM21_07_Zrn47	78	0.41	0.0744	0.0033	1.7462	0.1045	0.1705	0.0061	-0.37	1014.8	33.4	1023.6	39.6	1044.4	91.6	1014.8	33.4	2.8
M2_SM21_07_Zrn48	116	0.26	0.0816	0.0026	2.3362	0.0828	0.2080	0.0054	0.27	1218.0	28.9	1221.3	24.8	1224.6	62.2	1218.0	28.9	0.5
M2_SM21_07_Zrn49	308	0.09	0.0798	0.0025	2.3765	0.0903	0.2178	0.0067	0.40	1269.8	35.4	1234.0	27.2	1185.2	63.5	1269.8	35.4	-7.1
M2_SM21_07_Zrn50	185	0.16	0.0771	0.0030	1.9346	0.0731	0.1820	0.0054	0.55	1077.8	29.5	1092.7	25.5	1118.3	77.7	1077.8	29.5	3.6
M2_SM21_07_Zrn51	206	0.45	0.0809	0.0022	2.2998	0.0730	0.2055	0.0053	0.26	1204.8	28.6	1211.0	22.4	1213.3	52.7	1204.8	28.6	0.7

Continúa

Continuación

SM21-07 Meta-basalto (s. Pochotepec) Espejo-Bautista et al., 2022

Zircón	U ppm	Th/U	Relaciones isotópicas corregidas						rho	Edades corregidas						Mejor edad		Discordancia %
			$\frac{Pb^{207}}{Pb^{206}}$	$\pm 2\sigma$	$\frac{Pb^{207}}{U^{235}}$	$\pm 2\sigma$	$\frac{Pb^{206}}{U^{238}}$	$\pm 2\sigma$		$\frac{Pb^{206}}{U^{238}}$	$\pm 2\sigma$	$\frac{Pb^{207}}{U^{235}}$	$\pm 2\sigma$	$\frac{Pb^{207}}{Pb^{206}}$	$\pm 2\sigma$	Ma	$\pm 2\sigma$	
M2_SM21_07_Zrn52	22	0.36	0.0769	0.0056	1.9043	0.1361	0.1788	0.0065	0.41	1059.6	35.2	1077.6	44.9	1083.0	146.0	1059.6	35.2	2.2
M2_SM21_07_Zrn53	26	0.41	0.0849	0.0059	2.3212	0.1369	0.2009	0.0080	0.58	1179.2	43.2	1211.8	41.2	1260.1	129.9	1179.2	43.2	6.4
M2_SM21_07_Zrn54	305	0.15	0.0816	0.0025	2.3468	0.0752	0.2088	0.0056	0.49	1222.5	30.1	1225.5	22.9	1228.4	58.9	1222.5	30.1	0.5
M2_SM21_07_Zrn55	52	0.05	0.0729	0.0054	1.6516	0.1245	0.1647	0.0056	0.16	982.4	30.7	979.5	49.9	971.0	153.1	982.4	30.7	-1.2
M2_SM21_07_Zrn56	47	0.07	0.0719	0.0081	1.5378	0.1420	0.1570	0.0062	0.70	939.6	34.9	937.8	57.1	895.8	231.1	939.6	34.9	-4.9
M2_SM21_07_Zrn57	95	0.33	0.0799	0.0030	2.1681	0.0857	0.1972	0.0056	0.39	1159.9	30.1	1167.5	27.7	1171.6	78.8	1159.9	30.1	1.0
M2_SM21_07_Zrn58	23	0.02	0.0726	0.0064	1.5327	0.1284	0.1552	0.0058	0.38	929.3	32.5	925.7	50.9	880.3	180.3	929.3	32.5	-5.6
M2_SM21_07_Zrn59	153	0.34	0.0766	0.0030	1.9355	0.0803	0.1829	0.0049	0.28	1083.0	26.6	1091.4	27.3	1095.6	77.5	1083.0	26.6	1.2
M2_SM21_07_Zrn60	29	0.03	0.0734	0.0055	1.5231	0.1051	0.1543	0.0055	0.39	924.3	30.9	935.0	45.3	943.3	152.9	924.3	30.9	2.0

SM21-28 Meta-andesita (s. Pochotepec)

Espejo-Bautista et al., 2022

Zircón	U ppm	Th/U	Relaciones isotópicas corregidas						rho	Edades corregidas						Mejor edad		Discordancia %
			$\frac{Pb^{207}}{Pb^{206}}$	$\pm 2\sigma$	$\frac{Pb^{207}}{U^{235}}$	$\pm 2\sigma$	$\frac{Pb^{206}}{U^{238}}$	$\pm 2\sigma$		$\frac{Pb^{206}}{U^{238}}$	$\pm 2\sigma$	$\frac{Pb^{207}}{U^{235}}$	$\pm 2\sigma$	$\frac{Pb^{207}}{Pb^{206}}$	$\pm 2\sigma$	Ma	$\pm 2\sigma$	
M2_SM21_28_Zrn02	152	0.21	0.0702	0.0036	1.4865	0.0729	0.1543	0.0043	-0.17	924.7	24.3	921.3	30.2	900.4	108.7	924.7	24.3	-2.7
M2_SM21_28_Zrn03	121	0.71	0.0749	0.0036	1.7245	0.0861	0.1677	0.0055	0.26	999.2	30.6	1014.2	32.3	1041.0	96.7	999.2	30.6	4.0
M3_SM21_28_Zrn04	732	0.15	0.0752	0.0020	1.8537	0.0627	0.1783	0.0049	0.53	1057.8	26.7	1063.7	22.5	1068.9	54.7	1057.8	26.7	1.0
M3_SM21_28_Zrn05	492	0.28	0.0735	0.0024	1.7093	0.0623	0.1683	0.0045	0.20	1002.8	24.8	1011.3	23.4	1021.2	66.9	1002.8	24.8	1.8
M3_SM21_28_Zrn06	692	0.07	0.0720	0.0019	1.5430	0.0536	0.1556	0.0048	0.67	931.9	26.6	946.8	21.4	981.7	53.7	931.9	26.6	5.1
M3_SM21_28_Zrn07	176	0.36	0.0714	0.0029	1.5209	0.0682	0.1541	0.0045	0.27	923.6	25.2	937.3	27.8	956.0	85.9	923.6	25.2	3.4
M3_SM21_28_Zrn08	378	0.16	0.0735	0.0020	1.7928	0.0646	0.1754	0.0050	0.35	1041.8	27.3	1041.3	23.3	1031.1	60.0	1041.8	27.3	-1.0
M3_SM21_28_Zrn09	144	0.35	0.0707	0.0020	1.5916	0.0539	0.1631	0.0043	0.40	974.0	23.9	968.9	22.8	948.6	62.6	974.0	23.9	-2.7
M3_SM21_28_Zrn10	742	0.18	0.0753	0.0018	1.8248	0.0535	0.1758	0.0045	0.51	1043.7	24.9	1053.8	19.2	1071.1	49.1	1043.7	24.9	2.6
M3_SM21_28_Zrn11	136	0.40	0.0748	0.0026	1.8203	0.0674	0.1764	0.0053	0.59	1047.3	29.2	1051.2	24.1	1052.8	69.2	1047.3	29.2	0.5
M3_SM21_28_Zrn12	152	0.43	0.0751	0.0024	1.8364	0.0647	0.1772	0.0048	0.77	1051.3	26.1	1056.8	23.5	1058.5	66.5	1051.3	26.1	0.7
M3_SM21_28_Zrn13	1516	0.01	0.0702	0.0022	1.4905	0.0520	0.1542	0.0042	0.24	924.2	23.6	926.2	21.2	929.5	64.0	924.2	23.6	0.6
M3_SM21_28_Zrn14	260	0.35	0.0720	0.0018	1.6220	0.0478	0.1631	0.0041	0.28	974.1	22.7	978.0	18.4	994.3	58.1	974.1	22.7	2.0
M3_SM21_28_Zrn15	121	0.55	0.0694	0.0027	1.5129	0.0676	0.1562	0.0042	0.41	935.5	23.6	934.0	27.2	923.7	65.4	935.5	23.6	-1.3
M3_SM21_28_Zrn16	112	0.57	0.0799	0.0027	2.3043	0.0830	0.2083	0.0058	0.17	1219.5	30.8	1211.2	25.5	1178.6	66.5	1219.5	30.8	-3.5
M3_SM21_28_Zrn17	123	0.26	0.0717	0.0024	1.7024	0.0622	0.1714	0.0047	0.17	1019.6	25.8	1007.1	23.2	970.1	65.2	1019.6	25.8	-5.1
M3_SM21_28_Zrn18	332	0.15	0.0784	0.0030	2.2233	0.1724	0.2024	0.0104	0.95	1186.7	55.6	1176.5	53.7	1142.6	75.9	1186.7	55.6	-3.9
M3_SM21_28_Zrn19	434	0.08	0.0742	0.0019	1.8325	0.0528	0.1783	0.0051	0.36	1057.3	27.9	1056.6	18.9	1049.0	46.4	1057.3	27.9	-0.8
M3_SM21_28_Zrn20	129	0.15	0.0749	0.0030	1.8758	0.1138	0.1780	0.0067	0.08	1055.8	36.7	1068.4	40.4	1078.2	97.3	1055.8	36.7	2.1
M3_SM21_28_Zrn21	50	0.37	0.0813	0.0046	2.2916	0.1843	0.2018	0.0099	0.72	1182.8	52.9	1192.9	56.5	1184.1	115.5	1182.8	52.9	0.1
M3_SM21_28_Zrn22	379	0.12	0.0722	0.0025	1.6213	0.0598	0.1618	0.0044	0.07	966.6	24.4	977.5	23.4	982.6	72.6	966.6	24.4	1.6
M3_SM21_28_Zrn23	32	0.24	0.0737	0.0054	1.5774	0.1072	0.1552	0.0061	-0.06	929.7	34.0	956.0	43.3	981.7	161.9	929.7	34.0	5.3
M3_SM21_28_Zrn25	69	0.25	0.0707	0.0033	1.5437	0.0749	0.1565	0.0051	0.02	936.9	28.3	944.6	30.6	969.1	93.4	936.9	28.3	3.3
M4_SM21_28_Zrn26	380	0.21	0.0718	0.0022	1.5476	0.0661	0.1543	0.0047	0.13	924.9	26.1	947.1	24.7	969.5	64.0	924.9	26.1	4.6
M4_SM21_28_Zrn27	250	0.29	0.0708	0.0024	1.5174	0.0628	0.1557	0.0045	0.67	932.7	25.0	940.9	28.2	940.7	68.5	932.7	25.0	0.8
M4_SM21_28_Zrn28	621	0.08	0.0713	0.0033	1.5352	0.0625	0.1551	0.0043	-0.53	929.6	23.9	944.2	24.6	958.8	89.8	929.6	23.9	3.0
M4_SM21_28_Zrn29	1032	0.10	0.0711	0.0025	1.5076	0.0503	0.1547	0.0055	0.57	926.7	30.3	932.8	20.1	951.9	72.8	926.7	30.3	2.6
M4_SM21_28_Zrn30	111	0.77	0.0733	0.0028	1.6781	0.0672	0.1650	0.0046	0.16	984.4	25.3	997.4	25.9	1000.1	78.8	984.4	25.3	1.6
M4_SM21_28_Zrn31	344	0.65	0.0745	0.0027	1.7499	0.0681	0.1698	0.0044	0.20	1011.0	24.1	1025.9	25.1	1044.7	72.3	1011.0	24.1	3.2
M4_SM21_28_Zrn32	361	0.07	0.0708	0.0025	1.5253	0.0591	0.1556	0.0042	0.19	932.1	23.6	939.4	23.7	940.6	73.0	932.1	23.6	0.9
M4_SM21_28_Zrn34	186	0.28	0.0710	0.0023	1.6407	0.0595	0.1660	0.0044	0.20	990.1	24.3	987.8	21.0	955.8	62.7	990.1	24.3	-3.6
M4_SM21_28_Zrn36	383	0.28	0.0739	0.0036	1.8232	0.0815	0.1774	0.0057	0.14	1052.7	31.3	1052.6	29.5	1025.0	101.5	1052.7	31.3	-2.7
M4_SM21_28_Zrn38	407	0.57	0.0711	0.0026	1.5306	0.0667	0.1550	0.0045	0.50	929.0	25.1	941.2	26.5	950.4	72.6	929.0	25.1	2.3
M4_SM21_28_Zrn39	247	0.50	0.0791	0.0022	2.1405	0.0673	0.1943	0.0051	0.18	1144.7	27.7	1161.1	22.0	1169.4	56.6	1144.7	27.7	2.1

SM21-13a Anfibolita (s. Pochotepec)			Espejo-Bautista et al., 2022															
Zircón	U ppm	Th/U	Relaciones isotópicas corregidas						rho	Edades corregidas						Mejor edad		Discordancia %
			$\frac{Pb^{207}}{Pb^{206}}$	$\pm 2\sigma$	$\frac{Pb^{207}}{U^{235}}$	$\pm 2\sigma$	$\frac{Pb^{206}}{U^{238}}$	$\pm 2\sigma$		$\frac{Pb^{206}}{U^{238}}$	$\pm 2\sigma$	$\frac{Pb^{207}}{U^{235}}$	$\pm 2\sigma$	$\frac{Pb^{207}}{Pb^{206}}$	$\pm 2\sigma$	Ma	$\pm 2\sigma$	
M4_SM21_13a_Zrn01	128	0.47	0.0705	0.0027	1.5325	0.0642	0.1590	0.0044	0.22	950.9	24.4	940.8	26.0	921.1	83.1	950.9	24.4	-3.2
M4_SM21_13a_Zrn02	499	0.0437	0.0722	0.0019	1.5663	0.0537	0.1581	0.0048	0.62	946.1	26.7	956.0	20.8	987.3	55.4	946.1	26.7	4.2
M4_SM21_13a_Zrn04	243	0.1385	0.0805	0.0023	2.2030	0.0792	0.2000	0.0058	0.60	1174.8	31.4	1179.8	25.2	1200.0	55.6	1174.8	31.4	2.1
M4_SM21_13a_Zrn05	232	0.2122	0.0717	0.0024	1.5556	0.0548	0.1590	0.0043	0.04	951.0	23.7	951.5	21.8	964.9	68.7	951.0	23.7	1.4
M4_SM21_13a_Zrn06	138	0.5860	0.0724	0.0027	1.5895	0.0599	0.1617	0.0042	0.18	965.9	23.5	969.0	26.1	982.9	74.6	965.9	23.5	1.7
M4_SM21_13a_Zrn08	253	0.06	0.0739	0.0022	1.6616	0.0541	0.1654	0.0045	0.02	986.3	24.8	992.7	20.7	1028.1	58.9	986.3	24.8	4.1
M4_SM21_13a_Zrn10	302	0.05	0.0711	0.0034	1.5277	0.0857	0.1571	0.0045	0.52	940.4	25.2	940.4	34.9	952.9	102.1	940.4	25.2	1.3
M4_SM21_13a_Zrn11	310	0.0572	0.0714	0.0023	1.5667	0.0600	0.1587	0.0052	0.43	949.5	28.8	955.5	24.0	972.1	72.0	949.5	28.8	2.3
M4_SM21_13a_Zrn12	1177	0.2609	0.0713	0.0019	1.4657	0.0528	0.1505	0.0046	0.73	903.5	25.5	916.0	21.7	962.5	54.0	903.5	25.5	6.1
M4_SM21_13a_Zrn13	1236	0.2134	0.0701	0.0018	1.5088	0.0453	0.1569	0.0040	0.33	939.7	22.1	933.4	18.5	927.5	52.2	939.7	22.1	-1.3
M4_SM21_13a_Zrn14	106	0.43	0.0695	0.0035	1.5010	0.0744	0.1575	0.0047	-0.12	942.9	26.3	932.5	33.2	895.0	118.7	942.9	26.3	-5.4
M4_SM21_13a_Zrn15	954	0.1454	0.0750	0.0020	1.8169	0.0558	0.1766	0.0047	0.26	1048.2	25.7	1050.7	20.2	1062.1	53.8	1048.2	25.7	1.3
M4_SM21_13a_Zrn16	29	0.3542	0.0766	0.0062	1.9632	0.1731	0.1868	0.0078	0.42	1103.4	42.6	1101.4	68.6	1104.3	172.7	1103.4	42.6	0.1
M4_SM21_13a_Zrn18	320	0.10	0.0736	0.0028	1.5779	0.0712	0.1563	0.0054	0.47	935.8	30.2	964.3	30.4	1028.7	85.6	935.8	30.2	9.0
M4_SM21_13a_Zrn19	220	0.5168	0.0715	0.0025	1.5478	0.0563	0.1578	0.0042	0.02	944.7	23.3	947.4	22.8	951.0	71.6	944.7	23.3	0.7
M4_SM21_13a_Zrn21	464	0.11	0.0801	0.0036	2.2993	0.2319	0.2068	0.0136	0.97	1209.7	72.4	1198.2	70.4	1185.8	87.9	1209.7	72.4	-2.0
M4_SM21_13a_Zrn22	478	0.10	0.0729	0.0020	1.6827	0.0516	0.1674	0.0044	0.12	997.4	24.3	1000.9	19.6	1009.2	61.4	997.4	24.3	1.2

Zircón	U ppm	Th/U	Relaciones isotópicas corregidas						rho	Edades corregidas				Mejor edad		Discordancia %		
			$\frac{Pb^{207}}{Pb^{206}}$	$\pm 2\sigma$	$\frac{Pb^{207}}{U^{235}}$	$\pm 2\sigma$	$\frac{Pb^{206}}{U^{238}}$	$\pm 2\sigma$		$\frac{Pb^{206}}{U^{238}}$	$\pm 2\sigma$	$\frac{Pb^{207}}{U^{235}}$	$\pm 2\sigma$	$\frac{Pb^{207}}{Pb^{206}}$	$\pm 2\sigma$		Ma	$\pm 2\sigma$
MI_SM21_35_Zrn01	78	0.69	0.0733	0.0041	1.6678	0.0905	0.1662	0.0056	0.06	991.1	30.7	993.5	35.2	998.3	119.8	991.1	30.7	0.7
MI_SM21_35_Zrn02	139	0.33	0.0755	0.0027	1.7872	0.0659	0.1728	0.0049	0.11	1027.1	26.7	1038.9	24.2	1080.7	64.7	1027.1	26.7	5.0
MI_SM21_35_Zrn03	226	0.03	0.0814	0.0035	2.1047	0.0959	0.1888	0.0048	0.14	1114.8	25.8	1148.3	32.1	1219.2	88.4	1114.8	25.8	8.6
MI_SM21_35_Zrn04	1283	0.23	0.0733	0.0021	1.6371	0.0507	0.1632	0.0048	0.30	974.7	26.4	984.3	19.6	1018.8	56.9	974.7	26.4	4.3
MI_SM21_35_Zrn05	153	0.10	0.0713	0.0026	1.5645	0.0640	0.1591	0.0045	0.16	951.5	24.9	953.4	25.2	957.3	81.8	951.5	24.9	0.6
MI_SM21_35_Zrn06	37	0.62	0.0718	0.0048	1.5572	0.1022	0.1586	0.0051	0.04	948.6	28.6	948.1	41.7	935.0	145.6	948.6	28.6	-1.5
MI_SM21_35_Zrn07	33	0.27	0.0736	0.0054	1.8458	0.1054	0.1840	0.0082	-0.07	1088.3	45.0	1058.9	38.0	996.3	139.1	1088.3	45.0	-9.2
MI_SM21_35_Zrn08	173	0.14	0.0721	0.0037	1.5716	0.0719	0.1597	0.0049	-0.21	955.2	27.1	958.0	27.7	976.1	98.0	955.2	27.1	2.1
MI_SM21_35_Zrn09	72	0.40	0.0743	0.0035	1.7684	0.0868	0.1723	0.0050	0.00	1024.4	27.6	1035.4	29.1	1035.4	101.7	1024.4	27.6	1.1
MI_SM21_35_Zrn10	200	0.07	0.0715	0.0024	1.5592	0.0528	0.1592	0.0041	-0.24	952.0	22.8	952.9	20.8	960.0	67.6	952.0	22.8	0.8
MI_SM21_35_Zrn11	41	0.42	0.0716	0.0035	1.5535	0.0759	0.1587	0.0048	0.11	949.2	26.9	947.5	30.7	937.0	103.6	949.2	26.9	-1.3
MI_SM21_35_Zrn12	70	0.16	0.0810	0.0054	2.3364	0.1261	0.2095	0.0070	-0.26	1225.8	37.7	1220.4	38.3	1193.1	137.4	1225.8	37.7	-2.7
MI_SM21_35_Zrn13	39	0.64	0.0728	0.0049	1.5629	0.0958	0.1577	0.0061	0.03	943.6	33.8	951.1	37.5	967.6	131.5	943.6	33.8	2.5
MI_SM21_35_Zrn14	529	0.19	0.0705	0.0021	1.5393	0.0493	0.1595	0.0042	0.11	953.9	23.4	945.8	19.6	938.8	59.4	953.9	23.4	-1.6
MI_SM21_35_Zrn15	21	0.34	0.0888	0.0050	2.8016	0.1466	0.2321	0.0095	0.12	1344.3	49.4	1351.1	38.2	1371.1	107.3	1344.3	49.4	2.0
MI_SM21_35_Zrn16	113	0.22	0.0709	0.0028	1.6065	0.0680	0.1658	0.0044	0.15	988.8	24.1	970.8	26.9	959.9	69.2	988.8	24.1	-3.0
MI_SM21_35_Zrn17	860	0.28	0.0771	0.0017	1.9700	0.0565	0.1868	0.0049	0.58	1103.9	26.5	1105.1	19.2	1122.2	44.1	1103.9	26.5	1.6
MI_SM21_35_Zrn18	76	0.19	0.0725	0.0024	1.5862	0.0566	0.1600	0.0044	0.12	956.6	24.3	962.8	22.3	982.8	69.2	956.6	24.3	2.7
MI_SM21_35_Zrn19	110	0.19	0.0690	0.0031	1.4826	0.0631	0.1576	0.0050	-0.12	943.5	28.0	922.1	26.3	917.3	75.0	943.5	28.0	-2.9
MI_SM21_35_Zrn21	100	0.24	0.0718	0.0042	1.6801	0.0963	0.1712	0.0056	0.02	1018.7	30.9	997.3	35.5	949.8	117.6	1018.7	30.9	-7.3
MI_SM21_35_Zrn22	197	0.40	0.0714	0.0028	1.5392	0.0642	0.1573	0.0040	-0.02	941.7	22.5	943.9	25.8	950.8	83.0	941.7	22.5	1.0
MI_SM21_35_Zrn23	145	0.49	0.0729	0.0029	1.6603	0.0642	0.1653	0.0047	0.16	986.0	25.7	991.3	24.7	1022.7	66.4	986.0	25.7	3.6
MI_SM21_35_Zrn24	130	0.34	0.0718	0.0034	1.5427	0.0741	0.1573	0.0047	0.06	941.5	26.4	943.9	29.5	971.3	88.2	941.5	26.4	3.1
MI_SM21_35_Zrn26	125	0.43	0.0708	0.0035	1.5169	0.0716	0.1567	0.0047	-0.07	938.5	21.4	934.7	29.4	926.7	105.5	938.5	26.1	-1.3
MI_SM21_35_Zrn27	34	0.26	0.0741	0.0060	1.6043	0.1383	0.1584	0.0058	0.22	947.4	32.3	955.9	52.2	973.0	156.7	947.4	32.3	2.6
MI_SM21_35_Zrn28	119	0.28	0.0756	0.0029	1.6704	0.0709	0.1617	0.0045	0.35	966.0	24.9	994.2	26.9	1062.9	78.7	966.0	24.9	9.1
MI_SM21_35_Zrn29	102	0.22	0.0737	0.0041	1.8213	0.0998	0.1810	0.0061	0.13	1072.2	33.1	1049.7	37.0	1007.2	117.7	1072.2	33.1	-6.5
MI_SM21_35_Zrn32	56	0.21	0.0789	0.0037	2.0888	0.1064	0.1934	0.0066	0.30	1139.4	35.6	1141.0	35.1	1145.9	99.2	1139.4	35.6	0.6
MI_SM21_35_Zrn33	129	0.22	0.0706	0.0025	1.5206	0.0598	0.1573	0.0044	0.22	941.4	24.5	936.4	24.2	926.5	76.6	941.4	24.5	-1.6
MI_SM21_35_Zrn34	68	0.33	0.0758	0.0049	1.8001	0.1092	0.1746	0.0066	-0.03	1036.8	36.1	1040.8	38.6	1050.0	131.8	1036.8	36.1	1.3
MI_SM21_35_Zrn35	57	0.31	0.0768	0.0041	1.7299	0.1003	0.1645	0.0050	0.27	981.2	27.9	1013.2	36.7	1075.1	108.2	981.2	27.9	8.7
MI_SM21_35_Zrn36	240	0.24	0.0707	0.0023	1.5404	0.0568	0.1588	0.0045	0.35	950.0	25.0	945.2	22.7	937.7	66.5	950.0	25.0	-1.3
MI_SM21_35_Zrn37	924	0.20	0.0701	0.0020	1.4759	0.0450	0.1533	0.0038	-0.32	919.6	21.4	920.1	18.3	924.0	57.6	919.6	21.4	0.5
MI_SM21_35_Zrn38	167	0.13	0.0732	0.0029	1.5866	0.0628	0.1593	0.0043	0.11	952.9	23.7	962.6	24.7	1013.0	74.6	952.9	23.7	5.9
MI_SM21_35_Zrn40	117	0.34	0.0737	0.0030	1.6761	0.0721	0.1660	0.0045	0.15	989.7	25.0	996.5	27.3	1011.4	82.9	989.7	25.0	2.1
MI_SM21_35_Zrn41	96	0.29	0.0716	0.0030	1.5667	0.0630	0.1593	0.0043	-0.10	952.6	24.2	954.5	25.6	981.4	87.0	952.6	24.2	2.9
MI_SM21_35_Zrn42	42	0.47	0.0726	0.0040	1.5962	0.0873	0.1606	0.0051	0.08	959.8	28.2	962.0	35.3	973.1	109.1	959.8	28.2	1.4
MI_SM21_35_Zrn43	405	0.28	0.0804	0.0020	2.2303	0.0666	0.2012	0.0052	0.43	1181.9	27.7	1189.8	20.9	1202.0	48.5	1181.9	27.7	1.7
MI_SM21_35_Zrn44	101	0.08	0.0740	0.0043	1.7162	0.1032	0.1686	0.0051	0.15	1004.5	27.9	1011.6	38.3	1021.5	118.6	1004.5	27.9	1.7
MI_SM21_35_Zrn45	59	0.22	0.0836	0.0039	2.4530	0.1289	0.2134	0.0065	0.34	1246.3	34.5	1253.3	37.8	1260.4	95.3	1246.3	34.5	1.1
MI_SM21_35_Zrn46	197	0.12	0.0724	0.0022	1.6008	0.0526	0.1607	0.0042	0.12	960.6	23.3	969.1	20.7	985.7	61.7	960.6	23.3	2.5
MI_SM21_35_Zrn47	69	0.23	0.0729	0.0044	1.6058	0.0967	0.1604	0.0053	0.05	958.8	29.3	967.1	36.6	970.1	120.5	958.8	29.3	1.2
M2_SM21_35_Zrn48	854	0.20	0.0798	0.0017	2.1855	0.0609	0.1982	0.0050	0.57	1165.7	26.7	1175.9	19.3	1190.1	42.2	1165.7	26.7	2.0
M2_SM21_35_Zrn49	119	0.14	0.0728	0.0029	1.5248	0.0698	0.1519	0.0046	0.46	911.3	25.9	938.3	28.6	995.2	84.3	911.3	25.9	8.4

Continúa

Continuación

SM21-35 Leucosoma (s. Pochotepec) Espejo-Bautista et al., 2022

Zircón	U ppm	Th/U	Relaciones isotópicas corregidas						rho	Edades corregidas						Mejor edad		Discordancia %
			$\frac{Pb^{207}}{Pb^{206}}$	$\pm 2\sigma$	$\frac{Pb^{207}}{U^{235}}$	$\pm 2\sigma$	$\frac{Pb^{206}}{U^{238}}$	$\pm 2\sigma$		$\frac{Pb^{206}}{U^{238}}$	$\pm 2\sigma$	$\frac{Pb^{207}}{U^{235}}$	$\pm 2\sigma$	$\frac{Pb^{207}}{Pb^{206}}$	$\pm 2\sigma$	Ma	$\pm 2\sigma$	
M2_SM21_35_Zrn50	38	0.53	0.0702	0.0052	1.5537	0.1210	0.1602	0.0051	0.14	957.6	28.4	949.5	44.0	884.6	149.1	957.6	28.4	-8.3
M2_SM21_35_Zrn51	127	0.23	0.0719	0.0045	1.5500	0.0932	0.1563	0.0053	0.00	935.9	29.8	946.4	36.5	947.8	128.1	935.9	29.8	1.3
M2_SM21_35_Zrn52	48	0.50	0.0727	0.0048	1.7263	0.1136	0.1724	0.0052	0.03	1025.0	28.5	1010.1	42.1	946.0	138.3	1025.0	28.5	-8.3
M2_SM21_35_Zrn53	45	0.68	0.0693	0.0035	1.5221	0.0797	0.1592	0.0054	0.17	952.0	30.0	934.0	31.7	868.0	103.6	952.0	30.0	-9.7
M2_SM21_35_Zrn54	169	0.09	0.0710	0.0023	1.5073	0.0522	0.1540	0.0042	0.34	923.3	23.3	931.5	21.0	941.8	65.1	923.3	23.3	2.0
M2_SM21_35_Zrn55	204	0.16	0.0722	0.0024	1.6122	0.0593	0.1615	0.0042	0.11	965.0	23.4	972.9	23.0	976.4	69.8	965.0	23.4	1.2
M2_SM21_35_Zrn57	90	0.23	0.0713	0.0032	1.5862	0.0684	0.1612	0.0050	-0.01	963.0	27.5	962.3	27.0	941.7	91.5	963.0	27.5	-2.3
M2_SM21_35_Zrn58	97	0.17	0.0705	0.0035	1.5693	0.0765	0.1608	0.0048	-0.11	960.8	26.7	954.8	29.5	937.8	111.5	960.8	26.7	-2.5
M2_SM21_35_Zrn59	149	0.08	0.0805	0.0025	2.2272	0.0820	0.1998	0.0058	0.44	1173.8	31.1	1187.9	26.0	1200.5	62.7	1173.8	31.1	2.2
M2_SM21_35_Zrn60	123	0.15	0.0715	0.0030	1.5776	0.0703	0.1591	0.0047	0.10	951.7	26.1	965.5	31.5	973.2	99.4	951.7	26.1	2.2
M2_SM21_35_Zrn61	118	0.36	0.0715	0.0029	1.5693	0.0644	0.1582	0.0045	0.01	946.8	24.8	955.1	24.9	959.7	78.2	946.8	24.8	1.3
M2_SM21_35_Zrn62	42	0.53	0.0731	0.0053	1.5967	0.1099	0.1583	0.0047	-0.26	947.4	26.0	969.0	40.6	969.7	152.2	947.4	26.0	2.3
M2_SM21_35_Zrn63	83	0.25	0.0740	0.0038	1.7785	0.0942	0.1733	0.0055	0.16	1030.3	30.4	1033.9	34.6	1042.1	91.6	1030.3	30.4	1.1
M2_SM21_35_Zrn64	95	0.36	0.0707	0.0044	1.5630	0.0951	0.1598	0.0046	-0.14	955.5	25.5	951.4	38.1	910.7	135.4	955.5	25.5	-4.9
M2_SM21_35_Zrn65	51	0.63	0.0740	0.0061	1.5737	0.1036	0.1573	0.0058	0.00	941.5	32.2	968.2	50.5	988.7	173.7	941.5	32.2	4.8
M2_SM21_35_Zrn66	58	0.33	0.0816	0.0052	2.4480	0.1861	0.2161	0.0103	0.54	1260.2	54.7	1250.1	53.8	1211.4	122.6	1260.2	54.7	-4.0
M2_SM21_35_Zrn67	164	0.43	0.0725	0.0061	1.6020	0.1340	0.1595	0.0042	-0.16	953.8	23.4	967.7	54.4	972.5	192.0	953.8	23.4	1.9
M2_SM21_35_Zrn68	59	0.44	0.0707	0.0041	1.5699	0.0874	0.1600	0.0053	0.02	956.3	29.2	954.3	34.5	911.6	117.8	956.3	29.2	-4.9
M2_SM21_35_Zrn69	90	0.23	0.0700	0.0037	1.4278	0.0835	0.1465	0.0045	0.41	881.1	25.4	896.4	35.8	899.2	115.4	881.1	25.4	2.0
M2_SM21_35_Zrn70	187	0.05	0.0707	0.0026	1.4860	0.0562	0.1511	0.0040	0.01	906.9	22.6	922.8	23.1	932.2	76.7	906.9	22.6	2.7
M2_SM21_35_Zrn71	86	0.40	0.0749	0.0041	1.7624	0.0957	0.1697	0.0057	0.09	1010.1	31.7	1027.6	35.4	1034.4	112.9	1010.1	31.7	2.3
M2_SM21_35_Zrn72	96	0.42	0.0729	0.0035	1.5293	0.0729	0.1509	0.0049	0.15	905.8	27.2	939.1	29.0	985.6	96.0	905.8	27.2	8.1
M2_SM21_35_Zrn73	60	0.61	0.0701	0.0032	1.5417	0.0723	0.1582	0.0051	0.20	946.3	28.3	943.0	28.8	918.6	85.5	946.3	28.3	-3.0
M2_SM21_35_Zrn74	168	0.47	0.0719	0.0029	1.5775	0.0746	0.1572	0.0054	0.03	940.8	29.8	957.7	28.5	962.4	78.6	940.8	29.8	2.2
M2_SM21_35_Zrn75	20	0.27	0.0745	0.0059	1.6274	0.1250	0.1604	0.0061	0.21	958.0	34.3	973.7	51.9	991.9	148.7	958.0	34.3	3.4
M2_SM21_35_Zrn77	89	0.48	0.0728	0.0045	1.6501	0.1060	0.1628	0.0053	0.21	972.2	29.4	986.6	41.0	988.4	127.3	972.2	29.4	1.6
M2_SM21_35_Zrn78	44	0.51	0.0759	0.0046	1.7862	0.0980	0.1698	0.0063	-0.02	1010.7	34.6	1035.3	35.6	1048.2	123.2	1010.7	34.6	3.6
M2_SM21_35_Zrn79	57	0.20	0.0818	0.0039	2.2980	0.1231	0.2013	0.0071	0.39	1181.3	38.1	1203.6	37.8	1206.2	94.0	1181.3	38.1	2.1
M2_SM21_35_Zrn80	68	0.42	0.0709	0.0038	1.5941	0.0871	0.1614	0.0050	0.15	964.5	28.0	963.6	34.8	919.8	113.1	964.5	28.0	-4.9

SM21-34 Leucosoma (s. Pochotepec)

Espejo-Bautista et al., 2022

Zircón	U ppm	Th/U	Relaciones isotópicas corregidas						rho	Edades corregidas				Mejor edad		Discordancia %		
			$\frac{Pb^{207}}{Pb^{206}}$	$\pm 2\sigma$	$\frac{Pb^{207}}{U^{235}}$	$\pm 2\sigma$	$\frac{Pb^{206}}{U^{238}}$	$\pm 2\sigma$		$\frac{Pb^{206}}{U^{238}}$	$\pm 2\sigma$	$\frac{Pb^{207}}{U^{235}}$	$\pm 2\sigma$	$\frac{Pb^{207}}{Pb^{206}}$	$\pm 2\sigma$		Ma	$\pm 2\sigma$
M3_SM21_34_Zrn01	86	0.54	0.0683	0.0038	1.4023	0.0811	0.1499	0.0051	0.39	900.3	28.7	886.3	34.5	876.2	135.4	900.3	28.7	-2.8
M3_SM21_34_Zrn02	79	0.62	0.0713	0.0055	1.5040	0.0987	0.1539	0.0065	-0.17	922.3	36.3	929.4	40.7	936.0	166.4	922.3	36.3	1.5
M3_SM21_34_Zrn03	138	0.64	0.0715	0.0041	1.5253	0.0846	0.1558	0.0052	-0.02	933.2	28.8	938.4	34.4	950.4	122.9	933.2	28.8	1.8
M3_SM21_34_Zrn04	450	0.17	0.0697	0.0021	1.4932	0.0491	0.1556	0.0039	0.02	932.0	21.9	927.0	19.9	912.2	60.9	932.0	21.9	-2.2
M3_SM21_34_Zrn05	121	0.26	0.0699	0.0032	1.3168	0.0616	0.1366	0.0041	0.14	825.3	23.3	851.0	27.0	904.7	95.9	825.3	23.3	8.8
M3_SM21_34_Zrn06	520	0.08	0.0725	0.0017	1.6669	0.0473	0.1673	0.0043	0.29	997.1	23.9	995.5	17.9	994.8	48.0	997.1	23.9	-0.2
M3_SM21_34_Zrn07	111	0.39	0.0745	0.0035	1.7517	0.0781	0.1712	0.0049	-0.13	1018.5	26.9	1025.9	28.2	1038.0	90.1	1018.5	26.9	1.9
M3_SM21_34_Zrn08	68	0.47	0.0698	0.0037	1.4079	0.0740	0.1473	0.0044	-0.06	885.6	24.5	889.0	31.0	890.4	113.9	885.6	24.5	0.5
M3_SM21_34_Zrn09	52	0.40	0.0747	0.0038	1.7402	0.0946	0.1701	0.0058	0.30	1012.4	32.0	1019.9	35.2	1036.3	104.1	1012.4	32.0	2.3
M3_SM21_34_Zrn10	41	0.55	0.0714	0.0045	1.5956	0.0976	0.1635	0.0051	0.04	975.9	28.4	960.8	38.3	906.7	130.6	975.9	28.4	-7.6
M3_SM21_34_Zrn11	471	0.47	0.0719	0.0019	1.5912	0.0479	0.1614	0.0041	0.11	964.7	22.7	966.1	18.7	976.8	53.7	964.7	22.7	1.2
M3_SM21_34_Zrn12	489	0.53	0.0729	0.0019	1.6475	0.0514	0.1647	0.0043	0.40	982.9	23.9	987.8	19.4	1005.2	51.8	982.9	23.9	2.2
M3_SM21_34_Zrn13	561	0.04	0.0705	0.0018	1.4969	0.0442	0.1546	0.0042	0.31	926.8	23.4	928.8	18.1	938.9	53.3	926.8	23.4	1.3
M3_SM21_34_Zrn14	1064	0.26	0.0716	0.0019	1.5503	0.0556	0.1577	0.0046	0.74	943.8	25.6	949.8	22.2	971.7	52.5	943.8	25.6	2.9
M3_SM21_34_Zrn16	226	0.41	0.0718	0.0028	1.6214	0.0677	0.1651	0.0047	0.20	984.9	25.9	977.0	26.3	969.1	79.3	984.9	25.9	-1.6
M3_SM21_34_Zrn18	1227	0.11	0.0697	0.0015	1.4729	0.0397	0.1540	0.0039	0.41	923.5	21.9	919.1	16.3	918.1	44.9	923.5	21.9	-0.6
M3_SM21_34_Zrn19	1199	0.16	0.0717	0.0016	1.5261	0.0471	0.1556	0.0043	0.72	931.9	23.7	940.2	18.8	973.9	46.6	931.9	23.7	4.3
M3_SM21_34_Zrn20	102	0.31	0.0689	0.0030	1.3210	0.0621	0.1402	0.0044	0.32	845.6	25.0	851.3	27.6	866.5	92.9	845.6	25.0	2.4
M3_SM21_34_Zrn21	775	0.09	0.0708	0.0017	1.5624	0.0449	0.1616	0.0040	0.27	965.6	22.4	954.9	17.8	946.8	49.8	965.6	22.4	-2.0
M3_SM21_34_Zrn23	222	0.23	0.0759	0.0022	1.8795	0.0617	0.1810	0.0052	0.33	1072.2	28.1	1072.8	21.9	1084.2	58.4	1072.2	28.1	1.1
M3_SM21_34_Zrn24	120	0.36	0.0721	0.0026	1.5768	0.0632	0.1599	0.0045	0.26	956.1	25.2	958.9	24.7	972.5	74.5	956.1	25.2	1.7
M3_SM21_34_Zrn26	369	0.20	0.0710	0.0023	1.5025	0.0541	0.1552	0.0042	0.20	929.9	23.3	930.6	21.9	950.1	65.9	929.9	23.3	2.1
M3_SM21_34_Zrn27	91	0.33	0.0713	0.0034	1.5220	0.0786	0.1564	0.0050	0.27	936.3	27.7	934.2	30.5	930.5	96.8	936.3	27.7	-0.6
M3_SM21_34_Zrn28	35	0.44	0.0703	0.0044	1.5184	0.0929	0.1585	0.0052	0.08	948.4	28.7	931.5	36.7	883.5	124.9	948.4	28.7	-7.3
M3_SM21_34_Zrn29	47	0.71	0.0761	0.0044	1.7817	0.0844	0.1740	0.0056	-0.16	1033.7	30.9	1034.5	31.5	1046.2	120.2	1033.7	30.9	1.2
M3_SM21_34_Zrn30	1002	0.13	0.0698	0.0016	1.3868	0.0390	0.1451	0.0037	0.36	873.6	20.8	883.0	16.6	920.1	47.6	873.6	20.8	5.1
M3_SM21_34_Zrn31	168	0.40	0.0708	0.0036	1.4341	0.0746	0.1483	0.0040	0.02	891.3	22.4	900.2	30.4	925.1	101.9	891.3	22.4	3.7
M3_SM21_34_Zrn32	119	0.34	0.0770	0.0040	1.7452	0.0905	0.1662	0.0046	-0.07	990.8	25.5	1022.1	33.9	1096.4	108.2	990.8	25.5	9.6
M3_SM21_34_Zrn33	527	0.16	0.0713	0.0022	1.5180	0.0458	0.1558	0.0043	-0.27	933.5	24.0	937.5	18.5	962.0	64.1	933.5	24.0	3.0
M3_SM21_34_Zrn34	590	0.28	0.0707	0.0019	1.5105	0.0475	0.1558	0.0042	0.26	933.4	23.2	934.1	19.1	945.1	54.9	933.4	23.2	1.2
M3_SM21_34_Zrn35	414	0.14	0.0757	0.0022	1.8228	0.0561	0.1766	0.0046	0.16	1048.2	25.0	1052.8	20.1	1077.6	57.5	1048.2	25.0	2.7
M3_SM21_34_Zrn36	111	0.44	0.0739	0.0028	1.6625	0.0687	0.1644	0.0048	0.26	981.2	26.7	991.3	26.3	1048.1	66.1	981.2	26.7	6.4
M4_SM21_34_Zrn37	210	0.44	0.0707	0.0025	1.4970	0.0601	0.1542	0.0048	0.43	924.6	26.9	928.8	24.6	945.5	71.1	924.6	26.9	2.2
M4_SM21_34_Zrn38	159	0.21	0.0728	0.0025	1.6455	0.0649	0.1650	0.0045	0.38	984.4	24.8	985.2	25.6	990.4	74.1	984.4	24.8	0.6
M4_SM21_34_Zrn39	200	0.39	0.0710	0.0021	1.5170	0.0516	0.1560	0.0045	0.34	934.5	25.3	935.9	20.6	947.1	62.5	934.5	25.3	1.3
M4_SM21_34_Zrn40	252	0.21	0.0694	0.0027	1.4771	0.0600	0.1557	0.0045	0.10	932.7	25.2	919.7	24.8	898.6	82.8	932.7	25.2	-3.8
M4_SM21_34_Zrn41	337	0.09	0.0716	0.0025	1.5337	0.0644	0.1566	0.0044	0.51	937.9	24.5	943.0	26.5	993.0	48.1	937.9	24.5	5.5
M4_SM21_34_Zrn42	237	0.43	0.0714	0.0037	1.5158	0.0751	0.1553	0.0045	-0.17	930.4	24.9	934.6	30.7	948.8	109.4	930.4	24.9	1.9
M4_SM21_34_Zrn43	374	0.06	0.0702	0.0022	1.4236	0.0505	0.1474	0.0038	0.27	886.1	21.1	898.3	21.3	929.3	65.1	886.1	21.1	4.6
M4_SM21_34_Zrn44	208	0.37	0.0710	0.0021	1.5104	0.0688	0.1549	0.0063	0.80	927.8	34.9	931.2	27.8	948.7	61.0	927.8	34.9	2.2
M4_SM21_34_Zrn45	676	0.24	0.0701	0.0019	1.4069	0.0484	0.1458	0.0038	0.58	877.5	21.4	891.0	20.4	925.8	56.2	877.5	21.4	5.2
M4_SM21_34_Zrn46	407	0.51	0.0680	0.0023	1.3228	0.0455	0.1416	0.0037	-0.10	853.4	21.1	855.2	19.8	862.8	68.3	853.4	21.1	1.1
M4_SM21_34_Zrn47	169	0.29	0.0727	0.0039	1.5415	0.0772	0.1552	0.0051	-0.07	929.9	28.1	945.9	30.9	992.0	110.0	929.9	28.1	6.3
M4_SM21_34_Zrn48	100	0.54	0.0735	0.0028	1.6830	0.0627	0.1666	0.0045	-0.06	993.4	25.0	999.8	23.4	1006.4	74.5	993.4	25.0	1.3
M4_SM21_34_Zrn49	285	0.24	0.0736	0.0022	1.6122	0.0557	0.1586	0.0041	-0.02	949.1	22.9	973.7	21.7	1032.1	67.5	949.1	22.9	8.0
M4_SM21_34_Zrn50	902	0.18	0.0717	0.0017	1.5273	0.0422	0.1552	0.0039	0.16	930.2	21.7	941.2	16.9	973.5	47.6	930.2	21.7	4.4

6.2. Elementos traza en zircón

JG24 Meta-anortosita		Espejo-Bautista et al., 2021																				
Zircón	P	Sc	Ti	Y	Nb	La	Ce	Pr	Nd	Sm	Eu	Gd	Tb	Dy	Ho	Er	Yb	Lu	Hf	Pb	Th	U
Zircon_36	12.0	216.0	26.2	157.0	1.4	0.0	7.0	0.0	0.5	1.2	0.4	4.2	1.3	13.8	4.4	20.7	41.4	8.9	11600.0	16.1	26.3	80.1
Zircon_37	220.0	196.0	32.6	171.0	1.4	0.0	7.4	0.0	0.6	1.1	0.4	4.5	1.5	16.0	5.4	22.4	43.0	9.4	10200.0	12.9	31.2	68.7
Zircon_38	177.0	179.0	29.9	141.0	1.4	0.0	6.0	0.0	0.4	1.1	0.3	3.6	1.2	12.4	4.5	19.2	36.8	8.0	10250.0	13.6	27.3	82.6
Zircon_39	20.0	239.0	32.5	38.7	2.0	0.0	2.9	0.0	0.2	0.3	0.5	0.8	0.3	3.0	1.3	5.7	16.7	4.3	14000.0	7.1	8.3	34.6
Zircon_40	64.0	222.0	40.8	88.0	1.8	0.0	6.5	0.0	0.3	0.5	0.3	1.9	0.6	6.4	2.5	11.9	32.6	8.0	14000.0	19.7	17.1	82.9
Zircon_41	119.0	161.0	31.3	73.0	1.3	0.0	6.1	0.0	0.3	0.5	0.3	2.1	0.5	6.0	2.1	10.3	22.6	5.1	9410.0	17.3	25.7	97.0
Zircon_42	193.0	173.0	39.2	154.0	1.0	0.0	6.3	0.0	0.6	0.9	0.4	4.1	1.2	14.1	4.7	20.6	42.4	8.6	8270.0	16.9	23.0	85.0
Zircon_43	133.0	174.0	65.0	177.0	1.1	0.0	6.5	0.0	0.9	1.9	0.4	6.6	1.9	19.6	5.9	23.4	38.5	6.9	7710.0	34.0	42.7	202.0
Zircon_44	52.0	147.0	29.4	160.0	0.7	0.0	5.4	0.0	0.5	1.0	0.4	4.5	1.2	14.0	5.0	22.2	44.1	9.3	7440.0	14.7	25.4	82.8
Zircon_45	50.0	188.0	34.9	158.0	1.3	0.0	6.8	0.0	0.6	1.1	0.4	4.4	1.3	14.0	4.8	20.8	38.6	8.0	9920.0	13.5	29.0	69.9
Zircon_46	-1.0	194.0	38.2	181.0	1.3	0.0	7.3	0.0	0.8	1.0	0.3	5.0	1.5	16.5	5.6	24.4	45.0	9.3	10800.0	12.2	32.5	62.8
Zircon_47	60.0	189.0	35.9	240.0	5.8	0.0	5.5	0.1	0.7	1.5	0.4	5.6	2.0	22.9	8.4	35.5	75.0	14.7	8500.0	31.8	20.8	188.0
Zircon_49	90.0	186.0	27.5	121.0	0.9	0.0	4.5	0.0	0.4	1.0	0.4	3.3	1.1	11.4	3.8	16.7	37.3	8.0	9290.0	8.3	28.3	42.3
Zircon_50	190.0	195.0	37.3	184.0	1.1	0.0	2.7	0.0	0.5	1.0	0.3	5.1	1.5	17.5	6.3	26.2	54.9	11.2	8140.0	11.6	32.7	62.2
Zircon_51	190.0	184.0	21.8	161.0	0.8	0.0	3.1	0.0	0.3	0.8	0.3	3.7	1.4	15.0	5.1	23.0	48.3	10.2	8050.0	11.6	29.0	69.7
Zircon_52	96.0	186.0	19.8	14.3	3.1	0.1	1.2	0.0	0.2	0.2	0.2	0.2	0.1	1.0	0.5	2.0	7.8	1.9	11480.0	4.9	4.6	26.5
Zircon_54	-2.0	182.0	28.4	180.0	1.3	0.0	6.7	0.1	0.5	1.2	0.4	4.9	1.6	16.9	5.5	24.1	41.8	9.6	10500.0	12.8	41.4	79.5
Zircon_56	-50.0	157.0	30.3	170.0	0.9	0.0	6.8	0.0	0.7	1.2	0.4	5.2	1.5	15.6	5.3	22.8	43.5	9.2	9910.0	10.9	28.0	57.2
Zircon_57	55.0	152.0	24.1	159.0	0.9	0.0	6.4	0.0	0.5	1.1	0.4	4.7	1.3	14.7	5.1	21.5	42.1	8.7	10080.0	10.5	27.7	58.3
Zircon_58	40.0	199.0	33.8	183.0	1.0	0.0	2.8	0.0	0.3	1.0	0.4	5.0	1.5	16.4	6.2	26.4	55.7	11.9	8060.0	14.4	34.9	75.7
Zircon_59	-40.0	166.0	25.4	138.1	1.5	0.0	5.1	0.0	0.4	1.0	0.2	3.3	1.1	12.3	4.3	19.7	46.4	10.0	8460.0	13.8	21.0	75.0
Zircon_60	10.0	175.0	21.9	351.0	1.4	0.0	7.7	0.1	1.0	1.7	0.7	8.9	2.9	30.7	11.0	47.4	99.0	21.2	8700.0	33.7	69.3	167.0
Zircon_61	110.0	142.2	19.7	128.7	0.9	0.0	4.3	0.0	0.4	0.7	0.2	3.0	1.0	11.0	3.8	17.9	40.1	9.0	7530.0	11.4	21.3	74.5
Zircon_62	100.0	135.3	22.9	101.5	1.1	0.0	5.4	0.0	0.4	0.5	0.2	2.6	0.8	8.9	2.9	13.4	31.0	7.0	7260.0	16.7	33.9	104.9
Zircon_63	90.0	155.0	25.2	146.0	1.1	0.0	5.2	0.1	0.5	1.0	0.2	3.7	1.0	12.7	4.4	19.9	45.8	9.5	8150.0	14.7	28.2	93.0
Zircon_64	270.0	206.0	29.5	283.0	0.7	0.0	2.8	0.0	0.5	1.3	0.5	8.7	2.4	26.9	9.1	38.1	63.1	14.9	8090.0	4.1	15.3	25.0
Zircon_65	40.0	161.0	20.9	179.0	1.1	0.0	4.9	0.0	0.3	1.1	0.3	4.4	1.2	15.3	5.5	24.8	58.0	12.1	8390.0	15.7	26.0	95.5
Zircon_66	90.0	168.0	26.4	195.0	1.2	0.0	5.7	0.0	0.6	1.0	0.4	4.7	1.6	16.9	5.8	26.5	60.0	12.9	8730.0	17.6	31.3	97.1
Zircon_67	100.0	192.0	31.3	172.0	0.9	0.0	2.7	0.0	0.4	0.9	0.3	4.2	1.4	15.5	5.9	25.3	53.7	11.0	9310.0	9.0	14.3	49.5
Zircon_68	77.0	190.0	6.5	296.0	0.7	0.0	5.2	0.0	0.2	0.6	0.2	4.8	2.0	24.6	10.0	46.5	104.0	22.1	9560.0	23.5	31.6	130.5
Zircon_69	220.0	184.0	8.1	301.0	0.8	0.0	3.8	0.0	0.2	0.7	0.3	4.5	1.9	25.1	9.8	50.4	115.0	24.9	8790.0	15.4	20.2	92.3
Zircon_70	182.0	202.0	31.8	226.0	1.0	0.0	2.8	0.0	0.6	1.2	0.3	6.1	2.1	21.1	7.7	32.4	62.1	14.3	7510.0	6.3	22.2	37.6
Zircon_71	170.0	155.0	23.7	133.0	0.6	0.0	2.2	0.0	0.1	0.7	0.2	3.4	1.0	11.5	4.1	18.1	40.3	8.4	8650.0	8.6	12.6	47.4
Zircon_72	68.0	141.6	25.4	118.5	1.4	0.0	5.4	0.0	0.4	0.5	0.2	3.2	1.0	10.4	3.9	16.4	34.2	7.5	8400.0	15.9	31.2	98.6
Zircon_73	50.0	141.0	18.7	126.0	1.0	0.0	4.3	0.0	0.5	0.7	0.1	3.3	1.0	10.8	3.9	17.8	39.8	8.2	7880.0	11.4	17.9	63.5
Zircon_74	90.0	162.0	20.8	118.9	0.6	0.0	2.2	0.0	0.2	0.6	0.2	2.8	0.9	10.6	3.8	17.0	35.2	7.8	9130.0	10.1	15.5	62.0
Zircon_75	55.0	172.0	29.3	174.0	1.0	0.0	2.4	0.0	0.4	0.9	0.3	4.3	1.4	15.7	5.7	25.7	52.1	11.3	7020.0	6.3	17.9	35.0
Zircon_76	320.0	189.0	21.0	257.0	1.2	0.0	13.0	0.1	1.7	2.4	0.8	10.1	2.5	25.7	8.1	31.1	52.9	10.4	8680.0	4.4	12.5	21.7
Zircon_77	130.0	189.0	23.0	237.0	0.9	0.0	12.8	0.1	1.6	2.6	0.8	8.7	2.4	24.3	7.5	28.6	50.6	9.9	8950.0	3.8	11.5	20.8

*Valores en ppm

JG42 Meta-anortosita		Espejo-Bautista et al., 2021																					
Zircón	P	Sc	Ti	Y	Nb	La	Ce	Pr	Nd	Sm	Eu	Gd	Tb	Dy	Ho	Er	Yb	Lu	Hf	Pb	Th	U	
Zircon_01	310.0	480.0	52.0	1080.0	3.0	0.0	7.9	0.4	6.5	10.2	2.7	36.8	10.5	112.0	37.4	154.0	258.0	50.0	19700.0	52.8	85.3	153.5	
Zircon_02	40.0	500.0	58.0	810.0	2.7	0.0	6.2	0.1	3.5	6.1	1.9	22.7	7.2	82.0	28.3	117.0	210.0	41.5	22100.0	39.3	49.0	104.8	
Zircon_03	20.0	347.0	40.0	343.0	2.2	0.0	3.2	0.2	1.7	3.5	2.2	10.5	3.1	36.3	11.2	47.0	97.0	20.6	15700.0	11.8	10.3	48.5	
Zircon_04	0.0	321.0	37.0	197.0	1.3	0.0	2.1	0.0	0.6	0.5	0.6	5.4	1.7	20.6	7.0	30.0	58.0	12.2	13400.0	5.7	7.4	18.6	
Zircon_05	-180.0	420.0	84.0	970.0	3.5	0.0	29.0	0.2	3.1	6.5	1.5	28.9	11.1	92.0	31.0	129.0	225.0	44.0	19700.0	21.5	31.8	55.7	
Zircon_06	80.0	420.0	81.0	840.0	3.9	0.2	7.0	0.8	8.3	18.0	23.0	36.0	12.6	135.0	28.0	99.0	180.0	35.3	24500.0	27.5	12.2	68.7	
Zircon_07	-320.0	412.0	54.0	466.0	3.5	0.0	15.3	0.1	1.2	2.5	0.5	10.8	3.4	38.5	14.0	65.0	131.0	28.6	20800.0	60.5	68.5	150.8	
Zircon_08	-100.0	361.0	47.0	276.0	1.6	0.0	3.3	0.0	0.7	2.1	0.3	8.3	2.1	25.7	10.1	39.9	82.0	17.1	18000.0	15.3	16.4	42.9	
Zircon_09	-60.0	720.0	97.0	1270.0	3.9	0.0	9.7	0.2	2.3	6.1	2.5	37.0	11.8	128.0	43.0	209.0	290.0	58.0	27300.0	49.8	64.3	97.9	
Zircon_10	30.0	490.0	73.0	800.0	3.5	0.0	4.9	0.0	0.8	2.6	1.4	24.0	7.6	78.0	28.0	106.0	201.0	39.0	23400.0	33.5	66.3	104.1	
Zircon_11	60.0	366.0	46.0	584.0	2.0	0.0	4.1	0.0	0.9	2.8	1.1	17.2	5.2	59.0	19.3	85.0	139.0	28.0	19200.0	24.5	59.5	88.6	
Zircon_12	150.0	470.0	50.0	295.0	2.3	0.0	4.5	0.0	0.4	1.4	0.3	6.3	1.9	28.1	8.8	45.0	92.0	18.4	24800.0	19.0	18.2	51.7	
Zircon_13	110.0	480.0	42.0	1140.0	2.5	0.0	7.2	0.1	3.3	7.4	2.4	35.0	10.7	119.0	39.5	158.0	257.0	48.3	21800.0	45.3	80.3	130.0	
Zircon_14	0.0	446.0	42.0	266.0	1.5	0.0	3.8	0.1	0.4	1.3	0.5	6.9	2.2	25.0	9.2	38.9	89.0	16.8	20700.0	10.8	9.5	27.7	
Zircon_15	160.0	345.0	63.0	390.0	3.1	0.0	17.0	0.1	1.5	3.6	0.7	12.7	3.4	34.6	12.2	49.0	92.0	18.7	18700.0	11.8	15.6	30.3	
Zircon_16	240.0	328.0	59.0	330.0	2.8	0.0	14.9	0.1	1.6	2.4	0.7	10.1	3.2	32.8	10.9	42.2	79.0	16.4	17100.0	7.6	11.1	22.3	

*Valores en ppm

JG50 Meta-anortosita		Espejo-Bautista et al., 2021																					
Zircón	P	Sc	Ti	Y	Nb	La	Ce	Pr	Nd	Sm	Eu	Gd	Tb	Dy	Ho	Er	Yb	Lu	Hf	Pb	Th	U	
Zircon_17	20.0	480.0	48.0	430.0	2.1	0.0	3.6	0.0	0.6	1.6	0.9	10.1	3.0	36.1	13.5	59.0	124.0	29.6	18500.0	8.0	19.4	28.3	
Zircon_18	0.0	394.0	69.0	330.0	1.8	0.0	2.9	0.0	0.4	2.2	0.7	9.6	2.5	29.0	9.3	49.0	94.0	22.2	17200.0	7.5	17.5	26.8	
Zircon_19	260.0	381.0	61.0	630.0	2.1	0.0	4.4	0.0	0.8	3.5	1.6	15.9	5.1	56.0	20.6	89.0	179.0	41.0	15500.0	10.3	33.8	37.0	
Zircon_20	150.0	300.0	55.0	407.0	2.1	0.0	3.3	0.0	0.3	1.2	0.6	6.3	2.7	35.1	13.9	63.0	163.0	34.5	13000.0	6.6	15.3	23.4	
Zircon_21	90.0	257.0	41.5	401.0	1.5	0.0	2.6	0.0	0.4	1.0	0.3	7.3	2.5	32.6	12.6	63.3	150.0	34.9	12400.0	6.1	17.9	25.8	
Zircon_22	0.0	245.0	34.0	93.0	1.1	0.0	2.6	0.0	0.4	1.6	0.6	5.0	1.4	11.1	3.1	11.0	13.5	2.7	12500.0	8.3	19.1	29.9	
Zircon_24	200.0	365.0	41.2	443.0	2.1	0.0	2.8	0.0	0.3	0.9	0.5	7.0	2.5	35.7	14.5	76.0	192.0	47.6	9980.0	8.3	21.0	38.2	
Zircon_25	240.0	239.0	48.0	485.0	1.6	0.0	3.7	0.0	0.5	1.6	0.6	7.5	3.3	38.6	15.3	73.0	165.0	39.6	9600.0	9.5	17.7	30.9	
Zircon_26	70.0	234.0	25.9	60.0	0.9	0.0	2.1	0.0	0.2	0.5	0.5	3.6	1.1	7.3	1.8	5.3	6.5	1.2	15500.0	3.6	12.1	13.2	
Zircon_28	120.0	351.0	55.0	439.0	1.6	0.0	2.9	0.0	0.3	1.0	0.4	6.7	2.6	34.4	14.3	69.0	175.0	42.2	12600.0	8.0	18.3	31.3	
Zircon_29	-10.0	184.0	24.2	33.6	0.7	0.0	1.9	0.0	0.1	0.8	0.3	3.1	0.6	5.8	1.1	3.4	4.2	0.8	11400.0	6.6	18.0	33.4	
Zircon_30	15.0	208.0	31.5	63.4	1.0	0.0	2.2	0.0	0.2	0.8	0.3	3.3	0.8	6.2	2.1	7.8	17.6	3.7	12900.0	7.8	22.8	36.9	
Zircon_31	170.0	153.0	22.6	36.1	0.7	0.0	1.3	0.0	0.1	0.4	0.3	2.1	0.5	5.1	1.2	3.3	3.7	0.7	9100.0	3.6	20.1	23.3	
Zircon_32	205.0	193.0	19.3	168.0	1.1	0.0	1.5	0.0	0.2	0.6	0.3	3.6	1.3	14.8	5.6	25.4	60.0	14.1	8870.0	4.4	17.0	26.1	
Zircon_33	84.0	180.0	35.8	201.0	0.8	0.0	1.4	0.0	0.2	0.4	0.1	2.5	1.3	16.0	6.7	32.6	84.3	18.7	5970.0	25.8	58.5	127.1	
Zircon_34	50.0	188.0	33.3	190.0	1.5	0.0	2.1	0.0	0.1	0.6	0.3	3.7	1.2	15.3	6.1	29.4	64.6	16.9	7490.0	6.6	16.5	35.3	
Zircon_48	200.0	211.0	39.7	379.0	1.9	0.0	2.8	0.0	0.4	1.3	0.6	6.5	2.3	29.7	12.1	59.4	144.0	33.4	7500.0	7.9	20.5	38.4	

*Valores en ppm

JG55 Ortogneis de Sn Agustín		Espejo-Bautista et al., 2021																			
Zircón	P	Sc	Ti	Y	Nb	La	Ce	Pr	Nd	Sm	Eu	Gd	Tb	Dy	Ho	Er	Yb	Lu	Hf	Pb	Th
JG55-03_Zrn-01	230.0	193.3	4.4	279.0	0.5	0.0	1.3	0.0	0.2	0.6	0.4	4.1	1.5	20.4	9.0	44.1	106.4	24.5	7060.0	6.6	71.5
JG55-03_Zrn-02	220.0	179.2	28.6	147.3	0.5	0.0	0.8	0.0	0.1	0.2	0.2	1.7	0.7	10.8	4.4	24.5	62.5	15.4	8070.0	4.8	52.1
JG55-03_Zrn-05	200.0	164.9	10.5	119.9	0.5	0.0	1.8	0.0	0.1	0.3	0.2	2.3	0.7	8.7	3.7	17.7	40.9	9.2	9160.0	5.3	46.7
JG55-03_Zrn-06	240.0	168.9	10.5	186.0	0.9	0.0	13.3	0.1	1.0	1.7	1.0	7.3	1.9	16.4	5.3	20.4	38.9	8.3	9060.0	9.9	88.5
JG55-03_Zrn-07	310.0	195.6	12.1	382.0	1.0	0.0	18.3	0.3	4.3	5.1	2.4	16.7	4.2	38.7	11.6	43.9	79.0	15.9	9050.0	14.0	150.0
JG55-03_Zrn-11	710.0	208.0	38.3	951.0	1.9	0.0	16.6	0.1	2.0	4.8	0.6	22.5	6.6	79.5	32.1	143.0	309.0	63.8	7490.0	16.1	127.0
JG55-03_Zrn-12	180.0	164.0	8.7	127.8	0.4	0.0	1.0	0.0	0.1	0.1	0.2	1.6	0.6	8.5	3.8	19.2	49.5	11.9	7990.0	4.0	39.1
JG55-04_Zrn-14	130.0	201.0	9.4	350.0	1.2	0.0	17.4	0.3	3.0	4.2	2.3	14.3	3.8	34.3	9.8	37.1	61.8	12.8	8310.0	13.8	181.0
JG55-04_Zrn-16	30.0	182.0	460.0	143.0	0.6	0.0	1.6	0.0	0.2	0.5	0.3	2.3	0.8	11.4	4.7	22.3	54.2	13.9	8350.0	10.5	207.1
JG55-04_Zrn-17	166.0	160.5	3.5	103.7	0.5	0.0	1.1	0.0	0.2	0.3	0.2	1.5	0.7	7.8	3.1	16.7	41.1	9.6	7740.0	6.6	111.0
JG55-04_Zrn-18	670.0	155.0	4.7	86.1	0.4	0.0	0.7	0.0	0.1	0.4	0.1	0.6	0.4	5.8	2.8	14.1	37.5	9.3	7150.0	4.2	32.2
JG55-04_Zrn-19	180.0	193.0	13.3	168.0	0.7	0.0	4.2	0.1	0.3	0.6	0.4	2.9	0.8	11.1	5.0	26.2	67.0	16.6	9200.0	12.6	69.8
JG55-04_Zrn-22	210.0	157.0	4.5	151.0	0.4	0.0	1.0	0.0	0.0	0.3	0.2	1.9	0.8	11.0	4.9	24.7	59.2	14.3	6260.0	4.9	42.9
JG55-04_Zrn-23	190.0	169.0	18.2	168.0	0.3	0.0	1.0	0.0	0.0	0.2	0.1	1.2	0.6	9.2	4.6	27.1	81.2	21.5	11050.0	9.4	37.9
JG55-04_Zrn-24	20.0	213.0	12.0	344.0	0.7	0.0	7.1	0.1	0.8	1.3	0.6	6.0	2.2	25.0	10.1	49.0	123.0	30.9	9950.0	35.0	159.8
JG55-04_Zrn-25	230.0	199.0	23.7	305.0	1.2	0.0	15.2	0.1	2.6	2.5	1.2	9.2	2.6	25.4	8.9	42.1	99.2	22.4	13300.0	147.8	305.0
JG55-04_Zrn-29	90.0	157.8	4.5	106.3	0.5	0.0	0.6	0.0	0.0	0.2	0.2	1.2	0.4	7.7	3.1	17.0	45.9	10.6	6620.0	5.0	76.4
JG55-04_Zrn-30	70.0	166.3	4.9	125.9	0.4	0.0	0.9	0.0	0.1	0.3	0.2	1.1	0.6	8.8	3.9	19.7	53.5	13.5	8750.0	6.4	78.6
JG55-04_Zrn-31	180.0	192.0	9.7	232.0	0.7	0.0	4.7	0.1	0.3	0.9	0.5	4.8	1.5	18.6	7.4	34.8	89.1	20.6	10760.0	25.0	264.9
JG55-04_Zrn-32	2790.0	200.0	16.7	377.0	1.0	2.6	15.4	1.0	6.3	2.5	1.2	8.5	2.5	28.6	11.6	56.4	137.0	32.1	8310.0	17.6	168.0
JG55-04_Zrn-34	350.0	166.5	5.5	112.1	0.3	0.1	1.2	0.1	0.2	0.1	0.2	1.4	0.7	8.2	3.7	18.2	44.5	10.7	8360.0	6.7	62.7
JG55-04_Zrn-35	360.0	170.0	8.9	201.0	0.4	0.0	1.3	0.0	0.7	0.7	0.3	4.1	1.3	16.5	6.4	33.0	78.1	17.8	8980.0	6.5	58.8
JG55-04_Zrn-36	320.0	166.0	23.0	111.0	0.4	0.0	0.9	0.0	0.1	0.3	0.2	1.1	0.4	7.8	3.5	17.6	54.3	13.1	9550.0	7.6	46.8
JG55-04_Zrn-37	280.0	167.9	12.7	125.7	0.4	0.0	0.9	0.0	0.1	0.2	0.2	1.9	0.7	9.3	3.8	18.8	46.1	10.7	7580.0	4.3	55.9
JG55-04_Zrn-38	330.0	151.1	5.5	93.8	0.4	0.0	0.9	0.0	0.0	0.2	0.2	1.5	0.6	6.8	2.8	14.2	36.5	8.7	7330.0	7.2	138.3
JG55-04_Zrn-39	630.0	185.0	42.3	440.0	0.5	0.0	4.5	0.2	3.8	7.4	0.1	22.2	5.2	47.8	13.7	50.5	69.6	14.3	12170.0	125.3	223.0
JG55-04_Zrn-40	224.0	176.3	6.3	331.0	0.4	0.0	1.1	0.0	0.4	1.1	0.8	5.9	2.1	26.7	11.0	49.6	111.0	25.4	7090.0	9.9	128.0
JG55-04_Zrn-41	270.0	147.0	13.4	66.2	0.4	0.0	0.7	0.0	0.0	0.2	0.1	0.7	0.3	3.8	2.5	12.3	31.1	7.9	6470.0	6.0	24.4
JG55-04_Zrn-42	210.0	150.0	14.7	55.2	0.4	0.0	1.2	0.0	0.2	0.1	0.2	1.1	0.3	4.1	2.1	10.1	26.9	6.7	6590.0	9.8	43.5

*Valores en ppm

JG18 Esquisto pelítico (U. Esla)		Espejo-Bautista et al., 2021																			
Zircón	P	Ti	Y	Nb	La	Ce	Pr	Nd	Sm	Eu	Gd	Tb	Dy	Ho	Er	Yb	Lu	Hf	Pb	Th	U
JG18-01_Zrn-b-01	572.0	46.6	276.0	0.2	0.0	2.8	0.3	5.6	9.1	0.2	26.8	5.6	38.8	9.3	30.8	40.2	6.8	9630.0	5.9	47.3	64.6
JG18-01_Zrn-b-03	421.0	15.0	241.0	0.3	0.0	1.8	0.3	4.5	10.6	0.9	28.7	5.3	35.7	8.1	24.1	27.2	4.5	11450.0	21.1	15.8	272.0
JG18-01_Zrn-b-05	429.0	25.6	263.0	0.3	0.0	2.0	0.2	3.1	6.9	0.6	23.4	5.3	38.0	8.7	25.6	30.9	5.3	10670.0	11.4	19.2	160.0
JG18-01_Zrn-b-07	365.0	24.5	252.7	0.2	0.0	1.2	0.1	1.6	5.1	0.3	20.1	4.7	35.4	8.8	26.9	39.2	6.7	10600.0	10.5	5.0	124.8
JG18-01_Zrn-b-10	272.0	11.2	93.8	0.3	0.0	3.8	0.2	3.4	4.6	0.3	9.9	2.0	12.7	3.2	9.5	11.2	1.8	10810.0	38.8	222.0	499.0
JG18-01_Zrn-b-12	361.0	9.2	192.0	0.2	0.1	2.4	0.3	4.1	7.9	0.7	20.0	3.9	28.9	6.2	17.0	21.0	3.4	9080.0	10.8	34.9	191.9
JG18-01_Zrn-b-14	492.0	45.4	284.0	0.3	1.0	3.6	0.9	9.9	12.4	2.0	28.6	6.2	37.9	8.8	26.0	29.4	5.0	10340.0	20.7	13.8	156.2
JG18-01_Zrn-b-18	191.0	33.6	234.6	0.3	0.0	1.7	0.1	0.8	2.2	0.2	10.2	2.8	23.9	7.8	29.1	47.4	9.2	10260.0	18.6	67.6	251.4
JG18-01_Zrn-b-20	345.0	14.6	366.0	0.5	0.2	1.9	0.2	2.4	5.4	0.4	23.8	5.6	46.0	13.0	45.2	66.8	13.3	10320.0	14.5	77.0	249.0
JG18-01_Zrn-b-21	276.0	27.7	201.0	0.3	0.0	6.0	0.4	6.3	9.9	0.4	28.2	5.8	36.0	7.1	16.3	15.2	2.9	9340.0	79.2	79.4	706.0
JG18-01_Zrn-b-23	445.0	37.7	326.0	0.3	0.0	3.5	0.3	5.1	10.4	0.8	27.9	6.3	46.0	10.2	29.8	32.5	5.2	12300.0	46.5	22.1	322.0
JG18-01_Zrn-n-02	360.0	81.0	712.0	1.1	0.0	5.2	0.1	4.0	8.4	0.7	31.9	8.5	81.2	23.8	85.7	115.0	20.9	10170.0	107.8	497.0	860.0
JG18-01_Zrn-n-04	467.0	16.6	232.0	0.3	0.0	1.7	0.2	3.0	6.3	0.7	17.1	4.0	29.1	8.0	25.6	36.9	6.9	10110.0	19.6	23.6	331.0
JG18-01_Zrn-n-06	381.0	20.2	214.1	0.3	0.0	2.5	0.3	4.2	8.1	1.0	22.6	4.7	31.8	6.5	19.0	23.6	4.0	10630.0	27.3	21.4	357.0
JG18-01_Zrn-n-08	323.0	86.8	889.0	1.2	0.0	7.1	0.4	6.8	10.9	0.9	41.3	10.9	99.6	31.1	112.2	164.0	28.3	9490.0	138.3	542.0	911.0
JG18-01_Zrn-n-09	409.0	12.6	191.0	0.2	0.0	1.7	0.3	3.6	7.2	1.3	22.6	4.6	30.5	5.7	14.7	16.0	2.7	10350.0	18.2	8.3	289.0
JG18-01_Zrn-n-11	305.0	10.3	220.0	0.3	0.0	0.8	0.1	1.3	2.9	0.8	15.2	4.7	33.9	6.9	19.4	38.5	8.6	10900.0	14.2	8.4	257.0
JG18-01_Zrn-n-13	484.0	50.8	247.0	0.3	0.0	2.4	0.3	4.9	8.1	0.8	24.1	4.7	35.5	8.1	23.8	27.2	4.5	10540.0	24.1	13.5	189.1
JG18-01_Zrn-n-17	181.0	23.1	402.0	1.2	0.0	4.5	0.1	1.2	2.2	0.2	11.3	4.1	42.4	13.9	54.9	84.0	16.3	11300.0	96.3	209.6	478.0
JG18-01_Zrn-n-19	466.0	14.7	582.0	1.0	0.6	4.2	0.4	6.0	8.5	1.9	33.8	8.1	73.2	19.8	70.0	104.2	22.2	9460.0	25.8	191.6	399.0
JG18-01_Zrn-n-22	244.0	44.8	203.0	0.2	0.0	1.8	0.1	2.8	6.5	0.8	27.7	6.3	37.5	6.4	14.0	8.4	1.0	12500.0	36.0	30.6	212.5
JG18-01_Zrn-n-24	479.0	35.0	285.0	0.3	0.0	3.2	0.3	5.8	8.6	1.0	23.5	5.6	40.5	9.3	26.0	28.9	4.6	10230.0	34.6	24.9	356.0
Zircon_01_JGE-18	-470.0	15.7	258.3	0.3	0.4	2.6	0.2	4.8	9.3	1.0	27.3	5.5	38.2	8.3	22.1	22.3	3.6	13160.0	17.2	12.4	194.1
Zircon_10_1	-120.0	7.6	239.4	0.4	0.0	2.8	0.3	5.1	9.6	1.0	23.8	4.6	33.1	8.0	24.8	34.5	6.9	11650.0	20.3	16.8	271.4
Zircon_100	5000.0	12.7	628.0	0.6	0.0	0.6	0.1	1.0	4.3	0.4	31.6	9.4	81.6	19.9	61.7	73.4	14.1	14970.0	16.5	4.8	214.0
Zircon_103	1000.0	19.2	435.9	0.2	0.0	0.6	0.0	1.0	2.5	0.6	19.8	6.7	57.1	14.3	44.9	61.8	12.1	13880.0	26.8	4.3	198.3
Zircon_104	200.0	10.8	524.0	0.6	0.0	0.8	0.1	1.2	4.8	0.6	29.3	9.3	74.4	18.9	60.1	95.8	21.3	13810.0	36.4	8.9	343.0
Zircon_105	-300.0	18.7	238.5	0.2	0.0	1.6	0.1	2.0	8.0	0.4	25.2	5.1	35.7	7.6	22.0	25.1	4.1	12090.0	12.4	1.8	127.7
Zircon_106	1000.0	10.4	334.2	0.9	0.0	0.7	0.1	1.3	6.2	0.5	30.5	6.4	45.5	11.0	33.7	41.1	7.9	18940.0	24.3	8.3	320.2
Zircon_107	-500.0	19.5	376.0	1.2	0.0	7.7	0.1	2.8	4.5	0.6	15.8	4.2	39.3	12.6	51.2	97.2	19.4	11630.0	37.9	68.9	310.9
Zircon_108	1000.0	24.5	308.0	0.6	0.0	2.1	0.1	1.4	3.6	0.7	14.1	4.1	35.2	9.4	41.1	73.3	15.1	12430.0	74.1	15.9	610.0
Zircon_109	1000.0	10.0	257.7	0.2	0.0	1.3	0.1	1.5	7.6	0.3	25.5	5.5	37.2	8.6	25.8	28.2	4.8	12970.0	15.9	2.5	201.7
Zircon_11_1	490.0	31.2	227.4	0.4	0.0	2.6	0.3	5.8	7.6	0.7	18.7	4.5	28.2	7.0	22.4	31.9	5.0	11420.0	38.0	18.4	262.0
Zircon_110	0.0	14.4	305.4	0.5	0.0	1.2	0.1	1.8	6.4	0.2	22.0	5.2	41.3	9.5	30.3	40.2	8.2	12870.0	18.3	14.1	245.2
Zircon_12_1	-830.0	31.3	306.6	0.7	0.1	2.7	0.4	6.3	12.3	0.9	30.0	5.5	43.1	10.3	30.9	41.4	7.1	12500.0	19.9	13.8	211.6
Zircon_13_1	120.0	13.4	189.9	0.3	0.0	3.6	0.3	7.3	12.2	1.0	25.9	4.4	27.9	5.9	15.6	16.0	2.1	12680.0	34.6	33.6	410.9
Zircon_14_1	-360.0	15.0	188.7	0.2	0.0	3.4	0.4	7.1	11.5	1.1	25.2	4.4	28.9	5.7	16.5	16.2	2.2	12490.0	32.6	33.9	399.5
Zircon_15_1	-210.0	14.9	306.4	0.5	0.0	2.8	0.3	5.6	9.1	1.0	24.8	5.3	40.9	10.0	30.6	39.2	6.8	12170.0	19.0	30.1	220.6
Zircon_16_1	-360.0	11.2	455.6	0.3	0.0	2.7	0.3	6.0	12.2	0.3	42.5	9.1	63.1	14.6	42.7	44.7	6.9	10970.0	6.3	23.0	76.1
Zircon_17_1	-660.0	26.6	231.4	0.6	0.0	2.4	0.3	4.5	8.5	0.8	20.3	4.6	30.4	7.2	22.0	30.8	6.4	11090.0	28.5	15.8	249.8
Zircon_18_1	170.0	28.0	241.7	0.3	0.0	2.8	0.3	6.4	8.7	0.7	24.0	4.6	35.6	7.5	24.8	24.6	4.4	12070.0	25.8	16.4	218.8
Zircon_19_1	-270.0	11.2	247.3	0.4	0.0	1.0	0.0	1.3	5.5	0.2	19.6	4.7	34.4	8.0	25.2	31.4	6.4	13480.0	20.3	11.5	261.5
Zircon_2_1	-280.0	12.2	329.5	0.2	0.0	1.7	0.2	4.3	9.4	1.0	30.6	6.3	44.2	10.6	34.6	38.8	6.8	12280.0	17.2	12.6	205.3
Zircon_20_1	-220.0	26.7	145.0	0.4	0.0	2.4	0.1	2.6	4.0	0.3	19.6	3.8	23.8	4.7	12.0	11.5	1.9	11760.0	33.8	31.0	288.0
Zircon_21_1	-510.0	22.1	319.6	0.5	0.0	2.6	0.4	5.7	9.8	0.9	28.1	6.2	46.0	9.7	30.0	38.3	7.2	12160.0	19.0	14.0	234.6
Zircon_22_1	190.0	35.1	304.6	0.8	0.0	1.0	0.1	1.6	7.6	0.4	29.5	6.1	43.2	9.7	29.5	43.3	10.1	12170.0	12.4	3.5	166.5
Zircon_23_1	-190.0	21.2	350.7	0.5	0.0	1.8	0.0	1.3	6.8	0.5	32.4	7.3	48.7	10.8	33.6	44.9	9.1	12500.0	13.7	4.6	187.9
Zircon_24_1	-140.0	22.6	540.0	0.4	0.0	0.6	0.0	0.3	1.4	0.4	12.9	5.2	53.0	16.5	61.9	85.4	16.3	12140.0	64.5	11.0	345.0

Continúa

Continuación

JG18 Esquisto pelítico (U. Esla)	Espejo-Bautista et al., 2021																				
Zircón	P	Ti	Y	Nb	La	Ce	Pr	Nd	Sm	Eu	Gd	Tb	Dy	Ho	Er	Yb	Lu	Hf	Pb	Th	U
Zircon_25_I	-420.0	113.0	254.3	1.2	0.0	0.7	0.0	0.8	1.5	0.5	11.9	3.6	32.1	8.2	22.9	31.8	6.3	13370.0	63.0	6.7	579.0
Zircon_26_I	-20.0	23.0	161.6	0.3	0.0	2.0	0.2	3.1	5.6	0.6	17.3	3.4	22.7	5.3	15.3	19.4	3.8	12210.0	39.8	11.9	322.7
Zircon_27_I	-620.0	11.5	293.0	0.2	0.0	2.1	0.3	4.7	9.8	1.2	27.2	5.9	42.6	9.5	27.3	30.1	5.0	11740.0	17.8	15.4	229.7
Zircon_28_I	-290.0	26.4	312.0	0.6	0.0	3.2	0.4	5.8	11.6	0.9	29.7	6.1	42.2	10.4	33.7	56.5	12.9	11650.0	56.7	22.9	354.0
Zircon_29_I	-280.0	23.7	332.5	0.4	0.0	1.5	0.2	2.9	6.2	0.8	22.1	6.0	43.0	10.7	38.7	59.4	12.9	11860.0	43.7	11.2	298.7
Zircon_3_I	10.0	34.1	277.1	0.2	0.0	2.9	0.4	6.0	11.8	0.9	28.7	6.0	41.9	9.1	27.0	29.9	4.8	12380.0	28.7	14.6	188.2
Zircon_30_I	280.0	26.0	179.0	0.9	0.3	2.4	0.4	2.7	3.4	1.4	12.9	3.2	22.5	5.1	18.5	49.4	15.3	12710.0	11.0	7.0	109.0
Zircon_31_I	-260.0	11.7	810.0	1.7	0.4	4.8	0.2	1.9	5.8	1.0	23.8	7.1	76.3	26.8	121.4	236.3	49.5	11590.0	51.0	82.7	648.0
Zircon_32_I	-140.0	10.2	329.0	0.4	0.0	1.6	0.1	2.5	7.0	0.7	19.2	4.9	39.3	10.2	31.8	40.1	6.6	12310.0	14.2	10.8	256.0
Zircon_33_I	50.0	7.3	337.8	0.3	0.1	1.5	0.1	3.0	6.7	1.1	28.0	6.1	45.5	11.1	33.9	45.4	9.1	12040.0	15.1	3.2	212.1
Zircon_34_I	0.0	13.6	244.1	0.3	0.0	1.6	0.2	3.9	7.6	0.4	22.7	4.8	35.6	8.4	24.4	27.4	5.0	11470.0	28.5	19.9	332.0
Zircon_35_I	210.0	6.7	319.4	0.3	0.1	1.9	0.3	4.3	13.1	0.9	39.8	7.5	46.9	10.4	29.4	32.5	5.1	11840.0	20.2	6.8	267.6
Zircon_36_I	-150.0	39.6	160.5	0.3	0.0	4.6	0.5	6.0	6.3	0.5	15.0	3.0	21.8	5.5	17.5	19.8	3.3	11580.0	48.3	57.2	245.7
Zircon_37_I	-100.0	8.6	308.0	0.8	0.0	3.7	0.0	1.0	3.1	0.7	16.3	4.0	33.5	9.4	38.3	82.0	18.4	11620.0	48.0	36.4	680.0
Zircon_38_I	-300.0	7.8	288.0	0.4	0.0	2.1	0.2	4.0	7.8	0.7	25.4	5.8	39.8	9.6	31.2	54.0	10.9	11510.0	34.8	18.2	451.0
Zircon_39_I	-40.0	25.4	567.0	0.5	0.0	2.0	0.1	2.1	4.0	0.6	20.4	6.2	60.2	19.2	84.0	148.0	29.1	10940.0	84.2	43.3	649.0
Zircon_4_I	-60.0	18.9	167.6	0.2	0.0	3.4	0.4	5.3	6.5	0.6	15.1	3.3	23.0	5.6	16.7	19.9	3.1	12100.0	40.9	57.2	392.0
Zircon_40_I	-530.0	12.4	436.0	0.8	0.0	2.1	0.0	2.4	5.0	0.8	16.9	4.5	43.4	14.1	62.6	165.8	39.8	11850.0	45.8	23.5	524.0
Zircon_41	430.0	12.5	327.5	0.2	0.2	2.1	0.3	4.9	10.0	0.9	27.7	6.1	47.7	10.7	31.7	36.6	6.2	11800.0	23.3	16.9	287.1
Zircon_42	-390.0	20.5	213.0	0.2	0.0	1.9	0.2	3.5	7.4	0.6	22.4	4.3	30.6	6.8	19.9	21.9	3.6	10690.0	26.4	16.6	218.4
Zircon_43	-170.0	17.4	361.0	0.4	0.1	2.0	0.2	4.4	10.1	0.9	34.8	7.0	47.3	12.0	37.6	51.7	9.5	10840.0	22.9	16.1	294.8
Zircon_44	-310.0	13.0	560.2	0.7	0.0	0.4	0.0	0.9	5.7	0.2	38.4	9.5	72.2	18.0	59.0	73.9	12.6	19170.0	19.6	2.6	240.8
Zircon_45	-260.0	28.2	182.8	0.2	0.0	3.4	0.4	5.2	9.6	0.7	24.7	4.1	27.3	5.5	15.7	15.6	2.3	11860.0	49.3	26.1	372.3
Zircon_46	-910.0	13.5	200.0	0.5	0.0	3.4	0.4	6.8	13.8	1.5	25.1	4.6	29.8	6.5	17.1	20.8	4.3	12820.0	36.7	36.7	426.3
Zircon_47	460.0	14.8	233.9	0.1	0.0	1.9	0.1	2.4	5.5	0.3	20.5	4.5	32.6	7.0	22.0	25.6	3.9	10410.0	11.4	1.9	136.0
Zircon_48	-270.0	14.8	224.0	0.4	0.2	4.4	0.3	4.9	7.5	0.8	17.7	3.8	28.6	7.3	25.7	46.4	9.4	11180.0	33.1	61.4	371.0
Zircon_49	220.0	32.2	222.5	0.2	0.0	0.4	0.0	0.5	2.0	0.6	17.5	5.5	41.0	7.1	16.4	16.9	2.7	10670.0	23.4	3.5	183.0
Zircon_5	610.0	32.6	393.0	0.7	0.1	5.2	0.3	3.4	7.3	0.8	23.7	5.6	45.4	12.6	48.1	85.9	18.6	11670.0	31.8	39.1	320.9
Zircon_50	320.0	5.6	131.4	0.6	0.0	2.6	0.0	0.2	0.5	0.2	2.0	0.7	10.0	4.6	22.6	60.5	12.4	6020.0	15.5	29.9	81.6
Zircon_51	50.0	11.1	258.3	0.3	0.0	2.3	0.2	3.3	8.2	0.6	23.7	5.1	37.5	8.3	23.8	24.5	3.6	13990.0	13.2	2.5	177.9
Zircon_52	10.0	17.0	190.7	0.3	0.0	1.1	0.0	1.4	4.4	0.3	15.1	4.2	29.1	6.2	17.7	19.6	3.2	13630.0	49.7	16.6	424.9
Zircon_53	-750.0	13.3	305.6	0.3	0.1	2.1	0.3	5.0	10.5	1.0	29.2	6.2	44.7	10.0	29.7	33.7	5.0	12570.0	15.7	12.7	201.2
Zircon_54	-270.0	25.2	199.8	0.3	0.0	2.6	0.2	4.6	8.2	0.6	23.7	4.8	31.4	6.9	18.6	21.2	3.6	12290.0	22.3	15.1	180.3
Zircon_55	-1100.0	14.8	1383.0	3.6	1.3	25.5	0.2	4.6	8.3	1.3	37.3	12.1	126.3	46.0	203.6	376.0	73.3	11880.0	93.8	386.0	781.0
Zircon_56	-680.0	24.0	269.0	0.3	0.0	2.5	0.2	3.6	8.1	0.9	23.5	4.8	33.4	8.7	28.9	41.3	7.7	12180.0	47.2	19.6	371.0
Zircon_57	-480.0	11.2	431.7	0.3	0.0	0.8	0.1	0.8	2.9	0.2	24.5	6.7	58.0	13.5	41.6	49.5	6.0	15850.0	16.5	1.9	188.9
Zircon_58	-610.0	19.1	308.0	0.7	0.1	2.5	0.3	4.9	9.1	1.0	26.5	5.8	44.2	10.2	30.5	42.8	9.3	12570.0	25.5	11.2	223.8
Zircon_6	-230.0	10.9	550.0	1.1	0.0	3.7	0.1	1.6	6.2	0.5	23.3	6.2	54.8	18.8	74.9	130.0	25.6	11720.0	28.3	72.0	358.0
Zircon_60	-230.0	43.6	405.1	4.6	0.0	2.0	0.1	1.3	2.4	0.7	10.8	4.4	43.8	12.6	41.9	51.0	7.2	11600.0	38.2	65.8	653.4
Zircon_61	-400.0	41.1	265.0	0.3	0.0	2.6	0.3	5.1	11.1	1.1	27.0	5.7	36.9	8.5	25.0	30.8	6.0	12140.0	40.1	12.4	253.1
Zircon_62	440.0	17.0	230.9	0.3	0.0	2.3	0.3	6.1	9.5	1.1	26.0	5.2	35.4	7.9	23.0	27.4	4.6	11100.0	16.6	16.4	216.2
Zircon_63	-280.0	21.6	350.0	0.7	0.2	2.8	0.3	3.9	5.2	1.0	17.2	4.2	35.5	11.5	49.0	105.0	28.0	11860.0	89.5	30.0	720.0
Zircon_64	-560.0	18.9	252.0	1.2	0.0	0.6	0.0	1.2	2.4	0.5	8.7	2.5	23.7	7.7	39.7	148.0	38.6	12600.0	41.5	15.0	421.0
Zircon_65	150.0	22.8	721.0	3.1	0.0	24.5	0.0	1.0	3.0	0.5	14.4	5.0	61.6	23.9	113.8	254.9	53.6	12490.0	111.0	145.9	638.0
Zircon_66	150.0	8.7	260.5	0.5	0.0	1.1	0.1	1.0	4.2	0.3	19.3	4.5	36.7	8.5	25.1	28.1	4.8	12970.0	6.5	2.0	99.6
Zircon_67	-540.0	24.3	250.6	0.2	0.0	2.7	0.3	5.9	9.3	0.3	26.4	5.1	35.8	8.3	24.9	27.2	4.7	11510.0	14.6	7.5	141.0
Zircon_68	-230.0	12.2	243.8	0.1	0.0	1.5	0.1	1.8	8.6	0.4	28.6	5.4	36.3	7.7	21.4	24.2	3.4	11370.0	16.0	10.2	203.0
Zircon_69	-550.0	35.5	278.3	0.3	0.0	2.5	0.3	5.5	10.5	1.0	26.1	5.6	41.2	9.1	25.3	29.3	4.6	11920.0	54.0	13.8	312.9
Zircon_7	-180.0	14.7	285.2	0.5	0.1	2.3	0.4	6.3	11.6	1.2	30.2	6.2	42.7	9.3	28.2	34.6	6.2	11820.0	15.2	15.7	168.0
Zircon_70	-640.0	19.7	402.0	0.7	0.0	5.2	0.2	3.3	7.1	0.7	21.9	6.1	47.1	13.2	48.2	83.0	16.6	11730.0	41.8	34.2	381.0
Zircon_71	20.0	12.2	834.0	0.6	0.1	2.3	0.2	3.4	5.9	1.0	24.5	7.0	79.4	27.8	128.5	278.2	61.4	12640.0	74.3	61.9	775.0
Zircon_72	-800.0	7.4	490.7	0.7	0.0	0.8	0.1	1.7	11.2	0.8	50.5	10.9	72.8	15.3	50.7	57.2	9.6	19040.0	21.4	3.2	276.4

Continúa

Continuación

JG18 Esquisto pelítico (U. Esla)		Espejo-Bautista et al., 2021																			
Zircón	P	Ti	Y	Nb	La	Ce	Pr	Nd	Sm	Eu	Gd	Tb	Dy	Ho	Er	Yb	Lu	Hf	Pb	Th	U
Zircon_73	330.0	8.1	468.0	0.3	0.1	3.3	0.5	9.0	22.8	1.4	61.0	11.4	74.2	15.3	42.8	40.3	6.2	12110.0	21.5	27.2	291.6
Zircon_74	-1900.0	14.9	237.5	0.2	0.0	2.4	0.2	4.8	9.9	0.7	26.0	5.2	33.0	7.7	22.9	26.5	4.6	11960.0	14.0	19.6	160.5
Zircon_75	-590.0	17.8	91.4	0.2	0.0	0.7	0.1	1.0	2.2	0.4	6.5	2.0	14.2	2.8	8.7	16.9	4.0	12930.0	28.2	6.0	219.8
Zircon_77	-1000.0	26.0	219.4	0.2	0.0	2.6	0.2	5.8	8.8	0.5	23.2	4.4	31.3	7.2	21.7	27.0	4.5	12310.0	21.3	33.9	155.0
Zircon_78	-400.0	11.8	259.5	0.5	0.0	1.1	0.1	1.8	5.0	0.2	22.1	4.7	38.0	8.9	26.8	34.0	5.7	13520.0	10.8	15.0	147.4
Zircon_79	-1410.0	14.6	250.0	1.1	0.0	1.9	0.1	1.1	3.0	0.4	11.8	3.2	26.4	8.4	33.7	66.2	13.7	12220.0	95.0	28.0	941.0
Zircon_8	-290.0	15.4	233.6	0.4	0.0	2.1	0.3	5.3	9.7	0.9	22.1	4.9	32.4	7.7	21.8	29.7	6.3	11340.0	22.3	17.5	249.9
Zircon_80	-200.0	18.6	446.0	1.4	0.5	3.0	0.1	1.6	5.7	0.7	20.1	5.0	51.2	16.2	63.0	114.0	24.7	11410.0	43.0	19.4	527.0
Zircon_81	800.0	45.1	313.2	0.7	0.0	2.9	0.4	6.2	12.6	1.6	32.7	6.4	43.8	10.3	30.4	37.2	7.5	11940.0	40.5	16.0	295.9
Zircon_82	-1400.0	10.2	405.0	0.9	0.0	1.4	0.1	2.5	7.5	0.7	21.3	5.3	45.8	13.7	55.0	113.0	23.5	12410.0	39.0	28.9	540.0
Zircon_83	-800.0	11.0	267.4	0.5	0.0	1.6	0.1	2.6	6.3	0.4	24.4	5.3	37.6	8.5	24.8	25.6	4.2	13580.0	20.6	13.6	270.6
Zircon_84	800.0	23.8	213.3	0.9	0.0	3.3	0.3	4.7	6.9	0.6	18.0	3.5	27.2	6.9	25.1	57.6	15.8	12210.0	56.7	58.4	456.0
Zircon_85	-100.0	20.0	136.8	0.2	0.0	0.6	0.0	0.7	1.5	0.6	10.8	3.1	19.8	4.0	12.2	17.9	3.9	12240.0	79.8	4.8	747.0
Zircon_86	-1900.0	18.6	363.4	0.3	0.3	4.3	0.6	10.6	16.1	0.4	38.6	7.6	54.1	11.7	33.2	38.6	7.7	11050.0	10.8	73.4	142.6
Zircon_87	-700.0	13.3	711.0	1.1	0.2	2.8	0.1	2.2	5.8	0.9	26.6	7.7	71.4	23.2	102.2	218.0	45.1	11540.0	43.9	92.1	551.0
Zircon_88	-1200.0	38.1	223.9	0.3	0.0	3.3	0.4	6.3	10.2	1.0	27.2	4.7	31.8	7.3	22.6	23.6	3.8	11950.0	31.4	16.3	161.5
Zircon_89	-2800.0	11.5	561.0	0.2	0.0	0.7	0.1	0.8	4.3	0.5	38.9	10.4	80.4	18.6	51.9	54.7	8.9	9460.0	2.3	0.9	29.3
Zircon_9	-450.0	9.3	267.5	0.2	0.0	2.8	0.2	4.7	12.5	1.2	37.7	6.4	39.3	8.5	25.0	25.4	4.1	12560.0	25.2	20.9	333.3
Zircon_90	-7300.0	16.2	968.0	2.9	5.8	29.1	1.1	6.9	9.5	1.0	31.7	8.8	89.2	32.2	146.0	314.0	65.7	10830.0	57.8	366.0	538.0
Zircon_91	5000.0	16.2	537.0	1.1	0.0	13.0	0.1	1.9	3.8	0.7	16.1	4.6	48.6	17.1	77.3	175.0	38.6	12250.0	71.3	94.5	521.0
Zircon_92	2100.0	15.3	671.0	1.6	0.0	9.9	0.2	4.5	10.4	0.8	35.4	8.5	77.2	24.1	95.0	159.8	31.0	10920.0	27.0	126.7	364.8
Zircon_93	-30000.0	12.8	318.0	0.7	0.0	0.9	0.1	1.3	5.4	0.1	28.1	5.9	44.7	10.3	32.1	38.5	6.2	17200.0	33.7	13.1	371.0
Zircon_94	-10000.0	12.9	247.4	0.4	0.0	2.4	0.1	2.6	6.3	0.8	23.1	4.8	34.9	8.0	22.9	30.0	6.7	12690.0	15.7	3.8	198.6
Zircon_95	-160000.0	13.9	214.7	0.7	0.0	2.5	0.2	2.8	6.1	0.5	18.5	4.2	30.2	7.0	21.7	34.5	8.4	12270.0	14.6	3.2	185.2
Zircon_96	-26000.0	25.2	228.7	0.2	0.0	1.5	0.2	2.8	6.4	0.9	23.8	5.1	34.0	7.8	22.3	30.8	6.1	10960.0	29.8	11.1	288.0
Zircon_97	-800.0	22.9	248.1	0.2	0.0	1.9	0.1	2.7	7.4	0.3	26.3	5.2	36.5	8.3	23.7	26.0	4.2	11610.0	19.8	1.9	192.0
Zircon_98	10500.0	31.3	237.0	0.3	0.0	3.2	0.6	8.1	11.1	1.1	28.4	5.3	35.2	8.0	22.6	24.0	4.1	11690.0	27.5	15.2	138.5
Zircon_99	4100.0	13.3	609.0	1.1	0.1	10.3	0.2	5.0	8.5	0.8	27.6	7.0	63.8	20.5	83.8	144.0	28.7	11030.0	36.3	111.9	332.0

*Valores en ppm

JG46 Para-anfibolita (U. Etna)		Espejo-Bautista et al., 2021																				
Zircón	P	Sc	Ti	Y	Nb	La	Ce	Pr	Nd	Sm	Eu	Gd	Tb	Dy	Ho	Er	Yb	Lu	Hf	Pb	Th	U
JG46-01_Zrn-b-101	640.0	135.3	8.4	928.0	15.8	0.0	12.7	0.1	1.0	2.7	0.4	11.5	4.5	58.5	26.8	148.5	408.0	92.0	12790.0	87.5	81.6	878.0
JG46-01_Zrn-b-103	560.0	141.2	6.0	694.0	4.8	0.0	15.4	0.1	1.1	2.1	0.6	12.8	4.8	57.7	22.7	103.0	196.9	40.1	9640.0	7.5	14.7	82.1
JG46-01_Zrn-b-105	1350.0	169.6	7.5	2080.0	17.7	0.0	25.5	0.1	1.9	5.1	0.5	34.9	13.8	183.4	72.4	314.0	571.0	114.8	10510.0	13.9	80.5	133.1
JG46-01_Zrn-b-107	540.0	102.5	8.4	813.0	26.2	0.0	11.5	0.0	0.2	1.2	0.1	8.6	3.6	50.9	21.5	110.4	212.0	38.8	12270.0	33.0	71.0	293.0
JG46-01_Zrn-b-116	190.0	115.3	3.9	175.7	0.8	0.0	4.6	0.0	0.1	0.2	0.1	1.9	0.9	11.9	5.4	29.7	83.3	20.8	9840.0	3.4	11.6	53.6
JG46-01_Zrn-b-123	160.0	182.9	21.8	68.2	0.9	0.0	5.1	0.1	0.8	1.2	0.4	4.4	1.0	8.0	2.3	7.9	12.8	2.2	8000.0	2.4	6.7	29.8
JG46-01_Zrn-b-128	650.0	147.0	41.4	1600.0	7.8	0.0	25.4	0.1	2.3	4.6	0.6	26.9	10.5	128.0	51.1	247.0	496.0	103.0	11400.0	15.3	64.8	96.9
JG46-01_Zrn-b-132	447.0	157.0	5.3	1070.0	4.9	0.0	17.2	0.1	0.8	3.0	0.8	18.1	6.6	83.3	34.8	179.0	445.0	99.0	9430.0	26.5	61.9	217.0
JG46-01_Zrn-b-33	673.0	177.6	17.9	1075.0	4.4	0.4	15.3	0.2	2.1	3.2	0.5	17.1	7.0	87.4	35.3	170.8	398.0	92.3	11170.0	4.3	28.9	45.6
JG46-01_Zrn-b-37	430.0	144.4	12.5	458.0	1.0	0.0	8.6	0.1	1.0	1.2	0.7	8.6	3.2	37.5	15.0	69.4	139.4	30.1	8680.0	0.8	0.4	7.3
JG46-01_Zrn-b-39	870.0	136.4	9.3	1423.0	12.3	0.0	23.9	0.1	1.0	3.3	0.6	19.2	8.0	111.1	45.7	232.6	597.0	139.3	10310.0	19.6	176.0	144.1
JG46-01_Zrn-b-41	450.0	139.0	4.8	394.0	1.5	0.0	9.8	0.0	0.4	1.1	0.3	5.9	2.3	30.7	12.9	62.7	152.6	35.0	10230.0	6.1	13.7	101.3
JG46-01_Zrn-b-43	1100.0	116.5	6.6	2261.0	18.9	0.0	66.9	0.1	1.7	5.6	1.6	35.5	13.4	180.7	73.3	334.0	560.0	104.1	8560.0	34.3	256.0	248.0
JG46-01_Zrn-b-51	1330.0	277.0	11.4	2150.0	6.7	0.0	15.1	0.1	1.7	5.7	0.8	42.9	15.9	191.6	73.2	313.0	566.0	122.7	9470.0	9.4	37.4	80.2
JG46-01_Zrn-b-54	260.0	139.5	16.9	71.7	0.7	0.0	5.0	0.0	0.6	1.0	0.3	3.7	1.0	8.7	2.2	8.0	9.5	1.7	7860.0	1.1	0.9	8.7
JG46-01_Zrn-b-58	480.0	168.7	11.2	336.0	1.1	0.0	11.4	0.0	0.6	1.0	0.4	6.5	2.3	26.9	10.7	50.1	112.6	24.8	10360.0	5.7	71.5	78.2
JG46-01_Zrn-b-68	460.0	122.8	5.3	406.0	3.3	0.0	11.3	0.0	0.5	1.0	0.3	4.9	2.1	28.2	12.3	63.4	136.0	25.3	8060.0	19.1	138.5	204.0
JG46-01_Zrn-b-74	370.0	157.9	20.6	104.1	0.6	0.0	3.3	0.0	0.5	1.0	0.2	3.0	0.9	8.4	3.3	15.9	37.8	9.8	8700.0	4.0	3.0	35.7
JG46-01_Zrn-b-77	1160.0	118.4	6.4	1633.0	18.4	0.0	20.0	0.0	0.8	2.8	0.2	19.9	8.8	127.2	52.9	261.0	510.0	99.2	10500.0	15.0	32.8	133.0
JG46-01_Zrn-b-80	870.0	107.8	10.2	729.0	2.0	0.0	12.0	0.1	1.1	2.2	0.5	12.3	4.5	55.7	22.6	105.8	203.8	41.2	9130.0	3.2	7.8	45.3
JG46-01_Zrn-b-82	160.0	134.6	2.5	98.8	0.6	0.0	3.3	0.0	0.0	0.0	0.1	1.3	0.5	6.5	2.4	15.1	45.4	11.9	9030.0	2.0	12.2	39.2
JG46-01_Zrn-b-84	320.0	121.0	5.3	289.2	0.6	0.0	5.4	0.0	0.4	0.6	0.3	4.9	1.7	22.6	9.3	45.1	114.8	27.8	7630.0	2.3	6.6	24.6
JG46-01_Zrn-b-88	250.0	136.7	47.7	152.5	0.8	0.0	4.1	0.0	0.5	0.7	0.2	3.0	1.0	11.8	4.8	22.7	52.1	11.8	7460.0	2.5	5.8	24.1
JG46-01_Zrn-b-91	440.0	153.5	13.5	185.6	0.8	0.0	6.2	0.1	0.5	1.1	0.3	4.6	1.5	15.9	5.9	27.7	63.5	13.7	8010.0	2.5	7.1	26.5
JG46-01_Zrn-b-95	300.0	121.1	3.3	286.0	0.8	0.0	7.9	0.0	0.1	0.3	0.1	2.9	1.3	19.3	8.5	47.5	134.7	34.0	9200.0	2.4	15.0	48.7
JG46-01_Zrn-n-100	650.0	103.2	9.8	852.0	14.2	0.0	11.9	0.0	0.3	1.1	0.1	8.2	3.8	58.3	26.6	139.0	332.0	67.0	11730.0	33.3	65.6	274.0
JG46-01_Zrn-n-102	1080.0	115.1	4.2	1323.0	15.1	0.0	36.0	0.1	1.2	3.6	0.7	22.6	8.2	106.1	43.7	192.0	334.0	64.2	7370.0	25.3	133.0	222.5
JG46-01_Zrn-n-104	1290.0	126.8	7.6	1863.0	73.6	0.2	51.1	0.2	3.7	7.9	1.4	44.2	14.4	173.0	62.8	268.0	390.0	64.6	7670.0	104.0	561.0	699.0
JG46-01_Zrn-n-106	180.0	129.9	18.0	80.3	0.8	0.0	6.0	0.1	0.7	1.7	0.3	5.3	1.2	9.8	2.6	8.8	10.3	1.7	7770.0	1.0	0.5	7.4
JG46-01_Zrn-n-108	600.0	139.5	7.4	1007.0	27.3	0.1	19.0	0.1	0.6	1.8	0.4	7.7	3.2	51.6	26.8	161.8	446.0	91.0	13790.0	74.5	334.0	908.0
JG46-01_Zrn-n-110	194.0	137.7	17.2	175.2	0.7	0.0	5.9	0.0	0.7	0.7	0.4	4.5	1.3	15.1	5.5	25.7	57.9	12.7	8370.0	3.1	8.4	22.9
JG46-01_Zrn-n-111	250.0	129.5	4.5	228.9	0.6	0.0	4.5	0.0	0.1	0.5	0.1	3.2	1.1	14.9	6.5	37.6	104.6	26.6	9930.0	8.8	62.6	160.9
JG46-01_Zrn-n-112	397.0	212.0	22.3	150.3	1.0	0.0	6.8	0.0	1.0	1.6	0.4	5.9	1.5	15.6	5.3	22.7	46.1	9.8	8940.0	4.8	44.4	43.3
JG46-01_Zrn-n-113	1530.0	130.9	9.7	2910.0	6.2	0.0	25.5	0.1	1.5	4.2	0.4	31.4	14.2	202.0	92.2	453.0	815.0	158.3	9830.0	35.7	109.8	295.0
JG46-01_Zrn-n-114	210.0	124.7	7.1	373.0	2.9	0.0	12.8	0.0	0.2	0.6	0.2	3.7	1.5	22.2	10.8	64.8	196.8	45.1	12590.0	44.4	114.1	541.2
JG46-01_Zrn-n-115	400.0	136.0	12.0	690.0	22.3	0.0	16.0	0.0	0.0	0.7	0.1	3.8	2.0	33.5	17.4	111.0	280.0	56.0	15200.0	59.3	80.1	367.1
JG46-01_Zrn-n-117	990.0	124.0	6.4	1712.0	17.3	0.3	34.1	0.2	1.8	3.6	0.7	22.8	9.7	133.3	54.9	270.0	585.0	116.9	10500.0	17.7	143.1	198.5
JG46-01_Zrn-n-118	260.0	107.6	1.6	510.0	3.0	0.0	15.9	0.0	0.1	0.5	0.1	5.1	2.2	31.8	15.5	84.9	239.0	57.8	13240.0	17.7	38.4	225.0
JG46-01_Zrn-n-119	347.0	128.6	17.6	358.0	1.2	0.0	9.1	0.0	0.3	0.4	0.2	4.6	1.9	27.7	11.8	58.0	140.6	31.6	8760.0	15.3	24.4	102.0
JG46-01_Zrn-n-120	396.0	138.5	12.4	517.0	1.5	0.0	10.5	0.1	0.9	1.9	0.5	10.2	3.7	44.3	17.4	84.3	194.1	44.2	9700.0	6.8	43.4	55.7
JG46-01_Zrn-n-121	541.0	111.3	14.5	1279.0	2.1	0.0	8.1	0.0	0.9	3.2	0.5	23.3	9.0	110.1	43.7	191.8	347.0	68.9	8620.0	8.2	23.6	65.8
JG46-01_Zrn-n-122	429.0	161.0	12.8	595.0	2.1	0.0	14.7	0.1	0.9	2.0	0.5	10.6	3.9	49.7	20.3	95.7	211.0	47.7	11340.0	14.3	111.1	111.8
JG46-01_Zrn-n-124	147.0	156.4	20.8	40.2	0.7	0.0	4.5	0.1	0.7	1.0	0.4	3.0	0.6	4.9	1.3	4.0	6.2	1.2	7110.0	2.5	5.6	26.9
JG46-01_Zrn-n-125	269.0	121.9	23.4	137.0	0.7	0.0	9.4	0.1	1.4	1.6	1.0	6.6	1.7	14.8	4.5	15.0	19.6	3.4	7300.0	12.9	65.1	117.7
JG46-01_Zrn-n-126	184.0	178.0	3.3	357.0	0.8	0.0	7.0	0.0	0.3	0.8	0.4	4.7	1.8	25.5	10.9	55.6	156.0	37.1	9200.0	2.7	13.4	38.8
JG46-01_Zrn-n-127	910.0	120.8	3.9	1290.0	15.8	1.7	22.9	0.6	3.2	2.6	0.5	15.9	6.6	93.5	40.7	202.0	469.0	107.7	10420.0	35.5	101.0	332.0
JG46-01_Zrn-n-129	232.0	129.2	9.0	287.0	0.5	0.1	6.4	0.1	0.8	1.1	0.6	5.2	1.8	22.8	9.0	42.5	93.3	19.7	7790.0	3.4	8.4	48.3

Continúa

Continuación

JG46 Para-anfibolita (U. Etna)		Espejo-Bautista et al., 2021																				
Zircón	P	Sc	Ti	Y	Nb	La	Ce	Pr	Nd	Sm	Eu	Gd	Tb	Dy	Ho	Er	Yb	Lu	Hf	Pb	Th	U
JG46-01_Zrn-n-130	138.0	164.0	15.5	103.7	0.8	0.0	4.9	0.0	0.3	0.7	0.2	2.2	0.7	8.1	3.3	14.9	35.6	7.8	8450.0	4.1	9.5	38.6
JG46-01_Zrn-n-131	270.0	134.5	12.5	951.0	1.4	0.0	8.8	0.1	1.9	3.9	0.5	22.9	7.5	85.0	31.5	140.0	243.0	46.7	9050.0	24.3	97.3	231.0
JG46-01_Zrn-n-133	376.0	109.6	16.0	932.0	3.4	0.0	15.6	0.1	1.0	2.6	0.4	17.2	6.4	80.7	31.4	133.8	249.0	48.5	9490.0	3.1	5.5	21.0
JG46-01_Zrn-n-31	350.0	126.3	6.4	526.0	1.1	0.0	12.9	0.1	1.0	2.0	0.5	10.8	3.7	42.8	16.5	79.6	167.8	36.4	6890.0	10.8	106.1	92.2
JG46-01_Zrn-n-32	370.0	112.4	142.0	879.0	22.6	0.0	12.5	0.0	0.6	1.8	0.3	10.5	4.3	60.1	27.8	139.0	352.0	77.4	8110.0	44.3	109.0	376.0
JG46-01_Zrn-n-34	790.0	135.8	4.2	1290.0	35.0	0.0	20.5	0.0	0.4	1.4	0.3	8.6	4.9	77.0	39.1	217.0	654.0	142.0	14160.0	46.3	76.1	514.0
JG46-01_Zrn-n-35	190.0	138.6	14.6	40.9	0.5	0.0	4.8	0.1	0.7	1.3	0.4	3.2	0.7	5.1	1.4	4.3	7.3	1.4	7160.0	6.2	11.7	56.5
JG46-01_Zrn-n-36	420.0	127.7	9.5	643.0	12.0	0.0	12.2	0.1	0.3	1.0	0.3	9.0	3.3	45.1	19.7	107.1	312.0	76.6	9690.0	74.8	62.8	768.0
JG46-01_Zrn-n-38	790.0	131.7	4.8	1104.0	12.3	0.0	17.0	0.1	0.6	1.9	0.2	12.2	5.9	81.3	35.6	191.0	529.0	132.0	9790.0	24.7	72.3	245.0
JG46-01_Zrn-n-40	600.0	118.6	7.6	762.0	16.8	0.0	14.3	0.1	0.2	0.5	0.2	5.7	2.8	45.4	22.2	128.4	361.0	73.0	12630.0	76.8	123.7	738.1
JG46-01_Zrn-n-42	580.0	141.7	6.9	760.0	33.6	0.0	23.6	0.0	0.5	1.0	0.2	7.9	3.4	48.8	22.7	117.3	265.0	56.0	14250.0	54.4	42.8	580.0
JG46-01_Zrn-n-44	335.0	137.8	15.5	73.2	0.8	0.0	5.0	0.0	0.7	1.0	0.2	3.9	1.0	8.8	2.3	8.2	10.8	2.0	7600.0	0.7	1.0	6.2
JG46-01_Zrn-n-45	397.0	151.8	14.1	538.0	0.9	0.0	10.9	0.1	1.0	2.1	0.7	10.8	3.8	46.1	17.2	79.7	160.3	34.1	9280.0	7.9	58.9	59.0
JG46-01_Zrn-n-46	200.0	137.1	6.2	79.5	0.6	0.0	5.9	0.1	1.0	1.6	0.3	5.0	1.2	10.6	2.7	9.2	13.0	2.5	6950.0	1.3	7.5	16.0
JG46-01_Zrn-n-47	300.0	106.9	6.1	288.0	1.1	0.0	17.9	0.1	0.8	0.8	0.3	4.1	1.5	19.6	8.4	49.4	118.2	26.5	8720.0	9.0	71.6	116.0
JG46-01_Zrn-n-48	140.0	125.0	11.6	52.0	0.8	0.0	11.0	0.1	0.9	1.5	0.2	4.0	0.8	6.3	1.7	6.9	10.6	1.8	9620.0	3.9	43.7	38.8
JG46-01_Zrn-n-49	340.0	170.0	23.3	458.0	1.6	0.0	4.5	0.0	0.6	1.5	0.2	8.2	3.0	38.0	14.8	65.6	123.6	25.2	9310.0	9.7	18.6	64.5
JG46-01_Zrn-n-50	319.0	131.2	24.6	30.5	1.2	0.0	4.9	0.1	0.6	0.9	0.2	2.7	0.5	3.7	0.8	2.8	3.1	0.5	8010.0	2.7	1.5	22.7
JG46-01_Zrn-n-52	620.0	130.5	11.7	877.0	10.5	0.0	11.5	0.0	0.2	0.6	0.3	8.3	4.0	61.2	27.2	151.0	431.0	100.2	9990.0	114.5	63.3	913.0
JG46-01_Zrn-n-53	190.0	150.9	12.8	329.0	0.7	0.0	9.7	0.1	0.8	1.6	0.3	5.9	2.4	26.2	10.2	48.4	100.3	21.6	8420.0	5.7	62.6	65.0
JG46-01_Zrn-n-55	460.0	120.5	11.7	607.0	1.0	0.0	6.5	0.1	1.1	2.7	0.3	15.0	4.6	51.9	20.1	87.0	156.7	32.1	8520.0	23.9	58.6	178.0
JG46-01_Zrn-n-56	380.0	92.8	13.4	368.0	2.4	0.0	8.7	0.0	0.1	0.4	0.2	3.0	1.3	20.3	10.1	62.4	234.0	54.0	8440.0	18.2	30.1	99.9
JG46-01_Zrn-n-57	311.0	101.9	10.7	461.0	6.2	0.0	9.0	0.0	0.0	0.3	0.1	3.2	1.5	24.5	12.7	74.5	169.0	26.7	9860.0	82.3	24.7	583.0
JG46-01_Zrn-n-59	510.0	110.0	13.7	548.0	8.5	0.0	16.6	0.0	0.2	0.4	0.1	4.1	2.1	33.3	16.0	85.9	172.5	31.1	14170.0	28.8	263.0	245.0
JG46-01_Zrn-n-60	170.0	137.7	13.0	269.0	0.9	0.0	4.0	0.0	0.5	1.4	0.4	6.2	2.0	24.5	9.7	45.0	89.0	20.2	6190.0	21.0	38.4	167.0
JG46-01_Zrn-n-61	1090.0	131.5	11.0	1435.0	20.2	0.0	28.3	0.1	1.2	3.7	0.4	19.7	8.1	107.8	43.8	220.0	463.0	95.0	12730.0	34.8	120.3	281.0
JG46-01_Zrn-n-62	280.0	125.8	7.9	605.0	0.8	0.0	10.1	0.0	1.0	1.7	1.0	10.3	3.6	42.8	17.9	92.7	255.0	65.5	9140.0	9.3	67.1	143.4
JG46-01_Zrn-n-63	260.0	143.9	3.1	259.0	0.6	0.0	5.7	0.0	0.3	0.7	0.3	3.9	1.6	18.5	7.8	40.3	113.4	29.8	9110.0	3.7	43.3	65.8
JG46-01_Zrn-n-64	420.0	133.9	16.9	469.0	6.3	0.0	7.6	0.1	0.8	1.8	0.5	10.1	3.0	36.1	15.7	75.1	158.0	32.1	10540.0	4.4	2.1	38.5
JG46-01_Zrn-n-65	260.0	106.2	21.3	422.0	0.6	0.0	9.7	0.0	0.8	1.4	0.6	7.8	2.9	36.2	13.6	64.0	139.2	29.6	7860.0	1.4	4.1	12.6
JG46-01_Zrn-n-66	190.0	180.5	4.6	405.0	0.5	0.0	6.1	0.0	0.6	1.3	0.5	6.9	2.4	30.5	12.8	62.4	163.0	40.1	7890.0	1.7	14.5	31.6
JG46-01_Zrn-n-67	410.0	134.0	4.3	662.0	6.7	0.0	12.1	0.1	0.8	1.0	0.3	6.9	2.6	36.9	18.7	108.4	241.1	45.9	8910.0	49.8	186.6	559.0
JG46-01_Zrn-n-69	550.0	151.1	19.0	443.0	1.2	0.0	9.5	0.1	0.8	1.8	0.5	9.3	3.2	39.1	15.1	68.0	140.6	30.9	9260.0	3.2	19.3	30.4
JG46-01_Zrn-n-70	400.0	141.3	4.1	218.0	0.6	0.0	7.9	0.0	0.6	1.0	0.4	4.7	1.5	17.9	6.9	31.1	66.0	13.9	6460.0	4.1	41.2	54.8
JG46-01_Zrn-n-71	900.0	102.2	8.9	1444.0	24.6	0.0	68.7	0.1	1.8	3.7	1.3	23.9	9.4	116.1	44.7	203.2	328.0	55.8	9700.0	8.8	65.5	74.7
JG46-01_Zrn-n-73	380.0	168.1	27.5	182.0	0.7	0.0	3.7	0.0	0.2	1.2	0.3	4.3	1.4	15.6	5.7	25.5	60.6	14.0	10730.0	99.0	39.3	908.0
JG46-01_Zrn-n-75	265.0	134.8	2.0	207.0	0.3	0.0	3.4	0.0	0.1	0.3	0.1	1.8	0.9	13.0	6.1	35.1	111.7	31.0	6640.0	0.8	6.4	12.9
JG46-01_Zrn-n-76	386.0	113.9	7.9	573.0	10.1	0.0	12.4	0.0	0.3	0.8	0.2	5.9	2.6	37.2	17.2	94.5	232.0	48.0	8960.0	21.8	32.2	295.0
JG46-01_Zrn-n-78	900.0	114.9	11.3	1206.0	16.3	0.0	39.7	0.1	1.8	3.9	1.0	21.9	7.7	98.3	38.8	179.8	400.0	84.4	11210.0	9.7	50.5	66.7
JG46-01_Zrn-n-79	820.0	115.4	7.2	925.0	3.5	0.0	20.1	0.1	2.0	4.0	1.0	17.4	6.0	73.1	27.6	124.4	223.5	42.3	8010.0	3.4	5.5	48.4
JG46-01_Zrn-n-81	50.0	134.3	5.1	10.7	0.6	0.0	16.5	0.1	1.8	3.9	1.1	6.9	0.7	2.5	0.3	0.8	0.4	0.1	6680.0	26.4	32.4	270.0
JG46-01_Zrn-n-83	560.0	111.2	4.1	353.0	1.8	0.0	8.2	0.0	0.3	0.9	0.1	3.4	1.7	24.2	11.0	59.1	160.9	38.6	8610.0	34.6	80.8	293.6
JG46-01_Zrn-n-86	830.0	138.9	5.6	1216.0	21.3	0.3	24.0	0.1	1.0	1.9	0.4	13.4	5.8	82.4	37.5	196.0	509.0	114.9	11570.0	27.3	84.7	345.0
JG46-01_Zrn-n-87	330.0	149.9	49.0	175.5	1.0	0.0	4.8	0.0	0.4	0.7	0.3	3.6	1.1	14.1	5.6	25.8	60.4	14.1	8070.0	3.3	7.6	32.5
JG46-01_Zrn-n-89	640.0	156.1	7.2	760.0	2.1	0.0	10.2	0.0	0.6	1.8	0.5	12.7	4.9	63.2	25.9	124.0	275.0	61.1	9710.0	8.5	48.6	72.4
JG46-01_Zrn-n-90	60.0	114.0	17.2	135.6	0.6	0.0	8.1	0.1	0.5	0.7	0.5	3.7	1.1	12.3	4.5	19.7	47.5	11.4	7500.0	25.5	91.1	214.6
JG46-01_Zrn-n-92	280.0	142.1	22.3	150.2	0.9	0.0	5.7	0.0	0.5	0.7	0.3	3.4	1.1	13.6	4.6	20.6	47.6	10.1	7490.0	3.8	6.4	23.8
JG46-01_Zrn-n-93	1160.0	169.8	18.0	1446.0	6.9	0.0	17.4	0.1	1.6	3.7	0.5	23.2	8.6	115.5	46.4	228.9	567.0	138.9	9920.0	8.0	54.8	60.3
JG46-01_Zrn-n-94	750.0	149.7	6.5	1158.0	5.3	0.0	25.4	0.1	1.1	2.9	0.4	18.6	6.9	92.0	38.6	195.0	536.0	134.6	11580.0	10.3	79.7	96.1
JG46-01_Zrn-n-96	400.0	99.2	6.4	432.0	4.3	0.0	15.1	0.0	0.2	0.5	0.2	4.3	1.8	26.0	12.5	70.8	228.0	53.9	10370.0	34.4	96.1	295.6
JG46-01_Zrn-n-97	310.0	133.9	11.3	171.6	0.9	0.0	4.6	0.0	0.6	0.9	0.2	4.3	1.3	14.5	5.6	24.7	51.0	10.7	7370.0	2.0	4.6	18.8
JG46-01_Zrn-n-99	1890.0	175.8	9.8	2870.0	13.1	0.0	23.7	0.2	2.6	7.6	0.6	45.8	18.6	240.0	93.9	428.0	784.0	159.0	10340.0	15.7	48.9	121.2

Continúa

Continuación

JG46 Para-anfibolita (U. Esla)		Espejo-Bautista et al., 2021																				
Zircón	P	Sc	Ti	Y	Nb	La	Ce	Pr	Nd	Sm	Eu	Gd	Tb	Dy	Ho	Er	Yb	Lu	Hf	Pb	Th	U
JG46-02_Zrn-b-02	560.0	146.6	19.6	765.0	15.1	0.0	16.1	0.0	0.4	1.3	0.3	9.7	3.6	54.0	23.6	116.6	222.0	39.8	12700.0	26.8	138.0	202.0
JG46-02_Zrn-b-03	360.0	215.0	23.9	203.0	1.0	0.0	8.2	0.1	1.6	2.5	0.3	14.4	3.2	25.2	6.6	21.4	28.3	5.0	12160.0	12.6	16.7	123.8
JG46-02_Zrn-b-05	250.0	169.0	6.0	295.0	0.7	0.0	3.9	0.0	0.1	0.6	0.3	3.4	1.4	19.3	8.7	47.2	141.7	37.8	9250.0	5.1	23.4	68.6
JG46-02_Zrn-b-07	770.0	228.0	15.0	1169.0	3.1	0.0	12.4	0.1	1.4	3.2	1.1	21.0	7.9	100.9	40.5	189.0	443.0	101.2	12940.0	3.4	15.6	27.7
JG46-02_Zrn-b-10	460.0	166.8	22.3	229.0	1.1	0.0	5.5	0.0	0.4	0.9	0.2	4.4	1.7	18.9	7.6	34.0	70.4	14.8	8860.0	2.2	3.9	16.6
JG46-02_Zrn-b-12	570.0	189.2	13.7	538.0	1.3	0.0	11.5	0.1	0.7	1.5	0.5	9.2	3.8	46.4	17.7	82.3	181.8	40.4	11780.0	7.0	42.6	52.7
JG46-02_Zrn-b-13	1300.0	384.0	11.4	1408.0	4.9	0.0	16.4	0.1	2.3	6.6	0.9	43.1	13.3	141.0	48.6	196.8	354.0	83.5	12620.0	5.6	26.4	38.5
JG46-02_Zrn-b-15	500.0	196.2	15.6	55.4	0.7	0.0	5.4	0.1	0.7	1.2	0.5	3.5	0.8	6.5	1.8	6.4	8.9	1.7	8220.0	4.6	7.2	35.1
JG46-02_Zrn-b-18	1040.0	178.3	23.6	1342.0	4.7	0.0	33.8	0.1	2.7	6.1	1.7	32.6	10.2	123.3	46.1	201.6	364.0	76.1	10100.0	20.5	70.1	146.6
JG46-02_Zrn-b-20	390.0	194.8	20.2	187.0	1.0	0.0	6.5	0.1	1.2	2.4	0.8	9.3	2.2	21.8	6.1	20.6	25.6	4.5	7700.0	4.0	6.7	25.8
JG46-02_Zrn-b-22	1660.0	177.3	173.0	2350.0	7.9	0.1	23.4	0.1	2.4	6.4	0.8	38.4	14.7	193.0	78.4	363.0	703.0	144.8	10870.0	25.3	88.0	168.0
JG46-02_Zrn-b-24	1240.0	230.0	11.9	2180.0	23.5	0.0	38.3	0.1	2.0	5.8	0.9	38.5	14.4	184.0	71.2	336.0	758.0	161.2	18800.0	20.3	74.1	179.1
JG46-02_Zrn-b-25	650.0	175.0	10.0	589.0	18.5	0.0	22.8	0.0	0.5	1.3	0.3	8.0	3.2	43.1	18.6	92.3	220.0	51.5	14290.0	17.3	26.7	118.1
JG46-02_Zrn-b-28	220.0	340.0	29.1	315.0	1.7	0.0	5.2	0.0	0.3	1.0	0.5	6.1	2.2	25.0	9.3	40.1	85.6	18.7	15020.0	293.5	96.1	2060.0
JG46-02_Zrn-b-30	640.0	191.9	18.3	863.0	9.3	0.0	7.3	0.1	1.0	2.1	0.7	13.0	5.2	69.7	28.4	135.1	255.0	46.7	13990.0	9.0	3.8	59.5
JG46-02_Zrn-b-32	490.0	191.0	22.3	364.0	1.5	0.0	12.9	0.0	0.8	1.3	0.4	7.5	2.6	31.0	11.7	54.4	115.0	25.3	11300.0	9.5	53.7	56.4
JG46-02_Zrn-b-34	1020.0	174.0	12.2	1025.0	21.8	0.0	20.6	0.1	0.9	1.6	0.4	9.2	3.7	58.3	28.5	167.0	382.0	75.4	10420.0	158.5	260.0	1012.0
JG46-02_Zrn-b-36	200.0	148.2	8.0	223.0	1.1	0.0	6.1	0.0	0.1	0.5	0.1	2.3	1.0	14.3	6.7	35.3	105.5	24.1	11790.0	4.9	12.9	62.1
JG46-02_Zrn-b-38	1080.0	213.0	15.5	1260.0	6.3	0.0	19.5	0.1	1.5	3.7	0.7	22.9	8.7	112.7	42.5	188.0	332.0	66.5	12290.0	14.8	100.1	100.3
JG46-02_Zrn-b-40	530.0	159.3	5.0	731.0	2.9	0.0	13.5	0.0	0.4	1.2	0.4	9.6	4.0	54.1	23.9	117.2	291.0	69.5	10890.0	1.4	23.1	22.9
JG46-02_Zrn-b-41	440.0	160.9	14.8	441.0	1.2	0.0	6.9	0.0	0.3	0.9	0.4	6.1	2.5	32.0	13.5	71.9	179.6	41.3	9860.0	63.0	91.2	424.0
JG46-02_Zrn-b-44	313.0	144.6	11.0	38.6	0.7	0.0	4.7	0.0	0.5	0.7	0.3	2.6	0.5	4.0	1.2	4.5	9.2	2.1	7510.0	5.6	19.6	49.3
JG46-02_Zrn-b-46	340.0	140.4	15.2	81.0	0.8	0.0	4.5	0.1	0.4	0.7	0.2	2.2	0.7	7.7	2.4	9.7	17.4	3.6	7410.0	2.6	5.0	22.6
JG46-02_Zrn-b-48	1730.0	119.7	11.6	3000.0	17.4	0.0	42.5	0.1	2.7	7.5	1.1	53.5	19.6	251.0	97.4	437.0	813.0	173.7	8180.0	43.9	155.6	275.0
JG46-02_Zrn-b-50	290.0	121.8	6.0	177.1	0.5	0.0	4.7	0.0	0.2	0.5	0.1	2.4	1.0	11.5	5.3	27.0	78.7	20.1	7590.0	1.9	8.7	27.6
JG46-02_Zrn-n-01	1480.0	150.0	31.0	2770.0	40.1	1.4	33.8	0.4	2.5	5.7	0.9	36.2	13.5	198.0	85.4	408.0	747.0	143.0	9160.0	47.5	244.2	423.0
JG46-02_Zrn-n-04	710.0	167.0	23.1	1044.0	2.4	0.1	9.1	0.1	0.9	3.0	0.3	18.7	6.3	81.9	34.7	166.0	338.0	72.8	8020.0	62.5	101.1	377.6
JG46-02_Zrn-n-06	260.0	180.6	5.8	378.0	0.7	0.0	4.6	0.0	0.2	0.9	0.3	4.5	1.8	26.1	11.3	61.1	180.2	46.6	9440.0	2.4	13.4	35.9
JG46-02_Zrn-n-08	630.0	141.2	20.2	722.0	6.2	0.0	12.8	0.0	0.3	0.9	0.4	7.1	3.4	47.5	21.5	114.0	291.0	63.2	12890.0	24.4	65.0	184.1
JG46-02_Zrn-n-09	520.0	149.0	26.3	518.0	2.0	0.1	6.3	0.0	1.2	2.4	0.3	11.0	3.5	42.2	17.2	73.2	151.7	32.3	10330.0	49.8	37.6	381.0
JG46-02_Zrn-n-11	910.0	149.0	6.7	881.0	4.5	0.1	22.6	0.1	0.8	1.6	0.7	9.4	4.2	57.8	25.3	138.7	330.0	66.7	9900.0	41.3	324.0	347.0
JG46-02_Zrn-n-14	1000.0	216.0	7.1	1410.0	10.9	0.0	22.4	0.1	1.0	3.0	0.3	20.6	8.4	108.8	46.2	212.0	369.0	68.8	13100.0	35.5	353.5	272.2
JG46-02_Zrn-n-16	750.0	198.0	20.4	794.0	4.8	0.1	5.8	0.1	0.4	0.9	0.3	8.6	4.2	56.2	27.0	132.4	271.0	54.9	10490.0	70.0	105.7	566.0
JG46-02_Zrn-n-17	1290.0	160.1	14.9	1240.0	3.4	0.0	34.9	0.1	1.7	4.6	1.3	26.8	9.6	114.8	41.7	189.7	333.0	67.8	11060.0	23.3	63.9	147.5
JG46-02_Zrn-n-19	770.0	202.0	16.0	1000.0	2.8	0.0	5.1	0.1	0.5	2.7	0.5	16.1	6.4	80.3	34.2	165.0	332.0	70.2	10170.0	51.8	78.9	371.0
JG46-02_Zrn-n-23	1280.0	164.0	15.6	1820.0	39.0	0.0	38.7	0.1	1.1	2.1	0.4	13.8	6.3	93.0	47.1	300.0	855.0	174.0	14600.0	332.5	331.1	1767.0
JG46-02_Zrn-n-26	1240.0	172.5	36.0	1710.0	41.0	0.1	37.0	0.1	1.3	2.5	0.5	17.9	6.4	102.5	50.0	284.0	737.0	162.2	9700.0	83.8	235.9	495.0
JG46-02_Zrn-n-27	360.0	211.0	29.0	66.9	0.4	0.0	0.4	0.0	0.0	0.3	0.2	2.5	0.6	7.0	2.0	6.6	8.2	1.6	12480.0	36.9	1.8	157.2
JG46-02_Zrn-n-29	720.0	151.2	15.8	716.0	35.8	0.0	21.7	0.0	0.3	0.5	0.2	4.3	2.4	37.2	19.5	127.0	323.0	66.9	17600.0	92.8	48.5	595.0
JG46-02_Zrn-n-31	670.0	208.0	25.0	1300.0	8.1	4.7	36.1	2.4	12.4	4.4	1.0	17.8	6.7	89.0	40.0	193.0	391.0	76.0	13500.0	29.5	164.6	260.7
JG46-02_Zrn-n-33	1010.0	170.0	7.0	1004.0	9.3	0.3	28.6	0.2	1.7	2.5	0.7	12.9	4.8	65.5	29.2	151.0	306.0	57.6	8740.0	84.5	508.0	463.0
JG46-02_Zrn-n-35	1080.0	138.3	216.0	987.0	23.5	7.4	40.0	2.0	8.2	2.7	0.6	10.5	3.5	56.3	27.5	150.3	282.0	44.5	10720.0	93.0	216.9	598.0
JG46-02_Zrn-n-37	670.0	157.0	9.0	720.0	4.2	0.0	18.1	0.0	0.3	0.5	0.3	7.1	3.7	46.8	24.1	122.0	268.0	52.3	10400.0	28.3	104.0	173.0
JG46-02_Zrn-n-39	1220.0	175.0	10.4	1750.0	21.5	0.0	32.7	0.1	1.3	4.6	0.7	24.2	10.3	142.6	57.4	276.0	574.0	114.3	13150.0	56.8	158.8	440.0
JG46-02_Zrn-n-42	520.0	162.2	12.8	340.0	0.9	0.0	6.1	0.0	0.4	1.2	0.4	6.1	2.2	28.2	10.8	51.9	109.0	24.5	8980.0	5.4	43.5	35.9
JG46-02_Zrn-n-43	180.0	150.8	10.3	258.0	1.7	0.3	7.8	0.1	1.2	1.0	0.2	4.5	1.5	16.9	8.1	47.2	142.0	32.5	9300.0	55.0	198.0	642.0
JG46-02_Zrn-n-45	140.0	174.0	17.9	456.0	1.8	0.0	10.1	0.1	0.8	3.2	0.5	10.7	3.4	37.2	13.6	62.1	118.0	23.5	10990.0	76.0	155.0	677.0
JG46-02_Zrn-n-47	1200.0	134.7	11.7	1922.0	106.6	0.0	35.9	0.0	0.5	1.9	0.3	13.3	7.1	109.1	53.7	316.0	999.0	227.0	12170.0	87.5	123.3	739.0
JG46-02_Zrn-n-49	287.0	122.9	13.9	139.3	0.6	0.0	8.6	0.0	0.3	0.8	0.6	3.2	1.1	12.6	4.6	19.7	49.0	10.9	7820.0	31.4	99.2	244.0
Zircon_01	181.0		0.8	2680.0	21.7	0.0	37.7	0.1	2.8	8.8	1.1	57.1	20.2	247.0	92.1	398.0	714.0	145.7	13450.0	12.4	80.5	89.5
Zircon_02	135.0		1.1	1407.0	10.9	0.0	12.8	0.0	1.0	3.5	0.5	22.9	9.3	119.5	48.2	233.0	537.0	119.6	12230.0	12.6	48.7	91.4
Zircon_03	170.0		0.8	1860.0	1.9	0.0	17.3	0.1	1.8	5.1	2.6	31.4	11.4	145.4	59.3	272.0	531.0	108.6	8320.0	11.8	192.0	77.1

Continúa

Continuación

JG46 Para-anfibolita (U. Esla)		Espejo-Bautista et al., 2021																				
Zircón	P	Sc	Ti	Y	Nb	La	Ce	Pr	Nd	Sm	Eu	Gd	Tb	Dy	Ho	Er	Yb	Lu	Hf	Pb	Th	U
Zircon_04	215.0		0.8	1670.0	9.1	0.0	21.2	0.1	1.7	4.8	0.6	28.8	11.6	146.2	55.8	253.0	487.0	101.4	13140.0	8.0	39.8	67.8
Zircon_05	60.0		1.3	1027.0	9.3	0.0	18.2	0.0	0.5	2.0	0.4	12.9	5.1	73.7	33.3	161.0	312.0	63.4	11590.0	25.3	161.0	209.0
Zircon_06	223.0		1.1	1164.0	13.7	0.0	15.8	0.0	1.0	3.6	0.5	19.5	7.7	97.8	38.8	184.6	422.0	94.8	12430.0	12.7	33.9	87.6
Zircon_07	120.0		1.3	987.0	12.6	0.0	12.4	0.1	1.1	3.4	0.5	18.1	7.1	85.1	33.4	154.0	307.0	69.7	11720.0	16.8	45.5	103.1
Zircon_08	240.0		0.7	3060.0	47.0	0.0	41.6	0.1	1.8	6.3	1.4	43.2	18.4	251.0	99.5	445.0	716.0	128.3	13720.0	26.8	66.4	212.0
Zircon_09	-80.0		1.0	1066.0	14.8	0.0	15.6	0.0	0.5	1.2	0.6	8.4	3.7	59.4	30.7	181.0	360.0	68.4	13750.0	72.5	211.0	672.0
Zircon_10	90.0		1.2	1502.0	24.6	0.0	27.4	0.1	0.7	1.7	0.6	15.3	5.9	91.7	44.5	240.0	489.0	92.2	11830.0	152.8	379.0	1041.0
Zircon_11	-150.0		0.7	1080.0	8.6	0.0	18.1	0.0	0.7	2.0	0.4	14.4	5.7	86.1	35.5	179.0	424.0	99.0	12930.0	31.7	163.0	248.0
Zircon_12	-160.0		1.5	870.0	1.9	0.0	13.0	0.0	1.0	2.4	0.6	16.2	5.8	79.4	29.7	141.0	276.0	59.9	14700.0	5.3	41.5	53.6
Zircon_13	590.0		0.7	1850.0	8.5	0.0	40.7	0.1	1.4	5.0	1.2	32.1	11.9	157.3	61.6	283.0	523.0	94.6	15290.0	70.5	222.1	483.0
Zircon_14	130.0		1.2	1210.0	4.9	0.0	27.4	0.0	0.7	3.6	0.9	20.3	7.6	101.0	40.2	187.0	350.0	67.4	12350.0	26.5	117.0	170.0
Zircon_15	310.0		0.8	1763.0	12.3	0.0	18.4	0.1	1.3	4.5	0.5	29.3	12.1	154.8	60.1	273.0	500.0	101.0	12740.0	12.3	61.0	94.2
Zircon_16	1060.0		0.7	3150.0	25.7	0.0	36.9	0.1	3.0	9.6	0.7	60.2	22.4	276.0	103.9	450.0	768.0	146.4	12660.0	18.5	92.8	131.8
Zircon_17	-1000.0		0.7	2120.0	4.2	0.0	36.2	0.1	1.4	3.5	1.1	24.0	9.7	139.2	62.8	345.0	949.0	215.0	10880.0	21.7	269.0	300.0
Zircon_18	-1900.0		0.8	980.0	3.0	0.0	17.7	0.1	1.4	3.3	0.6	17.6	6.7	83.0	33.5	152.6	298.0	62.2	11770.0	6.7	4.3	47.9
Zircon_19	1400.0		2.8	1640.0	22.1	1.1	25.0	0.3	2.4	1.9	1.0	12.0	5.9	91.0	44.6	258.0	490.0	86.9	12000.0	159.0	873.0	1148.0
Zircon_20	2000.0		2.6	453.0	7.6	84.0	198.0	21.9	93.8	15.1	5.2	14.8	2.6	31.0	13.2	76.5	182.0	41.4	13590.0	94.8	99.7	558.0
Zircon_21	880.0		1.5	1310.0	23.9	0.0	16.7	0.0	0.5	3.0	0.3	18.5	7.8	111.8	43.7	200.0	368.0	81.1	12460.0	30.0	208.0	187.0
Zircon_22	800.0		0.6	538.0	1.6	0.0	9.7	0.0	0.1	0.5	0.2	4.9	2.1	34.5	15.5	90.1	272.0	63.2	14360.0	12.2	40.4	169.4
Zircon_23	630.0		1.1	958.0	9.1	0.0	19.7	0.1	0.6	1.9	0.5	11.2	5.0	69.4	31.1	154.0	374.0	80.5	12870.0	47.5	60.2	409.0
Zircon_24	-40.0		1.0	1455.0	6.5	0.0	19.3	0.1	1.9	4.0	0.9	25.8	9.6	126.5	49.6	232.0	487.0	104.9	12500.0	9.7	59.4	80.1
Zircon_25	180.0		1.2	2410.0	9.6	0.0	54.4	0.1	3.0	7.3	1.0	44.6	15.3	199.0	75.4	350.0	787.0	172.0	12160.0	15.5	42.1	109.5
Zircon_26	180.0		0.9	1860.0	13.2	0.1	22.8	0.1	1.0	2.5	0.9	20.7	7.8	113.9	52.2	272.0	519.0	100.5	12840.0	102.8	459.0	759.0
Zircon_27	170.0		0.9	1660.0	9.7	0.0	22.3	0.0	1.0	4.0	0.7	24.1	9.0	134.0	53.7	256.0	492.0	99.0	13300.0	19.1	82.3	171.0
Zircon_28	-240.0		1.5	2450.0	38.3	0.0	49.6	0.1	1.7	5.0	0.5	30.1	13.4	184.0	82.8	412.0	988.0	226.0	13910.0	21.8	61.6	206.0
Zircon_29	90.0		0.7	1074.0	8.0	0.0	15.1	0.0	1.4	2.6	0.4	19.0	7.0	87.0	35.7	163.0	319.0	69.2	12230.0	8.4	45.3	95.3
Zircon_30	-340.0		1.1	2210.0	8.5	0.2	20.8	0.2	2.7	8.2	0.6	48.4	17.6	206.0	75.6	320.0	591.0	128.4	11030.0	10.7	48.0	77.6
Zircon_31	20.0		0.7	787.0	1.8	0.0	12.9	0.0	1.0	2.6	0.9	13.9	5.1	64.3	25.7	125.4	329.0	79.3	11840.0	10.8	92.0	84.5
Zircon_32	-100.0		0.7	1570.0	22.1	0.0	40.7	0.1	1.7	3.6	1.1	23.1	9.0	123.0	48.5	237.0	511.0	102.4	11840.0	56.0	381.0	370.0
Zircon_33	140.0		0.8	947.0	5.5	0.0	21.1	0.0	1.1	2.2	0.5	13.4	5.2	74.5	30.9	150.1	293.0	56.4	12590.0	16.7	61.1	149.9
Zircon_34	70.0		1.8	2070.0	6.4	0.0	17.7	0.1	1.9	4.9	0.8	35.4	13.4	185.0	71.4	320.0	705.0	150.0	12900.0	12.8	81.2	108.6
Zircon_35	110.0		1.7	2480.0	22.1	0.0	19.9	0.0	0.8	3.1	0.8	21.7	11.0	174.0	76.4	426.0	1390.0	350.0	12000.0	46.5	19.4	350.0
Zircon_36	-70.0		5.0	1870.0	8.7	0.0	23.9	0.1	1.7	4.8	0.9	28.1	11.3	146.0	59.2	294.0	655.0	145.0	12880.0	7.9	71.3	58.5
Zircon_37	-80.0		1.1	1860.0	10.1	0.0	25.4	0.1	1.7	4.5	0.5	28.9	11.2	145.3	60.4	289.0	678.0	163.0	12580.0	13.8	70.8	84.8
Zircon_38	-340.0		1.0	1945.0	30.5	0.0	33.0	0.0	1.1	3.5	0.5	23.6	9.5	135.1	60.2	310.0	600.0	109.9	11150.0	167.3	610.0	1384.0
Zircon_39	-270.0		1.1	1073.0	7.3	0.0	15.8	0.0	0.8	2.5	0.5	17.6	6.5	86.0	34.1	162.0	307.0	63.3	11980.0	26.1	191.0	185.0
Zircon_40	-200.0		0.8	1150.0	11.5	0.0	25.1	0.0	0.4	1.6	0.4	13.0	5.2	77.5	34.8	176.3	327.0	59.0	14150.0	50.3	579.0	337.0

*Valores en ppm

JG30 Meta-granitoide milonítico		Espejo-Bautista et al., 2021																				
Zircón	P	Sc	Ti	Y	Nb	La	Ce	Pr	Nd	Sm	Eu	Gd	Tb	Dy	Ho	Er	Yb	Lu	Hf	Pb	Th	U
Zircon_1	500.0	25.4	3353.0	11.2	0.0	16.8	0.2	3.1	10.6	4.0	75.8	25.6	302.8	107.5	462.0	845.0	172.7	12470.0	160.3	1718.0	4740.0	
Zircon_10_2	540.0	62.8	135.1	0.4	0.0	7.1	0.6	7.7	7.4	0.3	14.1	2.7	19.7	4.5	13.6	16.3	2.5	12620.0	15.0	138.3	109.0	
Zircon_11_2	-40.0	69.7	137.1	0.3	0.1	7.5	0.6	8.5	7.8	0.3	14.2	2.6	19.1	4.5	14.3	16.7	2.8	12880.0	14.0	112.5	98.1	
Zircon_12_2	-920.0	53.3	238.2	0.9	0.0	4.3	0.3	5.5	7.0	0.2	11.7	2.7	25.0	7.6	31.7	69.3	15.0	12560.0	50.4	542.0	387.9	
Zircon_14_2	310.0	42.5	719.0	0.8	0.2	4.9	0.5	5.4	7.4	0.4	21.4	6.3	68.3	24.9	101.9	163.0	32.5	12180.0	27.0	295.0	202.0	
Zircon_16_2	80.0	69.0	201.9	0.3	0.0	5.7	0.8	10.9	11.6	0.3	18.1	3.6	28.9	6.6	19.6	24.0	3.4	12490.0	60.0	806.0	350.3	
Zircon_17_2	-1000.0	4.8	2680.0	2.2	0.0	4.6	0.0	1.2	2.3	1.5	30.3	14.7	199.0	85.6	402.0	857.0	186.0	11680.0	56.3	201.0	1580.0	
Zircon_18_2	910.0	61.9	772.0	2.0	0.0	3.9	0.5	7.4	10.5	0.8	23.5	6.4	70.8	24.9	126.1	390.0	89.1	12560.0	167.5	263.3	1372.0	
Zircon_19_2	-40.0	11.6	1891.0	9.0	0.0	5.1	0.0	0.8	3.6	0.8	27.2	12.0	152.3	63.5	296.4	579.0	120.3	14710.0	108.3	685.0	2710.0	
Zircon_2_2	-170.0	440.0	315.1	2.3	0.0	4.0	0.5	6.9	9.2	0.3	22.1	4.5	39.6	10.2	37.7	56.1	10.7	12590.0	32.1	206.9	240.6	
Zircon_20_2	600.0	57.2	407.0	1.3	0.0	2.4	0.2	3.5	6.3	0.7	18.9	4.8	43.0	13.2	60.1	181.0	43.7	11870.0	84.8	137.7	730.0	
Zircon_22_2	190.0	28.9	1750.0	3.9	0.1	3.8	0.1	1.1	2.8	0.9	26.6	10.7	138.0	55.0	242.0	516.0	112.0	13510.0	54.0	350.0	1560.0	
Zircon_23_2	1000.0	18.9	5570.0	4.5	0.0	51.4	0.2	6.4	20.7	11.8	148.3	48.2	531.0	185.8	729.0	1157.0	219.1	9290.0	42.3	607.0	1167.0	
Zircon_24_2	0.0	16.1	4550.0	3.7	0.0	42.5	0.1	3.3	13.4	8.6	109.7	39.7	434.0	153.9	623.0	933.0	177.0	9140.0	39.0	510.0	1014.0	
Zircon_25_2	1100.0	18.1	8230.0	7.5	0.1	67.4	0.5	8.7	28.9	17.5	212.7	70.8	768.0	266.0	1080.0	1670.0	319.0	8520.0	55.5	975.0	1620.0	
Zircon_26_2	590.0	48.6	333.0	1.2	0.0	3.8	0.2	2.8	4.3	0.6	11.1	3.0	31.1	10.5	47.6	119.0	27.6	12150.0	20.8	87.4	179.0	
Zircon_27_2	1400.0	37.0	3550.0	12.6	4.0	17.9	1.3	10.6	11.6	1.8	76.0	27.2	315.0	110.8	466.0	809.0	159.8	18020.0	143.3	2180.0	4250.0	
Zircon_28_2	600.0	57.6	234.6	0.9	0.0	6.4	0.4	7.0	8.0	0.3	16.5	3.6	28.3	7.8	28.3	48.0	10.4	12440.0	28.3	530.2	239.6	
Zircon_29_2	1700.0	66.6	220.0	0.3	0.0	7.0	0.6	8.1	9.0	0.4	21.4	3.8	30.1	7.2	23.2	30.5	5.5	12310.0	34.8	701.0	246.8	
Zircon_3_2	-1000.0	27.1	1343.0	1.0	0.0	1.5	0.0	0.4	0.8	0.5	16.4	6.8	97.4	45.0	224.0	532.0	124.1	10570.0	18.7	84.9	522.9	
Zircon_30_2	900.0	25.0	1860.0	4.2	0.4	6.0	0.1	1.2	5.3	1.5	44.0	15.1	174.0	62.0	265.0	494.0	104.0	14030.0	73.0	880.0	2340.0	
Zircon_31_2	-590.0	58.9	199.8	0.7	0.0	4.2	0.4	7.0	7.4	0.2	11.6	2.5	24.0	6.5	24.3	41.5	7.9	12050.0	53.6	647.0	394.8	
Zircon_32_2	150.0	42.9	289.0	0.5	0.0	8.4	0.1	2.0	4.0	0.7	15.1	3.4	30.2	9.8	40.8	74.0	14.3	11140.0	21.5	43.6	162.0	
Zircon_33_2	-520.0	42.0	866.0	1.5	0.0	6.3	0.4	6.1	7.6	0.7	22.0	6.6	79.9	29.4	127.7	249.7	51.6	12360.0	31.8	335.6	584.0	
Zircon_34_2	100.0	33.1	1373.0	6.1	0.0	4.7	0.2	2.7	6.4	0.9	36.5	11.6	132.1	43.8	183.5	331.0	66.4	16230.0	108.0	1175.0	3220.0	
Zircon_35	1040.0	48.3	398.0	1.4	0.1	4.4	0.5	7.2	10.7	0.4	20.9	4.9	44.4	13.6	49.9	97.8	18.2	12150.0	19.3	414.0	219.9	
Zircon_4_2	350.0	72.9	214.5	0.3	0.1	7.0	0.9	12.8	13.3	0.5	21.5	4.8	31.0	7.4	22.1	24.0	4.2	12620.0	45.6	739.0	320.1	
Zircon_5_1	300.0	74.7	1282.0	0.9	0.0	3.5	0.4	7.1	8.5	0.2	29.7	10.0	117.4	41.2	173.6	330.0	64.8	11960.0	58.1	212.0	459.0	
Zircon_6_1	1300.0	25.4	1689.0	5.7	0.0	6.8	0.2	4.3	5.9	0.7	29.4	11.7	151.2	59.0	247.8	454.0	90.1	13130.0	62.4	460.0	1511.0	
Zircon_7_1	2100.0	16.7	2142.0	3.6	0.1	5.8	0.1	1.7	5.7	1.8	40.4	14.7	182.7	67.8	299.0	568.0	121.2	11140.0	40.5	273.0	1171.0	
Zircon_8_1	900.0	59.4	527.0	0.9	0.0	6.4	0.3	5.6	7.5	0.4	16.5	4.3	45.2	17.1	84.3	257.0	63.9	12450.0	67.0	221.0	458.0	
Zircon_9_1	900.0	65.5	178.9	0.4	0.0	6.3	0.6	10.4	10.7	0.3	18.1	3.7	26.4	5.6	18.7	21.5	3.7	13580.0	57.1	815.0	358.2	

*Valores en ppm

SM21-04b													
Zircón	La	Ce	Pr	Nd	Sm	Eu	Gd	Tb	Dy	Ho	Er	Yb	Lu
M2_SM21_04b_Zrn01	0.0196	6.8329	0.1543	1.0230	3.1498	0.2064	24.3359	11.6356	170.2723	71.0788	372.2647	751.6880	152.7776
M2_SM21_04b_Zrn02	0.2116	6.8342	0.5011	3.1398	1.1863	0.1422	8.8854	5.8999	89.7840	41.6079	214.7985	473.5661	103.2589
M2_SM21_04b_Zrn03	0.0296	7.4092	0.1361	1.8749	3.9978	0.1808	25.2351	8.4252	104.2146	39.1154	180.9984	315.6602	63.1630
M2_SM21_04b_Zrn04	0.0000	11.6249	0.1041	0.3756	1.2984	0.0826	14.3128	5.6711	89.8849	37.2740	194.0956	408.5878	84.6712
M2_SM21_04b_Zrn05	0.7641	8.3723	0.5093	4.3614	7.1891	0.6408	32.7553	10.5839	123.6434	43.1340	192.9162	318.5786	61.3629
M3_SM21_04b_Zrn07	0.0000	5.5412	0.0920	0.4217	2.2645	0.1201	15.3684	7.0209	105.6104	45.4596	239.2875	493.3909	100.9953
M3_SM21_04b_Zrn08	1.7091	20.1730	0.5036	3.1809	4.9825	0.4217	33.9903	13.1905	176.0769	68.4761	348.7913	677.7750	135.4808
M3_SM21_04b_Zrn09	0.0000	8.5425	0.0878	0.8113	2.5873	0.3706	19.6693	8.5019	124.9798	52.1892	272.2882	561.7143	117.3309
M3_SM21_04b_Zrn10	0.0086	8.4814	0.2452	2.3939	6.4860	0.8923	44.8578	16.3636	232.3809	91.7651	439.3939	829.1061	168.1505
M3_SM21_04b_Zrn11	0.0016	18.1528	0.1067	0.8461	2.4914	0.1868	16.7797	6.2396	82.7482	31.9256	157.6409	295.2965	59.1962
M3_SM21_04b_Zrn12	8.4049	49.6996	2.0062	10.6053	8.8758	1.5381	41.9193	14.3546	174.9853	66.2538	306.7770	550.4522	106.3166
M3_SM21_04b_Zrn14	0.1618	7.9997	0.3931	4.4655	7.7094	0.4192	36.1760	11.0214	127.9296	45.1856	204.7009	338.9326	65.3397
M3_SM21_04b_Zrn15	1.2753	8.1375	1.1352	7.3215	4.0948	1.2103	9.6153	3.1289	39.9240	18.1927	106.6506	335.4615	76.5771
M3_SM21_04b_Zrn16	2.6687	28.1549	1.9615	9.8645	5.8275	0.3014	22.0788	7.3949	91.4253	35.2567	168.7864	314.0609	63.8031
M3_SM21_04b_Zrn17	1.5525	26.8319	1.2519	7.3915	6.3039	1.6265	20.9887	7.3649	102.2220	41.8592	219.3652	515.9074	103.8290
M3_SM21_04b_Zrn18	0.0037	4.4713	0.1003	0.3891	1.7182	0.1013	17.9284	8.3118	132.4080	57.7169	304.5920	650.3722	135.7266
M3_SM21_04b_Zrn19	0.0409	11.6742	0.0920	0.7890	2.0209	0.2363	16.6152	6.6793	101.7458	43.2744	228.7527	501.4148	100.9999
M3_SM21_04b_Zrn20	0.0000	8.4127	0.0980	0.9420	2.9037	0.1839	23.9761	11.2648	162.8035	68.7324	360.2844	743.9671	154.0641
M3_SM21_04b_Zrn21	10.0758	38.6776	6.5141	38.3064	25.3907	4.8625	50.7655	13.1903	166.4014	65.0304	340.8913	955.5272	202.5566
M3_SM21_04b_Zrn22	0.0781	7.1681	0.3957	5.4019	9.1224	1.4633	49.0816	15.2988	180.8394	65.1062	296.2352	502.6792	96.6338
M3_SM21_04b_Zrn23	0.0043	6.9247	0.1236	0.7840	2.4767	0.1701	15.8982	6.6258	95.8443	39.1712	199.3135	395.5861	80.6132
M3_SM21_04b_Zrn24	0.0740	75.6388	0.4815	6.3468	9.1873	1.9695	34.2982	8.6579	87.2197	28.0319	121.8729	221.5014	46.9617
M3_SM21_04b_Zrn25	3.4511	44.6725	2.7456	17.9401	8.2193	0.5562	29.4813	8.8490	112.1782	42.6799	202.5060	379.1873	78.3049
M3_SM21_04b_Zrn26	0.0000	3.6910	0.0958	0.2778	1.3355	0.0601	10.1676	5.2942	89.0448	38.2388	218.0258	585.9851	122.7313
M3_SM21_04b_Zrn27	0.2922	19.1746	0.2090	1.0855	1.8860	0.2717	13.6640	5.9308	83.0107	34.3709	180.3852	365.0485	76.1828
M3_SM21_04b_Zrn28	0.0057	4.8716	0.1623	1.4005	4.3875	0.3311	33.0120	12.4837	166.2766	66.7442	314.5307	580.0608	119.2659
M3_SM21_04b_Zrn29	15.4273	54.6804	6.2469	26.4404	8.8245	0.6345	32.4189	13.1175	187.7992	76.3648	403.7269	788.3781	157.0271
M3_SM21_04b_Zrn30	0.1379	10.3293	0.4434	2.1408	5.4086	0.4499	37.7502	16.1349	225.4974	90.4231	457.8749	880.7926	176.1267
M3_SM21_04b_Zrn31	0.0000	1.9664	0.3379	0.2896	1.0889	0.5868	6.1210	1.3424	8.7988	1.5383	3.6626	2.7478	0.4822
M3_SM21_04b_Zrn32	0.7753	19.7017	1.1343	7.7124	5.4615	0.3123	23.7378	8.6223	117.4997	45.8544	228.0851	433.1737	89.2694
M3_SM21_04b_Zrn33	28.9864	119.2808	19.5001	113.8041	41.1744	1.2609	80.4235	19.4918	205.2648	67.9039	300.5871	486.9097	93.4061
M3_SM21_04b_Zrn34	0.0109	6.4322	0.3042	0.7188	2.8374	0.3220	18.4809	7.8709	118.0933	49.1209	263.5042	525.0054	109.2416
M3_SM21_04b_Zrn35	0.0458	8.6329	0.4074	3.0885	5.9764	0.8203	29.9550	10.1237	120.0404	43.9718	205.1942	345.6005	69.5783
M3_SM21_04b_Zrn36	0.3254	23.8273	0.4916	2.1674	3.7151	0.4068	18.8210	7.5773	99.1388	41.1893	205.4339	413.4825	89.0126
M3_SM21_04b_Zrn37	0.1252	5.7317	0.3592	0.6000	1.1247	0.1502	4.9365	2.0645	25.8268	8.9287	42.3706	72.4903	14.0273
M3_SM21_04b_Zrn38	0.0166	7.1464	0.2852	1.7087	3.8189	0.2124	21.7596	7.8084	93.2522	33.6421	157.9412	261.4251	51.2545
M3_SM21_04b_Zrn39	0.0000	4.5971	0.2525	0.4502	2.5783	0.1436	21.8790	10.4271	161.9638	68.2140	377.9867	797.7963	162.6654
M4_SM21_04b_Zrn40	5.8099	57.9439	2.6935	15.5055	14.5471	3.0204	56.8624	18.6554	215.0440	78.1232	381.2889	706.4491	140.5854
M4_SM21_04b_Zrn41	0.0238	7.2814	0.3511	2.9260	6.2855	0.4979	41.5729	16.3294	224.4118	85.0673	433.2159	775.2021	156.5580
M4_SM21_04b_Zrn42	0.0189	15.8094	0.2983	1.5241	4.4490	0.6366	24.2619	9.2709	118.7325	47.1778	231.5640	433.7553	89.2761
M4_SM21_04b_Zrn43	0.0433	4.7752	0.2352	0.4845	1.8711	0.1241	15.2829	7.5066	118.3700	50.1303	279.0276	594.4553	122.5325
M4_SM21_04b_Zrn44	0.0120	6.0933	0.2384	0.5643	1.7973	0.1072	12.5267	5.0186	73.3956	30.6160	163.7202	334.0470	69.2869
M4_SM21_04b_Zrn45	0.2303	18.2130	0.4049	1.9218	2.2002	0.2445	13.2207	5.0607	68.2828	30.0337	163.3097	388.7521	87.7889
M4_SM21_04b_Zrn46	0.0952	22.5773	0.6216	8.4332	14.9811	2.1306	65.0768	20.8354	236.2148	81.2830	361.8466	569.6349	108.6242
M4_SM21_04b_Zrn48	0.1745	54.3821	0.5662	7.1172	11.6352	0.9258	62.0261	21.0591	256.7667	87.1489	427.2900	709.7202	136.0275
M4_SM21_04b_Zrn49	0.0381	7.4496	0.3936	4.8293	8.3853	1.4307	48.4081	14.7295	170.6927	59.1285	260.5434	412.5323	80.7478
M4_SM21_04b_Zrn50	0.7578	31.7196	1.4348	10.4279	14.3573	0.8998	69.1523	23.7270	292.6042	108.1904	504.6233	851.0339	164.1642
M4_SM21_04b_Zrn51	0.0278	11.9011	0.2365	1.2406	3.1090	0.2682	16.9695	6.1786	78.7595	29.9235	148.0121	277.7277	56.0047
M4_SM21_04b_Zrn52	0.0647	13.8207	0.3832	4.6180	7.4994	0.8714	44.8126	14.8674	189.2704	66.4401	308.7618	514.4262	98.9936

Continúa

**Continuación
SM21-04b**

Zircón	La	Ce	Pr	Nd	Sm	Eu	Gd	Tb	Dy	Ho	Er	Yb	Lu
M4_SM21_04b_Zrn53	0.7408	14.0072	0.6400	4.6794	5.5877	0.6845	29.9965	11.5331	154.2088	62.4144	329.6133	663.7456	135.7151
M4_SM21_04b_Zrn54	0.0050	12.4215	0.1978	1.2175	3.6145	0.1963	27.2736	11.9973	165.8441	67.5237	342.8876	635.6829	126.7909
M4_SM21_04b_Zrn55	0.0153	5.5183	0.2301	1.4794	4.9924	0.0948	35.4142	11.3210	135.0473	42.8700	183.1202	260.7969	49.7650
M4_SM21_04b_Zrn56	0.1904	6.6841	0.5806	4.5355	8.0125	0.3185	48.9567	24.0496	372.4587	155.4238	829.4321	1720.4693	337.6381
M4_SM21_04b_Zrn57	0.0537	61.7088	0.8616	11.0278	20.9614	1.2291	109.3915	38.8136	473.2316	168.9738	777.8344	1248.2388	237.1837
M4_SM21_04b_Zrn58	3.4214	21.8817	3.1484	18.3897	14.2698	3.5690	38.1690	14.2370	193.4511	78.6622	425.6320	959.5687	201.7320
M4_SM21_04b_Zrn59	0.1964	56.4728	0.7059	8.8474	16.3200	1.0264	90.6574	29.7870	342.5571	118.9996	530.9156	787.9192	148.7789
M4_SM21_04b_Zrn60	0.1348	19.9534	0.3376	2.4903	5.5090	0.3271	32.0264	11.6908	136.6459	51.3458	242.2480	418.4823	80.7786
M4_SM21_04b_Zrn61	1.4958	25.2037	0.8140	3.6827	4.3577	0.3984	27.0346	10.0805	127.9688	50.2369	248.6038	456.8350	91.0038
M4_SM21_04b_Zrn62	0.0576	32.3979	0.4827	6.3863	11.0191	1.5064	64.4245	21.7049	269.6578	95.4238	454.8598	720.5860	141.2964
M4_SM21_04b_Zrn63	0.0089	10.3052	0.2057	1.2462	4.0500	0.3181	33.1390	14.9496	216.7931	90.6845	472.6707	908.8570	181.5576
M4_SM21_04b_Zrn64	0.0307	10.9205	0.4160	4.3523	7.3306	1.3784	33.3299	10.5752	119.7941	42.2438	189.2642	314.4822	63.5660
M4_SM21_04b_Zrn65	2.4837	26.7197	1.5610	11.3227	12.6605	0.6901	59.9998	21.7519	264.2331	98.9283	458.7008	766.0727	144.3100
M4_SM21_04b_Zrn66	0.0125	11.8598	0.1997	1.1152	2.6191	0.4448	15.1923	4.7335	54.5705	22.6373	110.1379	262.1046	61.8974
M4_SM21_04b_Zrn67	0.0000	5.0872	0.1871	0.6679	2.9567	0.1289	16.4315	4.9800	63.3687	23.7944	115.4724	209.7460	42.6411
M4_SM21_04b_Zrn68	0.0044	10.2571	0.2732	2.5595	6.7105	0.2604	39.9956	14.0938	181.7688	66.0904	313.8289	524.2976	103.2818
M4_SM21_04b_Zrn69	14.8094	66.1733	7.9864	44.6272	22.9933	2.1486	73.9582	21.2979	243.6856	83.2564	365.4785	568.6229	108.0073
M4_SM21_04b_Zrn70	6.1160	37.6851	4.9773	26.6851	15.9860	3.9903	30.1058	8.4255	94.9876	34.3576	175.8599	393.3482	79.4003
M4_SM21_04b_Zrn71	0.2186	9.1072	0.2445	1.3384	4.0659	0.2130	26.9293	11.3808	166.7450	67.8827	351.0459	681.4159	133.8011
M4_SM21_04b_Zrn72	0.2360	3.9062	0.7802	5.8231	5.5238	0.3412	26.6693	8.8636	114.7472	43.5921	208.3614	382.4654	77.2923
M4_SM21_04b_Zrn73	0.0111	23.5059	0.2834	2.3487	5.3090	0.5702	34.8828	13.7566	184.5891	71.9573	356.0875	663.0121	129.1351
M4_SM21_04b_Zrn74	0.0218	7.7061	0.2328	1.6508	4.6845	0.6545	28.2839	11.0868	144.2369	56.5129	279.3997	531.0401	107.2173
M4_SM21_04b_Zrn75	0.0944	11.8184	0.3037	3.0187	6.5776	0.6610	39.7168	15.0597	198.7184	79.1656	395.0532	759.8198	153.1127
M4_SM21_04b_Zrn76	10.2212	68.1431	10.2362	66.5694	52.8682	17.0777	147.2284	40.6235	447.8998	144.7812	674.7119	1458.5509	285.9335
M4_SM21_04b_Zrn77	80.8037	130.9895	15.6493	65.2528	14.0134	1.8922	28.3609	7.5434	83.3944	29.1617	133.3019	239.1924	47.1311
M4_SM21_04b_Zrn78	0.0780	6.0644	0.2579	1.8997	5.4799	0.7746	37.2301	15.7826	222.8379	89.2629	459.4607	897.7621	181.2151
M4_SM21_04b_Zrn79	0.0621	13.3321	0.1416	0.8599	2.5714	0.1505	19.9929	8.5431	127.4286	54.3230	282.1060	587.2162	119.7853
M4_SM21_04b_Zrn80	0.2468	8.8486	0.4271	4.6524	10.0430	0.9855	61.6929	25.4271	341.7041	134.2650	683.0984	1305.3372	255.9801
M4_SM21_04b_Zrn81	0.0000	9.2165	0.1747	1.1715	2.1576	0.3463	14.2254	5.5879	83.8953	37.3551	216.6145	581.4794	132.0960
M4_SM21_04b_Zrn82	0.0714	13.7333	0.2074	1.1083	3.8457	0.3469	24.9646	11.8067	159.1999	63.9182	322.5052	622.1857	123.6657
M4_SM21_04b_Zrn83	0.0000	5.1187	0.1512	0.6835	2.4848	0.2026	20.6371	10.3199	160.4797	69.0141	370.7610	784.9671	159.2382
M4_SM21_04b_Zrn84	0.2544	2.8334	0.3144	1.8629	2.5196	0.7719	13.1153	4.7864	66.7333	27.0671	146.7079	380.2637	78.3702
M4_SM21_04b_Zrn85	0.0420	1.7611	0.4030	5.4709	10.2431	0.3654	58.8458	19.2743	232.3547	83.7118	378.0494	621.4454	122.1571
M4_SM21_04b_Zrn86	1.5823	11.8514	1.4054	7.5829	7.7731	1.9610	30.1237	13.5088	203.8973	85.2798	449.9360	1035.9047	208.4280
M4_SM21_04b_Zrn87	0.3250	11.4989	0.3303	4.8974	8.0279	1.0190	46.6354	16.5499	222.1049	84.7300	417.3465	792.4370	157.9842
M4_SM21_04b_Zrn88	0.3394	61.8918	0.7164	10.4510	17.6344	1.2822	84.4917	27.3442	333.2364	121.0117	571.3391	978.2979	188.4682
M4_SM21_04b_Zrn89	0.0894	15.1334	0.3179	2.4378	5.2680	0.6590	33.6028	11.9140	154.7536	52.4074	261.5313	448.8631	84.0299
M4_SM21_04b_Zrn90	0.0814	8.5277	0.1815	1.4910	3.2940	0.5015	19.0619	6.4907	80.8253	31.8640	155.8596	334.0442	71.7495
M4_SM21_04b_Zrn91	0.2023	12.3611	0.2832	1.1218	1.4278	0.1999	12.2025	5.5223	73.1632	32.6962	176.0149	370.8329	75.2641
M4_SM21_04b_Zrn92	0.8185	6.0341	0.5306	3.5184	7.2491	0.3095	53.3821	24.4912	354.0115	140.8856	709.7642	1293.4983	247.1217
M4_SM21_04b_Zrn93	0.0688	26.9555	0.2071	0.8976	2.2252	0.4090	10.3916	3.8830	52.4968	21.2288	109.4631	251.8100	55.9088
M4_SM21_04b_Zrn94	0.1776	29.5375	0.5005	4.5787	7.5113	0.4589	41.8138	15.1920	195.5405	72.6959	350.0355	623.2237	120.5432
M4_SM21_04b_Zrn95	0.2580	25.4698	0.4116	3.9605	7.9969	0.7042	50.6426	18.8314	257.4931	101.0600	511.2530	967.3705	190.0912
M4_SM21_04b_Zrn96	2139.2937	3694.0944	396.2796	1376.7572	171.5525	3.8055	147.7329	23.2887	216.7798	75.8643	371.3609	762.9106	156.0563

*Valores en ppm

SM21-06

Zircón	La	Ce	Pr	Nd	Sm	Eu	Gd	Tb	Dy	Ho	Er	Yb	Lu
M2_SM21_06_Zrn01	0.0000	3.2990	0.1144	0.8303	2.5155	0.2266	18.5716	7.6119	103.2545	41.0225	209.2372	392.1015	78.7986
M2_SM21_06_Zrn02	0.0294	5.6330	0.1313	1.1121	3.6761	0.4291	28.3994	15.3933	248.0122	105.5794	566.4968	1184.2165	237.9764
M2_SM21_06_Zrn04	0.3503	8.8500	0.3855	2.1663	2.7356	0.1590	14.3584	4.8634	59.8787	23.4634	113.3185	197.7968	39.0197
M2_SM21_06_Zrn05	0.0314	15.0602	0.1362	1.1054	2.1794	0.1070	11.3516	3.8230	47.5743	18.0336	86.5565	153.5798	31.6228
M2_SM21_06_Zrn06	0.0000	0.5117	0.1433	1.0167	4.0533	0.0696	34.6146	14.4051	165.0791	52.2321	208.4473	266.4384	45.6463
M2_SM21_06_Zrn07	0.0473	4.5863	0.2690	3.5349	8.0072	0.1311	18.6419	4.2777	33.7957	7.9655	25.7326	28.1488	4.1926
M2_SM21_06_Zrn08	0.8111	8.9267	0.4426	3.3024	4.1280	0.4021	22.3720	7.0901	82.0227	30.0301	141.3087	233.8238	47.4376
M4_SM21_06_Zrn09_1	0.1385	59.0026	1.3370	12.1559	18.6596	5.3056	54.0696	16.4543	170.7068	54.2748	251.1086	480.7799	92.5666
M4_SM21_06_Zrn10	0.8116	131.1711	0.9357	7.9156	12.2118	4.9174	34.0301	8.5223	93.8254	30.9872	156.0614	468.3575	102.1894
M4_SM21_06_Zrn11	0.9886	13.5724	0.8353	5.7057	2.7574	0.5363	6.8796	1.5547	19.1429	7.3453	38.5097	94.6346	22.2003
M4_SM21_06_Zrn13	0.0000	0.9852	0.1439	1.3566	4.5298	0.1189	22.3473	5.0171	40.9675	7.8752	24.4956	33.1592	7.0769
M4_SM21_06_Zrn14	0.0418	2.6781	0.2208	2.1412	4.9611	0.1659	32.4914	12.2564	161.8755	63.9134	301.2093	540.9118	106.0691
M4_SM21_06_Zrn15	0.0000	8.2414	0.1907	2.0456	4.7127	0.3216	26.3112	9.2920	116.2390	42.8098	204.4021	340.0024	65.4248
M4_SM21_06_Zrn16	0.0000	6.9846	0.0857	0.5341	2.1879	0.2923	15.6234	6.0151	86.1609	36.0387	189.9938	399.9350	82.7296
M4_SM21_06_Zrn17	0.7832	12.6900	0.8780	4.0324	4.7151	1.1180	18.4876	7.8128	113.6861	47.9727	261.9024	621.1721	135.8016
M4_SM21_06_Zrn18	0.0000	41.2242	0.1205	1.0363	4.5958	1.3095	34.7545	12.4420	159.9578	63.6270	311.5652	551.8612	110.5017
M4_SM21_06_Zrn19	0.2645	4.2330	0.2643	0.8610	1.0476	0.2496	1.7518	0.5903	8.5733	3.9862	28.5633	106.0118	30.6214
M4_SM21_06_Zrn20	0.0144	1.5189	0.1150	0.1124	0.0711	0.1084	1.9434	0.6520	10.2140	4.4922	26.0144	66.8529	16.2491
M4_SM21_06_Zrn21	0.0696	2.6234	0.1531	0.6293	0.1606	0.0679	1.0013	0.3931	5.5826	2.7348	19.3388	72.1733	21.8835
M4_SM21_06_Zrn22	0.0199	5.1733	0.0885	0.2022	0.3495	0.1463	3.6884	1.2060	18.2180	8.5705	51.4082	167.3813	36.9572
M4_SM21_06_Zrn23	0.0000	27.8989	0.2015	1.9829	3.2570	0.9942	10.7206	2.7252	28.7548	9.5948	43.1525	75.9293	15.1658
M4_SM21_06_Zrn24	0.0000	4.6957	0.1531	1.7405	4.7885	0.2791	31.0534	11.4178	150.0029	57.7363	283.1720	503.6191	99.5253
M4_SM21_06_Zrn25	0.0071	21.4588	0.1247	1.0068	2.4072	0.2651	12.4947	4.5365	60.9308	22.8266	113.5582	226.2052	46.6254
M4_SM21_06_Zrn26	0.0000	0.9889	0.1153	0.7672	3.0236	0.1232	20.6325	7.2806	74.8579	21.2634	79.0547	100.0005	18.4459
M4_SM21_06_Zrn27	0.0039	24.3696	0.1564	1.3027	3.8392	0.8638	18.2574	5.3416	54.7220	17.8489	78.2386	122.9784	22.2300
M4_SM21_06_Zrn28	0.0000	6.8926	0.1090	0.6607	2.2379	0.2966	18.0100	7.1942	94.7700	33.1695	151.4669	280.8840	56.2116
M4_SM21_06_Zrn29	0.0000	5.1256	0.1058	0.6846	3.6880	0.2642	28.6500	8.2852	70.6462	18.3093	58.8397	74.9267	14.0139
M4_SM21_06_Zrn30	0.0063	25.3751	0.1507	1.2142	2.9684	0.6494	15.5416	5.6346	78.0940	32.8246	174.8927	388.3958	85.3236
M4_SM21_06_Zrn31	0.1216	21.9491	0.2295	2.8467	5.7404	0.5622	29.1124	10.5575	130.5699	49.0896	239.5713	441.0122	87.7398
M4_SM21_06_Zrn32	0.0209	4.1452	0.1409	0.2636	5.6328	0.4318	36.0585	13.3986	169.0354	60.4343	271.9930	445.6085	84.3892
M4_SM21_06_Zrn33	0.1255	17.9999	0.1956	1.2203	2.8529	0.2373	13.8051	4.4382	52.4927	18.8879	82.7099	139.8877	26.4451
M4_SM21_06_Zrn34	0.0000	6.5918	0.0802	0.3903	2.3586	0.3688	18.2625	8.3496	115.7376	40.4654	173.1352	276.2972	52.0443
M4_SM21_06_Zrn35	0.0000	3.4480	0.1208	1.4941	4.1900	0.0486	29.5239	11.4348	152.9440	56.6108	272.9614	510.2920	91.0032
M4_SM21_06_Zrn36	0.1344	5.6984	0.2986	3.0541	6.8137	0.1160	38.3399	14.2444	176.2853	65.0816	301.5142	494.6840	92.9368
M4_SM21_06_Zrn37	0.0100	7.1541	0.1774	1.7782	5.0854	0.5497	34.3956	13.6408	186.6374	73.8439	361.5101	654.2405	128.6124
M4_SM21_06_Zrn38	0.0000	5.8722	0.0501	0.0699	0.1706	0.1036	0.7007	0.3790	5.6614	2.8989	20.1731	71.8509	19.6747
M4_SM21_06_Zrn39	0.0399	4.9639	0.3560	5.2344	11.9585	0.2497	71.5432	25.3561	335.1563	132.9609	637.4117	1009.1543	187.7116
M4_SM21_06_Zrn40	68.2826	207.1378	25.3042	111.4090	23.0174	1.3959	30.2516	6.1705	60.9044	21.1366	101.0176	183.7947	37.2441
M4_SM21_06_Zrn41	0.0535	18.0454	0.1755	2.3985	4.6248	0.1714	26.0816	9.2825	118.4115	46.0179	215.1086	387.1203	75.6773
SM21_06_Zrn42	5.7786	61.4062	1.4096	6.7579	4.6617	0.4199	17.9112	5.9026	71.5217	26.8923	131.3780	250.5062	48.9671
SM21_06_Zrn43	0.0169	32.4211	0.1123	1.7347	2.9952	0.6418	14.0444	3.7112	44.7931	15.9588	80.1019	159.6826	33.3085
SM21_06_Zrn44	0.0000	22.4392	0.0465	0.8406	1.6997	0.3820	9.1133	2.8817	36.9771	14.3916	75.0237	167.7277	35.8607
SM21_06_Zrn45	22.4249	69.8540	9.1526	56.3444	19.3758	0.9915	46.5883	14.0119	159.5008	58.2564	268.8141	461.2377	88.9868
SM21_06_Zrn46	0.0000	4.2248	0.0734	1.5033	3.3507	0.2814	17.0462	5.9980	68.3457	26.8699	120.9698	209.8075	40.6230
SM21_06_Zrn47	0.0000	4.4859	0.0116	0.6600	1.0192	0.2321	5.3581	1.3814	12.0098	3.3792	12.6804	16.7061	2.8318
SM21_06_Zrn48	0.0071	1.9388	0.1346	3.0250	9.5384	0.3969	55.9777	16.8537	163.0819	43.3353	149.9889	176.7534	29.6782
SM21_06_Zrn49	0.0331	7.0762	0.0536	0.8039	2.7299	0.3323	17.7939	7.2569	97.0801	34.2788	158.4916	328.2157	66.2471
SM21_06_Zrn50	0.0000	31.1000	0.1093	2.4708	5.6577	1.5870	28.2394	8.0003	84.7011	27.9411	117.5863	182.0983	34.0938
SM21_06_Zrn51	0.0281	14.6609	0.2740	5.4559	9.0355	1.0253	41.1409	12.8578	151.0956	54.2957	248.4506	433.7281	84.8983
SM21_06_Zrn52	0.0189	17.7709	0.1007	1.3405	2.3035	0.3151	12.5677	4.1507	54.8339	21.1147	103.8309	206.2985	41.1405

Continúa

Continuación

SM21-046

Zircón	La	Ce	Pr	Nd	Sm	Eu	Gd	Tb	Dy	Ho	Er	Yb	Lu
SM21_06_Zrn53	0.0000	29.7928	0.0911	1.9626	4.5468	0.8344	19.8542	6.0355	78.4932	30.8707	152.1199	315.1429	68.1243
SM21_06_Zrn54_I	0.2921	13.0819	0.3386	3.2388	4.7361	0.3413	26.6727	9.1929	124.2912	49.5095	259.6518	554.9376	117.2285
SM21_06_Zrn55	0.0000	63.8657	0.0590	1.7398	4.6714	1.3314	34.4759	12.2161	159.3175	61.3954	298.4476	523.5831	102.1191
SM21_06_Zrn56	0.0219	1.1768	0.0132	0.2051	0.3243	0.1400	2.0913	0.7029	9.7042	4.3160	24.2496	60.0853	14.2911
SM21_06_Zrn57	0.0321	33.0857	0.3985	6.2186	7.9082	2.4820	24.8920	5.8220	56.7596	16.9237	71.1606	114.6816	21.9102
SM21_06_Zrn58	0.0233	3.6248	0.0546	1.5129	5.1769	0.2276	37.1967	14.9148	203.6448	80.8275	393.2709	708.8947	135.4913
SM21_06_Zrn59	0.5201	21.0262	0.6091	4.0746	3.9557	0.3922	18.6913	6.8650	84.5856	32.7128	160.5121	296.9093	58.4764
SM21_06_Zrn60	0.3928	55.5473	0.3671	3.3984	4.5816	0.5486	25.7334	9.8053	121.4388	43.4894	196.4926	326.7771	61.3029
SM21_06_Zrn62	0.0104	9.1231	0.0596	0.8197	3.1994	0.3159	21.0200	7.5594	101.8928	38.2013	182.0841	334.2389	66.3389
SM21_06_Zrn63	0.0071	1.7578	0.0609	1.3521	4.8699	0.0247	33.7331	14.0107	181.7354	66.3359	310.3623	536.1811	96.6882
SM21_06_Zrn64	0.0000	2.1983	0.0746	1.1066	2.9230	0.0319	16.1635	6.2663	78.8467	29.9549	146.9776	264.6650	53.4218
SM21_06_Zrn65	0.2292	7.7180	0.2113	2.8377	6.3181	0.7024	38.3301	14.3452	186.5046	70.9605	332.1216	570.6999	108.5486
SM21_06_Zrn66	0.1070	33.4613	0.4306	3.2877	4.0483	1.8643	17.0218	5.7155	72.8620	29.6006	175.7115	474.9083	117.1547
SM21_06_Zrn67	0.0208	7.1073	0.3818	6.4172	14.5190	0.3126	72.6188	24.5497	311.5450	122.4289	601.5547	999.5725	181.0458
SM21_06_Zrn68	10.3412	65.8643	9.5627	56.3017	18.3219	0.5942	35.9723	9.7045	106.6711	38.6822	188.0658	348.1957	68.0381

*Valores en ppm

SJ15

Zircón	La	Ce	Pr	Nd	Sm	Eu	Gd	Tb	Dy	Ho	Er	Yb	Lu
M1_SJ15_Zrn01	0.1919	19.4329	0.3427	2.4581	3.7505	0.8343	19.9562	5.7845	69.2118	22.7916	105.1064	186.2401	37.4974
M1_SJ15_Zrn02	0.4026	10.8646	0.2769	0.7427	0.8763	0.2819	3.9555	1.6016	20.0042	8.6848	48.7431	128.4245	32.9612
M1_SJ15_Zrn03	0.0000	0.0850	0.1242	0.0000	0.1365	0.0209	1.2552	1.0744	19.1780	8.3309	40.9351	64.3271	12.7321
M2_SJ15_Zrn04	0.0021	10.5202	0.1898	1.0934	2.4992	0.5196	13.9394	5.0840	63.9258	25.3976	128.2357	255.1829	55.1907
M2_SJ15_Zrn05	0.1213	0.7178	0.1732	0.3254	0.3189	0.0785	2.2991	1.0643	18.4814	10.2842	83.8211	412.0926	108.4692
M2_SJ15_Zrn06	0.0000	3.6607	0.2046	1.0121	2.0982	0.3547	15.0776	5.5096	74.8382	29.1571	143.1553	257.1056	52.3727
M2_SJ15_Zrn07	1.4645	5.2657	1.1345	5.2227	3.5809	0.7786	7.3826	3.1145	49.6601	22.9102	154.9518	577.2662	132.7840
M2_SJ15_Zrn08	0.0000	7.3686	0.2056	1.2792	4.2052	0.5503	27.0312	9.4614	115.0725	42.1481	198.8666	330.5270	64.9429
M2_SJ15_Zrn09	0.0189	0.1658	0.1045	0.1878	0.3089	0.0870	1.9442	0.9637	18.0034	8.7328	55.4864	195.0975	46.8802
M2_SJ15_Zrn10	0.0140	14.8645	0.1945	1.1089	3.6514	0.0915	19.3489	6.8382	80.0790	27.1000	120.3378	181.3794	33.1555
M2_SJ15_Zrn11	0.0102	0.0617	0.1298	0.0000	0.2742	0.0172	2.3901	1.4468	23.7388	8.1257	34.9748	46.6703	8.3083
M2_SJ15_Zrn12	0.0126	0.2473	0.1754	0.0264	0.4682	0.0826	4.1433	2.3935	48.7686	23.2652	126.8026	314.7936	70.9570
M2_SJ15_Zrn13	0.0305	6.3993	0.2073	1.4924	3.7791	0.3874	15.3609	5.2896	67.6645	26.4411	133.2925	293.6355	69.3537
M2_SJ15_Zrn14	0.0076	6.0628	0.1231	0.5469	1.7337	0.1619	9.8928	3.4965	42.8736	15.9673	74.9975	125.4332	25.6133
M2_SJ15_Zrn15	0.0104	0.1734	0.1247	0.0883	0.3861	0.0510	3.9865	2.5541	40.4630	15.6229	69.8745	101.2297	18.3844
M2_SJ15_Zrn16	0.0000	0.9759	0.2450	1.5717	7.7408	0.1107	60.6646	25.3937	362.6239	140.2815	688.2245	1174.6489	223.5286
M2_SJ15_Zrn17	0.0000	0.1408	0.1305	0.0315	0.8422	0.0911	8.7862	5.1888	78.5580	29.9114	135.8820	190.7699	37.8298
M2_SJ15_Zrn18	0.2061	0.8720	0.2292	0.7617	0.8373	0.0998	7.0028	4.4400	76.4721	28.2173	128.8232	235.4481	48.9270
M2_SJ15_Zrn19	0.0097	9.5647	0.1961	0.9745	2.8610	0.1339	22.8189	9.7709	137.2275	56.8647	294.2128	565.1190	117.8403
M2_SJ15_Zrn20	0.0000	0.2144	0.0948	0.0782	0.5982	0.0865	7.5718	4.8772	86.6724	36.4214	188.8594	311.7030	63.5825
M2_SJ15_Zrn21	0.0252	8.3847	0.1522	0.5597	1.6250	0.1174	9.8685	3.5431	48.2247	18.9545	94.8369	169.0136	33.1996
M2_SJ15_Zrn22	0.0000	0.1545	0.1170	0.0379	0.3423	0.0478	3.6758	2.7385	49.1175	22.2708	116.5546	213.9537	44.9988
M2_SJ15_Zrn23	0.0046	3.3232	0.2564	2.5238	4.5494	1.1512	23.1988	7.3933	84.6765	28.9641	128.0971	201.9350	39.1109
M2_SJ15_Zrn24	0.0000	0.0700	0.1284	0.0073	-0.0067	0.0344	0.5245	0.4637	7.8464	2.5828	10.1686	13.1783	2.2744
M2_SJ15_Zrn25	0.0000	7.6629	0.1232	0.4311	1.7404	0.2318	12.0952	4.9918	69.0960	29.1281	149.6657	294.7135	62.0545
M2_SJ15_Zrn26	0.0320	10.0473	0.3758	4.5623	7.4024	2.0470	43.9751	13.8108	172.1438	66.7493	333.0257	597.9569	122.1908
M2_SJ15_Zrn27	0.0705	8.9426	0.2123	0.9577	2.1442	0.4190	10.9514	3.9022	46.0159	17.3963	81.0047	147.8306	29.7087
M2_SJ15_Zrn29	0.0020	7.7633	0.1899	1.0476	2.2561	0.3310	14.0194	5.1161	71.0032	27.2647	136.2112	266.4145	55.3072
M2_SJ15_Zrn30	0.0255	4.3739	0.2836	2.8239	5.2248	1.0674	23.2707	6.6175	77.9958	24.8483	111.8401	180.5337	34.4095
M2_SJ15_Zrn31	0.2949	0.4736	0.3438	0.9993	0.6750	0.2035	3.9276	2.5264	45.2847	21.0672	120.4403	310.4165	72.2740
M3_SJ15_Zrn32	0.0163	12.3362	0.1271	0.5211	1.4856	0.1605	12.7095	5.5013	79.6225	35.9247	201.2482	454.8850	102.4137
M3_SJ15_Zrn33	0.0000	1.9400	0.1234	0.2136	0.4874	0.1596	4.5205	1.9599	32.4764	15.7004	100.8339	289.0406	64.6800
M3_SJ15_Zrn34	0.0138	14.7864	0.2565	2.8062	7.0785	1.4120	48.9327	17.8449	237.8771	92.6269	458.0868	860.8146	179.6407
M3_SJ15_Zrn35	0.0590	8.1380	0.5082	5.4038	9.3803	1.4405	35.6269	8.7573	89.9128	27.7694	111.9530	161.1886	31.5891
M3_SJ15_Zrn36	0.0157	0.1037	0.1326	0.0557	0.0759	0.0280	0.9699	0.5612	9.3844	3.9163	23.6790	83.0931	21.3423
M3_SJ15_Zrn37	0.0246	11.4485	0.2649	2.4887	5.9487	1.0256	30.6376	11.6085	156.1434	64.9841	341.7991	704.4821	150.0346
M3_SJ15_Zrn38	0.0000	6.0175	0.1005	0.6116	1.6220	0.0919	8.6730	3.2070	40.2792	15.5826	77.7917	146.9625	29.7234
M3_SJ15_Zrn39	0.0200	2.2239	0.2820	3.3228	8.1390	0.1477	48.5227	18.5359	230.0757	89.1890	423.9012	736.9744	147.2894
M3_SJ15_Zrn40	0.2532	9.3978	0.4680	4.4080	8.1129	0.9619	37.7964	12.4185	142.8998	50.6758	233.9032	377.3639	76.9343
M3_SJ15_Zrn42	2.3428	3.4374	1.2955	7.1253	3.5371	0.9745	6.5046	2.5314	33.6654	13.8018	77.0312	184.8246	41.0359
M3_SJ15_Zrn43	2.0698	5.1440	1.3540	6.5317	3.3213	0.8091	6.9083	2.7976	40.7427	18.4851	129.7268	555.8152	137.9914
M3_SJ15_Zrn44	0.0000	13.5497	0.1682	1.3621	2.8752	0.8697	16.2904	6.1070	79.4779	32.3278	173.4371	384.9144	88.3427
M3_SJ15_Zrn45	0.0667	16.0179	0.2491	1.4825	2.8908	0.9276	15.0625	5.1960	67.8537	27.4132	148.8885	356.3412	84.3376
M3_SJ15_Zrn46	0.0507	5.9577	0.5316	7.1294	10.7573	1.9206	50.2782	14.8629	166.0251	55.9822	245.3339	378.1181	72.3861
M3_SJ15_Zrn47	0.0475	0.4447	0.1310	0.2159	0.7302	0.1546	9.3982	5.8445	105.0812	45.3856	235.7154	429.9311	86.6538
M3_SJ15_Zrn48	0.0122	7.3591	0.1173	0.6134	1.9592	0.3893	15.7224	6.8091	99.9887	43.5548	249.3143	581.4431	131.8822
M3_SJ15_Zrn49_1	0.0582	5.9192	0.0980	0.8399	0.2782	0.2249	20.3134	1.2884	40.4021	12.3953	101.2604	330.4723	73.0477
M3_SJ15_Zrn49_3	0.3517	1.5175	0.2123	1.3505	0.9754	0.2663	5.6436	3.5297	69.3206	36.6202	265.7598	1029.0743	232.4360
M3_SJ15_Zrn50	0.0394	19.4387	0.1476	0.7974	1.9487	0.8256	12.9877	4.5573	58.6876	23.5125	123.1024	264.0371	57.1041
M3_SJ15_Zrn51	0.0131	0.2340	0.1224	0.0611	0.2696	0.0224	3.5583	2.2841	39.0686	16.9514	89.3370	172.8134	36.9912

Continúa

Continuación

SJ15

Zircón	La	Ce	Pr	Nd	Sm	Eu	Gd	Tb	Dy	Ho	Er	Yb	Lu
M3_SJ15_Zrn52	0.0077	1.8723	0.1425	0.1692	0.1925	0.1403	1.8103	1.2190	22.7714	12.4531	94.6046	436.3060	102.0351
M3_SJ15_Zrn53	0.0056	28.1792	0.2286	2.1601	3.8024	0.9416	22.4244	7.4853	90.0592	34.7436	171.1554	320.8403	67.8983
M3_SJ15_Zrn54	0.0359	0.2604	0.1321	0.1549	0.3277	0.0748	3.2895	2.5513	44.9609	20.2472	112.2602	256.1411	57.5251
M3_SJ15_Zrn55	0.0000	10.1962	0.1010	0.7113	1.6495	0.1498	17.2112	7.7533	114.4487	52.9438	304.0626	689.8394	157.7270
M3_SJ15_Zrn56	0.2030	0.3991	0.1757	0.2844	0.4218	0.1734	2.0037	0.8777	9.5480	3.5765	20.8149	87.1969	23.0449
SJ15_Zrn57	1.7669	16.9583	0.9131	5.2974	3.5408	0.7403	13.1429	4.4865	59.3432	22.7077	124.2296	344.8651	76.6491
SJ15_Zrn58_a	0.4629	17.6549	0.5025	2.4158	3.3494	0.5012	13.8878	4.6220	63.7248	23.8930	121.3783	252.0705	52.4268
SJ15_Zrn58_b	3.5178	21.7166	2.1934	11.6716	6.1163	1.3787	17.0018	5.4330	67.9297	28.1995	166.0892	552.6281	118.4726
SJ15_Zrn59_a	0.0142	5.3818	0.0278	0.7355	1.3455	0.2327	8.9812	3.4310	41.4430	16.5408	80.8825	167.1976	34.5687
SJ15_Zrn59_b	0.1641	6.6599	0.0565	1.3242	0.9336	0.1544	7.9371	4.0180	81.0503	31.6806	165.8780	357.5060	70.9268
SJ15_Zrn60	0.0000	3.3074	0.0143	0.3161	0.2688	0.0957	3.9945	2.1419	35.8806	17.7964	136.0914	709.1240	178.2328
SJ15_Zrn61	0.0804	0.3853	0.0139	0.2449	0.6353	0.1196	6.5474	3.9420	67.6296	28.5679	141.1032	286.4680	57.4799
SJ15_Zrn62	0.0026	4.4117	0.0247	0.4449	1.3279	0.0606	8.4787	3.5357	48.0247	19.5203	97.7015	191.6650	40.5415
SJ15_Zrn63	0.4788	1.5081	0.1551	0.4866	0.1938	0.1592	4.9905	2.7071	46.9014	18.8750	112.1374	364.0410	77.2611
SJ15_Zrn64_a	0.0000	17.7729	-0.0022	0.2444	1.1714	0.2865	4.1708	1.7523	22.4265	8.7850	48.6799	116.9678	27.8940
SJ15_Zrn64_b	0.0289	3.7618	0.0272	0.1829	0.5401	0.1834	3.1426	1.4519	20.9687	10.6104	76.1352	288.5064	64.7449
SJ15_Zrn65	0.0132	20.6120	0.1312	2.1400	3.4801	1.3008	17.7587	5.9836	65.2017	23.9610	111.2100	196.0114	39.7421
SJ15_Zrn66	0.0019	0.1197	0.0020	0.0617	0.3416	0.0370	2.8030	1.9028	37.5862	18.1548	109.5824	285.0742	64.3932
SJ15_Zrn67	0.0285	0.5610	0.0190	0.0840	0.1969	0.0448	2.0506	1.4890	29.4776	14.6472	87.6629	224.4376	55.9166
SJ15_Zrn68	0.0265	17.1116	0.1905	3.7287	6.1717	2.0735	33.0295	10.4306	120.2569	43.1852	199.0367	356.5014	73.5223
SJ15_Zrn70	0.0196	2.9790	0.0103	0.2092	0.8181	0.2171	5.4888	3.0364	50.4476	23.5547	144.5366	519.5651	124.4256
SJ15_Zrn71	3.0194	9.3898	1.5263	7.8428	4.0595	1.0151	7.3266	2.7167	38.0059	16.2487	103.3717	380.6849	86.5489
SJ15_Zrn72	0.0140	0.0742	0.0119	0.0643	0.1059	0.0198	0.9563	0.5522	9.5316	5.3549	40.9484	202.4307	51.1934
SJ15_Zrn73	0.0051	1.7546	0.1049	2.1094	4.5914	0.3122	25.9210	9.0324	116.8014	45.7241	224.9258	404.4360	83.7221
SJ15_Zrn74	0.0000	0.8719	0.0045	0.0558	0.0621	0.0481	1.0277	0.6917	13.0952	7.3945	48.4293	163.1949	37.8817
SJ15_Zrn75	0.0217	3.4682	0.0662	0.5906	1.3527	0.1606	9.8221	3.9937	59.6977	29.1687	193.8355	731.2700	171.4533
SJ15_Zrn76	11.4132	74.6011	2.3017	8.1165	3.8130	0.6423	12.7804	3.8717	44.0695	16.3351	81.6019	182.3453	39.9690
SJ15_Zrn77	0.0338	0.6547	0.0211	0.2874	0.9395	0.2100	11.3611	7.5366	125.8179	51.4423	245.5152	386.5927	71.9024
SJ15_Zrn78	0.0632	3.8837	0.0446	0.8618	1.6056	0.2080	10.1525	3.6737	46.5425	17.7450	86.4203	162.7314	32.2640
SJ15_Zrn79	0.4314	6.0073	0.3732	2.3029	2.4910	0.3823	11.2701	3.8226	50.7193	19.3823	94.1804	191.5095	39.0475

*Valores en ppm

SM21-04													
Zircón	La	Ce	Pr	Nd	Sm	Eu	Gd	Tb	Dy	Ho	Er	Yb	Lu
M3_SM21_04_Zrn01	0.0557	14.5748	0.1559	0.9306	1.2407	0.6266	6.9959	2.3477	26.3118	10.7174	55.1679	130.8462	31.0999
M3_SM21_04_Zrn02	0.0000	25.7536	0.1471	1.2058	2.7440	1.1495	15.5852	4.5763	51.3805	18.8149	90.5102	179.4329	39.0922
M3_SM21_04_Zrn03	0.0022	8.6189	0.1820	1.4333	3.6334	2.5124	20.5829	6.9392	83.3755	30.8646	148.4328	278.5930	62.2034
M3_SM21_04_Zrn04	0.0000	19.4785	0.0899	0.4761	1.3953	0.7525	11.5491	4.2865	59.6361	26.7652	155.6550	419.3799	107.0332
M3_SM21_04_Zrn05	0.0524	8.4213	0.2044	1.7772	2.7389	1.0987	12.3610	3.7044	46.6920	17.4043	91.1902	197.2944	45.6785
M3_SM21_04_Zrn06	0.0411	15.4713	0.1021	0.4351	1.3267	0.5226	6.4535	2.1490	24.5793	9.5331	49.4217	109.3677	25.6715
M3_SM21_04_Zrn07	0.0041	6.6325	0.1431	0.8880	1.5942	0.8168	8.2813	2.6729	33.7187	13.0807	71.4017	166.8080	41.8824
M4_SM21_04_Zrn08	0.0275	8.0536	0.1836	1.9044	5.9230	1.1302	36.3894	12.4196	175.3480	70.0853	326.6245	602.7076	126.4132
M4_SM21_04_Zrn09	0.1626	38.0093	0.3281	1.6555	3.7615	2.3028	24.9073	7.9354	101.2152	37.3221	179.7833	378.6522	85.2604
M4_SM21_04_Zrn10	0.0018	17.8280	0.2743	2.6397	4.4659	1.8298	19.7090	5.9646	72.1387	27.8355	140.3274	298.8714	68.2792
M4_SM21_04_Zrn11	0.0437	15.9261	0.2722	3.6187	11.6322	2.2989	97.0410	35.4235	468.9834	177.1757	809.1606	1335.8827	259.6347
M4_SM21_04_Zrn12	5.5776	24.7876	2.8048	19.2275	9.0694	1.0770	34.9174	11.8203	154.5840	62.4351	303.1525	532.0563	110.4288
M4_SM21_04_Zrn13	0.0149	19.9929	0.2469	1.6201	3.7548	1.2827	14.9950	4.5425	51.2983	18.9729	98.4901	222.1883	51.7381
M4_SM21_04_Zrn14	7.1350	24.7653	2.1368	7.9392	2.4386	0.7404	6.5243	1.9326	22.8523	8.7742	45.4019	102.9402	24.1743
M4_SM21_04_Zrn15	0.0023	8.2040	0.1967	2.7446	7.8425	0.7815	56.2748	20.1226	270.9951	107.9068	508.8022	850.3721	170.5928
M4_SM21_04_Zrn16	0.0000	10.5709	0.2071	2.5218	4.7985	1.4454	21.2177	6.8930	84.0744	33.0773	173.0393	397.7858	95.8956
M4_SM21_04_Zrn17	0.0000	15.5658	0.0906	0.3770	1.2741	0.4573	7.1885	2.1027	27.8338	10.0646	53.8874	125.4700	29.7829
M4_SM21_04_Zrn18	0.0000	28.8956	0.1852	1.6047	3.2391	1.5287	19.9988	7.1887	91.1266	37.1487	194.0759	418.0956	96.6611
M4_SM21_04_Zrn19	0.1379	14.4318	0.2173	1.6444	4.6576	0.4880	33.7005	13.2968	186.5689	78.7968	408.3224	795.4390	171.7197
M4_SM21_04_Zrn20	0.0047	19.6999	0.0990	0.3767	2.0030	0.4168	14.9035	5.6474	73.5991	29.6868	149.2218	294.6677	61.0046
M4_SM21_04_Zrn21	0.0058	22.4948	0.2059	1.8710	4.3632	1.3776	27.4284	9.3206	121.5781	45.7205	221.0748	395.7228	82.4657
M4_SM21_04_Zrn22	0.0076	5.8158	0.2138	1.8286	2.9633	1.2322	9.7896	2.9212	32.5151	12.2178	61.9247	138.2904	32.6199
M4_SM21_04_Zrn23	0.0052	3.1007	0.1794	2.2049	5.1123	0.1438	31.9342	10.9917	134.5747	48.1075	224.2111	373.3964	73.5885
M4_SM21_04_Zrn24	0.0077	13.1450	0.1176	0.5558	1.6349	0.5997	7.2045	2.3604	29.2781	12.0913	66.0153	161.2594	39.3513
M4_SM21_04_Zrn25	0.0062	33.8461	0.1536	1.0859	3.0578	1.1897	15.6014	5.1257	58.2822	22.8842	118.3767	264.6017	62.6861
M4_SM21_04_Zrn26	13.4568	49.2317	4.6080	24.2614	15.7221	3.8986	66.6600	21.4894	256.6639	98.1091	494.3500	999.2860	218.9600
M4_SM21_04_Zrn27	0.0000	8.5367	0.0973	0.3616	0.6878	0.3556	2.6558	0.8433	13.2888	5.4932	33.4273	84.9620	20.0424
M4_SM21_04_Zrn28	0.0000	11.2887	0.1103	0.7190	1.6684	0.7143	7.4671	2.6625	32.4843	13.0479	67.4383	154.6509	36.5654
M4_SM21_04_Zrn29	0.0078	11.7554	0.1888	2.5050	8.5347	1.2145	58.2343	21.1216	286.4666	109.6739	531.2804	850.8917	169.1649
M4_SM21_04_Zrn30	0.0018	0.9058	0.0622	0.0000	0.1374	0.0682	0.9740	0.5322	9.7172	5.7904	42.2723	158.4291	41.7061
M4_SM21_04_Zrn31	0.0434	10.6784	0.3724	3.8603	6.2304	1.2781	31.4484	9.2113	110.0531	38.0467	173.2590	289.3631	61.0412
M4_SM21_04_Zrn32	0.0000	17.4960	0.1248	0.7634	2.8598	1.2126	25.5436	10.6415	147.9483	64.5495	358.4952	824.2707	197.0195
M4_SM21_04_Zrn33	0.0000	16.4726	0.0795	0.5199	1.3469	0.6196	7.1961	2.0811	26.6691	10.7634	55.0314	129.1720	31.8850
M4_SM21_04_Zrn34	0.0168	30.1346	0.1546	1.4183	3.9834	1.0619	24.5868	7.6837	89.2975	31.6143	146.3325	264.3569	52.2946
M4_SM21_04_Zrn35	8.9793	37.6900	3.8608	19.2994	10.7016	0.7124	42.9545	15.1815	204.7146	82.1805	429.9100	862.7232	189.8727
M4_SM21_04_Zrn36	0.0335	22.8552	0.1464	1.2219	3.2477	1.4233	18.4748	6.1542	68.2413	23.9433	112.2502	210.3147	42.9413
M4_SM21_04_Zrn37	0.0063	8.8470	0.2089	1.7439	2.2111	0.9622	8.4226	2.4024	27.6130	11.1550	58.8126	142.9076	34.9819
M4_SM21_04_Zrn38	0.0312	13.9288	0.1208	1.2962	2.6288	0.9687	12.1736	3.8807	46.7340	18.1746	92.6775	232.9918	61.0807

*Valores en ppm

SM21-05

Zircón	La	Ce	Pr	Nd	Sm	Eu	Gd	Tb	Dy	Ho	Er	Yb	Lu
M2_SM21_05_Zrn01	0.0139	3.8205	0.2541	2.9649	6.1207	1.4373	25.3379	7.7023	84.4211	28.4384	130.7838	222.9287	44.2769
M2_SM21_05_Zrn02	0.0129	6.6199	0.1811	2.2933	5.5957	1.4025	30.0571	9.2666	110.3541	40.0534	186.7447	317.6188	63.9276
M2_SM21_05_Zrn03	0.0022	4.3153	0.1754	1.4238	3.0549	0.9212	17.9678	6.1674	76.9555	29.6839	142.6847	248.3306	50.9354
M2_SM21_05_Zrn04	0.0133	8.5218	0.3067	4.0065	8.3291	2.0880	37.6622	11.5736	132.4052	46.9800	215.1345	382.2860	77.2821
M2_SM21_05_Zrn05	0.0161	3.0075	0.2805	2.3701	4.1186	1.1824	17.8995	5.8983	62.6816	20.6382	91.0108	150.7532	30.6261
M2_SM21_05_Zrn06	0.0039	1.5144	0.1105	0.2660	0.5600	0.1425	2.8437	0.8580	8.1502	2.6873	11.2491	20.4845	4.2916
M2_SM21_05_Zrn07	0.0332	8.4860	0.2958	4.9825	10.1563	2.8263	51.3941	15.6449	176.0026	58.0469	260.1586	456.1204	91.9427
M2_SM21_05_Zrn08	0.0000	3.1804	0.1272	0.7454	1.8264	0.8335	12.4174	4.5005	50.3278	17.8641	83.7979	145.2674	30.2560
M2_SM21_05_Zrn09	0.0029	1.4071	0.0645	0.2146	0.5840	0.2171	3.0819	0.8472	8.2723	2.4543	8.7775	13.0940	2.2756
M2_SM21_05_Zrn10	0.0263	6.9835	0.4476	5.7845	10.8357	2.9553	49.0853	13.8753	153.6535	49.9913	220.1489	342.2739	69.4101
M2_SM21_05_Zrn11	0.0000	2.2046	0.1291	0.9259	1.2532	0.3838	6.8899	2.1333	27.3927	10.1796	49.0302	107.8637	23.7381
M2_SM21_05_Zrn12	0.0045	8.1369	0.2241	3.1475	6.5740	1.8158	43.1580	14.8644	173.5799	62.3268	274.8219	436.2942	85.5200
M2_SM21_05_Zrn13	0.0000	0.7429	0.1051	0.0706	0.3306	0.1469	2.6175	0.8979	11.4342	5.0201	27.7659	63.9955	15.3195
M2_SM21_05_Zrn14	0.0226	5.3300	0.1916	1.7366	4.0606	1.2463	20.8315	7.2430	89.3066	32.3893	154.2128	287.7002	61.4734
M2_SM21_05_Zrn15	0.0044	3.2753	0.1441	1.5252	2.9528	0.8394	15.9141	5.0945	63.3152	24.5203	119.5632	222.7553	47.8754
M2_SM21_05_Zrn16	0.0000	0.8398	0.0702	0.0987	0.4933	0.1697	2.6166	0.8991	10.8937	4.0878	19.1543	40.4029	9.1573
M2_SM21_05_Zrn17	0.0000	3.3953	0.1231	1.2187	2.8548	0.8645	15.6816	4.8620	60.2128	22.7820	110.2867	198.6006	41.4197
M2_SM21_05_Zrn18	0.0000	4.7628	0.1962	2.0835	6.3340	1.4037	29.8635	9.2224	99.3775	34.3355	159.3120	260.0973	53.3373
M2_SM21_05_Zrn19	0.0628	6.3724	0.4603	6.4266	10.7610	2.9948	50.1591	13.5329	146.4285	48.3219	206.2275	326.0933	66.5152
M2_SM21_05_Zrn20	0.0522	13.1370	0.5420	8.2684	17.4212	4.5451	89.4618	25.2197	263.7261	83.3929	338.7848	472.6680	89.2932
M2_SM21_05_Zrn21	0.0000	0.5145	0.0857	0.0644	0.2440	0.1417	1.7381	0.5624	8.1273	2.9567	13.2947	27.3712	5.8856
M2_SM21_05_Zrn22	0.0028	0.4139	0.1109	0.0482	0.2841	0.0929	1.3441	0.5182	6.3193	2.6780	15.5498	44.5801	11.7807
M2_SM21_05_Zrn23	0.0110	7.1486	0.1847	2.6613	5.7896	1.4520	34.5468	11.5026	135.7504	47.6239	215.5360	356.8563	70.1920
M2_SM21_05_Zrn24	0.0000	0.3230	0.0754	0.0702	0.1237	0.0500	0.7076	0.2428	2.9617	1.2010	5.1741	9.4707	1.8265
M2_SM21_05_Zrn25	0.0726	4.6647	0.2997	3.6974	7.7453	1.9776	32.1496	9.7097	109.9139	38.5719	169.4377	285.8858	57.7575
M2_SM21_05_Zrn26	0.0000	0.9193	0.0711	0.2309	0.4444	0.1722	2.3223	0.8420	8.9444	3.0231	13.9446	26.1653	5.1037
M2_SM21_05_Zrn27	0.0000	0.4702	0.0803	0.0000	0.0823	0.0363	1.2010	0.3027	4.0493	1.6132	8.9410	20.6686	4.2249
M2_SM21_05_Zrn28	0.0110	8.3534	0.2103	2.9368	7.5985	2.2060	42.8956	13.8962	168.6741	64.3669	314.3142	624.4123	136.5297
M2_SM21_05_Zrn29	0.0000	0.4671	0.0775	0.0000	0.1215	0.0946	1.5053	0.5813	7.0566	3.0563	16.4376	41.3524	10.5761
M2_SM21_05_Zrn30	0.0217	11.6927	0.7149	10.4381	19.4485	5.2044	71.8984	18.8929	199.1609	61.9437	267.8426	424.0940	84.2087
M2_SM21_05_Zrn31	0.0038	5.4661	0.2222	2.2516	4.8976	1.3542	28.3347	9.5721	119.9328	45.3957	214.1277	364.0081	74.8456
M2_SM21_05_Zrn32	0.0000	0.3711	0.0822	0.0000	0.1191	0.0545	0.8367	0.3664	4.8620	2.0856	11.0783	26.6452	6.1262
M2_SM21_05_Zrn33	2.4596	5.7799	0.5696	2.4096	2.7300	0.8957	13.9804	4.4786	52.9895	19.2583	89.1064	161.4964	32.9568
M2_SM21_05_Zrn34	0.0000	1.4021	0.0806	0.0971	0.4068	0.1410	1.7647	0.5639	4.7931	1.4431	5.5487	7.7970	1.6093
M2_SM21_05_Zrn35	0.0000	1.4543	0.0515	0.1793	0.6789	0.2032	3.2921	0.9975	9.6004	2.8225	10.2347	16.5274	3.2573
M2_SM21_05_Zrn36	0.0064	4.6164	0.3509	3.2848	6.5620	1.7112	33.6352	9.9365	111.1041	38.1483	167.3249	278.0231	56.6868
M2_SM21_05_Zrn37	0.1872	23.9888	1.3953	17.7795	29.4862	7.0096	111.1273	31.6646	332.9700	116.0613	521.0369	863.1595	170.3661
M2_SM21_05_Zrn38	0.0034	1.3678	0.1290	0.1431	0.4759	0.1641	2.6509	0.6995	7.1069	2.4026	9.4440	16.3820	3.6171

*Valores en ppm

SM21-21													
Zircón	La	Ce	Pr	Nd	Sm	Eu	Gd	Tb	Dy	Ho	Er	Yb	Lu
M2_SM21_21_Zrn01	0.0236	24.5316	0.1472	1.7864	4.2458	2.6415	31.7627	10.2839	123.7844	48.1611	246.1433	516.9391	118.2981
M2_SM21_21_Zrn02	0.0000	18.4194	0.0823	0.6872	1.7436	1.0811	10.7543	3.6311	49.4013	20.0199	109.2123	262.6040	63.0438
M2_SM21_21_Zrn03	0.0000	22.6999	0.1696	2.1414	5.5568	3.3184	37.3654	11.4399	145.2310	56.1767	286.2729	613.2663	141.0045
M2_SM21_21_Zrn04	0.0000	24.6458	0.1520	1.2773	2.9355	1.6590	19.4658	7.1574	90.6871	37.6041	200.1038	459.7740	109.1484
M2_SM21_21_Zrn05	0.0000	10.8617	0.0956	0.9247	1.2484	0.8673	9.4258	3.2777	46.5923	19.8466	113.2371	278.9887	69.6557
M2_SM21_21_Zrn06	0.0050	24.7987	0.0814	0.5330	1.5980	0.9777	12.9668	4.5527	60.6925	23.4987	127.4752	301.5523	72.2216
M2_SM21_21_Zrn07	0.0031	9.3068	0.0856	0.8544	1.7115	0.8216	9.7252	3.0055	42.6122	18.0011	101.6473	255.9979	65.3241
M2_SM21_21_Zrn08	0.0035	23.4703	0.0725	0.5316	1.7729	0.8752	12.6774	4.3565	56.2376	23.4504	125.8215	300.8840	72.6533
M2_SM21_21_Zrn09	0.0000	22.2197	0.1334	1.2718	2.7798	1.6027	20.1265	6.8348	89.7204	36.4459	190.7214	431.4823	99.3961
M2_SM21_21_Zrn10	0.0264	17.6207	0.0809	0.5123	1.7973	0.6288	7.8768	2.6286	33.6060	13.9166	79.5815	197.8069	48.2120
M3_SM21_21_Zrn11	0.0171	21.5532	0.3124	5.1759	9.5524	3.6942	48.8114	16.1317	205.8088	78.7154	395.9505	800.8619	174.7667
M3_SM21_21_Zrn12	0.0024	16.7472	0.1320	1.2562	3.0564	1.8419	21.3757	7.3737	89.5145	35.8719	184.3256	408.5677	95.0625
M3_SM21_21_Zrn13	0.0029	19.7099	0.1205	0.7059	2.0486	1.1888	14.7889	5.4558	70.7417	28.7632	155.7936	364.0313	88.1570
M3_SM21_21_Zrn14	0.0000	18.7364	0.0686	0.3510	1.5112	0.8080	10.1670	3.4753	42.4360	17.2014	92.2746	219.3593	52.4552
M3_SM21_21_Zrn15	0.0000	18.9624	0.1622	1.3441	3.2162	1.9964	23.4350	7.8873	96.8208	38.6428	199.0819	439.3069	103.4797
M3_SM21_21_Zrn16	0.0000	25.7365	0.1133	0.7306	2.3084	1.1382	15.3554	5.9686	82.6430	36.6843	203.6554	508.5324	123.2111
M3_SM21_21_Zrn17	0.0000	22.1103	0.0907	0.7224	1.7669	1.1317	12.9975	5.1905	74.2058	31.6111	182.5455	464.0856	114.3223
M3_SM21_21_Zrn18	0.0059	28.4269	0.0678	0.8449	2.6582	1.2775	18.2621	6.7882	94.6860	40.8412	220.9455	537.6879	125.8592
M3_SM21_21_Zrn19	0.0000	19.0776	0.0768	0.4106	1.4589	0.7903	9.1613	3.2234	43.7567	18.1446	96.0628	238.2719	57.9657
M3_SM21_21_Zrn20	0.0000	28.6505	0.1363	0.6570	2.5394	1.4574	20.0761	7.1336	100.7424	42.6840	236.6857	554.9103	132.5872
M3_SM21_21_Zrn21	0.0338	17.9645	0.2734	2.8124	4.5836	2.7641	27.2279	8.5210	106.1767	39.7756	199.4603	445.0221	103.2786
M3_SM21_21_Zrn22	0.0000	23.4414	0.1096	0.6739	2.1399	1.3061	14.6970	5.2515	74.1563	31.9735	176.9407	433.0021	104.2300
M3_SM21_21_Zrn23	0.0067	11.7848	0.1485	1.0348	2.7515	1.2568	12.6541	4.1453	52.8731	21.0451	115.6241	275.3854	66.9685
M3_SM21_21_Zrn24	0.0099	21.9536	0.1994	2.2360	5.9178	3.4885	37.2368	11.6368	133.5959	50.6233	253.9561	515.6165	118.1725
M3_SM21_21_Zrn25	0.0000	19.4258	0.0713	0.7499	1.7963	0.7567	11.2198	3.8248	49.2481	21.0446	113.0592	272.2055	67.5843
M3_SM21_21_Zrn26	0.0433	14.6259	0.3564	4.9932	6.7712	4.4144	32.1267	9.7478	105.0868	39.5533	195.6552	431.3255	97.3192
M3_SM21_21_Zrn27	0.0024	19.6189	0.1369	1.8602	4.3284	2.5435	28.3302	9.1133	114.0263	44.6287	228.7373	497.8741	117.0103
M3_SM21_21_Zrn28	0.0144	31.6877	0.1541	1.7694	4.3334	2.1839	25.5510	8.8857	113.2987	46.3281	246.9248	538.0729	129.0214
M3_SM21_21_Zrn30	0.0067	29.4345	0.1374	1.3604	4.1671	2.5580	28.7018	9.0025	110.6735	42.7891	220.0802	480.3537	113.4271
M3_SM21_21_Zrn31	0.0321	17.9160	0.5108	5.5240	9.3447	4.5501	37.9898	11.1424	125.1094	44.3521	214.8415	459.6782	105.0472
M3_SM21_21_Zrn32	0.0000	21.8197	0.1278	0.7642	1.6834	1.0951	13.6481	4.8223	64.8644	27.8982	153.8003	376.0523	91.4859
M3_SM21_21_Zrn33	0.0042	37.5079	0.1045	1.5408	4.7178	2.5556	35.1499	12.1156	161.4902	63.3205	321.6722	695.0592	154.6270
M3_SM21_21_Zrn34	0.0000	12.5540	0.0643	0.2788	0.8383	0.9634	7.2959	3.1827	38.7958	16.0019	89.8204	222.8184	52.9534
M3_SM21_21_Zrn35	0.0000	25.2763	0.1933	2.4170	5.6808	3.2133	32.2088	10.2387	124.2635	45.4460	225.6598	473.2397	107.8446
M3_SM21_21_Zrn36	0.0000	15.3589	0.1168	1.2195	2.6240	1.7511	19.8390	6.4601	84.5777	34.6333	186.6676	426.5100	101.5158
M3_SM21_21_Zrn37	0.0067	31.4367	0.1008	1.1484	3.2146	1.3124	21.0505	7.2423	97.9164	41.8649	232.3262	562.1978	135.0198
M3_SM21_21_Zrn38	0.0000	12.9058	0.0906	0.4441	1.3493	0.8099	8.4220	2.7819	33.9298	13.6449	75.6757	190.0930	47.7560
M3_SM21_21_Zrn39	0.0000	45.0164	0.0772	1.2197	3.0281	1.5761	21.7849	7.8342	101.1917	41.6219	224.0139	515.1653	122.0891
M3_SM21_21_Zrn40	0.0000	36.6121	0.1079	1.5492	6.3819	3.5880	54.4862	22.0591	299.8674	118.9885	597.4316	1140.6782	235.5631
M3_SM21_21_Zrn41	0.0000	14.0227	0.1433	1.2541	2.9108	1.9526	20.0651	7.2271	89.7339	35.2449	183.5065	388.8698	92.4798
M3_SM21_21_Zrn42	0.0084	12.7683	0.1092	0.6946	1.4979	0.9699	10.3096	3.8016	49.5645	20.5687	113.4424	270.3301	66.8776
M3_SM21_21_Zrn43	0.0190	16.0189	0.1077	0.9053	2.9559	1.7105	18.6809	5.9315	78.1887	31.1352	167.2552	370.7808	87.7802
M3_SM21_21_Zrn44	0.0071	24.3308	0.1101	1.1285	2.5366	1.8217	20.6917	7.0881	91.3128	36.5835	193.5785	442.9191	104.4366
M3_SM21_21_Zrn45	0.0212	19.6013	0.1635	0.7923	3.0755	1.8126	19.3696	5.9593	77.1563	30.9246	162.1728	375.1524	87.7793
M3_SM21_21_Zrn46	0.0000	23.6475	0.1136	0.9610	2.2801	1.2549	14.6163	5.3886	70.5697	28.5855	156.6330	365.4958	90.6728
M3_SM21_21_Zrn47	0.0000	26.0440	0.0761	0.9146	1.9816	1.0313	14.3809	5.2560	82.0439	35.0688	195.8371	470.5456	115.1415
M3_SM21_21_Zrn48	0.0204	12.4257	0.2775	3.4842	5.6455	3.1361	28.5612	8.0380	92.5962	33.8764	168.3523	354.3584	81.1357
M3_SM21_21_Zrn49	0.0000	3.4925	0.0771	0.3566	0.6218	0.4012	3.8657	1.3715	18.0124	7.3162	38.1130	97.6540	24.6245
M3_SM21_21_Zrn50	0.0024	42.2950	0.0785	1.2041	3.4401	1.2272	21.8267	8.4236	112.2992	48.5941	269.3107	659.2904	151.6202

*Valores en ppm

SM21-26

Zircón	La	Ce	Pr	Nd	Sm	Eu	Gd	Tb	Dy	Ho	Er	Yb	Lu
M4_SM21_26_Zrn01	1.9651	89.6606	1.6782	18.0098	27.9375	4.7016	123.5607	38.2621	431.1965	151.4023	669.9747	1033.3436	197.0590
M4_SM21_26_Zrn02	1.8794	41.0730	1.1624	12.5663	18.0257	3.6778	88.1810	28.5307	337.2063	122.3553	551.3958	885.8824	172.7365
M4_SM21_26_Zrn03	43.3330	150.0961	16.8400	84.7168	33.7720	6.3821	113.0367	33.5878	385.2200	136.2374	624.7172	998.6075	194.0637
M4_SM21_26_Zrn04	1.6764	24.9540	0.8262	5.8526	9.8421	2.0410	48.4133	16.0742	200.4266	76.4454	367.4028	656.5300	128.9957
M4_SM21_26_Zrn05	2.5167	68.2746	1.5479	14.8730	22.0464	3.9865	112.8812	36.8175	429.8006	153.3946	704.1761	1126.8939	218.9180
M4_SM21_26_Zrn06	23.1188	78.6551	8.8386	45.7214	18.3788	3.7951	63.8052	19.3264	223.6308	81.0894	386.1971	657.3542	134.4306
M4_SM21_26_Zrn07	0.2355	15.6582	0.3068	3.6334	6.8881	1.9397	39.4781	13.1530	168.3253	63.5956	307.0435	538.4603	109.3970
M4_SM21_26_Zrn08	0.2533	19.0127	0.3265	3.5762	6.7120	2.1224	41.6881	12.8583	177.0141	65.6248	307.5643	536.3412	111.5037
M4_SM21_26_Zrn09	2.9369	26.6585	1.4067	9.4891	11.7082	2.5364	59.0548	18.8253	231.3166	84.5779	405.3166	687.8320	140.0981
M4_SM21_26_Zrn10	0.5488	20.1937	0.3343	2.8587	5.2362	1.2759	31.4475	11.7492	149.6679	59.2721	297.8708	542.8754	113.3182
M4_SM21_26_Zrn11	0.0159	21.7423	0.2108	2.7568	6.3239	1.8662	39.7278	14.1592	171.2155	63.1879	301.4462	512.5579	104.3878
M4_SM21_26_Zrn12	5.4663	39.5700	2.0736	12.0533	8.8220	1.8956	44.2384	14.2401	177.3119	65.2972	302.9287	518.6148	103.6701
M4_SM21_26_Zrn13	0.0472	9.1005	0.0967	1.3608	2.8161	0.9246	17.0498	5.5538	70.4564	27.4741	136.5479	255.6773	53.1895
M4_SM21_26_Zrn14	0.1657	14.0473	0.2017	1.7744	3.9258	0.9450	22.4046	7.9294	100.1139	38.5422	187.0065	353.1439	70.1346
M4_SM21_26_Zrn15	0.0309	81.3465	0.3706	6.8797	17.6882	2.9421	92.1998	29.3540	346.0919	125.1412	554.9461	868.1554	165.6617
M4_SM21_26_Zrn16	3.6377	24.2162	1.2701	4.5221	3.9493	0.6359	20.4710	7.5481	100.3725	40.3028	212.5109	464.4415	103.9545
M4_SM21_26_Zrn17	0.0184	12.8162	0.1316	1.2662	3.0002	0.5713	19.9231	6.5469	85.3263	34.0344	169.9619	319.2477	66.4788
M4_SM21_26_Zrn18	1.3627	109.2736	0.9136	12.3466	29.7071	5.5505	162.1137	49.7645	589.1370	203.1597	916.1733	1411.7092	270.7743
M4_SM21_26_Zrn19	0.9217	23.2577	0.3740	3.1774	5.6073	0.4868	27.9018	9.6593	121.9885	47.0313	236.3227	422.6224	88.1267
M4_SM21_26_Zrn20	63.2997	168.5511	21.7656	106.4056	32.0647	5.2495	74.9275	20.7970	239.8512	85.2770	399.1737	660.8722	132.0405
M4_SM21_26_Zrn21	0.0060	14.2673	0.1385	2.0963	3.8041	0.7185	25.1030	8.7754	111.3942	44.3845	223.4783	416.3414	86.9698
M4_SM21_26_Zrn22	57.5190	199.8975	21.6902	104.8423	36.0639	6.0924	105.8146	29.4397	313.8750	111.0236	498.6090	793.8576	156.8984
M4_SM21_26_Zrn23	4.0688	25.1991	1.6434	9.5565	6.7011	1.5412	30.2688	10.4818	131.6394	49.7357	241.7026	420.0618	85.5197
M4_SM21_26_Zrn24	1.0829	13.8365	0.6313	2.6808	3.9247	1.0208	19.2224	6.2792	87.3176	33.1474	160.9925	306.2142	62.7747
M4_SM21_26_Zrn25	1.8206	20.4230	0.8057	4.8246	5.7516	1.4338	30.9761	9.8829	132.1422	49.8353	238.3726	423.4925	85.8707
M4_SM21_26_Zrn26	0.6336	78.4711	1.1930	16.6310	35.4577	8.1422	181.4984	55.3974	642.6488	224.2104	994.5449	1566.3192	298.1348
M4_SM21_26_Zrn27	0.0497	15.3650	0.2671	3.7577	8.6822	1.9186	44.6447	15.1210	188.4564	71.2859	329.5048	576.4639	114.1956
M4_SM21_26_Zrn28	0.1861	24.8507	0.2410	2.6840	6.7078	1.5960	39.4207	13.9200	178.5505	66.4420	323.2122	563.4994	112.4269
M4_SM21_26_Zrn29	1.0305	67.3241	0.9581	13.3680	24.2516	5.4045	132.1748	41.9004	484.0746	171.3530	773.8963	1230.7257	238.3798
M4_SM21_26_Zrn30	6.8766	38.3090	2.6666	14.9710	9.1594	2.1200	42.7959	13.9734	184.7545	70.0780	332.9204	607.9040	123.4435
M4_SM21_26_Zrn31	0.3471	25.5431	0.4376	5.1004	10.6342	2.7161	60.8761	20.3179	255.9264	95.1477	457.9432	776.5060	155.5754
M4_SM21_26_Zrn32	0.1151	10.9035	0.1562	1.5023	3.0008	0.8873	17.7525	6.4416	80.1583	30.5404	145.0013	282.3210	58.7595
M4_SM21_26_Zrn33	0.8096	36.3039	0.5531	7.5689	14.0342	2.9431	71.9243	22.6167	280.5959	103.6940	483.6667	930.5679	197.7692
M4_SM21_26_Zrn34	0.1113	148.1896	0.8211	14.9685	25.6374	4.4386	112.7719	32.7428	361.2719	120.8780	520.1229	783.9910	148.8265
M4_SM21_26_Zrn35	3.6314	31.3357	1.6978	14.1311	9.5186	3.0708	41.1077	12.7634	154.5407	55.6407	264.4003	467.0724	93.0003
M4_SM21_26_Zrn36	0.2109	21.5586	0.2029	2.5893	5.8301	1.8816	35.8097	11.8668	151.0567	53.9740	249.0733	439.6883	87.2875
M4_SM21_26_Zrn37	0.0627	10.5314	0.1527	1.7769	3.4043	1.1687	24.0485	7.7603	100.9959	39.4717	192.6310	353.5270	74.8021
M4_SM21_26_Zrn38	4.8918	48.3151	1.8975	10.7419	7.1174	1.1643	34.1926	12.4018	167.7242	66.6119	345.1023	662.3873	128.7538
M4_SM21_26_Zrn39	0.1822	30.1783	0.3134	3.6511	8.2457	2.3379	54.1248	17.8657	218.2616	80.1222	376.3543	630.7129	126.2809
M4_SM21_26_Zrn42	12.8963	54.6713	5.1632	25.3636	9.2085	0.9426	27.3107	9.0628	116.0398	43.7633	222.1344	421.3847	87.5973
M4_SM21_26_Zrn43	1.0250	19.8694	0.5234	6.3981	10.1479	2.3862	57.0808	17.4213	205.2184	76.3115	355.1430	609.7253	122.9238
M4_SM21_26_Zrn44	2.3603	66.9224	1.5541	16.3278	20.0972	6.1480	138.9767	43.4623	517.9788	182.0963	813.4038	1285.7842	247.2917
M4_SM21_26_Zrn45	0.6528	24.8588	0.5486	8.0035	15.1434	3.3813	75.2053	22.8031	271.4471	99.6186	451.6698	751.6850	147.6476

*Valores en ppm

SM21-33													
Zircón	La	Ce	Pr	Nd	Sm	Eu	Gd	Tb	Dy	Ho	Er	Yb	Lu
MI_SM21_33_Zrn01	0.0000	6.5359	0.1868	0.6372	1.7261	0.6141	7.5116	2.5272	31.7357	12.5090	62.6464	136.1014	29.3150
MI_SM21_33_Zrn02	0.0087	17.8144	0.3504	1.6102	2.9350	0.6979	16.5828	6.0172	77.5264	31.6197	157.6508	330.0960	68.8981
MI_SM21_33_Zrn03	0.0000	23.0344	0.3265	1.5265	4.1898	0.3439	19.4567	7.1459	90.9889	36.0530	184.1546	359.5321	75.6547
MI_SM21_33_Zrn04	0.0104	27.6717	0.3314	1.5578	3.9618	0.5050	24.1792	8.8933	113.6487	43.7545	217.1545	426.1629	87.6600
MI_SM21_33_Zrn05	0.0000	5.9445	0.2165	0.6160	1.2781	0.4866	6.4071	2.3026	29.9426	11.9422	59.5377	127.3756	27.7986
MI_SM21_33_Zrn06	0.0000	6.4905	0.2572	0.4192	1.1172	0.3980	5.4468	1.9266	24.2583	9.3267	47.0758	108.5904	24.3120
MI_SM21_33_Zrn07	0.0038	11.3041	0.3012	1.1826	2.8752	0.6683	8.8655	2.3243	25.1843	8.0709	33.6829	55.6738	10.7573
MI_SM21_33_Zrn08	0.0000	19.2441	0.3601	1.3229	3.0872	0.6217	13.0529	4.1193	45.5384	16.7569	75.9579	134.5494	28.3388
MI_SM21_33_Zrn09	0.0093	11.8316	0.3002	1.0583	2.0231	0.5083	9.3667	2.1577	19.0362	5.6022	24.5387	41.2832	8.9855
MI_SM21_33_Zrn10	0.0038	10.3916	0.2530	0.8366	2.8484	0.2999	20.9403	8.4415	117.4473	45.2816	213.9688	365.9647	69.1477
MI_SM21_33_Zrn11	0.0000	19.8174	0.2959	1.6867	3.4545	0.7615	13.0473	3.6638	41.3477	13.3362	56.8606	93.7409	18.5886
MI_SM21_33_Zrn12	-0.0001	18.4416	0.2336	1.1398	2.9203	0.3591	15.8934	5.7693	78.1768	30.7911	158.7921	330.6328	67.9542
MI_SM21_33_Zrn13	-0.0003	12.9683	0.1969	0.6254	1.6418	0.3324	9.9999	3.5609	48.4367	18.9936	95.9212	196.8312	40.7739
MI_SM21_33_Zrn14	0.0000	21.1392	0.2716	1.5749	2.5449	0.5882	10.8795	3.4048	42.8973	17.1284	85.1880	173.4952	36.1159
MI_SM21_33_Zrn16	0.0024	16.7107	0.3240	1.1729	2.7790	0.4753	17.2759	6.1119	79.8073	29.8076	151.9413	308.7609	64.7954
MI_SM21_33_Zrn18	0.0029	18.8619	0.3313	1.4698	2.5031	0.6229	10.6874	3.4286	37.0818	12.6849	58.0375	110.0168	21.5290
MI_SM21_33_Zrn19	0.0026	21.2573	0.2578	1.1150	3.1235	0.2646	18.9416	8.3987	125.3189	54.1153	285.5421	564.3043	112.0096
MI_SM21_33_Zrn20	0.0240	19.3262	0.3497	3.1786	3.8938	1.3940	12.0554	2.1389	16.9516	3.7419	11.8706	13.9907	2.4414
MI_SM21_33_Zrn21	0.0146	23.0162	0.3498	1.2970	2.5351	0.5366	14.8547	4.6391	59.5987	23.4598	117.1551	232.7684	48.3525
MI_SM21_33_Zrn22	0.0000	21.7243	0.2740	1.0816	2.9921	0.2860	20.9285	7.9185	105.4959	42.6775	207.7757	405.4713	80.7244
MI_SM21_33_Zrn23	0.0036	15.7507	0.2544	1.0452	2.6178	0.3191	13.5706	4.8445	60.4592	23.0663	113.5747	209.4936	42.8062
MI_SM21_33_Zrn24	0.0044	16.7754	0.2632	1.0229	1.7927	0.4032	11.7763	4.0908	49.6993	18.5896	92.4029	176.9411	36.4385
MI_SM21_33_Zrn25	0.0000	23.9736	0.2470	0.9492	2.9478	0.3001	18.5211	7.3550	105.0612	41.4005	207.8596	408.2666	80.8210
MI_SM21_33_Zrn26	0.0093	22.0487	0.4315	2.8007	4.2196	1.1121	13.1102	2.7716	25.3017	6.5126	22.4533	29.4338	5.2435
MI_SM21_33_Zrn27	0.0065	16.1368	0.2627	1.5955	3.0796	0.4440	12.0843	4.0009	43.0534	15.1822	64.3946	107.7833	20.6544
MI_SM21_33_Zrn28	0.0217	7.4200	0.2772	0.6323	1.5162	0.5490	8.5359	2.8103	38.4493	14.7970	74.5536	168.8838	37.0851
M2_SM21_33_Zrn29	0.0000	11.9363	0.3909	1.3620	6.4127	1.1857	40.9844	13.9747	175.1139	67.7629	313.5986	540.5491	109.3947
M2_SM21_33_Zrn30	0.0071	18.3358	0.2800	2.4213	3.9981	1.0144	12.6519	2.7372	24.9603	6.7975	26.6884	39.3449	8.0201
M2_SM21_33_Zrn31	0.0082	11.7956	0.2250	0.7813	1.9993	0.4233	12.1935	4.4663	63.5691	25.4549	129.1858	252.4360	53.3730
M2_SM21_33_Zrn32	0.0445	13.3472	0.3300	1.3214	2.3186	1.1613	13.2473	4.6918	58.6786	22.3779	108.8015	212.4998	42.8312
M2_SM21_33_Zrn33	0.0321	22.7366	0.2780	1.7636	4.0362	0.8655	15.2231	3.7575	40.8302	13.3186	63.1124	99.0694	19.7627
M2_SM21_33_Zrn34	0.0000	6.3169	0.2632	0.4801	1.8562	0.6266	8.5494	2.9676	37.0113	14.5207	70.1574	151.2344	32.0653
M2_SM21_33_Zrn35	0.0079	25.9792	0.2211	1.1110	3.6157	0.2152	17.3047	7.4084	97.8499	39.1542	197.3616	393.6715	77.6766
M2_SM21_33_Zrn36	0.0043	17.4489	0.2447	1.1317	2.4320	0.4283	13.2177	4.5004	58.4048	22.1556	108.0288	204.9912	40.2605
M2_SM21_33_Zrn37	0.0000	11.0397	0.2636	1.1669	2.2435	0.5189	8.7694	2.4962	24.9897	8.5814	37.8597	70.3193	14.9348
M2_SM21_33_Zrn38	0.0120	18.3812	0.2725	1.1615	2.7456	0.3437	16.3528	5.9135	72.9538	28.4900	147.2821	300.4627	63.7877
M2_SM21_33_Zrn39	0.0039	19.8504	0.3343	1.2309	2.6261	0.3218	16.0035	5.9419	77.4017	32.3210	161.1058	344.3049	72.8190
M2_SM21_33_Zrn40	0.0103	21.6198	0.2942	1.3749	2.8109	0.6818	12.2565	3.4571	35.5467	11.4421	48.4647	83.2098	16.5525
M2_SM21_33_Zrn41	0.0000	19.5332	0.2971	1.0834	2.4445	0.5297	9.8133	2.8618	29.2087	9.7945	41.8925	71.0867	13.4170
M2_SM21_33_Zrn42	0.0123	18.0443	0.2076	0.7392	2.7961	0.3332	20.2066	7.8900	113.4715	45.6093	235.3027	463.1480	93.8413
M2_SM21_33_Zrn43	0.0173	14.8414	0.2537	1.1706	2.0895	0.5850	10.1673	3.0356	35.5032	12.7597	62.5357	120.2150	25.2652
M2_SM21_33_Zrn44	0.0076	21.1091	0.2540	1.3258	2.8566	0.6962	11.2909	3.4513	38.5043	12.8850	57.4341	107.1222	22.4748
M2_SM21_33_Zrn45	0.0000	4.4301	0.2205	0.3770	1.0490	0.3146	3.7999	1.4751	19.3132	7.2413	37.8628	83.1046	18.9877
M2_SM21_33_Zrn46	0.0000	22.2243	0.2906	1.1929	3.2953	0.3025	22.1515	9.2268	134.4427	54.9422	269.2646	507.8824	96.5259
M2_SM21_33_Zrn47	0.0064	4.9292	0.2362	1.1304	3.8797	0.7953	23.8333	8.5011	109.7836	48.2907	268.7014	707.3095	156.4867
M2_SM21_33_Zrn48	0.0482	20.7126	0.3194	0.5300	2.6374	0.2316	15.2118	4.7928	49.8029	21.1626	121.9781	209.3563	42.7037
M2_SM21_33_Zrn49	0.0001	13.8600	0.2728	1.0619	2.8190	0.3568	23.1691	11.0971	168.6846	70.5695	359.7599	666.5614	127.9285
M2_SM21_33_Zrn50	0.0092	21.4286	0.2857	1.0511	3.1070	0.4346	18.8459	6.3982	91.8622	38.7918	206.9076	430.2095	90.4632
M2_SM21_33_Zrn51	0.0019	8.5939	0.1793	0.7378	2.4404	0.4741	16.7680	6.4935	95.5860	40.0330	217.5025	465.8315	99.6181

Continúa

**Continuación
SM21-33**

Zircón	La	Ce	Pr	Nd	Sm	Eu	Gd	Tb	Dy	Ho	Er	Yb	Lu
M2_SM21_33_Zrn52	0.0046	15.7407	0.2421	1.1169	2.8370	0.6307	12.6563	3.8775	44.3653	14.8579	66.7860	120.6908	24.2172
M2_SM21_33_Zrn53	0.0104	9.8044	0.2422	1.0556	1.8458	0.6147	7.8796	2.1811	23.3759	7.7377	33.5323	59.8435	12.0149
M2_SM21_33_Zrn54	0.0000	8.0848	0.2202	0.4298	1.5566	0.2845	8.0608	3.1155	42.3280	17.7118	94.0438	210.1697	44.4234
M2_SM21_33_Zrn55	0.0000	17.7720	0.2501	1.4084	2.0729	0.6466	8.6688	2.6324	28.1242	10.3862	49.7654	94.6418	19.9748
M2_SM21_33_Zrn56	0.0070	21.1451	0.2633	1.6280	3.8453	0.3716	24.4350	8.4880	109.7143	42.3252	201.0908	378.7589	75.6493
M2_SM21_33_Zrn57	0.0090	20.4562	0.2834	1.5136	3.5911	0.4666	19.8993	6.6410	89.5663	34.3655	174.2754	346.5195	73.7522
M2_SM21_33_Zrn58	0.0000	10.9526	0.2091	1.2090	3.6684	0.7309	24.4157	9.8723	120.9909	44.9903	207.1904	355.5610	69.1425
M2_SM21_33_Zrn61	0.0000	23.9343	0.2404	1.3867	1.2576	0.6146	4.3166	1.1932	14.9752	5.6833	27.7447	58.5441	12.8721
M2_SM21_33_Zrn62	0.0000	17.2722	0.2606	1.7247	3.3229	0.7500	15.0728	4.4076	46.9933	15.6902	71.8084	120.6818	24.4777
M2_SM21_33_Zrn63	0.0588	15.2241	0.2422	1.6050	2.4953	0.6518	8.8821	2.0327	19.1790	5.6457	23.5545	39.8949	8.8557
M2_SM21_33_Zrn64	0.0465	8.8761	0.2336	0.6419	1.3178	0.5203	8.4065	3.4302	44.7631	18.1356	93.3641	200.6721	41.6408
M2_SM21_33_Zrn65	0.0000	5.9885	0.2194	0.3984	1.2049	0.4504	6.0447	1.9968	25.9543	9.7601	50.2577	110.4995	24.5424
M3_SM21_33_Zrn66	0.0037	5.3739	0.2013	0.4788	1.0305	0.3138	4.6977	1.6457	19.3348	7.3509	35.4887	71.0351	15.2031
M3_SM21_33_Zrn67	0.0000	16.1208	0.2124	1.0998	2.4690	0.6339	11.2244	2.9840	31.2334	9.6829	38.4328	56.8748	10.6273
M3_SM21_33_Zrn68	0.0040	11.9442	0.2367	1.0312	2.2410	0.5029	12.1071	3.7790	42.6343	13.8883	55.4729	78.4857	14.5662
M3_SM21_33_Zrn69	0.0000	14.5815	0.2786	1.0679	2.8216	0.5661	15.6425	5.0480	58.6760	22.3545	106.9198	206.3689	43.5225
M3_SM21_33_Zrn70	0.0000	4.0790	0.2205	0.5277	1.1076	0.3948	4.7942	1.7026	23.9172	8.9728	45.4298	96.7660	20.6649
M3_SM21_33_Zrn67	74226.1118	0.0000	16.1208	0.2124	1.0998	2.4690	0.6339	11.2244	2.9840	31.2334	9.6829	38.4328	56.8748
M3_SM21_33_Zrn68	73258.4645	0.0040	11.9442	0.2367	1.0312	2.2410	0.5029	12.1071	3.7790	42.6343	13.8883	55.4729	78.4857
M3_SM21_33_Zrn69	73554.9775	0.0000	14.5815	0.2786	1.0679	2.8216	0.5661	15.6425	5.0480	58.6760	22.3545	106.9198	206.3689
M3_SM21_33_Zrn70	73543.8406	0.0000	4.0790	0.2205	0.5277	1.1076	0.3948	4.7942	1.7026	23.9172	8.9728	45.4298	96.7660

*Valores en ppm

SM21-07

Zircón	La	Ce	Pr	Nd	Sm	Eu	Gd	Tb	Dy	Ho	Er	Yb	Lu
M1_SM21_07_Zrn01	0.0317	15.0303	0.1863	1.5887	2.0255	0.8784	6.4328	1.3829	9.3974	2.2662	7.6624	8.8294	1.5825
M1_SM21_07_Zrn02	0.0000	7.6981	0.1108	0.8657	1.7709	0.3313	13.1573	4.5797	61.2742	23.9992	115.6700	208.3320	42.6142
M1_SM21_07_Zrn03	0.0218	8.0862	0.1273	0.6311	1.1365	0.3817	7.7928	2.5028	32.1751	12.6687	67.0906	156.1487	34.8597
M1_SM21_07_Zrn04	0.1407	6.5523	0.2330	1.0326	1.1343	0.5336	4.3388	1.1811	9.6807	3.1701	12.3138	20.4275	5.3428
M1_SM21_07_Zrn05	17.5756	41.5791	2.6800	9.8268	2.7036	1.0444	16.7551	5.0207	63.3477	24.3177	115.3470	213.6715	43.8266
M1_SM21_07_Zrn06	0.1080	6.6295	0.2666	1.3558	1.6736	0.6425	4.5435	1.0398	8.1642	2.0654	7.1326	9.2531	2.1974
M1_SM21_07_Zrn07	0.0125	14.6832	0.2050	1.7207	2.9889	1.5183	10.7188	2.1025	15.4539	3.5202	11.4337	9.9618	1.7171
M1_SM21_07_Zrn08	0.0000	6.4225	0.0988	0.2939	1.3488	0.8215	10.6640	4.3746	64.6120	28.4257	150.0678	327.6013	72.8220
M1_SM21_07_Zrn09	0.0191	10.2355	0.1439	0.9396	2.2158	0.5854	6.0847	1.3143	9.6466	2.3194	6.5229	7.5318	1.1449
M1_SM21_07_Zrn10	0.0000	2.9113	0.1337	0.4469	0.5648	0.1924	2.7034	0.8907	10.0460	3.9301	20.6601	54.6916	13.9178
M1_SM21_07_Zrn11	0.0000	10.1493	0.1133	0.3719	1.7529	0.1693	10.6326	3.8420	50.8549	19.4089	97.3232	187.1640	38.3092
M1_SM21_07_Zrn12	0.1667	8.7091	0.1592	0.9384	0.7335	0.2570	4.6265	1.3843	16.6848	6.1122	30.5370	58.3904	12.9403
M1_SM21_07_Zrn13	0.0000	6.5888	0.0673	0.3621	0.6701	0.1232	4.9737	1.4842	19.6386	7.1139	34.8139	64.5980	13.1110
M1_SM21_07_Zrn14	0.0111	8.8278	0.1317	0.5663	0.9548	0.4010	3.4388	0.7184	7.4097	2.1066	7.7624	11.7186	2.0482
M1_SM21_07_Zrn15	0.0100	5.1138	0.1072	0.9229	2.2068	0.7933	8.8622	2.8426	35.0253	14.6060	81.9079	207.6850	52.3125
M1_SM21_07_Zrn16	0.0138	4.3652	0.1438	0.5621	1.0761	0.2753	4.1609	0.9994	10.2636	3.2228	11.8835	20.8842	4.3212
M1_SM21_07_Zrn17	0.0049	3.5371	0.1435	0.8383	1.6174	0.4930	6.0275	1.5185	12.5422	3.1131	11.4916	11.6090	1.8602
M1_SM21_07_Zrn18	0.1030	4.9371	0.1681	0.9396	1.4516	0.3664	4.5790	0.9650	8.0091	1.9425	6.0917	6.2028	1.0674
M1_SM21_07_Zrn19	0.0071	5.2014	0.0994	0.9473	1.8680	0.4186	14.6670	5.1022	69.9305	28.9725	146.2819	282.8501	61.8285
M1_SM21_07_Zrn20	0.0140	5.1158	0.1365	0.5826	0.8430	0.1528	4.2370	1.2355	14.6750	4.4852	20.8558	34.8856	7.4032
M1_SM21_07_Zrn21	0.0062	6.2578	0.2328	0.4626	1.1349	0.2739	3.0249	0.7052	7.5780	2.3064	10.7273	17.5477	3.7023
M1_SM21_07_Zrn22	0.0000	12.6217	0.1268	0.4557	1.0783	0.2819	3.5683	1.0025	13.3857	4.0152	17.8136	28.1618	5.5740
M2_SM21_07_Zrn23	0.0035	8.8761	0.0770	0.4064	1.4371	0.2272	8.7606	3.0012	39.0289	15.7125	76.2891	146.2821	29.8122
M2_SM21_07_Zrn24	0.0000	14.6894	0.1339	0.5873	1.1408	0.5204	3.1241	0.5419	3.5794	0.7774	2.7658	2.3201	0.4456
M2_SM21_07_Zrn25	0.0000	13.1584	0.1857	1.2832	4.1283	0.5075	23.3083	8.0977	100.2996	38.8624	183.0167	319.6051	65.1791
M2_SM21_07_Zrn26	0.0877	4.1189	0.1405	0.7544	2.0677	0.4221	13.7016	5.5493	71.6024	26.9245	131.9569	250.2868	52.6519
M2_SM21_07_Zrn27	0.0025	5.0547	0.1627	1.1917	1.6569	0.6993	6.8232	1.4235	11.6608	2.6227	7.5717	7.0660	1.1612
M2_SM21_07_Zrn28	0.0623	4.4752	0.1303	0.4929	1.1039	0.4672	5.2488	1.3975	15.6317	5.2601	22.6855	36.0313	6.8845
M2_SM21_07_Zrn29	0.0113	13.1750	0.1563	0.9100	1.7327	0.3057	9.5073	3.1325	37.0948	12.9505	59.7846	95.8679	19.7420
M2_SM21_07_Zrn30	0.0954	18.4194	0.2614	2.1268	3.2116	0.4698	15.5619	4.8344	56.9584	21.2505	99.1642	169.7116	34.3712
M2_SM21_07_Zrn31	0.0000	20.2960	0.1335	1.3389	2.4702	0.3822	13.1994	4.6858	62.2253	22.9645	114.8934	225.1540	46.6000
M2_SM21_07_Zrn32	0.0000	11.8177	0.0965	0.1913	0.6320	0.1434	5.7476	2.4179	37.2911	16.3215	86.3906	169.8392	36.6325
M2_SM21_07_Zrn33	0.0000	14.4008	0.1300	0.7554	1.6293	0.1909	13.6144	5.0110	67.3322	25.8795	131.5073	244.1917	50.0824
M2_SM21_07_Zrn34	0.0131	5.7370	0.1208	0.5021	1.1966	0.3028	6.6737	2.1098	26.3160	9.4057	44.9799	79.5563	15.7158
M2_SM21_07_Zrn35	0.0817	12.5583	0.5469	5.7908	9.9904	1.2767	47.8596	14.7165	171.9212	58.8966	263.8229	413.5023	78.1560
M2_SM21_07_Zrn36	0.0000	23.5897	0.3034	2.6060	4.6548	1.6901	13.6406	2.0586	15.0541	3.2324	9.0111	7.4247	1.2663
M2_SM21_07_Zrn37	0.0000	7.0466	0.2137	0.8665	1.4251	0.3861	5.0826	1.3449	13.5109	4.0309	16.1301	26.7598	5.5628
M2_SM21_07_Zrn38	0.0174	9.6320	0.2092	2.4861	5.3544	0.5699	28.2025	8.7552	103.5370	36.9477	170.8737	274.2534	53.1314
M2_SM21_07_Zrn39	0.0111	4.4513	0.1062	0.6809	1.3825	0.3625	4.4026	1.0235	8.7601	2.2650	7.4211	8.5945	1.3398
M2_SM21_07_Zrn40	0.0000	4.0888	0.1473	0.6262	1.3795	0.3066	4.0746	1.0336	7.5543	1.9076	6.0596	6.8474	1.0446
M2_SM21_07_Zrn41	0.0957	7.5296	0.1307	1.0001	2.9655	0.9072	18.8692	6.2007	74.2482	27.3848	121.2531	206.0192	40.0553
M2_SM21_07_Zrn42	0.3119	8.5638	0.3597	3.3937	7.5254	1.6015	40.4817	13.1386	154.2976	56.5597	251.7793	410.5079	80.6027
M2_SM21_07_Zrn43	0.0000	7.7655	0.1492	0.8218	1.2327	0.5391	5.7353	1.5490	15.8705	5.1047	23.2379	38.8512	7.8729
M2_SM21_07_Zrn44	0.1027	14.1413	0.1268	1.3782	2.4698	0.6367	16.0894	5.0070	63.9345	23.3703	120.6859	245.6514	51.3716
M2_SM21_07_Zrn45	0.8456	10.3830	0.4605	3.1192	4.0711	0.6572	22.0147	6.8449	83.3013	31.0763	145.3784	230.6549	45.4019
M2_SM21_07_Zrn46	0.0161	4.7285	0.1098	0.4389	1.3972	0.2921	5.4456	1.5506	17.0674	5.0305	22.9185	34.7741	7.5350
M2_SM21_07_Zrn47	0.0000	8.4424	0.0949	0.5581	2.8288	0.4361	14.6171	5.0939	60.1488	21.2069	97.7986	163.5229	30.3573
M2_SM21_07_Zrn48	0.0046	8.1531	0.0853	0.4838	1.1572	0.1942	7.2705	3.0868	42.0699	16.9256	84.9979	164.7715	34.2687
M2_SM21_07_Zrn49	0.0598	12.3751	0.1177	2.0712	5.4722	0.6474	28.0265	10.0544	121.8832	44.4551	203.5062	331.4370	63.6842
M2_SM21_07_Zrn50	-0.0003	6.3612	0.0665	0.2239	0.8994	0.1729	6.3433	1.8444	29.4639	12.0940	61.6361	133.8613	28.9180
M2_SM21_07_Zrn51	0.0999	12.1031	0.4168	4.7688	8.1565	1.1078	44.3578	14.8952	171.9679	62.7999	282.8183	443.2734	86.4139

Continúa

Continuación**SM21-07**

Zircón	La	Ce	Pr	Nd	Sm	Eu	Gd	Tb	Dy	Ho	Er	Yb	Lu
M2_SM21_07_Zrn52	0.0554	7.9147	0.1739	1.2108	1.9816	0.6064	6.5361	1.7490	19.2403	6.1558	26.1332	42.4398	8.7576
M2_SM21_07_Zrn53	0.0041	9.5092	0.1113	0.5716	1.5428	0.2650	6.7124	2.2988	28.8573	10.8648	54.1151	106.4854	23.0246
M2_SM21_07_Zrn54	0.0024	6.1370	0.0944	0.5129	1.1611	0.2695	8.1959	2.8849	37.5484	15.4151	77.2715	167.8663	37.2114
M2_SM21_07_Zrn55	0.0000	4.8852	0.1227	0.8912	0.8360	0.2945	3.2133	0.8047	7.6699	1.5502	6.4016	6.5344	1.1225
M2_SM21_07_Zrn56	0.0323	4.5506	0.2081	0.9489	1.3162	0.3393	5.4146	1.4158	12.9149	3.7093	13.6162	16.2121	2.8196
M2_SM21_07_Zrn57	0.0633	7.0237	0.1712	1.3470	2.6346	0.2851	11.2591	3.5927	45.7815	17.3927	79.9212	145.5402	30.3955
M2_SM21_07_Zrn58	0.0109	4.0957	0.1496	0.7711	1.3389	0.4007	4.6013	1.1949	9.3941	2.7072	8.2035	9.9631	1.7304
M2_SM21_07_Zrn59	0.0027	9.2861	0.1199	0.6586	1.8658	0.2412	11.5087	4.6018	60.2168	24.2803	118.2055	217.6465	44.8468
M2_SM21_07_Zrn60	0.0593	4.6929	0.1281	0.6056	1.1967	0.3964	3.8243	0.8257	7.0130	1.5839	5.2536	5.3780	0.9046

*Valores en ppm

SM21-28													
Zircón	La	Ce	Pr	Nd	Sm	Eu	Gd	Tb	Dy	Ho	Er	Yb	Lu
M2_SM21_28_Zrn01	0.0022	8.1513	0.1306	1.6255	3.0929	0.7375	15.1933	4.8304	57.8995	20.6448	96.4613	167.1711	33.6463
M2_SM21_28_Zrn02	0.0074	7.9145	0.1253	1.1657	1.9745	0.5693	6.7730	1.9259	17.4373	5.1401	19.9228	30.3278	5.8943
M2_SM21_28_Zrn03	0.0044	43.1058	0.2220	3.9435	7.4634	0.5731	33.4841	10.7925	130.7374	50.3109	241.8439	469.0984	96.3230
M3_SM21_28_Zrn04	0.4111	6.5234	0.0997	0.5320	0.8483	0.1845	7.1682	3.5972	56.4255	26.8686	166.0551	486.3696	114.6457
M3_SM21_28_Zrn05	0.0001	7.7462	0.0527	0.2649	0.8673	0.0893	6.2859	2.5779	36.0119	15.3997	83.4470	171.4362	37.3793
M3_SM21_28_Zrn06	0.0000	3.2929	0.1112	1.3595	3.4666	0.1657	18.8536	6.8216	88.7083	31.1380	142.5534	284.7405	57.4274
M3_SM21_28_Zrn07	0.0187	1.6445	0.0949	0.7786	1.4051	0.0847	4.1788	1.1591	13.0022	4.4539	18.2685	33.8370	5.2113
M3_SM21_28_Zrn08	0.0147	11.7637	0.1034	1.3683	2.7455	0.4653	16.9233	6.7247	96.0537	40.3934	229.0536	579.5189	124.8664
M3_SM21_28_Zrn09	0.0000	16.7227	0.1458	2.2544	3.6587	0.7262	16.7086	4.8480	56.1971	21.0770	93.8818	166.7734	32.6427
M3_SM21_28_Zrn10	0.0000	3.6176	0.0830	0.6071	2.7461	0.0767	20.9242	9.0049	124.8147	50.7970	272.6608	580.4401	125.4563
M3_SM21_28_Zrn11	0.0000	13.7805	0.1465	2.0754	4.1942	0.4777	18.9957	5.7491	65.2642	23.4033	110.9367	180.4018	36.6632
M3_SM21_28_Zrn12	0.0000	16.1299	0.1030	1.1236	2.4778	0.2113	12.7891	4.4932	55.6142	21.2977	104.1119	199.8111	40.6129
M3_SM21_28_Zrn13	0.0000	0.3461	0.0536	0.2555	0.7718	0.0752	8.0628	5.1689	72.4258	26.4709	114.4872	221.6692	45.2863
M3_SM21_28_Zrn14	0.0074	24.3928	0.2672	4.0619	8.1445	0.1836	42.5363	13.8302	162.7127	62.6390	311.7232	569.5015	112.8286
M3_SM21_28_Zrn15	0.0042	14.8844	0.1308	1.4549	2.8874	0.4505	5.5846	0.7717	3.9840	0.7778	2.6548	2.6132	0.3453
M3_SM21_28_Zrn16	0.0001	15.9068	0.1481	1.4406	3.0586	0.6991	17.1660	5.6568	71.0086	26.7058	132.1588	268.2271	57.5752
M3_SM21_28_Zrn17	0.0025	1.7882	0.0871	0.8571	2.1746	0.2896	10.6014	3.0365	33.4187	10.2804	37.3491	45.5370	7.9126
M3_SM21_28_Zrn18	0.0001	8.0369	0.0578	1.2416	3.0842	0.2022	18.7896	6.4194	86.8738	35.2382	179.6392	361.3637	77.5260
M3_SM21_28_Zrn19	0.0221	19.6014	0.1090	1.0908	2.1053	0.5070	10.4744	3.1225	35.4126	12.7330	59.1370	114.8721	24.7247
M3_SM21_28_Zrn20	0.0001	8.3243	0.0920	1.1528	1.9109	0.4657	9.2970	2.9969	33.6336	12.0350	56.0333	104.0085	21.8227
M3_SM21_28_Zrn21	-0.0002	6.6278	0.2502	2.0788	3.9204	1.0866	18.7672	5.6967	69.2866	23.4353	111.4637	213.7978	42.7084
M3_SM21_28_Zrn22	0.0177	38.8305	0.1252	1.4300	4.9679	0.2219	31.1854	10.3371	110.3572	35.3684	150.5150	245.4223	51.0239
M3_SM21_28_Zrn23	0.0130	30.2726	0.1561	1.7709	3.7170	0.3670	15.6449	4.9594	56.1805	20.1456	93.9357	165.0274	33.3027
M3_SM21_28_Zrn24	0.0000	7.4204	0.0795	0.7903	1.4406	0.2205	8.1985	3.0636	39.3309	15.3457	75.8644	147.9092	31.5255
M3_SM21_28_Zrn25	0.0026	11.3945	0.1460	1.7266	3.3089	0.3992	14.0298	4.4291	51.0432	18.6001	83.5885	143.7805	28.8727
M4_SM21_28_Zrn26	0.0000	8.4579	0.1369	1.5048	2.2416	0.2200	11.4339	4.1006	51.5580	19.5344	96.5012	185.1378	37.5914
M4_SM21_28_Zrn27	0.0000	9.1722	0.0442	0.6355	1.5518	0.2064	12.7718	4.6932	59.1290	23.8738	115.5459	203.7573	43.7005
M4_SM21_28_Zrn28	0.2697	11.4372	0.1583	0.8863	2.0498	0.0924	16.4173	7.7852	127.4870	58.1008	340.4333	791.3623	171.8962
M4_SM21_28_Zrn29	0.0000	11.5313	0.0638	0.6208	2.1541	0.3396	13.9156	4.8005	73.8694	33.9495	220.4501	746.8065	183.1707
M4_SM21_28_Zrn30	0.0357	28.7146	0.3136	3.5301	5.4491	2.2646	22.2932	6.2648	67.7600	23.1835	106.0437	189.1977	40.2568
M4_SM21_28_Zrn31	0.0145	5.3604	0.2720	3.5972	5.1118	0.1843	12.2215	2.3856	18.3066	3.9387	13.1224	14.9630	2.7506
M4_SM21_28_Zrn32	0.0192	16.7872	0.2258	2.1105	6.3030	0.2888	41.3950	14.8676	164.4455	55.4058	239.5225	352.3108	64.2402
M4_SM21_28_Zrn33	0.0000	13.2075	0.1519	0.4737	1.5840	0.2041	11.7084	4.0114	62.5475	25.6098	140.4834	369.6382	97.7942
M4_SM21_28_Zrn34	0.0000	3.9429	0.1243	1.1186	3.2206	0.1579	18.1704	6.7124	88.3262	33.8109	163.9854	292.7799	59.2474
M4_SM21_28_Zrn35	0.0136	29.5557	0.1095	1.3253	2.5743	1.5744	16.1069	4.7130	56.5581	21.3261	100.4904	194.4293	40.6961
M4_SM21_28_Zrn36	0.0037	9.2024	0.2125	3.0888	7.9699	1.0330	45.0628	14.3425	171.6397	63.0942	293.0862	505.4081	102.1480
M4_SM21_28_Zrn37	0.1882	9.3220	0.1450	0.6624	1.1727	0.6295	7.0526	2.6188	30.1369	11.5321	56.7320	116.3354	26.3535
M4_SM21_28_Zrn38	0.0000	17.8470	0.0552	1.2044	2.0628	0.0758	13.3275	4.6654	57.9631	20.5147	95.9425	166.5946	34.8764
M4_SM21_28_Zrn39	38.2063	145.3103	20.3585	93.5428	27.5201	1.8964	69.0868	19.6221	231.0766	81.3063	380.0183	562.1053	106.0455
M4_SM21_28_Zrn40	0.0668	3.5139	0.0671	0.5575	1.0436	0.1452	5.2353	1.6715	22.2875	8.2117	43.3682	88.5340	19.9580

*Valores en ppm

SM21-13a													
Zircón	La	Ce	Pr	Nd	Sm	Eu	Gd	Tb	Dy	Ho	Er	Yb	Lu
M4_SM21_13a_Zrn01	0.0154	20.3798	0.2921	3.9541	7.7029	0.2065	39.8563	11.4348	111.9232	33.3892	129.5134	180.1993	32.9616
M4_SM21_13a_Zrn02	0.0000	18.4703	0.2288	3.9059	10.0952	0.2624	42.3820	9.8807	78.5799	18.9242	61.7966	71.4364	11.7417
M4_SM21_13a_Zrn04	0.0000	5.0439	0.0822	0.7455	2.3008	0.2967	17.5215	6.9590	96.5027	42.3494	239.0480	569.8196	120.7911
M4_SM21_13a_Zrn05	0.0060	12.3968	0.2050	2.7173	5.1604	0.5296	18.7482	3.9176	35.5373	9.6056	34.1702	42.4952	6.9856
M4_SM21_13a_Zrn06	0.0882	12.9708	0.8006	9.7672	13.9558	1.3968	42.0045	10.6088	103.9240	31.7006	134.3128	202.2566	39.3852
M4_SM21_13a_Zrn07	0.1131	10.7228	0.3619	4.3245	7.0042	1.1788	33.1731	9.4450	93.6857	30.8755	127.6787	197.7313	38.6587
M4_SM21_13a_Zrn08	0.0025	3.3882	0.0431	0.8780	3.5323	0.3464	19.5609	6.7798	75.1819	23.0660	90.0319	131.4983	25.4324
M4_SM21_13a_Zrn10	0.0660	13.8007	0.3449	3.5927	9.1672	0.8404	34.3897	8.3166	72.8427	19.4157	66.1824	84.6637	16.2064
M4_SM21_13a_Zrn11	0.0289	10.7504	0.1817	3.9127	8.9318	0.5867	36.0894	9.2343	87.0060	23.4114	82.5168	95.3130	16.1512
M4_SM21_13a_Zrn12	0.0723	23.7923	0.1681	1.5720	4.3739	0.1867	21.7723	7.0599	93.6380	40.6474	222.8253	490.2654	107.1795
M4_SM21_13a_Zrn13	0.0368	20.1099	0.1221	1.3272	3.3922	0.1723	20.7046	7.2726	100.5355	43.7855	244.8516	538.5647	114.5097
M4_SM21_13a_Zrn14	0.0000	5.6426	0.0778	0.3627	0.2436	0.3238	2.9094	1.0615	13.3454	5.0227	24.9192	57.4036	12.8305
M4_SM21_13a_Zrn15	0.0267	10.2791	0.0666	0.5917	1.1474	0.3186	9.4958	3.4826	56.7069	26.5427	160.8906	437.0229	103.6136
M4_SM21_13a_Zrn16	0.0000	7.6469	0.0797	0.5805	1.4739	0.3234	8.5432	2.5954	30.6554	11.4732	53.0875	98.1126	20.4948
M4_SM21_13a_Zrn17	0.0000	7.5218	0.0682	0.3780	0.8877	0.2615	6.1231	2.1377	26.8057	10.1290	49.6893	100.3765	20.7478
M4_SM21_13a_Zrn18	9.8559	33.1209	4.1386	18.9824	4.7627	0.7443	13.9093	4.6865	71.9135	31.6136	188.6212	485.6035	108.3103
M4_SM21_13a_Zrn19	0.3953	12.9525	0.2529	2.3857	4.0810	0.7655	18.9261	5.5585	66.4798	23.3922	104.5530	182.5341	38.4520
M4_SM21_13a_Zrn20	0.0210	6.7128	0.0763	1.0740	4.5669	0.3192	27.9666	13.0351	182.1327	73.4889	343.1916	622.1880	117.9200
M4_SM21_13a_Zrn21	0.0000	4.2434	0.0998	1.5874	4.2337	0.5600	27.2288	9.4906	125.0466	50.6201	246.1976	430.7975	86.4986
M4_SM21_13a_Zrn22	0.0024	10.3671	0.0723	0.6443	2.2539	0.2906	13.7117	5.5019	71.2470	29.2735	150.5792	300.0888	63.4540

*Valores en ppm

SM21-35

Zircón	La	Ce	Pr	Nd	Sm	Eu	Gd	Tb	Dy	Ho	Er	Yb	Lu
M1_SM21_35_Zrn01	0.0000	62.0297	0.7148	3.9030	12.4268	1.0167	66.9435	23.1407	278.0543	99.5989	455.8592	744.9770	148.8477
M1_SM21_35_Zrn02	0.0034	44.7503	0.4465	2.2886	6.7608	0.3943	42.6954	15.4595	210.7555	80.9844	398.4384	700.1053	134.5234
M1_SM21_35_Zrn03	0.0216	29.4760	0.4818	0.6624	1.8431	0.1758	22.5138	11.4745	191.6808	85.6300	499.9721	1184.6305	233.4231
M1_SM21_35_Zrn04	0.0664	23.7035	0.5392	1.0061	2.9330	0.3391	14.9157	6.4337	96.1646	46.1207	300.6973	777.9818	164.1560
M1_SM21_35_Zrn05	0.0016	33.7771	0.4093	1.4620	6.5317	0.3060	42.7022	17.4291	231.4300	86.3651	401.0734	626.0308	118.2746
M1_SM21_35_Zrn06	0.0026	41.3429	0.4841	2.8050	7.0248	0.8351	37.5243	11.2151	126.6028	43.1608	192.2775	316.7576	65.5105
M1_SM21_35_Zrn07	0.0092	60.9100	0.5776	0.9029	3.1080	0.3875	20.3627	8.7568	115.4829	48.2210	261.5197	513.9119	105.9440
M1_SM21_35_Zrn08	0.0058	57.5274	0.4954	4.1577	9.6366	0.7788	66.4219	24.3947	306.5838	109.8127	507.5361	830.0353	161.5537
M1_SM21_35_Zrn09	0.0146	39.3040	0.5401	2.8813	6.4890	1.1500	33.5935	10.6286	123.3795	43.7310	203.3739	353.6155	73.6849
M1_SM21_35_Zrn10	0.0035	46.4389	0.4843	2.7109	8.4522	0.4603	63.9566	26.3797	351.9567	135.9777	632.2555	979.8174	186.2099
M1_SM21_35_Zrn11	0.0166	46.7868	0.5141	3.2592	8.8126	0.9294	48.0976	15.3603	186.5516	65.5666	298.2557	498.6669	99.2119
M1_SM21_35_Zrn12	0.0108	37.7930	0.3970	1.1368	5.3203	0.5438	46.3077	20.3762	320.2381	131.7456	636.9926	1187.7937	216.3473
M1_SM21_35_Zrn13	0.0000	41.5528	0.4555	3.7378	6.7350	0.8350	33.2009	9.0780	100.3660	34.6006	151.0477	255.8496	53.6823
M1_SM21_35_Zrn14	0.1828	30.8096	0.3471	1.0888	1.3239	0.3797	7.7619	3.6685	52.1895	23.4649	150.1364	401.8339	94.3996
M1_SM21_35_Zrn15	0.0000	46.5950	0.3261	0.7580	3.4003	0.4662	20.9509	8.2708	115.1074	48.2236	272.1800	542.6384	104.8977
M1_SM21_35_Zrn16	0.0065	25.5642	0.3333	1.4784	3.8619	0.6255	19.6690	6.2932	81.0435	30.6022	148.8524	280.1956	58.4292
M1_SM21_35_Zrn17	0.0000	39.8807	0.3399	0.4595	1.4761	0.5024	9.5475	3.6999	60.1453	27.6374	171.1523	460.8519	103.3100
M1_SM21_35_Zrn18	0.0053	37.6178	0.4819	2.4237	5.4668	0.7000	28.5835	9.8351	116.5878	42.7355	201.2284	356.1704	72.1681
M1_SM21_35_Zrn19	0.0233	22.6932	0.3738	1.1288	4.1754	0.3974	22.9327	9.7589	128.2581	51.7470	256.7353	463.8407	92.1474
M1_SM21_35_Zrn21	0.0023	29.4800	0.3214	1.1234	4.2416	0.2880	36.5986	16.2122	242.1027	101.1000	526.1121	991.4241	214.3305
M1_SM21_35_Zrn22	0.0115	28.6095	0.3894	2.1531	4.3363	0.6788	22.0215	6.5431	81.9312	29.4390	141.3811	262.9520	55.8413
M1_SM21_35_Zrn23	0.0029	35.9199	0.4742	1.9961	6.5102	1.0045	40.4198	14.0190	176.4862	65.2109	312.6220	549.9090	111.0597
M1_SM21_35_Zrn24	0.0037	35.8414	0.4003	3.3810	6.5068	1.1069	29.5227	9.0369	101.2760	36.4457	173.0715	335.5519	71.1657
M1_SM21_35_Zrn25	0.0062	30.6722	0.3643	1.3136	4.0815	0.2704	31.3688	15.5241	227.9674	93.9042	491.5874	957.2444	191.8076
M1_SM21_35_Zrn26	0.0000	32.6202	0.4689	1.9703	5.2831	0.9493	24.7798	7.9395	94.1020	32.9486	159.6813	285.4952	59.9884
M1_SM21_35_Zrn27	0.0055	19.2449	0.3040	1.4069	3.7775	0.2954	29.7165	12.1183	167.1709	63.6956	304.8151	479.1351	89.3190
M1_SM21_35_Zrn28	0.0015	54.9374	0.6187	5.0246	12.0625	0.9793	71.9798	24.5496	293.8033	102.7035	454.6094	723.9072	143.0242
M1_SM21_35_Zrn29	0.0199	35.2665	0.3186	1.1312	3.9061	0.3605	28.4347	12.1591	168.0367	68.7232	346.4761	641.7705	127.0024
M1_SM21_35_Zrn31	0.0000	1.0486	0.2283	0.0000	0.2107	0.0244	0.3226	0.2439	5.0470	3.0807	25.3970	121.6928	37.5221
M1_SM21_35_Zrn32	0.0000	27.7109	0.3453	1.5137	5.3845	0.3012	40.0865	17.3835	248.8297	100.0418	480.8323	819.4460	161.2661
M1_SM21_35_Zrn33	0.0083	39.2298	0.3590	2.7227	6.4631	0.6285	41.4862	14.3604	178.7965	66.9174	308.9148	551.4810	116.0526
M1_SM21_35_Zrn34	0.0000	16.5574	0.3061	1.3513	3.5975	0.3657	23.3829	8.9349	113.3702	41.3185	189.8277	305.8928	60.7857
M1_SM21_35_Zrn35	0.0094	44.2701	0.2937	0.8477	3.0230	0.4512	21.7595	9.0814	133.0439	56.6481	310.2982	642.4354	133.0306
M1_SM21_35_Zrn36	0.0000	41.8077	0.2622	0.5577	1.1252	0.2804	6.7577	2.8170	37.1592	16.7750	93.4271	237.1804	54.4138
M1_SM21_35_Zrn37	0.0184	29.8400	0.3124	0.6321	1.3060	0.6209	7.6012	3.0306	44.7911	19.8600	119.0946	300.6929	68.9412
M1_SM21_35_Zrn38	0.0116	46.9509	0.4093	2.9795	8.2652	0.5837	52.0869	19.4289	243.0921	91.0864	419.8653	698.0683	138.9325
M1_SM21_35_Zrn39	0.0039	33.3699	0.3661	2.7221	5.7998	1.0282	27.2902	7.6172	86.4469	30.3158	135.9997	233.3779	50.6370
M1_SM21_35_Zrn40	0.0165	27.4002	0.3629	2.1977	4.7125	0.7921	27.2370	8.9673	115.1423	43.4496	211.8990	392.2673	83.0172
M1_SM21_35_Zrn41	0.0000	27.0893	0.3661	1.8691	4.2089	0.6356	21.0993	6.6413	82.7044	30.7875	151.0810	292.1273	62.4673
M1_SM21_35_Zrn42	0.0000	29.8458	0.4050	2.3620	4.2458	1.0277	22.1353	6.6370	75.4990	27.0241	125.1026	228.7662	49.3741
M1_SM21_35_Zrn43	0.0017	68.3733	0.2680	0.5453	1.8327	0.5018	10.7253	4.6706	69.1193	32.8488	199.0484	492.6092	111.8060
M1_SM21_35_Zrn44	0.0152	42.0048	0.2566	1.1381	3.9888	0.3206	25.4848	10.1775	142.7971	59.8398	298.0837	539.8973	105.7770
M1_SM21_35_Zrn45	0.0090	34.6962	0.3401	2.4985	7.9153	0.5513	58.7077	25.4669	359.0983	143.9034	692.2649	1142.4846	226.1953
M1_SM21_35_Zrn46	0.0535	43.4276	0.4065	2.7460	7.3244	0.6902	44.1208	15.5564	193.9892	71.9217	332.9179	565.1120	112.7883
M1_SM21_35_Zrn47	0.0178	34.9742	0.3780	2.6881	5.3221	0.8113	26.1726	7.3371	85.1361	31.5746	148.4057	283.2857	62.3450
M2_SM21_35_Zrn48	0.1949	30.5918	0.2707	0.2328	0.5033	0.1535	3.6031	1.4203	23.3836	12.0766	81.4774	255.8273	65.1096
M2_SM21_35_Zrn49	0.0059	32.1941	0.3962	2.2592	4.8428	0.5703	30.9974	12.3449	172.1659	69.7744	343.1804	610.6086	120.3723
M2_SM21_35_Zrn50	0.0051	34.2626	0.4499	2.7942	6.0729	0.9173	31.1074	9.9557	117.9434	42.6882	192.8454	342.7629	69.7038
M2_SM21_35_Zrn51	0.0448	42.1674	0.3738	2.6943	6.0336	0.7820	35.5188	12.3486	156.2578	59.0796	290.2531	539.1633	112.7717
M2_SM21_35_Zrn52	0.0163	34.1552	0.3717	2.1382	5.8950	0.5429	34.8134	11.9105	146.1334	53.7475	247.3142	410.1918	80.9791

Continúa

**Continuación
SM21-35**

Zircón	La	Ce	Pr	Nd	Sm	Eu	Gd	Tb	Dy	Ho	Er	Yb	Lu
M2_SM21_35_Zrn53	0.0000	31.7984	0.4248	2.4713	5.5524	0.9264	24.0465	7.2489	80.4939	27.9783	125.7832	218.3438	46.7658
M2_SM21_35_Zrn54	0.0000	45.2012	0.3829	2.2871	8.0983	0.4790	54.2889	22.1017	296.0387	114.0197	542.0017	906.7296	177.6301
M2_SM21_35_Zrn55	0.0000	49.1541	0.4557	3.1762	8.2584	0.6646	51.9619	19.0649	245.4483	91.9332	438.0273	719.8900	139.7597
M2_SM21_35_Zrn56	0.0088	17.5990	0.2893	1.0175	2.6600	0.3307	15.4220	5.5059	75.3367	29.9080	152.9593	318.7451	71.1893
M2_SM21_35_Zrn57	0.0088	51.3517	0.4970	3.1224	10.1364	0.7439	59.7855	21.2575	253.9443	91.2300	410.6964	665.0297	132.4756
M2_SM21_35_Zrn58	0.0104	57.7590	0.4891	3.9274	10.7875	0.7676	65.2462	24.1825	297.1138	107.3127	486.0665	807.7712	160.1479
M2_SM21_35_Zrn59	0.0000	29.3814	0.2549	0.6710	2.4015	0.4445	23.1898	11.9908	194.9554	89.0035	507.5582	1259.3750	272.2816
M2_SM21_35_Zrn60	0.0018	45.7740	0.4294	2.7146	8.1738	0.6346	49.0851	17.6307	216.0620	80.8994	377.5866	618.2487	125.3870
M2_SM21_35_Zrn61	0.0000	25.2147	0.3570	2.1243	3.9692	0.6736	19.9569	6.6852	82.0357	30.0244	148.2423	287.8152	61.5489
M2_SM21_35_Zrn62	0.0046	33.0375	0.2919	1.8828	5.7303	0.5483	35.9840	12.3723	156.1537	58.5714	269.8376	448.6875	88.0161
M2_SM21_35_Zrn63	0.0156	34.5610	0.3185	2.9065	6.2487	1.0932	29.8632	9.1695	105.9322	38.8401	183.1221	339.4034	74.0424
M2_SM21_35_Zrn64	0.0099	41.9684	0.4106	3.3845	8.1889	0.8466	40.2244	13.0369	157.9165	57.6761	264.6497	450.1309	94.0323
M2_SM21_35_Zrn65	0.0091	36.3624	0.4111	2.5321	7.0855	1.0463	28.0011	8.0624	88.3433	32.0139	140.8265	246.4827	52.5169
M2_SM21_35_Zrn66	0.0000	80.3135	0.2869	1.3117	3.3262	0.5692	24.1550	10.0609	138.2029	57.9233	312.2663	629.5315	125.6156
M2_SM21_35_Zrn67	0.0098	28.1170	0.3869	2.0533	4.6257	0.8622	21.4873	7.4456	92.5468	34.1291	165.9325	317.8456	66.3098
M2_SM21_35_Zrn68	0.0024	35.4411	0.3640	2.6579	5.7889	0.9250	32.1797	10.5066	123.0703	44.4560	202.4940	344.6027	72.3456
M2_SM21_35_Zrn69	0.0130	33.4040	0.3620	2.7936	4.7093	0.9273	24.3721	7.0653	83.0771	30.1582	144.8782	282.6182	62.0859
M2_SM21_35_Zrn70	0.0000	32.8880	0.2996	1.4531	4.1533	0.2791	35.4440	16.3329	246.4693	101.1919	500.1194	887.6674	171.4529
M2_SM21_35_Zrn71	0.0134	41.8253	0.3801	3.3436	7.0074	0.8590	36.6149	11.7005	134.6561	47.4729	210.7050	370.9962	76.1051
M2_SM21_35_Zrn72	-0.0001	25.2015	0.3008	1.7047	4.0361	0.7151	18.0768	5.8466	71.8991	25.9833	125.2257	229.4685	49.3094
M2_SM21_35_Zrn73	0.0103	39.2154	0.3941	2.7124	5.8364	1.0374	29.7349	8.0096	88.0931	30.9578	137.1646	248.1920	54.1306
M2_SM21_35_Zrn74	0.0000	38.0178	0.3694	2.5324	4.8216	0.8183	24.5607	7.5449	86.2735	29.8657	142.0714	267.8468	58.0747
M2_SM21_35_Zrn75	0.0113	20.9327	0.2303	0.8446	2.6802	0.2929	17.9417	7.1664	99.9417	38.0992	183.6759	331.2059	62.3375
M2_SM21_35_Zrn76	0.0000	33.2098	0.4134	2.3296	4.4606	0.7792	24.7253	6.5404	78.1737	27.3528	132.0823	247.0114	53.2034
M2_SM21_35_Zrn77	0.0108	42.1691	0.3891	3.4855	6.3813	1.0172	32.5689	9.1518	106.4055	37.4192	168.5374	310.4116	66.1023
M2_SM21_35_Zrn78	0.0000	37.0374	0.2903	2.1931	5.4822	0.5830	33.9340	11.6169	145.7164	54.4815	251.8075	438.2621	87.7420
M2_SM21_35_Zrn79	0.0022	35.6662	0.2762	0.8885	2.2894	0.3287	16.5020	6.5832	91.0501	38.2961	194.9638	379.7193	78.1315
M2_SM21_35_Zrn80	0.0055	38.2440	0.3551	3.3740	5.9441	0.9105	28.3681	7.8669	87.8229	32.3551	143.6781	262.2008	56.4713

*Valores en ppm

SM21-34 El Águila leucosome

Zircón	La	Ce	Pr	Nd	Sm	Eu	Gd	Tb	Dy	Ho	Er	Yb	Lu
M3_SM21_34_Zrn02	0.0326	15.6130	0.4047	2.3580	5.5022	1.3940	21.4948	6.6223	82.8637	29.6578	142.7337	254.9975	54.8022
M3_SM21_34_Zrn03	0.0000	10.1407	0.2004	0.5474	1.2288	0.3473	9.3373	3.3834	44.4381	17.1645	91.0431	181.3116	39.2060
M3_SM21_34_Zrn04	0.0018	12.6961	0.1907	0.3290	1.1466	0.2629	6.1812	2.6849	40.0142	19.1922	113.1252	294.5906	71.0197
M3_SM21_34_Zrn05	0.0191	11.7901	0.2133	0.6257	1.4937	0.3534	7.1433	2.6308	35.8082	14.2785	76.9391	170.6739	39.8665
M3_SM21_34_Zrn06	0.0658	9.0922	0.2058	0.6041	1.2372	0.2830	7.3314	2.9145	45.8528	21.4112	140.0252	441.4759	113.5939
M3_SM21_34_Zrn07	0.0000	12.5862	0.1651	0.3862	1.5410	0.3450	9.7757	3.1345	39.6238	15.4810	84.1646	177.1306	40.3352
M3_SM21_34_Zrn08	0.0000	10.6651	0.1969	0.7711	1.9512	0.4006	8.9199	3.3378	42.0967	16.5319	85.5719	167.2163	35.8345
M3_SM21_34_Zrn09	0.0135	13.9263	0.2204	1.1470	2.2303	0.4117	11.5405	4.1713	53.6609	19.7268	98.3919	185.8643	39.0191
M3_SM21_34_Zrn10	0.0070	15.2065	0.2457	1.6499	2.9699	0.7771	15.8372	5.0971	64.5971	23.3711	113.0038	212.9123	44.2970
M3_SM21_34_Zrn11	0.0219	16.9997	0.2233	0.7497	1.9654	0.6220	12.1322	3.7389	50.9749	19.8892	100.3371	201.6289	44.4760
M3_SM21_34_Zrn12	0.0000	15.7756	0.1951	0.8226	2.1141	0.6750	12.1757	4.4414	60.7035	24.3075	124.2704	265.1043	57.8257
M3_SM21_34_Zrn13	0.0000	13.9210	0.1375	0.2732	1.3140	0.1745	6.6857	2.5644	38.4169	17.8160	102.6613	268.3284	69.7544
M3_SM21_34_Zrn14	0.0884	9.3457	0.1845	0.7320	1.1381	0.3952	6.5116	3.2655	61.4501	33.0574	223.8303	716.9151	169.9076
M3_SM21_34_Zrn16	0.0132	39.0962	0.2236	1.1392	3.9910	0.2940	30.1216	11.0243	151.0003	62.5314	306.5241	574.8358	117.0872
M3_SM21_34_Zrn17	0.0000	13.9299	0.2210	1.2500	2.3037	0.3710	10.0137	3.5921	44.3419	18.6448	91.4475	211.6059	47.3920
M3_SM21_34_Zrn18	0.0112	9.4515	0.1838	0.5639	0.8348	0.2243	6.4679	2.7313	49.7472	26.5228	193.6965	657.1023	157.1492
M3_SM21_34_Zrn19	0.0000	13.1438	0.1577	0.7849	1.3335	0.2308	8.0044	3.4597	54.7709	26.8493	182.1853	586.4482	141.8003
M3_SM21_34_Zrn20	0.0640	14.3781	0.2369	0.6492	1.7222	0.3412	10.0134	3.7708	49.1257	21.7999	117.6564	253.9745	58.7038
M3_SM21_34_Zrn21	0.0025	16.2551	0.1693	0.4209	1.4354	0.2567	9.5682	4.4290	67.3709	31.2737	182.5687	454.6812	104.6264
M3_SM21_34_Zrn22	0.0000	12.5348	0.2110	0.5913	1.3434	0.2864	9.2496	2.7636	39.9256	16.8573	98.0340	235.4414	55.0940
M3_SM21_34_Zrn23	0.0062	14.8863	0.1546	0.8541	2.0936	0.3780	11.3747	3.8725	54.3743	22.2055	117.3840	282.1890	70.6567
M3_SM21_34_Zrn24	0.0025	40.0063	0.1815	1.1293	3.5074	0.1645	21.4576	7.9037	100.0865	37.1828	167.7095	265.8485	52.5408
M3_SM21_34_Zrn25	0.0000	14.2310	0.1990	0.9214	1.7899	0.6228	10.3961	3.7812	48.2324	18.5120	91.5520	181.3751	40.1549
M3_SM21_34_Zrn26	0.0097	10.6566	0.1848	0.7682	1.6260	0.3459	8.8152	2.7431	38.6139	15.4729	92.9718	305.2876	84.9340
M3_SM21_34_Zrn27	0.0038	16.7400	0.1848	1.1395	2.4463	0.4696	14.7222	5.0256	62.7947	24.5100	125.4211	261.9202	56.2703
M3_SM21_34_Zrn28	0.0030	22.6447	0.1522	0.8891	2.4944	0.3713	14.1719	4.6841	57.7014	22.7282	109.0847	209.7848	44.4154
M3_SM21_34_Zrn29	0.0141	17.4949	0.2392	2.1869	4.6833	1.1554	24.6543	7.3171	84.5411	30.5517	138.6592	247.3131	50.5867
M3_SM21_34_Zrn30	0.0000	9.9372	0.1563	0.4064	1.0936	0.2211	7.9372	3.8096	62.9114	30.1771	190.5303	511.8750	114.3690
M3_SM21_34_Zrn31	0.0000	17.7374	0.2176	0.7652	2.5114	0.5908	11.9125	4.4873	57.6893	21.9828	114.4340	241.3150	54.6003
M3_SM21_34_Zrn32	0.0072	30.4246	0.1842	1.1282	2.5139	0.3795	21.5005	7.1974	96.9444	39.1980	195.9756	369.1231	76.4393
M3_SM21_34_Zrn33	0.0038	17.0627	0.1766	0.7456	1.7897	0.2885	11.2788	4.0759	61.2406	27.6796	163.4779	465.9722	110.7838
M3_SM21_34_Zrn34	0.0373	8.4784	0.1623	0.5869	1.0631	0.2043	7.8378	3.9116	69.4341	34.3938	208.5055	501.8772	107.9549
M3_SM21_34_Zrn35	-0.0002	30.6886	0.1727	0.6640	2.9196	0.3223	23.3932	10.1901	149.4879	64.9685	348.0346	740.4506	164.2580
M3_SM21_34_Zrn36	0.0081	15.2110	0.1706	1.0198	2.4666	0.4245	14.0187	4.6710	59.2808	23.1003	112.9951	218.3214	46.2267
M4_SM21_34_Zrn37	0.0000	13.4076	0.1620	0.6601	1.6592	0.4240	10.2670	3.8613	52.1639	21.3267	115.0503	237.9488	56.3134
M4_SM21_34_Zrn38	0.0125	28.1654	0.2125	0.9469	3.0766	0.2205	19.6601	7.5775	97.4278	37.0249	176.2316	306.5979	64.0413
M4_SM21_34_Zrn39	0.0000	29.8251	0.2213	1.2996	2.6520	0.3099	15.8970	5.7328	71.4885	27.3731	131.7574	231.6256	49.9587
M4_SM21_34_Zrn40	0.0049	17.7210	0.1259	0.6366	1.4335	0.2980	11.4075	4.1169	56.4394	24.0839	128.8272	283.7327	62.1694
M4_SM21_34_Zrn41	0.0054	13.7659	0.1695	0.3966	1.7473	0.4549	11.1384	4.7899	77.5272	34.9918	192.0055	437.7997	101.8329
M4_SM21_34_Zrn42	0.0000	12.9368	0.1858	0.5698	1.3725	0.3649	8.2586	3.0013	38.7310	15.1790	79.3399	184.3656	43.9497
M4_SM21_34_Zrn43	0.0023	10.0237	0.1372	0.5035	0.8644	0.2676	5.3531	2.1700	31.8899	14.6233	85.0574	235.6926	62.4905
M4_SM21_34_Zrn44	0.0000	15.3652	0.1875	1.3534	2.2515	0.6173	13.6452	4.5383	60.2654	24.4025	128.5414	238.0061	52.2781
M4_SM21_34_Zrn45	0.0018	17.1208	0.1552	0.6738	1.6598	0.3325	11.2028	4.1722	64.2662	30.8133	189.7258	447.5619	89.0858
M4_SM21_34_Zrn46	0.0000	29.0201	0.1525	0.7607	2.0965	0.3801	17.3670	7.3129	103.1602	44.3380	232.7586	492.3612	103.0797
M4_SM21_34_Zrn47	0.0000	30.0268	0.1892	1.3857	2.8001	0.4465	15.3281	5.3705	65.3174	26.5059	129.0687	247.0171	53.6514
M4_SM21_34_Zrn48	0.0113	12.4202	0.1865	0.8337	2.3620	0.4476	11.9463	4.6134	57.3922	23.1805	118.8247	232.6624	49.7590
M4_SM21_34_Zrn49	0.0020	17.9590	0.1578	0.8244	2.1382	0.4155	13.8213	5.3308	69.3918	29.0646	151.7670	323.2097	68.5832
M4_SM21_34_Zrn50	0.0288	10.2522	0.1303	0.5405	1.4545	0.3568	8.5546	3.7813	65.1744	33.3882	214.3521	531.0203	106.0271

*Valores en ppm

